REACTION ENGINEERING *for* POLLUTION PREVENTION

ELSEVIER

EDITED BY MARTIN A. ABRAHAM AND ROBERT P. HESKETH

Reaction Engineering for Pollution Prevention

by Martin A. Abraham, Robert P. Hesketh, Robert P. Hesketh (Editor)

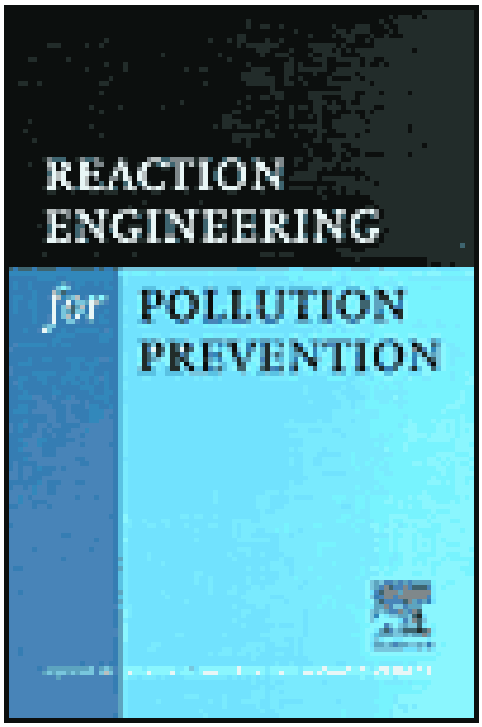

- ISBN: 0444502157
- Pub. Date: February 2000
- Publisher: Elsevier Science & Technology Books

Preface

In 1997, the Catalysis and Reaction Engineering division of the American Institute of Chemical Engineers was initiated to afford researchers in the reaction engineering community a greater opportunity to participate in the national discussion. It was decided that one of the initial programming events of the new division would be a Topical Conference on Environmental Reaction Engineering and Catalysis. Shortly thereafter, the division teamed up with the North American Catalysis Society to organize the Second World Congress on Environmental Catalysis, and the Topical Conference on Environmental Reaction Engineering became a separate entity. This Topical Conference took place at the AIChE 1998 Annual meeting in Miami Beach, Florida. We would like to acknowledge the members of the topical conference organizing committee, who helped to develop the technical sessions on which this book is based: John C. Friedly, MIT Practice School, Jan J. Lerou, Dupont USA, Yuri Matros, Matros Technologies, Jonathan Phillips, The Pennsylvania State University, Peter Smirniotis, University of Cincinnati, and Theodore Tsotsis, University of Southern California.

Coordinated by Michael Harold, 1st Vice-Chair of the division and Martin Abraham, Topical Conference Programming Chair, six separate sessions were organized, with over 50 technical presentations. Authors of these presentations were then invited to prepare their work as a full-length manuscript for publication. Each manuscript was carefully reviewed by experts in the field and revised based on the reviewer's comments before inclusion in this volume.

In the context of this book, we define environmental reaction engineering as the use of reaction engineering principles, including reactor design, for the development of processes that provide an environmental benefit. With regard to pollution prevention, we focus primarily on new reaction and reactor technologies that minimize the production of undesirable side-products (pollutants), but also consider the use of reaction engineering as a means of treating wastes that are produced through other means. Thus, we cover topics ranging from reactive distillation (for a cleaner production of MTBE) to photocatalytic oxidation (for treatment of air pollutants). Environmental reaction engineering is distinct from environmental catalysis - here we are focused on the reaction or the reactor whereas environmental catalysis focuses more closely on the development of the catalyst and the underlying surface science.

The papers contained within this book have been classified into topics that are related to those of the individual sessions from the AIChE meeting. We begin with a section on environmentally benign combustion. The three papers discuss methods of reducing the formation of PAHs and NO_x, as well as other environmentally sensitive combustion products. Next is a contribution from Heavy Industries Co. in Japan describing their efforts to capture the combustion exhaust gases for recycle into the combustion process. This paper serves as a bridge to a series of three papers on CO_2 sequestration, including contributions from two U.S. national laboratories. Our inclusion of CO_2 sequestration represents our recognition of the importance of the growing

concentration of carbon dioxide in the atmosphere, and the role the chemical reaction engineering has on contributing to these increased levels.

The next section contains a collection of contributions that involve the use of a catalyst to support the reaction. We begin with a paper describing catalytic reforming of methane using CO_2, a process with implications to the carbon dioxide sequestration issue of the previous section. Two papers on unsteady catalysis follow, one involving the selective catalytic reduction of NO_X the other involving oxidation of VOCs. Continuing the theme of VOC oxidation, we then present two papers on photocatalytic oxidation of VOCs, followed by two papers on photocatalysis for the treatment of organic compounds in wastewater.

Next is a section on the use of supercritical fluid solvents as environmentally friendly media for chemical reactions. Three papers involve reaction in supercritical CO_2, all discussing the potential for selective chemistry within this benign medium. A final paper in this section considers the use of supercritical water as a medium for the conversion of cellulose to useful chemicals. This process is beneficial not only for its use as a benign reaction solvent but also because of the possibility of converting renewable resources into valuable chemical feedstocks.

Finally, a series of papers is presented in which novel reactor designs are utilized to obtain product yields not possible in conventional reactor systems. These include the use of reactor-absorber system, reactive distillation, and reactive membranes.

The book concludes with a chapter that was contributed by the editors and discusses the educational aspects of pollution prevention. We have included this chapter because we believe that it is necessary for future generations of engineers to be trained to design processes that are inherently environmentally benign. This can only be achieved by assembling resource materials for educators. The chapter describes some of the materials that are available and provides direction onto where the interested reader should go for further information. It is our hope that this last chapter will spark the creative instincts of the researchers using the materials contained within this book to develop new resources for pollution prevention education.

It is our hope that this book provides a reasonable cross-section of the field of environmental reaction engineering at this point in time. Certainly, the broad spectrum of topics included indicates the diversity of this area, and the vibrant nature of the ongoing research. As the field continues to grow, we expect to see continued interest in pollution prevention and benign processing, and expect reaction engineers to be at the forefront of developments in this area. One can only do so much to treat a waste in an effluent stream. However, the possibilities of producing desirable products without the formation of waste byproducts is bounded only by the creativity of the reaction engineer.

In closing, we would like to take this opportunity to thank all of the individuals who have contributed to this effort. Specifically, we thank all of the individuals who contributed papers to this book, and all of those who took time from their busy schedules to review these papers and provide comments for the authors. We thank the Catalysis and Reaction Engineering division of the AIChE, and the AIChE itself, for providing us with

the permission to produce this book based on the Topical Conference. We also recognize the efforts of the individual session organizers, who made the Topical Conference a valuable compilation of research in this area. Finally, we recognize Elsevier Science for providing us the opportunity to organize this book.

Martin Abraham
Professor, Chemical and Environmental Engineering
The University of Toledo

Robert Hesketh
Associate Professor, Chemical Engineering
Rowan University

LIST OF CONTRIBUTORS

Martin A. Abraham
Dept. of Chemical & Environmental Engineering
The University of Toledo
2801 W. Bancroft St.
Toledo, OH 43606
USA

Tadafumi Adschiri
Dept. of Chemical Engineering
Tohoku University
Aoba-ku, Sendai 980-8579
JAPAN

K. Arai
Dept. of Chemical Engineering
Tohoku University
Aoba-ku, Sendai 980-8579
JAPAN

N. Arai
Research Center for Advanced Energy Conversion
Nagoya University
Nagoya
JAPAN

G. Balasubramanian
Dept. of Civil and Environmental Engineering
741 Baldwin Hall
University of Cincinnati
P.O. Box 210071
Cincinnati, OH 45221-0071
USA

I. Baudin
Lyonnaise Des Eaux
CIRSEE
Le Pecq
France

Eric J. Beckman
University of Pittsburgh
1249 Benedum Hall
Chemical Engineering Dept.
Pittsburgh, PA 15261
USA

Arun C. Bose
US Department of Energy
Federal Energy Technology Center
Pittsburgh, PA 15236-0940
USA

G. A. Bunimovich
Matros Technologies, Inc.
14963 Green Circle Dr.
Chesterfield, MO 63017
USA

Darryl P. Butt
Los Alamos National Laboratory
Mail Stop H846
Los Alamos, NM 87545
USA

G. B. Combes
University of New South Wales
School of Chemical Engineering
Sydney, NSW 2052
AUSTRALIA

S. N. Danov
Research Center for Advanced Energy Conversion
Nagoya University
Nagoya
JAPAN

Hugo de Lasa
University of Western Ontario
Faculty of Engineering Science
Chemical Reactor Engineering Center
London, Ontario
CANADA N6A 5B9

F. Dehghani
University of New South Wales
School of Chemical Engineering
Sydney, NSW 2052
AUSTRALIA

A. K. Dillow
University of Minnesota
Dept. of Chemical Engineering and
Materials Science
Minneapolis, MN 55455
USA

Dionysios D. Dionysiou
Dept. of Civil and Environmental
Engineering
741 Baldwin Hall
University of Cincinnati
P.O. Box 210071
Cincinnati, OH 45221-0071
USA

Can Erkey
Department of Chemical Engineering
University of Connecticut
Storrs, CT 06269-3222
USA

Z. Fang
Dept. of Chemical Engineering
Tohoku University
Aoba-ku, Sendai 980-8579
JAPAN

Pio Forzatti
Politecnico di Milano
Piazza Leonardo da Vinci 32
20133 Milano
ITALY

Neil R. Foster
University of New South Wales
School of Chemical Engineering
Sydney, NSW 2052
AUSTRALIA

Y. Fukushima
Dept. of Chemical Engineering
Tohoku University
Aoba-ku, Sendai 980-8579
JAPAN

T. Furuhata
Research Center for Advanced Energy
Conversion
Nagoya University
Nagoya
JAPAN

Shigeo Goto
Nagoya University
Dept. of Chemical Engineering
Furo-cho, Chikusa-ku
Nagoya, Aichi-ken 464-8603
JAPAN

D. Hâncu
University of Pittsburgh
1249 Benedum Hall
Chemical Engineering Dept.
Pittsburgh, PA 15261
USA

Robert P. Hesketh
Dept. of Chemical Engineering
Rowan University
201 Mullica Hill Rd.
Glassboro, NJ 08028-1701
USA

H. Ibrahim
University of Western Ontario
Faculty of Engineering Science
Chemical Reactor Engineering Center
London, Ontario
CANADA N6A 5B9

H. Itoh
Nagoya University
Dept. of Chemical Engineering
Furo-cho, Chikusa-ku
Nagoya, Aichi-ken 464-8603
JAPAN

Jiří Jirát
Prague Institute of Chemical Technology
Dept. of Chemical Engineering
Techniká 5
166 28 Prague 6
CZECH REPUBLIC

T. Kiga
Ishikawajima-Harima Heavy Industries Co.
2-16 Toyosu 3-Chome, Koto-ku
Tokyo 135-8733
JAPAN

Milan Kubíček
Prague Institute of Chemical Technology
Dept. of Mathematics
Technická 5
166 28 Prague 6
CZECH REPUBLIC

Klaus S. Lackner
Los Alamos National Laboratory
Mail Stop H846
Los Alamos, NM 87545
USA

J. M. Laîné
Lyonnaise Des Eaux
CIRSEE
Le Pecq
France

Luca Lietti
Politecnico di Milano
Piazza Leonardo da Vinci 32
20133 Milano
ITALY

G. Q. (Max) Lu
Department of Chemical Engineering
The University of Queensland
St. Lucia, QLD 4072
AUSTRALIA

F. P. Lucien
University of New South Wales
School of Chemical Engineering
Sydney, NSW 2052
AUSTRALIA

Miloš Marek
Prague Institute of Chemical Technology
Dept. of Chemical Engineering
Techniká 5
166 28 Prague 6
CZECH REPUBLIC

Yu. Sh. Matros
Matros Technologies, Inc.
14963 Green Circle Dr.
Chesterfield, MO 63017
USA

Ivan Milosavljevic
Air Liquide
1, chemin de la Porte des Loges
Les Loges en Josas
78353 Jouy en Josas Cedex
FRANCE

S. Miyamae
Ishikawajima-Harima Heavy Industries Co.
2-16 Toyosu 3-Chome, Koto-ku
Tokyo 135-8733
JAPAN

Harvey M. Ness
US Department of Energy
Federal Energy Technology Center
Pittsburgh, PA 15236-0940
USA

Isabella Nova
Politecnico di Milano
Piazza Leonardo da Vinci 32
20133 Milano
ITALY

M. Okawa
New Energy and Technology Dev. Dept.
Electric Power Development Co., Ltd.
6-15-1, Ginza, Chuo-ku
Tokyo 104-8165
JAPAN

Nesrin Olten
University of California, Los Angeles
5531 Boelter Hall
Los Angeles, CA 90095
USA

D. R. Palo
Department of Chemical Engineering
University of Connecticut
Storrs, CT 06269-3222
USA

Sean I. Plasynski
US Department of Energy
Federal Energy Technology Center
Pittsburgh, PA 15236-0940
USA

Pluton Pullumbi
Air Liquide
1, chemin de la Porte des Loges
Les Loges en Josas
78353 Jouy en Josas Cedex
FRANCE

A. T. Quitain
Nagoya University
Dept. of Chemical Engineering
Furo-cho, Chikusa-ku
Nagoya, Aichi-ken 464-8603
JAPAN

Ajay K. Ray
National University of Singapore
Dept. of Chemical and Environmental
Engineering
10 Kent Ridge Crescent
Singapore, 119260

C. R. Roach
Monsanto Enviro-Chem Systems, Inc.
P.O. Box 14547
St. Louis, MO 63178
USA

M. Sasaki
Dept. of Chemical Engineering
Tohoku University
Aoba-ku, Sendai 980-8579
JAPAN

Daniel J. Seery
United Technologies Research Center
East Harford, CT 06108
USA

Selim M. Senkan
University of California, Los Angeles
5531 Boelter Hall
Los Angeles, CA 90095
USA

František Štěpánek
Prague Institute of Chemical Technology
Dept. of Chemical Engineering
Techniká 5
166 28 Prague 6
CZECH REPUBLIC

Vadim O. Strots
Matros Technologies, Inc.
14963 Green Circle Dr.
Chesterfield, MO 63017
USA

M. T. Suidan
Dept. of Civil and Environmental
Engineering
741 Baldwin Hall
University of Cincinnati
P.O. Box 210071
Cincinnati, OH 45221-0071
USA

K. Suzuki
Ishikawajima-Harima Heavy Industries Co.
1 Shinnakahara, Isogo-ku, Yokohama
Kanagawa 235-8501
JAPAN

H. Teng
National Institute of Materials and Chemical
Research
1-1 Higashi, Tsukuba 305
JAPAN

Enrico Tronconi
Politecnico di Milano
Piazza Leonardo da Vinci 32
20133 Milano
ITALY

Savvas Vasileiadis
ZiVaTech
15549 Dearborn St.
North Hills, CA 91343
USA

M. Wakatsuki
University of Tokyo
7-3-1 Hongo, Bunkyo-ku
Tokyo, 113-8656
JAPAN

Shaobin Wang
Department of Chemical Engineering
The University of Queensland
St. Lucia, QLD 4072
AUSTRALIA

Christopher H. Wendt
Los Alamos National Laboratory
Mail Stop H846
Los Alamos, NM 87545
USA

K. Yamada
University of Tokyo
7-3-1 Hongo, Bunkyo-ku
Tokyo, 113-8656
JAPAN

Toshihiko Yamada
Ishikawajima-Harima Heavy Industries Co.
2-16 Toyosu 3-Chome, Koto-ku
Tokyo 135-8733
JAPAN

Akihiro Yamasaki
University of Tokyo
7-3-1 Hongo, Bunkyo-ku
Tokyo, 113-8656
JAPAN

Hiroshi Yamashita
Dept. of Mechanical Engineering
Nagoya University
Furo-cho, Chikusa-ku
Nagoya, Aichi 464-8603
JAPAN

Y. Yanagisawa
University of Tokyo
7-3-1 Hongo, Bunkyo-ku
Tokyo, 113-8656
JAPAN

D. Zhao
New Energy and Industrial Technology
Development Organization
Nagoya
JAPAN

Zoe Ziaka
ZiVaTech
15549 Dearborn St.
North Hills, CA 91343
USA

Hans-J. Ziock
Los Alamos National Laboratory
Mail Stop H846
Los Alamos, NM 87545
USA

Table of Contents

Section 2: Catalytic Reactions

Section 3: Supercritical Fluids

Section 4: Reactor Design and Miscellaneous Contributions

Reaction Engineering for Pollution Prevention
M.A. Abraham and R.P. Hesketh (Editors)

POLYCYCLIC AROMATIC HYDROCARBON FORMATION IN COUNTER-FLOW PROPYLENE DIFFUSION FLAME

Nesrin Olten and Selim M. Senkan*

Chemical Engineering Department, 5531 Boelter Hall, UCLA, Los Angeles, CA 90095

The detailed structure of an opposed flow propylene diffusion flame has been determined at a strain rate of 37.7 s^{-1}, with particular attention given to aromatics and polycyclic aromatic hydrocarbons (PAH). Flame sampling was achieved by using quartz microprobe coupled to an on-line Gas Chromatograph/ Mass spectrometer (GC/MS). Packed columns connected to a thermal conductivity detector (TCD) were used for separation and quantification of major species, and a capillary column directly interfaced to a mass spectrometer was used for minor and trace species. Temperature measurements were done by using a 0.075 mm diameter Pt/Pt+13%Rh thermocouple (R type, Omega) that was coated with silica to reduce catalytic reactions on the bare wire surface. A total of 84 species concentration profiles were determined.

Introduction

Pollution control and environmental regulations enacted since the early 1970's target the protection of public health and the environment [1]. In these laws, a substance is considered as a pollutant if it has been perceived to have an adverse effect on human health and the environment. In recent years, increasing numbers of substances appear to pose such threats; the earlier Clean Air Act listed seven hazardous substances between 1970 and 1989, and now approximately 300 compounds are listed as hazardous.

Combustion processes significantly contribute to air pollution as a consequence of production and emission of nitrogen oxides (NO_x), sulfur oxides (SO_x if sulfur is present in the fuel), unburned hydrocarbons, such as benzene, naphthalene, soot and polycyclic aromatic hydrocarbons (PAH). PAH's are of particular concern, because some isomers are potent carcinogens. Gaseous pollutants produced and emitted from combustion processes may be reduced either by removing them from effluent streams or by changing the process conditions, i.e. pollution prevention. In order to accomplish the latter, a good understanding of the underlying physical and chemical processes that are responsible for the formation and destruction of the toxic products is necessary. Creating laboratory scale combustion and studying the structures of flames is a way to better understand the flame chemistry. One-dimensional premixed and diffusion flames are generally used for this purpose. Counter-flow diffusion flames are particularly attractive systems to study the detailed structure of flames, because they provide spatially wider reaction zones than premixed flames.

There are a large number of studies on diffusion flames starting with Burke and Schumann in 1928 [2] and others [3,4,5]. To understand the transport processes and chemical kinetics in strained, laminar, counter-flow diffusion flames, a number of theoretical [6-10] and experimental [9,11-13] studies have also been performed over the years. The main motivation for these studies was to attempt to model turbulent non-premixed combustion as a collection of strained laminar flamelets and also to model pollutant formation. With advanced computer and laboratory instrumentation, the flame studies in recent years have become even more sophisticated. Yet our understanding of the issues related to the formation of trace combustion byproducts, such as aromatics and PAH's are still at an early stages of development, inadequate to formulate predictive models.

Recently, we started an experimental program investigating the formation mechanisms of PAH in counter-flow diffusion flames. We started with the smallest hydrocarbon fuel, methane [14] followed by ethane flame [15]. These studies provided the first information on the detailed structures of the saturated hydrocarbon fuels in laminar, counter-flow diffusion flames at low strain rates. We further expanded these studies to explore the impact of unsaturated hydrocarbons as fuels on the formation of PAH [16, 17]. In these reports, we studied ethylene flames at different strain rates and reported their detailed flame structures. In the present study, we discussed the detailed structure of a propylene flame at the same strain rate as the ethylene flame studied previously [16]. Propylene is an intermediate species in the combustion of propane fuel [18]. Previously, Westbrook and Pitz [19] proposed a pyrolysis and oxidation mechanism of propane and propylene, and Burcat and Radhakrishnan [18] studied the propylene oxidation in a shock tube. However, these earlier studies did not address issues related to the formation of aromatics and PAH.

Results and Discussion

The operating conditions of the propylene flame studied are shown in Table-1. It is well known that PAH are formed in fuel rich premixed flames and on the fuel side of the diffusion flames. This is why the fuel composition in the fuel stream was kept at higher ratios compared to the oxygen composition in the oxidizer stream. These flow conditions were chosen so that the strain rate was the same as the ethylene flame studied before [16]; however the fuel side composition was kept at 50% instead of 75% used in the ethylene flame since larger propylene levels resulted in excessive sooting which lead to the early termination of sampling due to the plugging of the sampling probe. The composition used in the present work also yields the same carbon density as in the ethylene flame. The burner separation distance also had to be increased to 1.6 cm to keep the strain rate the same as the ethylene flame since propylene is a denser fuel than ethylene. Both fuel and oxidizer sides were diluted with Argon.

The temperature measurements were done by using Pt/Pt+%13Rh thermocouple with 0.075 mm wire diameter. It was coated with silica in order to prevent catalytic reactions on the surfaces, and to minimize the hydrogen embrittlement of the thermocouple. Further details on experimental procedure can be found in reference [16].

The strain rate of the flame was calculated as $37.7s^{-1}$ using the following equation [13]:

$K = (-2V_o/L)\{1+(V_f/V_o)(\rho_f/\rho_o)^{0.5}\}$, $[s^{-1}]$

where K is the strain rate and V_o,V_f, ρ_f, ρ_o and L are the oxidizer outlet velocity, fuel outlet velocity, fuel density, oxidizer density and burner separation distance, respectively.

Measurements of the stable species and temperature profiles were made along the streamline on the axis of symmetry. Composition profiles were measured by gas sampling from within the flame using a quartz micro-probe and analyzed by on-line GC/MS system. The quartz sampling micro-probe orifice diameter was kept about 150 micron to withdraw samples in the sooting region of the flame. The location of the tip of the sampling probe with reference to the edge of the fuel burner surface was determined by the use of a cathetometer, having a reading accuracy of ± 0.01mm. The sampling probe used resulted in a 2 mm shift of the composition profiles towards the fuel side. The magnitude of the shift was determined from temperature measurements, since the flame disturbances introduced by the thermocouple was small compared to the probe. The profiles must be interpreted after taking this shift into consideration.

The flame was visually stable and flat under the conditions studied. It exhibited the characteristics of a sooting flame with a bright yellow and orange luminous zones and a thin blue zone in the oxidizer side. CO_2 and H_2O were the major combustion products with peak mole fractions of 0.09 and 0.26, respectively. The peak mole fraction of CO and H_2 was measured as 0.08 and 0.035, where the levels of pyrolysis products were maximized. As seen in Figure 1, the maximum flame temperature was measured to be about 1450°C, which corresponded to the location where stoichiometric combustion took place (after taking into account the shift in concentration profiles) . Corrections for radiation were not included in the temperature profiles, since different procedures give somewhat different corrected temperatures. Thus the data are reported here should allow the reader to make their own corrections. Previously it has been shown that for similar flames, the trends in concentration and temperature profiles remain the same [20].

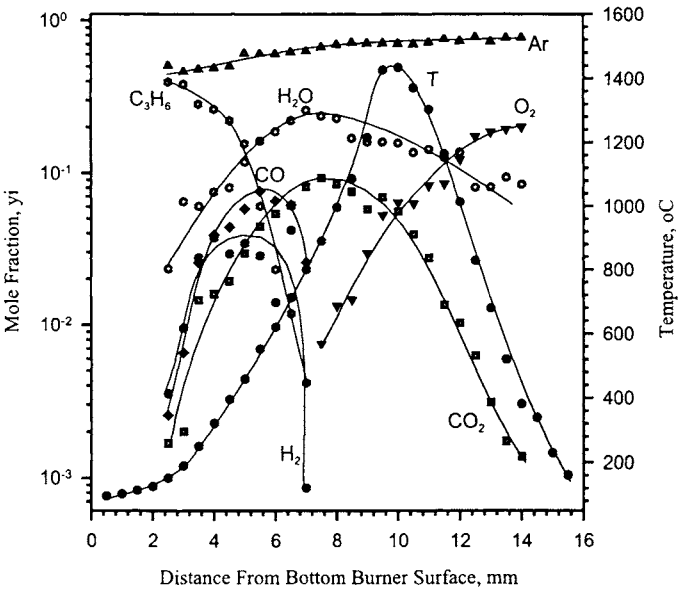

Fig. 1: Major species mole fraction and temperature profiles

As shown in Figure 2, the levels of the pyrolysis products reached their maxima in the fuel side of

the flame. CH_4 was the most abundant pyrolysis product detected. It reached a peak mole fraction of about 0.02, exceeding the level of C_2H_2, which was the most abundant hydrocarbon intermediate in the ethylene flames. Benzene was the most abundant aromatic byproduct, reaching levels of 2300 ppm, while cyclopentadiene was the smallest ring compound detected at 300 ppm. In Figure 3, the mole fraction profiles of polycyclic aromatic hydrocarbons are shown. The formation and growth of PAH's and soot particles has been proposed to occur via Hydrogen-Abstraction-Carbon-Addition (HACA) reactions in which acetylene plays a vital role [21, 22]. In addition, propargyl (C_3H_3) and allene (C_3H_4) species have also been suggested to play important roles during the initial ring formation process [23-25]. Similarly, cyclopentadiene has been suggested to be a possible precursor for naphthalene formation [26]. As seen in Figure 2, a large number of substituted benzenes were also produced. This result, however is not surprising, having such high levels of benzene and propylene as pyrolysis products. The peak mole fractions were 493 ppm for phenylacetylene, 253 ppm for toluene, and 156 ppm for styrene.

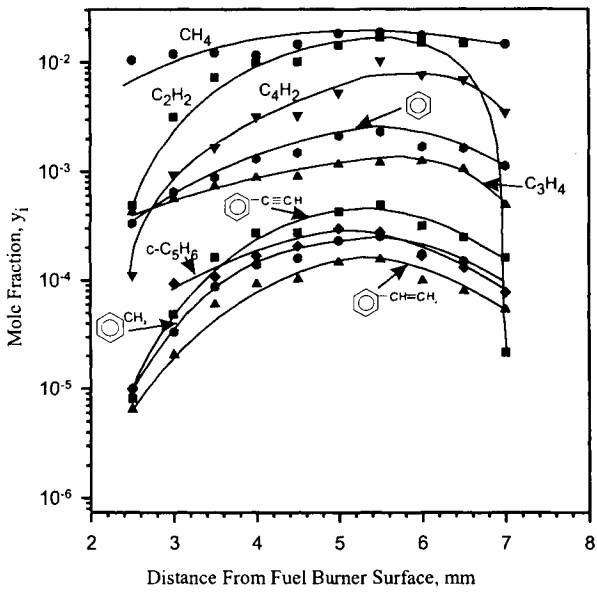

Fig. 2: Pyrolysis products, benzene and substituted benzene profiles

Naphthalene (536 ppm peak mole fraction) and pyrene (66 ppm) were the most abundant polycyclic aromatics found in the flame, a result consistent with flames studied previously [14-17]. Acenaphtylene was formed at 324 ppm maximum level. Acetylene addition to naphthalene is one possible route to acenaphtylene formation [21]. As evident from Figure 3, all PAH reached their maxima at the same flame location, which was about 2.5 mm below maximum flame temperature location, again after taking the shifts in consideration in concentration profiles. There was also a shift in peak location of PAH's with increasing size towards the fuel side, that was also observed in ethylene flames. The largest PAH detected was benzo(a)pyrene (mass 252) along with its two isomers perylene and benzo(k)fluoranthene at peak mole fractions of 4 ppm, 4 ppm and 2 ppm, respectively. The maxima and the sharper decrease of the PAH's in the oxidizer side of the flame are consistent with the abundance of oxygen and higher flame temperatures [27].

Conclusion

Detailed measurements provided here represent the first comprehensive flame chemistry data for propylene diffusion flames, and should be useful for the development and validation of detailed chemical kinetic mechanisms (DCKM) of combustion of hydrocarbons with regard to the formation of toxic byproducts.

Acknowledgements

This research was supported, in part, by The National Science Foundation, U.S. Environmental Protection Agency, the UCLA Center for Clean Technology.

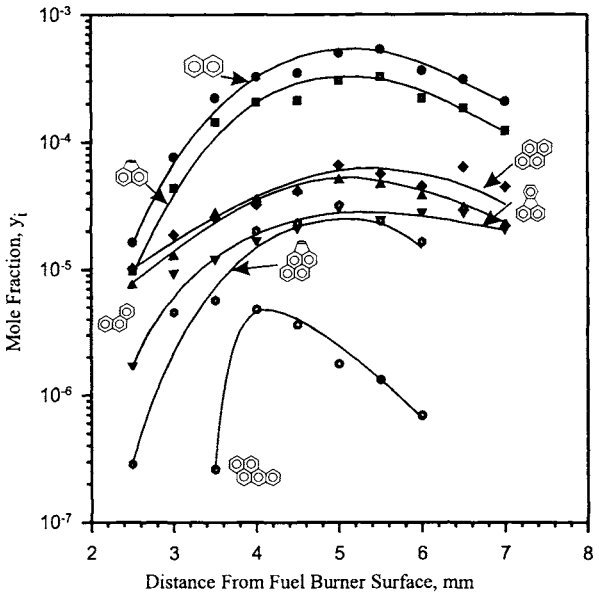

Fig.3 : Polycyclic aromatic hydrocarbon profiles

References

1. Peirce, J., Weiner, R.F., Vesilind P.A., "*Environmental Pollution and Control*" Butterworth-Heinemann, 4th ed., 1998.
2. Burke, S. P. and Schumann, T. E. W., *Ind. Eng. Chem.*, 20: 998-1004 (1928).
3. Wohl, K., Gazley, C. and Kapp, N., *Third Symposium on Combustion*, Baltimore: Williams and Wilkins, 1949, p. 288.
4. Hottel, H. C. Hawtorn, W. R., *Third Symposium on Combustion*, Baltimore: Williams and Wilkins, 1949, p. 254.
5. Fay, J.A., *J. Aero. Sci.*, 21: 681 (1954).
6. Dixon-Lewis, G., David, T., Gaskell, P.H., Fukutani, S., Jinno, H., Miller, J.A., Kee, R. J., Smooke, M. D., Peters, N., Effelsberg, E., Warnatz, J., and Behrendt, F., *Twentieth Symposium (International) on Combustion*, The Combustion Institute, 1984, p. 1893.
7. Miller, J. A., Kee, R. J., Smooke, M. D., and Grcar, J. F., paper # WSS/CI 84-20 presented at the *1984 Spring Meeting of the Western States section of the Combustion Institute*, University of Colorado, Boulder, CO, April 2-3, (1984)
8. Liew, S. K., Bray, K. N. C., and Moss, T. B., *Combust. Flame* 56: 199 (1984).
9. Hahn, W. A., and Wendt, J. O. L., *Eighteenth Symposium (International) on Combustion*, The Combustion Institute, 1981, p. 121.

10. Ishizuka, S., and Tsuji, H., *Comb. Sci. and Tech.* 37: 171 (1984).

11. Tsuji, H., and Yamaoka, J., *Thirteenth Symposium (International) on Combustion*

12. Tsuji, H., *Prog. Energy Combust. Sci.* 8: 93 (1983).

13. Seshadri, K. and Puri, I., *Combust. Flame* 65:137-150 (1986).

14. Vincitore, A.M. and Senkan, S.M., *Comb. Sci. and Tech.* 130: 233-246 (1997).

15. Vincitore, A.M. and Senkan, S.M., *Combust. Flame* 114: 259-266 (1997).

16. Olten, N. and Senkan, S. M., *Combust. Flame,* in press (1999).

17. Olten, N. and Senkan, S. M, *Mediterrenean Combustion Symposium*, submitted (1999).

18. Burcat, A., and Radhakrishnan, K., *Combust. Flame* 60, 157-169 (1985).

19. Westbrook, C. K., and Pitz, W. J., *Comb. Sci. Tech.* 37: 117-152 (1983).

20. Farrow, R. L., Mattern, P. L., and Rahn L.A., *Applied Optics* 21: 3119 (1982)

21. Frenklach, M., and Wang, H., *Twenty-Third Symposium (International) on Combustion*, The Combustion Institute, Pittsburgh, 1990, pp. 1559-1566.

22.Frenklach, M., and Wang, H., in *Soot Formation in Combustion* (H. Bockhorn,Ed.), Springer-Verlag, Berlin, 1994, pp. 165-192.

23. Pfefferle, L. D., Bermudez, G., and Boylr, J., in *Soot Formation in Combustion* (H. Bockhorn,Ed.), Springer-Verlag, Berlin, 1994, pp. 25-49.

24. Stein, S. E., Walker, J. A., Suryan M. M., and Fahr, A., *Twenty-Third Symposium (International) on Combustion*, The Combustion Institute, Pittsburgh, 1990, pp. 85-90.

25. Senkan, S. M., and Castaldi, M., *Combust. Flame*, 107: 141-150 (1996).

26. C. F. Melius, Colvin, E. M., Marinov, N. M., Pitz, W. J., Senkan, S.M., *Twenty-Sixth Symposium on Combustion,* The Combustion Institute, Pittsburgh, PA, 1996, pp 685-692.

27. Homann, K. H., *Twentieth Symposium on Combustion,* The Combustion Institute, Pittsburgh, PA, 1984, pp. 857-870.

Reaction Engineering for Pollution Prevention
M.A. Abraham and R.P. Hesketh (Editors)

REDUCTION OF DIOXINS AND FURANS IN INCINERATION

Ivan Milosavljevic and Pluton Pullumbi

Air Liquide
Les Loges en Josas, 78350 Jouy en Josas Cedex; France
Phone: +33 1 39 07 61 69; Fax: +33 1 39 56 98 10
E-mail: ivan.milosavljevic@airliquide.com

In the present study the Molecular Electrostatic Potentials (MEPs) were used as a tool to characterize the relative stabilities and reactive properties of a number of halogen substituted dibenzo-p-dioxins ("dioxins") and dibenzo-furans ("furans"). That work was initiated in order to better explain experimental results obtained on an industrial municipal solid waste (MSW) incinerator. The goal of the experiments was to examine the effects of oxygen enrichment of combustion air on the incinerator operational and environmental performances. Among other results, it was observed that the emission of dioxins and furans decreased during the oxygen enriched incinerator functioning. The reason for this might have been twofold: combustion improvement (precursor destruction resulting in smaller amount of pollutants formed) and dioxins and furans destruction (by oxidation of formed pollutants). The goal of the MEP modeling was to examine the effects of oxygen on destruction of already formed dioxins and furans. As a result of both studies (experimental and modeling), it was concluded that the observed decrease in dioxins and furans emissions was due solely to the combustion improvement inside the incinerator which resulted from oxygen enrichment. This conclusion was further corroborated by examining the oxidation kinetics of two known dioxins and furans precursors.

1. INTRODUCTION

It is planned that only non-ultimate waste (the waste that cannot be recycled or used for its energy content) be accepted in European landfills starting from 2005. As landfills become more and more saturated, while people continue generating more and more waste, incineration will be more used as a form of thermal recycling. Today it represents anywhere from 5% to 60%, depending on a country [1]. In France, approximately one third of municipal solid waste (MSW) is burned in about 300 incinerators of various capacity and age [2]. However, in many cases MSW incineration pollutes; widely known pollutants, such as NOx, CO and particles, and some less known, such as halogenated compounds, are formed. For example, it is estimated that MSW incineration is responsible for about 25% of the overall emissions of

dioxins [3]. It would not be surprising if a correlation between the incinerator age and the amount of the pollutants rejected exists.

Thus, at least in some European countries, a need to renew the incinerator park exists solely from the point of view of their environmental performance. It is preferred that this renewal takes place before 2005, preferably without the capacity loss.

Following tests done on an industrial MSW incinerator [4], we believe that oxy-combustion can be used in order to reduce emissions of some pollutants and, in particular, dioxins and furans. This improvement of the incinerator performance can be done with the capacity increase. Of course, oxygen enrichment has a beneficial effects for any installation, whether old or new.

2. EXPERIMENTAL AND COMPUTATIONAL DETAILS

2.1 EXPERIMENTAL

The objective of the tests done was to examine the effect of oxygen enrichment on several parameters (and also that the improvement of one parameter does not imply the deterioration of another one):

- decrease of the amount of polluting gases (CO, NOx and dioxins/furans emissions),
- decrease of the carbon content in the bottom ash,
- furnace throughput increase and operational flexibility improvement.

The incinerator used for tests is presented schematically in Figure 1. The installation consists of the following components (as in sequence of the MSW processing): arrival and manipulation of the MSW, furnace, bottom ash handling system, boiler and heat dissipation system, flue-gas clean-up, electrostatic precipitator and the stack.

The incineration furnace is of a reciprocated Stoker type. There are three grates in the furnace: the first one where the MSW arrives and where it is preheated and dried, the second one where it is almost completely combusted and the third one where the final burnout of the residual bottom ash carbon takes place. The primary air arrives underneath the grates. The secondary air arrives from the sides of the furnace by refractory plates. At the end of the furnace (after the third grate) the flue gases enter the boiler and the bottom ash falls into the handling system.

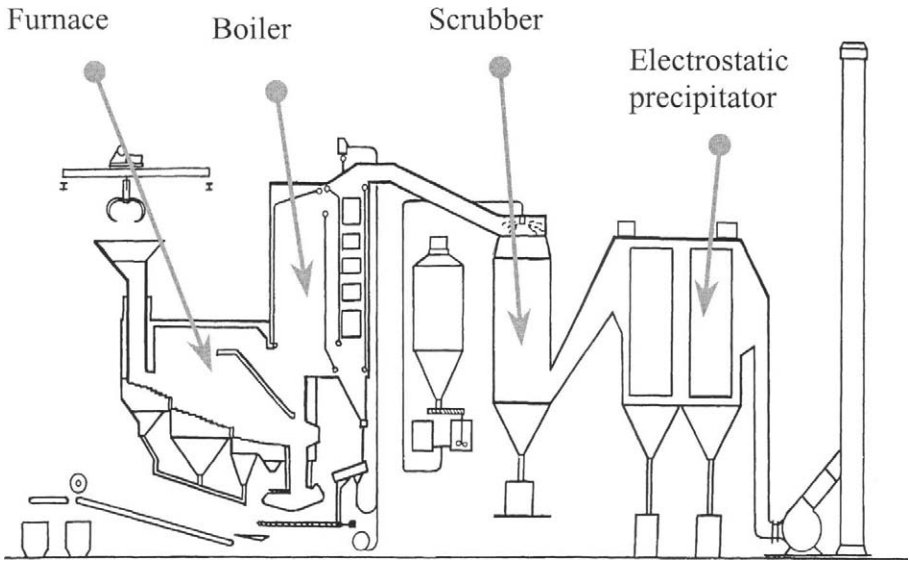

Figure 1. The incinerator used for tests

After the boiler, flue gases pass to the semi-wet clean-up. This process neutralizes HCl and SO_2. Before rejecting the flue gas at the stack they are cleaned from dust in the electrostatic precipitator.

Tests were done in two different configurations:

(a) second grate primary air enrichment
(b) second and third grate primary air enrichment.

In both configurations the flue gas volume was kept constant. This means that as air was enriched with oxygen and as throughput increased, the amount of air had to decrease. Consequently, there was less gas flowing through the system per unit of waste.

Air was enriched globally (to 23.8% in one part of the primary air), i.e. oxygen was injected in the air pipe and the enriched air was transported to the furnace by means of an air pipe. Oxygen was injected by means of a swirl injector (***OXYNATOR™***), a device developed to assure very homogeneous mixture of oxygen with air in a very short distance.

Standard gas analyses (O_2, CO_2, CO, NOx, SOx) were performed in the boiler and the stack. Dioxins and furans samplings were done in the stack for 6 hours per sample. The analyses of the collected samples were done subsequently by GC-MS technique (subcontracted to a registered laboratory). Bottom ash unburned carbon was determined on several samples by heating them at 500°C in air for 4 hours. Leaching behavior for the bottom and fly ash samples was examined.

The following results were obtained for treatment capacity and average gas emissions:
- treatment capacity: +10%
- dioxins: -70% (decrease from 1.5 ng TEQ/Nm^3 to 0.5 ng TEQ/Nm^3)
- CO_2 : 10% increase that corresponded to the treatment capacity increase
- CO: -70% (in average decrease from 25 ppm to 7 ppm at 11% oxygen in the flue gas)
- NOx: -10% (in average decrease from 160 ppm to 145 ppm at 11% oxygen in the flue gas)
- SOx : no change was observed
- bottom ash: -40% residual carbon (in average from 3.8 % to 2.2 %)
- ash leaching: no changes were observed

2.2 COMPUTATIONAL DETAILS

The objectives of the molecular modeling were twofold: to explain better the results obtained experimentally and to examine the possibility of using modeling as a tool of predicting dioxins and furans properties which influence the emissions from a MSW incinerator.

The molecular mechanics (MM) and molecular dynamics (MD) calculations were carried out with the Discover program of the MSI molecular modeling package [8]. The PCFF force field was used to perform the geometric optimizations and molecular dynamic simulations on both anomers. The Van der Waals potential was set to zero at 10 Å and the automatic parameter assignment was used for the PCFF forcefield. The conjugate gradient algorithm has been used for the minimization of both species combined with Newton Raphson one. The quantum mechanical semiempirical calculations were performed with the PM3 (parametric method 3) as implemented in MSI [8] molecular modeling package. The medium integration mesh with a relaxed core treatment the electrons using a standard basis set has been adopted in all Faststructure calculations [8]. The simulations of the mechanisms of formation of benzene (precursor for dioxin or dibenzofuran formation) have been performed using the Faststructure code for realizing a simulated annealing with " scattering boundary conditions ". Single point DFT calculations on faststrucure-optimized geometries have been performed using the Dmol program [8] to determine the MEPs of the most stable geometries.

Many indices of reactivity have been introduced during the last 10 years, like atomic charges, bond orders, free valences, frontier electron densities, fukui functions and the Molecular Electrostatic Potentials (MEP). Unlike many of the above mentioned parameters quantities used to rationalize the reactivity, the MEP is a real physical property which can be either determined experimentally by X-ray and electron diffraction methods or calculated from the calculated electronic wave function.

Any charge distribution creates a potential $V(\mathbf{r})$ in the space as defined by the following equation:

$$V(\mathbf{r}) = Z_i / |\mathbf{R}_i - \mathbf{r}| + \vee \rho(\mathbf{r}')d\mathbf{r}' / |\mathbf{r} - \mathbf{r}'| \quad (1)$$

Where $V(\mathbf{r})$ is the electrostatic molecular potential, Z_i is the charge on nucleus i located at $\mathbf{R}_i$ and $\rho(\mathbf{r}')$ is the electron density function of the given molecule at point $\mathbf{r}'$. This equation

contains a summation over the nuclear point charges and an integration over the "continuous" negative electron distribution. The sign of V(**r**) at any point out of the molecular region reflects which of the nucleus (+) or the electron density (-) has a major effect.

3. RESULTS AND DISCUSSION

The result obtained during the tests on the incinerator was that the average dioxins and furans emissions were decreased by a factor of three when oxygen enrichment was used. The reason for this observation was searched in the available literature. It was noted in [9] that there are four sources of dioxins and furans in incineration:

1. introduced in the incinerator with the waste
2. formed in the flame
3. formed from the fly ash at temperatures about 500°C
4. *de novo* synthesis (formation on the fly ash surface) at about 300°C.

Seeker [9] also notes that sources 1 and 3 are not very significant in a Stoker type incinerator. Therefore, dioxins and furans are either formed in the flame or by *de novo* synthesis. The parameters that influence the formation of dioxins and furans can be found in the literature [5]. The formation in the flame is favored by:

- free chlorine presence
- low combustion temperature
- precursor (hydrocarbon).

The *de novo* synthesis is favored by:

- temperature window at about 300°C
- heavy metals in the ash
- residual carbon in the ash (solid phase)
- precursor (hydrocarbon in the gas phase)
- the presence of water vapor.

The reasons for the experimentally observed decrease of dioxins and furans emissions can be examined by using the above parameter list. It is known [5] that dioxins and furans can be formed from macromolecular carbon structures (by *de novo* synthesis) and from small organic molecules (precursors). Also, there exist a correlation between the quantity of fly ash and dioxins and furans emissions [6]. In the tests discussed in this communication, it is believed that both of those phenomena were altered. Carbon structures (macromolecular as well as precursors) were better combusted thanks to faster kinetics which resulted from higher oxygen concentration. On the other hand, the quantity of fly ash was reduced since the total amount of gas flowing through the system was reduced.

The kinetic hypothesis can be confirmed by a simple study of benzene and chlorobenzene combustion [10]:

$$r = A Y_F^a Y_O^b \exp(-\frac{E}{RT}) \qquad (2)$$

where:
r – reaction rate [mol/m^3 s]
A – pre – exponential [mol/m^3 s]
Y – mass fraction
F – fuel
O – oxygen
a – reaction order with respect to fuel
b – reaction order with respect to oxygen
E – activation energy
R – gas constant
T – temperature

Using equation (2), the reaction time at a constant temperature can be calculated. Two cases were examined: isothermal combustion (at 1000 K) of benzene (C_6H_6) and of chlorobenzene (C_6H_5Cl). These two molecules were chosen since they are probable precursors in the dioxins and furans formation. The kinetic parameters are given by Delplanque et al [10], i.e.:

Table 1: Kinetic parameters used in this study (adopted from [10])

Fuel	a	b	E 10^8 J/kmol	A 10^9 SI
Benzene	-0.10	1.85	1.25	1.1
Chlorobenzene	1.00	1.00	0.96	$8x10^{-5}$

The results from this calculation for benzene and chlorobenzene are shown in Figures 2a and 2b, respectively. There are two main conclusions that can be drawn from Figure 2: the two compounds examined react much faster in oxygen than in air and chlorobenzene needs approximately 3 orders of magnitude more time to achieve the same degree of conversion. If these two conclusions are combined, it can be seen that oxygen enrichment might have a significant effect on the destruction and removing efficiency (DRE) of these two compounds.

While it seems clear that oxygen enrichment had very positive effect on the combustion of dioxins and furans precursors, it is not clear whether it had any effects on already formed pollutants. In order to check this, mathematical modeling (MEP study) was used.

One of the first applications of the MEP was to determine reactivity maps in order to explain and predict the sites of electrophilic attack on a molecule. An approaching electrophile would

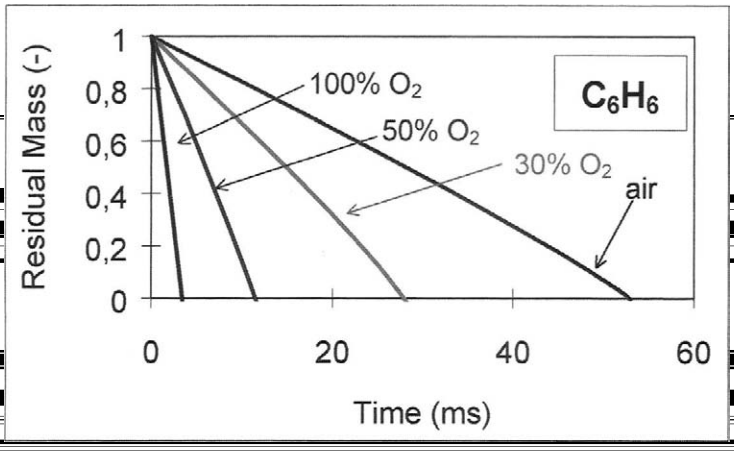

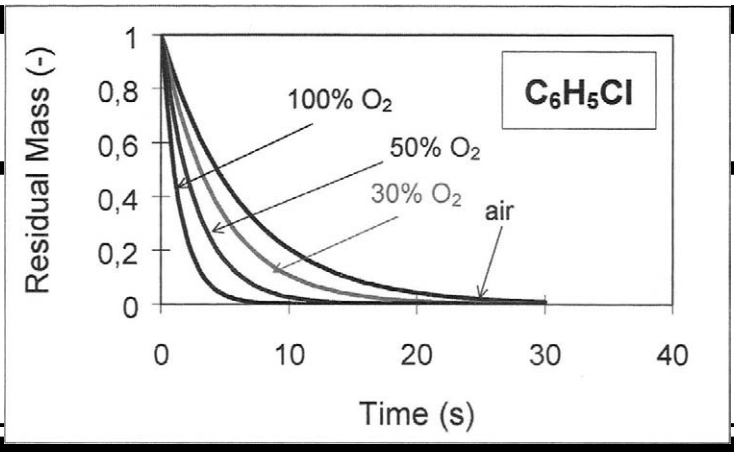

2,3,7,8-tetrachlorodibenzo-p-dioxin (TCDD), dibenzofuran and 2,3,7,8 tetrachlorodibenzofuran (TCDF). The analysis of the MEP pattern indicates that the attack of the CO bonds in chlorinated compounds (the toxic

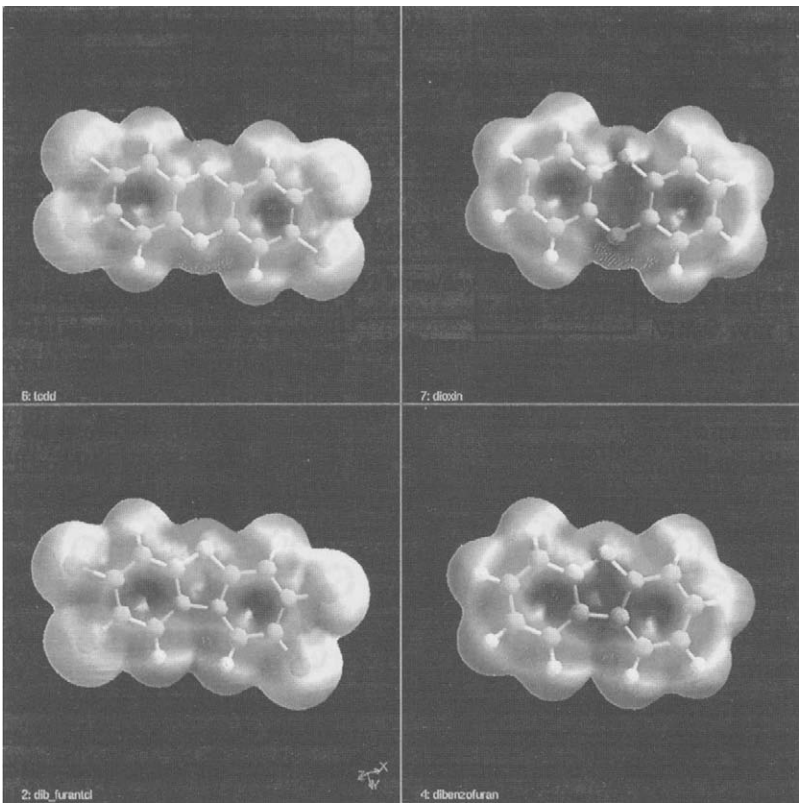

Figure 3. Structures of dibenzo-p-dioxin (upper right), 2,3,7,8-tetrachlorodibenzo-p-dioxin (upper left), dibenzofuran (lower right) and 2,3,7,8 tetrachlorodibenzofuran (lower left)

members of the family) is less favored than in the unsubstituted ones. This finding suggests that the use of oxygen for the abatement of the toxic dioxins would not react selectively with these compounds.

In our study of the mechanisms of dioxins and furans formation we observed that the formation of propagyl radicals was an important pathway for their synthesis. The runs carried out with the faststructure program showed that these radicals were easily formed. Due to their structure and electron delocalization effects they are quite stable with a reduced number of possible reaction channels. As the benzene formation resulted from efficient collisions of propagyl radicals with unsaturated molecular species the introduced oxygen in the simulated system gave rise to new products reducing the number of propagyl radicals and unsaturated

hydrocarbons implying less effective collisions corresponding to benzene formation. It should be noticed that this simulation result corresponds to our particular starting point. Exploration of other possible scenarios in order to correctly, computationally, examine the effect of oxygen

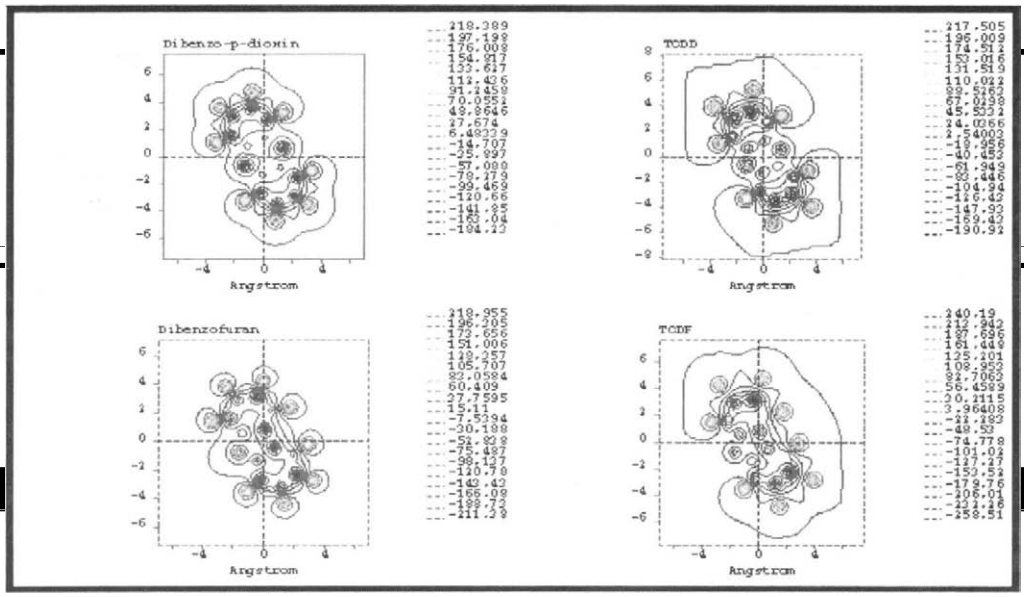

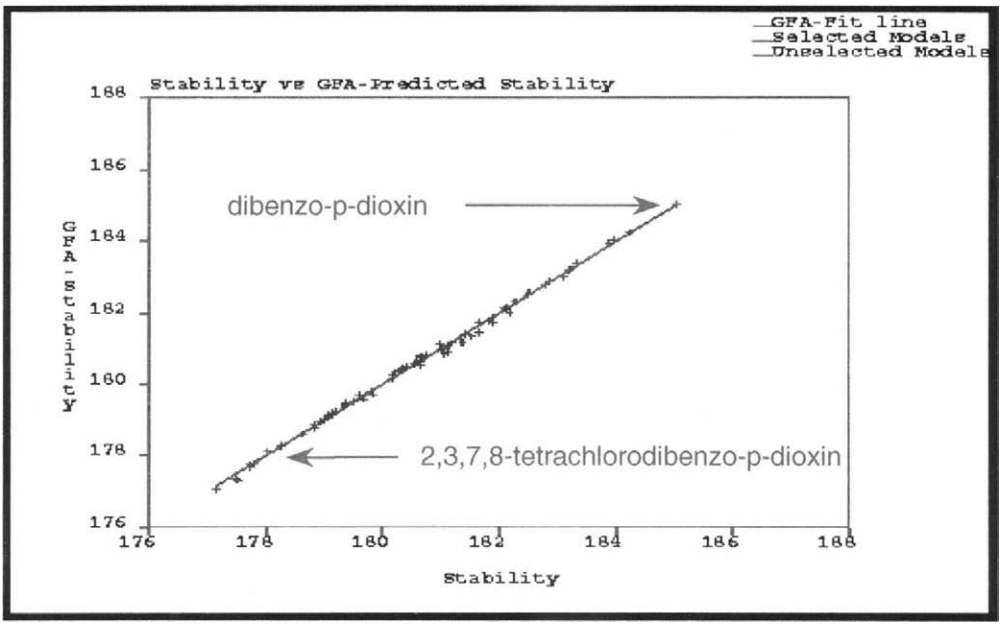

Figure 5. QSAR predicted stabilities for chlorine-substituted dibenzodioxins

4. CONCLUSIONS

Concentrations of dioxins and furans were measured in the flue gas of a municipal waste incinerator. It was observed that oxygen enrichment of air has a positive effect on dioxins and furans destruction. It was postulated that oxygen enrichment affects the combustion in the incinerator and that the destruction efficiency is the reason of observed phenomena. It was also postulated that oxygen enrichment might not have an effect on already formed dioxins and furans. These hypotheses were confirmed by the molecular modeling study. It was shown that dioxins and furans that were already formed cannot be easily decomposed by increasing oxygen partial pressure inside the furnace. This is mainly due to the presence of the electron-withdrawing chlorine atoms which modify the electrostatic potentials of the parent molecules reducing the reactivity of the heterocycles towards electrophilic reactants.

REFERENCES

1. EPA information (www.epa.gov), 1998
2. ADEME, ITOM 6, Sixième Inventaire des installations de traitement, de transit ou de mise en décharge des déchets ménagers et assimilés en France, 1995
3. Page 25, C&EN, June 29, 1998; CBNS, Queens College, CUNY Flushing, NY (www.qc.edu/CBNS), 1996; ADEME, 1997

4. I. Milosavljevic, O. Charon, M. Degrand and J. De Freitas ; *Int. Conference on Incineration and Thermal Treatment Technologies*, Salt Lake City, UT, USA, May 1998
5. R. Addink and K. Olie; *Environmental Science & Technology*, **29**(6), 1425, 1995 and the references cited therein
6. R. G. Barton, W. D. Clark, W. S. Lanier and W. R. Seeker; *Chemosphere*, **20**(10-12) 1825, 1990
7. Lecomte ; C. *Adv. in Mol. Struct. Research,* **1**, 261, 1995
8. MSI, *Molecular Simulation package*, San Diego, California, 4.0.0, 1997.
9. W. R. Seeker *23rd International Symposium on Combustion*, pp. 867-885, 1990
10. J. – P. Delplanque, R. H. Rangel and W. A. Sirignano, *23rd International Symposium on Combustion*, pp. 887-894, 1990

Reaction Engineering for Pollution Prevention
M.A. Abraham and R.P. Hesketh (Editors)

A numerical study on NOx reduction by steam addition in counterflow diffusion flame using detailed chemical kinetics

H. Yamashita[a], D. Zhao[b], S.N. Danov[c], T. Furuhata[c] and N. Arai[c]

[a] Department of Mechanical Engineering, Nagoya University,
Chikusa-ku, Nagoya, 464-8603, Japan
[b] New Energy and Industrial Technology Development Organization, Japan
[c] Research Center for Advanced Energy Conversion, Nagoya University, Japan

In order to improve thermal efficiency of gas turbine system and better control NOx emission, the injection of steam into a gas turbine combustor has been employed. The numerical analysis has been performed by using the detailed elementary reaction mechanisms including NOx formation. The effect of flow field on the chemical reaction has been investigated by using the methane-air counterflow diffusion flame aiming at the elucidation of the NOx reduction mechanism due to the steam injection. The influence of the amount of steam, the method of injection, the preheated air and fuel temperature has been investigated. The results show that the steam injection is effective for the reduction of NOx emission, and the reduction mechanism of NOx emission is clarified.

1. INTRODUCTION

Gas turbines provide generators with an advantageous solution in their search for high thermal efficiency and cost effective power generation. But the development of high efficiency gas turbines has met a barrier. The traditional technology improvement is to rise firing temperature at turbine inlet (TIT). However, this has drawbacks. It will increase emissions to the atmosphere and subject the entire system to higher temperature and stresses. Therefore, the temperature of combustion gases is reduced by decreasing the fuel/air equivalence ratio and introducing a large amount of diluting (secondary) air [1]. This, however, decreases the efficiency due to the increased power consumption for supplying secondary air and increased heat losses.

In order to save energy and better control NOx emission, authors have proposed a two stage combustion technology and high-pressurized steam injection for a gas turbine combustor [2,3]. In this system a significant improvement of thermal efficiency and reducing NOx emission can be expected under the condition of fuel-rich combustion and steam injection. The high-pressure steam is generated in a waste heat recovery boiler. Before applying the system into practical power generation, it is important to elucidate the

combustion characteristics under the conditions of steam existence and predict NOx reduction by numerical analysis.

Some prior works have already discussed the effect of steam injection on NOx formation. Miller and Bowman [4] pointed out that decreasing flame temperature by injecting steam can control NOx formation and that the reaction between H_2O and radical CH would contribute to the decrease of prompt NO. Recently, Li et al. [5] reported that with the same amount of water addition, the higher fuel/air equivalence ratio could lead to the larger NOx reduction for a counterflow double flame, which was formed by fuel-rich mixture and water-atomized air.

Although many studies have shown that steam injection can control NOx formation, the NOx reduction mechanism has not been explained clearly yet. In this study, the methane, a principal ingredient of the natural gas, was used as a fuel, and the GRI-Mech [6] was employed for the detailed elementary chemical reaction mechanisms including NOx formation. The basic combustion characteristics had been studied by chemical equilibrium calculations in the previous study [7]. In the present study, the effect of flow field on chemical reactions was also investigated by using a counterflow diffusion flame, which was one of the basic configurations of diffusion flames.

2. ANALYTICAL MODEL AND COMPUTATIONAL PROCEDURE

A previously developed calculation code [8] was used for the calculation of counterflow diffusion flame. Figure 1 shows the outline of an analytical model of the counterflow diffusion flame in two-dimensional Cartesian coordinates. Two opposing jet planes are infinitely wide, and the fuel and air are spouted from the left jet side and the right side, respectively. Assuming a two-dimensional potential flow field, the stream function depends only on x, and velocities u and v are given as follows:

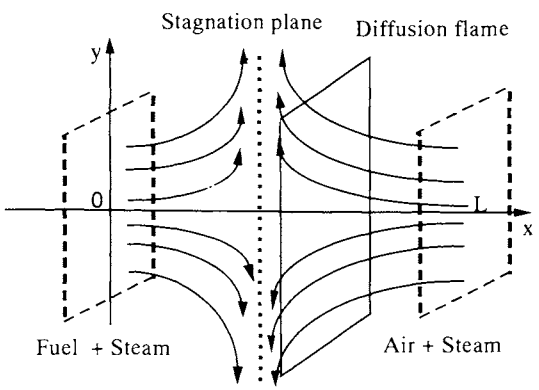

Fig. 1. Theoretical model of counterflow diffusion flame

$$u = \frac{U}{\rho} \qquad v = \frac{y}{\rho}\frac{dU}{dx} \tag{1}$$

where ρ is density , u and v are velocities in x- and y-direction, respectively.

Assuming that 'similar' solutions can be applied to the calculation of temperature and concentration fields, the conservation equations can be presented as follows:
Energy conservation equation

$$\rho u c_p \frac{dT}{dx} - \frac{d}{dx}\left(\lambda \frac{dT}{dx}\right) + \sum_{k=1}^{K} \rho Y_k V_k c_{p,k} \frac{dT}{dx} + \sum_{k=1}^{K} w_k h_k = 0 \tag{2}$$

Species conservation equations

$$\rho u \frac{dY_k}{dx} + \frac{d}{dx}(\rho Y_k V_k) - w_k = 0 \qquad (k = 1, \cdots, K) \tag{3}$$

where T is temperature, c_p is specific heat capacity at constant pressure, λ is thermal conductivity, while Y_k, V_k, h_k and w_k represent mass fraction, diffusion velocity, specific enthalpy and mass production rate of species k, respectively.

The boundary conditions of the temperature and the concentration field are given at two jet planes of distance L, and the left and right jet plane positions are at x=0 and x=L, respectively. The boundary conditions are as follows:

$x = 0$:

$$u = u_{fuel}, \quad v = 0 \Rightarrow U = \rho_{fuel} u_{fuel}$$

$$T = T_{fuel}, \quad Y_{CH4} = Y_{CH4,0} \; Y_{H2O} = Y_{H2O,0}$$

$x = L$:

$$u = u_{air}, \quad v = 0 \Rightarrow U = \rho_{air} u_{air} \tag{4}$$

$$T = T_{air}, \quad Y_{O2} = Y_{O2,L}, Y_{N2} = Y_{N2,L}, Y_{H2O} = Y_{H2O,L}$$

where U(x) is the linear expression of x in the following manner:

$$U(x) = \frac{\rho_{fuel} u_{fuel} - \rho_{air} u_{air}}{L} x + \rho_{fuel} u_{fuel} \tag{5}$$

The distance L was assumed 15mm, and velocities u_{fuel} at the fuel jet plane and u_{air} at the air jet plane were assumed to be 1m/s. Then, the velocity gradient (strain rate) $(u_{fuel}+u_{air})/L$ was $133.3s^{-1}$. The temperatures on the fuel and the air jet plane were assumed 400K. The amounts $Y_{H2O,0}$ of the addition of steam were 0.05, 0.1 and 0.3 in the mass fraction, and the steam was added to the fuel side or the air side.

GRI mechanism [6], containing the NOx formation reactions, was used as a chemical kinetic mechanism, It involves 49 species and 279 elementary reactions. The thermodynamic parameters and transport properties were obtained from CNEMKIN data base [9].

3. RESULTS AND DISCUSSION

This chapter shows the calculation results of the counterflow diffusion flame by using a detailed chemical kinetic mechanism, for which the NO formation is chiefly ruled with the prompt mechanism. Especially, the flame structure and the distributions of the temperature and NO concentration and related species for the case with steam addition are shown. Moreover, an emission index (EI_{NO}) [10] was introduced in order to evaluate NO emission characteristic quantitatively, and the reduction mechanism of NOx due to the steam addition was examined comparing with the influences of the amount of the steam addition and the addition method.

EI_{NO} is defined as a ratio of the NO mass production rate M_{NO} [g/(m^2·s)] to the fuel (methane) mass consumption rate -M_{CH4} [kg/(m^2·s)] per unit area of the flame zone, and it is given by the following expression:

$$M_k = \int_0^L w_k dx \qquad [\mathrm{kg}/(\mathrm{m}^2 \cdot \mathrm{s})]$$
$$EI_{NO} \equiv \frac{M_{NO}}{-M_{CH4}} \qquad [\mathrm{g}/\mathrm{kg}] \tag{6}$$

where w_{NO} and w_{CH4} are mass production rate of NO and CH_4.

Though it is known that the flame structure depends on the velocity gradient, i.e. the strain rate in the counterflow diffusion flame [11], it depends on 'the momentum gradient' more strictly. Therefore, if all other conditions are kept the same, the flame temperature decreases with an increase in the momentum gradient. The momentum gradient changes due to the change of density on the jet plane by adding steam even if the velocity gradient is the same. When steam is added to the air side, the injection velocity at the air jet plane was assumed to 1.05m/s for keeping the momentum gradient unchanged, because the difference of molecular weight of the air and steam is rather large.

In the case of the jet plane temperature 400K, the distributions of the axial velocity and momentum are shown in Fig.2 for three steam addition methods: no steam adding, adding steam to fuel side and adding steam to air side with mass fraction Y_{H2O}=0.1. The position of the stagnation point is almost the same for the three steam addition methods, and almost no variation of the momentum gradient is observed.

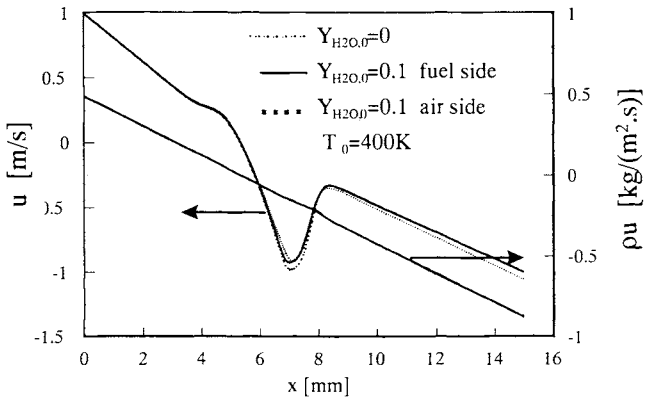

Fig. 2. Distributions of axial velocity and momentum of counterflow diffusion flames

3.1. Case without steam addition

The concentration distributions of major species and temperature distribution are shown in Fig.3(a), and the concentration distributions of CH, HCN and N which closely relate to NO formation are shown in Fig.3(b). The broken line and the dot-dash-line in the figure show the positions of the stagnation plane and the maximum temperature corresponding to the flame position, respectively. The maximum values of the concentrations of reaction products H_2O and CO_2 and the flame temperature are located on the air side further apart from the stagnation plane, and the flame zone is formed at this position. The maximum temperature is 2139K. As shown in this figure, the distribution of HCN concentration is chiefly on the fuel side of the reaction zone, while NO is produced on the air side of the reaction zone, and a part of NO is oxidized to NO_2 on the further air side.

3.2. Case with steam addition to fuel side

The flame structure and the concentration distributions of NO, NO_2, CH, HCN and N are shown in Fig.4(a) and Fig.4(b) in the case where the steam is added to the fuel side with mass fraction Y_{H2O}=0.1. The flame structure is the same as in the case without steam addition in the foregoing section, and though the steam concentration distribution is different on the fuel side, the maximum value of steam concentration is only slightly higher. The maximum temperature falls down to 2038K and the peak of NO concentration decreases to about 7.5×10^{-5}. All concentrations of CH, HCN and N decrease.

3.3. Case with steam addition to air side

The flame structure and the concentration distributions of NO, NO_2, CH, HCN and N are shown in Fig.5(a) and Fig.5(b) in the case where the steam is added to the air side with mass fraction Y_{H2O}=0.1. The steam concentration increases clearly not only in the air side but also in the reaction zone. The maximum temperature remarkably decreases to 1879K and the

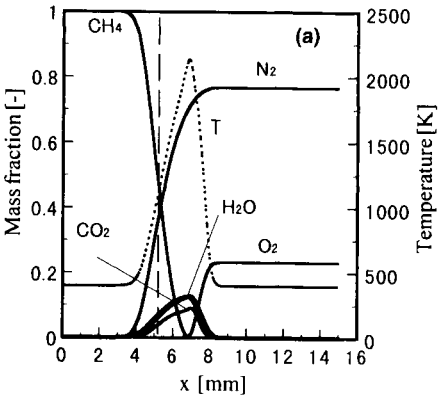

(a) Distributions of major species concentration and maximum temperature

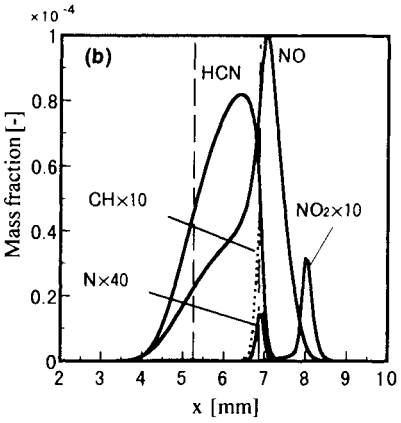

(b) Concentration distributions of NO, NO_2, CH, HCN and N

Fig. 3. The flame structure and NOx formation (Without steam addition)

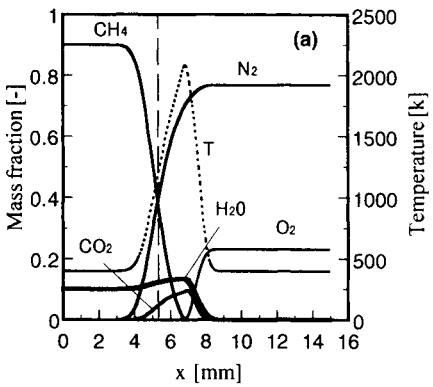

(a) Distributions of major species concentration and maximum temperature

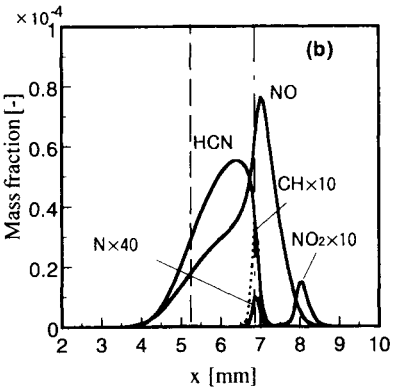

(b) Concentration distributions of NO, NO_2, CH, HCN and N

Fig. 4. The flame structure and NOx formation (With steam addition to fuel side)

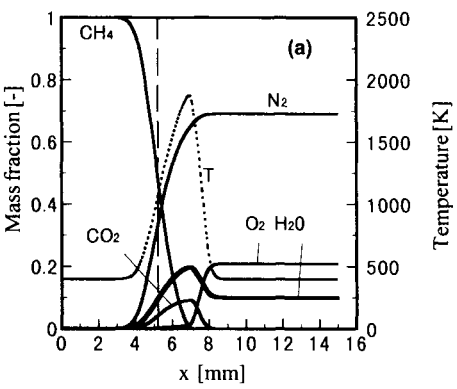

(a) Distributions of major species concentration and maximum temperature

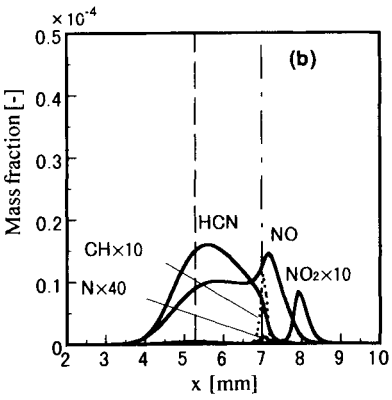

(b) Concentration distributions of NO, NO_2, CH, HCN and N

Fig. 5. The flame structure and NOx formation (With steam addition to air side)

combustion reaction considerably weakens. Moreover, the peak of the NO concentration decreases to about 1.5×10^{-5}, and the concentration distributions of radicals CH, HCN and N are also considerably different from the case of the foregoing sections. Thus, it has been understood that the addition method of steam strongly influences the combustion characteristic and the NOx formation.

3.4. Effect of addition method on steam concentration in the reaction zone

The effect of steam addition on NOx formation is examined with respect to the relation between flow field characteristics and steam addition method in the counterflow diffusion flame.

As shown in Fig.3(a), Fig.4(a) and Fig.5(a) in the case where the steam is added to the fuel side, the steam concentration distribution is almost the same as those without steam addition excluding the fuel side, and the maximum value of steam concentration is slightly higher. That is because the flame zone is located on the air side away from the stagnation point, and the steam cannot enter the flame zone from the fuel side by convection, and the diffusion of the steam produced in the flame zone decreases only slightly. On the other hand, when steam is added to the air side, the steam concentration increases significantly not only in the air side but also in the reaction zone, because the steam enters the flame zone via convection. Thus, it is thought that the method to add steam to the air side is a very effective way for controlling the flame temperature and the reduction of the NOx formation.

3.5. Comparison of emission index of NO (EI_{NO})

In the case of the jet plane temperature 400K, effects of both the amount and the method of steam addition on the emission index of NO are shown together in Table 1. The maximum values of flame temperature and NO concentration are also shown in the table for reference. It can be seen from this table that NO formation is suppressed even if steam is added to either the fuel side or the air side, and the amount of the reduction of NO can be enlarged by increasing the amount of steam addition. The NO formation can be decreased more effectively in the case of steam addition to the air side even with a small amount of steam.

Table 1 Combustion characteristics and predicted NO emission index

Added side	$Y_{H_2O,0}$ [-]	T_{MAX} [K]	$Y_{NO,MAX}$ [ppm]	EI_{NO} [g/kg]
----	0.0	2139	100.7	0.703
Fuel	0.1	2090	76.2	0.584
	0.3	2038	57.2	0.479
Air	0.05	1961	22.6	0.219
	0.1	1879	10.1	0.107

3.6. Effect of steam addition on NO formation

It is known that the formation of NO is governed by the prompt NO mechanism in the methane-air counterflow diffusion flame, which has comparatively high strain rate in the present calculation [11]. Figure 6 shows the profiles of NO production rate with the steam addition for various elementary reactions which contribute significantly to the NO formation. As seen from Fig.6, the production rate of thermal NO via the elementary reaction (R179) is very small, NO is produced mainly by the elementary reactions (R180 and R214), and consumed by the elementary reactions (R274 and R249). It is therefore clear that the prompt NO mechanism controls the formation of NO regardless of the steam addition. Namely, NO is produced principally through the reaction route showed in Fig.7. Especially, N-radical necessary for NO formation is chiefly generated by reaction R240 in the GRI-Mech mechanism.

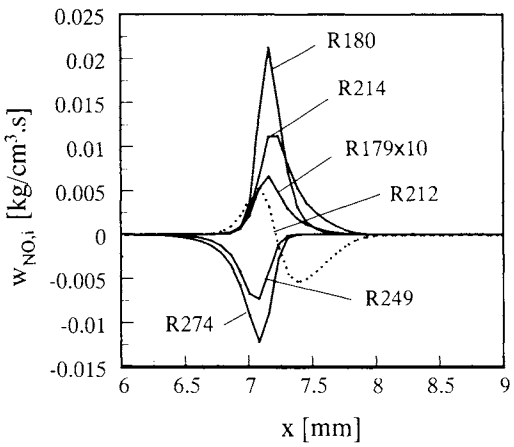

R179: $N+O_2 = NO+O$
R180: $N+OH = NO+H$
R212: $H+NO+M = HNO+M$
R214: $HNO+H = H_2+NO$
R249: $CH_2+NO = H+HNCO$
R274: $HCCO+NO = HCNO+CO$

Fig. 6. Profiles of NO mass production rate by various elementary reactions (T_0=400K, $Y_{H2O,0}$=0.05, Steam addition to the air side)

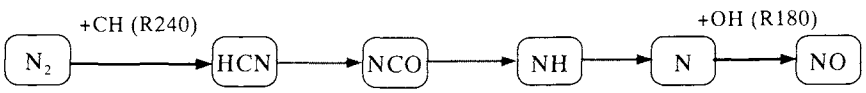

R240: $CH+N_2 = HCN+N$

Fig. 7. Schematic mechanism of prompt NO formation

The mass production rates of NO, HCN and CH together are shown in Figs.8(a-c) in order to get better understanding of NO reduction mechanism by the steam addition. The production rates of NO decrease according to an increase in the amount of steam addition, and it becomes extremely small when steam is added to the air side. Moreover, the mass production rates of HCN and CH become small as well as that of NO. Therefore, the decreases in the flame temperature and in the concentrations of HCN and N related to

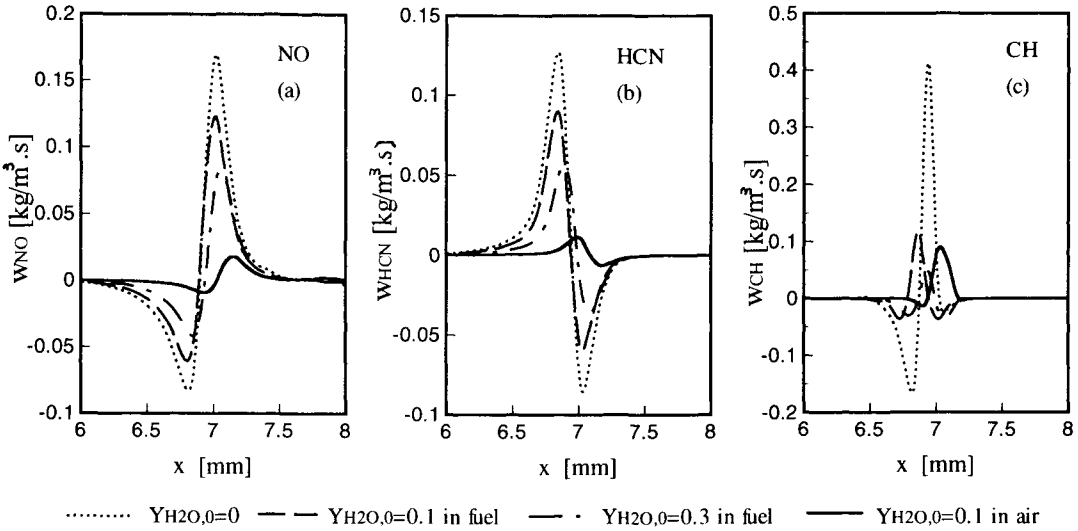

Fig. 8. Mass production rate distributions of NO, HCN and CH

prompt NO formation, play an important role for reduction mechanism of NOx by steam addition.

Li et al. [5] pointed out that the decreases in concentrations of HCN and N were caused by the consumption of decomposition products CH and CH_2 of methane due to the reaction with water. We should examine this reduction mechanism of NOx distinguishing a physical effect of decrease of the flame temperature from a chemical effect of suppression of reaction R240, etc.

3.7. Effects of initial temperature on maximum flame temperature and NO emission index

The effect of initial temperature on the maximum flame temperature and the NO emission index are shown in Figs.8 and 9 in the case of no steam addition and steam addition to the air side with mass fraction $Y_{H2O,0}$=0.05 and 0.1. As the initial temperature increases, the maximum flame temperature and the NO emission index increase.

The relations between the NO emission index and the maximum flame temperature, which is derived from the above figures, are shown in Fig.10. It can be seen from this figure that even if they are compared under the conditions of the same maximum flame temperature, the NO emission index decreases by increasing the amount of steam addition. This indicates that there exists the chemical reaction effect of steam addition on the reduction of NO as well as the physical effect of steam addition, that is, the decrease of flame temperature.

The relations between NO mass production rate, CH_4 mass consumption rate and maximum flame temperature are shown in Fig.11. This figure indicates that as the amount of steam addition increases, the NO mass production rate decreases more than the CH_4 mass consumption rate. Moreover, the CH_4 mass consumption rate is almost independent of the maximum flame temperature, but the NO mass production rate increases very steeply with increase of the maximum flame temperature.

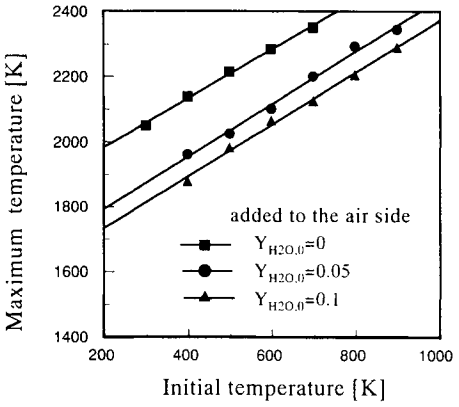

Fig. 9. Effect of initial temperature on maximum flame temperature

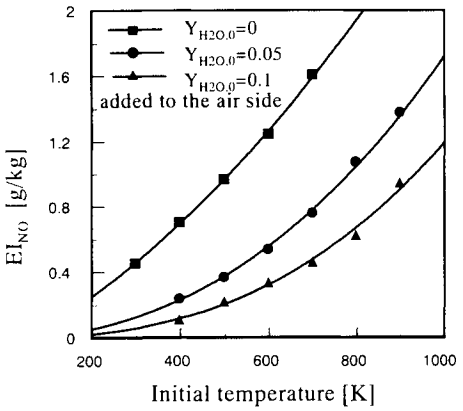

Fig. 10. Effect of initial temperature on NO emission index

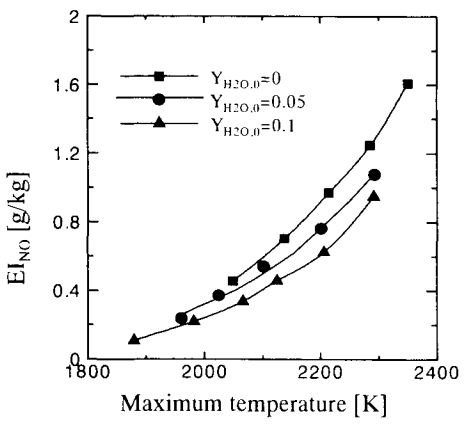

Fig. 11. The relation between emission index of NO and maximum flame temperature

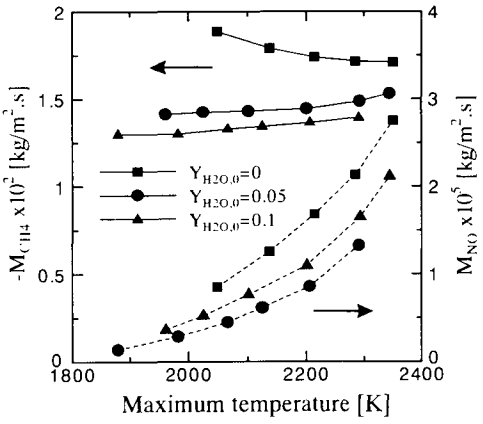

Fig. 12. The relations between NO mass production rate, CH_4 mass consumption rate and maximum flame temperature

3.8. The chemical kinetic effects of steam addition on NO formation

In order to examine the chemical kinetic effects of the steam addition on the NO formation, the concentrations of HCN, CH and N, which are important to the NO formation, under the two conditions of T_0=600K and $Y_{H2O,0}$=0, and T_0=800K and $Y_{H2O,0}$=0.05 are shown Fig.13. Although the maximum temperature are almost in agreement under these condition, the concentrations of HCN, CH and N decrease remarkably with the steam addition to the air side.

Figure 14 shows the emission index $EI_{NO,i}$ for various elementary reactions which contribute significantly to the NO formation. As seen from the figure, the elementary reactions for NO formation and consumption are both suppressed. In comparison with

decreases in the $EI_{NO,i}$ for the NO consumption, the degrees of the decreases in the $EI_{NO,i}$ for the NO formation are greater. The detailed discussion on chemical kinetic effects of the steam addition on the NO reduction has been described in our previous paper[12].

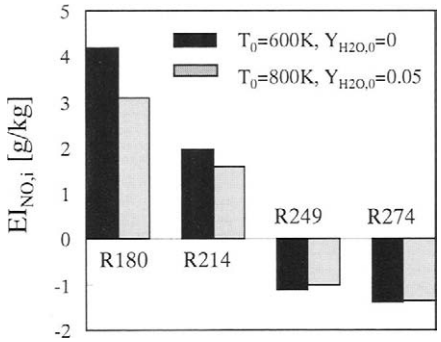

Fig. 13. Contributions to NO emission index from various elementary reactions

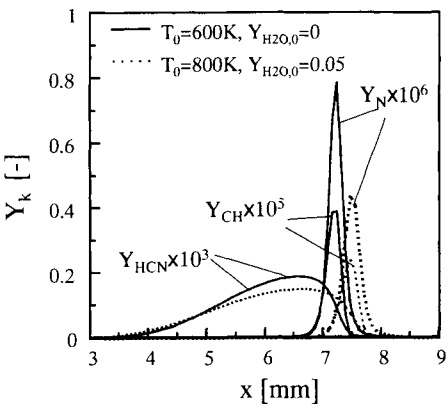

Fig. 14. Profiles of mass fraction of species HCN,CH and N

4. CONCLUSIONS

This paper has used the counterflow diffusion flame calculations of methane air flame in order to elucidate of the NOx reduction mechanism by the steam addition. This study has led to the following conclusions.

1. In the fuel-rich combustion with steam existing, a significant reduction of NOx can be attained due to the double effect of the fuel-rich mixture and steam addition.
2. On the point of view of steam addition method, adding steam to air side is more effective even with a small amount of steam. It is extremely important that the addition steam reaches the reaction zone.
3. The decreases in flame temperature and in concentration of CH, HCN and N related to prompt NO formation are very important with respect to the reduction of NOx by steam addition.
4. As the initial temperature increases, and the maximum flame temperature and the NO emission index increase. Even if they are compared under the conditions of the same maximum flame temperature, the NO emission index decreases by increasing the amount of steam addition.

ACKNOWLEDGMENT

This research was supported by the Proposal-Based New Industry Creative Type Technology R&D Promotion Program (Project ID No.97E02-002) from the New Energy and Industrial Technology Development Organization (NEDO) of Japan.

REFERENCES

1. J.Chomiak, *Combustion - a study in theory, fact and application*, Abacus Press, New York, P410 (1990).
2. N.Arai, N.Kobayashi, K.Nakano and A.Matsunami, Proposal of Chemical Gas Turbine and Characteristics of Pressurized Low-NOx Combustion, *Pacific RIM Int. Conf. on Environmental Control Combustion Processes*, Paper 6A, Hawaii, USA (1994).
3. N.Arai and N.Kobayashi, Challenges for Development of Highly Efficient Gas Turbine System: The Chemical Gas Turbine System, *Proceedings of the ASME Int. Joint Power Generation Conf.*, Volume 1, 423-430, Denver, USA (1997).
4. J.A.Miller and C.T.Bowman, Mechanism and Modeling of Nitrogen Chemistry in Combustion, *Prog. Energy Combust. Sci.,* 15, 289-338(1989).
5. S.C.Li, N.Llincic and F.A.Williams, Reduction of NOx Formation by Water Sprays in Strained Two-Stage Flames, *ASME J. Eng. for Gas Turbines and Power*, 119, 836-843(1997).
6. GRI, http://www.me.berkekey.edu/gri_mech/, (1995).
7. H. Yamashita, D. Zhao, S. N. Danov, T. Furuhata and N. Arai, Numerical Analysis of NOx Reduction by Steam Injection Using Detailed Chemical Kinetics, *Second Trabzon International Energy and Environment Symposium*, 68, Trabzon, Turkey(1998).
8. H.Yamashita, Numerical Study on NOx Production of Transitional Fuel Jet Diffusion Flame, *Trans. Jan. Soc. Mech. Eng.,* (in Japanese), Vol.65, No.630, B, 783-789(1999)
9. R. J. Kee, F.M.Rupley and J.A.Miller, The Chemkin Thermodynamic data base, *Sandia National Laboratories Report*, SAND87-8251(1987).
10. T. Takeno and M. Nishioka, Species Conservation and Emission Indices for Flames Described by Similarity Solutions, *Combustion and Flame*, 92, 465-468(1993).
11. T. Takeno and M. Nishioka, NO Formation Mechanisms of Methane Air flames, *Nensho Kenkyu, Combustion Society of Japan*, (in Japanese),111, 3-15(1998).
12. D.Zhao, H.Yamashita, T.Furuhata and N.Arai, Consideration of Chemical Kinetics on Mechanism of NOx Reduction by Steam Addition, *Kagaku Kogaku Ronbunshu, The Society of chemical Engineers, Japan*, (in Japanese), to be published(1999).

Reaction Engineering for Pollution Prevention
M.A. Abraham and R.P. Hesketh (Editors)

Experimental studies on the capture of CO_2, NOx and SO_2 in the oxygen/recycled flue gas coal combustion system

T. Yamada[a], T. Kiga[a], S. Miyamae[a], K. Suzuki[b] and M. Okawa[c]

[a]Power Plant Division, Ishikawajima-Harima Heavy Industries Co.,Ltd., 3-2-16, Toyosu, Koto-ku, Tokyo, 135-8733, Japan

[b]Technical Development, Ishikawajima-Harima Heavy Industries Co.,Ltd., 1, Shinnakahara, Isogo-ku, Yokohama, Kanagawa, 235-8501, Japan

[c]New Energy and Technology Development Department, Electric Power Development Co.,Ltd., 6-15-1, Ginza, Chuo-ku, Tokyo, 104-8165, Japan

ABSTRACT

The oxygen/recycled flue gas (O_2/RFG) combustion system is one of the candidates to recover CO_2 from pulverized-coal firing boiler. Characteristics for NOx, SO_2 and CO_2 emission from the system were investigated through combustion tests in the 1.2MWt test furnace. From the results, the amount of NOx emitted from the stack is much less than ordinary air combustion, because recycled NOx is decomposed in flame. In O_2/RFG combustion, the desulfurization rate is about twice higher than that in air combustion and it is found that sulfur is effectively absorbed in ash. Almost 100 % pure CO_2 in the system can be successfully recovered in liquid. Experimental studies using a drop tube furnace were also performed to clear the desulfurization mechanism in CO_2-rich atmosphere. The results suggested that the direct desulfurization by $CaCO_3$ would be promoted in O_2/RFG combustion.

1. INTRODUCTION

The oxygen/recycled flue gas (O_2/RFG) combustion system is expected to be one of the promising systems on CO_2-recovery from pulverized-coal power plants, because it has the advantage of high plant efficiency and easy CO_2 recovery.[1] In this system, pulverized coal is fired with the mixture of oxygen and recycled flue gas. Accordingly, flue gas so rich in CO_2 can be obtained that it can be directly recovered and poured into the ground, or CO_2 can be extracted only by removing water through compression. Also, combustion proceeds under a CO_2-based atmosphere while pulverized coal is normally burnt with air, which is a N_2-based oxidant. Since CO_2 is a well-known radiative gas having a higher specific heat than N_2, it is supposed that the combustion characteristics in the system will be considerably different from that in a normal combustion system. Also the oxidant contains NOx and SO_2

recycled with flue gas. Therefore, studies were conducted to clarify the characteristics of pulverized coal combustion in the system.

Our previous studies in the area were laboratory-scale combustion testing using a vertical electrically heated flow reactor[2], numerical computational analysis[3] on its test results and the industrial-scale combustion test using a 1.2MWt horizontal cylindrical furnace[1]. These studies provided much information on the combustion characteristics in O_2/RFG. One characteristic is a very vague ignition point and lower flame temperature in O_2/RFG combustion, and the other is the remarkably lower NOx and SO_2 emissions.[1-3] In order to make the phenomena clear several kinds of experimental studies were carried out. In addition, CO_2 recovery from actual flue gas was demonstrated in the 1.2 MWt industrial scale testing to confirm the possibility to recover pure CO_2. In this paper, test results in 1.2MWt test furnace will be introduced and some discussions based on the experimental studies will be presented.

2. NOx AND SO_2 EMISSIONS AND CO_2 RECOVERY

Our previous studies on industrial-scale combustion test facilities showed that NOx emissions from the O_2/RFG combustion system were greatly reduced to about 25 % compared with conventional air combustion. On the other hand, the staged combustion is normally applied to coal fired boilers to reduce NOx emissions, NOx reduction down to about 25 % is attained compared with non-staged combustion. Accordingly, staged combustion tests for the O_2/RFG combustion system were carried out in the industrial scale testing. The transition of sulfur in the system was also investigated in the test since previous industrial scale tests had indicated that the system produced remarkably lower SO_2 emissions. The O_2/RFG combustion system is also characterized with direct CO_2 recovery from the flue gas. However, flue gas from pulverized coal combustion includes the impurities, N_2, O_2, NOx and so on for CO_2 recovery. Studies were therefore performed to demonstrate the separation of pure CO_2 from flue gas.

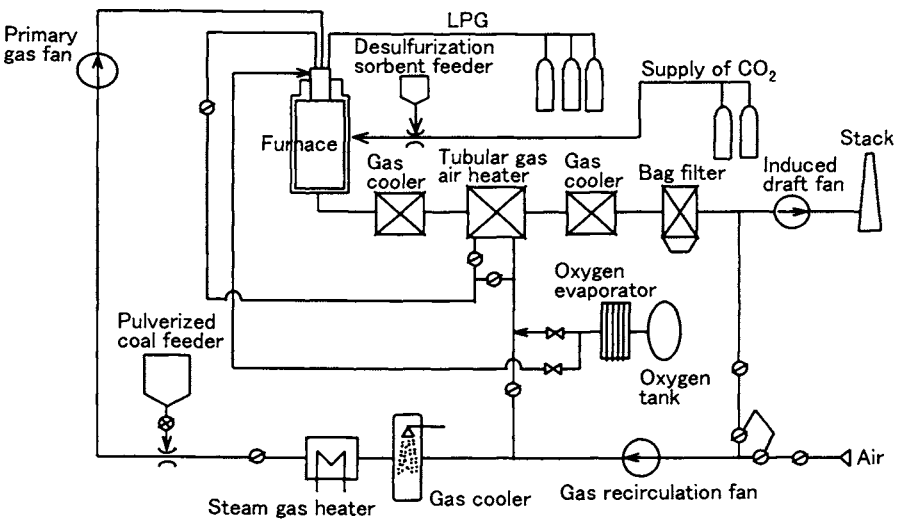

Fig. 1. The flow diagram of 1.2 MWt industrial-scale combustion test facilities

2.1. Experiment

Test on O_2/RFG combustion of pulverized coal was conducted using 1.2MWt industrial-scale test facilities shown in Figure 1. The furnace is a vertical cylindrical type with a water jacket lined with refractory. Its size is 1.3 m in diameter and 7.5 m in length. In the O_2/RFG combustion, the greater part of flue gas was taken out at the downstream of a bag filter and was recycled to be used as primary gas for transporting pulverized coal and as secondary gas for combustion. Oxygen was supplied from a liquefied oxygen tank through an evaporator and was mixed with secondary gas. A part of oxygen could be directly injected into the burning area through the center of the burner to help the combustibility. A part of secondary gas is taken out and injected into the furnace through three staged-air-ports for staged combustion.

Combustion tests were performed for normal air-blown combustion and O_2/RFG combustion at the constant flue gas oxygen concentration of 3.5%. In the O_2/RFG combustion tests, oxygen concentration in the flue gas was controlled in 3.5 % by oxygen flow rate, and oxygen concentration in the burner wind box was controlled in 30 % by recirculation gas flow rate. Two kinds of bituminous coal, whose properties are listed in Table 1, were fired at the firing rate of 100 kg/h. In case of desulfurization test, desulfurizing sorbent $CaCO_3$ (average diameter ; 8.4 mm) was directly injected into the furnace to adjust the Ca/S mol ratio.

2.2. Results and discussions

2.2.1. NOx emission

Figure 2 shows the relationship between the excess oxygen ratio λ_1 at the burner and the conversion ratio η_N of fuel nitrogen into NOx when coal A was fired for air combustion and O_2/RFG combustion with or without direct O_2 injection. Where, since the flame temperature was 1,400 ℃ at most, η_N was calculated assuming that NOx was produced from only organic nitrogen in coal. It can be seen from the figure that in air combustion, η_N takes a very high value over 30 % without staging, while it decreases rapidly down to 5-7 % by staging. On

Table 1 Coal properties

Coal		A	B
Heating value	(MJ/kg)	28.5	29.6
Fuel ratio	(−)	2.1	1.6
Proximate analysis			
Moisture	(%, ad.)	2.8	3.3
Ash	(%, dry)	15.8	12.7
Volatile matter	(%, dry)	27.5	33.7
Fixed carbon	(%, dry)	56.7	53.7
Ultimate analysis			
Carbon	(%,dry)	70.4	72.7
Hydrogen	(%,dry)	4.3	4.7
Oxygen	(%,dry)	1.4	1.6
Nitrogen	(%,dry)	7.9	8.2
Sulfur	(%,dry)	0.3	0.8

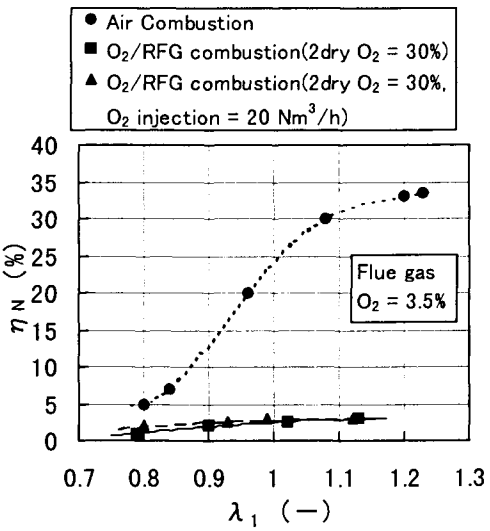

Fig. 2. The relationship between the excess oxygen ratio λ_1 at the burner and the conversion ratio η_N of fuel nitrogen into NOx

the other hand, η_N is remarkably low around 3 % in O_2/RFG combustion even without staging. It must be noted that the amount of NOx emission is reduced to the level which can not be attained in air-blown combustion even with deep staging. The reason is because NOx in recycled flue gas is mostly decomposed in flame. However, η_N is reduced to only a half or one third at most by staging in O_2/RFG combustion because the decomposition of NOx in staged gas is not so active due to a lack of reducing components.

2.2.2. SO_2 emission

Limestone or dolomite is a well-known good sorbent removing SO_2 from combustion gases in a fluidised bed burning coal.[4-7] The typical desulfurization process is said as follows. CaO is first produced in a porous condition by heating limestone or dolomite through calcination reaction represented by the following equation.

$$CaCO_3 \Leftrightarrow CaO + CO_2 \quad (1)$$

And then CaO reacts with SO_2 as following overall reaction.

$$CaO + SO_2 + 1/2\ O_2 \Leftrightarrow CaSO_4 \quad (2)$$

As mentioned above, Ca in the ash seems to play an important role in low SO_2 emission in O_2/RFG combustion.

A survey was therefore conducted on the behavior of sulfur components to confirm the relationship between sulfur absorbed in ash at the furnace and sulfur exhausted from the stack. Combustion tests were carried out using two coals shown in Table 1 for the various Ca/S mol ratios with injecting $CaCO_3$ into the furnace. Figure 3 shows the results on the desulfurization rate η_D, that is the ratio of the amount of sulfur captured in the system to sulfur content in coal, for both O_2/RFG combustion and air combustion. In O_2/RFG combustion, a good relationship can be seen between η_D and Ca/S ratio indepent on the kind of coal, and η_D

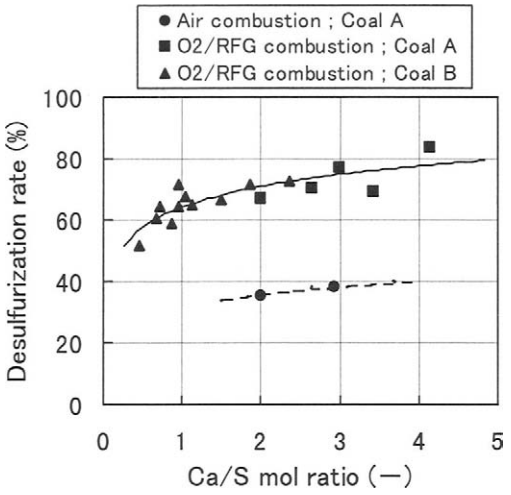

Fig. 3. Comparison of desulfurization rate between O_2/RFG combustion and air combustion

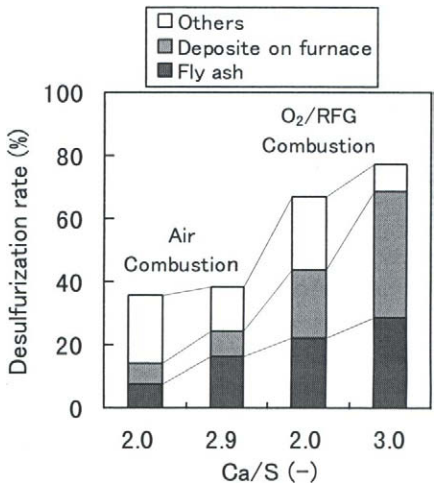

Fig. 4. The details of desulfurization rate

gradually increases with the increase of Ca/S mol ratio. Also, it is clearly found that the value of η_D in O_2/RFG combustion is about twice higher than that in air combustion. Figure 4 shows the details of sulfur captured in the system for the case that Ca/S mol ratios are 2.0 and about 3.0. It is found from the figure that the sulfur is mainly absorbed in ash for both cases, almost a half in fly ash and another half in deposit on furnace wall. The results mean that the η_D becomes higher in the O_2/RFG combustion because the sulfur is effectively absorbed in ash. Higher SO_2 concentration in O_2/RFG combustion is beleived to promote desulfurization.

2.2.3. CO_2 Recovery

In order to confirm the performance of the CO_2 recovery system applied to O_2/RFG combustion system, CO_2 recovery facilities shown in figure 5 were combined with 1.2MWt combustion test facilities. The facilities were composed of a gas cooler, two flue gas compressors and a pressure vessel. A part of recycled flue gas was taken out from the

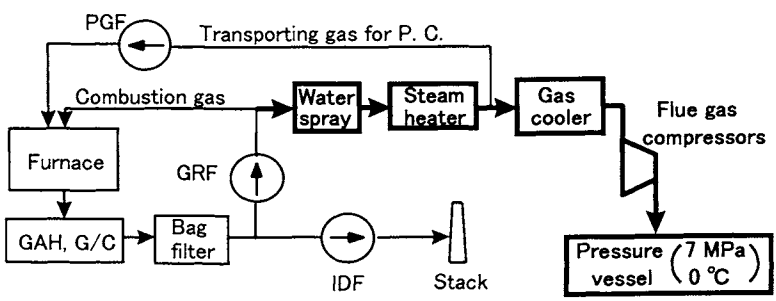

Fig. 5. Flow diagram to recover CO_2 in O_2/RFG combustion (bold)

primary gas line after the water spray and steam heater to reduce H_2O content in flue gas. The rest of H_2O in flue gas was lastly drained in the gas cooler before the flue gas compressors. Test was conducted at the condition of 7 MPa and 0 ℃ in the pressure vessel when coal A was fired, and chemical analysis of liquefied flue gas was carried out using gas chromatography. The component in liquid recovered in the pressure vessel was almost 100 % pure CO_2, as was theoretically supposed, and impurities of NOx, SO_2 and so on were not detected. The test proceeded very successfully and it was confirmed that O_2/RFG combustion was one of the easy systems for CO_2 recovery from pulverized coal fired power plants.

3. FUNDAMENTAL TEST ABOUT DESULFURIZATION

O_2/ RFG combustion system is characterized with combustion under a CO_2-rich atmosphere. In such CO_2-rich condition it is said that the calcination reaction denoted by the equation (1) is not easy to proceed. Therefore, it is supposed that the desulfurization reaction will be considerably different from that in normal air combustion. Tests were carried out using a drop tube furnace to investigate the desulfurization characteristics in O_2/RFG combustion.

3.1. Experiment

The fundamental desulfurization characteristics in O_2/RFG combustion were experimentally studied using a vertical electrically heated flow reactor. The schematic

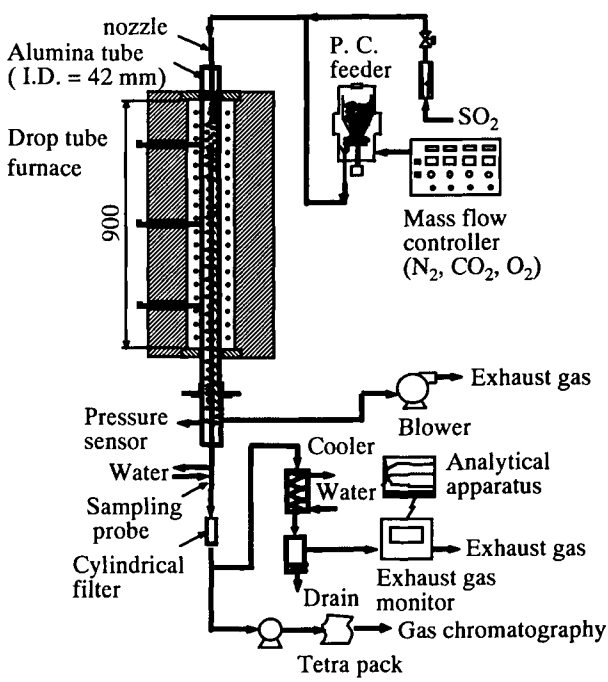

Fig. 6. Drop tube furnace apparatus

diagram of the equipment is shown in figure 6. The reactor body was an alumina tube (47 mm in inner diameter and 1.2 m in length), which was heated in a three-element electric furnace with a 900 mm long heating part. Gas supplied as oxidant was a mixture of 21% O_2, 79% CO_2 or N_2 and 3,000ppm SO_2 and it was divided into two streams, primary gas and secondary gas. Each constituent gas was supplied through mass flow controller. Pulverized $CaCO_3$ (8.4 mm in average diameter, the same sorbent used in 1.2MWt combustion test) was fed from the top of the reactor through a turntable-type microfeeder and it was carried by primary gas. Gas was sampled using a sampling probe inserted from the bottom end of the reactor. The sampling probe was a water-cooled triple tube, and the temperature of cooling water was kept to 70 ℃ so as to prevent a water vapor in sampled gas from condensing. The sampling piping connecting to the sampling probe was also heated to around 100 ℃ for the same reason. Experiments were carried out under O_2/N_2 or O_2/CO_2 atmosphere at the furnace temperature between 750 and 1350 ℃. Pulverized $CaCO_3$ feed rate was controlled to 0.5 g/min in order to keep Ca/S mol ratio to be 3.5.

3.2. Results and discussions

Firstly, the temperature profile in the reactor was examined because the specific heat of CO_2 was much higher than that of N_2 and some difference in temperature distribution was expected between O_2/CO_2 and O_2/N_2 atmosphere. As shown in figure 7, gas temperature became stable at the distance of 300 mm from the nozzle in both atmospheres, and it was confirmed that the difference of temperature between O_2/N_2 and O_2/CO_2 atmosphere could be ignored. Then, experiments were carried out to investigate the effect of oxygen concentration and temperature on the desulfurization rate. Figure 8 shows the dependence of the desulfurization rate on oxygen concentration under the O_2/N_2 or O_2/CO_2 at 1,250 ℃. The desulfurization rate was calculated from the difference of SO_2 concentration at the exit of reactor with or without feeding $CaCO_3$. From a result, it is suggested that desulfurization characteristics are scarcely depended on oxygen concentration because a very small amount of oxygen is needed for $CaCO_3$ to react with SO_2 of 3000 ppm. Figure 9 shows the affect of

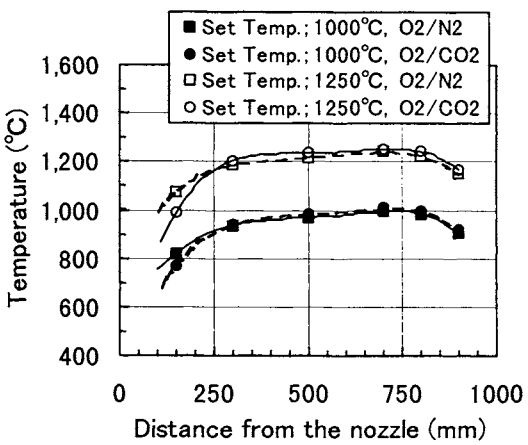

Fig. 7. Temperature profile at the O_2/N_2 and O_2/CO_2 atmosphere

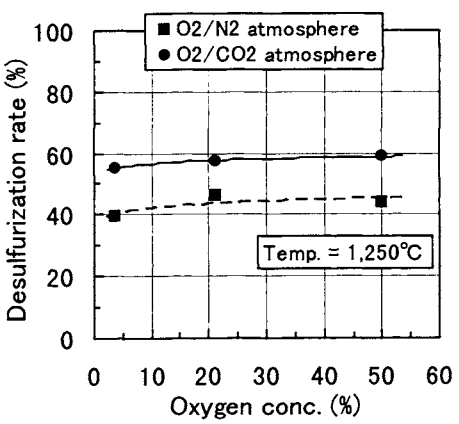

Fig. 8. The dependence on O_2 conc. at the O_2/N_2 and O_2/CO_2 atmosphere

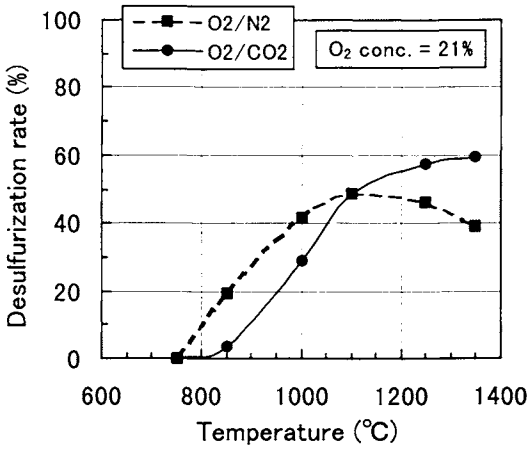

Fig. 9. The temperature dependence at the O_2/N_2 and O_2/CO_2 atmosphere

temperature when supplied oxygen concentration was 21%. From the figure, in the O_2/N_2 atmosphere, although desulfurization does not occur at 750 ℃, the desulfurization rate increases as temperature increases from 750 ℃. After it reaches to a peak value of about 50 % at around 1,100 ℃, it gradually decreases with increase of temperature. Since the calcination reaction easily proceeds in O_2/N_2 atmosphere without CO_2, the dominant desulfurization reaction is thought to be proceeded through the calcination as shown in equation (1) and (2). The decrease of desulfurization rate at higher temperature is thought to be due to the decomposition of $CaSO_4$.

On the other hand, in the O_2/CO_2 atmosphere, the desulfurization initiation temperature is around 850 ℃, which is higher than that in O_2/N_2 atmosphere, and η_D increases as temperature increases. η_D takes lower value than in O_2/N_2 atmosphere up to about 1,100 ℃, however it continues increasing at above 1,100 ℃ taking higher values than in the O_2/N_2 atmosphere. The results seem to mean that both the calcination of $CaCO_3$ and the decomposition of $CaSO_4$ are delayed in O_2/CO_2 atmosphere. The process will be explained as follows. That is, due to the delay of the calcination reaction, which is easily understood in CO_2-rich condition, the dispersion of SO_2 and O_2 into the limestone particle is promoted. Accordingly, the desulfurization will occur even at inside of the limestone particle, where the following direct desulfurization may also occur.

$$CaCO_3 + SO_2 + 1/2\ O_2 \Leftrightarrow CaSO_4 + CO_2 \quad (3)$$

Since $CaSO_4$ is distributed relatively, widely and deeply in the particle, the decomposition reaction of $CaSO_4$ is not so active in the O_2/CO_2 atmosphere.

4. CONCLUSIONS

In O_2/RFG combustion, to make clear the characteristics of NOx and SO_2 emissions and to demonstrate of CO_2 recover from the actual esxhaust gas, studies have been carried out using 1.2MWt combustion test facilities and a drop tube furnace. The followings are concluded in O_2/RFG combustion.

- The conversion ratio of fuel nitrogen into NOx is remarkably low. This is mainly due to the decomposition of recycled NOx in the flame.
- The desulfurization rate is twice higher than that in air combustion and sulfur is effectively absorbed in ash, because higher SO_2 concentration in O_2/RFG combustion is beleived to promote desulfurization.
- Almost 100% pure liquefied CO_2 was easily recovered in pulverized-coal O_2/RFG combustion and it is also suggested that impurities can be separated from liquefied CO_2.
- The results of experimental studies on desulfurization mechanism suggested that the direct desulfurization by $CaCO_3$ would be promoted under O_2/CO_2 atmosphere.

REFERENCES

1. T. Yamada, T. Kiga, M. Okawa, K. Omata, N. Kimura, K. Arai, T. Mori and M. Kato, *JSME Int. J.*, Vol. 41, No. 4, (1998) 1017-1022.
2. K. Kimura, S. Takano, T. Kiga, S. Miyamae, Y. Noguchi and Y. Tanaka, *Proceedings of JSME-ASME Int. Conf. on Power Eng.-93*, Vol. 1 (1993) 487-492.
3. S. Watanabe, Y. Endo, T. Kiga, N. Kimura and M. Okawa, *Proceedings of the 1997 Int. Joint Power Generation Conf.*, EC-Vol. 5, Vol. 1 (1997) 239-246.
4. M. J. H. Snow, J. P. Longwell and A. F. Sarofim, *Ind. Eng. Chem. Res.*, 27, (1988) 268-273.
5. J. B. Illerup, K. Dam-Johansen and K. Lunden, *Chem. Eng. Sci.*, Vol. 48, No. 11, (1993) 2151-2157.
6. C. Tullin, G. Nyman and S. Ghardashkhani, *Energy & Fuels*, 7, (1993) 512-519.
7. Z. Ye, W. Wang, Q. Zhong and I. Bjerle, *Fuel*, Vol. 74, No. 5, (1995) 743-750.

Reaction Engineering for Pollution Prevention
M.A. Abraham and R.P. Hesketh (Editors)

The Need and Options Available for Permanent CO_2 Disposal

Hans-J. Ziock*, Darryl P. Butt**, Klaus S. Lackner, Christopher H. Wendt
Los Alamos National Laboratory, Los Alamos, NM 87545, USA

Inexpensive, readily available energy is the cornerstone of modern society and the basis of a decent standard of living. The high probability of future restrictions on CO_2 emissions has put in question the use of fossil fuels, the largest, most convenient, and most cost-effective energy resource available. The rapidly growing world population, the need for an improved standard of living worldwide, and the nearly linear dependence of the standard of living on energy consumption, all coupled with the magnitude of today's CO_2 emissions point to an impending crisis. We briefly review the problem and look at the available options. We conclude that for the foreseeable future, fossil fuels will continue to dominate the world energy market, but that CO_2 disposal will be required. Of the possible disposal options, mineral sequestration of CO_2 appears as an extremely promising, permanent, and environmentally benign disposal option.

1. INTRODUCTION

Abundant, clean, low cost energy is critical to the future of not only the U.S., but also the world as a whole. Present day energy sources at best provide only two of these three properties. If environmental impact would not limit energy production, cost and abundance become the driving terms. Fossil fuels are by far the lowest cost energy source currently available. Today they account for ~85% of the world's energy supply. After some concern about their long-term availability in the past decades, it is now realized that there are sufficient reserves to last for centuries to come. For instance, global coal reserves are put at 10,000 gigatons (Gt)[1], whereas the world's yearly consumption of carbon is only ~6 Gt. The only remaining issue for fossil fuels today is their environmental impact, in particular, the large CO_2 emissions resulting from their use. The emissions will continue to grow rapidly as the world population roughly doubles in the next 50 years and it strives to achieve, if not exceed, the standard of living found in the U.S. today. In turn, the effects of CO_2, which include global warming, ocean acidification, and ecological change, will also increase well beyond a non-negligible level. To set the scale, the atmospheric CO_2 concentration has risen by 30% over its pre-industrial age value of 280 ppm to over 365 ppm today. Yearly increases are accelerating from their present value of 1.7 ppm/yr and would already be ~3 ppm/yr were it not for a rather large driving force that drives the CO_2 level back towards its

* Corresponding Author: Mail Stop H846, Phone: 505-667-7265; fax: 505-665-7920; E-mail: ziock@lanl.gov.
** Now with Ceramatec, Inc., Salt Lake City, UT 84119.

pre-industrial equilibrium value. The size of the associated sinks and their capacity is currently not well known.

The competitors to fossil fuels face their own problems. The promise of unlimited nuclear power, too cheap to meter, has never come to pass, and today in the U.S., nuclear power is a factor of ~2 more expensive than fossil power. Nuclear power also faces environmental issues of its own, which still remain unaddressed. Furthermore nuclear power creates serious proliferation problems and is opposed by a substantial fraction of the U.S. population. Despite these problems, some other countries have adopted nuclear power. These countries typically view a lack of domestic fuel as a more pressing problem. When coupled with the spiraling fossil fuel prices of the 70's the decision to adopt nuclear power was not difficult for these countries. Given that fossil fuel reserves are abundant in the U.S., that the price escalation of the 70's was not permanent, and that there are widespread public concerns that exist about nuclear power, the main purpose that nuclear power serves today is to set an upper price bound. For fossil fuels to remain viable, their cost including CO_2 disposal must remain under that of nuclear power and all other alternative energy sources. Of course, it is possible that nuclear energy becomes more attractive with technology improvements. However, the same can be said for fossil energy, which starts from a much better economic position.

Most renewable energy sources are more expensive than nuclear power and thus areat an even greater disadvantage. The majority of renewable energy forms ultimately derive their energy from sunlight. The energy density in sunlight is very low. This is further aggravated by the low conversion efficiencies of most solar collectors (photoelectric devices ~ 10–15% efficient, plants ~ 1% efficient). The more price competitive renewable energy sources such as hydroelectric and wind, which rely on natural energy concentrators, are too scarce to satisfy global energy demand. Thus, they do not provide a viable solution to the overall problem.

Attempts to use biological means to achieve disposal of anthropogenic CO_2 will at best provide temporary relief. Biological approaches will have a huge impact on the environment if they attempt to address the full scale of the future problem. Photosynthesis requires energy to turn CO_2 into organic carbon. The energy required is more than is obtained in the combustion of coal. Given the dilute nature of sunlight (~200 W/m^2 global average) and the typical efficiency of plants to sink carbon (~1%), anthropogenic CO_2 emissions that are 10 times that of today would require an area of almost $1/15^{th}$ of the world total surface area. As atmospheric CO_2 levels were in equilibrium before the industrial revolution, attempts to store large amounts of additional carbon as biomass will take one away from the natural biological equilibrium that had existed previously. Unless biomass is sequestered itself, for example in the deep ocean, biological solutions will have to artificially maintain a level of stored biomass that is substantially higher than the natural level. This would imply a legacy for future generations who would have to continuously pay for today's carbon dioxide emissions.

Low cost energy is imperative not only from a competitive point of view, but more importantly it is the generator of wealth, as energy is used to produce virtually all products. This is illustrated in Fig. 1, where it is shown that there is a linear relation between energy

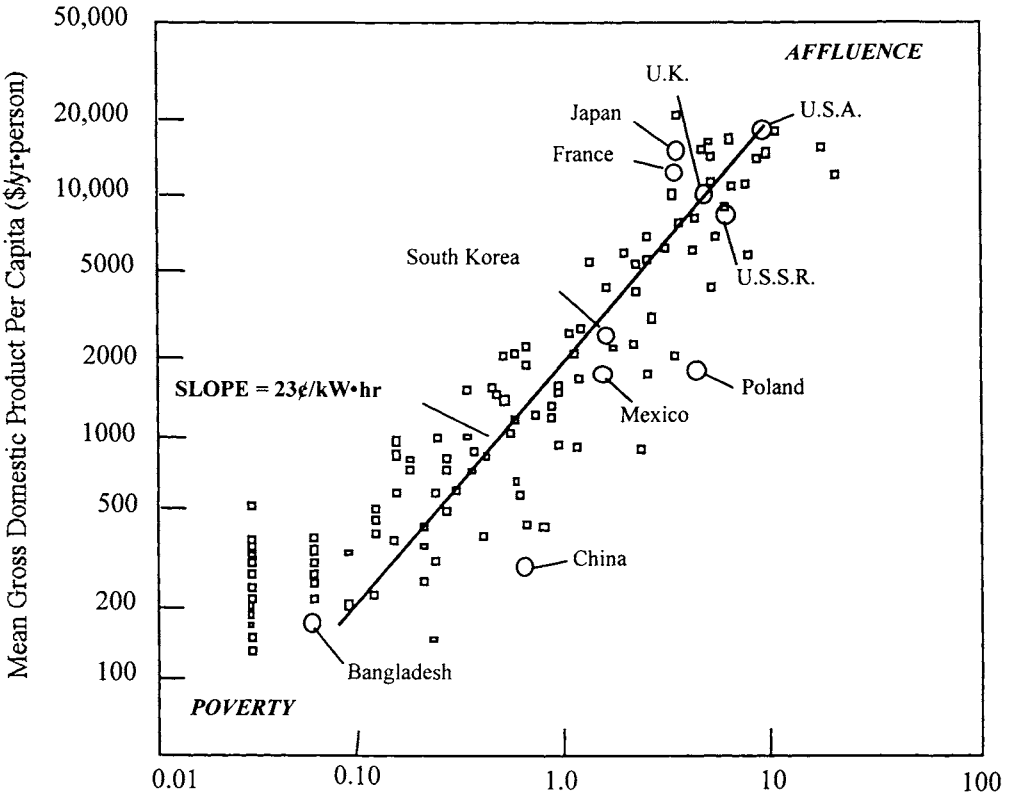

Fig. 1. The relation between energy consumption and GDP, which is essentially equivalent to wealth[2]. Although plotted on a log-log scale, the relation is indeed linear as shown by the line which corresponds to 23¢ of GDP/kW-hr of raw energy consumption. Even though there is a scatter of about a factor of 2 for the individual points, the overall relation is valid over two orders of magnitude.

consumption per person and gross domestic product (GDP) per person. The relation holds over several orders of magnitude, from the richest to the poorest countries. It is the poor counties that can least afford high energy prices as they have little money to spend on energy supply. An immediate corollary is that with increasing energy prices, poorer countries will have an ever more difficult time extracting themselves from poverty. These countries, which dominate the world population, are the ones that most desperately need low energy prices. Due to their large populations, they will also in time be the world's dominant energy consumers and therefore CO_2 emitters. If CO_2 disposal is not low cost, it will not be adopted by the poorer countries who would be tempted to adopt the cheapest solution which is to emit the CO_2 into the atmosphere.

The task before us is to find a means of disposing CO_2 from the combustion of fossil fuels at a cost that keeps fossil energy competitive with all major alternative energy sources. This will be demanded by the free market economy. In addition to low cost, any proposed solution for disposing of CO_2 must have the following additional features:

- Acceptable to the population at large,
- Able to deal with the scale of fossil fuel reserves,
- Provide a permanent means of disposal (leave no legacy issues for future generations),
- Consume little or no net energy, and
- Be environmentally sound.

For the last item, it is important to emphasize that this must really be measured on a relative scale. Given the scale of global energy consumption and its likely substantial increase in the future, any energy source will have a measurable impact on the environment; the relevant concern is the relative size of the impact.

2. MINERAL CO_2 DISPOSAL

It was suggested by Seifritz[3] that it might be possible to dispose of CO_2 in the form of mineral carbonates. We have investigated this option in considerable detail and find it is indeed an extremely promising option. Mineral sequestration is a disposal option that achieves the criteria put forward in the above section.

CO_2 reacts exothermically with silicates of alkaline earth metals to form thermodynamically stable carbonates that are environmentally benign. The carbonation reactions are actually part of the natural carbon cycle and huge deposits of stable carbonates exist in the form of magnesium and calcium carbonates. Magnesium and calcium ions are also responsible for most of the CO_2 storage in the oceans, without the otherwise associated lowering of pH. In nature, the carbonation reactions operate on a time scale much too slow to deal with current manmade emissions.

The silicates of alkaline earth metals are of particular interest due to their large abundance in the Earth's crust[4]. After more careful evaluation[5], we have chosen to pursue magnesium silicates, as these are available in huge deposits throughout the world[6]. Furthermore, the magnesium silicate deposits contain a very large weight-percentage of magnesium oxide (35-50%), which is the basic component needed to form the carbonate. Magnesium silicates of interest are olivines and serpentines. The deposits are sections of the oceanic crust/upper mantle, which were thrust up onto land. As such, they are found in extensive deposits at present and former continental boundaries as shown in Fig. 2. The most prevalent useful silicate deposits are in the form of serpentinite, which is a relatively soft rock. The nature and hardness of the deposits make them suitable to open pit mining. The mining and initial ore processing operations that are involved are similar to that in the copper industry. The scale of an operation required for a 1 GW coal-fired power plant operating at 33% efficiency is nearly identical to that of large open pit copper mines currently in operation[7]. It is also important to note that the serpentine mining operation, in terms of earth moved, is less than 1/3 the size of the strip mining operation typically required to obtain the coal that feeds the power plant. In terms of surface area disturbed, it is even smaller

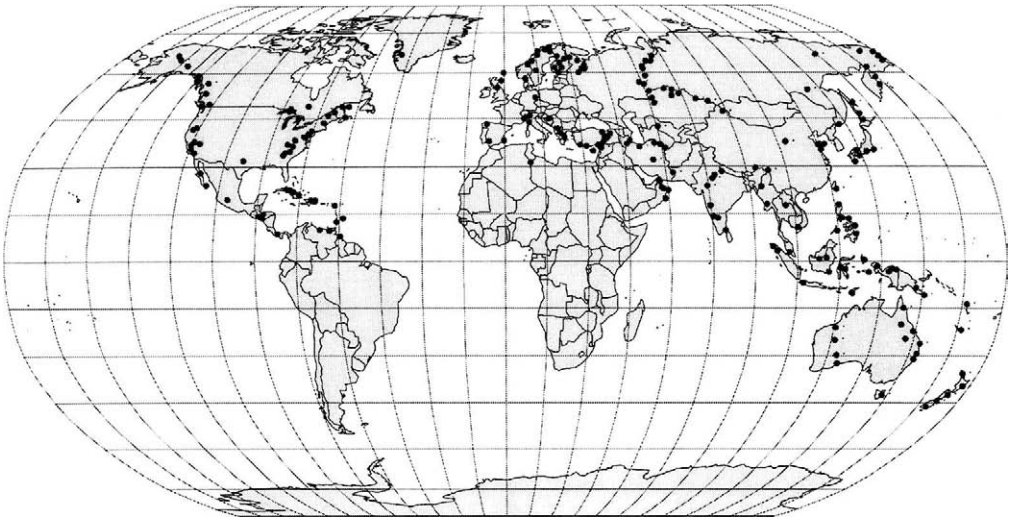

Fig. 2. Known major peridotite or serpentinite deposits. As can be seen, the deposits tend to lie along continental margins or former continental boundaries.

given the large thickness of typical serpentinite deposits relative to coal deposits. Based on the volumes involved and the cost of the combined operations of mining, crushing, milling, and disposal of the tailings in the copper industry, which are very similar to the needed up front processing for the CO_2 disposal operation, one can derive an estimate of \$9/ton of CO_2

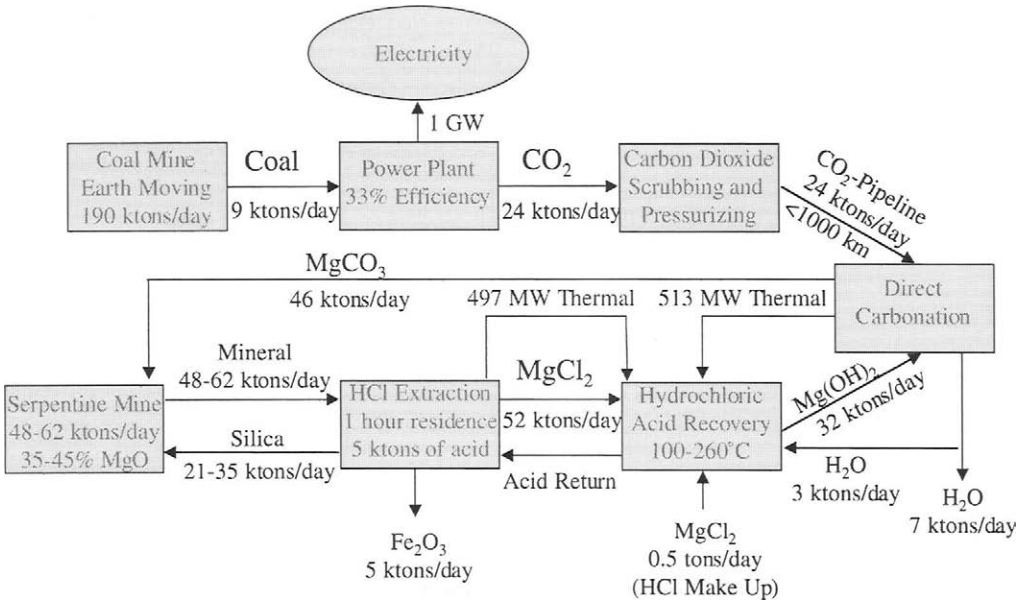

Fig. 3. Material and heat flows for the aqueous HCl mineral carbonation process for a coal-fired 1 GW electric power plant assumed to run at 33% efficiency. Coal strip mining is assumed. The indicated heat flows are idealized values. The input heat is likely to be considerably greater than given and only a fraction of the output heat will be useful.

required processing equipment, the cost of any required make-up feedstock other than serpentine, and the possible need for external energy input.

We have established one reaction series as a proof of principle which showed that the overall carbonation process can be carried out in a useful and affordable time frame[8]. The reaction series is based on the dissolution of the serpentine in a hydrochloric acid bath to yield $MgCl_2$ along with water and silica. Through a series of steps, the hydrochloric acid is recovered for reuse and $Mg(OH)_2$ is formed and subsequently carbonated. The material and heat flows for this process are shown in Fig. 3. Although the kinetics of this process have been shown to be favorable, the process is found to require substantial inputs of external energy in spite of the fact that it is exothermic overall by 63.6 kJ/mole CO_2 for pure serpentine. The need to input external heat is due to the loss of otherwise useful heat by the aqueous and therefore necessarily low temperature steps, the repeated need to remove water by evaporation, and the deep energy well of the $MgCl_2 \cdot 6H_2O$, which is a necessary intermediate product. We have examined the thermodynamics of the hydrated $MgCl_2$ system over a broad temperature and pressure range in a series of internal reports[9,10,11], which are partially summarized in a recent conference presentation[12]. This analysis identifies the limiting step in terms of heat input as the partitioning of Mg(OH)Cl into $Mg(OH)_2$ and

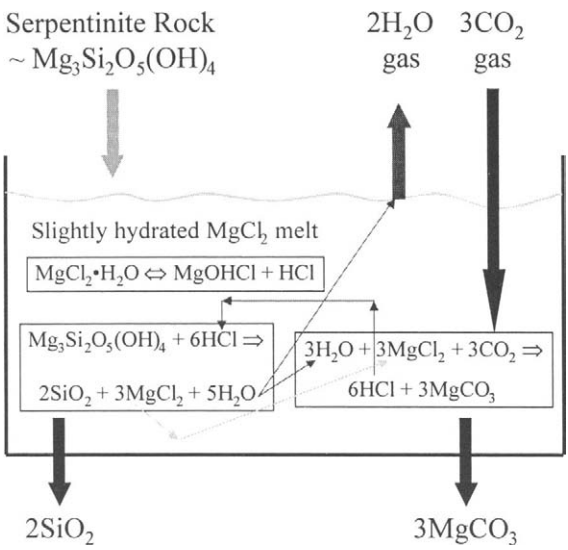

Fig. 4. A schematic diagram of the molten salt process.

$MgCl_2 \cdot nH_2O$, which, regardless of temperature and pressure, is found to require a value of at least 6 for n.

While investigating the overall $MgCl_2 \cdot nH_2O$ system we identified various alternative reaction routes including reduced water versions of the aqueous process and molten salt processes. Although considerable reductions in the need for external energy input were achieved for the reduced water aqueous processes, a version that required no external energy input was not found. However, a slightly hydrated (n = 1–2) molten salt process was identified from which net heat could in theory be extracted. The process is sketched in Fig. 4 and takes place as a continuous process in a single reaction vessel. The process relies on the existence of a significant partial pressure of HCl which is built up in the melt at higher temperatures (~300°C) as an equilibrium is established between $MgCl_2 \cdot H_20$ and Mg(OH)Cl + HCl. Although the thermodynamics do not quite favor the self-sustaining dissolution of serpentine in such a melt, this situation is nearly achieved as the Gibbs free energy for this process approaches zero. Thermodynamic calculations show that the simultaneous introduction of a substantial CO_2 partial pressure (20-30 atm) does result in a self-sustaining reaction, provided the CO_2 partial pressure is maintained. In such a situation, the CO_2 reacts with the $MgCl_2$ and water to yield $MgCO_3$ and HCl, the latter being recycled. In this process the starting, slightly hydrated, $MgCl_2$ molten salt is not consumed. Instead, it effectively acts as a catalyst, and in all likelihood provides the kinetics typically associated with molten salt reactions. The predictions of the thermodynamic calculations have yet to be established. We are just beginning to investigate this process experimentally. The corrosive nature of the process coupled with the required elevated temperatures and pressures has limited the work achieved to date. Additional issues that will need to be addressed include the continual dilution of the salt by the water produced from the serpentine, the required separation of the SiO_2 and $MgCO_3$ from the molten salt, the corrosive nature of the process, and the potential formation of various sorel cements[13].

Another reaction process that we are pursuing is the direct gas solid reaction between CO_2 and serpentine, or some of the decomposition products of serpentine. At temperatures of ~ 500°C and pressures of ~ 300 atm, the reaction proceeds rapidly to completion. As the reaction takes place in a single step, heat extraction is again possible. Furthermore, unlike the molten salt process, in this case the end products are pure and thus no separation steps are needed. The issue that remains to be addressed is the needed lowering of the pressure, which

is required to make the process economical. This must be done without compromising the kinetics that are achieved at the higher temperatures allowed by the higher pressures. ($MgCO_3$ becomes unstable, decomposing into MgO and CO_2, at these temperatures when at

lower pressures.)

As a final route for mineral sequestration we are looking at the feasibility of using underground disposal through the injection of supercritical CO_2. Unlike conventional underground CO_2 disposal options, our goal is to choose appropriate injection sites where the CO_2 is able to chemically bind with the strata into which it is injected. Such an approach would again yield permanent disposal of the CO_2, unlike other underground disposal options where there always exists the potential for the CO_2 to escape at a later date. This idea was pursued for a short period of time[14,15], but before a thorough understanding of the feasibility of this option could be established, the work stopped due to a lack of funding. This underground disposal option opens up additional areas for CO_2 disposal given that much lower concentrations of the appropriate binding minerals are now allowable. The allowable time scale for the carbonation reactions also becomes much longer than in an industrial process as one no longer has to pay for the large holding volumes required. Furthermore, longer reaction times are actually desired. The rock is apt swell upon carbonation thereby sealing off channels through which the injected fluid could otherwise flow. One would prefer time constants that allow the strata in the large area fed by a single well to be thoroughly permeated with CO_2 before significant swelling occurs. Time scales measured in years are appropriate; long enough to keep well numbers and therefore costs down, yet short

[5] Fraser Goff and K. S. Lackner, "Carbon Dioxide Sequestering Using Ultramafic Rocks." Environmental Geocsciences, **5**, #3 (1998), pp. 89-101.

[6] R. G. Coleman, *Ophiolites*, Springer-Verlag, Berlin: (1977).

[7] Klaus S. Lackner, Darryl P. Butt and Christopher H. Wendt, "Magnesite Disposal of Carbon Dioxide," The Proceedings of the 22nd International Technical Conference on Coal Utilization & Fuel Systems, March 16-19, 1997, Clearwater, Florida, U.S.A, pp. 419-430.

[8] Klaus S. Lackner, Darryl P. Butt & Christopher H. Wendt, "Progress on Binding CO_2 in Mineral Substrates," Energy and Conservation Management, **38** Suppl, S259-S264, (1997).

[9] C.H. Wendt, D.P. Butt, K.S. Lackner, and H-J Ziock, "Thermodynamic Calculations for Acid Decomposition of Serpentine and Olivine in $MgCl_2$ Melts- I: Description of Concentrated $MgCl_2$ Melts," Los Alamos National Laboratory Report, LAUR-98-4528, July 27, 1998, 22 pp.

[10] C.H. Wendt, D.P. Butt, K.S. Lackner, and H-J Ziock, "Thermodynamic Calculations for Acid Decomposition of Serpentine and Olivine in $MgCl_2$ Melts- II: Reaction Equilibria in $MgCl_2$ Melts," Los Alamos National Laboratory Report, LAUR-98-4529, October 7, 1998, 28 pp.

[11] C.H. Wendt, D.P. Butt, K.S. Lackner, Raj Vaidya, and H-J Ziock, "Thermodynamic Calculations for Acid Decomposition of Serpentine and Olivine in $MgCl_2$ Melts- III: Heat Consumption in Process Design," Los Alamos National Laboratory Report, LAUR-98-5633, November 25, 1998, 23 pp.

[12] Christopher H. Wendt, Darryl P. Butt, Klaus S. Lackner & Hans-Joachim Ziock, "Thermodynamic Considerations Of Using Chlorides To Accelerate The Carbonate Formation From Magnesium Silicates," to appear in the proceedings of the Fourth International Conference on Greenhouse Gas Control Technologies, Interlaken, Switzerland, August 30 - September 2, 1998.

[13] W. F. Cole and T. Demeduck, Aust. J. Chem., **8** (1955), 234.

[14] E.H. Perkins and W. D. Gunter, "Mineral traps for carbon dioxide," in *Aquifer Disposal of Carbon Dioxide, Hydrodynamic and Mineral Trapping – Proof of Concept*, Brian Hitchon (editor), Geoscience Publishing Ltd., (1996), 93-113.

[15] W. D. Gunter, B. Wiwchaw and E.H. Perkins, "Autoclave experiments and geochemical modeling," in *Aquifer Disposal of Carbon Dioxide, Hydrodynamic and Mineral Trapping – Proof of Concept*, Brian Hitchon (editor), Geoscience Publishing Ltd., (1996), 115-141.

Reaction Engineering for Pollution Prevention
M.A. Abraham and R.P. Hesketh (Editors)

An analysis of the disposal of anthropogenic CO_2 in the ocean via a submerged hydrate crystallizer

A. Yamasaki[a], H. Teng[b], M. Wakatsuki[a], Y. Yanagisawa[a], and K. Yamada[a]

[a] Department of Chemical System Engineering, The University of Tokyo,
7-3-1 Hongo, Bunkyo-ku, Tokyo, 113-8656, Japan

[b] National Institute of Materials and Chemical Research
1-1 Higashi, Tsukuba 305, Japan.

A new scenario for disposal of the anthropogenic CO_2 in the ocean is proposed. In this scenario, liquid CO_2 is injected through a submerged pipeline into a crystallizer located at a depth between 450 and 500 m in the ocean, where the injected liquid CO_2 is converted completely into hydrate particles via a crystallization process and then the hydrate particles are released into the ocean. Because of being heavier than seawater, the hydrate particles will sink and will be sequestrated in the ocean. This proposed scenario has been simulated experimentally and the simulation results, including the effect of agitation on the formation process of CO_2 hydrate particles, are reported in this study.

1. INTRODUCTION

It has become an urgent issue for the human being to mitigate the global warming: studies have shown that the global temperature might increase by 2-5 °C over the next century if no actions of reducing the CO_2 emission are taken [1]. Disposal and capture of the anthropogenic CO_2 in the ocean has been considered as a promising counteraction to the global warming [2]. Following ocean disposal scenarios have been proposed to date: (1) disposing gaseous CO_2 in shallow waters (< 200 m); (2) disposing liquid CO_2 in intermediate-depth waters (500 - 1500 m); (3) disposing liquid CO_2 in deep waters (> 3000 m); (4) disposing CO_2 in the form of dry ice; and (5) disposing CO_2 in the form of hydrate. Among these five scenarios, disposal of CO_2 hydrate in the ocean is less discussed in the literature due to insufficient understanding of the behavior of CO_2 hydrate in the ocean.

CO_2 hydrate is a clathrate compound. The crystalline structure of CO_2 hydrate is formed by linkage of water molecules via hydrogen bonding and CO_2 molecules are included, but not bonded, in the water cavities (cages). If every water cavity in a unit hydrate crystal is occupied by a CO_2 molecule, the chemical formula for CO_2 hydrate is $8CO_2 \cdot 46H_2O$ or $CO_2 \cdot 5.75H_2O$. Based on the phase diagram for the CO_2-water system [3], the stable CO_2 hydrate forms only when the system is at a high pressure and a low temperature ($p > 45$ bar and $T < 283$ K). The characteristics of CO_2 hydrate make the ocean disposal of CO_2 in the hydrate form have following advantages over other disposal methods: (1) being denser than seawater, the CO_2 hydrate released will sink in the ocean; and (2) because the rate of mass

transfer of CO_2 from the hydrate to seawater is smaller than that from gaseous, liquid or solid CO_2 to seawater in the hydrate formation region [4], the environmental impact induced by the ocean disposal of CO_2 in the hydrate form will be smaller than those by other disposal methods. Ocean disposal of CO_2 in the form of hydrate was proposed previously in a USDOE report [5]. In that proposed scenario, the liquid CO_2 captured from a thermal power plant is injected into a vessel (located at a depth of 600 m in the ocean) where the CO_2 is assumed to react with seawater and form CO_2 hydrate, and then the hydrate particles produced in the vessel can be disposed of in the ocean; because the hydrate particles are denser than seawater, the released hydrate particles descend to the seabed and are sequestered there. However, laboratory simulations of the ocean disposal process showed that when liquid CO_2 was injected into seawater the CO_2 effluent broke up into droplets and hydrate formed only as a thin film on the surface of the CO_2 droplets [6, 7]. Because the thickness of the hydrate film was very thin (in order of 10^{-5} m), the hydrate film had little effect on the bulk density of the CO_2 droplets. This implies that the CO_2 droplets covered with a hydrate film may have positive buoyancy and, thus, they may ascend to the ocean surface if the disposal depth is less than 3000 m where CO_2 becomes denser than seawater. Other hydrate disposal scenarios also can be found in the literature [8-11]. In these proposals, the hydrate is assumed to be formed in a reactor either on land or at the ocean surface. Because hydrate formation requires a high pressure and a low temperature, production of hydrate in these proposed methods would consume considerable energy for cooling and pressurizing the seawater. In addition, a pipeline blockage induced by agglomeration of hydrate particles [12] may be encountered during transporting of the hydrate particles to the disposal site where the pressure and temperature of seawater must meet the requirement by hydrate stability.

2. A NEW OCEAN DISPOSAL SCENARIO

Here we propose a new scenario for ocean disposal of anthropogenic CO_2 (Figure 1). In this scenario, CO_2 emitted from thermal power plants is captured and liquefied, and then the liquid CO_2 is transported through a submerged pipeline into a hydrate crystallizer located at a depth between 450 and 500 m in the ocean where the temperature and pressure of the seawater can satisfy those required by hydrate formation. Because the ambient seawater is used as a water source, no energy is required for pumping, pressurizing, or cooling the seawater. In the crystallizer, the seawater and liquid CO_2 introduced into the crystallizer will react to form hydrate particles. The sizes of the hydrate particles are controlled by a properly-designed crystallization process with a well organized internal circulation and agitation. Only the hydrate particles that reach desired sizes will be released. Via the crystallizer, liquid CO_2 can be converted completely into hydrate particles. Since CO_2 hydrate is denser than seawater, the hydrate particles released from the crystallizer will descend to the bottom of the ocean. Because dissolution of the hydrate particles occurs only as a surface phenomenon, the bulk density of the hydrate particles will not be disturbed during hydrate dissolution in the ocean. In addition, via controlling the particle sizes and number density of the negatively-buoyant particle plume, the environmental impact due to hydrate dissolution may be controlled at an allowable level.

Although the equilibrium conditions for formation of CO_2 hydrate have been studied intensively, they are not of much help in understanding the crystallization process proposed above because the hydrate formation in the submerged crystallizer is largely a kinetic process.

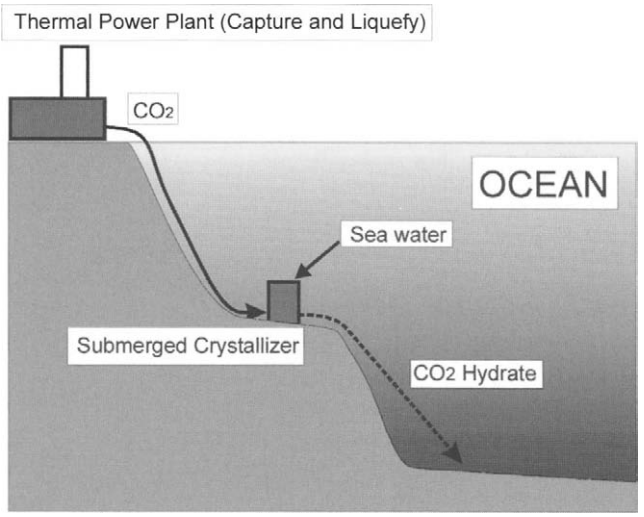

Fig. 1. Conceptual draw for the new ocean disposal scenario.

In order to evaluate the new ocean-disposal scenario, it is necessary to understand the CO_2 hydrate crystallization process at pressures and temperatures corresponding to those at depths between 450 and 500 m in the ocean and the parameters that may influence the crystallization process. For this purpose, we constructed a laboratory-scale CO_2 hydrate crystallizer to simulate the hydrate crystallization process. We believe that the laboratory simulation can offer useful information on understanding the newly-proposed disposal scenario and properly-designing the crystallization process.

3. EXPERIMENTAL

The hydrate crystallizer that we developed is shown schematically in Figure 2. The main part of the experimental apparatus was a high-pressure, low-temperature, batch-type reactor. The reactor had a coaxial structure: an inside Pyrex-glass tube with 100-mm in inside diameter, 5-mm in wall thickness, and 250-mm in length; and an outside polycarbonate tube with 120-mm in inner diameter, 60-mm in thickness, and 250-mm in length. The coaxial structure was so designed from the following two considerations: (1) the polycarbonate tube can stand pressures up to 200 bar but may react with CO_2 when it is in contact with CO_2; (2) the reactivity of Pyrex glass with CO_2 is negligibly low; however, it cannot stand a high pressure (the estimated maximum pressure for the Pyrex tube is only 20 bar). In the tests water was introduced to the gap between the Pyrex and polycarbonate tubes and liquid CO_2 and water were introduced into the inside of the Pyrex tube. The difference in pressures of

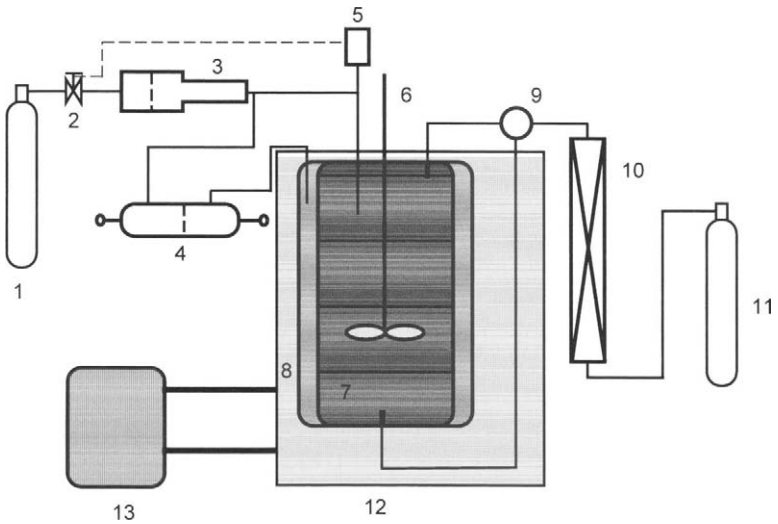

Fig. 2. Schematic drawing for the experimental apparatus

1. N_2 cylinder (for pressure controller), 2. Solenoidal valve, 3. Pressure controller, 4. Pressure equilibrator, 5. Pressure sensor, 6. Agitator, 7. Pyrex glass tube, 8. Polycarbonate tube, 9. Three-way valve, 10. Heat exchanger, 11. CO_2 cylinder, 12. Water bath, 13. Cooling unit.

fluids in the Pyrex tube and in the gap between the Pyrex and polycarbonate tubes was controlled by a piston-type pressure equilibrator. Under a perfect condition the difference in pressures inside and outside of the Pyrex tube could be zero. The pressure of the reactor was controlled by a piston-type pressure controller with an accuracy of ±0.2 bar. The reactor was immersed in a thermal bath through which the temperature of the reactor was controlled within an accuracy of ±0.1 °C. Deionized water and carbon dioxide with minimum purity of 99.99 % were used in all the tests conducted.

The typical experimental pressure and temperature were, respectively, 45 bar and 6 °C which simulated the pressure and temperature of seawater at 450 m in the ocean. Pre-cooled liquid CO_2 at about 8-10 °C and 50 bar was introduced into the reactor by a plunger pump. The tests were conducted at different initial CO_2 content (the corresponding mole fractions of CO_2 fell in a range between 0.015 and 0.035) in the reactor. The experiments were conducted both with and without agitation. The agitation was performed by a three-paddle propeller located downwards 50 mm from the top of the reactor. The speed of the agitator could vary in a range from 0 to 740 rpm. Because the materials of the reactor were transparent, the process of hydrate formation was observed and video-recorded with a CCD camera.

4. RESULTS AND DISCUSSION

4.1 Influence of the initial reactor pressure on hydrate formation

Liquid CO_2 was introduced into the reactor at two different initial reactor pressures. For the case of low initial reactor pressures, a certain amount of water was first introduced into the reactor at a normal pressure, and then liquid CO_2 was introduced into the reactor through a nozzle at the top of the reactor. Because of a continuous injection of liquid CO_2 the system was pressurized. At the early stage of the injection during which the system pressure was low, the liquid CO_2 entered the reactor vaporized immediately and a gaseous CO_2 phase formed at the top of the water (Figure 3(a)). In this case, hydrate was observed to form at the water-CO_2 interface and then was dissolved rapidly into the water. The pressure of the reactor increased as more CO_2 was introduced, and when the pressure of the reactor was high enough the CO_2 entered the system became a liquid phase although it was still at the top of the water (Figure 3(b)), due to the fact that at given conditions liquid CO_2 is less dense than water. Once the CO_2 in the system became liquid, a thin hydrate film reappeared at the CO_2-water interface and it grew rapidly to a thickness of about 0.1 mm in a period of several tens of seconds. The hydrate interphase and the two liquid phases were apparently stable because no noticeable changes could be observed in a period of several hours if no external disturbance (i.e., agitation) was added to the system.

For the case of high initial reactor pressures, the water filled in the reactor was pressurized (water pressure > 45 bar) before liquid CO_2 was introduced. Then liquid CO_2 was injected into the pressurized water through a nozzle (with a 2-mm diameter orifice) located at the bottom of the reactor. In this case, a thin CO_2 hydrate film was observed to form rapidly on

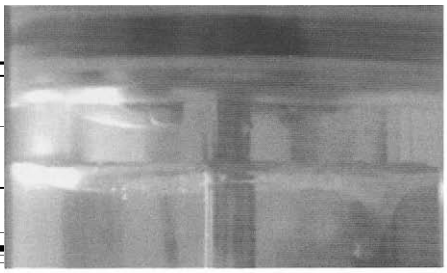

(a)

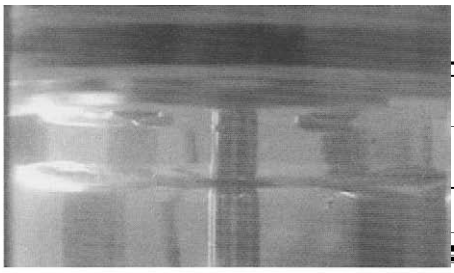

(b)

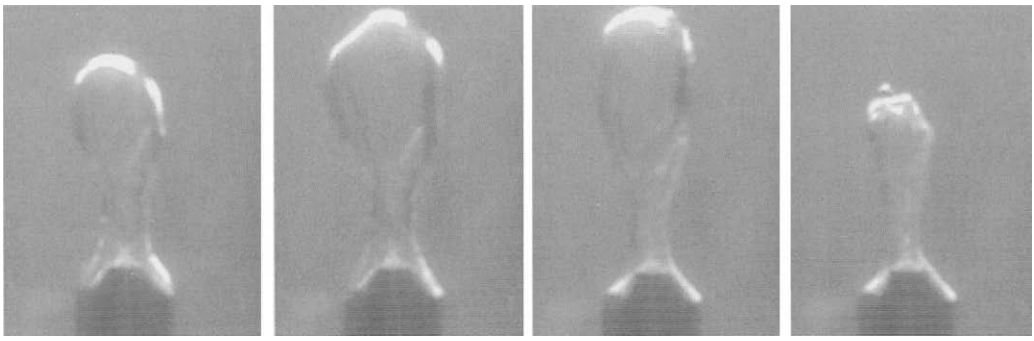

(1) (2) (3) (4)

Fig. 4. Injection process of liquid CO_2 into water phase.
(1)→(2)→(3)→(4)

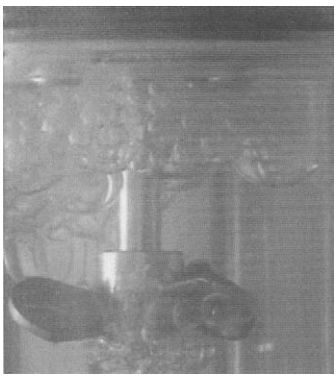

Fig. 5. Grape-like structure of CO_2 droplets covered with hydrate film.
(p=45 bar, T=6°C).

The above experimental observations indicate that no hydrate particles could be produced simply by injection of liquid CO_2 into water, even if the thermodynamic conditions for hydrate formation are satisfied. Instead, hydrate forms only as a thin interphase between the liquid CO_2 and water phases.

4.2 Influence of agitation on hydrate formation

Because CO_2 is liquid under conditions at depths ≥ 450 m in the ocean, the effect of agitation on the hydrate kinetics was studied for hydrate formation from the liquid CO_2-water system. In our experiments, agitation was found to affect the formation kinetics dramatically as was reported in the formation kinetics for many other hydrates [12]. When the agitation was started, the liquid CO_2 phase broke up into many small droplets and these droplets were

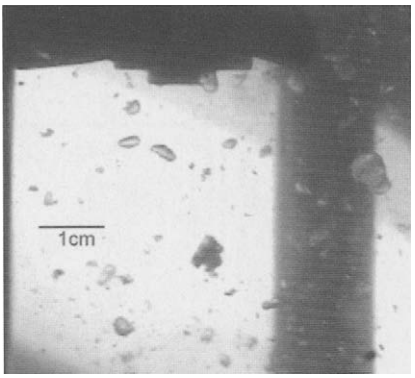

Fig. 6. Liquid CO_2 droplets and hydrate particles.

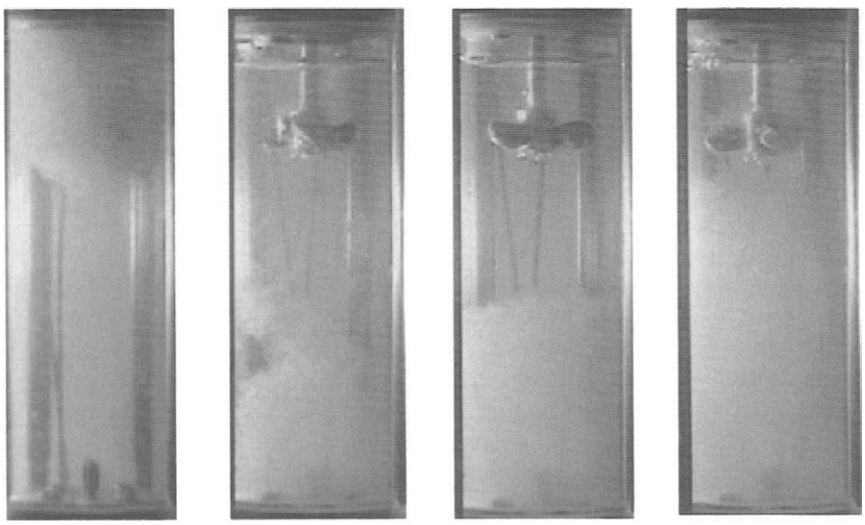

Fig. 7. Formation of CO_2 hydrate cluster for different agitation periods. Agitation time: (a) 10 min, (b) 15 min, (c) 20 min, (d) 30 min, at 740 rpm. (p=45 bar, T=6°C).

dispersed throughout the water phase. Simultaneously small opaque particles (presumably being hydrate particles) appeared in the CO_2-water mixture (Figure 6). When the agitation was stopped after a short agitation time (< 15 min at 740-rpm agitator speed), the CO_2 droplets and particles ascended to the top of the reactor where they agglomerated to form a cluster with a dimension of several centimeter (Figure 7(a)). It was obvious that both the CO_2

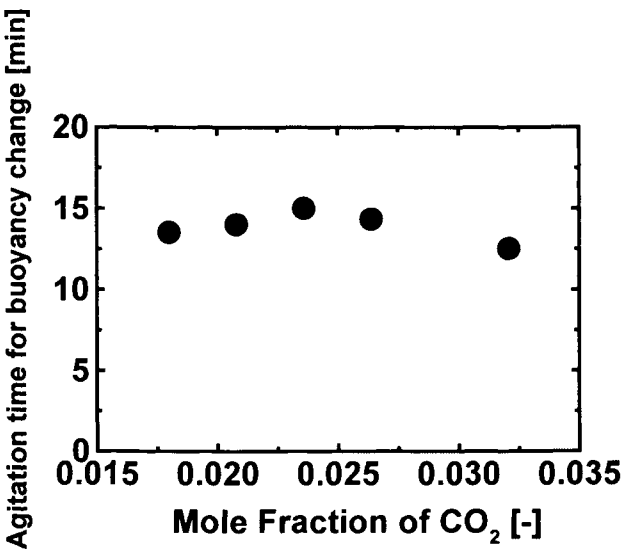

Fig. 8. Effect of the initial ratio of CO_2 and water on the critical agitation time for buoyancy change.

droplets and hydrate particles had positive buoyancy and, as a result, the cluster had positive buoyancy. The forces for formation of the cluster of particles and droplets were not strong and the cluster broke up into smaller particles easily when the agitation was resumed. It was observed that as long as the agitation stopped the dispersed particles always tended to form a cluster. However, the sizes of hydrate particles increased with increase in the agitation time, and buoyancy of the particles became negative when the total agitation time exceeded 15 min. In this case, the cluster was formed at the bottom of the reactor when the agitation stopped (Figure 7(b)). Further agitation resulted in more particles in the mixture and a larger cluster when the agitation stopped (Figure 7(c) and (d)). The hydrate particles formed after the change in the buoyancy of the cluster had negative buoyancy. There was no significant difference in the effect of the agitation after the cluster structure was observed.

Figure 8 shows the relationship between the time when the particle buoyancy becomes negative and the initial CO_2 content in the reactor. It is seen from Fig.8 that no obvious mole fraction dependence is in evidence in the mole fraction range between 0.015 and 0.035. Note that when the initial mole fraction of CO_2 was 0.015, the hydrate particles formed dissolved in the water phase after a short agitation period (a few minutes). In comparison, the critical agitation time (at which the particles buoyancy changes from positive to negative) was found to be influenced considerably by changes in speeds of the agitator. Figure 9 shows the dependence of the critical time on the speed of the agitator. It is seen in Fig.9 that the critical time decreases dramatically with increase in the agitator speed.

The change in the particles buoyancy may be explained as follows. Under the agitation, the liquid CO_2 phase becomes a dispersed phase formed by many small dispersed CO_2 droplets

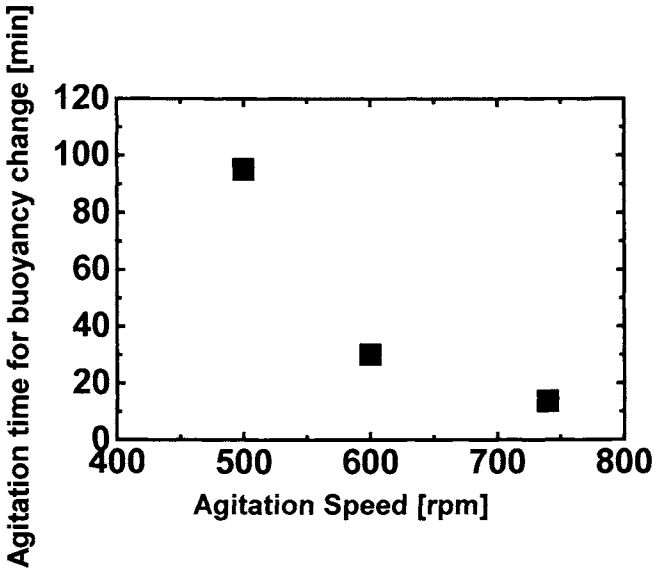

Fig. 9. Relationship between the agitation speed and the critical agitation time for buoyancy change.

covered with a hydrate film in the system. When the dimensions of the droplets and the thickness of the hydrate film become comparable, the droplets should be considered as particles. The hydrate surfaces of the particles may serve as the growth centers for the crystallization, i.e., at these surfaces hydrate crystals may grow continuously. The bulk density of the particles depends on the growth of the hydrate crystal or the thickness of the hydrate layer. When the hydrate layer is sufficiently thick that the bulk density of the particle droplets becomes larger than that of water, the buoyancy of the particles changes from positive to negative.

The experimental results demonstrated that CO_2 hydrate particles can be formed from a liquid CO_2-water two-phase system with a limited induction period. And, as long as a proper agitation is performed the hydrate particles produced will be negatively buoyant and such particles will sink in the ocean.

4.3 Sedimentation of hydrate particles released in the ocean

Because of being denser than seawater, the hydrate particles released from the crystallizer will descend to the ocean bottom. During this sinking process, the hydrate particles will dissolve slowly in the ocean because the hydrate is chemically unstable in seawater that is highly unsaturated with CO_2. However, dissolution of the hydrate occurs only as a surface phenomenon. Thus, the shrinkage of a CO_2 hydrate particle may be modeled on the basis of mass conservation as

$$-d(4\pi r^3 C_h/3)/dt=4\pi r^2 k(C_l-C_w), \quad (1),$$

where C_h the CO_2 concentration in the hydrate, C_l the CO_2 solubility in seawater, and C_w the CO_2 concentration in seawater; r the radius of the hydrate particle, and k is the overall mass-transfer coefficient. Noting that $C_w << C_l$, Eq. (1) may be rewritten in the form of the particle shrinkage rate as:

$$dr/dt=-k(C_l/C_h). \quad (2).$$

Integration of Eq. (2) gives

$$r=r(0) - k(C_l/C_h)t, \quad (3),$$

where $r(0)$ is the initial radius of the hydrate particle and t is the time. Sedimentation of a hydrate particle may be studied on the basis of the following relationship for force balance [13]:

$$m(dV/dt)=G-F_d, \quad (4),$$

where m is mass of the hydrate, V is the particle velocity, and G and F_d are the buoyant and drag forces given by the following equations:

$$G=(4/3)\pi r^3(\rho_h-\rho_w)g, \quad (5),$$

$$F_d=(1/2)C_d\rho_w AV^2, \quad (6),$$

where ρ_w is the density of the ambient seawater, ρ_h the density of the hydrate particle, and A the cross-sectional area of the particle. The drag coefficient C_d in Eq.(6) depends on the Reynolds number Re:

$$C_d=24/Re \qquad (0 \le Re \le 2), \quad (7),$$

$$C_d=18.5/Re^{0.6} \qquad (2 \le Re \le 500), \quad (8),$$

$$C_d=0.44 \qquad (500 \le Re \le 2\times 10^5). \quad (9).$$

Since the time for a hydrate particle to reach its terminal velocity is much shorter in comparison with that for its full dissolution, it may be assumed that the hydrate particle moves in its terminal velocity during the entire process of dissolution. The traveling distance of the hydrate particle during the dissolution process thus can be determined by the terminal velocity and dissolution time via integration of Eq.(4). Figure 10 shows the calculated traveling distance as a function of dissolution time. The properties used in the computation are: k= 10^{-7}m/s [14], ρ_w = 1,030 kg/m^3, and ρ_h = 1,130kg/m^3. It is seen in Fig.10 that the dissolution distance increases dramatically as the particle size increases and that hydrate particles with sizes of several centimeters would travel several hundred meters before they

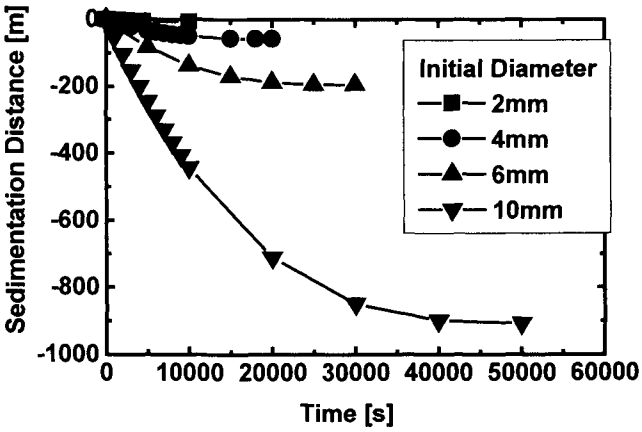

Fig. 10. Sedimentation distance of CO_2 hydrate particles disposed in the ocean.

dissolve completely in seawater. Since smaller hydrate particles dissolve fully in a short travelling distance which may result in a larger increase in the CO_2 concentration in the local seawater, smaller hydrate particles may induce a bigger environmental impact. Also, the ocean current and ocean turbulence may have a stronger influence on the small particles than on large particles. Therefore, large hydrate particles may be favorable to lessening the marine environmental impact.

5. CONCLUSIONS

A new scenario for the CO_2 ocean disposal was proposed in this work. The key part of the disposal process is a hydrate crystallization process in a submerged reactor. The feasibility of this proposed scenario was examined by a laboratory simulation. The simulation results supported the proposed concept. It has been demenstrated by the experiments that a proper agitation is necessary for formation of the CO_2 hydrate particles in the reactor. Our analysis of dissolution of the hydrate particles in the ocean indicates that larger hydrate particles may be favorable to a less environmental impact induced by the hydrate dissolution.

REFERENCES

1. A. Ravkin, Global Warming: Understanding the Forecast, Abbeville Press, New York, 1992.
2. C.F. Baes, S. E. Beall, D.W. Lee, and G. Marland, The collection, disposal, and storage of carbon dioxide, in Interactions of Energy and Climate (ed. by W. Bach et al.), Reidel Publishing Company, New York,1980.
3. N. M. Steinberg, DOE Report, US-DOE/CH/00016-2 (1984).

4. K. Y. Song and R. Kobayashi, SPE Formation Evaluation, (1987) 500.
5. Y. Fujioka, Y. Shindo, K. Takeuchi and H. Komiyama, Int. J. Energy Res., 18 (1994) 765.
6. I. Aya, K. Yamane and N. Yamada, HTD, ASME, 215 (1992) 17.
7. Y. Shindo, Y. Fujioka, K. Takeuchi and H. Komiyama, Int. J. Chem. Kinetics, 27 (1995) 569.
8. T. Austvik and K.P. Løken, Energy Conv. Mgmt., 33 (1992) 659.
9. T. Austvik and K.P. Løken, Energy Conv. Mgmt., 34 (1993) 1081.
10. A. Saji, H. Yoshida, H. Sakai, T. Tanii, and T. Kamata, Energy Conv. Mgmt., 33 (1992) 643.
11. A. Saji, H. Noda, Y. Takamura, T. Tanii, T. Tanaka, H. Kitamura and T. Kamata, Energy Conv. Mgmt., 36 (1995) 493.
12. E. D. Sloan, Jr., Clathrate Hydrate of Natural Gases, Dekker, New York, 1990.
13. M. M. Clark, Transport Modeling for Environmental Engineers and Scientists, John Wiley and Sons, New York, 1996.
14. H. Teng, A. Yamasaki, Int. J. Heat Mass Transfer, 41 (1998) 4315.

Reaction Engineering for Pollution Prevention
M.A. Abraham and R.P. Hesketh (Editors)

CARBON DIOXIDE MITIGATION VIA COMBUSTION MODIFICATION: AN OVERVIEW OF U.S. DEPARTMENT OF ENERGY'S POWER SYSTEMS TECHNOLOGY R&D PROGRAM

Arun C. Bose*, Sean I Plasynski, and Harvey M. Ness
US Department of Energy, Federal Energy Technology Center, Pittsburgh, PA 15236
and
Daniel J. Seery, United Technologies Research Center, East Hartford, CT 06108

SUMMARY

The Federal Energy Technology Center of the U. S. Department of Energy (DOE) sponsors a wide range of RD&D (research, development, and demonstration) programs to maximize the utilization of vast domestic carbon-based resources while simultaneously responding to global environmental concerns.

DOE, in partnership with United Technologies Research Center (UTRC) and Foster Wheeler Development Corporation (FWDC), is focussing on its Combustion 2000 Program aimed at developing a beyond state-of-the-art, inherently low polluting High Performance Power System (HIPPS) for the 21st century. HIPPS represents a new way of burning coal to deliver clean, low-cost electricity.

DOE is partnering with an industrial team, led by Air Products and Chemicals Inc., to develop and demonstrate a new air separation technology based on dense ceramic membrane materials that conduct both oxygen ions and electrons through membrane walls. These novel materials can separate oxygen from air at high temperatures and pressures at essentially 100% oxygen selectivities. Air Products calls these materials Ion Transport Membranes (ITM).

Availability of lower-cost oxygen would make oxygen-enriched combustion of coal-fired boilers more industrially acceptable and oxygen-blown Integrated Gasification Combined Cycle (IGCC) would be more economically attractive as the next-generation power producing choice. A DOE-industry partnership has quantified the benefits of membrane-derived oxygen integrated with an IGCC plant and currently is doing simulation studies using oxygen-enriched combustion mode for advanced pulverized coal-fired power system configurations. The oxygen-enriched combustion mode would produce CO_2-enriched flue gas streams that are easier to handle for subsequent disposal or recycle.

This paper reviews two HIPPS designs, a non-cryogenic oxygen production technology, and discusses on-going research.

* To whom correspondences should be addressed.

INTRODUCTION

Industrial nations have made significant progress in reducing emissions of NOx, SO_2, and particulates from coal-fired boilers. Attention is now focussed on the reduction of the anthropogenic emissions of CO_2, the greenhouse gas believed to cause global warming. While capture, disposal, and sequestration is one approach for CO_2 remediation, an enabling technology to capture, concentrate, and dispose of billions of tons of dilute CO_2 streams from a variety of power plant locations has not evolved yet. Inherently low CO_2 emitting power production plants are more desirable and future power plants should be designed to allow source reduction of CO_2.

High-purity oxygen is a key requirement for many advanced energy technologies – including the Department of Energy's (DOE) proposed "Vision 21" concept for a futuristic power plant/energy complex. But extracting oxygen from the air is both capital- and energy-intensive. Today, for large-scale oxygen production, massive refrigeration units are required to cool air to about 275 °F below zero, the temperature at which air becomes a liquid and oxygen can be separated.

DOE recently initiated a new research project to explore an entirely different, a high-temperature membrane-based process, to produce high-quality oxygen. The potential exists to cut the cost of oxygen production by nearly one-third compared to the conventional technology.

Environmental attributes, although necessary, are alone not sufficient for commercial success. Translating environmental benefits into economic and pricing terms is the reality. DOE's Power Systems development program is based upon this conviction. HIPPS and non-cryogenic oxygen production technologies are government-industry partnerships focused for innovations that are responsive to market reality and successful commercial deployment.

1. HIGH PERFORMANCE POWER SYSTEM (HIPPS)

The HIPPS technology embodies an indirectly-fired cycle (IFC) that is particularly attractive because of its inherently high thermal efficiency relative to other advanced coal-fired technologies. IFC is applicable to new plants as well as for repowering and retrofitting applications. In an Indirectly Fired Combined Cycle (IFCC), as embodied in HIPPS, air compressed to the turbine inlet pressure, is heated in a coal-fired High Temperature Advanced Furnace (HITAF) and then expanded in a turbine to produce more than half of the cycle's power output. The baseline efficiency of a HIPPS plant is 47% and the efficiency improvement translates to significant reductions in carbon dioxide (CO_2) emissions.

In an IFC, the working fluid does not come in contact with the corrosive coal combustionenvironment. A concept HIPPS plant is presented in Figure 1.

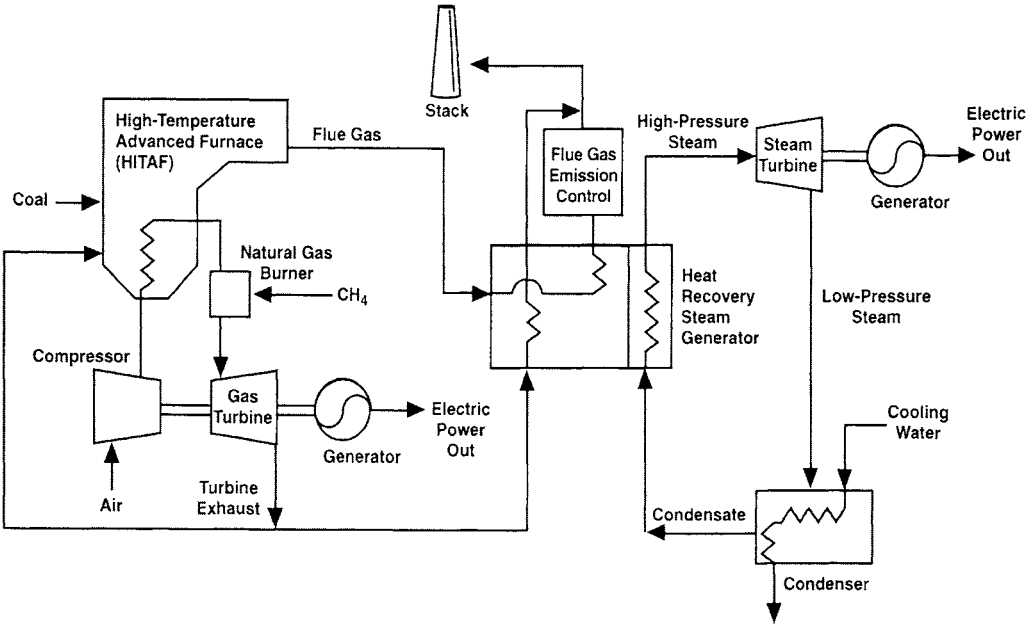

Fig.1. Concept for the Indirectly Fired High Performance Power System

The HIPPS design allows point source CO_2 emissions reduction. As a result of increased efficiency and advanced combustion technology, CO_2 emissions are significantly reduced. The bar chart in Figure 2 compares HIPPS to conventional Pulverized Coal Combustion (PCC) boilers in terms of CO_2 emission reduction.

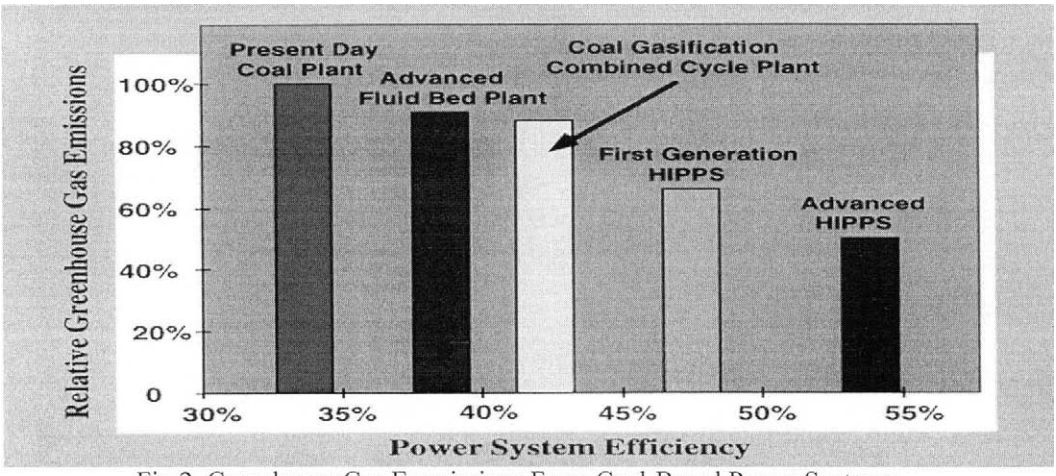

Fig.2 Greenhouse Gas Emmissions From Coal-Based Power Systems

2. THE UTRC HIPPS CONCEPT

The UTRC concept is developing an inherently low CO_2 emitting coal-fired power plant based on thermodynamic optimization of indirectly fired combined cycle configurations using a topping Brayton cycle and a bottoming Rankine cycle. Clean air, the working fluid, is heated in a HITAF. The HITAF extracts heat from coal combustion with a radiative air heater and a convective air heater connected in series. For ash handling considerations, the radiative air heater operates in slagging mode. The basic layout of UTRC HIPPS is shown in Figure 3. Heat recovered from the turbine exhaust air and from the furnace flue is used to raise steam for the steam turbine. The UTRC HIPPS technology embodiment allows a baseline efficiency of 47% and efficiencies approaching 55% are realizable using advanced cycles. The major component development need for the HIPPS plant is the HITAF.

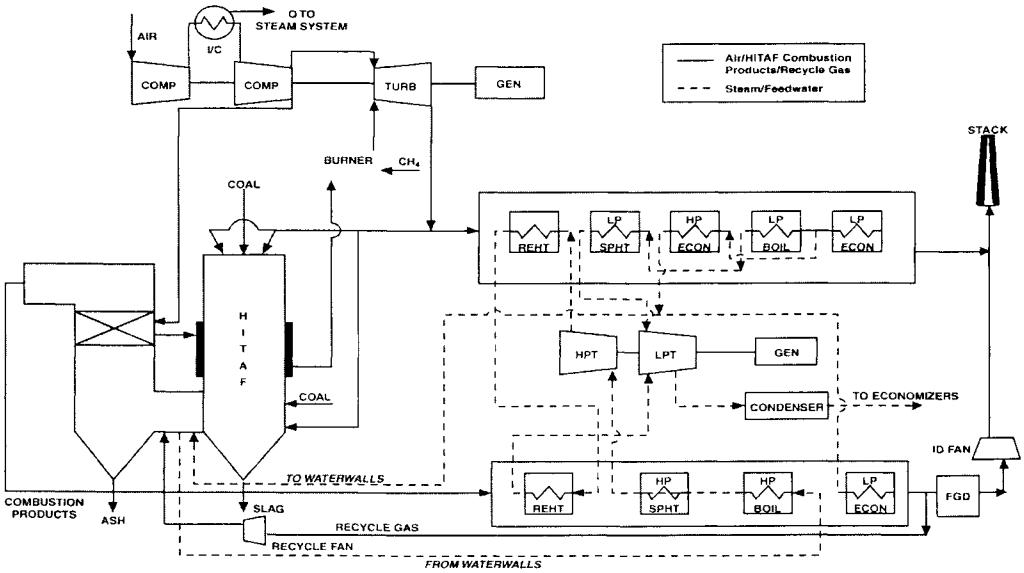

Fig.3. HIPPS Combined Cycle
United Technologies

3. CYCLE OPTIMIZATION STUDY

The baseline cycle is only one case of a family of cycles that is being studied. The goal is to find the optimum cycle to exploit the HIPPS technology. The baseline system uses a heavy frame gas turbine and a 2400 psi/1000 °F/1000/°F reheat bottoming cycle to give 47.1% overall efficiency.

An optimization study for several advanced cycles for improving efficiency is currently in progress. Several advanced HIPPS cycles are shown in Figure 4. The aero-derivative gas turbine uses the same steam system as the Rankine cycle. To realize most of the coal heat, humid air turbine (HAT) cycles are necessary. These cycles are based on a high compression

ratio gas turbine with inter-cooling. The advanced steam-heavy frame cycle has not been optimized yet, but it can be assumed that efficiencies near 50% can be achieved. Preliminary analysis of the advanced steam aero-derivative cycle indicates efficiency improvements by over three percentage points compared to the baseline cycle. The advanced HAT is based on aero-derivative turbine and requires a HITAF exit temperature near 2900 °F. At these conditions, efficiencies over 54% are achievable.

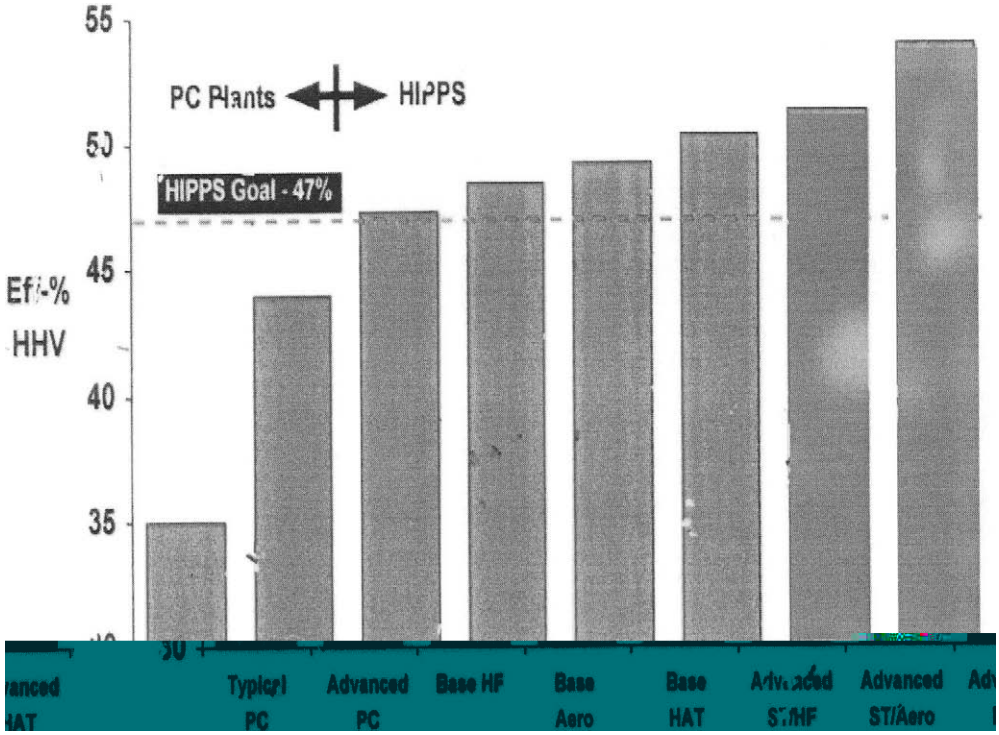

Fig.4 Efficiency of Coal-Fired Systems

4. RESULTS AND DISCUSSION OF UTRC HIPPS

Experimental work for the HITAF development is currently under progress at the Energy and Environmental Research Center of the University of North Dakota (UNDEERC). UNDEERC has built a 30 ft. tall by 6 ft. diameter, 3 MM Btu/hour slagging furnace combustion system for the development of the HITAF and for obtaining design, scaleup, and operating data for a planned 50 MM Btu/hour proof-of-concept scale test.

The baseline design requires the Radiative Air Heater (RAH) section of the HITAF to heat the working fluid (air) from 1300 °F to 1700 °F. Up to 35% natural gas combustion is required to raise the air temperature to the 2500 °F required by the turbine. Results to date have achieved several important objectives.

Air can be heated to 1700 °F in the RAH panel of the HITAF using oxide-dispersed strengthened alloys. Thermal and mechanical stresses as well as corrosion by slag and ash can be controlled. The combined heat transfer of the RAH and the Convective Air Heater (CAH) has demonstrated that the DOE efficiency goal can be exceeded to achieve nearly 55% overall efficiency. This translates into approximately a 40% reduction of CO_2, including the nearly 12% reduction due to fuel substitution (natural gas-fired duct heater).

A recent successful test of the key UTRC HIPPS component, the HITAF, achieved temperature capabilities up to 2000 °F. This has surpassed design expectations and validated the novel concept of the indirectly fired combined cycle (IFCC) configuration. In this test, the radiant heater panel of the RAH was successfully operated to heat the pressurized working fluid to 2000 °F. This success shows that an overall thermal efficiency nearing 55% (HHV) is achievable when HIPPS is ready for commercial deployment. The successful test has also opened the path to a nearly all-coal HIPPS plant with minimal need for a natural gas-fired temperature boost.

An important step came when UTRC developed a method to weld a special alloy capable of withstanding intense heat. UTRC also developed ceramic tiles that can survive the heat and corrosive environment inside the furnace. The recent successful test has shown that the RAH of the HITAF can be constructed with currently available materials - a combination of metallic and refractory materials for the panel and metal alloys for the hot air transporting tubes. However, the materials are not available in commercial quantities.

HIPPS has been tested for both bituminous (high-rank) coals and lignite, but it can be configured to use a variety of other fuels. It could run on biomass fuels, other opportunity fuels, and also liquid fuels. Another advantage of HIPPS is that it can be retrofitted in older plants for less than the cost of building new conventional coal-fired plants. The retrofitting would improve thermal efficiencies of existing plants and thus decrease CO_2 emissions.

Coal ash, if low in carbon content, is a valuable raw material in the cement-making process. The UTRC HIPPS technology generates very low carbon ash that would be readily marketable for cement-making and other applications and the market could be substantial.

5. THE FWDC HIPPS CONCEPT

FWDC is developing an all coal-fired system utilizing a pyrolyzer to convert coal to fuel gas and char. The fuel gas is sent to a turbine combustor, and the char is burned in FWDC's version of the HITAF (Figure 5). An arch-fired combustor design is utilized for burning the char. The gas turbine air is heated in the HITAF using tube banks and further heated to the turbine inlet temperature by a combustor fired with the fuel gas. In addition to achieving the HIPPS goal of 47% overall efficiency, this configuration allows integration of sophisticated emission control technologies, such as, those developed by the DOE-sponsored Low Emissions Boiler Systems (LEBS) program.

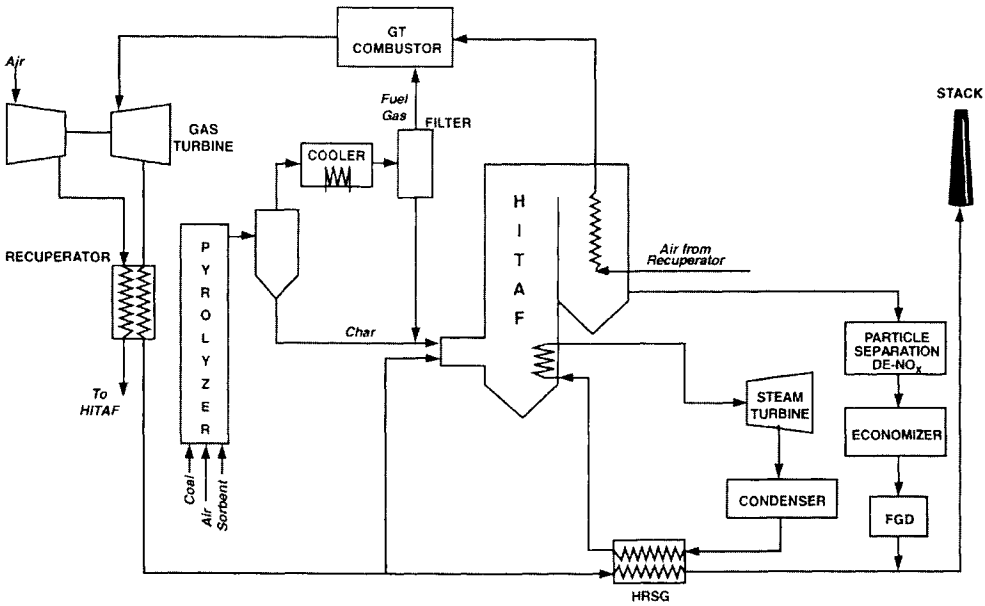

Fig.5. All Coal Fired High Performance Power System

6. RESULTS AND DISCUSSIONS OF FWDC HIPPS

Pyrolyzer tests were conducted in a pilot-scale fluidized bed pyrolyzer with a coal feed rate approximating 500 lb/hour. The results will be used to develop computer models to predict pyrolyzer performance. Pulverized Pittsburgh No. 8 coal was fed to the pyrolyzer along with limestone that acted as a desulfurizing agent. The pyrolyzer operates at a temperature of 1700-1800 °F and a pressure of 240 lb/sq in. The conversion of carbon in the feed coal to fuel gas ranges from 50% to 60%. The gas contains approximately equal amounts (6-10%) of CO, H_2, and the balance consists of H_2O, CH_4, NH_3, and N_2. A typical char contains 64% carbon, 33% ash, 1% N, and 1% sulfur.

A key challenge is the transport of hot char to the fuel burners and efficient combustion using gas turbine exhaust as the oxidant in the furnace. Laboratory tests have shown excellent combustibility of Pittsburgh No. 8 char. In ignition characteristics, the char was similar to anthracite, but once ignited, the char reactivity was higher than low-volatile bituminous coals. The reason for the char's high reactivity is attributed to the high surface area of 160 m^2/g compared to coal at 2-20 m^2/g. Arch-firing has been used for anthracite and low-volatile coals. The burners are fired downward and secondary air is added along the flamepath to help stabilize the flame. Pilot-scale char combustion tests are now planned in a 30 MM Btu/hr arch-fired furnace.

7. NON-CRYOGENIC OXYGEN PRODUCTION TECHNOLOGY

This innovative gas separation technology is based on a class of dense ceramic materials that conduct oxygen ion at high temperature. The process is called the ITM Oxygen Technology. The process can be illustrated by a two concentric cylinder configuration where the inner tube is made of ITM. When an ITM air separation module is heated to a desired temperature, oxygen in the preheated air flowing through the annulus of the two-cylinder configuration is ionized on the outer surface of the inner membrane tube and the oxygen ions then pass through the wall of the ceramic membrane to the inside surface. On the inner side of the membrane, the ions reform into a stream of pure oxygen, releasing electrons that travel back through the membrane to repeat the ionizing process with incoming oxygen (Figure 6).

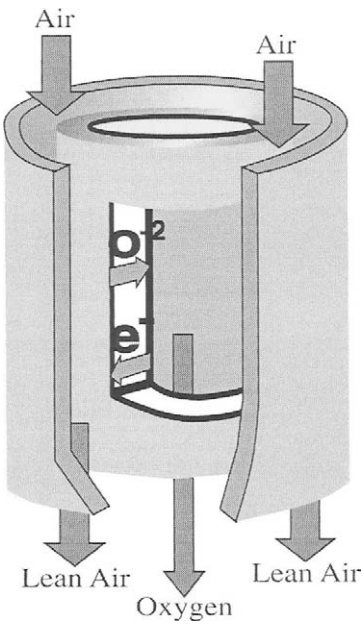

Fig.6. ITM Oxygen Technology

The new project will be carried out in three phases. In the first phase, research will focus on laboratory-scale development to verify that ion transport membrane is technically viable for oxygen separation. A 0.1 ton-per-day, laboratory-scale membrane module will be designed and built for testing and process concept validation purposes.

In the second phase, the process will be scaled up through two test facilities: a 1 ton-per-day unit and a 5-ton-per-day unit. Both will be run under simulated commercial conditions to obtain design, engineering, cost and scale-up data. In the third phase, a 25 to 50 ton-per-day "proof-of-concept" facility will be built as the final step toward commercial readiness.

8. ITM-DERIVED OXYGEN AND OXYGEN-BLOWN IGCC PLANTS

A recent DOE-industry joint study quantified the impact of ITM oxygen technology on IGCC plants. The economic evaluation has indicated that a high-temperature ITM-based oxygen generation process, when integrated with an IGCC system, has the potential to lower oxygen cost by 31%, capital cost by $114/kW, and increase the overall thermal efficiency of the power plant. The proposed ITM Oxygen Technology would produce high-purity oxygen at a much lower specific equivalent energy consumption compared to cryogenic tonnage oxygen. These benefits would reduce the cost of electric power and also significantly lower CO_2 emissions. Cryogenic oxygen is already being used in a new generation of power plants that rely on coal gasification. Availability of lower-cost oxygen would make oxygen-blown Integrated Gasification Combined Cycle a more economic power producing choice.

9. OXYGEN-ENRICHED COMBUSTION WITH FLUE GAS RECYCLE FOR COAL-FIRED UTLITY BOILERS

One at-source CO_2 reduction concept is to use a mixture of oxygen (O_2) and carbon dioxide as the oxidant instead of air in stationary combustion processes. The result is a sequestration-ready CO_2-enriched flue gas stream that contains no nitrogen and requires much smaller process equipment to capture, concentrate, and dispose of the carbon dioxide. The flue gas composition is primarily CO_2 and water. A portion of the flue gas, following the hot gas clean-up operation, may also be recycled by mixing it with pure oxygen. In addition, the O_2 -

coal combustion or gas turbine inlet temperature on the other side, is not the most energy-efficient power plant design and may not be acceptable to electricity producing industries. Instead, if a technology can be available that would use the power plant's heat sources to thermally energize an air separation process and would produce lower-cost oxygen, such a technology would enhance the acceptance of a O_2-CO_2 combustion mode of coal-fired boilers by the electric utility industry sector, especially to comply with voluntary or involuntary carbon emission regulations.

10. LOOKING FORWARD

The HIPPS approach provides regulated pollutant reduction nearly 90% more than required by the current National Source Performance Standard and has the highest CO_2 mitigation potential of any coal burning option while generating lower-cost electricity. Opportunities for HIPPS include new plants in the U.S. and developing countries, and repowering and upgrading of existing plants. The recent tests of the RAH, the key UTRC HIPPS component with temperature capabilities of 2000 °F and excellent char combustibility for the FWDC concept, have demonstrated the soundness of the design.

Oxygen-enriched combustion could increase the efficiency of high-temperature furnaces and minimize the formation of nitrogen oxide pollutants, a major contributor to smog and ground-level ozone. Cryogenically derived oxygen is already being used in a new generation of power plants that rely on coal gasification. Lower-cost oxygen may be used to improve the economics and environmental performance of more traditional coal-burning power generation technologies.

In the HIPPS configuration, pure oxygen will be fed to the HITAF to support combustion of coal or char. It would be desirable to design all future power plants on an oxygen-enriched mode of combustion using a mixture of oxygen and carbon dioxide as the oxidant. This combustion modification would generate a CO_2-enriched flue gas that is easy to capture for partial recycle and disposal. Further, the advancements of air separation and gas turbine technologies offer new integration opportunities to improve oxygen-blown Integrated Gasification Combined Cycle performance and reduce consumer cost of electricity.

BIBLIOGRAPHY

D.J. Seery, J.J. Sangiovanni, F.J. Cogswell and C.E. Bird, "Engineering Development of a Coal-Fired High Performance Power Generating System," International Joint Power Generation Conference, Denver, CO, November, 1997.

D.J. Seery, F.L. Robson and J.D. Ruby,"Engineering Development of a Coal-Fired High Performance Power Generating System," International Joint Power Generating Conference, Houston, TX, October 1996.

F.L. Robson, J.D. Ruby and D.J. Seery,"Repowering with High Performance Power Plant Systems (HIPPS)," American Power Conference, Chicago, 1996.

F.L. Robson, J.D. Ruby and D.J. Seery "High Performance Power Systems (HIPPS) for the 21st Century," 22nd International Technical Conference on Coal Utilization & Fuel Systems, Clearwater, Florida, 18-21 March 1997.

F.L. Robson, J.D. Ruby and D.J. Seery "Greenhouse Gas Reduction Through the Use of High Performance Power Systems," International Joint Power Generation Conference, Denver, CO, November 1997.

D.J. Seery, J.J. Sangiovanni, F.J. Cogswell and C.E. Bird, "Engineering Development of a Coal-Fired High Performance Power Generating System," International Joint Power Generation Conference, Denver, CO, November 1997.

D.J. Seery, J.J. Sangiovanni, F.L. Robson and J.D. Ruby, "Engineering Development of a Coal-Fired High-Performance Power Generating System," International Joint Power Generation Conference, October 1996.

N.S. Bornstein and D. J. Seery, "Progress in Using ODS Alloys in the HITAF Air Heater," Materials and Components, No. 136, October 1, 1998.

M. Torpey et al., "Design and Development of a Pulverized Char Combustor for the High Performance Power System," Advanced Coal-Based Power and Environmental Systems '98 Conference, Federal Energy Technology Center, Morgantown, WV, July 21-23, 1998.

J. Shenker and A. Grove, "Coal-Fired Combined-Cycle Power Generating System Using a Pyrolyzer and High-Temperature Furnace," International Power Generation Conference, Atlanta, GA, Oct.18-22, 1992.

J. Shenker, "Development of a High-Performance Coal-Fired Power Generating System with a Pyrolysis Gas and Char-Fired High Temperature Furnace," Ninth Annual Coal Preparation, Utilization and Environmental Control Contractors Conference, July 19-22, 1993.

J. Shenker and A. Grove, "Coal - Energy and the Environment," Tenth Annual International Pittsburgh Coal Conference, September 20-24, 1993.

J. Shenker and A. Grove, "Char Combustor Considerations for a Partial Gasification-Based Combined-Cycle Power Generation System," Joint ASME/IEEE Power Generation Conference, Kansas City, KS, October 19-22, 1993.

J. Shenker, "Characteristics of Char Combustion in a High Temperature Advanced Furnace for the High Performance Power System," 22nd International Technical Conference on Coal Utilization & Fuel Systems, Clearwater, Florida, 18-21 March 1997.

J. Shenker, "Development of a High-Performance, Coal-Fired Power Generating System with a Pyrolysis Gas and Char-Fired High-Temperature Furnace," Eleventh Annual Coal

Preparation, Utilization and Environmental Control Contractors Conference, Pittsburgh, July 12-14, 1995.

R. E. Richards, S. Russek, and J. Xu, "Advanced Integration Concepts for Oxygen Plants and Gas Turbines in Gasification/IGCC Facilities," 15th Annual International Pittsburgh Coal Conference, September 14-18, 1998.

Reaction Engineering for Pollution Prevention
M.A. Abraham and R.P. Hesketh (Editors)

Reaction kinetics and deactivation of Ni-based catalysts in CO_2 reforming of methane

Shaobin Wang and G.Q. (Max) Lu*

Department of Chemical Engineering, The University of Queensland,
St. Lucia, QLD 4072, Australia

The kinetics and deactivation of methane reforming with carbon dioxide over unpromoted and ceria promoted Ni/γ-Al_2O_3 catalysts were studied. Activation energies and an exponential rate relationship for CO production and reactant partial pressures were obtained. Based on the results, a reaction mechanism and a Langmuir-Hinshelwood type of kinetic model were proposed. The performance of these two catalysts at 700 °C showed that Ni/γ-Al_2O_3 and Ni/CeO_2-Al_2O_3 catalysts deactivated at rates of 8.1×10^{-4} and 1.3×10^{-4} min^{-1}, respectively. Deactivation of these catalysts can be attributed to carbon deposition.

1. INTRODUCTION

CO_2 reforming of methane to synthesis gas ($CO_2 + CH_4 \rightarrow 2\ CO + 2H_2$) has been proposed as one of the most promising processes for utilisation of these greenhouse gases [1]. Ni and noble metal catalysts have been found effective for this reaction [1,2]. Most of the researches in the past decade have been focused on the preparation of catalysts and evaluation of catalytic performance. Relatively less work has been conducted on the reaction kinetics.

Some researchers studied the reforming kinetics and obtained the reaction rate expressed approximately by a simple power-law equation [1]. On the other hand, through the use of partial pressure data and mechanistic information, other researchers have derived complex rate expressions to quantify the reaction kinetics. The earliest report of a Langmuir-type rate expression for CH_4-CO_2 reforming was presented by Lewis et al. for a Cu/SiO_2 catalyst [3]. Bodrov et al. [4,5] studied CH_4-CO_2 reforming on a nickel foil catalyst and fitted their data to an expression originally used to describe the kinetics of steam reforming of methane. Richardson and Paripatyadar [6] studied the CO_2/CH_4 reforming kinetics over Rh/Al_2O_3 at a pressure of 1 atm. Using linear regression analysis, a rate equation was obtained as follows:

$$r = \frac{k_R K_{CO_2} K_{CH_4} P_{CO_2} P_{CH_4}}{(1 + K_{CO_2} P_{CO_2} + K_{CH_4} P_{CH_4})^2} \qquad (1)$$

Calculated and measured rates were correlated with a regression coefficient of 0.988. Zhang and Verykios [7] also provided a rate expression, derived from a Langmuirian model assuming that methane dissociation was the rate-determining step. The model supposedly fitted the experimental data reasonably well. However, they did not provide the values for adsorption and kinetic parameters. Bradford and Vannice [8] reported a kinetic model for the CH_4-CO_2 reforming reaction which successfully described the reaction kinetics over Ni/MgO and Ni/TiO_2 catalysts. Mark and Maier [9] proposed a kinetic model for this reaction over Ir/Al_2O_3 catalyst in the temperature range 500-850 °C.

We have recently reported Ni/γ-Al_2O_3 and ceria-promoted Ni/γ-Al_2O_3 catalysts exhibiting high and stable activities in an integral fixed-bed reactor [10,11]. In this paper, the kinetics and deactivation of Ni/γ-Al_2O_3 and Ni/CeO_2-Al_2O_3 in CO_2-CH_4 reforming under differential conditions are investigated.

2. EXPERIMENTAL

Ni/γ-Al_2O_3 catalyst was prepared by wetness impregnation using $Ni(NO_3)_2 \cdot 6H_2O$ as a nickel precursor in a desired concentration and a commercial γ-Al_2O_3(S_{BET}=190 m^2/g). The resulted solution was stirred at 80 °C to evaporate water and dried in an oven at 103-105 °C overnight. The samples were then calcined in air at 500 °C for 4 h. The ceria-promoted catalyst was prepared by a consecutive impregnation method described as above using metal nitrates. The Ni and promoter laodings were all kept at 5 wt%. The surface areas determined by N_2 adsorption for Ni/γ-Al_2O_3 and Ni/CeO_2-Al_2O_3 are 145 and 146 m^2/g, respectively.

1-5 mg catalysts with a particle size of about 60 μm were diluted with α-Al_2O_3 powder with similar particle size to make 50 mg sample and loaded in a fixed-bed reactor with an inner diameter of 10 mm and catalyst bed length 1-2 mm. Conversions were usually controlled to be significantly lower than those defined by thermodynamic equilibrium (<10%). Before reaction, catalysts were reduced in 10%H_2/He flow at 500 °C for 1 h. To determine the apparent activation energies, the reforming reaction was performed with a feed composition of CO_2:CH_4:He=15:15:70 with a total flow rate of 360 ml/min over a temperature range of 500-700 °C. The partial pressure dependencies were studied by maintaining 0.15 atm of one reactant and varying the other reactant between pressure of 0.02-0.15 atm. A balance gas of He was adjusted to maintain a total gas flow rate of 360 ml/min and a total absolute pressure of one atm. In those above measurements, the initial reaction rate was determined after 3 min of reaction gas flow was introduced into the reactor. The reactants and products were analysed with a Shimadzu GC-17A equipped with a TCD. Calculations by the Weisz criterion indicate that the reaction proceeded in kinetic control regime under the reaction conditions [12].

3. RESULTS AND DISCUSSION

3.1. Activation energy

The dependency of reaction rate on temperature was measured at 500-700 °C. The initial reaction rates for CH_4 and CO_2 consumption as well as CO production versus temperature over Ni/γ-Al_2O_3 and Ni/CeO_2-Al_2O_3 catalysts are shown in Figure 1, and activation energies thus obtained are

listed in Table 1. It is seen that CO production over Ni/CeO_2-Al_2O_3 is slightly higher than that over Ni/γ-Al_2O_3. However, the two catalysts do not show much difference in the apparent activation energies. The apparent activation energies for CH_4 or CO_2 consumption are lower than those for CO production over the same catalyst. This suggests that the reaction routes and kinetics of CO formation is probably different from those of CH_4 and CO_2 consumption. In addition, activation energies may vary at different reactant conversion. Kroll et al. [13] found that activation energy decreases when increasing CH_4 or CO_2 conversion.

It is noted that activation energies for CH_4 and CO_2 consumption are similar within the experimental error over Ni/Al_2O_3. However, activation energy for CO_2 consumption overNi/CeO_2-Al_2O_3 is higher than that for CH_4 consumption. The difference is possibly due to the effect of promoter CeO_2. The addition of CeO_2 resulted in changes in the surface properties of Ni/Al_2O_3 and created the interstitial surface CeO_x on the nickel surface, which may increase the activation barrier for CO_2 consumption [14]. Due to the insensitivity of H_2 in TCD, detection of lower concentrations of H_2 was very difficult without larger errors. Hence, no activation energy for the H_2 formation was obtained. Bradford and Vannice [8] have studied the reaction kinetics of CO_2-CH_4 reforming over several Ni catalysts, Ni/C, Ni/MgO, Ni/SiO_2, and Ni/TiO_2. They found that the apparent activation energies for all gases reaction over Ni-based catalysts were very similar, giving values between 80-100 kJ/mol.

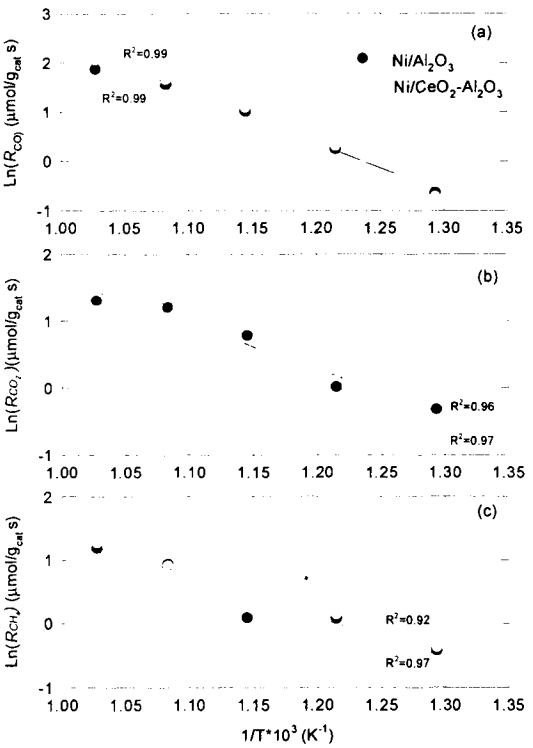

Fig.1 Arreheius plots for reaction rate in CO_2-CH_4 reforming. (a) CO (b) CO_2 (c) CH_4

Table 1
Activation energies for CH_4-CO_2 reaction.

Catalyst	E_{CO}(kJ/mol)	E_{CH_4}(kJ/mol)	E_{CO_2}(kJ/mol)
Ni/γ-Al_2O_3	80.5±5.2	50.9±8.5	56.1±6.6
Ni/CeO_2-Al_2O_3	87.0±5.3	50.5±5.4	77.0±8.0

Olsbye et al. [15] reported that the activation energy for CO production amounted to 90 kJ/mol for Ni/La_2O_3-Al_2O_3 catalyst. These values are much similar to the results for CO production

obtained in this research. Tokunaga and Ogasawara [16] obtained activation energy for CH_4 consumption over Ni/Al_2O_3 of 92.4 kJ/mol. However, Osaki et al. [17] found that activation energies for CH_4 consumption were about 33 kJ/mol over supported Ni catalysts, Ni/TiO_2, Ni/MgO, Ni/SiO_2, and Ni/Al_2O_3. Lower activation energies for CH_4 consumption ranging 40-76 kJ/mol were also reported [18]. These observations are close to the values for CH_4 and CO_2 consumption in this investigation. Therefore, it is deduced that the wide range of apparent activation energy over Ni-based catalysts reported in the previous research and obtained in this work may be attributed to the varying catalyst system and reaction conditions. In practice, a heterogeneous catalyst may have a distribution of catalytic active sites with different intrinsic activation barriers for the chemical reaction of interest.

3.2. Dependencies of partial pressure and kinetic model

The dependencies of the rate of CO production on the partial pressures of CH_4 and CO_2 were determined in a broad temperature range over two catalysts and are plotted in Figures 2 and 3. As can be seen, a linear dependency of CO production rate on CH_4 partial pressure is observed. While the relationship between CO production rate and CO_2 partial pressure varies depending on CO_2 pressure. At lower CO_2 partial pressure (<6 kPa), the reaction rate increases with increasing pressure. As the CO_2 pressure reached about 6 kPa, the CO formation rate levels off at all temperatures.

The reaction orders with respect to pressures of CH_4 and CO_2 were determined from a simple power law equation

$$R_{CO} = kP_{CH_4}^{a} P_{CO_2}^{b} \tag{2}$$

Table 2 gives a summary of the extracted reaction orders and parameter k values at various temperatures. It is seen that the reaction order with respect to CH4 pressure is close to first order at all temperatures for both catalysts. The reaction order with respect to PCO2 approaches zero at high partial pressure (>6 kPa). These results are in agreement with findings of Rostrup-Nielsen and Hansen [19]. They reported a zero-order dependence on P_{CO_2} and a first-order dependence on P_{CH_4} over Ni/Mg(Al)O catalyst.

Table 2
Reaction order based on simple power law.

Tem (°C)	Ni/Al_2O_3			Ni/CeO_2-Al_2O_3		
	CH_4	CO_2*	k($\mu mol/g_{cat}.s\ kPa^2$)	CH_4	CO_2*	k($\mu mol/g_{cat}.s\ kPa^2$)
500	1.05	0.83	0.25	1.08	0.73	0.52
550	1.08	0.85	0.55	1.04	0.97	1.18
600	1.00	1.11	1.38	1.12	0.94	3.06
650	0.93	1.61	2.64	1.06	0.60	4.54
700	0.90	1.77	3.83	1.10	0.55	7.27

* $P_{CO_2} < 6$ kPa

Olsbye et al.[15] also reported similar results for a Ni/La_2O_3-Al_2O_3 catalyst in CO_2-CH_4 reforming at 700-900 °C. Takano et al. [18] found similar results over Ni/Al_2O_3 for this reaction. For CO_2 partial pressure lower than 8.4 kPa, the reaction order with respect to P_{CO_2} is almost unity, and for CO_2 pressure in the range of 8.4-67.6 kPa, the order is zero. Based on the k values at various temperatures, the activation energies over two catalysts according to Eq.2 were estimated as 88.2 and 83.6 kJ/mol, respectively. It is seen that these values are close to the results reported in Table 1.

In the previous section, it was shown that the activation energy for CO production is higher than that for either CH_4 or CO_2 consumption. Catalytic reaction of CO_2 reforming of methane involves first chemisorption of CH_4 and CO_2 on active sites. The lower activation energies for CH_4 or CO_2 consumption may suggest that chemisorption steps of the two reactants are relatively easier, and CO formation step is rate controlling.

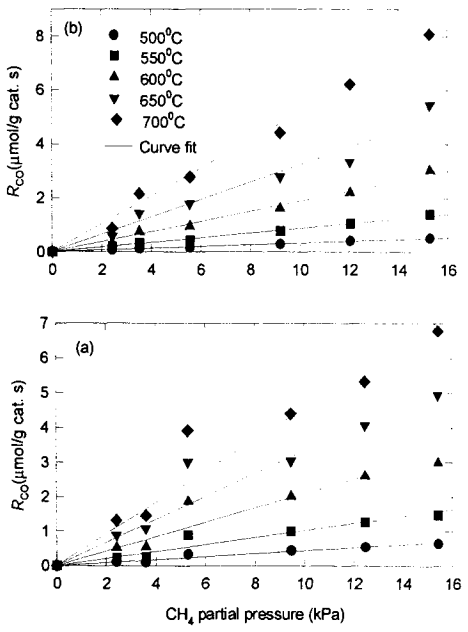

Fig.2 Relationship between CO production rate and CH_4 partial pressure
(a) Ni/Al_2O_3 (b) Ni/CeO_2-Al_2O_3

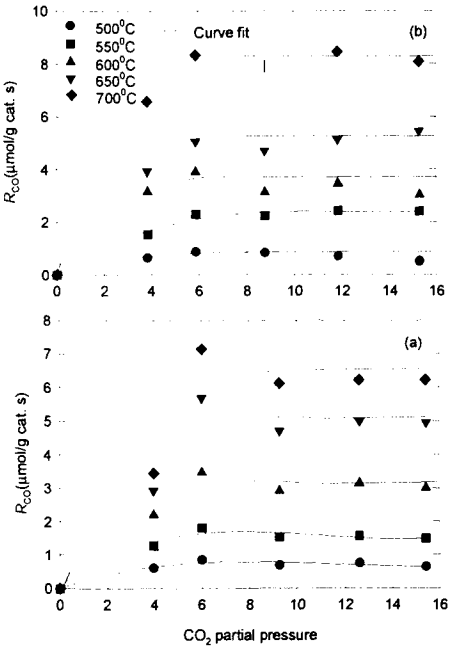

Fig.3 Relationship between CO production rate and CO_2 partial pressure.
(a) Ni/Al_2O_3 (b) Ni/CeO_2-Al_2O_3

The reaction mechanism can, therefore, be simplified as follows:

$$CH_4 + * \rightarrow CH_4* \quad (3)$$

$$CO_2 + * \rightarrow CO_2* \quad (4)$$

$$CH_4^* + CO_2^* \rightarrow 2\,CO + 2\,H_2 + 2\,^* \quad (5)$$

The rate for CO production is expressed as

$$r = k\,[CH_4^*][CO_2^*] \quad (6)$$

Where k is the rate constant, $[CH_4^*]$ and $[CO_2^*]$ are the surface concentrations for adsorbed CH_4 and CO_2. According to the dependencies of the reaction rate(Eq.2) on CH_4 or CO_2 partial pressure described above, methane showed first order and CO_2 exhibited first order at lower partial pressure and zeroth order at high pressures. Assuming a Langmuir adsorption for chemisorbed CH_4 and CO_2

$$[CH_4^*] = \frac{K_1 P_{CH_4} C_{CH_4}}{(1 + K_1 P_{CH_4})} \quad (7)$$

$$[CO_2^*] = \frac{K_2 P_{CO_2} C_{CO_2}}{(1 + K_2 P_{CO_2})} \quad (8)$$

where K_1, K_2 are the adsorption equilibrium constants for CH_4 and CO_2, respectively. C_{CH_4} and C_{CO_2} represent the CH_4 and CO_2 concentrations corresponding to a monomolecular layer on the catalyst. Hence, replacing the variables in Eq (6), the rate for CO production will be

$$r = \frac{k_1 P_{CH_4} P_{CO_2}}{(1 + K_1 P_{CH_4})(1 + K_2 P_{CO_2})} \quad (9)$$

where $k_1 = kK_1K_2C_{CH_4}C_{CO_2}$. Olsbye et al. [15] investigated the kinetics of CO_2-reforming reaction over Ni/La_2O_3-Al_2O_3 and obtained the same rate expression.
At a fixed CH_4 partial pressure, if P_{CO_2} is higher, i.e., $K_2P_{CO_2} >> 1$, Eq. (9) is approximated by

$$r = \frac{k_1' P_{CH_4}}{(1 + K_1 P_{CH_4})} \quad (10)$$

where $k_1' = k_1/K_2$, which explains that the reaction order is zeroth order with respect to CO_2 partial pressure. If P_{CO_2} is lower, i.e. $K_2P_{CO_2} << 1$, Eq. (9) will be approximated as

$$r = \frac{k_1 P_{CH_4} P_{CO_2}}{(1 + K_1 P_{CH_4})} \quad (11)$$

The reaction is of the first order with respect to CO_2 partial pressure. Similarly, at a fixed CO_2 pressure, if $K_1P_{CH_4} << 1$, Eq, (9) is simplified to

$$r = \frac{k_1 P_{CH_4} P_{CO_2}}{1 + K_2 P_{CO_2}} \quad (12)$$

Under this condition, the reaction is of the first order with respect to CH_4 partial pressure.The experimental data (Figure 2 and 3) were fitted to the model (Eq.9) and the best fit was obtained with the constants presented in Table 3. It is seen that the values of equilibrium constant K_2 are generally higher than K_1, which explains the reason why activation energy for CO_2 consumption is greater than that of methane consumption. The reaction constant of k_1 is around 0.2- 1.0 $\mu mol/g_{cat}.s\ kPa^2$. Olsbye et al. [14] reported a value of 0.4 $\mu mol/g_{cat}.s\ kPa^2$ for Ni/La_2O_3-Al_2O_3 catalyst.

Table 3
Kinetic parameters for model of reaction rate.

Temp (°C)	Ni/Al_2O_3			Ni/CeO_2-Al_2O_3		
	k_1 ($\mu mol/g_{cat}.s\ kPa^2$)	K_1 (kPa^{-1})	K_2 (kPa^{-1})	k_1 ($\mu mol/g_{cat}.s\ kPa^2$)	K_1 (kPa^{-1})	K_2 (kPa^{-1})
500	0.20±0.04	$(8.2\pm0.2)\times10^{-4}$	4.3±0.8	1.0±0.3	$(5.0\pm0.5)\times10^{-10}$	22.8±1.1
550	0.29±0.04	$(1.5\pm0.3)\times10^{-2}$	2.3±0.6	0.21±0.09	$(7.6\pm1.3)\times10^{-10}$	1.5±0.2
600	0.24±0.03	$(2.3\pm0.3)\times10^{-2}$	0.80±0.4	1.0±0.07	$(3.6\pm0.2)\times10^{-10}$	4.6±0.4
650	0.25±0.05	$(2.0\pm0.2)\times10^{-2}$	0.50±0.2	0.32±0.02	$(1.6\pm0.6)\times10^{-10}$	0.9±0.2
700	0.32±0.04	$(3.5\pm0.3)\times10^{-2}$	0.43±0.2	0.68±0.05	$(1.3\pm0.3)\times10^{-10}$	1.2±0.3

3.3. Deactivation of catalysts

Deactivation of two catalysts versus time in differential conditions was conducted at 700 °C (Figure 4). The deactivation of Ni/CeO_2-Al_2O_3 proceeded significantly slower than that of Ni/Al_2O_3. During the 6 h testing, Ni/CeO_2-Al_2O_3 lost its initial activity by 75% whereas Ni/Al_2O_3 lost 97% of its initial activity. The corresponding deactivation rates for Ni/Al_2O_3 and Ni/CeO_2-Al_2O_3 catalysts were estimated to be 8.1×10^{-4} and 1.3×10^{-4} min^{-1}, respectively. The difference is believed to be resulted from more severe coking on Ni/Al_2O_3 catalyst. Coking measurements in TGA and fixed-bed reactor indicated that carbon content in CO_2 reforming of methane on Ni/Al_2O_3 was two times as great as on Ni/CeO_2-Al_2O_3 under the same reaction conditions. The stability tests of these two catalysts in integral conditions also showed that ceria-promoted Ni/Al_2O_3 exhibited longer activity, which is similar to the results [11].

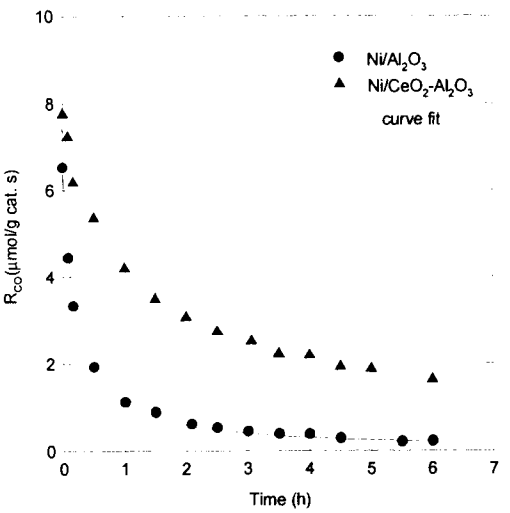

Fig.4 Deactivation of catalyst versus time in CO_2 reforming of methane.

Many types of expressions have been used for modeling deactivation. Most frequently, time-dependent models are used. Simple correlations of how the activity, γ , varies with time are commonly employed. In these correlations γ is defined as [20]:

$$r = r^0 \gamma(t) \tag{13}$$

where r is the reaction rate at time t, and r^0 is the reaction rate at time t=0. The activity, γ, can be modeled using zeroth-, first-, and second-order deactivation forms [20].

$$\gamma(t) = 1-\alpha t \tag{14}$$

$$\gamma(t) = \exp(-\alpha t) \tag{15}$$

$$\gamma(t) = 1/(1+\alpha t) \tag{16}$$

where α is a constant associated with catalyst deactivation and varies with reaction conditions. Froment and Bischoff [21] discussed the problems using models that treat deactivation as a simple function of time. They stressed that different reaction conditions would result in different values of the constant α , and that the constant is actually a function of reaction conditions. Further, they argued that expressions showing the activity is a function of the coke content C_c, for example $\gamma=\exp(-\alpha C_c)$, are more useful. Volter and Kurschner [22] studied the conversion of methylcyclopentane over Pt and Pt-Sn catalysts and found that the coke caused the deactivation in an almost linear fashion. Larson [23] reported that activity of propane dehydrogenation declined with increasing amount of coke and followed the equation of $\gamma=\exp(-\alpha C_c)$.

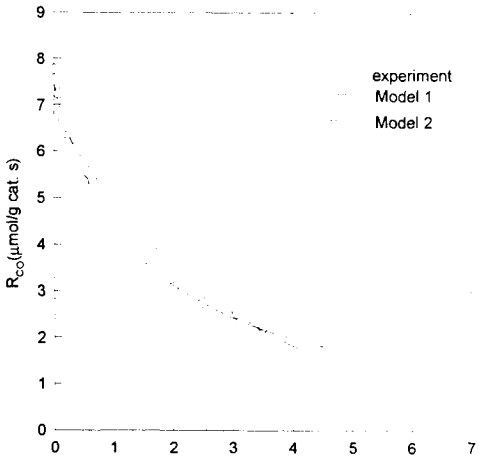

Fig.5 Comparison of experiment and models for catalyst activity over Ni/CeO_2-Al_2O_3.

In this investigation, Figure 4 shows clearly that deactivations of Ni/Al_2O_3 and Ni/CeO_2-Al_2O_3 catalysts in CO_2 reforming of methane were not of zeroth order. Hence, two other models were employed to model the catalyst deactivation and a typical result is shown in Figure 5. As seen, second order deactivation is better in fitting the experimental data. Using this model the parameters, α and r^0 , were obtained for two catalysts (Table 4). It is seen that α is much larger for Ni/Al_2O_3 catalyst.

Table 4
Parameter values for deactivation models.

Catalyst	Parameters	
	α (h^{-1})	r^0 ($\mu mol/g_{cat}\ s$)
Ni/Al_2O_3	5.06	6.44
Ni/CeO_2-Al_2O_3	0.69	7.42

Catalyst deactivation in CO_2 reforming of methane is generally ascribed to carbon deposition and metal sintering, in which coking is the major cause. When performing deactivation studies, correlation between coke concentration and activity can often be obtained in the reforming reaction, dehydrogenation and methanation. We have studied carbon deposition over these two catalysts at 700 °C with CH_4: CO2 =1:1 using a thermogravimetric analysis [12].

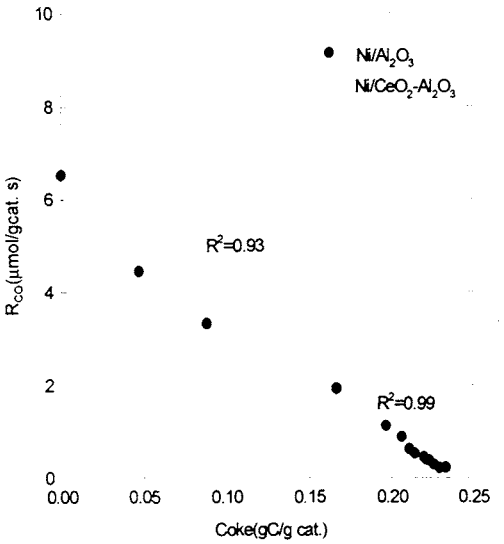

Fig.6 Relationship between catalyst activity and carbon deposition over Ni-based catalysts.

Comparison of coking profile on catalyst and the catalyst deactivation behaviour in CO_2 reforming of methane, it could be found that the curve shapes are conversely similar, which suggests that coking is responsible for the catalyst deactivation. Figure 6 presents the relationship between reaction rate and coke content for Ni/Al_2O_3 and Ni/CeO_2-Al_2O_3catalysts. It is seen that reaction rate has an inversely linear relation with coke content, not as the exponential relation [23]. This result is similar to the observation of Volter and Kurschner [22].

4. CONCLUSION

The kinetics of the CO_2 reforming of methane was investigated over Ni/γ-Al_2O_3 and Ni/CeO_2-Al_2O_3 catalysts at temperatures 500-700 °C under the conditions of normal pressure with a 1:1 mixture of CH_4 and CO_2. The reaction mechanism was found much similar over two catalysts and the activation energies were around 80 kJ/mol based on CO production. A Langmuir-Hinshelwood type of expression can be used to model the reaction. Deactivation of catalysts Ni/γ-Al_2O_3 and Ni/CeO_2-Al_2O_3 in differential conditions was directly correlated with amount of carbon deposition though Ni/CeO_2-Al_2O_3 showed lower deactivation rate.

Acknowledgement- Financial support by the Australian Commonwealth Department of Education under the TIL program is greatly acknowledged.

REFERENCES

1. S. Wang, G.Q. Lu, and G.J. Millar, Energy & Fuels, 10 (1996), 896.
2. J.H. Edwards and A. M. Maitra, Fuel Processing Tech., 42 (1995), 269.
3. W.K. Lewis, E.R. Gilliland, and W.A. Reed, *Ind. Eng. Chem.*, 41 (1949),1227.
4. I.M. Bodrov, and L.O. Apel'baum, *Kinet. Catal.*, 8 (1967), 379.

5. I.M. Bodrov, L.O. Apel'baum, and M.I. Temkin, *Kinet. Catal.*, 5 (1964), 696.
6. J.T. Richardson, and S.A. Paripatyadar, *Appl. Catal.*, 61 (1990), 293.
7. Z.L. Zhang and X.E. Verykios, *Catal. Today*, 21 (1994), 589.
8. M.C.J. Bradford, and M.A. Vannice, Appl. Catal. A., 142 (1996), 97.
9. M.F. Mark, F. Mark, and W.F. Maier, *Chem. Eng. Technol.*, 20 (1997), 361.
10. S. Wang, and G.Q. Lu, Appl. Catal. A., 169 (1998), 272.
11. S. Wang and G.Q. Lu, Appl. Catal. B., 19 (1998), 267.
12. S. Wang, Ph.D thesis, The University of Queensland, 1998.
13. V.C.H. Kroll, G.J. Tjatjopoulos, and C. Mirodatos, Stud. Surf. Sci. Catal., 119(1998), 753.
14. A. Trovarelli, Catal. Rev. Sci. Eng., 38(1996), 439.
15. U. Olsbye, T. Wurzel, and L. Mleczko, Ind. Eng. Chem. Res., 36 (1997), 5180.
16. O. Tokunaga, and S. Ogasawara, React. Kinet. Catal. Lett., 39 (1989), 69.
17. T. Osaki, T. Horiuchi, K. Suzuki, and T. Mori, J. Chem. Soc.,Faraday Trans., 92 (1996), 1627.
18. A. Takano, T. Tagawa, and S. Goto, , J. Chem. Eng. Jpn., 27 (1994), 723.
19. J.R. Rostrup-Nielsen, and J.H.B. Hansen, J. Catal., 1993, 144 (1993), 38.
20. J.B. Butt and E.E. Petersen(eds.), Activation, Deactivation, and Poisoning of Catalysts, Academic Press Inc., San Diego, 1988.
21. G.F. Froment, and K.B. Bischoff (eds.), Chemical Reactor Analysis and Design, John Wiley & Sons, New York, 1979.
22. J. Völter, and U. Kürschner, , Appl. Catal. A., 8 (1983), 167.
23. M. Larson, Ph.D thesis, Chalmers University of Technology, 1997.

Reaction Engineering for Pollution Prevention
M.A. Abraham and R.P. Hesketh (Editors)

Unsteady-state kinetics of $DeNO_x$-SCR catalysis

Luca Lietti, Isabella Nova, Enrico Tronconi, Pio Forzatti

Dipartimento di Chimica Industriale e Ingegneria Chimica "G. Natta", Politecnico di Milano, P.zza L. Da Vinci 32, 20133 Milano, Italy

A dynamic model of the SCR catalysis, describing both the $DeNO_x$ and the SO_2 oxidation reaction for industrial SCR monolith reactors, is presented. The model relies on the fundamentals of both the SCR reactions and the SO_2 oxidation reaction investigated under transient conditions, and allows combined predictions of NO_x reduction efficiency, NH_3 slip and SO_3 emission levels for changes in the operating conditions of industrial SCR monolith reactors.

1. INTRODUCTION

The Selective Catalytic Reduction (SCR) of NO_x by ammonia is a world-wide commercial technology for NO_x abatment from power plant flue gases [1-3]. The process is based on the reaction among nitrogen oxides contained in the flue gases (essentially nitrogen monoxide) with oxygen and injected ammonia according to the stoichiometry:

$$4\,NO + 4\,NH_3 + O_2 \rightarrow 4\,N_2 + 6\,H_2O$$

If SO_2 is present in the combustion gases, as occurring in the combustion of S-bearing fuels, SO_2 oxidation also occurs as a side reaction:

$$SO_2 + \tfrac{1}{2}\,O_2 \rightarrow SO_3$$

Even very small SO_2 conversions are highly undesired since they cause deposition of ammonium sulfates in the cold parts of the plant [4].

Commercially available catalysts are made up of a TiO_2 anatase carrier supporting the active components, i.e. V_2O_5 and WO_3 (or MoO_3). Vanadia is active in the reduction of NO_x but also in the undesired oxidation of SO_2 to SO_3, accordingly its content is kept low, below 1.0 % w/w. WO_3 (or MoO_3) is employed in larger amounts (nearby 6 or 10 % w/w for MoO_3 and WO_3, respectively); they act both as "chemical" and "structural" promoters by enlarging the temperature window of the SCR reaction and by improving the mechanical, structural and morphological properties of the catalysts [5-8]. Commercial catalysts are shaped in the form of honeycomb monoliths or plates: such

structures afford low pressure drops and high attrition resistance while providing geometric surface areas comparable to those of packed beds of catalyst pellets [9].

SCR-DeNO$_x$ reactors are often involved in transient operations associated e.g. with startup, shutdown or load variations. Under such conditions, maintaining pollutants below the emission limits may become more critical than during steady-state operation. This has stimulated in the last years a growing interest towards the study of the dynamics of SCR reactors in view of a possible development of predictive control systems of SCR plants able to avoid pollutants emission peaks during transient conditions. Furthermore, the understanding of the dynamics of the SCR catalysis is of importance also in the development of forced unsteady operation of SCR reactors (as e.g. in flow reversal processes for power stations [10-13]) and in the purification of exhaust gases from non-stationary sources (e.g. diesel engines of heavy trucks [14]), which involves fast transients primarily associated with load variations.

For all of these applications, reliable engineering analysis calls for a dynamic mathematical model of the SCR reactor. If properly grounded on the physico-chemical fundamentals of the SCR chemistry, such a model can be in principle more helpful in rationalizing the complexities of the reacting system under transient conditions.

Such investigation was performed in our labs: a dynamic model of the SCR reactor was developed based on a detailed knowledge of both the dynamics of the DeNO$_x$-SCR reaction and of the simultaneously occurring $SO_2 \rightarrow SO_3$ oxidation reaction. As a first stage of our study, the dynamics of the DeNO$_x$-SCR reaction was investigated. To avoid complications and difficulties associated with the presence of diffusional limitations, which are typically encountered under real SCR conditions over monolith catalysts, the dynamics of the DeNO$_x$-SCR reaction was investigated in the kinetic regime in a microreactor system over powder catalyst samples. The transient response method was adopted for this purpose, by applying perturbations to the reacting system (e.g. step or linear changes in the inlet reactant concentration) and analyzing the transient response. The characteristics of the response reflect the nature of the sequence of steps underlying the kinetics of the reaction: therefore valuable mechanistic and dynamic aspects of the reaction could be derived. Aiming at the analysis of the single steps of the reaction, the adsorption-desorption of the reactants (e.g. ammonia and NO) was at first investigated, and then their surface reaction was addressed. Quantitative kinetic indications were then obtained by analyzing the results of the transient response experiments by using a dynamic model of the reacting system.

Once the major features of the DeNO$_x$-SCR reaction under transient conditions in a chemical regime were secured, drawing from previous activities in steady-state modelling of SCR monolith reactors [15-17], we developed an introductory 1D unsteady heterogeneous model of the DeNOx reaction in monolith honeycomb catalysts, based on analytical approximations of the reactant intraporous concentration profiles.

The second stage of the study involved the analysis of the dynamics of the SO_2 to SO_3 oxidation reaction. In previous papers we have systematically investigated the effects of operating conditions, feed composition and catalyst design parameters in the oxidation of SO_2 to SO_3 under steady-state conditions over honeycomb deNOxing catalysts [18-20]. It was shown that, due to the low SO_2 conversion values (typically lower that 1 %), the SO_2 to SO_3 oxidation reaction operates under chemical control.

Also, it was shown that a kinetic interaction exists between SO_2 oxidation and NO_x reduction and that the oxidation of SO_2 to SO_3 may influence the reduction of NO_x by affecting the level of sulfates present on the surface of the catalyst. In this study, the SO_2 oxidation reaction was examined under transient conditions as well and the dynamics of the reaction was investigated by the transient response method. Finally, a dynamic kinetic model of SO_2 oxidation over SCR monolith catalysts was also developed and is herein presented, based on a detailed mechanism of the catalyst sulfate coverage which accounts for the interaction with NO_x reduction. The model has been validated against transient experiments both in the absence of the De-NO_x reaction and with its simultaneous occurrence.

2. EXPERIMENTAL

2.1. Catalysts

Ternary V_2O_5-WO_3/TiO_2 model and commercial catalysts were used in the various experiments.

The model catalyst (V_2O_5 = 1.47 % w/w, WO_3 = 9 % w/w) was prepared by dry impregnation of a home-made TiO_2 anatase support with a hot water solution of ammonium paratungstate and citric acid, followed by drying and calcination at 823 K. Vanadium was then introduced by dry impregnation of the calcined WO_3/TiO_2 sample with a hot water solution of ammonium metavanadate and oxalic acid, followed by drying and calcination at 823 K [20]. The XRD analysis showed that the catalyst is monophasic and constituted by TiO_2 in the polymorphic form of anatase. The specific surface area of the sample is 80 m^2/g. The V and W surface coverage (θ_V and θ_W, respectively), calculated as reported by Vermaire and van Berge [21] and by Bond and Tahir [22], are $\theta_V = 0.12$ and $\theta_W = 0.67$ ($\theta_{Ti} = 0.21$).

Commercial V_2O_5-WO_3/TiO_2 catalysts having different V_2O_5 contents (0.6 – 1 % w/w) and WO_3 loading near 9 % w/w were also used, either in the form of monolithic samples or as granules, obtained by crushing and sieving the monolithic samples. The vanadium loading was uniformly distributed across the wall thickness of the monoliths or of the granules. Monolithic samples had square channels, with pitch and wall half-thickness near 7 and 0.6 mm, respectively. Catalyst samples with 9 channels, 15 cm in length, were cut from commercial modules and loaded in the test reactor.

2.2. Transient adsorption-desorption of the DeNO$_x$-SCR reactants and reactivity experiments under kinetic regime (powder catalysts)

The transient NH_3 and NO adsorption-desorption study and NO + NH_3 reaction were performed in a flow-microreactor system constituted by a quartz tube (8 mm o.d., 6 mm i.d.) directly connected to a mass spectrometer (UTI 100C) via a leaking system allowing fast transfer of the gases from the reactor to the quadrupole mass analyzer (traveling time lower than 2 s). The reactor was inserted into an electric furnace and the catalyst temperature was measured and controlled by means of a K-type thermocouple directly immersed in the catalyst bed.

The feed gases (NH_3 in He, NO in He, O_2 in He and Ar (inert tracer) in He), whose flow rates were measured and controlled by mass flow controllers (Brooks 5850 TR), were mixed in a single stream before entering the reactor. Both step changes and linear variations in the inlet reactant concentrations with time were performed. In the first case a four-port valve was used to perform the abrupt switches in the inlet reactant concentration, whereas linear changes in the inlet reactant concentrations were imposed by externally driving in a linear fashion the set point values of the mass flow meter-controllers with a Personal Computer. In both cases care was taken in minimizing all possible dead volumes in the lines before and after the reactor and in eliminating pressure and flow changes upon switching of the reactants.

Transient NH_3 (or NO) adsorption-desorption experiments were performed by imposing step-wise or linear perturbations in the NH_3 (or NO) reactor inlet concentration at various temperatures in flowing He + O_2, while maintaining the overall flow rate constant. At the end of the experiments, the catalyst were heated up to 773 K under temperature programming at 15 K/min in order to completely desorb the reactants still adsorbed over the catalyst surface (Temperature Programmed Desorption, TPD).

The dynamics of the NH_3 + NO SCR reaction was investigated by imposing step-wise perturbations in the NH_3 (or NO) reactor inlet concentration while keeping constant the concentrations of the other reactants. Additional conditions are reported in the figure captions.

2.3. Transient $DeNO_x$-SCR reactivity experiments under real conditions (monolith catalysts)

Experimental transient data of NO reduction were obtained in a lab-scale flow reactor over commercial "high-dust" monolith honeycomb V_2O_5-WO_3/TiO_2 catalysts. Monolith samples with nine channels, 15 cm in length, were cut from commercial modules, wrapped with quartz wool and forced into the test reactor to prevent bypass. Synthetic gas mixtures from high-pressure bottles (300-560 ppm NO, 1000-1200 ppm SO_2, 2-2.6% v/v O_2, 10-12.6% v/v H_2O, balance N_2) were pre-heated to the desired reaction temperature, mixed with ammonia (300-500 ppm NH_3) at the top of the reactor to prevent side reactions, and then admitted to the reactor. The gases flowing out of the reactor were passed in an aqueous solution of phosphoric acid to trap unconverted ammonia. NO/NO_x were detected in a chemiluminescence analyzer (Beckman, model 955). Further details on the experimental apparatus and on the analytical methods are given elsewhere [18].

Transient experiments consisted in reactor start-up (NH_3 injection into the NO-containing feed stream) and shut-down procedures corresponding to various NH_3/NO feed ratios (0.6 - 1.2) and operating temperatures (270 - 380 °C), as well as in step changes of the inlet concentration of either NO or NH_3. During the experiments, the H_2O, O_2 and SO_2 reactor inlet concentrations were kept constant. In view of these transient runs, special care was devoted to minimize the dead volumes existing in the rig. Blank start-up runs indicated that a lag time of less than 10 s was typically associated with the test reactor transients.

2.4. Transient $SO_2 \rightarrow SO_3$ reactivity experiments

Transient $SO_2 \rightarrow SO_3$ reactivity experiments were performed in the same rig used for the $DeNO_x$-SCR reactivity experiments over commercial monolith honeycomb V_2O_5-WO_3/TiO_2 catalysts. The experimental plan was designed in order to cover the dynamic effects associated with step changes of the major operating variables, namely temperature, Area Velocity (AV), feed concentrations of SO_2, H_2O and O_2, over an experimental field representative of industrial SCR operation. In line with the SCR technical literature, AV is herein defined as the ratio of the volumetric feed flow rate to the geometric surface area of the catalyst. The following variable ranges were investigated: T = 350 - 380 °C, $C°_{SO_2}$ = 160 - 1917 ppm, H_2O feed content = 3.3 - 9.7% v/v, O_2 feed content = 0.1 - 5% v/v, AV = 5 - 7.8 $Nm^3/(m^2\ h)$. In the runs with simultaneous occurrence of SO_2 oxidation and NO reduction, NO and NH_3 feed concentrations in the range 200 - 400 ppm were also used. The SO_3 content of the outlet gases was determined by condensing sulfuric acid at 90 °C in a glass spiral, followed by off-line analysis with an ionic chromatograph Dionex Model Quick. The mean sampling time was 45 minutes, much shorter than the typical system response time; sampling was more frequent during fast transients.

3. RESULTS AND DISCUSSION

3.1. Transient kinetics of the adsorption-desorption of NH_3 and NO and of the SCR reaction

3.1.1. NH_3 and NO adsorption-desorption

The transient kinetics of the adsorption-desorption of the SCR reactants (NH_3 and NO) were investigated at first. Step and linear changes of the reactor inlet NH_3 (or NO) concentration were performed for this purpose, and the transient response was analyzed. In the case of NH_3, a typical result obtained with a rectangular step feed in flowing He + O_2 over a ternary V_2O_5-WO_3/TiO_2 model catalyst at 280 °C is presented in Figure 1A, where the dashed line represents the ammonia inlet concentration. The results of the TPD experiment obtained upon heating the catalyst at the end of the ammonia rectangular step are also reported. The figure shows that upon the NH_3 step addition (at t = 0 s), the ammonia outlet concentration slowly increased with time and approached the ammonia inlet concentration (700 ppm) only after ≈ 500 s. The shaded area included between the ammonia inlet and outlet concentration traces is proportional to the amount of NH_3 adsorbed over the catalyst surface. A similar behavior is apparent upon ammonia shut-off (t = 750 s): the outlet NH_3 concentration slowly decreases with time due to the desorption of previously adsorbed ammonia. Complete desorption of NH_3 was achieved upon subsequent heating of the catalyst (TPD experiment).

The study of NH_3 adsorption/desorption process was also performed by imposing linear variations of the inlet ammonia concentration over a commercial catalyst (Figure 1B, dashed line). In this case the outlet NH_3 concentration shows a large dead-time (400 s), and then increases with time showing a shoulder near 500 s. The final steady state

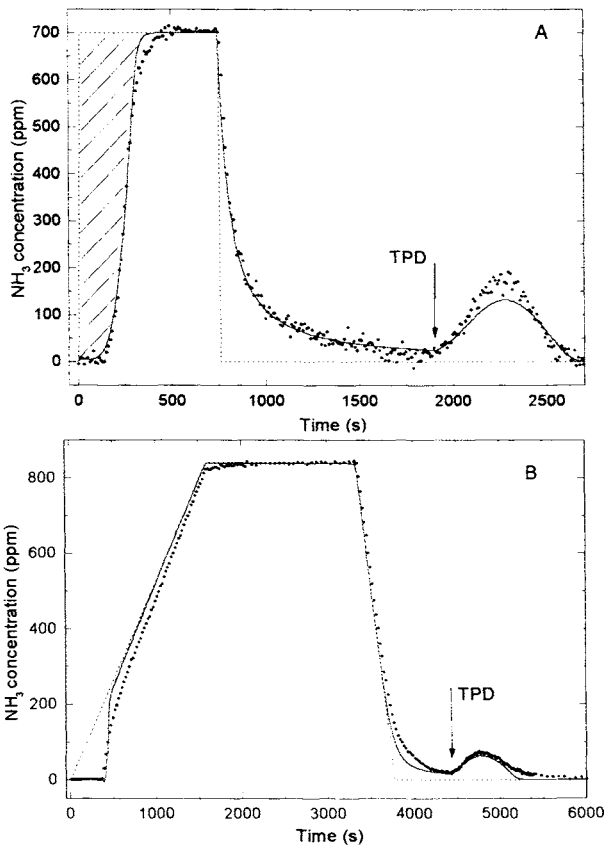

Figure 1. Dynamic adsorption-desorption of NH_3: A) step changes of the NH_3 inlet concentration over a model V_2O_5-WO_3/TiO_2 catalyst (V_2O_5 = 1.47 % w/w; WO_3 = 9 % w/w) at 280°C. NH_3 step addition at t = 0, shut off at t = 750 s and thermal desorption (TPD). Dashed lines: ideal inlet NH_3 concentration; symbols: experimental data; solid lines: model fit (Temkin-type coverage dependence: $k°_a$=0.487 m^3/mol s, $k°_d$=2.67 E+5 1/s, $E°_d$= 22.9 kcal/mol, γ=0.405, Ω_{NH3}=270 m^3/mol); B) linear changes of the NH_3 inlet concentration (0 → 840 → 0 ppm) over a commercial WO_3-V_2O_5/TiO_2 catalyst (V_2O_5 = 0.6 % w/w; WO_3 = 9 % w/w). at 300°C followed by thermal desorption (TPD). Dashed lines: ideal inlet NH_3 concentration; symbols: experimental data; solid lines: model fit (Temkin–type coverage dependence: $k°_a$= 33.87 m^3/mol s, $k°_d$=2.2 E+6 1/s, $E°_d$= 23.0 kcal/mol, γ=0.256,

value is reached after 1700 s. In line with the transient step experiments, also in this case the presence of the dead-time in the outlet NH_3 concentration clearly indicates that NH_3 strongly adsorbs on the catalyst surface. During the negative ramp, the ammonia outlet concentration decreases less than the NH_3 inlet concentration due to the presence of previously adsorbed species. Again, complete NH_3 desorption was achieved upon the subsequent TPD experiment.

NH_3 adsorption-desorption experiments were performed at different temperatures (data not reported in the figure). On increasing the catalyst temperature the variations in the ammonia outlet concentration during both the adsorption and desorption steps are faster and the amount of ammonia adsorbed on the catalyst surface is reduced, in line with the increased rates of the adsorption-desorption processes and with the exothermicity of the NH_3 adsorption process. The area of the TPD desorption trace is also significantly reduced. At temperatures above 350 °C, formation of N_2 and H_2O was observed (figure 2), indicative of the occurrence of the ammonia oxidation reaction.

Rectangular and linear variations of the reactor inlet concentration were also performed with the other SCR reactant (NO) at different temperatures in He + O_2 over both model and commercial V_2O_5-WO_3/TiO_2 catalysts (figure 3). In all cases the outlet NO concentration curves

closely resemble that of the inlet NO concentration. This indicates that NO does not appreciably adsorb onto the catalyst surface, in line with literature indications [23,24].

3.1.2. NH_3 + NO reaction

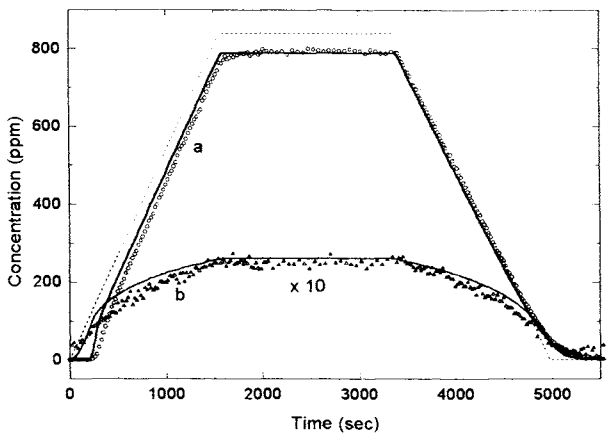

Figure 2. Dynamic adsorption-desorption of NH_3 over a commercial WO_3-V_2O_5/TiO_2 catalyst (V_2O_5 = 0.6 % w/w; WO_3 = 9 % w/w) at 400°C following linear variations of the inlet ammonia concentration (0 → 840 → 0 ppm). Dashed lines: ideal inlet NH_3 concentration; trace a: NH_3 experimental data; trace b: N_2 experimental data; solid lines: model fit ($k°_a$= 33.87 m^3/mol s, $k°_d$=2.2 E+6 1/s, $E°_d$= 23.0 kcal/mol, γ=0.256, Ω_{NH3}=270 m^3/mol, $k°_{ox}$= 3.25 E+6 1/s, $E°_{ox}$= 28.8 kcal/mol).

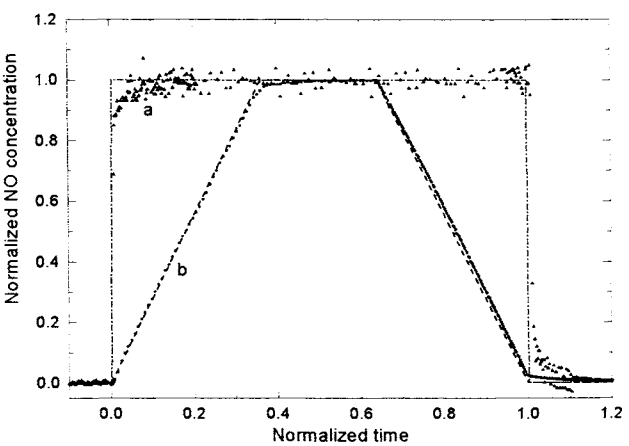

Figure 3. Dynamic adsorption-desorption of NO: step addition and shut off on a model V_2O_5-WO_3/TiO_2 catalyst (V_2O_5 = 1.47 % w/w; WO_3 = 9 % w/w) at 280 °C (dash-dotted line: inlet NO concentration, trace a: NO outlet concentration); linear variations on a commercial V_2O_5-WO_3/TiO_2 catalyst (V_2O_5 = 0.6 % w/w; WO_3 = 9 % w/w) at 300°C (dash line: inlet NO concentration, trace b: NO outlet concentration).

The dynamics of the SCR reaction was investigated upon performing step changes of the NH_3 reactor inlet concentration in flowing He + NO + O_2, and step changes of the NO reactor inlet concentration in flowing He + NH_3 + O_2. Figure 4 shows typical results obtained over the model V_2O_5-WO_3/TiO_2 sample upon performing step changes of the NH_3 inlet concentration (dashed line) at 220 °C in flowing He + NO 700 ppm + O_2 1% v/v. The figure reports the evolution with time of the outlet concentrations of ammonia (trace a), nitrogen oxide (trace b) and nitrogen (trace c).

Upon the NH_3 step feed (t = 0 s), the NO reactor outlet concentration decreased due to the occurrence of the SCR reaction. The evolution with time of the ammonia, NO and N_2 concentrations show different transient behaviors: the ammonia concentration profile exhibits a dead time (≈ 250 s) and then slowly increases with time on stream to the new steady-state value. On the other hand, the NO concentration trace does not show any dead time and reaches its steady-state value more rapidly if compared with NH_3. The evolution with time of N_2 and of H_2O (not reported

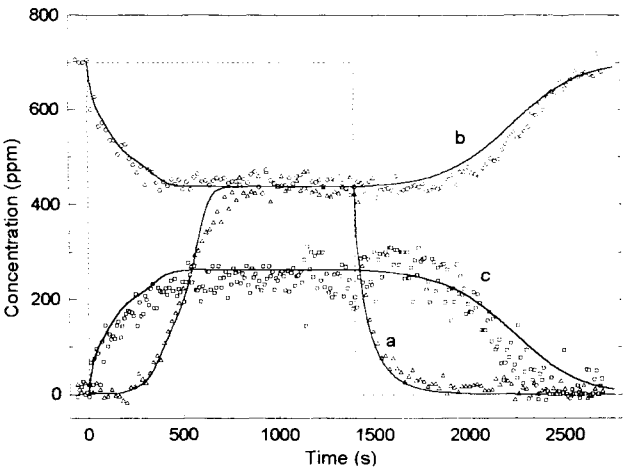

Figure 4. Step feed and shut off of NH_3 in He + O_2 (1 % v/v) + NO (700 ppm) over a WO_3-V_2O_5/TiO_2 model catalyst (V_2O_5 = 1.47 % w/w; WO_3 = 9 % w/w) at 220°C. Dashed lines: ideal inlet NH_3 concentration; symbols: experimental data (a: ammonia, b: NO, c: nitrogen concentration); solid lines: model fits (Temkin-type coverage dependence and "modified θ_{NH_3} kinetics": $k°_a$=0.487 m^3/mol s, $k°_d$=2.67 E+5 1/s, $E°_d$= 22.9 kcal/mol, γ=0.405, Ω_{NH3}=270 m^3/mol, $k°_{NO}$=7.19 E+5 1/s, $E°_{NO}$= 14.2 kcal/mol, $\theta^*_{NH_3}$ = 0.121).

in the figure) is symmetrical to that of NO. No formation of other species (e.g. N_2O) was observed, thus indicating the occurrence of a genuine SCR process. NH_3 and NO show a different transient behavior also upon the NH_3 shut-off, performed at t = 1250 s. Indeed while the NH_3 concentration rapidly dropped to zero, the NO concentration signal was not affected for several minutes. Then the NO concentration began to increase up to the inlet concentration value. Again the N_2 concentration trace is symmetrical to that of NO. Similar results were also obtained over a commercial catalyst sample by imposing linear variations in the inlet NH_3 concentration, instead of step changes [25].

The transient responses shown in figure 4 are typical of a reaction involving a strongly adsorbed species (NH_3) and a gas-phase or weakly adsorbed species (NO). Indeed, in correspondence of the increase of the ammonia feed content, the ammonia outlet concentration slowly increases with time on stream, being NH_3 itself involved in adsorption-desorption processes. On the other hand, NH_3-related reactive species are readily formed leading to the immediate consumption of gaseous NO. Along similar lines, upon decreasing the NH_3 inlet concentration, ammonia adsorbed species are still available for the reaction, and accordingly NO is still consumed. It is worth noting that upon decreasing the inlet NH_3 concentration (either in a step-wise manner or linearly) the rate of NO consumption is not affected for several minutes. This clearly indicates that the rate of the SCR reaction does not depend on the ammonia surface concentration above a characteristic "critical" value of the NH_3 coverage.

Similar evolutions of the concentrations of ammonia, nitrogen oxide and nitrogen with time on stream were obtained by performing the experiments at higher temperatures. In particular, on increasing the reaction temperature: i) the steady-state concentration of NO is lowered; ii) the delay in restoring the NO concentration upon decreasing the NH_3 inlet concentration is reduced. Such temperature effects are explained by the higher rates both of NH_3 desorption and of the surface reaction, which result in a higher conversion of NO but also in a significant depletion of the adsorbed

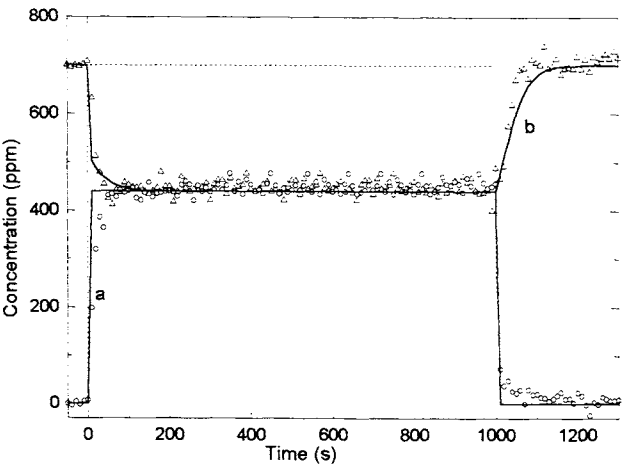

Figure 5. Results of NO step feed (t = 0 s) and shut off (t = 1000 s) experiments in He + O_2 (1% v/v) + NH_3 (700 ppm) over a WO_3-V_2O_5/TiO_2 model catalyst (V_2O_5 = 1.47 % w/w; WO_3 = 9 % w/w) at 220°C: dashed line: ideal inlet NO concentration; trace a: NO outlet concentration; trace b: NH_3 outlet concentration; solid lines: model predictions.

ammonia. Under these conditions (low NH_3 surface coverage) the rate of NO consumption becomes directly dependent on the ammonia surface concentration, so that the temporal evolution of NO follows closely that of NH_3.

The dynamics of the SCR reaction was also investigated by performing changes in the NO inlet concentration in NH_3 + O_2 constant. Figure 5 shows typical results obtained upon performing a step variation of the NO inlet concentration, respectively. The figure reports the evolution with time of the ammonia (traces b) and nitrogen oxide (traces a) reactor outlet concentrations. Upon increasing the NO inlet concentration (t = 0 s) the NH_3 reactor outlet concentration immediately decreases due to the occurrence of the SCR reaction, and a parallel evolution of N_2 and of water (not reported in the figure) is observed. The evolution with time on stream of the ammonia and NO reactor outlet concentrations following the NO inlet concentration changes significantly differs from those shown in the case of NH_3 (figure 4). In particular, no significant delays are observed in the system responses upon imposing variations in the NO inlet concentration. Similar results were also obtained by performing linear variations in the NO inlet concentration [25]. These results further confirm that NO is not involved in an adsorption-desorption process on the catalyst surface, and that the SCR reaction occurs between a strongly adsorbed NH_3 species and a gas-phase or weakly adsorbed NO molecule.

3.1.3. Kinetic analysis of the transient experiments.

The results of the transient kinetics experiments shown in figures 1-5 were analyzed by a dynamic one-dimensional heterogeneous PFR model and fitted by nonlinear regression to provide estimates of the relevant kinetic parameters. On the basis of theoretical diagnostic criteria [26,27], the influence of both intraparticle catalyst gradients and external mass transfer limitations were estimated as negligible. Under these simplifying hypotheses, the unsteady-state model is based on the following equations:

- NH_3 mass balance on the catalyst surface:

$$\frac{\partial \theta_{NH3}}{\partial t} = r_a - r_d - r_{NO} - r_{ox} \quad (1)$$

- NH_3, NO and N_2 mass balances on the gas stream:

$$\frac{\partial C_{NH3}}{\partial t} = -v\frac{\partial C_{NH3}}{\partial z} + \Omega_{NH3} \cdot (r_a - r_d - r_{NO} - r_{ox}) \quad (2)$$

$$\frac{\partial C_{NO}}{\partial t} = -v\frac{\partial C_{NO}}{\partial z} + \Omega_{NH3} \cdot r_{NO} \quad (3)$$

$$\frac{\partial C_{N_2}}{\partial t} = -v\frac{\partial C_{N_2}}{\partial z} - \Omega_{NH3} \cdot (r_{NO} + 0.5 \cdot r_{ox}) \quad (4)$$

where the symbols are defined in the Notation. The following rate expressions were used for NH_3 adsorption and desorption from the catalyst surface:

$$r_a = k_a^o \cdot e^{-E_a / RT} \cdot C_{NH_3} \cdot (1 - \theta_{NH_3}) \quad (5)$$

$$r_d = k_d^o \cdot e^{-E_d / RT} \cdot \theta_{NH_3} \quad (6)$$

Different rate expressions were used for NH_3 desorption, including a simple Langmuir approach (that considers a constant value of the desorption activation energy E_d), and more complicate expressions (e.g. Freundlich- and Temkin-type coverage dependence of the desorption energies) that take into account the catalyst surface heterogeneity, in agreement with the physico-chemical characterization of the catalysts [28-30].

The following rate expression was used for NH_3 oxidation:

$$r_{ox} = k_{ox} \cdot \theta_{NH_3} \quad (7)$$

whereas different rate expressions were tested for the SCR reaction (r_{NO}), including first order kinetics in respect to θ_{NH_3} (eq. 8 a) and "modified" θ_{NH_3} kinetics (eq. 8 b):

$$r_{NO} = k_{NO} \cdot C_{NO} \cdot \theta_{NH_3} \quad (8a)$$

$$r_{NO} = k_{NO} \cdot C_{NO} \cdot \theta^*_{NH_3} \cdot (1 - e^{\theta_{NH_3} \; \theta^*_{NH_3}}) \quad (8b)$$

where $k_{NO} = k^{\circ}_{NO} \cdot e^{-E_{NO}/RT}$. In the case of eq. 8b, the rate of reaction is supposed to be essentially independent of the ammonia surface coverage above a critical NH_3 surface concentration ($\theta^{*}_{NH_3}$). This empirical rate expression is in line with the results of the experiments shown in Figure 4, which suggests that the rate of the SCR reaction is unaffected by changes of the ammonia surface concentration at high NH_3 coverage.

Eq. (1)-(4) were solved by standard numerical procedures [31, 32] and the data fit was performed on the experimental results shown in the figures 1-4, i.e. NH_3 adsorption-desorption experiments and runs with changes in the NH_3 reactor inlet concentration in flowing NO + O_2. The data fit is reported as solid lines in the same figures: it appears that the goodness of fit is satisfactory, being reproduced the most relevant features of all the experiments. The data fit shown in the figures was obtained by using a Temkin-type ($E_d = E^{\circ}_d \cdot (1 - \gamma \cdot \theta_{NH_3})$ desorption kinetics and the "modified" θ_{NH_3} kinetics for the SCR reaction. Indeed no satisfactory data fit was obtained by either considering simpler Langmuir-type adsorption desorption or a first order kinetics in θ_{NH_3} for the SCR reaction. These features are in line with: i) the presence of surface heterogeneity, i.e with the presence of distinct types of acid sites (e.g Lewis and/or Brønsted) characterized by different acid strengths [28-30,33-35]; ii) the presence of a "reservoir" of adsorbed ammonia species, possibly adsorbed onto poorly active (but most abundant) W and Ti sites, which is available for the reaction once the NH_3 gas-phase concentration is decreased.

Furthermore, preliminary data fits lead to values of the activation energy for NH_3 adsorption close to zero, and hence a non-activated ammonia adsorption process was considered in the model. The estimates of the kinetic parameters leading to the fits shown in the figures are reported in the figure captions. Values of the activation energy for ammonia desorption at zero coverage (E°_d) close to 23 kcal/mol were obtained for both the model and commercial catalyst samples, whereas values of the activation energy for the SCR reaction in the range 14-19 kcal/mol were obtained for the model and the commercial catalyst. These values compare well with literature data [36,37]. The model is also able to account for the formation of N_2 due to ammonia oxidation during the adsorption-desorption study of NH_3 (figure 2) over the commercial catalyst. In this case from the parameter estimates it was found that the rate of the ammonia oxidation is negligible in the presence of NO, i.e. under SCR conditions. It is worth emphasizing that the model accounts quite satisfactorily for large variations in the NH_3 surface coverage (θ_{NH_3} was estimated to vary in the range 0-0.8) and/or in the catalyst temperature (T = 493-623K). The soundness of the kinetic model is further confirmed by the analysis of the experiments performed by varying the NO reactor inlet concentration (figure 5), which could be nicely described on a purely predictive basis by using the kinetic parameters previously estimated. Also, it is worth of note that the same results and parameter estimates could be obtained either by analyzing simultaneously the whole bulk of experimental data, or by separate fit of the NH_3 adsorption-desorption data and of the NH_3 + NO reaction runs. This confirms the adequacy of the adopted

model for the description of the transient adsorption-desorption and reaction kinetics, as well as the virtual superposition of the two processes.

The analysis of the parameter estimates leads also to additional significant implications concerning the steady-state kinetics of the SCR reaction. Indeed calculation showed that the r_d/r_a ratio (i.e. the ratio of the rate of ammonia desorption to the rate of ammonia adsorption) at steady-state is considerably lower than 1 under typical operating conditions. Hence, it comes out that the assumption of equilibrated ammonia adsorption, which was used by several authors in the derivation of steady-state kinetic expressions for the SCR reaction [15,38,39], is not always applicable under steady-state $DeNO_x$ conditions.

3.2. Development of a transient kinetic model for the SCR monolith reactor.

3.2.1. Rate equations.

The results of the transient response study previously reported provided valuable mechanistic and kinetic information for the development of the dynamic model of the SCR reactor. In particular, the following information was obtained: i) NH_3 is strongly adsorbed on both model and commercial V_2O_5-WO_3/TiO_2 catalyst samples; ii) surface heterogeneity must be considered to describe the kinetics of NH_3 adsorption-desorption; iii) in contrast to NH_3, NO does not adsorb appreciably on the catalyst surface; iv) these data, along with the transient behavior of the SCR reaction upon step-wise and linear changes of the NH_3 or NO feed concentrations, are in line with a mechanism of the SCR reaction which involves a strongly adsorbed species (NH_3) and a gaseous or weakly adsorbed species (NO); v) the rate of the $DeNO_x$ reaction is virtually independent of the ammonia surface concentration for NH_3 coverage above a characteristic "critical" value. On these basis, a dynamic kinetic model for the monolithic SCR reactor was developed. Eqs. (5) and (6) were considered for ammonia adsorption and desorption, respectively, whereas the first order kinetics in θ_{NH_3} for the SCR reaction was considered at first (eq. 8a). The inhibiting effect of water on the SCR reaction was not considered in the $DeNO_x$ rate expression (eq. 8a) since such an effect is essentially constant over the concentration range of industrial interest ($5 < C_{H2O} < 12$ % v/v [18]), and hence was incorporated in the kinetic parameter estimates. No ammonia oxidation was considered, in the light of the poor relevance of such reaction over the considered V_2O_5-WO_3/TiO_2 commercial catalyst in the presence of NO.

3.2.2. Reactor model and mass balances.

By assuming negligible axial dispersion, negligible pressure drop and identical conditions within each channel of the honeycomb monolith catalyst [40] and adopting a 1D representation of the concentration field in the gas phase flowing inside the monolith channels, the following mass balance equations for NH_3 and NO in the bulk gas phase apply, with symbols explained in the Notation:

$$\frac{\partial C^{b}_{NH3}}{\partial t} = -\frac{v}{L}\frac{\partial C^{b}_{NH3}}{\partial z} - \frac{4}{d_h} k_{mat,NH3}\left(C^{b}_{NH3} - C^{W}_{NH3}\right) \qquad (9)$$

$$\frac{\partial C_{NO}^{b}}{\partial t} = -\frac{v}{L}\frac{\partial C_{NO}^{b}}{\partial z} - \frac{4}{d_h} k_{mat,NO}\left(C_{NO}^{b} - C_{NO}^{W}\right) \tag{10}$$

At any axial coordinate z, the bulk and wall concentrations of NO and NH_3 are related by the following gas - solid continuity equations:

$$k_{mat,NH3}\left(C_{NH3}^{b} - C_{NH3}^{W}\right) = s\, r_{NH3}^{eff} \tag{11}$$

$$k_{mat,NO}\left(C_{NO}^{b} - C_{NO}^{w}\right) = s\; r_{NO,1}^{eff} \tag{12}$$

In Eq.s (11)-(12), r_{NH3}^{eff} and $r_{NO,1}^{eff}$ are effective rates of NH_3 adsorption and of NO reduction per unit volume of catalyst, respectively, accounting for the influence of the strong intraporous diffusional limitations affecting the SCR-DeNO$_x$ reaction: they are defined by Eq.s (15) - (16) below.

Following the derivation outlined in [41], the mass balance for NH_3 adsorbed on the catalyst can be written as follows:

$$\Omega_{NH3}\cdot(1-x^*)\frac{\partial\bar{\theta}}{\partial t} = r_{NH3}^{eff} - r_{NO,1}^{eff} \tag{13}$$

where θ is the average NH_3 surface coverage across the "active" portion of the catalytic wall, with dimensionless thickness (1-x*), at any axial coordinate z. x* is given by [41]:

$$x^* = \frac{1}{\Phi_{NH3}}\cdot\ln\left[f\cdot\cosh(\Phi_{NH3}) + \sqrt{f^2\cdot\cosh^2(\Phi_{NH3}) - 1}\right] \tag{14}$$

with $\dfrac{C_{NH3}(x^*)}{C_{NH3}^{W}} = f$

Notice that, according to Eq. (14), only a reduced NH_3 adsorption capacity, corresponding to the active fraction of the catalyst wall thickness, is involved in SCR dynamics.

The effective rates per unit catalyst volume are evaluated approximately, assuming pseudo-first order kinetics, as

$$r_{NH3}^{eff} = \frac{k_{ads}C_{NH3}^{W}(1-\bar{\theta}) - k_{des}\bar{\theta}\cdot(1-x^*)}{\Phi_{NH3}}\tanh\Phi_{NH3} \tag{15}$$

and:

$$r_{NO,1}^{eff} = k_{NO,1} C_{NO}^{W} \bar{\theta} \frac{1 - \frac{\sinh(\Phi_{NO} x^*)}{\cosh \Phi_{NO}}}{\Phi_{NO}} \tanh \Phi_{NO} \qquad (16)$$

where Φ_{NH3}, Φ_{NO} are Thiele moduli defined as:

$$\Phi_{NH3} = s \cdot \sqrt{\frac{k_{ads} \cdot (1-\theta) - \frac{k_{des}\theta}{C_{NH3}^{W}}}{D_{eff,NH3}}} \quad , \quad \Phi_{NO} = s \cdot \sqrt{\frac{k_{NO,1} \cdot \theta}{D_{eff,NO}}}$$

3.2.3. Model validation.

The set of model PDEs, Eq.s (9)-(10), was solved numerically, using orthogonal collocation techniques [31] to approximate the unknown solutions $\bar{\theta}$(z,t), C_{NH3}(z,t), C_{NO}(z,t) along the axial coordinate. The resulting system of algebraic and ordinary differential equations (DAEs) was integrated in time using a library routine based on Gear's method [32], with self-adjusting step size and variable method order. Convergence of the solution was checked by varying the number of collocation points along z (typically 8 or 9 points were sufficient), and by the internal criteria of the DAE integrator.

Concerning the model parameters, local gas-solid mass and heat transfer coefficients were estimated from the analogy with the Graetz-Nusselt heat transfer problem [15], and effective intraporous diffusivities of NO and NH_3 were evaluated from the catalyst morphological properties according to Cunningham and Geankoplis [42], using a modified form of the Wakao-Smith random pore model recommended by Beeckmann [38] for SCR catalysts.

The present 1D dynamic model of the SCR-DeNO_x reaction system was validated by comparing its predictions with experimental transient data of NO reduction over a commercial monolith SCR catalysts. The data were obtained perturbing steady-state operation of the reactor by imposing step changes of the inlet reactant concentration (NH_3 or NO), and recording the system response with time.

Figure 6 shows a comparison between the experimental data and model predictions (solid lines) upon reactor start-up (NH_3 injection, t = 0 s) and shut-down (t = 500 s) for different values of the NH_3/NO feed ratio (α) at 360 °C. The model results were generated using the estimates of kinetic parameters reported in the figure caption. As apparent in the figure, the agreement between experiment and model fit is satisfactory. In line with results of microreactor experiments performed with powder catalysts (figures 1-5), both the data and the simulations show that different dynamics are associated with reactor start-up and shut-down. In fact the start-up transient following ammonia injection is associated with the buildup of NH_3 coverage: this process results from a competition between ammonia adsorption and NO reduction, the latter occurring at the expense of adsorbed NH_3. On the other hand NH_3 adsorption is absent after

ammonia shut-down: in this case depletion of preadsorbed NH_3 results primarily from its surface reaction with NO. Upon performing the same experiments at lower temperatures (i.e. 330 and 270 °C, data not reported for the sake of brevity), similar results were obtained. However in these cases smaller NO conversions were measured, and much slower responses were observed. Also, it was observed that on decreasing the reaction temperature the shut-down time becomes similar to the start-up time. In fact the rate of NO reduction decreases with decreasing temperature more markedly than the rate of ammonia adsorption due to the different activation energies of the two processes.

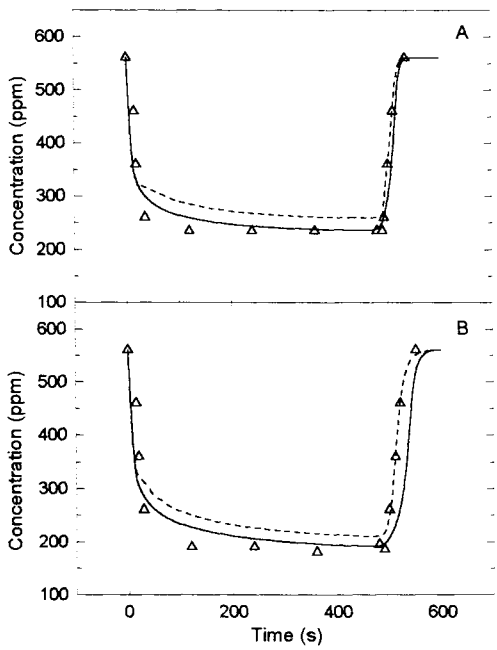

Figure 6. Experimental and simulated evolutions of the NO outlet concentration during reactor start-up and shut-down at T = 360 °C over a commercial WO_3-V_2O_5/TiO_2 monolith catalyst (V_2O_5 = 0.96 % w/w; WO_3 = 9 % w/w). C_{NO}^0 = 560 ppm, AV = 33 Nm/h. Solid lines: first order kinetics ($k°_{ads} = 8.5 \cdot 10^6$ $m^3_{gas}/(m^3_{cat}\ s)$; $E_{ads} = 9.0 \cdot 10^3$ cal/mol; $k°_d = 8.0 \cdot 10^8$ $mol/(m^3_{cat}\ s)$; $E°_d = 2.6 \cdot 10^4$ cal/mol; $\gamma = 0.32$; $k°_{NO} = 2.5 \cdot 10^{10}$ $m^3_{gas}/(m^3_{cat}\ s)$; $E_{NO} = 18.6 \cdot 10^3$ cal/mol; Ω = 210 mole NH_3/m^3_{cat}). Dashed line: "modified kinetics"($k°_{ads} = 3.0 \times 10^6$ $m^3_{gas}/(m^3_{cat}\ s)$; $E_{ads} = 9.0 \cdot 10^3$ cal/mol; $k°_d = 7.45 \cdot 10^8$ $mol/(m^3_{cat}\ s)$; $E°_d = 2.6 \cdot 10^4$ cal/mol; $\gamma = 0.32$; $k°_{NO} = 4.57 \cdot 10^{10}$ $m^3_{gas}/(m^3_{cat}\ s)$; $E_{NO} = 18.6 \cdot 10^3$ cal/mol; Ω = 210 mole NH_3/m^3_{cat} θ^* = 0.24) A) α= 0.8: $C_{NH3}^0 = 0 \rightarrow 448$ ppm (t=0 s), $C_{NH3}^0 = 448 \rightarrow 0$ ppm (t=500 s). B) α= 1: $C_{NH3}^0 = 0 \rightarrow 560$ ppm (t=0 s), $C_{NH3}^0 = 560 \rightarrow 0$ ppm (t=500 s)).

The fit of the data reported in figure 6 was also performed by using the "modified" θ_{NH_3} kinetics, i.e. eq. (8b). In this case the values of the activation energies for the NH_3 adsorption and desorption processes and for the SCR reaction obtained by the previous fit were retained. The model predictions obtained in this case are reported in figure 6 as dotted lines: no relevant differences are apparent with respect to the first-order θ_{NH_3} rate expression, but the shut-down dynamics is apparently more satisfactorily reproduced. The limited differences observed in this case between the first-order and the "modified" θ_{NH_3} kinetics can be likely associated to the lower NH_3 coverages attained during these experiments as compared to the same experiments performed with the powder catalyst, both due to the higher reaction temperatures and lower ammonia inlet concentrations. As a matter of facts, transient reactivity experiments performed over powder catalysts at high temperatures could be nicely fitted with the first-order θ_{NH_3} kinetics as well.

The values of the kinetic constants calculated according to the dynamic model were used to estimate the relative rates of NH_3 adsorption, desorption and

reaction at different temperatures, and results are reported in Table 1. In line with the data obtained over powder catalysts, also in this case it is apparent that NH_3 adsorption is the fastest process, with NO reduction becoming of comparable rate at the highest temperatures. NH_3 desorption is always slower than the surface reaction by at least one order of magnitude. The dynamic SCR reactor model here developed was successfully employed in simulating the evolutions of the NO outlet

Table 1
Characteristic rates in SCR-DeNO$_x$ over a commercial V_2O_5-WO_3/TiO_2 monolith catalyst. (Assumed conditions: $\theta = 0.1$, $C_{NO} = 200$ ppm, $C_{NH3} = 160$ ppm).

	T=270 °C	T=330 °C	T=350 °C	T=400 °C
r_{des}/r_{ads}	9.88E-04	4.83E-03	7.68E-03	2.18E-02
r_{NO}/r_{ads}	5.58E-02	1.35E-01	1.75E-01	3.11E-01

concentrations following step variations in the NO feed content. As an example Figure 7 illustrates the evolution of the SCR system upon three different step changes of the NO feed concentration. Again, the model was able to reproduce the characteristic times of the experimental transients. Both the data and the calculations indicated that such characteristic times were longer for runs 2 and 3 corresponding to final $C°_{NO}$ < 500 ppm, which implies an overstoichiometric NH_3 feed content (i.e. $\alpha > 1$). In fact, under such conditions the buildup of adsorbed ammonia, that is the controlling step in SCR dynamics, is not limited to the narrow active catalyst layer but entails the whole catalyst volume. It is noteworthy that the present

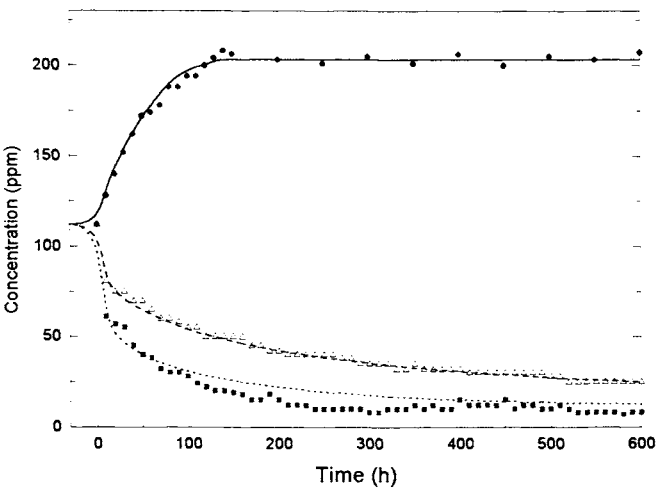

Figure 7. Experimental (points) and simulated (lines) evolutions of the NO outlet concentration following step variation of NO inlet concentration C_{NO}^0 at t = 0 s over a commercial WO_3-V_2O_5/TiO_2 monolith catalyst (V_2O_5 = 0.45 % w/w; WO_3 = 9 % w/w). (T = 350 °C, C_{NH3}^0 = 400 ppm, AV = 10 Nm/h). Filled circles: $C_{NO}^0 = 500 \rightarrow 600$ ppm. Up triangles: $C°_{NO} = 500 \rightarrow 400$ ppm. Squares: $C_{NO}^0 = 500 \rightarrow 300$ ppm. Solid lines: model fit ($k°_{ads} = 8.5 \cdot 10^6$ $m^3_{gas}/(m^3_{cat}\ s)$; $E_{ads} = 9.0 \cdot 10^3$ cal/mol; $k°_d = 8.0 \cdot 10^8$ mol/(m^3_{cat} s); $E°_d = 2.6 \cdot 10^4$ cal/mol; $\gamma = 0.32$; $k°_{NO} = 7 \cdot 10^7$ $m^3_{gas}/(m^3_{cat}\ s)$; $E_{NO} = 12.2 \cdot 10^3$ cal/mol).

dynamic model can predict the time response of SCR catalysts under such vastly different conditions of NH_3 coverage as corresponding to $\alpha < 1$ and $\alpha > 1$. The results of Figure 7 were confirmed by additional runs with either less marked step changes of NO feed content or with step changes of the NH_3 feed concentration.

3.3. Development of a transient kinetic model for the $SO_2 \rightarrow SO_3$ oxidation reaction.

3.3.1. Transient behavior of the $SO_2 \rightarrow SO_3$ oxidation reaction.

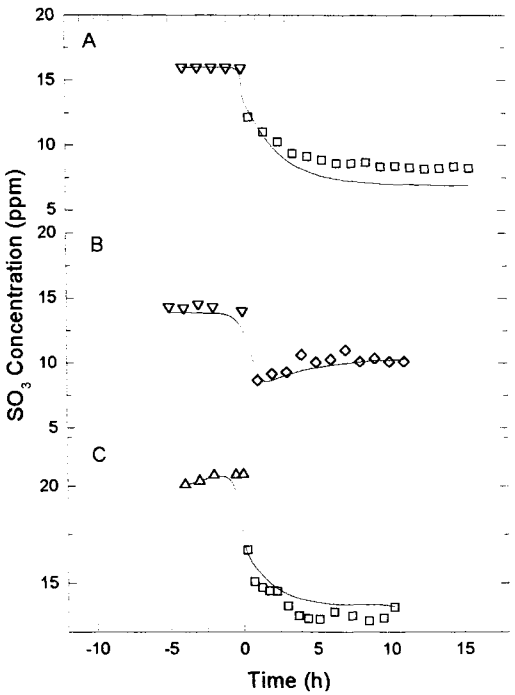

Figure 8. Experimental (symbols) and calculated (lines) temporal evolution of the SO_3 outlet concentration upon negative step changes at t=0 h over a commercial WO_3-V_2O_5/TiO_2 monolith catalyst (V_2O_5 = 0.6 % w/w; WO_3 = 9 % w/w) of: A) inlet SO_2 concentration (1278 → 639 ppm); B) reaction temperature (360 → 350°C); C) Area Velocity (7.8 → 5 Nm/h). Reaction conditions: T = 380 °C, $C^{\circ}_{SO_2}$ = 1278 ppm, AV = 7.8 $Nm^3/(m^2\ h)$, C°_{O2} = 2.6 % v/v , C°_{H2O} = 12.8 % v/v. Parameters estimates: Ω_{SO_3}= 8470 [moles SO_3/m^3 gas], k_{ad}= $2.16 \cdot 10^{-3}$ [m^3_{gas} /mole·s], k_{des}= $2.08 \cdot 10^{-4}$ [1/s], E°_{des}=11.75 [kcal/mol], k_{SO2}= $8.02 \cdot 10^{-6}$ $[(m^3_{gas}/mol)^{1+\alpha_{O2}-\alpha_w}/s]$, E°_{SO2} = 5.55 [Kcal/mol], K_{H2O}= 0.828 [m^3/mole], α_{ox} = 0.064, α_w= 0.211.

In previous papers [17-20] we have systematically investigated the effects of the operating conditions, feed composition and catalyst design parameters in the steady-state oxidation of SO_2 to SO_3 over honeycomb deNO$_x$ing catalysts. It was shown that under SCR conditions the SO_2 oxidation is a slow reaction (SO_2 conversion values lower than 1 % are typically measured) which occurs in a chemical controlled regime. Hence, as opposite to the DeNO$_x$-SCR reaction, the SO_2 to SO_3 oxidation reaction is not limited by diffusional resistances. Besides it was demonstrated that: i) in order to obtain steady state data in both the SO_2 to SO_3 oxidation and the DeNO$_x$ reaction the catalyst must be conditioned; ii) the DeNO$_x$ reaction is faster over sulfated catalysts; iii) the conditioning process involves the accumulation of sulfates at the catalyst surface; iv) conditioning requires a few hours in the case of the SO_2 oxidation, whereas it is much shorter for the DeNOx reaction; v) the catalyst active sites for SO_2 oxidation are not the same active sites for the DeNOx reaction; vi) the rate of SO_2 oxidation is slightly enhanced by NO_x and is strongly inhibited by NH_3; vii) the inhibiting effect of NH_3 is markedly reduced in

the presence of NO_x due to the occurrence of the SCR reaction. These observations clearly prove that a kinetic interaction exists between SO_2 oxidation and NO_x reduction and that the oxidation of SO_2 to SO_3 may influence the reduction of NO_x by affecting the level of sulfates present on the surface of the catalyst. In order to clarify the role of sulfates in the reactions of interest of the SCR process, in a previous paper a dynamic approach was applied [20], and the responses of the reacting system upon step-changing the operating conditions that affect the rate of the SO_2 oxidation (e.g. SO_2 concentration, temperature, water content, Area Velocity (AV)) was investigated. In the present study, a quantitative description of the dynamics of the SO_2 oxidation is attempted: a dynamic kinetic model of SO_2 oxidation over SCR monolith catalysts is herein presented, based on a detailed mechanism of the catalyst sulfate coverage which accounts for the interaction with NO_x reduction.

Figures 8 and 9 illustrate the measured temporal evolutions of the gaseous SO_3 concentration at the reactor outlet upon negative (Fig. 8) and positive (Fig. 9) step changes of the inlet SO_2 concentration, reaction temperature and Areas Velocity (parts A-C of the figures, respectively). The step changes were performed at t = 0. In the case of negative step changes in the SO_2 inlet concentration (1280 → 640 ppm, figure 8 A), the outlet SO_3 concentration slowly decreases with time and approaches the steady-state (ultimate) value in a monotonic way after a few hours. Along similar lines, when the inlet SO_2 concentration is increased (640 → 1920 ppm, figure 9 A), the outlet SO_3 concentration slowly increases with time and approaches the new steady-state value monotonically. Various runs performed by using different step changes indicated that the ultimate value is not influenced by the previous SO_2 concentration level. Similar dynamics are displayed by the system upon step changes of the feed flow rate, as shown in Figures 8 and 9 C. Again we observed a sudden response of the SO_3 emission followed by a much slower approach to the new steady-state. The fast initial transient was associated with the response of the gas-phase concentrations, whereas the longer subsequent evolution resulted from the buildup/depletion

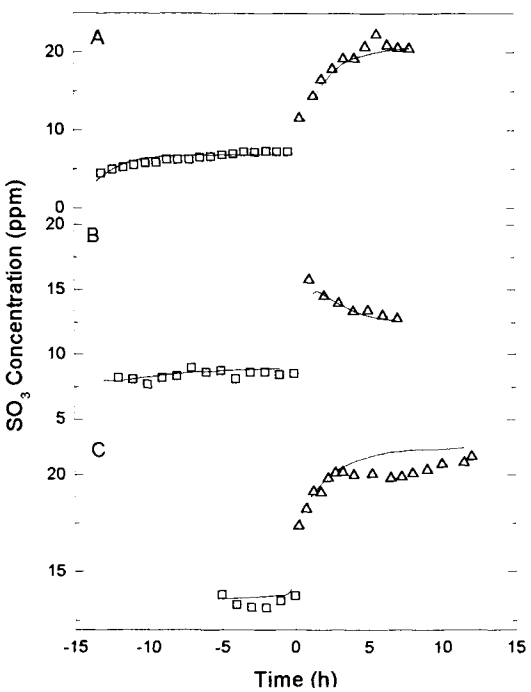

Figure 9. Experimental (symbols) and calculated (lines) temporal evolution of the SO_3 outlet concentration upon positive step changes at t=0 h over a commercial WO_3-V_2O_5/TiO_2 monolith catalyst (V_2O_5 = 0.6 % w/w; WO_3 = 9 % w/w) of: A) inlet SO_2 concentration (639 → 1917 ppm); B) reaction temperature (350 → 370°C); C) Area Velocity (5 → 7.8 Nm/h). Reaction conditions and parameters estimates as in figure 8.

dynamics of the surface sulfates. The negative step change of AV lead in fact to a higher gaseous concentration of SO_3, which lead in turn to a higher ultimate coverage. The situation was reversed upon restoring the initial AV value of 7.8 $Nm^3/(m^2\ h)$.

Step changes in the reaction temperature result in different dynamics (figures 8-9 B). Indeed the response is initially much faster, it first exceeds the ultimate value and then it approaches this value monotonically. As shown in Figure 8 B, a reduction of the temperature from 380 to 360 °C caused an initial, sudden decrease of the outlet SO_3 concentration, followed however by a slower recovery of the SO_3 emission level. Such a characteristic response is related to the accumulation of sulfates onto the catalyst: in fact, a temperature reduction leads to a decrease of the rate of SO_2 oxidation, but to a more significant decrease of the rate of SO_3 desorption in view of the activation energies of the two reactions. The net result is a buildup of sulfates at the catalyst surface, responsible for the observed negative overshoot of the SO_3 concentration level. In the following stages of the transient, however, the system slowly approached a new ultimate value of SO_3 concentration through re-equilibration of the rates of SO_3 generation, desorption and readsorption, resulting eventually in a greater SO_3 surface coverage at steady-state. On the contrary, upon step increases of the reaction temperature (figure 9 B), a peak of SO_3 emission was observed, resulting from decomposition of the surface sulfates, followed by a slow decline of C_{SO3} towards the new stationary value associated with a smaller sulfate coverage. These results were also confirmed by identical trends observed upon applying other step changes of the reaction temperature.

3.3.2. Model assumptions and reaction scheme.

The above reported data lead us to develop a dynamic kinetic model of SO_2 oxidation over SCR monolith catalysts, based on a detailed mechanism of the catalyst sulfate coverage. The model is based on the following reaction scheme:

$$SO_2 + \frac{1}{2}O_2 + \vartheta_f \xrightarrow{k_{SO_2}} \vartheta_{SO_3} \tag{17}$$

$$\vartheta_{SO_3} \underset{k_{ads,SO3}}{\overset{k_{des,SO3}}{\Leftrightarrow}} SO_3 + \vartheta_f \tag{18}$$

$$H_2O + \vartheta_f \Leftrightarrow \vartheta_{H_2O} \tag{19}$$

$$NH_3 + \vartheta_{SO_3} \Leftrightarrow \vartheta_{SO_3,NH_3} \tag{20}$$

Step (17) is the reaction of SO_2 with gaseous oxygen on a free active site, originating an adsorbed SO_3 molecule, which then undergoes desorption-readsorption on the active sites (step 18). Water from the gas phase can compete with SO_2 onto the catalyst active

sites (step 19) whereas ammonia, if present, can react with adsorbed SO_3 to give a surface ammonium sulfate, which blocks further desorption of SO_3 (step 20). This reaction represents the observed inhibiting effect of NH_3 on the SO_2 oxidation.

Under such assumptions, four types of catalytic sites are identified: i) sites occupied by SO_3 alone (also referred to sites with free SO_3), ii) sites occupied by SO_3 and ammonia (ammonium sulfates), iii) sites occupied by water, iv) free sites. The corresponding surface coverages are indicated in the following as $\vartheta_{SO3,f}$, $\vartheta_{SO3,NH3}$, ϑ_{H2O}, ϑ_f, respectively. By lumping the sites occupied by SO_3 alone and by SO_3 plus NH_3 into one only family of sites with overall surface coverage ϑ_{SO3}, the site balance is given by the following equation:

$$\vartheta_{SO3} + \vartheta_{H2O} + \vartheta_f = 1 \tag{21}$$

It was found that the adsorption-desorption dynamics of water and ammonia are much faster than SO_3 desorption, whose characteristic time is of the order of several hours. Hence, by assuming adsorption-desorption equilibrium of H_2O, the water surface coverage ϑ_{H2O} is calculated from Eq. (22), where the fraction of SO_3-occupied sites (ϑ_{SO3}) is assumed to be negligible in comparison to ϑ_{H2O} as the H_2O gas-phase concentration is greater than the SO_3 concentration by at least three orders of magnitude:

$$\vartheta_{H2O} = \frac{K_{H2O} \cdot C_{H2O}}{1 + K_{H2O} \cdot C_{H2O}} \tag{22}$$

In Eq.(22) K_{H2O} is the H_2O adsorption equilibrium constant.

Furthermore, considering equilibrium adsorption of NH_3 on SO_3-occupied sites, the volume - averaged fraction of SO_3-occupied sites free from adsorbed ammonia, $\overline{\vartheta}_{SO3,f}$, can be computed as a function of the overall fraction of SO_3-occupied sites $\overline{\vartheta}_{SO3}$. Indeed, in view of the difference in time scales between the $DeNO_x$ process and the SO_2 oxidation [19,20], we introduce a pseudo steady-state assumption for adsorption-desorption of NH_3 on sulfated sites,

$$0 \approx r_{ads,NH3,SO3} - r_{des,NH3,SO3} \tag{23}$$

By expressing the local rates as follows:

$$r_{ads,NH3,SO3} = k_{ads,SO3,NH3} C_{NH3}(x) \vartheta_{SO3,f} \tag{24}$$

$$r_{des,NH3,SO3} = k_{des,SO3,NH3} \vartheta_{SO3,NH3} \tag{25}$$

where $C_{NH3}(x)$ indicates that the ammonia concentration varies along the intraporous coordinate x due to the strong diffusional limitations associated with the DeNOx reaction.

On introducing the sites balance equation, and defining $K_{NH3,SO_3} = k_{ads,SO3,NH3}/k_{des,SO3,NH3}$,

$$K_{NH3,SO3}C_{NH3}(x)\vartheta_{SO3,f} = \vartheta_{SO3} - \vartheta_{SO3,f} \tag{26}$$

Introducing average coverages, represented by overbars, and integrating Eq. (26) over the catalyst wall half-thickness by making use of the approximate intraporous NH_3 concentration profile adopted by Tronconi et al. [41], the following expression is eventually obtained [43]:

$$\bar{\vartheta}_{SO3,f} = \frac{\bar{\vartheta}_{SO3}}{1 + \dfrac{K_{NH3,SO3} \cdot C^{W}_{NH3}}{\Phi_{NH3}}} \tag{27}$$

On an integral basis, Eq. (27) accounts for the variation of both C_{NO} and C_{NH3} along x, the transverse coordinate across the monolith wall thickness, due to strong intraporous concentration gradients caused by the fast DeNOx reaction [41]. In (27), $C_{NH3}{}^{W}$ is the NH_3 concentration at the catalyst wall, and Φ_{NH3} a suitable Thiele modulus correcting for intraporous diffusional resistances [41].

3.3.3. Rate expressions.

According to previous steady-state results [17,18] the SO_2 oxidation rate, Eq. (28), is first order in SO_2 concentration, exhibits a fractional order in O_2, and accounts for the promoting effect of NO_x and the inhibiting effects of water and ammonia,

$$r_{SO2} = \frac{k_{SO2} \cdot C_{SO2} \cdot C^{\alpha O2}_{O2} \cdot C^{-\alpha W}_{H2O}}{1 + K_{NH3}C_{NH3}(x)} \cdot \left[1 + A_{NO}C_{NO}(x)\right] \tag{28}$$

Again, notice that both C_{NO} and C_{NH3} vary along x, the transverse coordinate across the monolith wall thickness. Thus, Eq. (28) provides the local rate: the overall rate of reaction ($\bar{r}_{SO2}$) is obtained upon integrating this expression over the wall half thickness of the catalytic monolith, the overbar representing an average quantity.

Along similar lines, Eqs. (29) and (30) provide the average SO_3 adsorption and desorption rates, respectively:

$$\bar{r}_{ads,SO3} = k_{ads,SO3} \cdot C_{SO3} \cdot (1 - \bar{\theta}_{SO3} - \theta_{H2O}) \tag{29}$$

where a linear dependence on the gaseous SO_3 concentration and on the fraction of free sites was adopted, and, making use of Eq. (29),

$$\bar{r}_{des,SO3} = k_{des,SO3} \cdot \bar{\vartheta}_{SO3,f} = k_{des,SO3} \cdot \frac{\bar{\theta}_{SO3}}{1 + K_{NH3,SO3} \cdot C^{w}_{NH3} / \Phi_{NH3}} \tag{30}$$

which includes a linear dependence on the fraction of free SO_3 sites. Again, the overbars indicate that Eqs. (29) and (30) represent average rates of SO_3 adsorption and desorption over the catalyst wall half-thickness.

3.3.4. Mass balance equations.

Given the very limited SO_2 conversion (≈1%), the SO_2 concentration can be regarded as constant along the whole reactor. Water is in large excess, and its concentration is considered constant, too. So only unsteady mass balances for gaseous and adsorbed SO_3 are required, which take into account however the distributions of NH_3 and NO_x both along the monolith axial coordinate z and across the monolith walls, the latter gradients resulting from the intraporous diffusional resistances. The gas phase SO_3 mass balance yields accordingly

$$\frac{\partial C_{SO3}}{\partial t} = -\frac{v}{L} \cdot \frac{\partial C_{SO3}}{\partial z^*} - \Omega_{SO3} \frac{1-\varepsilon}{\varepsilon} \cdot \left(\bar{r}_{ads,SO3} - \bar{r}_{des,SO3}\right) \tag{31}$$

whereas Eq. (32) provides the mass balance for adsorbed SO_3,

$$\frac{\partial \bar{\vartheta}_{SO3}}{\partial t} = \bar{r}_{ads,SO3} - \bar{r}_{des,SO3} + \bar{r}_{SO2} \tag{32}$$

where symbols are defined in the Notation. The overbars imply that the rates are averaged over the catalyst wall thickness at every axial location z. The model equations were solved numerically by polynomial approximation [31] along the axial coordinate z, while the integration in time was carried out by the library routine LSODI [32].

3.3.5. Data fit.

Transient runs with SO_2 oxidation only were examined at first, i.e. with no NO and NH_3 in the reactor feed stream (data of figures 8 and 9). Hence the parameters A_{NO}, K_{NH3} and K_{NH3,SO_3} included in the unsteady kinetic model, Eqs. (21)-(32), were not significant. The 9 remaining adaptive parameters were estimated by global nonlinear regression, using the outlet SO_3 concentration as the experimental response. The model responses, obtained by using the parameter estimates reported in the figure captions, are shown in figures 8 and 9 as solid lines. In view of the measurement precision, the accuracy of the dynamic kinetic model in reproducing all of the observed trends was acceptable. Particularly, the occurrence of SO_3 emission peaks upon step increments of

the reaction temperature (Figure 9 B) was successfully predicted. In particular we may notice that the activation energy of SO_3 desorption ($\approx$ 23 kcal/mole) is in line with the expected strong interaction of SO_3 with the catalyst surface, and that the activation energy of the surface reaction (SO_2 oxidation, $\approx$ 11 kcal/mole) is close to the apparent activation energy estimated over this catalyst from steady-state data (~14 kcal/mole). The small value of the kinetic order α_{ox} results from operation under O_2 excess, whereas the extent of H_2O inhibition is consistent with previous steady-state data [17]. Notably, the parameter estimates assess that SO_3 desorption is the rate-determining step of the whole process, controlling the buildup or depletion of sulfate species on the catalyst surface.

Finally, the transient kinetics of SO_2 oxidation with simultaneously occurring $DeNO_x$ reaction was also addressed, though only in a limited number of experiments. For this purpose, the previous estimates of the adaptive parameters were retained, and the additional kinetic parameters A_{NO} and K_{NH3} in Eq. (28) were estimated from data obtained under steady-state conditions [17]. The NH_3 equilibrium constant of adsorption over sulfated sites, $K_{NH3,SO3}$, was simply set to a large value (10^6) due to the lack of adequate data for its accurate estimation. This is in line with the expectation that ammonia adsorption onto sulfated sites is largely favored, and was found adequate to reproduce qualitatively the observed trends of the data.

The model equations for SO_3 gas- and solid-phase balances were then included in the 1D dynamic model of the SCR-DeNOx monolith reactor previously reported, in order to couple the simulations of the temporal evolution of NO_x reduction and SO_2 oxidation.

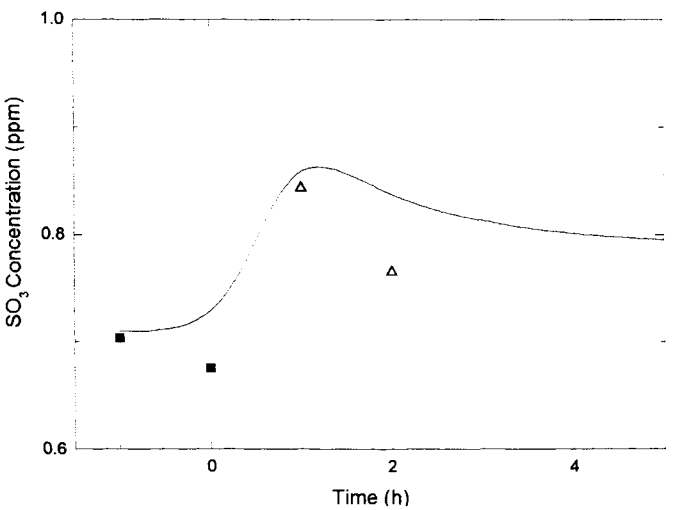

Figure 10 - Experimental (symbols) and calculated (lines) temporal evolution of the SO_3 outlet concentration upon step changes of the NH_3 feed concentration (400 $\rightarrow$ 350 ppm) at t=0 h over a commercial WO_3-V_2O_5/TiO_2 monolith catalyst (V_2O_5 = 0.6 % w/w; WO_3 = 9 % w/w). Reaction conditions: T = 380 °C, $C^\circ_{SO_2}$ = 1278 ppm, AV = 7.8 $Nm^3/(m^2\ h)$, C°_{H2O} = 12.8 % v/v, C°_{O2} = 2.6 % v/v, C°_{NO} = 200 ppm. Parameters estimates as in figure 8.

Eventually, the complete dynamic kinetic model was validated for simultaneously occurring $DeNO_x$ and SO_2 oxidation reactions by predictive comparison with transient data following step changes of the NH_3 inlet concentration. Figure 10 shows one of such comparisons for the temporal evolution of the SO_3 outlet concentration profile: both model and data exhibit a maximum in the SO_3 emission after a sudden drop in the feed concentration of ammonia. This response is associated

with the release of SO_3 originally blocked as surface ammonium sulfates. Notably, the introduction of SO_2 oxidation dynamics does not significantly increment the computational load for numerical model solution with respect to the dynamic model of the $DeNO_x$ reaction only. Accordingly, the simulation of typical SCR reactor transients can still be carried out in a fraction of the actual transient time. This is a prerequisite for application to predictive control systems of SCR reactors.

4. CONCLUSIONS

A dynamic model of the SCR catalysis, describing both the $DeNO_x$ and the SO_2 oxidation reaction, was here presented. The fundamentals of the SCR reactions under transient conditions were investigated by applying the transient response method, and then a heterogeneous 1-D model of SCR monolith reactors was developed. The major results of our study can be summarized as follows:

i) NH_3 is strongly adsorbed on V_2O_5-WO_3/TiO_2 model and commercial catalyst samples, and in both cases surface heterogeneity must be considered to describe the kinetics of NH_3 adsorption-desorption. A model assuming a non-activated NH_3 adsorption process and a Temkin-type coverage dependence of the desorption energy is well suited to represent the dynamic data, with value of the activation energy for desorption at zero-coverage close to 23 kcal/mol;

ii) in contrast to NH_3, NO does not adsorb appreciably on the catalyst surface. These data, along with the features of the transient behavior of the SCR reaction upon step-wise and linear changes of the NH_3 or NO reactor inlet concentrations, indicates that the $DeNO_x$ reaction involves a strongly adsorbed species (NH_3) and a gaseous or weakly adsorbed species (NO);

iii) the rate of the $DeNO_x$ reaction is virtually independent from the ammonia surface concentration for NH_3 coverage above a characteristic "critical" value. This is explained by assuming that a "reservoir" of adsorbed ammonia species, possibly adsorbed onto poorly active but most abundant W and Ti sites, are present on the catalyst surface and are available for the reaction occurring on the reactive V sites once the NH_3 gas-phase concentration is decreased;

iv) the observed dynamics could be nicely fitted according to a one-dimensional heterogeneous unsteady PFR model, superimposing the NH_3 adsorption-desorption process, with kinetics obtained by the independent ammonia adsorption study, to the SCR reaction. The most adequate rate expression for the DeNOx reaction is independent of the ammonia surface coverage at high θ_{NH_3}, and becomes first order in respect to the ammonia surface concentration only below a "critical" NH_3 coverage ($\theta^*_{NH_3}$);

v) a weak inhibiting effect of ammonia on the $DeNO_x$-SCR reaction was also observed at high ammonia surface coverages and at the lowest investigated temperatures;

vi) the analysis of the rate parameter estimates indicates that the assumption of equilibrated ammonia adsorption may be incorrect under steady-state DeNOx conditions, specifically at high temperatures;

vii) a simplified dynamic 1D model of the monolith SCR reactor incorporating the major features of the $DeNO_x$ transient kinetics revealed by the transient response study can effectively represent the dynamic behavior of SCR-$DeNO_x$ monolith reactors. The model was successfully fitted to a variety of transient NO reduction data collected over commercial SCR honeycomb catalysts at different temperatures, space velocities and NH_3/NO feed ratios;
viii) in line with the results obtained in the case of the microreactor system, the model analysis showed that the rate of ammonia adsorption is comparable to the rate of its surface reaction with NO, whereas NH_3 desorption is much slower. Hence also for commercial SCR monolith catalysts under industrial-type operating conditions the assumption of NH_3 adsorption - desorption equilibrium, commonly made for steady-state $DeNO_x$ kinetics, is incorrect;
ix) since NH_3 is strongly adsorbed on the catalyst, while NO is not, the dynamics of NO conversion is intrinsically faster than exhibited by the NH_3 slip. In fact, the model simulations indicate the possibility of peaks of NO emissions upon sudden changes in the operating variables while, only regular, monotonic variations of the NH_3 slip are predicted;
x) an unsteady kinetic model of the undesired SO_2 oxidation reaction was also derived which accounts satisfactorily for the observed transient effects resulting from step changes of the main variable settings in the absence of NO_x and NH_3;
xi) the treatment was also extended to account for the simultaneous occurrence of the $DeNO_x$ and the SO_2 oxidation reactions. The kinetic influence of the major reactants in the SCR process was introduced both in the rate expression for SO_2 oxidation (promoting action of NO, inhibition due to NH_3) and in that for SO_3 desorption (formation of surface ammonium sulfates). The peculiar transients observed upon varying the NH_3 feed content can thus be reproduced.
xii) the complete dynamic model of the SCR reactions in monolith catalysts, including both the $DeNO_x$ reaction and the parasite SO_2 oxidation reaction allows combined predictions of NO_x reduction efficiency, NH_3 slip and SO_3 emission levels for changes in the operating conditions of industrial SCR monolith reactors.

NOTATION

A_{NO} = parameter for NO promotion [m^3_{gas}/mol]
AV = area velocity [$Nm^3/(m^2\ h)$]
C_i = gas-phase concentration of species i [mol/m^3_{gas}]
D = molecular diffusivity [m^2/s]
d_h = hydraulic diameter of the monolith channels [m]
E_a = activation energy for NH_3 adsorption [kcal/mol]
E_d = activation energy for NH_3 desorption [kcal/mol]
E_d° = activation energy for NH_3 desorption at zero-coverage [kcal/mol]
E_{NO} = activation energy for the DeNOx reaction [kcal/mol]
k_a° = pre-exponential factor for NH_3 adsorption rate constant [m^3 / mol s]

k_{ads} = rate constant for NH_3 adsorption [$m^3_{gas}/(m^3_{cat}$ s)]
$k_{ads\ NH3,SO3}$ = rate constant for NH_3 adsorption on sulfated sites [m^3_{gas}/mol s]
$k_{ads\ SO3}$ = rate constant for SO_3 adsorption [m^3_{gas}/mol s]
k_d° = pre-exponential factor for NH_3 desorption rate constant [1/s]
k_{des} = rate constant for NH_3 desorption [moles/(m^3_{cat} s)]]
$k_{des\ NH3,SO3}$ = rate constant for NH_3 desorption from sulfated sites [1/s]
$k_{des\ SO3}$ = rate constant for SO_3 desorption [1/s]
k_{ox} = rate constant for ammonia oxidation [1/s]
k°_{NO} = pre-exponential factor for the DeNOx reaction rate constant [m^3 / mol s]
k_{NO} = kinetic constant for the DeNOx reaction rate constant [m^3 / mol s]
$k_{NO,1}$ = kinetic constant for the DeNOx reaction rate constant [$m^3_{gas}/(m^3_{cat}$ s)]
k_{SO2} = rate constant for SO_2 oxidation [$(m^3_{gas}/mol)^{1+\alpha_{O2}-\alpha_W}$/s]
K_{H2O} = equilibrium constant for H_2O adsorption [m^3_{gas}/mol]
K_{NH3} = parameter for NH_3 inhibition [m^3_{gas}/mol]
$K_{NH3,SO3}$ = equilibrium constant for NH_3 adsorption on sulfated sites [m^3_{gas}/mol]
k_{mat} = gas-solid mass transfer coefficient [$m^3_{gas}/(m^2_{cat}$ s)]]
L = monolith length [m]
R = ideal gas constant [cal / mol K]
r_a = rate of NH_3 adsorption [1/s]
r_d = rate of desorption [1/s]
r_{NO} = rate of NO consumption [1/s]
r_{NH3} = net rate of NH_3 adsorption [mol/(m^3_{cat} s)]
$r_{NO,1}$ = rate of NO reduction [mol/(m^3_{cat} s)]
$r_{ads,NH3,SO3}$ = rate of NH_3 adsorption on sulfated sites [1/s]
$r_{des,NH3,SO3}$ = rate of NH_3 desorption from sulfated sites[1/s]
$r_{ads,SO3}$ = rate of SO_3 adsorption [1/s]
$r_{des,SO3}$ = rate of SO_3 desorption [1/s]
r_{ox} = rate of ammonia oxidation [1/s]
r_{SO2} = rate of SO_2 oxidation [1/s]
s = half-thickness of monolith wall [m]
t = time [s]
v = gas linear velocity [m/s]
x = dimensionless monolith transverse (intraporous) coordinate
x* = coordinate of inner boundary of active region
z = reactor or monolith axial coordinate
Greek letters
α = NH3/NO molar feed ratio
α_{o2}, α_w = kinetic orders for O_2, H_2O
ε = void fraction
γ = parameter for the surface coverage dependence
θi = surface coverage of species i

$\theta^{*}_{NH_3}$ = parameter for the NH_3 surface coverage dependence

Φ_i = Thiele modulus of species i

Ω_{NH3} = catalyst NH_3 adsorption capacity [mol/m^3_{cat}]

Ω_{SO3} = catalyst SO_3 adsorption capacity [mol/m^3_{cat}]

Superscripts

b = bulk gas conditions

eff = effective rate

f = free sites

w = conditions at the monolith wall

° = conditions at reactor inlet

REFERENCES

1. H. Bosch and F.J.J. Janssen, Catal. Today, 2 (1988) 369.
2. F. Nakajima and I. Hamada, Catal. Today, 29 (1996) 109.
3. P. Forzatti and L. Lietti, Heterog. Chem. Rev. 3 (1996) 33.
4. S. Matsuda, T. Kamo, A. Kato and F. Nakajima, Ind. Eng. Chem. Res., 21 (1982) 48.
5. J.P. Chen and R.T. Yang, Appl. Catal. A: General, 80 (1992) 135.
6. L. Lietti, P. Forzatti and F. Bregani, Ind. Eng. Chem. Res., 35(11) (1996) 3884.
7. L. Alemany, L. Lietti, N. Ferlazzo, P. Forzatti, G. Busca, E. Giamello and F. Bregani, J. Catal., 155 (1995) 117.
8. L. Casagrande, L. Lietti, I. Nova, P. Forzatti and A. Baiker, Appl. Catal. B: Environmental, in press.
9. A. Beretta, E. Tronconi, G. Groppi and P. Forzatti, in "Structured Catalysts and Reactors" (J. Mouljin and A. Cybulski, Ed.s), Ch. 5, Marcel Dekker, New York (1997) 121.
10. D. Agar and W. Ruppel, Chem. Eng. Sci., 43 (1988) 2073.
11. L.N. Bobrova, A.S. Noskov and Y.S. Matros, Catal. Today, 17 (1993) 293.
12. K. Hedden, R. Ramanda Rao and N. Schon, Chem. Ing. Tech., 65 (1993) 1506.
13. A. Noskov, L. Bobrova, G. Bunimovich, O. Goldman, A. Zagoruiko and Y. Matros, Catal. Today, 27 (1996) 315.
14. S.L. Andersson, P.L.T. Gabrielsson and C.U.I. Odenbrand, AIChE J., 40(11) (1994) 1911.
15. E. Tronconi and P. Forzatti, AIChE J., 38 (1992) 201.
16. E. Tronconi, P. Forzatti, J.P. Gomez Martin and S. Malloggi, Chem. Eng. Sci., 47 (1992) 2401.
17. E. Tronconi, A. Beretta, A.S. Elmi, P. Forzatti, S. Malloggi and A. Baldacci, Chem. Eng. Sci., 49 (1994) 4277.
18. J. Svachula, N. Ferlazzo, P. Forzatti, E. Tronconi and F. Bregani, Ind. Eng. Chem. Res., 32 (1993) 1053.
19. C. Orsenigo, A. Beretta, P. Forzatti, J. Svachula, E. Tronconi, F. Bregani and A. Baldacci, Catal. Today, 27 (1996) 15.

20. C. Orsenigo, L. Lietti, E. Tronconi, P. Forzatti and F. Bregani, Ind. Eng. Chem. Res., 37 (1998) 2350.
21. D.C. Vermaire and P.C. van Berge, J. Catal., 116 (1989) 309.
22. G.C. Bond and S.F. Tahir, Appl. Catal., 71 (1991) 1.
23. T.Z. Srnak, J.A. Dumesic, B.S. Clausen, E. Törnqvist and N.Y. Topsøe, J. Catal., 135 (1992) 246.
24. N.-Y. Topsoe, J.A. Dumesic and H. Topsoe, J. Catal., 151 (1995) 241.
25. I. Nova et al., manuscript in preparation.
26. D.E. Mears, Ind. Eng. Chem. Process Des. Develop, 10(4) (1971) 541.
27. G. Froment and K. Bischoff, in "Chemical reactor analysis and design", I. Wiley, New York, 1979.
28. N.-Y. Topsøe, J. Catal., 128 (1991) 499.
29. G. Ramis, G. Busca, P. Forzatti, C. Cristiani, L. Lietti and F. Bregani, Langmuir, 8 (1992) 1744.
30. L. Lietti, P. Forzatti, G. Ramis, G. Busca and F. Bregani, Appl. Catal. B: Environmental, 3 (1993) 13.
31. B. Finlayson, in "Nonlinear Analysis in Chemical Engineering", McGraw Hill Eds. New York, 1980 .
32. A.C. Hindmarsh, in "Odepack: a systematized collection of ODE solvers", in Scientific Computing (R.S. Stepleman et al., Ed.s); North Holland, Amsterdam, 1983.
33. G. Ramis, G. Busca, F. Bregani and P. Forzatti, Appl. Catal., 64 (1990) 259.
34. G. Ramis, G. Busca, F. Bregani and P. Forzatti, Cat. Scie. Tec., 1 (1991) 189.
35. H. Schneider, S. Tschudin, M. Schneider, A. Wokaun, and A. Baiker, J. Catal., 147 (1994) 5.
36. W.C. Wong and K. Nobe, Ind. Eng. Chem. Prod. Res. Dev., 23 (1984) 564.
37. V.I. Marshneva, E.M. Slavinskaya, O.V. Kalinkina, G.V. Odegova, E.M. Moroz, G.V. Lavrova and A.N. Salanov, J. Catal., 155 (1995) 171.
38. J. Beeckmann and L. Hegedus, Ing. Eng. Chem. Res., 30 (1991) 969.
39. J.A. Dumesic, N.-Y. Topsøe, T. Slabiak, P. Morsing, B.S. Clausen, E. Tornqvist and H. Topsøe, in "New frontiers in catalysis", (Guczi, L. et al., Eds.), Denmark (1993).
40. E. Tronconi, L. Lietti, P. Forzatti and S. Malloggi, Chem. Eng. Sci., 51 (1996) 2965.
41. E. Tronconi, A. Cavanna and P. Forzatti, Ind. Eng. Chem. Res., 37 (1998) 2341.
42. R.S. Cunningham and C.J. Geankoplis, Ind. Eng. Chem. Fund., 7 (1968) 535.
43. E.Tronconi, C.Orsenigo, A.Cavanna, P.Forzatti, Ind. Eng. Chem. Res, in press.

Reaction Engineering for Pollution Prevention
M.A. Abraham and R.P. Hesketh (Editors)

Regenerative Catalytic Oxidizer Technology for VOC Control

V. O. Strots[a], G. A. Bunimovich[a], C. R. Roach[b], and Yu. Sh. Matros[a]

[a] Matros Technologies, 14963 Green Circle Dr., Chesterfield, MO 63017, USA

[b] Monsanto Enviro-Chem Systems, Inc., P. O. Box 14547, St. Louis, MO 63178, USA

Regenerative catalytic oxidizer technology is being increasingly used for air pollution control. The technology fundamentals, as well as examples of commercial applications, have been recently reviewed by Matros *et. al.* (1993) and Matros and Bunimovich (1996). In the 90s, substantial progress has been made both in understanding various factors affecting the performance of RCOs, and in process engineering and design. This paper presents several practically important technology issues, such as selection of optimum inert packing geometry and operation with slowly deactivating catalyst. It also discusses fundamental bases for novel process design features: retrofitting of regenerative catalytic thermal oxidizer into RCOs and improved strategy for auxiliary energy supply. Examples of applications of these new features are presented and discussed.

INTRODUCTION

The regenerative catalytic oxidizer (RCO) technology employs the concept of reverse flow operation in a fixed bed reactor. Developed in the mid-70s by Matros with co-workers (Matros, 1977, Boreskov and Matros, 1983), the technology has gained acceptance as an efficient method to control volatile organic compounds (VOC). RCOs have become increasingly accepted in the 90s, when more stringent air quality standards made the industry look for more effective, cost-saving solutions to remove VOC from waste air streams.

An RCO typically includes a fixed bed of catalyst placed between two beds of chemically inert heat retentive packing (Fig. 1,a). A control system initiates periodical reversals of the direction of gas flow through the beds. RCOs combine advantages of low-temperature catalytic oxidation and highly efficient regenerative heat transfer in porous media (both catalyst and inert packing) to produce the most energy efficient method of VOC oxidation.

Fundamentals of the technology, such as process model, methods for solving model equations, analysis of effects of process and design parameters on the reactor performance, the results of laboratory and pilot tests, and examples of commercial applications have been reported in a number of papers (Boreskov *et. al.*, 1984, Matros, 1989, Eigenberger and Nieken, 1988, 1994), and were recently summarized by Matros *et. al.* (1993) and Matros and Bunimovich (1996).

The published literature, although abundant and frequently overlapping, is usually confined to the discussion of process fundamentals, advantages, and most general aspects of unit design and operation. However, commercial applications has demonstrated that more detailed knowledge is necessary to resolve practical issues. The present paper discusses a number of such issues recently studied by the authors.

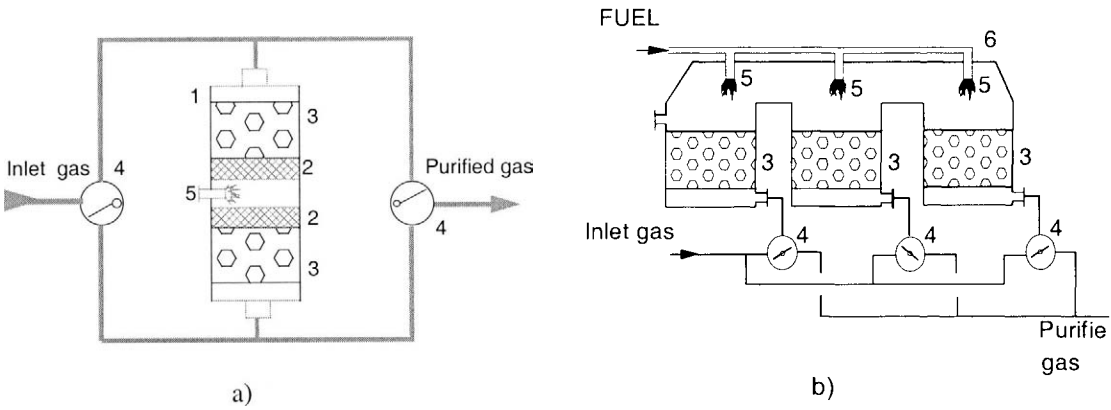

Fig. 1. Principal flow diagrams of regenerative catalytic (a) and thermal (b) oxidizers. 1: reactor, 2: catalyst bed, 3: ceramic packing, 4: switching valves; 5: burner, 6: combustion chamber.

One of these design aspects is the selection of optimum ceramic packing for heat regeneration. The packing surrounds the catalyst in order to preheat the gas flow before entering the catalyst bed (Fig. 1a). More diluted gas streams require larger amounts of packing. There exist a variety of packing materials that can be used in RCOs. While initial work was focused mainly on simplest types of packing, such as balls or Rashig rings, the latest research showed that random packing materials with advanced geometry or structured media provide a potential for great improvement in the process economics. This paper provides the results of comparison between a number of ceramic packing materials.

Industrial applications of catalytic methods for VOC control often cause deactivation of the catalyst through thermal sintering, poisoning or masking by the gas stream components. Deactivation of VOC oxidation catalysts is a broad and complex subject (Spivey and Butt, 1993). On practical side, it is important to understand the dynamics of unit performance while the catalyst deactivates, and develop strategies for process control and *in situ* catalyst regeneration. Examples of such strategies are discussed here.

An emerging area of RCO application is retrofitting of regenerative thermal oxidizers (RTOs) into catalytic units. RTO technology also periodical flow reversals for heat energy regeneration in ceramic packing media, but oxidation occurs homogeneously in gas phase at 800°C or higher (Fig 1,b). Comparison of RTO and RCO economics by Matros *et. al.* (1996) outlined the range of gas stream parameters where RCOs are preferable, and thus created a fundamental basis for RTO retrofitting applications. In this paper, we will discuss engineering approach to the retrofitting, options, and commercial unit operation examples.

CATALYST AND REACTION KINETICS

VOC oxidation catalysts usually represent two major classes of catalytically active materials: noble metals (Pt and Pd), and transition metal oxides. Noble metals have higher activity while oxide catalysts provide the advantage of lower cost. The RCO technology favors using oxide catalysts because it allows for easy compensation of lower activity by an

increase in the catalyst amount and/or temperature. The latter can be easily controlled by appropriate choice of the geometry and amount of catalyst and inert packing.

Catalyst activity determines the amount of catalyst (residence time), its operating temperature and, therefore, the required amount of ceramic packing. It is expressed a rate of reaction, *r*, which is a function of temperature and gas phase composition.

The reaction rate measurements referred to in this work were made in an isothermal gradientless reactor. First-order rate equations were found be fairly accurate for oxidation of many organic compounds at low concentrations and high temperatures:

$$r = k_o \exp\left(-E/RT\right) C_{VOC}.$$

MATHEMATICAL MODEL

Process simulation results were obtained using one-dimensional mathematical model (Matros, 1989, Matros and Bunimovich, 1995) that includes chemical reaction, intraparticle diffusion of reactants and products (via effectiveness factor), heat transfer between the surface of solid particles and the bulk of the gas phase, solid phase heat capacity, and mass and heat transport by convection. The model also includes adiabatic mixing of the process gas and flue gas generated by a fuel burner, or preheating of the process gas by an electric heater.

The most important dynamic factor governing dynamic behavior of the reactor is heat capacity of the solid. Gas flow temperature and composition were assumed to be in quasi-steady state in relation to solid phase temperature. At commercially used values of superficial velocity, > 0.5 m/sec, thermal conductivity of packed bed plays secondary role to interphase heat transfer. For typical VOCs concentrations, less than 1 g/m^3, catalyst or ceramic particles are nearly isothermal.

The mathematical description is represented by the system of equations:

$$\frac{1}{Pe_s}\frac{\partial^2 T}{\partial \xi^2} + \alpha(T-\theta) + \sum_j \Delta T_{ad,j} r_j(\theta, y) = \gamma_\theta \frac{\partial \theta}{\partial \tau}, \tag{1}$$

$$\alpha(\theta - T) - \frac{\partial \theta}{\partial \xi} = 0, \tag{2}$$

$$\beta_j(x_j - y_j) - \frac{\partial x_j}{\partial \xi} = 0, \tag{3}$$

$$\beta_j(x_j - y_j) - r_j(y,\theta) = 0, \tag{4}$$

The boundary conditions between catalyst and inert beds are:

$$\text{at } \xi = 0: \quad \frac{1}{Pe_s^{in}}\frac{\partial \theta_{in}}{\partial \xi_{in}} = \frac{1}{Pe_s}\frac{\partial \theta}{\partial \xi}, \quad T = T_{in}, \quad x_j = 0; \tag{5}$$

$$\text{at } \xi = 1: \quad \frac{\partial \theta}{\partial \xi} = 0; \tag{6}$$

Supply of additional energy, typically arranged for in the center of catalyst bed, results in an increase in the temperature of gas flow entering downstream portion of the catalyst. At a constant amount of energy supply, such an increase is represented by a constant parameter

ΔT_s. Therefore, the boundary condition for the second catalyst bed (dimensionless coordinate is given as ξ_2) depends on the outlet parameters after the first bed T^1_{out} and x^1_{out} as follows:

$$\text{at } \xi_2 = 0: \begin{cases} \dfrac{1}{Pe_s}\dfrac{\partial\theta}{\partial\xi} = \theta - T, \quad T = T^1_{out} + \Delta T_s + \alpha\dfrac{(1-\varepsilon)}{La_V}\left(\theta - T^1_{out} - \Delta T_s\right); & (7a) \\ x_j = x^1_{j.out}. & (7b) \end{cases}$$

The model (1 - 7) has been extensively tested through simulation of both pilot and commercial RCOs. An example of comparison of experimental and model generated temperature profile in a pilot RCO tested at an aluminum foil production facility in oxidation of mineral oils is given in Fig. 2.

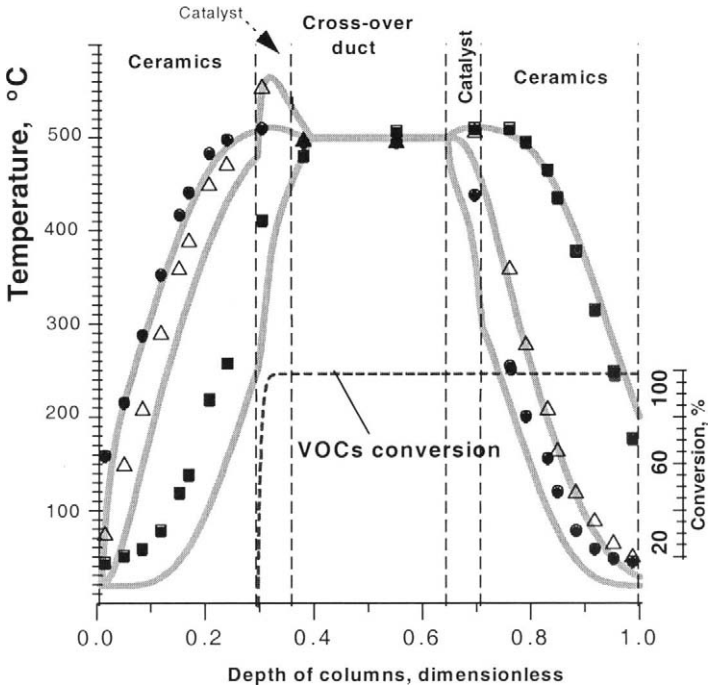

Fig. 2. Model predicted and experimental temperature and simulated VOC conversion profiles in a pilot RCO unit. Test results were obtained during testing at an aluminum foil production facility in oxidation of mineral oils.

CERAMIC PACKING

Heat transfer and accumulation properties of ceramic packing material strongly influence RCO performance. The rate of heat transfer affects the temperature gradients along the bed length which, in turn, determine the volume of material required to preheat the gas to the temperature of catalytic or thermal oxidation.

When an RCO operates with short cycles (relaxed steady state of reverse-flow reactor), the required volume of ceramic material is approximately inversely proportional to $a_V \cdot \Delta T$, where ΔT is difference between outlet and inlet temperatures in the oxidizer. This difference is composed of the temperature rise from VOC oxidation and auxiliary energy supply.

Process simulation was used to understand how the geometry of ceramic material affects the RCO performance. Five packings were considered: Intalox saddles, Ty-Pak ceramic packing from Norton Chemical Process Products Corp., monolithic ceramic foam, straight channeled monoliths, and stacked corrugated wave plates from Koch Engineering, Inc. The first three materials represent random packings while the latter two make regular structures.

The analysis was complicated by lack of sufficient information on heat transport properties and pressure drop of the packings. Some of the data could be derived from manufacturers' literature. For instance, Norton claimed that the Ty-Pak packing has the same mass transport coefficient as 25.4 mm saddles with lower pressure drop. Data from Koch indicate that the mass transfer rate in corrugated wave monolith with the smallest pitch is slightly higher than that for 25.4 mm saddles. In both cases we assumed that same ratios are applied for heat transport coefficients, given the analogy between mass and heat transport processes.

We further assumed that the heat transport coefficient α depends on superficial velocity of the gas flow in a random packing and corrugated wave monolith as

$$\alpha_{random} \sim U^{0.64} \tag{8}$$

For straight channeled monoliths, this coefficient was assumed to be independent on superficial velocity:

$$\alpha_{str.chan} \sim U^{0} \tag{9}$$

Heat accumulating capability of packed bed is determined by volumetric heat capacity of ceramic packing. If the heat capacity is low, shorter cycles are required. Usually, ceramic materials have the heat capacity close to 800 $J \cdot kg^{-1} \cdot K^{-1}$. At typical 60-70 % void fraction and 640 kg/m^3 density of ceramic bed, the volumetric heat capacity is about 540 $kJ \cdot m^{-3} \cdot K^{-1}$. Increase in the packed bed heat capacity without changes of transport properties means void fraction reduction which results in higher pressure drop.

Table 1 presents the results of pressure drop estimations for ceramic materials having similar efficiency regarding to heat transfer rate (expressed as equivalent size in mm). It turns out that Ty-Pak packing has ~ 1.3 times lower pressure drop than Intalox saddles of equivalent size, while corrugated wave packing provides for 2.5 times pressure drop reduction.

Figs. 3a and 3b illustrate heat transfer efficiency for various commercial packings, calculated at 16 °C and the same flow rate. Fig. 3b shows the data on a smaller scale. The data indicate that monolithic ceramic foam would have pressure drop much higher than other packings even at large channel sizes corresponding to 0.4 - 4 pores per linear cm (1-10 ppi). Straight channeled monolith is by far the most efficient material among those studied, i.e. it combines very high heat and mass transport rate with low pressure drop.

Superiority of the monolith results from laminar flow pattern inside the straight channels. In randomly packed materials and in wave plates the flow patterns are turbulent or intermediate between laminar and turbulent.

Table 1. Calculated relative pressure drop through the packing at 16 °C.

Linear velocity, Nm/sec	Pressure drop ratios for packings with equivalent sizes of 25.4 mm		
	saddles/ Ty-Pak, 25.4 mm	Ty-Pak / corrugated wave, 25.4 mm	saddles / corrugated wave, 38.1 mm
0.40	1.39	1.97	2.52
0.60	1.34	1.9	2.43
0.80	1.29	1.89	2.36
1.00	1.27	1.86	2.31
1.20	1.25	1.84	2.27

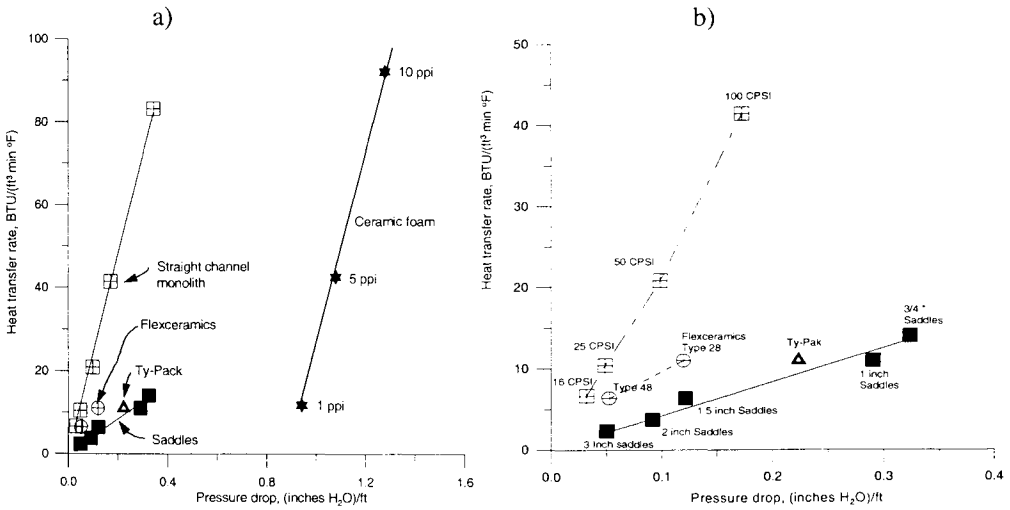

Fig. 3. Regenerative heat transfer efficiency vs. pressure drop for various ceramic materials. (Estimations at 0.80 Nm/sec linear velocity and 16 °C).

RCO OPERATION WITH DEACTIVATING CATALYST

During the catalyst operation, it gradually becomes less active and must be eventually replaced. The factors affecting the catalyst lifetime include high temperature, catalytic poisons and masking agents. Compounds of halogens and sulfur are the most common catalyst poisons (Spivey and Butt, 1993). Temperature control, poison tolerant catalysts and gas flow pretreatment are used to reduce the impact of catalyst deactivation. Nevertheless, it is necessary to understand the behavior of an RCO when the catalyst deactivates, and to develop strategies that ensure the required performance during the entire catalyst lifetime.

Example 1. *Sulfur poisoning of copper chromite catalyst.*

This example deals with the problem of catalyst poisoning in an RCO installed at an asphalt production facility. The gas flow contained ~ 1.5 - 2g/m^3 of hydrocarbons and up to 1,000 ppm of sulfur. The unit was loaded with a commercial catalyst containing copper chromite on γ-alumina. The catalyst has demonstrated good activity and lifetime in a large number of RCOs (Matros *et. al.*, 1991, 1993).

Testing the activity of catalyst samples after 3 months of operation showed that the catalyst was severely deactivated, with the residual activity of less than 10 % of initial value.

Earlier studies of poisoning of copper chromite catalysts by sulfur (Mulina *et. al.*, 1988, Khanmamedov *et. al.*, 1988, and Matros *et. al*, 1991) explained sulfur poisoning via formation of surface sulfates, and showed that poisoning was in most cases reversible. Further, Mulina *et. al.* (1988) and Matros *et. al* (1991) found that thermal treatment of the catalyst at 600 to 700 °C results in substantial restoration of the catalyst activity.

In our tests, poisoned catalyst samples were thermally treated in air at 600 to 800°C in order to determine the possibility and temperature range for the catalyst regeneration. The test results are shown in Figs. 5 and 6. These figures present the data on activity of fresh, poisoned and regenerated samples, measured as propane oxidation rate constant at 300°C. At 700°C, the catalyst slowly recovered its activity, achieving up to 80 % of the activity of fresh sample (Fig. 5). Activity of a fresh sample decreased slightly in the first 20 hours, then stabilized. At 800°C, regeneration initially accelerated, but longer exposure lead to the activity decline (Fig 6). Fresh catalyst activity also decreased, indicating that sintering was responsible for activity decrease.

These studies lead to the development of a method for *in situ* regeneration of catalyst. The procedure involves adding fuel to the RCO inlet, or turning on the burner, in order to increase the catalyst bed temperature to 700 - 750 °C, and keeping that temperature for several hours. With periodic regeneration, the catalyst has lifetime has been more than 4 years.

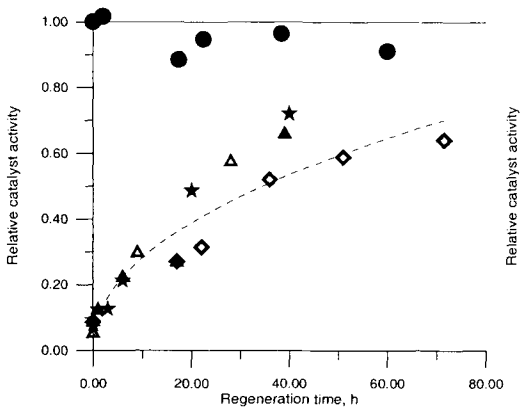

Fig. 5. Regeneration of poisoned catalyst at 700°C. ● - sample of fresh catalyst; other symbols - different samples of poisoned catalyst.

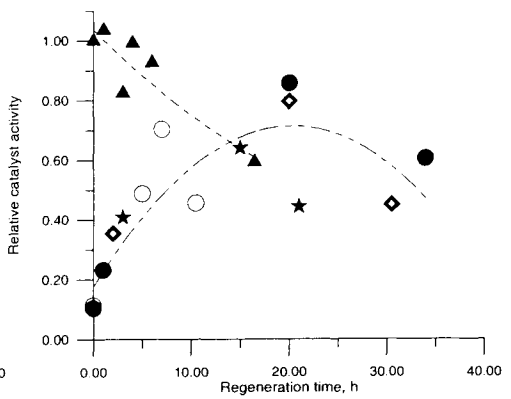

Fig. 6. Regeneration of poisoned catalyst at 800°C. ▲ - sample of fresh catalyst; other symbols - different samples of poisoned catalyst.

***Example B**. Effect of organic particulates*

There are many industries where VOC contaminated gas flows carry particulate matter (PM), sometimes in large quantities. The PM issue has two sides: potential catalyst deactivation via masking of its active surface or fouling its internal pores, and plugging of the catalyst and ceramic packing beds. Vast variety of compositions and size distributions of industrial particulates makes it difficult to develop universal solution for this problem. However, in cases where the PM is mostly of organic nature, thermal treatment provides such a solution. The effect of thermal treatment can be demonstrated on the example of catalyst operation in a wood industry application.

A mobile RCO demonstration unit was tested at a wood processing (veneer making) facility for one month. The unit was loaded with copper chromite catalyst. The gas contained 0.2 - 2.4 g/m^3 of hydrocarbons, and 0.8 - 1.1 g/m^3 of particulates, mostly or organic origins. Table 2 presents the dynamics of changes in conversion of hydrocarbons and CO during the 900 hours of the test. High conversion was achieved, however the trend to lower conversion has been identified.

Simultaneously, a catalyst testing unit (CTU) was operated at a similar facility. The unit consisted of a tubular insulated reactor with controlled input gas temperature. The design permitted sampling the catalyst from several locations along the gas flow.

The catalyst samples from the CTU were tested in propane oxidation (Table 3). Tests showed that the activity of samples closest to the unit inlet was 30 to 40 % lower than the activity of fresh catalyst. Samples farther from the inlet had higher activity. EDX analysis of the catalyst surface showed no contamination by sulfur, phosphorus or heavy metals.

Table 2. Conversion of hydrocarbons and CO during the RCO testing.

Catalyst bed temperature, °C	800	750	700	650	600
Hydrocarbon conversion, %					
10 h after start-up			99.1	96.2	95.2
100 h after start-up			98.6	97.5	94.4
900 h after start-up	98.3	98.1	97.0	95.2	92.9
CO conversion, %					
10 h after start-up			98.4	95.5	94.2
100 h after start-up			95.9	93.0	88.8
900 h after start-up	98.3	96.1	93.7	92.0	91.4

Table 3. Catalyst activity in propane oxidation at various stages of regeneration at 500 °C.

Sample	Rate constant at 300°C, s^{-1}, after regeneration time:						
	0 hr	0.5 hr	1 hr	3 hr	4.5 hr	13 hr	16 hr
Inlet, #1	0.69	0.87	0.86	0.89			1.02
Inlet, #2	0.77					0.95	
Middle, #1	0.77	0.90					
Middle, #2	0.80				1.05		
Outlet, #1	1.01					1.26	
Fresh catalyst	1.13						

Combustion of organic particles on VOC oxidation catalyst has close similarities to the combustion of soot in catalytic converters after diesel engines. Studies of PM oxidation for diesel exhaust aftertreatment showed that soot deposited on the filter burns out at 500-600 °C (Opris and Johnson, 1998), and the temperature can be reduced if there is good contact between carbonaceous particles with a catalytically active material (Summers *et. al.*, 1996).

In our tests, activity of the catalyst was slowly increasing during calcination at 500 °C (Table 3). Increase in the regeneration temperature to 600 °C resulted in complete recovery of the catalyst activity within 1 hour.

The tests showed viability of thermal treatment. The data also indicate that the catalyst does not significantly participate in the destruction of organic deposit.

The results of these experiments have been be used to simulate long-term RCO performance. The model assumed that all PM carried with the incoming gas flow is deposited on the catalyst bed. Uniform activity reduction was assumed to simplify the analysis. The model also included slow and irreversible deactivation of the catalyst as a result of aging process. A unit operating with energy addition was simulated, and the amount of energy was adjusted in order to achieve the required 95 % destruction of VOC, a-pinene in this example.

The resultant strategy of temperature control in the catalyst bed includes gradual increase in the amount of energy added to the oxidizer in order to compensate for the catalyst aging, with periodical increases that raised the maximum temperature up to 600 °C for about an hour (Fig. 7). Such excursions remove the accumulated deposits of organic materials.

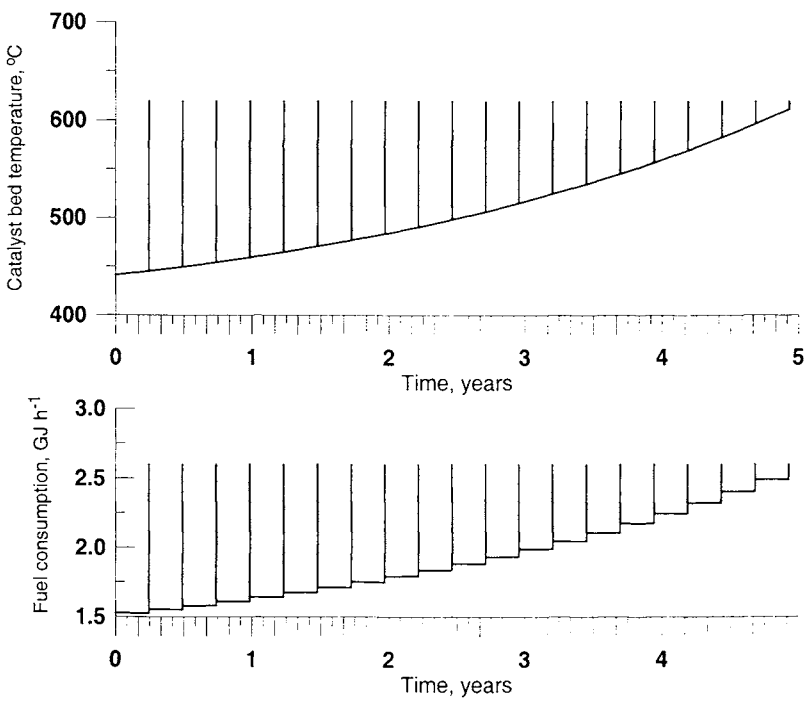

Fig. 7. Strategy of catalyst bed temperature control in an RCO with deactivating catalyst and periodical thermal regeneration of the catalyst.

RTO RETROFITTING

Regenerative thermal oxidation has traditionally been considered as one of the most cost effective solutions for VOC oxidation (see, for example, van der Vaart et al., 1994). This process technology uses homogeneous, gas phase oxidation of organic compounds. As in an RCO, periodical flow reversals in a heat regeneration media are used to preheat the inlet gas flow to the oxidation temperature, and to cool the outlet flow. Oxidation proceeds in a combustion chamber located between the beds, within the temperature range of 800 - 1000 °C. Residence time in the combustion chamber is typically 0.5 sec or more. One ore more fuel burners are usually installed in the chamber to maintain the combustion process. RTO systems often include more than two ceramic packed beds (Fig. 1, b). To achieve higher VOC destruction efficiency, each bed can be periodically purged by air to remove unreacted VOCs collected in the low temperature zone of the oxidizer and ceramics during part of the cycle.

The differences between RTO and RCO technologies can be demonstrated by a comparison of axial profiles of temperature and conversion (Fig. 4) obtained from computer simulation. An RTO process model is similar to the model (1) - (7), with equations modified in order to account for reactions occurring in the gas phase only. Reaction rate parameters used in these examples are given in Table 4.

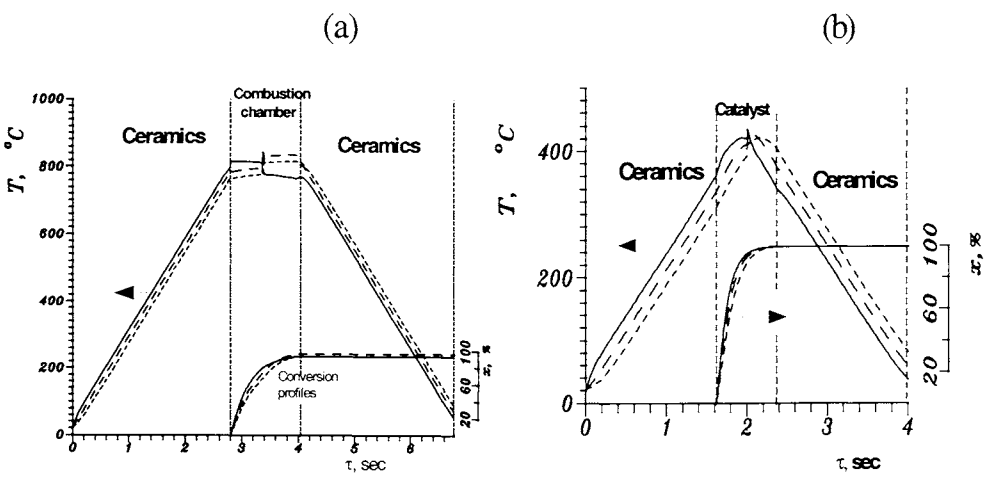

Fig. 4. Temperature (T) and conversion (x) profiles in regenerative thermal oxidizer (a) and reverse flow catalytic reactor (b) vs. residence time, τ. Solid, dashed and dotted lines represent the profiles at the beginning, middle, and end of the period between flow reversals for stabilized operation.

Table 4. Parameters of rate equations for RCO and RTO simulation.

	k at 573 K, s^{-1}	E_A, kcal/mol
catalytic oxidation	4.0	6.5
homogeneous oxidation	0.015	15

Matros *et. al.* (1994) presented economic analysis of RTO and RCO operation and determined that RCO technology is more efficient over a broad range of process conditions characterized by low concentration of VOC (or, adiabatic temperature rise of VOC oxidation). In particular, additional ongoing cost of catalyst replacement is less than the cost of electricity and supplemental fuel required to maintain the combustion temperature at $\Delta T_{VOC} < 95$ °C. At $\Delta T_{VOC} > 95$ °C, RTO is advantageous. For hydrocarbons, this threshold corresponds to VOC concentrations of ca. 3 g/m3.

There are three principal options in performing the retrofitting, each involving adding the amount of catalyst equal to 2 - 10 % of the original volume of ceramic packing. Table 5 presents the example of retrofitting a standard five-chamber RTO according to all three options. The unit was loaded initially with standard 1 in. (25.4 mm) ceramic saddles. The target conversion of VOC (toluene) is 95 %.

Option 1. Catalyst is added over existing beds of ceramic material. As a result, the oxidation temperature is reduced by 200 - 400 °C for the same input gas flow parameters and performance requirements. Pressure drop through the unit remains the same or decreases because lower reaction temperature compensates for packed bed volume increase. Process simulation results showed that the external energy requirement is reduced by 30-70 %.

Option 2. Catalyst replaces a small fraction of ceramic material in each bed. This option does not change the total height of packed beds and allows for pressure drop reduction. The fuel economy is slightly less than in Option 1.

Option 3. Substantial amount of ceramic packing, 40 to 60 % of initial quantity is removed and catalyst is loaded into the empty space. This option allows for a pressure drop reduction by 25 - 35 % at the same flow rate, or a flow rate increase by 15 - 25 % with pressure drop and destruction efficiency unchanged. Fuel consumption is still less than in the initial RTOs.

Table 5. Parameters of various options in retrofitting an RTO to RCO.

Parameter	Existing RTO	RCO after retrofitting		
		Option 1	Option 2	Option 3
Gas flow rate, Nm3/h	120,000	120,000	120,000	140,000
Inlet temperature, °C	20	20	20	20
Toluene concentration, ppm	100	100	100	100
Height of each ceramic packing bed, m	2.75	2.75	2.55	1.70
Height of catalyst bed, m	-	0.18	0.18	0.27
Volume of ceramic packing, m^3	108	108	101	66
Volume of catalyst, m^3	-	7.2	7.2	10.6
Maximum temperature in oxidizer, °C	790	480	480	450
Period between chamber switching, min	1	3	3	3
Outlet gas flow temperature, °C	66	47	49	57
Fuel consumption, MJ/s	1.27	0.42	0.52	0.90
Oxidizer pressure drop, kPa	4.48	4.46	4.28	4.48
Electric power consumption, kW·hr	231	230	221	231
Gas flow rate increase	-	-	-	15 %

CONCLUDING REMARKS

We have carried out a number of studies aimed at better understanding of factors affecting operation of regenerative catalytic oxidizers, and developed approaches to some of the problems encountered during operation of commercial RCO units.

Relation between heat transport properties and pressure drop through several commercial packings that could be used in RCOs has been investigated. The results show that straight-channeled monolithic media provides the best combination of these properties among the packings studied. Despite excellent performance, application of monolithic packing in RCOs remains very limited because of high price.

RCO operation with gradually deactivating catalyst was considered using two examples: poisoning of Cu-Cr catalyst by sulfur compounds at an asphalt production facility, and masking by organic deposits at a wood industry application. In both cases, satisfactory performance could be achieved with periodic thermal treatment of the catalyst in order to regenerate its activity. Optimum temperature conditions for regeneration are 700 - 750 °C for sulfur poisoned catalyst, and ~ 600 °C for a catalyst masked by carbonaceous deposits. Further, a model approach has been developed to predict the energy requirements for an RCO to meet performance criteria during several years long operating campaign.

Superior energy saving properties of RCO technology has been used for the development of basic approaches for retrofitting of regenerative thermal oxidizers into catalytic units. Depending on particular purposes of such retrofitting, a range of solutions have been suggested and investigated using computer process simulation. The solutions provide for either 30 - 70 % energy savings, or pressure drop (therefore, electrical energy use) reduction, or 15 - 25 % flow rate increase, or combination of all three.

NOTATION

a_V	external surface area of particles per unit volume of the bed
$C_{o,j}$, $C_{g,j}$ and $C_{s,j}$	concentrations of j-th VOC component at the bed inlet, in gas phase and on the particle surface, respectively
c_s, c_p	specific heat capacity of solid and gas
E_A	activation energy
h	gas-to-solid heat transfer coefficient
$K_{g,j}$	gas-to-solid mass transfer coefficient
k and k_0	rate constant and pre-exponential factor
l	axial coordinate, m
L and l	total bed length, m
P	pressure
Pe	$L\, u\, c_p\, \rho_g / \lambda_s$
R	gas constant
T	temperature of gas phase
t	time
u	linear gas flow velocity at NTP
x_j and y_j	conversion of j-th compound in the gas flow and on the catalyst pellet surface

α	$h\, a_V\, \tau_s / (c_p\, \rho_g)$, dimensionless gas-to-solid heat transfer coefficient
β_j	$K_{g,j}\, a_V\, \tau_s\, P / (R\, T)$, dimensionless gas-to-solid heat transfer coefficient
ΔH_j	heat of combustion of j-th compound, kcal/mol
$\Delta T_{ad,j}$	$(-\Delta H_j)\, C_{0,j} / (c_g\, \rho_g)$, adiabatic temperature rise of oxidation of j-th compound
γ_θ	$c_s\, \rho_s\, (1 - \varepsilon) / (c_g\, \rho_g)$, ratio of solid-to-ga heat capacities
ε	packed bed porosity
ρ_g and ρ_s	density of gas and bed frame
θ	temperature of frame phase
τ	t / τ_s, dimensionless time
τ_s	L / u, space time of gas mixture in packed bed
ξ	l / L, dimensionless axial coordinate

Subscripts:

in	inert packing

REFERENCES

Boreskov, G. K., and Matros,Y. S., (1983). Flow reversal of reaction mixture in a fixed catalyst bed, a way to increase the efficiency of chemical processes.*Appl. Catal., 5*, 337-342.

Boreskov, G. K., Matros, Y. S., Lugovskoy, V. I., Bunimovich, G. A., and Puzhilova, V. I., (1984). Unsteady-state process of complete oxidation in a fixed bed catalytic reactor. *Teor. Osnovy Khim. Tekhnol. (Theor. Fundam. of Chem. Technol.), 18,* 328-334.

Eigenberger, G., and Nieken, U., (1988). Catalytic combustion with periodic flow reversal, *Chem. Eng. Sci., 43*, 2109-2115.

Eigenberger, G., and Nieken, U., (1994). Catalytic cleaning of polluted air: Reaction engineering problems and new solutions, *Int. Chem. Eng., 34*, 4-16.

Khanmamedov, T. K., Kalinkin, A.V., Kundo, N.N., and Novopashina, V.M., (1988). XPS studies of active surface of Al-Cu-Cr catalysts for oxidation of tail gases from sulfur production. *React. Kinet. Catal. Lett., 37*, 83-88.

Matros, Y. S., (1977). Prospects for the use of unsteady-state processes in catalytic reactors. *Zhournal V. Kh. O. im. Mendeleeva (Journal of All-Union Chemical Society), 22*, 576-579.

Matros, Y. S., (1989). *Catalytic processes under unsteady-state conditions.* Studies in Surface Science and Catalysis, *43*, Elsevier.

Matros, Y. S., and Bunimovich, G. A., (1995). Control of volatile organic compounds by the catalytic reverse process. *Ind. Eng. Chem. Res., 34*, 1630-1640.

Matros, Y. S., and Bunimovich, G. A., (1996). Reverse flow operation in fixed bed catalytic reactors, *Catal. Rev.-Sci. Eng., 38*, 1-68.

Matros, Y. S., Noskov, A. S., and Chumachenko, V. A., (1993). Progress in *reverse-process* application to catalytic incineration problems. *Chem. Eng. and Proc., 32,* 89-98.

Matros Y. S, Bunimovich, G. A., Patterson, S. E., and Meyer, S. F., (1996). Is it economically feasible to use heterogeneous catalysts for VOC control in regenerative oxidizers? *Catal. Today, 27,* 307-313.

Matros Y. S., Noskov, A. S., and Chumachenko, V. A. (1991), K*atalitícheskoe obezvrezhivane otkhodyashchikh gasov promyshlennykh proizvodstv (Catalytic purification of industrial off-gases*). Novosibirsk: Nauka (in Russian).

Mulina, T. V., Filipov, A.V., and Chumachenko, V. A., (1988). CO oxidation over $CuCr/Al_2O_3$ catalysts in presence of SO_2. *React. Kinet. Catal. Lett., 37,* 95.

Opris, C. N., and Johnson, J. H., (1998). A 2-D computational modesl describing the flow and filtration characteristics of a ceramic diesel particulate trap, *Diesel Exhaust Aftertreatment, 1998,* SAE publication SP-1313, 149 - 175.

Spivey, J. J. and Butt, J. B., (1992). Literature review: Deactivation of catalysts in the oxidation of volatile organic compounds. *Catal. Today, 11*, 465-500.

Summers, J. C., Van Houtte, S., and Psaras, D., (1996). Simultaneous control of particulate and NO_x emissions from diesel engines, *Applied Catal. B., 10*, 139-156.

Van der Vaart, D. R., Marchand, E. G., and Bagely-Pride, A., (1994). Thermal and catalytic incineration of volatile organic compounds, *Critical Reviews in Environmental Science and Technology, 24*, 203.

Reaction Engineering for Pollution Prevention
M.A. Abraham and R.P. Hesketh (Editors)

Novel Photocatalytic Reactor for the Destruction of Airborne Pollutants

H. Ibrahim[a] and H. de Lasa[a]

[a] Chemical Reactor Engineering Center, Faculty of Engineering Science, University of Western Ontario, London, Ontario, Canada N6A 5B9

The photocatalytic conversion of a model pollutant (toluene) is studied in a newly designed Photo-CREC-Air reactor. In this unit, the TiO_2 is supported on a filter mesh with good contacting of near UV light, TiO_2 and air.

Photo-CREC-Air is designed with special features including a Venturi section and a heated perforated plate. The heated perforated plate minimizes water adsorption on the mesh and consequently water effects on the reaction rate.

Photo-CREC-Air performance is examined, in the present study, for four different toluene concentrations and two humidity levels. Following the insignificant toluene adsorption, a pseudo homogenous model is postulated for kinetic modeling. Initial photodegradation rates of toluene at 100° C in Photo- CREC-Air were determined in the 0.005-0.05 μmole/(gcat.s) range. Apparent quantum yields were in many cases greater than 100% and as high as 450 %.

1. Introduction

New legislation and environmental acts are placing more emphasis on the removal of undesired organic contaminants from air streams. Organic emissions, belonging to the Volatile Organic Compounds (VOCs) class, cause potentially significant public health risks. In this respect, photocatalytic oxidation using TiO_2 is an attractive technique, with potential applications for treatment of air in offices, buildings and refinery plants.

Several laboratory scale reactors have been developed using the UV/TiO_2 technology. Relevant configurations include:

a) Thin films of TiO_2 coated on the inner surface of reactor walls [1] ;
b) TiO_2 supported onto a porous fibrous mesh [2], monoliths [3-4], or honeycombs [5];
c) TiO_2 entrapped in supporting particles [6-9];
d) TiO_2 coated on optical fiber bundles [10].

2. Photo-CREC-Air

Even if some of the advantages of photocatalysis have been identified, there is, however, a need for novel photoreactors displaying high-energy efficiency and achieving total pollutant mineralization [11]. In this respect, Photo-CREC-Air is a novel unit [12] addressing this specific need. Photo-CREC-Air is designed with an inline fan, a Venturi section, a heated perforated plate, and an illuminated mesh section. In Photo-CREC-Air TiO_2 is supported on a filter mesh and this yields an optimal reactor configuration with high quantum yield.

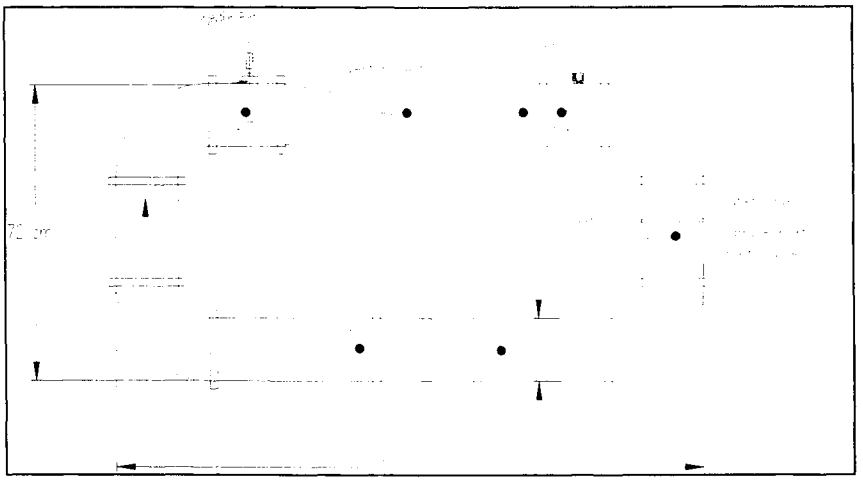

Figure 1: Overview of the Photo-CREC-Air unit and its associated internals. P1, P2, P3, P4, P5, P6, P7 represent the location of the pressure taps.

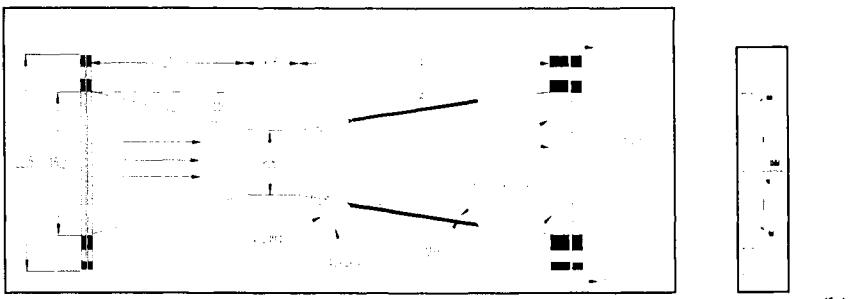

(a) (b)

Figure 2: a) Schematic diagram of the Venturi section including the reflector, the UV lamp, and the perforated heated plate, b) Schematic of the UV intensity and the velocity profiles in section A-A. Note that given dimensions are in cm.

A schematic diagram of the Photo-CREC-Air unit and of the corresponding air recirculation loop is described in Figure 1. The system has a total capacity of 65 L and it was built with a 15.2 cm ID exhaust pipe connected with four zinc-plated elbows. In the Venturi section, focused illumination of the reactor is achieved using lamps, reflectors and plexiglas windows (Figure 2).

The Venturi section was designed using classical Venturi equations with a corresponding C_v factor of 0.98 [13]. On this basis, the Venturi was made out of stainless tubing with the following components: a) a convergent section (21 cm), b) a straight section (6.8 cm), and c) a divergent section (34.2 cm). The upstream cone of the convergent section had an angle of 11° and the downstream section an angle of 7°. At the exit of the divergent section a fixed layer of a fibrous filter was located transverse to the flow with this fibrous mesh supporting the TiO_2. This design incorporates high mass transfer with a controlled pressure drop and establishes a "self-cleansing" system. The geometry of the Venturi was judged as very convenient given it allows to place the lamps close to the neck of the Venturi (Figure 2a). This position provides uniform irradiation of the complete mesh area (Figure 2b). The TiO_2 powder used was TiO_2 P25 supplied by Degussa Corporation. This TiO_2 had a BET surface area of 35-65 m^2/g, average primary particle size 21 nm, and a specific gravity of 3.7.

Illumination of the reactor was provided by two low-pressure mercury gaseous discharge lamps, Pen-Ray® lamps, each rated at 4 W. Lamps were designed for stable, low noise operation and had a rated lamp life of 5000 h. Lamps were placed inside two aluminum reflectors. These reflectors together with two-side mirrors focus light rays on the target mesh. Reflectors were designed using principles of classical optics.

A perforated plate was incorporated in the design as an extra support for the impregnated mesh. This perforated plate secures uniform distribution of fluid when in contact with the mesh. The plate is heated with two cartridge heaters of 150 W each and this ensures a free of water mesh and this is significant given the potential negative effect of adsorbed water on the photoreaction. The perforated heated plate had 144 holes each of them having 0.8-cm diameter.

3. Filter Selection

Three filters were studied to find the best TiO_2 support: Filtrete™, 3M blue pleated filter, Bionaire electrostatic charged filter. With this end, different tests were performed to examine catalyst loading, light transmittance, thermal resistance and water desorption. These tests revealed that the 3M blue pleated filter was the one providing the highest catalyst loading (50wt. %), allowed water to be desorbed completely at 100° C, displayed a high thermal resistance and provided good light transmittance (before and after impregnation). Consequently it was judged that the 3M blue pleated filter was the one displaying the best combination of the required properties.

Loading of 3M blue plated filters was studied using Scanning Electron Microscopy (SEM). It was concluded that TiO_2 was firmly attached with 2-μm aggregates of well-anchored 21-nm TiO_2 particles, uniformly distributed throughout the filter.

A TPD (Temperature Programmed Desorption) test was also performed to estimate the temperature at which the filters are essentially free of adsorbed water. It was found that a

typical desorption temperature is 100° C. Thus, this shows that having the heating plate holding the mesh at 100° C and above, allows adsorbed water to be removed from the mesh.

Light transmittance through the filters was another factor to secure efficient light penetration throughout the filter layer. Light transmittance in the 365 nm wavelength was measured using a PU 8625 UV/VIS Spectrophotometer supplied by Philips Light. The fraction of the focused light that made its way through the filter was used to define the transmitted light, T (optical density =log (I_o/I)=log (1/T)). This revealed that light transmittance in the 3M blue plated filter was 1-2.5 %.

Furthermore, the coating of TiO_2 on the mesh was accomplished by applying catalyst on the mesh gently spreading it with a soft painting brush. Then, acetone was sprayed on the mesh surface. Following this, there was a 20 minutes wait until acetone evaporated. The coating process was repeated several times (5-6 times) until 2-2.5 g of TiO_2 were deposited in 8.5-10 g of mesh. Additional details of the mesh preparation technique are reported in Ibrahim [14].

4. Evaluation of Photo-CREC-Air

Evaluation of the Photo-CREC-Air was developed using pressure, velocity and UV intensity measurements. Pressures were measured, as illustrated in Figure 1, at 7 locations with taps placed at various positions. It was noticed that there was a progressive pressure reduction along the unit path with a point of lowest pressure at the Venturi throat (P6). This pressure reduction is expected given the Venturi promotes a considerably velocity increase and as a result, given mass continuity, a pressure reduction. Following this, the pressure recovered in P5, once the vena contracta effect, was dissipated. There was also a further pressure drop due to the perforated plate in P4 and P5. Finally, the pressure recovered, given air re-compression, with the fan reaching at this point an above atmospheric pressure level.

An important indicator of unit performance was the gas radial velocity profile in the mesh close region. Gas velocities were measured at 12 radial positions at the fourth pressure tap (P4) using a Pitot tube. Velocity profiles were recorded both at low (20° C) and high temperature (97° C). In both cases the profile was parabolic in shape, close to symmetric, with a sharp velocity change in the outer mesh region and a less pronounced change in the core of the mesh. Thus, the gas contacted the mesh with uniform velocities, close to 3 m/s.

Regarding the irradiating light and its distribution measurements were developed using a UVX radiometer, supplied by UVP, equipped with a 365-nm sensor. The radiometer was mounted on a specially designed rotating plexiglas plate. This plate allowed measurements of UV intensity on the mesh surface at four circumferential positions: 0 degrees, 45 degrees, 90 degrees and 135 degrees. It was noticed that radiation tended to be quite uniform across the filter surface with most of the filter illuminated with 55 $\mu W/cm^2$.

4. Experimental Methods

Toluene was used as model pollutant to test the performance of the unit under the following experimental conditions: a) toluene concentration: 5.2-13.0 $\mu g/cm^3$, b) temperature: 20-100° C and c) water levels: less than 25.0 $\mu g/cm^3$ and about 32.0 $\mu g/cm^3$.

In a typical experiment, the reactor was filled with dry air bringing the final gauge pressure up to 13.8 kPa. This over-pressure provided an adequate internal pressure for taking a cumulative total of 8-L of samples. Following this, the plate heaters were turned "on" until a plate-desired temperature of 50-100° C was reached. The reactor contents were allowed to circulate and they were recycled for about half an hour before any samples were taken.

Note that during the first four hours of operation the UV light was not turned on, allowing the toluene to be adsorbed onto the TiO_2-mesh system. After that, light was turned on for 18-20 hours. Samples were withdrawn every 0.5-1 h, as necessary. In the case of experiments with high humidity levels, water was also injected into the reactor about thirty minutes before the toluene injection. Two GC units were used. One GC was equipped with a Poropak Q column 1.83 m long and 0.318 cm in diameter in conjunction with a thermal conductivity detector (TCD). The second GC was operated with a 25 m x 0.33-μm HP-1 capillary column that operated with a flame ionization detector (FID). Both GCs used helium as the carrier gas. Samples were collected in 1L Tedlar bags and injected manually. The Poropak-TCD analysis allowed the quantification of gas fractions of unconverted toluene, carbon dioxide, and water. Air was used, in this case, as an internal standard while all measurements of toluene and carbon dioxide were based on air peaks. The capillary column-FID analysis also allowed the evaluation of the formation of intermediate species.

5. Results and Discussion

A typical experiment consisted of two periods: a) an initial period of 4 hour duration with light source turned "off" and adsorption/condensation process being completed, b) a second period, typically lasting 18 hours, when the UV source was turned "on". In order to establish adequacy of the 4 hour initial period for completing adsorption-condensation phenomena, extended blank runs were developed lasting 18 hours. It was, in this way, confirmed that the model gas phase pollutant concentration change was completed in the initial 4 hours of the run. Thus, the adopted methodology, 4 hours with the light source turned "off" followed by 18 hours of light source turned "on", was considered as very adequate.

As stated above, combined capillary column-FID analysis allowed the investigation of intermediate photo-oxidation products. It was observed that during the more than 32 systematic runs, at four different toluene initial concentrations and two humidity levels, water and carbon monoxide were the only products formed with no indication of gas phase detectable intermediate species. This strongly suggested the complete combustion of toluene.

In order to provide a description of the results obtained, a model for toluene photo-oxidation in Photo-CREC-Air was developed. The main assumptions include: a) well mixed conditions in Photo- CREC-Air loop and this was justified given the intense gas recirculation; b) pseudo homogeneous model for the photocatalytic reaction and this was supported given the small amounts of adsorbed toluene on the mesh-heated plate system. Based on this, the following integrated equation was considered [12];

$$\ln(C_T/C_{To}) = -k_o t^* \quad (1)$$

"t" being the time elapsed from the instant the lamp was turned on and t^* a corrected time ($t^* = t\,(I/I_o)$). This corrected time t^* allows to refer the kinetic constants to the condition of a lamp

after 40 hours of operation with an incident UV intensity of 50 $\mu W/cm^2$. A typical C_T/C_{To} versus t^* is shown in Figure3.

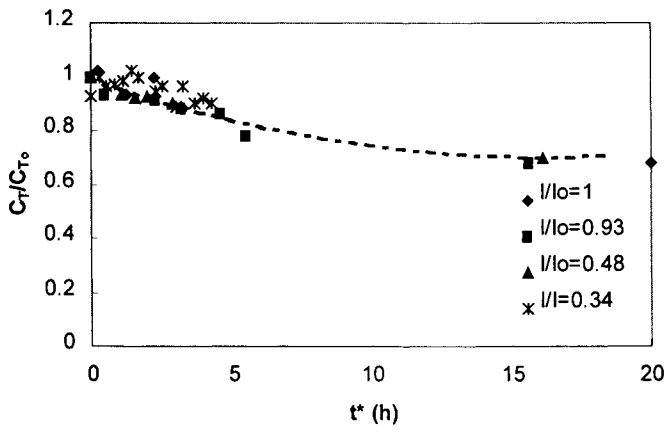

Figure 3: Typical (C_T/C_{To}) versus corrected time ($t^*=I/I_o$ t) during an experimental run with Photo-CREC-Air. Kinetic constant evaluated was 0.02 ±0.002 h^{-1} (95 % confidence interval) with R^2=0.9.

Once the kinetic constants k_o were calculated, quantum yields based on the photons absorbed by the TiO_2 on the mesh were determined by :

$$\varphi = \gamma [r_{mpo,max}] W N_A h c/[\lambda Q_{m,abs}] \quad (2)$$

where

$$r_{mpo,max} = -k_o C_{To} \quad (3)$$

Apparent quantum yields obtained were, except for the lowest toluene concentration, consistently bigger than 100%. (Figure 4). This confirmed the special character of photocatalytic oxidation reactions in air where one photon appears to be involved in more than one photocatalytic event and this suggests a chain decomposition mechanism.

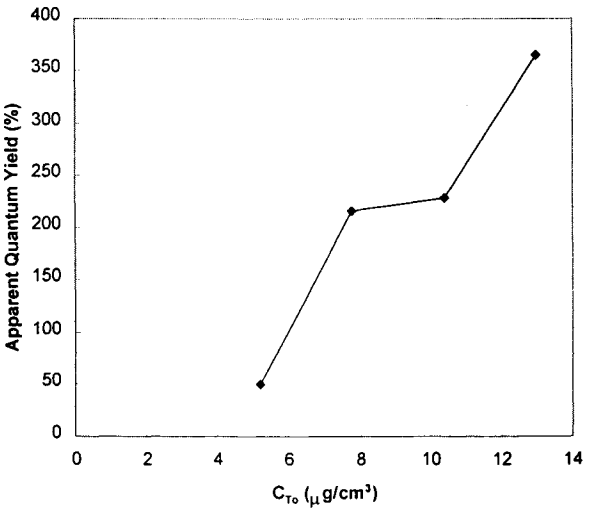

Figure 4: Apparent quantum yield assessed for the different toluene concentrations studied.

This finding is consistent with Luo and Ollis [15] who quoted quantum yields as high as 4 (400%) and Berman and Dong [16] who reported photoefficiencies of 590% for TCE, 220% for perchloroethylene, 920 % for methanol and 190% for ethanol. Moreover, the high levels of apparent quantum yields obtained in Photo-CREC-Air point towards its excellent performance.

6. Conclusions

The novel Photo-CREC-Air unit, described in the present study, is conceived with unique features for high-energy efficiency. There is a Venturi section and a heating plate to improve photo-oxidation of model pollutants (high apparent quantum yields). A first order, pseudo homogeneous model was found adequate for representing the photo-oxidation of toluene under the experimental conditions tested. Apparent quantum yields were promising and greater than 100% at the higher pollutant concentrations.

Acknowledgments

We would like to express our acknowledgment to the Natural Science and Engineering Research Council of Canada and the University of Western Ontario Research Office for their financial support.

Notation

C speed of light in vacuum (2.997×10^{10} cm/s).
C_T concentration of toluene.
C_{To} initial concentration of toluene.
h: Plank's constant (6.62×10^{-34} J.s).
k_o initial kinetic constant (h^{-1}).
I power of the lamp (W/cm^2).
I_o initial power of the lamp (W/cm^2).
N_A Avogadro number (6.023×10^{23} molecules/mole).
$Q_{m,abs}$ rate of light energy absorbed by the TiO_2 mesh in the photocatalytic reactor at 40 h of lamp operation ($9.1*10^{-3}$ W or 50 $\mu W/cm^2$ for a 182 cm^2 mesh area).
$r_{mp>o\ max}$: rate of model pollutant photo conversion based on corrected kinetic constants for a lamp after 40 hours of operation and gas phase toluene concentration once light is turned on.
t time elapsed from the instant the lamp was turned on (h).
t^* corrected time = $t\ I/I_o$ (h.).
W total catalyst weight used in the experiment (g).
λ wavelength (m).
γ stoichiometric coefficient, equals -1.
φ Quantum yield (%).

References

1. Jacoby, W.; Black, D.; Fennell, D.; Boulter, J.; Vargo, L.; George, M.; Dolberg, S, Journal of Air and Waste Management Association, v 46, 691-898, **1996**.
2. Peral, J., and Ollis, D., J.of Catal., v136, 554-565, **1992**.
3. Blanco, J., Avila, P., Bahamonde, A., Alvarez, E., Sanchez, B., and Romero, M., Catalysis Today, v29, 437-442, **1996**.
4. Obee, T., and Brown, R., Environ.Sci.Technol., v29(5), 1223-1231, **1995**.
5. Suzuki, K., in Photocatalytic Purification and Treatment of Water and Air: Proceedings of the 1st International Conference on TiO_2, 421-434, D. Ollis and H. Al-Ekabi (eds.), **1993**.
6. Dibble, L., and Raupp, G., Environ. Sci. Technol., v26(3), 492-495, **1992**.
7. Yamazaki-Nishida, S., Nagano, J., Phillips, L., Cervera-March, S., and Anderson, M., J.of Photochemistry and Photobiology A: Chemistry, v70, 95-99, **1993**.
8. Yamazaki-Nishida, S., Read, H., Nagano, J., Jarosch, T., Eddy, C., Cervera-March, S., and Anderson, M., J. Soil Contamination, v3(4), 363-378, **1994**.
9. Anderson, M., Yamazaki-Nishida, S., and Cervera-March, S., in Photocatalytic Purification and Treatment of Water and Air: Proceedings of the 1st International

Conference on TiO_2, 405-420, D. Ollis and H. Al-Ekabi (eds.), **1993**.

10. Peill, N., and Hoffmann, M., Environ. Sci. Technol., v30, 2806-2812, **1996**.
11. Serrano, B., and de Lasa, H., Ind. Eng. Chem. Res., v36, 4705-4711, **1997**.
12. de Lasa, H., and Ibrahim, H., USA Patent Application, **1998**.
13. McCabe, S., Smith, J., and Harriott, P., Unit Operations of Chemical Engineering. McGraw-Hill, Inc., Toronto, **1993**.
14. Ibrahim, H., M.E.Sc. Thesis, The University of Western Ontario, **1998**.
15. Luo, Y., and Ollis, D., J. Catal., v163, 1-11, **1996**.
16. Berman, E., and Dong, J., in Chemical Oxidation Technologies for the Ninties, 183-189, W. Eckenfelder et al. (eds), **1994**.

Reaction Engineering for Pollution Prevention
M.A. Abraham and R.P. Hesketh (Editors)

Thin film photocatalytic reactor for the destruction of organic contaminants in industrial wastewater and drinking water

D. D. Dionysiou[a], G. Balasubramanian[a], M. T. Suidan[a], I. Baudin[b] and J.-M. Laîné[b]

[a] Department of Civil and Environmental Engineering, University of Cincinnati, Cincinnati, OH 45221, U.S.A.

[b]Lyonnaise Des Eaux, Centre International de Recherche sur l'Eau et l'Environnement (CIRSEE), 38, rue du Président Wilson 78230, Le Pecq, France

A novel UV/TiO_2 rotating disk photocatalytic reactor (RDPR) has been developed for the photocatalytic degradation of toxic and hazardous organic compounds in industrial wastewater as well as in groundwater (drinking water application). The rotating disk photocatalytic reactor exhibits certain advantages, such as the formation of a thin film for the reaction, good mixing, use of air as oxygen source and effective immobilization of the TiO_2 catalyst. Other advantages include the flexibility of either catalyst reactivation or replacement during potential deactivation or poisoning. The rotating disk was covered on both sides with attached TiO_2 catalytic pellets and was rotated vertically in the reactor vessel. With half the disk exposed to air, the reaction occurred within a thin film of solution carried on the rotating disk. The effects of disk angular velocity (2 to 20 rpm), pH (3, 7, and 10), and initial contaminant concentration (32 to 320 μmol/l) on the degradation of 4-chlorobenzoic acid have been investigated. Degradation rates increased with disk angular velocity following a saturation-type dependancy. Higher degradation rates were observed at pH = 3.0 while the effect of initial contaminant concentration on the initial reaction rates followed the Langmuir-Hinshelwood model.

1. INTRODUCTION

TiO_2-assisted photocatalytic treatment of water has been considered for the refinement of polluted drinking water, surface water and groundwater as well as for the decomposition of nonbiodegradable and biocidal compounds, but the process is still in the experimental stage. More promising application areas include the production of ultrapure water for the pharmaceutical, microelectronic, and power generation industries and treatment of contaminated groundwaters in small- to medium-sized units [1-2]. Numerous organic compounds have been reported as being treated via TiO_2 photocatalysis. These include compounds of the classes of alkanes, haloalkanes, amines, ketones, dioxins, aldehydes, aliphatic alcohols, aliphatic carboxylic acids, alkenes, haloalkenes, aromatics, haloaromatics, phenols, aromatic carboxylic acids, surfactants, herbicides, pesticides and dyes. Examples of the above and a more complete list of organic compounds that were degraded using TiO_2 photocatalysis can be found in many reviews and in other papers [2-12]. Many of these organic compounds are classified as priority pollutants by the US EPA. Other environmental application of TiO_2 photocatalysis include the

photocatalytic oxidation for total organic carbon analysis [13], determination of dissolved organic nitrogen compounds in natural waters [14], water and air disinfection [15], removal of silver in photographic processing waste [16] and photoreduction of mercuric salt solutions [17].

For the destruction of various toxic compounds and contaminants, the TiO_2 (titania) catalyst is usually used in the form of colloidal suspensions in the aqueous medium or immobilized on various supports. The choice of colloidal suspensions results in higher reaction rates due to higher surface area and lesser mass transfer limitations but imposes the problem of separation of the catalyst from the effluent in a continuous operation. On the other hand, the use of immobilized catalyst on various substrates usually results in lower surface area for reaction and mass transfer limitations but eliminates the problem of catalyst separation.

Various support material that have been used to immobilize photocatalysts include glass (e.g., glass beads, fused-silica glass fibers, glass plates, glass tubes, porous Vycor glass, hollow glass microbeads, fiber optic cables), silica gel, ceramic, and stainless steel [18-27]. In most of those immobilization techniques, the TiO_2 is attached on the support material using TiO_2 slurry solutions or wet chemistry preparation methods (sol-gel techniques), followed by heat treatment of the obtained film.

The low photonic efficiencies of the current photocatalytic processes are the major reasons for their limited impact on current industrial processes for the degradation of organic contaminants [28] and give the impulse to the search for new designs and reactor configurations which will increase process efficiencies and will reduce the cost of the process. An alternative solution utilizes sunlight which has about 4% UV radiation. Solar photocatalytic treatment of water has been demonstrated at both the bench and pilot scale [29-34].

Large-scale implementation and commercialization of TiO_2 photocatalysis and other Advanced Oxidation Technologies (AOTs), for the destruction of pollutants in water and air are a joint aim of many researchers from both industry and academia. The annular photoreactor [2, 35-37], the packed bed photoreactor [38], the photocatalytic Taylor vortex reactor [39], the TiO_2 fluidized-bed reactor [40], the TiO_2-coated fiber optic cable reactor [25, 41-42], the falling film reactor [43] and the thin-film-fixed-bed sloping plate reactor [44] are different types of reactors that have been used for heterogeneous photocatalytic processes. However, commercialization and large scale application of TiO_2 photocatalysis in the industrial level has not been achieved.

Motivated by the need to apply this process in an industrial level, we developed in our laboratories a novel photocatalytic reactor: the RDPR. In this reactor, degradation of various toxic compounds in drinking water or wastewater streams can be carried out in batch or in continuous operations. In a closed reactor, heterogeneous reactions can simultaneously occur in both liquid and gas phase. Mixing of the solution in the reaction vessel is achieved by the rotating disk. In this type of reactor, the various organic contaminants in water are degraded in a thin film of liquid carried on the TiO_2-loaded rotating disk under UV illumination. The photocatalytic reactions occur in the upper semicircular part of the disk, which exposed to UV, and not in the bulk liquid in the reaction vessel. Various design parameters are important for controlling the degradation rates in the RDPR. Most important of those include the light intensity, the catalyst type and surface area, the liquid flow rate, the disk angular velocity, the residence time, and the type and concentration of the organic contaminants in the feed.

Immobilization of the catalyst, reaction within a thin liquid film, good mixing, and no demand for oxygenation other than oxygen uptake from the surrounding air are some of the advantages of the RDPR. Moreover, similar to rotating biological contactors (RBCs), an

established commercial technology for wastewater treatment [45], the RDPR can be an attractive technology for major environmental companies.

Beside the application of the RBC for the purification of wastewater [45-46], the rotating disk reactor has been extensively used in spin coating processes for the production of high quality coatings or films in lithography and microelectronic industries [47-51], in chemical vapor deposition methods for the preparation of super-contacting thin films [52-54], in chemical reactions using immobilized enzymes [55] and in other chemical reactions and solid dissolution into solvents [56-61].

This study focuses on the RDPR as a new type of reactor for the destruction of organic pollutants in water. The major goals of this work are the following: (a) to characterize the catalyst used in the RDPR, (b) to explain the important characteristics of the RDPR, and (c) to study the effect of disk angular velocity, pH, and initial contaminant concentration on the initial photocatalytic reaction rates of a model compound.

2. EXPERIMENTAL METHODS AND PROCEDURES

2.1. Rotating disk photocatalytic reactor

The RDPR includes the following major components: a reactor vessel, a rotating disk loaded with TiO_2 catalyst, the UV sources, a control system for angular velocity, a controller for the UV radiation units, and a pH control system. A schematic of the reactor is shown in Figure 1.

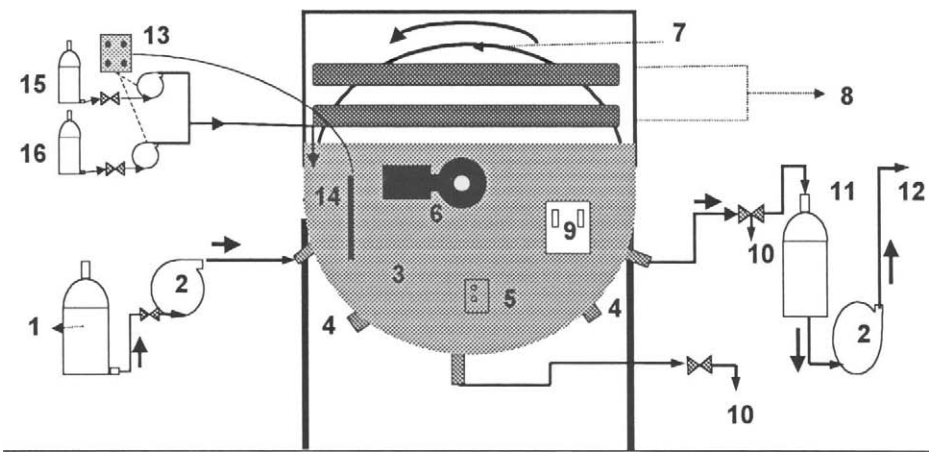

1: Feed Solution	**5: RPM Control**	**9 : UV Lamp Control**	**13: pH controller**
2: Pump	**6: Motor**	**10: Sampling Ports**	**14: pH meter**
3: Reactor Vessel	**7: Rotating Disk**	**11: Collection Vessel**	**15: Acid**
4: Sampling Ports	**8: UV Lamps**	**12: Effluent**	**16: Base**

Fig. 1. The Rotating Disk Photocatalytic Reactor (RDPR) and its major components.

The reaction vessel had a semicircular shape with an inner diameter of 52 cm, a gap thickness of 3.5 cm, and a maximum volumetric capacity of 3.5 l. The top section of the reactor is open to the atmosphere. Stainless steel 304 was the material used for the construction of the main body of the reactor as well as for the rotating disk support. The rotating disk had a diameter of 49.5 cm and a thickness of 0.32 cm. Stainless steel plates located parallel on the top part of the reaction vessel and next to the rotating disk prevented stray radiation from entering the reactor vessel. This was important for ensuring that the photocatalytic reactions occurred in the thin film of liquid carried on the rotating disk and not inside the reaction vessel.

The UV sources (Spectronics Corporation, Westbury, New York) were four 15-watt integrally filtered low pressure mercury UV tubes emitting 365 (±10) nm radiation with an intensity of 1100 $\mu W/cm^2$ (for each tube) measured at a distance of 25 cm. The UV tubes were mounted in pairs in two silver-anodized aluminum housings positioned horizontally at each side of the disk. The UV tubes were at a distance of 10 cm from each side of the exposed semicircular section of the rotating disk.

2.2. TiO_2 catalyst: characterization and immobilization

The type of TiO_2 catalyst used in the study (ST-B01, Ishihara Techno Corp., Japan) was in the form of composite ceramic balls (~6 mm in diameter). These catalytic balls were composed of an inner ceramic support (mainly SiO_2/Al_2O_3) and a layer of anatase TiO_2 particles attached on the surface of the support. Crystal morphology of the deposited active layer of TiO_2 was identified using X-ray diffraction (XRD, Siemens Kristalloflex D500 diffractometer, with CuK_a radiation) while the thickness of the active TiO_2 layer was determined with Scanning Electron Microscopy (SEM, Hitachi S-4000). Trace impurities and other metals on the surface of the ST-B01 ceramic balls were identified with Electron Diffraction X-Ray (EDX, Hitachi S-4000). The total surface area and total pore volume of the ST-B01 composite ceramic balls as well the total surface area of the active layer of TiO_2 particles were determined using BET analysis (Gemini 2360 V1.01, Micromeritics). Pore size and pore size distribution of the ST-B01 ceramic balls was measured with an Accelerated Surface Area and Porosimetry System (ASAP 2010, Micromeritics).

The TiO_2 composite ceramic balls were immobilized within individual cavities (with diameter of 0.6360 cm and a depth of 0.3175 cm) using 316 stainless steel woven wire cloth. The total number of attached TiO_2 composite ceramic balls was 7958.

2.3. Mixing patterns in the RDPR

Mixing in the RDPR was investigated using lithium chloride as tracer. In this process the reactor was operated in a continuous flow mode while the volume of liquid in the reactor vessel was fixed at 2950 ml. In order to avoid tracer deposition on the catalyst, the experiments were performed with equally sized (6 mm) solid glass beads substituting for the ST-B01 ceramic balls. The tracer was injected as a pulse input (V_{spike}=7 ml, C_{spike}=36.6 g LiCl/l) in the inlet of the reactor vessel and samples (10 ml) were taken from three locations in the reactor vessel (inlet zone, bottom of the reactor vessel, and outlet) at various time intervals. Atomic Absorption Spectroscopy (Perkin Elmer, AAnalyst 300 and AS 90 Autosampler) was employed for measuring the concentration of Li in the samples. The lithium chloride solutions as well as the lithium standards were prepared in 5% HNO_3 solution.

2.4. Rotating disk liquid holdup

Two different techniques, the potassium ferrioxalate actinometer [62-64] and the overflow method were used to determine the liquid holdup of the rotating disk loaded with glass beads. The overflow method only was used for determining the liquid holdup of the disk loaded with ST-B01. Details about how these two techniques were used in our study and the obtained results are explained elsewhere [65]. The liquid holdup (V_L) increase with disk angular velocity (ω) in the range of 2 to 41 rpm following a power law correlation,

$$V_L = c_1 \left(\omega \right)^{c_2} \tag{1}$$

with coefficients c_1 and c_2 of 133.9 and 0.32, respectively [65].

2.5. Light intensity distribution on the UV-illuminated rotating disk

A research radiometer (IL 1700 Research Radiometer/Photometer, International Light, Inc.) equipped with a super slim (2 mm thick) UV probe (SSL001A, International Light, Inc.) was used to measure the local light intensity at various positions on the rotating disk. The spectral response of the UV probe ranged from 260-400 nm with a 365 nm peak and a dynamic range from 300 nW/cm^2 to 1 W/cm^2. Local light intensity was measured using both radial and rectangular grid configurations and the details for this experimental procedure is explained elsewhere [65]. The average incident light intensity used in our study was 8.95 x 10^{-4} W/cm^2 and it was calculated based on the rectangular grid configuration. The data obtained based on the radial segmentation of the disk were used to obtained the local light intensity distribution shown in Figure 2.

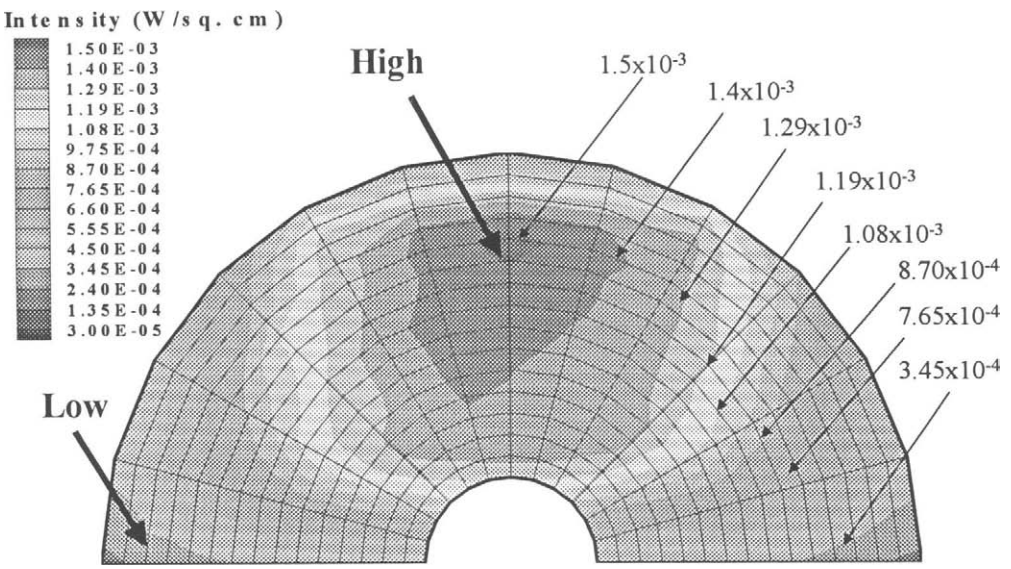

Fig. 2. UV light intensity distribution on the rotating disk.

2.6. Photocatalytic degradation of 4-chlorobenzoic acid

In a case study for determining certain characteristic parameters of the reactor and to better understand the limitations of the process, degradation of 4-chlorobenzoic acid (4-CBA) was investigated in triplicate experiments at 6 rpm, pH=3.3 and room temperature until complete mineralization of the compound was achieved. In other experiments, degradation of 4-CBA was investigated in the RDPR at different angular velocities (2 to 20 rpm), pH (3.0, 7.0 and 10.0) and different initial contaminant concentration (32 to 320 μmol/l). The photocatalytic experiments were carried out in a batch mode using 3.5 l solution and 10 mM KNO_3 for controlling the ionic strength. Control experiments were also performed as follows: (a) with UV radiation but without catalyst (replacement of ST-B01 catalyst with glass beads), (b) without UV radiation but with ST-B01 catalyst, and (c) with neither UV nor ST-B01 catalyst. 4-CBA was selected as a model compound in this study because it exhibits the following properties: (a) low volatility which is important since the RDPR is open to the atmosphere, (b) lack of reaction with molecular ozone during chlorine-ozone interactions [66] which is important in UV/O_3 processes for the purification of drinking water, and (c) measurement at low concentration by HPLC methods [67-68].

Before illumination, the 4-CBA solution was allowed to equilibrate for 180 min in darkness (absorption on the ST-B01 catalyst). In these experiments (during dark adsorption and reaction under UV illumination), 15 ml samples were taken to measure the 4-CBA concentration and the total organic carbon (TOC) using 20 ml glass interchangeable Perfektum® Micro-Mate® syringes (Popper & Sons, Inc.) with blunted stainless steel needles (15.2 cm). Filtration of all samples was performed immediately to remove any suspended TiO_2 particles detached from the surface of the ST-B01 catalyst by attrition. The first 5 ml of the filtrate were discarded and the remaining 10 ml of the solution were filtered directly into 20 ml Qorpak® amber borosilicate glass EPA vials (All-Pak) using 0.1 μm MAGNA nylon membrane filters (Micron Separations, Inc.) and Gelman syringe-type holders (Fisher Scientific). The vials were kept in the dark at room temperature and sample analysis was performed immediately after collection. Other operating parameters, such as dissolved oxygen (DO), pH and temperature were monitored during the experiments.

An HPLC (Hewlett Packard, Series 1050) equipped with a C-18 column (J&W Scientific) was employed for measuring the concentration of 4-CBA in the samples and the feed solution. The mobile phase was 70% v/v acetonitrile and 30% v/v sulfuric acid 0.01 N with flow rate of 0.2 ml/min. A TOC Analyzer (Shimadzu TOC-5000) was employed to measure the TOC of the samples. A DO meter (Corning) equipped with a temperature compensation probe was used to measure the DO and the temperature of the reaction liquid at specified time intervals. An LED pH/ORP controller (Cole-Parmer®) and a stable calomel reference, extra-slender neck (277 mm in length, 3.5 mm in diameter) glass-body pH electrode with temperature compensation (Cole-Parmer®) were used for pH adjustment of the reaction liquid using HNO_3 or KOH solution. Finally, a microprocessor pH/mV/ISE bench top meter (Orion, Model 720A) was used to measure the pH of the samples.

2.7. Chemicals

4-chlorobenzoic acid (99%) was obtained from Aldrich. Potassium nitrate (99.3%), potassium hydroxide (86.4%), lithium chloride (99.5%), lithium reference solution (1000 ppm ± 1%), acetonitrile (HPLC grade), sulfuric acid (95.7%), and nitric acid (68-71% w/w, trace metal grade) were obtained from Fisher. All chemicals were used as supplied.

3. RESULTS AND DISCUSSION

3.1. Characterization of TiO_2 catalyst

Some of the physicochemical characteristics of the ST-B01 catalyst used in our study are presented in Table 1.

Table 1
Physicochemical characteristics[1] of the ST-B01 ceramic balls

Property	Units	Value or Composition
ST-B01 ceramic balls		
Size	mm	~ 6
Specific gravity		2.8-3.2
Support material		
Composition		SiO_2 (60-80%), Al_2O_3 (15-35%), K_2O+Na_2O (5% max)
Active layer		
Composition		TiO_2

1: As given by the manufacturer.

The total surface area of the ST-B01 ceramic balls determined by the BET analysis was very small (3.8 m^2/g, Std. Err. = 0.5). However, the surface area of the attached TiO_2 particles was much higher (~50 m^2/g, Std. Err. = 0.1). This is important feature for obtaining higher photocatalytic degradation rates in the RDPR in comparison with pellets with lower external surface area (e.g., pellets coated with a thin continuous film of TiO_2). Assuming that the attached TiO_2 particles are spherical, non-porous, and one dimensional, their size is approximately 31 nm. The pore volume of ST-B01 was 0.0058 cm^3/g (Std. Err. = 0.0012) with an average pore diameter of approximately 18 nm. This shows that the porosity of this material is small which is important since only a small amount of liquid can be trapped inside the pores. Figure 3 shows XRD results for the crystal structure of the TiO_2 layer. The spherical symbols represent the intensities (%) of the various plains of the theoretical anatase TiO_2 spectrum obtained from the JCPDS-ICDD library for XRD spectra. The three numbers above the spherical symbols denote the Miller indices (h, k, l) of the corresponding crystal planes. Comparing the obtained spectrum (solid line) with the spherical symbols it can be easily proven that the attached TiO_2 powders belong to the anatase phase of TiO_2. The three peaks that did not belong to the anatase TiO_2 phase (star symbols) were identified as SiO_2 (silica) which is the major component of the support material.

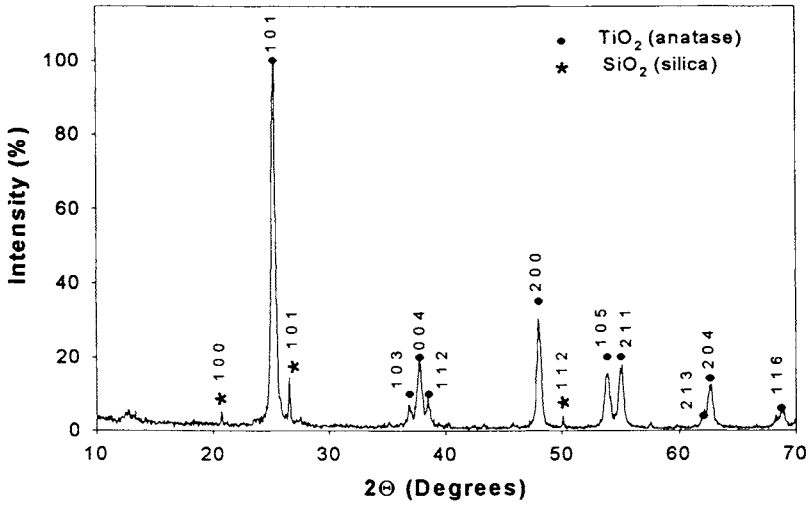

Fig. 3. XRD spectrum of powders obtained from the deposited active layer.

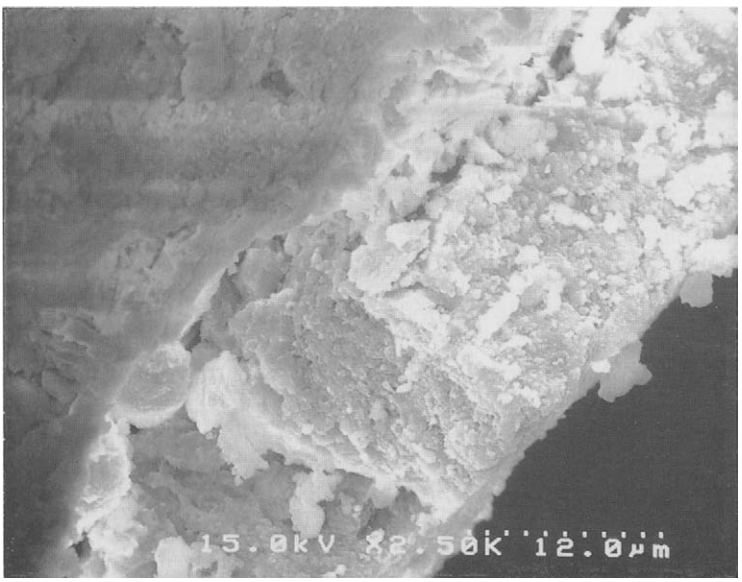

Fig. 4. SEM picture of a hemisphere of ST-B01.

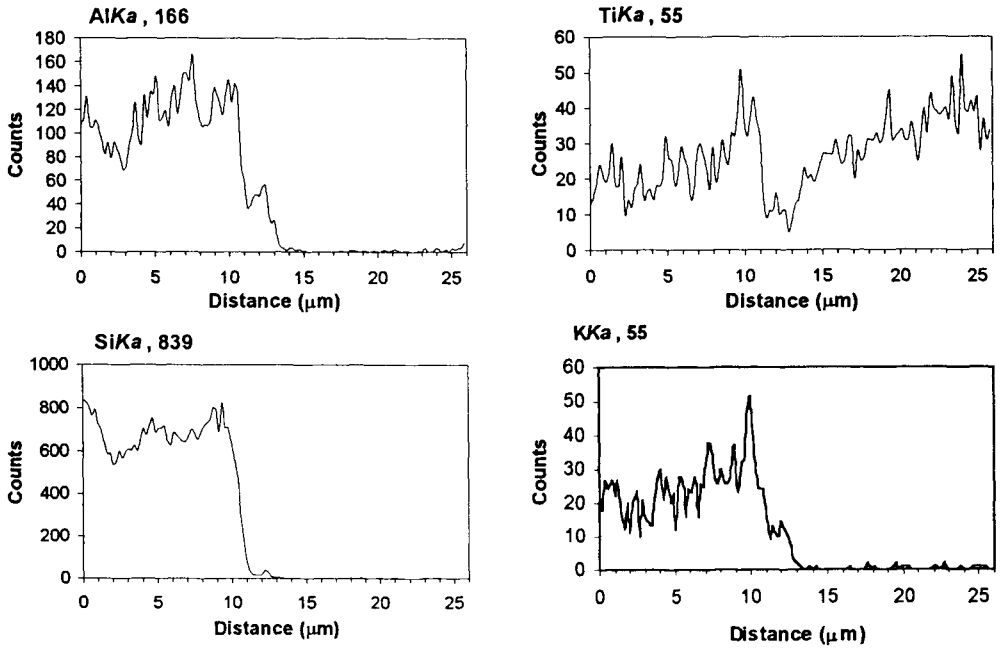

Fig. 5. EDX results across the TiO_2 deposited layer of ST-B01 for Al, Ti, Si, and K.

Figure 4, shows an SEM picture of a hemisphere of ST-B01 while Figure 5 presents EDX results across the TiO_2 deposited layer. In Figure 5 the distance is from the support to the outer point of the TiO_2 deposited layer. As can be shown from Figures 4 and 5, as well as from additional samples not presented here, the thickness of the TiO_2 layer varied from 10 to 30 μm. Figure 5 shows that in the attached TiO_2 layer there is only Ti (compared to the other elements: Si, Al, K) and that some TiO_2 powders have penetrated inside the support material due to the existence of some porosity in the support material. This result is further supported by the fact that the total surface area (5.3 m^2/g, Std. Err. = 0.4) and the porosity (0.0089 cm^3/g, Std. Err. = 0.0008) of the support material before the TiO_2 deposition were higher. Large TiO_2-layer thickness is very important for the conservation of the catalytic activity from the inner layers during catalyst attrition. EDX analysis also showed the existence of trace amount of other elements (V, Zn, P, Cl) other than the main elements of the support material and the deposited TiO_2 layer.

3.2. Mixing patterns in the RDPR

The results of the characteristics of mixing at different disk angular velocities and flow rates (Q) are presented in more details elsewhere [65]. Mixing in the RDPR proved to be close to that in an ideal Continuously Stirred Tank Reactor (CSTR) in the range of conditions investigated (ω was varied from 5 to 20 and Q was varied from 10 to 156 ml/min) [65] with the coefficients α and β of the equation [65, 69]:

$$\frac{C}{C_o} = a\, e^{\beta\left(-\frac{t}{\tau}\right)} \qquad (2)$$

being very close to 1. For the ideal CSTR the coefficients α and β are equal to1. In equation (2), C_o is the concentration in the reactor after the pulse input assuming instant ($t \to 0$) and ideal mixing (mg/l), C is the concentration of the tracer in the outlet (mg/l), τ is the residence time (sec), and t is the time after the pulse input (sec). Here, the characteristics of mixing at 5 rpm and 38.8 ml/min are presented as an example. Figure 6 shows the response of the lithium concentration after the pulse input in the RDPR. Figures 6a and 6c show that the tracer concentration was similar to that in an ideal CSTR. Figure 6b shows the initial response of the tracer and that some time was initially required to reach the concentration expected in a CSTR (assuming instantaneous mixing).

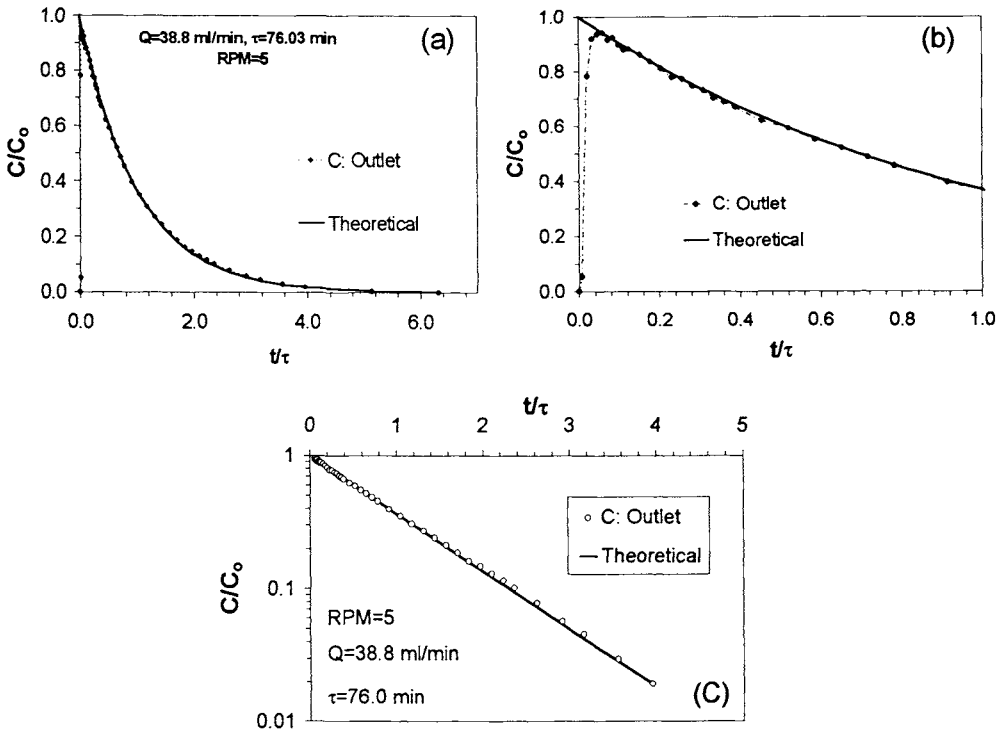

Fig. 6. Pulse input response of lithium chloride tracer in the RDPR at ω=5 rpm and Q=38.8 ml/min (τ=76.0 min); (a) full scale response, (b) response at initial times, (c) comparison with the response in an ideal CSTR.

It is believed that the following reasons are responsible for good mixing in the RDPR: (a) the fully three dimensional nature of the flow near the rotating disk [70], (b) the small thickness

of the gap of the reactor vessel, and (c) the shape of the reaction vessel. The ideal mixing behavior in the RDPR is important not only for the uniform distribution of organic contaminants in the reaction vessel and the adequate oxygenation of the reaction solution, but also to differentiate between non-ideal mixing and mass transfer limitations in future studies.

3.3. Photocatalytic degradation of 4-chlorobenzoic acid

3.3.1. Case study: mineralization of 4-CBA

Figure 7 shows results for the photocatalytic degradation of 4-CBA in the RDPR from one of the three experiments. For this experiment the initial contaminant concentration was 48 mg/l while the disk angular velocity was kept constant at 6 rpm.

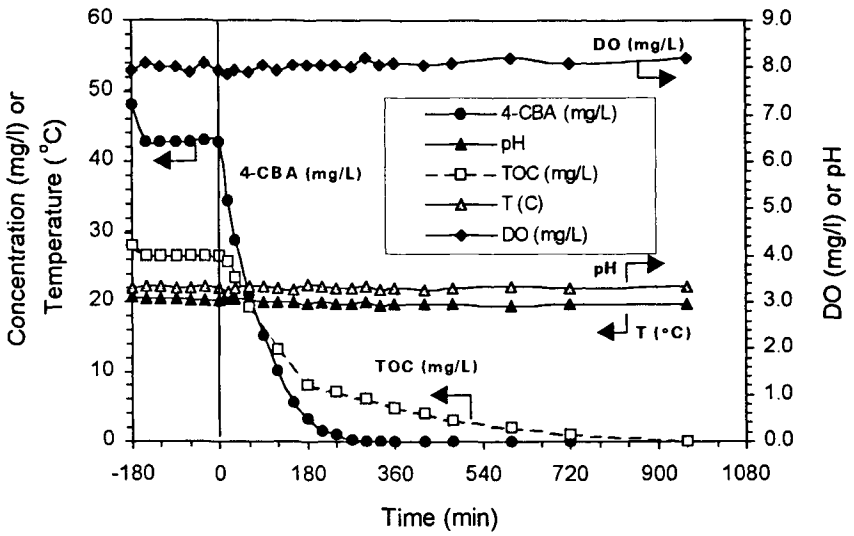

Fig. 7. Photocatalytic degradation of 4-CBA in the RDPR at ω=6 rpm and pH=3.3.

As shown in Figure 7, the temperature, DO, and pH of the reaction solution during the experiment were 293 (± 2) K, 8.0 (±0.3) mg/L, and 3.3 (± 0.2) respectively. Degradation of 4-CBA in the RDPR in the absence of TiO_2 catalyst and/or UV irradiation did not occurred. Spontaneous adsorption on the TiO_2 in the dark occurred immediately after the addition of the solution to the RDPR. Complete decomposition of 4-CBA was achieved in approximately 6 hrs but more than 12 hrs were needed for TOC removal. Beside the peak corresponding to 4-CBA during the HPLC analysis other peaks were observed suggesting the formation of intermediate products. Identification of intermediate products of 4-CBA photocatalytic degradation is currently investigated with HPLC and GC-MS and results will be reported in future studies. Complete mineralization of the three isomer compounds, (4-CBA, 3-CBA, 2-CBA) was observed from other investigators [71]. In their study, D'Oliveira and coworkers [71] identified chlorobenzene, 2-chlorophenol, and chlorohydroquinone as intermediate products for the photocatalytic degradation of 2-CBA.

3.3.2. Effect of angular velocity of the rotating disk

The initial degradation rates (r_0) of 4-CBA were investigated at different angular velocities, ω varying from 2 to 20 rpm. The reaction rates were determined after one hour of the initiation of the photocatalytic reactions. Figure 8 shows the results of the effect of disk angular velocity on the initial reaction rates. It was found that the reaction rates increased from 6.1 μmol/min at 2 rpm to 8.6 μmol/min at 20 rpm following a saturation type dependancy with the angular velocity:

$$r_0 = \frac{8.95\omega}{1.02 + \omega} \tag{3}$$

where r_0 is in μmol/min and ω is in rpm. It is believed that at low disk angular velocities (ω<6 rpm) the reaction rates were lower mainly due to smaller mass transfer coefficients resulting in more significant external mass transfer limitations. Low angular velocities also resulted in a larger time available per rotation leading to higher down flow of the liquid film due to gravitational forces. This could result in the absence of a liquid film in the upper part of the illuminated disk and thus to lower reaction rates. Determination of the mass transfer coefficients at several disk angular velocities will elucidate this problem and along with studies for the existence of mass transfer limitations in the RDPR will be an extensive subject in our future work.

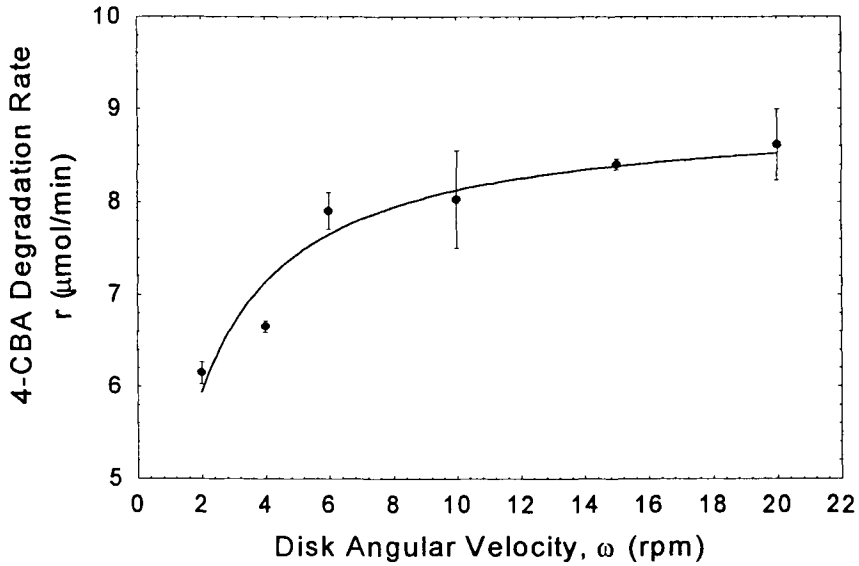

Fig. 8. Effect of disk angular velocity on the initial photocatalytic degradation rates of 4-CBA in the RDPR.

3.3.3. Effect of pH

The photocatalytic degradation of 4-CBA was investigated at 6 rpm and three different pH values: 3.0, 7.0, and 10.0. The r_0 values (determined after one hour of the beginning of photocatalytic experiment) were 8.3 (Std. Err. = 1.1), 5.1 (Std. Err. = 0.25), and 4.8 (Std. Err. = 0.17) μmol/min for pH values of 3.0, 7.0, and 10.0, respectively. The increase of the reaction rates at low pH values is mainly believed to occur due to the increase of adsorption of 4-CBA and intermediate products on the TiO_2 surface. The enhancement of adsorption of an organic molecule on the semiconductor surface will result in an enhancement of reaction rates since the molecule is at the vicinity of the catalyst surface where oxidizing species such as the hydroxyl radicals are formed. In general hydroxyl radicals are the major oxidizing species in this process and are formed after the activation by radiation of the TiO_2 catalyst leading to the electron-hole separation and water photosplitting on the semiconductor surface [72].

The effect of pH on adsorption and photocatalytic degradation of similar to 4-CBA compounds such as salicylic acid and 3-chlorosalicylic acid (among other related compounds) were investigated by Tunesi and Anderson [73] using suspended TiO_2 ceramic membranes. In their study, Tunesi and Anderson found that both adsorption (comparative studies at pH = 3.7 and 5.7) and photocatalytic degradation of salicylic acid (comparative studies at pH = 4, 7.5, and 9.5) increased with the increase of acidity of the solution. Similar results for adsorption were obtained for 3-chlorosalicylic acid [73].

3.3.4. Effect of initial concentration of 4-CBA

In a series of triplicate experiments, the effect of initial concentration on the degradation rates of 4-CBA was investigated at pH=3.0 and ω=6 rpm. The effect of initial concentration on the initial reaction rates (at one hour) is shown in Figure 9.

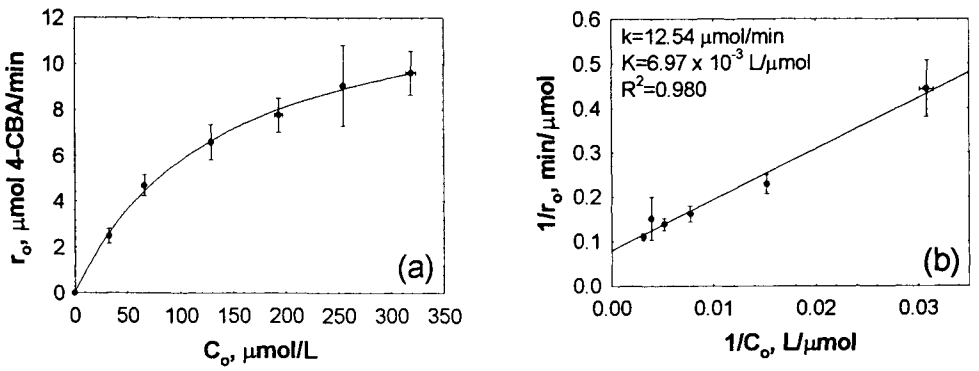

Fig. 9. Effect of initial contaminant concentration on the initial reaction rates.

In many previous studies, the Langmuir-Hinshelwood (L-H) model was used to describe the effect of contaminant concentration on the photocatalytic degradation of chlorinated aromatics and other organic compounds [22, 41, 74, 75]. In batch photocatalytic systems and in the absence of external mass transfer limitations, a general form of the L-H model for the reaction rate is [41]:

$$r_A = -\frac{1}{V}\left(\frac{dn_A}{dt}\right) = \frac{kK_AC_A}{1+K_AC_A+K_sC_s+\sum_1^n K_iC_i} \quad (4)$$

where r_A is the intrinsic reaction rate (mol/l/min), V is the reactor volume (l), n_A is the number of moles of the organic contaminant reacted, k is the reaction rate constant for the organic contaminant (mol/l/min), K_A, K_s, and K_i are the adsorption coefficients (l/mol) and C_A, C_s, C_i are the concentrations of the parent organic compound, the solvent, and the intermediate products (mol/l), respectively. Assuming, (a) low concentration of the intermediate products in the initial stage of the photocatalytic experiment, (b) similar binding characteristics on TiO_2 of the intermediate products and the parent compound ($K_A \approx K_i$), and (c) non-competitive adsorption for the same active sites on TiO_2 between the organic contaminant and the solvent, the equation for initial reaction rate takes the following form [18]:

$$r_A = \frac{k\,K_A\,C_{A_o}}{1+K_A\,C_{Ao}} \quad (5)$$

where C_{Ao} is the initial concentration of the parent compound. Linearization of equation (5) results in the following equation [18, 41]:

$$\frac{1}{r_{Ao}} = \frac{1}{k} + \frac{1}{k\,K_A}\frac{1}{C_{Ao}} \quad (6)$$

Using equation (6), the values for the reaction rate constant (k) and the absorption coefficient (K_A) for 4-CBA determined in our study were 12.5 μmol/l and 7.0 x 10^{-3} l/μmol, respectively. However, the obtained value for k and K_A are apparent values, since only the radiation incident on the disk (and not absorbed by TiO_2) was measured and the effect of mass transfer was not fully investigated in our study. Determination of the mass transfer coefficient and the degree of mass transfer limitations as well the effect of incident light intensity on the reaction rates and photonic efficiencies are the subjects of our current work.

4. CONCLUSIONS

The RDPR, a new type of photocatalytic reactor, proved to be an attractive choice for the decontamination of polluted water. Photocatalytic reactions occurred in a thin film of liquid carried on the rotating disk loaded with TiO_2 catalytic pellets and illuminated by UV radiation. Heterogeneous reactions in the thin liquid film around the vicinity of TiO_2 catalyst, immobilization of the catalyst, potential of catalyst replacement after deactivation, and no need of introducing oxygen in the reaction vessel are among the advantages of the RDPR. Photocatalytic studies in water using 4-CBA, as a model organic contaminant, showed that both TiO_2 catalyst and UV (365 nm) radiation were required for degradation. Although the time required for TOC removal was more than two times that required for 4-CBA degradation, complete mineralization was achieved. The photocatalytic reaction rates increased with the disk angular velocity in the range investigated (2 to 20 rpm). The increase of the reaction rates was higher when the disk angular

velocity increased from 2 to 6 rpm. Above 6 rpm, the reaction rates increased only slightly with the disk angular velocity. Comparison of degradation rates at pH values of 3.0, 7.0, and 10.0 showed that higher reaction rates were observed at pH=3.0 which is lower than the pKa of 4-CBA resulting in higher adsorption of the contaminant on the surface of the photocatalyst. The effect of initial concentration on the initial reaction rates showed that the degradation of 4-CBA in the RDPR obeys the Langmuir-Hinshelwood model. The obtained values for the reaction rate constant and the adsorption coefficient were 12.5 μmol/l and 7.0 x 10^{-3} l/μmol, respectively.

However, more studies are required for the implementation of the RDPR in large scale operations. Future project objectives are to evaluate and use other material and methods for TiO_2 catalyst immobilization on the rotating disk, improve the performance of the RDPR, and evaluate its performance in a pilot scale for the decontamination of natural waters.

5. ACKNOWLEDGMENTS

We are grateful to CIRSEE, Lyonnaise Des Eaux, France for the financial support and to Ishihara Techno Corporation for supplying samples of the ST-B01 catalyst. We are also grateful to Mr. Robert B. Fitzpatrick and Mr. Robert E. Muench for the construction of the RDPR.

REFERENCES

1. R. W. Matthews, *Chemistry and Industry*, (1988) 28.
2. O. Legrini, E. Oliveros and A. M. Braun, *Chem. Rev.*, 93 (1993) 671.
3. M. R. Hoffmann, S. T. Martin, W. Choi and D. W. Bahnemann, *Chem. Rev.*, 95 (1995) 69.
4. A. Mills, R. H. Davies and D. Worsley, *Chem. Soc. Rev.*, 22 (1993) 417.
5. D. F. Ollis, *Environ. Sci. Technol.* 19 (1985) 480.
6. D. F. Ollis and H. Al-Ekabi (eds.) Photocatalytic Purification and Treatment of Water and Air, Elsevier Science Publishers B. V., Amsterdam, The Netherlands (1993).
7. J.-C. D'Oliveira, C. Minero, C. Pelizzetti and P. Pichat, *J. Photochem. Photobiol. A: Chem.* 72 (1993) 261.
8. D. F. Ollis, E. Pelizzetti and N. Serpone, *Environ. Sci. Technol.*, 25 (1991) 1523.
9. E. Pelizzetti, C. Minero and V. Maurino, *Adv. Coll. Interface Sci.*, 32 (1990) 271.
10. N. Serpone and E. Pelizzetti (eds.), Photocatalysis-Fundamentals and Applications, Wiley, New York (1989).
11. N. Serpone, R. Terzian, H. Hidaka and E. Pelizzetti, *J. Phys. Chem.*, 98 (1994) 2634.
12. R. P. S. Suri, J. Liu, D. W. Hand, J. C. Crittenden, D. L. Perram and M. E. Mullins, *Water Environ. Res.*, 65 (1993) 665.
13. R. W. Matthews, M. Abdullah and G. K.-C. Low, *Anal. Chim. Acta* 233 (1990) 171.
14. K. Takeda and K. Fujiwara, *Wat. Res.* 30 (1996) 323.
15. W. A. Jacoby, P. C. Maness, E. J. Wolfrum, D. M. Blake and J. A. Fennell, *Environ. Sci. Technol.* 32 (1998) 2650.
16. M. Huang, E. Tso, A. K. Datye, M. R. Prairie and B. M. Stange, *Environ. Sci. Technol.* 30 (1996) 3084.
17. L. D. Lau, R. Rodriguez, S. Henery, D. Manuel and L. Schwendiman, *Environ. Sci.*

Technol. 32 (1998) 670.
18. H. Al-Ekabi and N. Serpone, *J. Phys. Chem.* 92 (1988) 5726.
19. H. Y. Ha and M. A. Anderson, *J. Environ. Eng.* 122 (1996) 217.
20. K. Hofstadler, R. Bauer, S. Novalic and G. Heisler, *Environ. Sci. Technol.* 28 (1994) 670.
21. K. Kato, A. Tsuzuki, Y. Torii, H. Taoda, T. Kato and Y. Butsugan, *J. Mat. Science* 30 (1995) 837.
22. R. W. Matthews, *J. Phys. Chem.*, 91 (1987) 3328.
23. Z. Mengyue, C. Shifu and T. Yaowu, *J. Chem. Tech. Biotechnol.*, 64 (1995) 339.
24. T. N. Obee, *Environ. Sci. Technol.* 30 (1996) 3578.
25. N. J. Peill and M. R. Hoffmann, *Environ. Sci. Technol.* 30 (1996) 2806.
26. Y. Takahashi and Y. Matsuoka, *J. Mat. Science* 23 (1988) 2259.
27. K. Tannakone, C. T. K. Tilakaratne and I. R. M. Kottegoda, *Wat. Res.* 31 (1997) 1909.
28. G. Chester, M. A. Anderson, H. Read and S. Esplugas, *J. Photochem. and Photobiol. A: Chem.*, 71 (1993) 291.
29. D. J. Alpert, J. L. Sprung, J. E. Pacheco, M. R. Prairie, H. E. Reilly, T. A. Milne and M. R. Nimlos, *Solar Energy Materials* 24 (1991) 594.
30. D. Bahnemann, D. Bockelmann and R. Goslich, *Solar Energy Materials* 24 (1991) 564.
31. D. M. Blake, J. Webb, C. Turchi and K. Magrini, *Solar Energy Materials* 24 (1991) 584.
32. J. E. Pacheco, M. R. Prairie and L. Yellowhorse, *J. of Solar Energy Engineering* 115 (1993) 123.
33. P. Reeves, R. Ohlhausen, D. Sloan, K. Pamplin, T. Scoggins, C. Clark, B. Hutchinson and D. Green, *Solar Energy* 48 (1992) 413.
34. J. Zhao, T. Wu, K. Wu, K. Oikawa, H. Hidaka and N. Serpone, *Environ. Sci. Technol.*, 32 (1998) 2394.
35. A. E. Cassano, C. A. Martin, R. J. Brandi and O. M. Alfano, *Ind. Eng. Chem. Res.* 34 (1995) 2155.
36. L. Jakob, E. Oliveros, O. Legrini and A. M. Braun, in Photocatalytic Purification and Treatment of Water and Air, D. F. Ollis and H. Al-Ekabi (eds.), Elsevier Science Publishers B. V., Amsterdam, The Netherlands, (1993), 511.
37. P. L. Yue, in Photocatalytic Purification and Treatment of Water and Air, D. F. Ollis and H. Al-Ekabi (eds.), Elsevier Science Publishers B. V., Amsterdam, The Netherlands, (1993), 495.
38. A. Sclafani, A. Brucato and L. Rizzuti, in Photocatalytic Purification and Treatment of Water and Air, D. F. Ollis and H. Al-Ekabi (eds.), Elsevier Science Publishers B. V., Amsterdam, The Netherlands, (1993), 533.
39. J. G. Sczechowski, C. A. Koval and R. D. Noble, *Chem. Eng. Sci.* 50 (1995) 3163.
40. A. Haarstrick, O. M. Kut and E. Heinzle, *Environ. Sci. Technol.* 30 (1996), 817.
41. D. F. Ollis, E. Pelizzetti and N. Serpone, in Photocatalysis: Fundamentals and Applications, N. Serpone and E. Pelizzetti (eds.), John Wiley & Sons, New York, (1989), 603.
42. N. J. Peill and M. R. Hoffmann, *Environ. Sci. Technol.* 32 (1998) 398.
43. H. C. Yatmaz, C. R. Howarth and C. Wallis, in Photocatalytic Purification and Treatment of Water and Air, D. F. Ollis and H. Al-Ekabi (eds.), Elsevier Science Publishers B. V., Amsterdam, The Netherlands, (1993), 795.
44. D. Bockelmann, R. Goslich, D. Weichgrebe and D. Bahnemann, in Photocatalytic

Purification and Treatment of Water and Air, D. F. Ollis and H. Al-Ekabi (eds.), Elsevier Science Publishers B. V., Amsterdam, The Netherlands, (1993), 771.
45. Metcalf & Eddy, Inc., Wastewater Engineering: Treatment, Disposal, and Reuse, McGraw-Hill, Inc., New York, (1991), 418-420.
46. D. D. Ravetkar and D. D. Kale, *Chem. Eng. Sci.* 36 (1981) 399.
47. W. J. Daughton and F. L. Givens, *J. Electrochem. Soc.* 129 (1982) 173.
48. S. A. Jeneke, *Ind. Eng. Chem. Fundam.* 23 (1984) 425.
49. J. H. Lai, *Polym. Eng. Sci.* 19 (1979) 1117.
50. T. C. Papanastasiou, A. N. Alexandrou and W. P. Graebel, *J. Reol.* 32 (1988) 485.
51. B. D. Washo, *IBM J. Res. Dev.*, 21 (1977) 190.
52. C. S. Chern, J. S. Martens, Y. Q. Li, B. M. Gallois, P. Lu and B. H. Kear, *Supercond Sci. Technol.* 6 (1993) 460.
53. M. E. Coltrin, R. J. Kee and G. H. Evans, *J. Electrochem. Soc.* 136 (1989) 819.
54. S. Joh and G. H. Evans, *Numer. Heat Transfer (Part A)* 31 (1997) 867.
55. P. Richter, B. L. Ruiz, M. Sánchez-Cabezudo and H. A. Mottola, *Anal. Chem.* 68 (1996) 1701.
56. X. Chen, K. Li and Y. Su, *Ind. Eng. Chem. Res.* 32 (1993) 453.
57. W. W. Hammerschmidt and W. Richarz, *Ind. Eng. Chem. Res.* 30 (1991) 82.
58. Ph. Hasler and W. Richarz, *Ind. Eng. Chem. Res.* 28 (1989), 38.
59. J. B. Melville and J. D. Goddard, *Ind. Eng. Chem. Res.* 27 (1988) 551.
60. M. M. Rahman and A. Faghri, *J. Heat Mass Transfer* 36 (1993) 189.
61. R. K. Ulrich, M. K. Koppaiah and V. K. Majmudar, *Can. J. Chem. Eng.* 69 (1991) 825.
62. S. L. Murov, I. Carmichael and G. L. Hug (eds.), Handbook of Photochemistry, 2nd Edition, Marcel Dekker, Inc. New York, (1993) 299-305.
63. J. G. Calvert and J. N. Jr. Pitts, Photochemistry, John Wiley & Sons, Inc. New York, (1966) 783-786.
64. C. G. Hatchard and C. A. Parker, *Proc. Roy. Soc. (London)* A235 (1956) 518.
65. D. D. Dionysiou, G. Balasubramanian, M. T. Suidam, A. P. Khodadoust, I. Baudin, J.-M. Laîné, *Wat. Res.* (Submitted for publication, 1999).
66. M. S. Siddiqui, *Wat. Res.* 30 (1996) 2160.
67. E. A. Dietz, N. J. Cortellucci and K. F. Singley, *J. Liq. Chromatogr.* 16 (1993) 3331.
68. Y. Magara, T. Aizawa, N. Matumoto and F. Souna, *Wat. Sci. Tech.* 30 (1994) 119.
69. K. R. Westerterp, W. P. M. van Swaaij and A. A. C. M. Beenackers, Chemical Reactor Design and Operation, 2nd Edition, J. Wiley, New York, (1984), 177-179.
70. H. Schlichting, Boundary-layer theory, 7th Edition, McGraw-Hill Book Company, Inc., New York, (1979), 102-107.
71. J.-C. D'Oliveira, W. D. W. Jayatilake, K. Tennakone, J.-M. Herrmann and P. Pichat, in New Frontiers in Catalysis: Proceedings of the 10th International Congress on Catalysis, Budapest, July 19-24, 1992, L. Guczi, F. Solymosi and P. Tétényi(eds.), Elsevier Science Publishers B. V., Amsterdam, The Netherlands, (1993), 2168.
72. E. Pelizzetti, C. Minero, *Electrochem. Acta* 38 (1993) 47.
73. S. Tunesi and M. Anderson, *J. Phys. Chem.* 95 (1991) 3399.
74. C. S. Turchi, D. F. Ollis, J. Catal. 122 (1990) 178.
75. J.-C. D'Oliveira, G. Al-Sayyed, P. Pichat, Environ. Sci. Technol. 24 (1990) 990.

Reaction Engineering for Pollution Prevention
M.A. Abraham and R.P. Hesketh (Editors)

Design and Development of Two Large-scale Photocatalytic Reactors for Treatment of Toxic Organic Chemicals in Wastewater

Ajay K. Ray*

Department of Chemical and Environmental Engineering
The National University of Singapore
10 Kent Ridge Crescent, Singapore 119260

Semiconductor photocatalysis is a newly emerging technology for elimination of harmful chemical compounds from air and water. It couples low energy ultraviolet light with semiconductors acting as photocatalysts overcoming many of the drawbacks that exist for the traditional water treatment methods. Recent literature has established the potential of this powerful technology to destroy toxic pollutants dissolved or dispersed in water. Nevertheless, new reactor design concept is necessary that must be able to address the two most important parameters, namely, uniform light distribution inside the reactor through the absorbing and scattering liquid to the catalyst, and must provide high surface areas for catalyst coating per unit volume of reactor. Two new design configuration for efficient photocatalytic reactors have been discussed that not only addresses the solution to both the above problems, but also have scale-up potential.

1. INTRODUCTION

The presence of toxic organic compounds in water supplies and in the discharge of wastewater from chemical industries, power plants and agricultural sources is a topic of global concern. The impurities can be destroyed completely by semiconductor photocatalysis technology [1]. In this process in-situ degradation of traces of organic substances is achieved. The process couples low energy ultraviolet light with semiconductors acting as photocatalysts overcoming many of the drawbacks that exist for traditional water treatment methods. The appeal of this process technology is the prospect of complete mineralization of pollutants to environmentally harmless compounds. The carbon containing pollutants are oxidised to carbon dioxide while the other elements bonded to the organic compounds are converted to anions such as nitrate, sulphate, or chloride. Literature has established that practically any pollutants that include aliphatics, aromatics, dyes, surfactants, pesticides and herbicides can be completely mineralised by this process into harmless substances [2].

Besides the advantage of complete destruction of toxic compounds and use of atmospheric oxygen as oxidants, TiO_2 based photocatalysis has many advantages over the other conventional chemical oxidation methods. The catalyst is cheap, biologically and chemically inert, insoluble under most conditions, photostable, non-toxic, reaction rate is relatively high if large surface area of catalyst is provided, can be used for extended period without substantial loss of its activity [3, 4]. Moreover, it uses very low energy ultraviolet

* E-mail: cheakr@nus.edu.sg, Fax: (65) 779 1936.

light resulting in energy requirement as low as 1-5 W/m^2 [5], and more importantly, can even be activated by sunlight.

Inspite of the potential of this promising technology, development of a practical water treatment system has not yet been successfully achieved. In the last few years, a large number of publications [6-11] have appeared based on laboratory scale studies with generally positive results for very diverse categories of toxic compounds in water. However, technical development to pilot scale level has not yet been successfully achieved although there are numerous patents approved worldwide.

There are several factors that impede the efficient design of photocatalytic reactor [12]. In this type of reactors, besides conventional reactor complications such as reactant-catalyst contacting, flow patterns, mixing, mass transfer, reaction kinetics, catalyst installation, temperature control etc., an additional engineering factor related to illumination of catalyst becomes relevant. It is also necessary to achieve efficient exposure of the catalyst to light irradiation. Without photons of appropriate energy content, the catalyst shows no activity. The problem of photon energy absorption has to be considered regardless of reaction kinetics mechanisms. The illumination factor is of utmost importance since the amount of catalyst that can be activated determines the water treatment capacity of the reactor. The high degree of interaction between the transport processes, reaction kinetics and light absorption leads to a strong coupling of physico-chemical phenomena and no doubt, it is the major obstacle in the development of a photocatalytic reactor [13].

The central problem in a photocatalytic reactor is focused on a uniform distribution of light to a large surface area of catalyst. For particular photoreactor geometry, scale-up in the axial and/or radial directions is constrained by the phenomenon of opacity, light scattering, depth of radiation penetration and local volumetric light absorption. The arrangement of light source - reactor system influences the reactor design in such a strong way that independent consideration is not possible. Moreover, the need for at least one of the reactor walls to transmit the chosen radiation imposes the utilisation of transparent materials, such as glass for the reactor construction, and thus imposes size limitations, sealing problems, and breakage risks.

The overall reaction rate of photocatalytic processes is usually slow compared to conventional chemical reaction rates due to low concentration level of the pollutants and therefore, there is a need to provide large amounts of active catalyst inside the reactor. Although the effective surface area of the porous anatase catalyst coating is high, there can only be a thin coating (about 1 μm thick) applied to a surface [5]. Thus, the amount of active catalyst in the reactor is limited, and even if individual degradation processes can be made relatively efficient, the overall conversion efficiency will still be low. This problem severely restricts the processing capacity of the reactor and the necessary time required to achieve high conversions are measured in hours, if not days [14].

Photocatalytic reactions are promoted by solid photocatalyst particles that usually constitute the discrete phase distributed within a continuous fluid phase in the reactor. Therefore, at least two phases, i.e. liquid and solid, are present in the reactor. The solid phase could be dispersed (SPD) [15] or stationary (SPS) within the reactor [14]. SPD photoreactors may be operated with the catalyst particles and the fluid phase(s) agitated by mechanical or other means. Depending on the means of agitation the photoreactor resembles that of slurry or fluidized bed reactors. In numerous investigations, an aqueous suspension of the catalyst particles in immersion or annular type photoreactors has been used. However, the use of suspensions requires the separation and recycling of the ultrafine (sub-micron size) catalyst from the treated liquid and can be an inconvenient, time consuming expensive process [16].

In addition, the depth of penetration of UV light is limited because of strong absorption by both catalyst particles and dissolved organic species [5]. Above problems could be avoided in SPS photoreactors in which photocatalyst particles are immobilised onto a fixed transparent surface, such as the reactor wall or a fibre mesh, or supported on particles, such as glass or ceramic beads, that are held in fixed positions in the photoreactor. However, immobilisation of catalyst on a support generates a unique problem [17]. The reaction occurs at the liquid-solid interface and usually only a part of the catalyst is in contact with the reactant. Hence, the overall rate may be limited to mass transport of the pollutant to the catalyst surface [5-13]. In addition, the rate of reaction is usually slow because of the low concentration level of the pollutant and therefore, there is a need for a reactor whose design provides a high ratio of illuminated immobilised catalyst to illuminated surface and provides the possibility of total reactor illumination [17].

A number of photocatalytic reactors have been patented in recent years but none has so far been developed to pilot scale level. Based on the manner in which catalyst is used, and the arrangement of the light source and reactor vessel, all photocatalytic reactor configuration fall under four categories. They are *slurry type* in which catalyst particles are in suspension form [15, 16], *immersion* type with lamp(s) immersed within the reactor [18], *external* type with lamps outside the reactor [19], and *distributive* type with the light distributed from the source to the reactor by optical means such as reflectors and light conductors [20, 21] or optical fibres [22]. Majority of reactors patented are variation of the slurry reactor, and classical annular reactor of immersion or external type in which catalyst is immobilised on reactor wall [23, 24], on pipes internally [25], on ceramic membranes [26], on glass wool matrix between plates [27], on semipermeable membranes embedded [28, 29] in water permeable capsules [30], on a mesh of fiberglass [31], on beads [32], on fused silica glass fibers [33], on porous filter pipes [34], on glass fiber cloth [35], etc. The reactors are either helical [36], spiral [37], shallow cross flow basins [38] or optical fiber [39]. However, all these reactor designs are limited to small scales by the low values of illuminated catalyst density. The only way to apply these systems for large-scale applications is by using large numbers of multiple units.

The parameter κ [21], namely illuminated specific surface area, helps to compare design efficiency of different photocatalytic reactors as it defines the efficacy to install as much active catalyst per unit volume of reaction liquid in the reactor. The parameter κ represents the amount of catalyst inside a reactor that is sufficiently illuminated so that it is active, and is in contact with the reaction liquid. Table 1 lists κ values for the four different classes of photocatalytic reactors. In a slurry reactor, small catalyst particles could provide large surface area for reaction but essentially most of the catalyst surface area will be inactive, particularly for large reactor dimensions as the catalyst particles will not receive enough light from the external light source. This happens since the organics and the liquid medium itself are absorbing light. This is especially true for large reactor dimensions, resulting in low efficiencies and the drawback of impossibility for scale up to commercial use applications. In addition, use of suspension requires separation and recycling of the ultrafine catalyst from the treated effluent by filtration, centrifugation or coagulation and flocculation. These add various levels of complexity to an overall treatment process and clearly decrease the economical viability of the slurry reactors. An external type reactor will always be limited by low values of κ. An immersion type reactor could be scaled-up to any dimension but when classical lamps of diameter between 0.07-0.1m are used, the κ value is very low even if it is assumed that the lamps occupy 75% of the reactor volume.

Many other new *innovative* type of reactor designs exist in literature, addressing specific problems and applications or others being designed especially for treating specific

types of pollutants. These are in the form of treatment agents containing novalak resins, photoelectro-chemistry or electro-photographic methods, use of magnetic or sound waves, photocatalysis and acoustics, catalyst particles coated with polymers as well as ion exchange process [17]. Others include the use of optical fibers as the source of illumination catalyst contained in removable filter units, and water permeable capsules containing the catalyst. Although, innovative in approach, the main problem associated with all these reactor configurations is again the issue of scale-up for commercial use purposes.

Table 1.
Comparison of κ, m^2/m^3, for different reactors

Photocatalytic reactor	κ, m^2/m^3	Parameters	κ, m^{-1}	Remarks
Slurry Reactor [19]	$\left[\frac{6C_C}{\rho_C}\right]\frac{1}{d_p}$	$d_P = 0.3$ μm $C_C = 0.5$ kg/m^3	2631[#]	scale-up not possible
External type - annular reactor [21]	$\frac{4d_0}{d_0^2 - d_i^2}$	$d_o = 0.2$ m $d_i = 0.1$m	27	scale-up not possible
Immersion type - with classical lamps [16]	$\left[\frac{4\varepsilon}{1-\varepsilon}\right]\frac{1}{d_o}$	$d_o = 0.09$ m $\varepsilon = 0.75$	133	scale-up possible but large V_R
Immersion type - with novel lamps [18]	$\left[\frac{4\varepsilon}{1-\varepsilon}\right]\frac{1}{d_o}$	$d_o = 0.0045$ m $\varepsilon = 0.75$	2667	scale-up possible with small V_R
Distributive type - with hollow tubes [22]	$\left[\frac{4\varepsilon}{1-\varepsilon}\right]\frac{1}{d_o}$	$d_o = 0.006$ $\varepsilon = 0.75$	2000	scale-up possible with small V_R

[#] The value will be much lower than 2631 m^{-1} as all the suspended catalyst particles will not be effectively illuminated. Catalyst concentration, $C_c = 0.5$ kg/m^3 is normally used. $\rho_c = 3800$ kg/m^3.

The scale-up has been severely limited by the fact that reactor configurations have not been able to address the two most important parameters, namely, light distribution inside the reactor through the absorbing and scattering liquid to the catalyst, and providing high surface areas for catalyst coating per unit volume of reactor [12]. The new reactor design concepts must provide a high ratio of activated immobilised catalyst to illuminated surface and must have a high density of active catalyst in contact with the liquid to be treated inside the reactor [14, 20].

2. TWO NEW DESIGNS OF LARGE-SCALE PHOTOCATALYTIC REACTOR

In order to overcome some of these deficiencies inherent in conventional photocatalytic reactor designs, a distributive type photocatalytic reactor design in which catalyst is fixed to a structure in the form of glass slabs (plates), rods or tubes inside the reactor have the greatest potential for scale-up. This will allow for high values of κ and will eliminate light passage through the reaction liquid. This is advantageous because when light approaches the catalyst through the bulk liquid phase, some radiation is lost due to absorption in the liquid. In particular, this effect is more pronounced for highly coloured dye pollutants as they are strong UV absorber and will therefore, significantly screen the TiO_2 from receiving UV light [5].

At National University of Singapore, we are considering scale-up configurations that contain both high surface areas to volume and efficient light distribution to the catalyst phase. Two ways above deficiencies inherent in conventional photocatalytic reactor designs can be overcome. First, by using a distributive type of photocatalytic reactor design in which catalyst

is fixed to a structure in the form of hollow glass tubes [21], and secondly, by using an immersion type reactor with very narrow diameter tube lamps [18]. The design based on hollow glass tubes allows for a much higher illuminated surface area per unit reactor volume [20], while the other design provides not only much higher values for active catalyst surface area but also the catalyst can be activated uniformly at its highest possible level [14]. Furthermore, the designs of the reactors are flexible enough to be scaled-up for commercial scale applications.

The limitation to the size of the reactor with light conductors is the UV transparency of the material and the light distribution to the catalyst particle [21]. The critical and probably the most intricate factor is the distribution of the available light in the conductors to the catalyst particles and to ensure that each particle receives at least the minimum amount of light necessary for activation. The reactor configuration conceptually applicable for photocatalysis, satisfying most of the above-mentioned requirements is a rectangular vessel in which light conductors as glass slabs (or rods) coated on its outside surface with catalysts are embedded vertically [20]. The lamps together with reflectors are placed on two sides of the reactor while liquid enters and exits from the other two sides. Light rays entering the conductor through one end is repeatedly reflected internally down the length and at each reflection come in contact with the catalyst present around the outer surface of the conductors. Thus, conducting materials might be considered as a means of light carrier to the catalyst. Since the ratio of the surface area on which catalyst is present to the light entering area could be as high as 500, evidently a very large catalyst area can be illuminated [17]. Moreover, with a large number of such light conducting material may be packed inside the reactor, the configuration provides a high total light transfer area and allows for a higher illuminated catalyst area per unit reactor volume. Densely packing the reactor with light conducting object, not only increases surface to volume ratio but also reduces the effective mass transfer diffusion length for the pollutant to catalyst surface [40].

The vital issue in the distributive type of reactor concept is how to introduce light from the external source efficiently into the light conductors, and likewise, how to get it out again at the proper location and in the apropos amount [21]. The predominant obstacle we came across in the use of glass slabs (or rods) as the light-conducting object is the occurrence of total internal reflection. It transpires when light travels from denser to rarer medium and is determined by the critical angle given by

$$\theta_c = \sin^{-1}\left[n_2 / n_1\right] \tag{1}$$

where n_1 and n_2 are the refractive indices of the denser and rarer medium respectively. In the case of light travelling from air, to glass to air (or water), the angle θ will always exceed the critical angle, θ_c, for the interface between glass and air (or water) irrespective of angle of incidence, α (0 to 90°) [21]. In other words, all the light rays that are entering through the top surface will experience the phenomena of total internal reflection and will come out axially rather than emerging from the lateral surface. However, refractive index of TiO_2 (between 2.4 to 2.8) is higher than that of glass (about 1.5) in the wavelength range of 200 to 400 nm and it is likely that total internal reflection would not take place when the glass surface is coated with titania. Nevertheless, if coating consists of small spheres of catalyst particles dispersed along the surface, the actual glass-titania interface will be small, as most of the glass surface will still be in contact with water. Therefore, it is best, if possible, to avoid the occurrence of total internal reflection entirely.

One way of avoiding total internal reflection is by surface roughening. Moreover, surface roughening assist in achieving better catalyst adhesion to the substrate. Both are

indeed found out to be the case experimentally [4]. In fact, when lateral surface was roughened by sand blasting most of the light emerged within few centimetres and hardly any light remained thereafter in the axial direction [20]. This is not only because roughening desist total internal reflection phenomena but also UV-transparency of most light conducting material is very poor [21]. Although the use of Quartz as light conductors will naturally help to overcome light transmission problem, it will certainly make the overall reactor set-up more expensive [21].

The total internal reflection problem can also be effectively avoided when the surface's light has to pass through are parallel instead of perpendicular. One such configuration [20] is a hollow glass tube coated on its surface with semiconductor catalysts. The hollow tube might be considered as a pore carrying light to the catalyst. In this novel configuration, light rays entering through one end of the hollow tube are repeatedly internally reflected down the length of the tube and at each reflection come in contact with the annular catalyst coating present around the outer surface of the tube. Although, total internal reflection could be avoided completely in this configuration the angle of incidence of light will be a critical factor. When light falls on the glass surface a part of it is reflected and the rest is transmitted. The ratio between the reflection and transmission of light is a strong function of angle of incidence. When the light beam is nearly parallel with the surface (α close to 0^{o}), most of the light is reflected and exits axially rather than laterally while for light rays with α close to 90^{o} most of the light will emerge laterally within few centimetres and barely any light will remain thereafter as reflection is only 4% for a glass-air interface [21]. Hence, it is important that in the design of reactor based on hollow tubes, light must be guided into the conductors at a very precise angle through a combination of optical lenses and reflectors.

During the development of this new concept of photocatalytic reactor based on multiple hollow tubes (MTR), we developed a unique new lamp design. These are extremely narrow diameter fluorescent tube lamps of low wattage emitting lights in the wavelength of our interest ($\lambda < 365$ nm). These new lamps [14] address many of the solutions to the problems that have restricted the development of technical scale photocatalytic reactors for water purification. These lamps are available in various shapes and lengths, and can be placed inside a reactor to form a variety of different configurations. Development of a reactor using these new lamps will provide all the advantages of the multiple tube reactor, plus the additional advantage that catalyst could be activated at its highest level. In the reactor, catalyst was deposited on the outer surface of the low wattage lamps using a dip-coating apparatus [14]. Thus, the main problem encountered in the development of a reactor based on multiple hollow tubes (MTR) was avoided. In the MTR concept, it is impossible to obtain a uniform light distribution along the length of the tubes and therefore, it will severely restrict the maximum length of tubes that can be used inside a reactor and thereby the overall performance of the reactor. The new lamps eliminated this drawback in the development of the MTR reactor concept, as the new design is capable of uniform light distribution over long tube lengths. Of course, this was possible with classical lamps too. However, the new lamps allow for a 50 to 100 times larger surface area for catalyst per unit reactor volume compared to a classical reactor design [17].

3. EXPERIMENTAL DETAILS

The reactors: Figure 1 shows schematic drawing of the novel bench-scale reactor system based on hollow tubes. The reactor (MTR) consists of a cylindrical vessel of diameter 0.056m within which 54 hollow Quartz glass tubes of diameter 0.006m coated on its peripheral surface with catalyst were placed. The tubes were held securely within the reactor

by two teflon end plates on which 54 holes were drilled. The reactor resembles that of a shell- and tube- heat exchanger with reaction liquid flowing through the shell-side over the outside surfaces of the coated tubes while light travels through the inside of hollow tubes. The tubes were arranged in triangular pitch of 0.007m thereby achieving a very high surface area per unit volume. The feed was introduced through four equally distributed ports at one end of the vessel thereby minimizing formation of any dead zones. Similarly, the exit flow from the reactor was collected through four ports distributed at the other end of the reactor. One end of each tube was closed to prevent any reaction liquid entering the inside of the tubes. The closed ends were also coated with aluminium for better utilisation of axially exiting light.

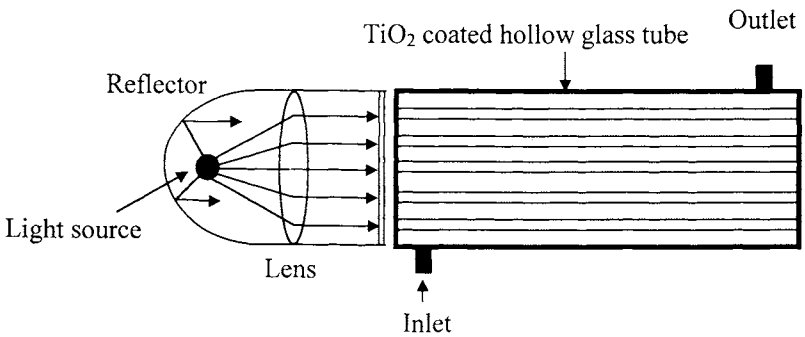

Figure 1. Schematic diagram of Multiple Tube Reactor (MTR)

The glass material used was quartz instead of Pyrex. Although quartz is expensive than Pyrex glass when glass slabs or rods are considered, but the price difference is not that appreciable when glass test tubes are considered. The quartz was used in the set-up particularly for two reasons: (a) transmission of light in Pyrex is very poor compared to quartz [25] and therefore, the length of hollow glass tubes that can be used in the reactor will be restricted, and (b) when using large number of 5-6 mm test tubes, use of quartz tubes will increase the strength of the reactor and it will be much easier to handle bundle of long but narrow diameter hollow test tubes without worrying about breakage of the tubes. Of course, if one use Pyrex tubes, reactor will be cheaper but then the length of the reactor has to be reduced.

The Tube light reactor, see figure 2, consists of a stainless steel flat top plate (0.132m x 0.016m) with 21 holes onto which another plate (0.248m x 0.132m) was welded. Twenty-one U-shaped lamps were placed around the latter plate and its end extended through the holes for electrical connections. Electrical wires were connected to the novel lamps through copper holders that are screwed around the lamp end. This part acts as a clamp for the lamps. The assembly was put in a rectangular stainless steel reactor vessel. Feed is introduced at the top of the vessel and is equally distributed over the width of the reactor through 5 inlet ports thereby minimizing formation of any dead zones. Similarly, the flow exits the reactor through 5 ports at the other end. The effective illuminated surface areas of the catalyst and the volume of the reactor are $0.15m^2$ and 5.36×10^{-4} m^3 respectively. The parameter κ, defined as total illuminated catalyst surface area that is in contact with reaction liquid per unit volume of liquid treated in the reactor volume, is equal to 618 m^2/m^3.

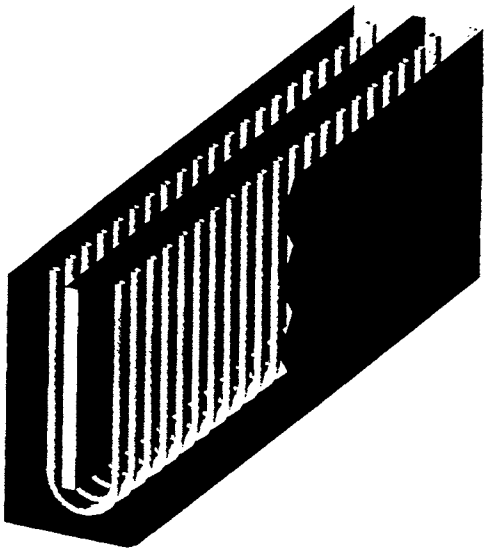

Figure 2. Schematic diagram of the Tube Light Reactor (TLR).

Lamps: The light source (Philips GBF 6436, 12V, 40W) used in MTR was a low voltage halogen lamp optically positioned in a lightweight highly glossy anodised aluminium reflector spanning 0.056m for a clearly defined beam spread. In addition, a condenser lens of focal length 0.04m were placed between the lamp and the reactor to obtain light beam at a half intensity beam angle between 2 to 4 degrees. The novel lamps (Philips NDF-U2 49-6W) used in TLR were specially developed by Philips Lighting for our experiments. The U-shaped lamps are 0.498m long and have a diameter of 0.0045m only. These operate at 1020V; produce 6W of which 15% is in the UV-A region. The light intensity ($\lambda < 380$ nm) on catalyst particles is 127.8 W/m^2.

Catalyst: Degussa P25 grade TiO_2 was used as catalyst for all the experiments. The crystalline product is nonporous primarily in the anatase form (70:30 anatase to rutile) and is used without further treatment. It has a BET surface area of (5.5 ± 1.5) x 10^4 m^2/kg and crystallite sizes of 30 nm in 0.1-0.3 μm diameter aggregates.

Catalyst immobilization: For better catalyst fixation and its durability, the glass surface of the tubes and the lamps on which titania was deposited were roughened by sand blasting. This makes the catalyst surface uneven but increases the strength and amount of catalyst per unit area that could be deposited. It is known that adherence of TiO_2 on quartz is poor than on Pyrex. However, when the glass surface was roughened the adherence improved appreciably. The glass surface was carefully degreased, cleaned with 5% HNO_3 solution overnight, washed with water and then dried. A 5% aqueous suspension of the catalyst was prepared with water out of Millipore Milli-Q water purification system. The suspension was mixed in an ultrasonic cleaner (Branson 2200) bath to obtain a milky suspension that remained stable for weeks. The lamp's surfaces were coated with catalyst by dip-coating apparatus [14] designed for coating catalyst. This is a completely automated equipment capable of immobilizing catalyst onto a variety of different shaped and sized substrates to any desired thickness by successive dipping of the objects into a suspension at controlled speed that can be varied between (0.4-4.0) x 10^{-4} m/s. Four 250 W infrared lamps were attached to a clamp that can be moved both vertically and horizontally for instant drying of the coating. After

coating, it was dried and then fired at a temperature of 300C. Catalyst coating thus obtained on a roughened glass surface was very stable. Hardly any catalyst washes away under running water. During experimentation less 2% was lost and that too after 100 hours of operation. In addition, roughening of glass surface helped in achieving better light distribution.

Model component: Special Brilliant Blue of Bayer (SBB, MW 812), of laboratory reagent grade (in 20% solution) was used (catalogue number 42735). This is an excellent model component [5] for characterization of a photocatalytic reactor as the dye is reactive only in presence of both TiO_2 and UV light, biologically not degradable, and present in wastewater streams from textile industries. The complete oxidation reaction of SBB dye is:

$$C_{43}H_{71}O_6N_3S_2Na + 64½\ O_2 \longrightarrow 43\ CO_2 + 32\ H_2O + 2\ H_2SO_4 + 3\ HNO_3 \qquad (2)$$

Analysis: Changes in SBB dye concentration were measured on-line by flowing a bypass stream of the dye from reactor outlet continuously through a bottom loader flow-through cuvet (Hellma, path length 0.001m) placed inside a Colorimeter (Vitatron Universal Photometer 6000) and was recorded continuously by a Kipp & Zonen (Model BD80) recorder. Up to 0.5 mol/m^3, the calibration line obeys the Beer-Lambert law with good precision and the absorptivity coefficient, ε (at λ_{max}= 605 nm), was found to be 5000 m^3/mol/m.

Experimental set-up: A gear pump (Verder model 2036) was used for pumping the reactant between the reactor and the reservoir via a flow-through cuvet placed inside a universal photometer (Vitatron 6000) for continuous on-line measurement of the model component (see figure 3). Two three-way glass valves were used between the water and specially designed reactant reservoir for initial zero setting of the analytical instrument before the start of an experiment, introduction of the reactant into the system, elimination of bubbles formed during experiment, and final flushing of the entire system.

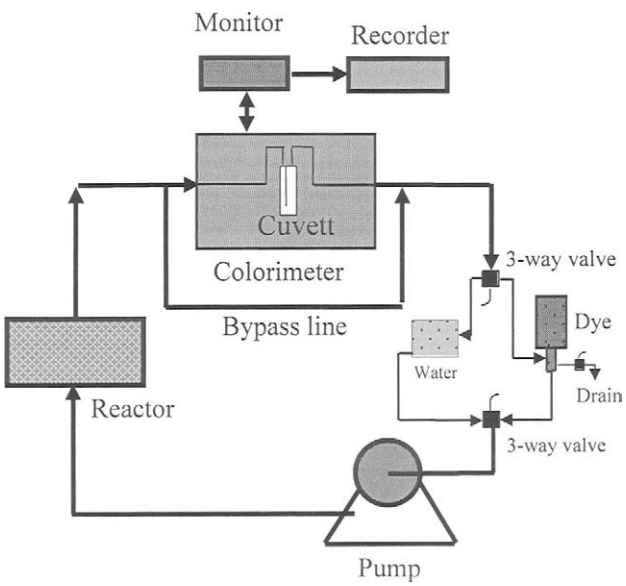

Figure 3. Experimental set-up

Evidence of complete mineralisation : The COD for SBB dye is given by

$$COD = y \cdot [M_{Oxygen}/M_{SBB\ dye}] \cdot n = 2.542\ y \quad (3)$$

where y is the concentration of the SBB dye in ppm, M_{Oxygen} and $M_{SBB\ dye}$ are the respective molecular weights and n for the dye is 64½. COD was measured for various virgin dye solutions, for liquid collected at the end of several experiments and for pure Milli-Q water. COD values for the virgin solutions were always equal to value calculated from equation (3) and that of the treated liquid and blank was zero. COD value for the final treated liquid shows that complete mineralisation occurred and for the present model component colorimetric analysis was justified as it was not merely measuring the decolorization of the dye.

Experimental procedure: At the start of every experiment the reactor was rinsed with Milli-Q water before zero-setting the analytical instrument. The reactor was then filled with the dye solution and it was ensured that no air bubbles remained in the system. The change in the dye concentration was continuously recorded. New silicon connecting tubes and fresh catalyst were found to adsorb the dye for about an hour, but no noticeable adsorption by the entire system was observed afterwards. Light was turned on only when the colorimeter reading was stabilized.

Experiments performed in the two reactors showed very promising results. The catalyst coatings on the glass tube and lamp surfaces were found durable, and the activity of the catalyst did not deteriorate even after 50 hours of experimentation. Figure 4 shows experimental results for the photocatalytic destruction of the SBB dye [5] in the MTR and TLR. Experimental results show that photocatalytic destruction of the dye pollutant is possible in both configurations. The figure reveals that 90% of the pollutant was degraded in about 100 minutes for the MTR and about 30 minutes for the TLR, although neither reactor was operated at optimum conditions.

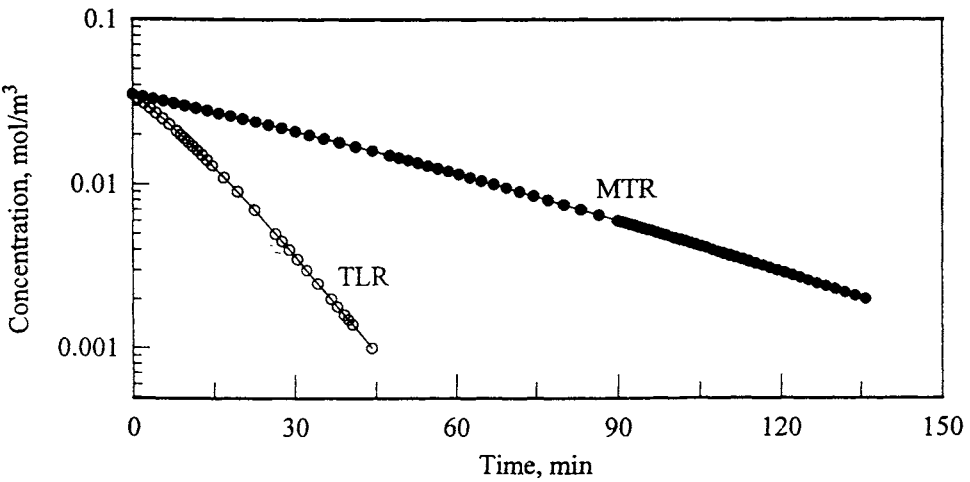

Figure 4. Experimental results for photocatalytic degradation of SBB dye in MTR and TLR.

Performance of the MTR can be instantly improved by decreasing the length of the hollow tubes used, as it is likely that the catalyst is inactive near the end of the tube away from the light source. In addition, the designs of the reactors are far from optimum with respect to mass transfer of pollutant to catalyst surface, flow distribution of reaction liquid, and efficiency of packing of the tubes/lamps inside the reactor. The reaction occurs at the

liquid-solid interface and mass transfer from the bulk of the liquid to the catalyst surface plays an important role in the overall rate of destruction of pollutants. Nevertheless, the designs of the reactors have the capability to be scaled-up to any dimensions, whereas the other two reactors are restricted only to a small reactor capacity.

The efficiency of the reactors (expressed in terms of moles converted per unit time per unit reactor volume per unit electrical power consumed) is compared with two different reactors [19] for the same model component (SBB dye) and same initial concentration (C_o= 0.024 mol/m^3). The slurry reactor (SR) consists of 20 tubes each of volume 7 x 10^{-5} m^3 containing 3 x 10^{-5} m^3 of liquid (with TiO_2 concentration of 0.5 kg/m^3), placed on a holder that rotates around a magnetic stirrer and is surrounded by 24 Philips TLK 40W/10R lamps. The classical annular reactor (CAR) was of 0.099m outside diameter and 0.065m inside diameter and 0.77m long, surrounded externally with 10 Philips TLK 40W/10R lamps. When the efficiencies of these test reactors are compared (see Table 2) with the experimental results of CAR and SR [19], an increase of about 695% and 259% was observed for TLR while 436% and 142% were observed for MTR respectively.

Table 2.
Reactor specifications, experimental conditions, and reactor performance efficiency for CAR, SR, TLR and MTR.

Photocatalytic reactor	CAR [21]	SR [21]	TLR [18]	MTR [22]
Volume of reactor, m^3	3.48 x 10^{-3}	1.4 x 10^{-3}	5.36 x 10^{-4}	1.23 x 10^{-3}
Catalyst surface area, m^2	0.18	3.7	0.15	0.51
Parameter κ, m^2/m^3	69	6139 #	618	1087
Flow rate, m^3/s	8.42 x 10^{-5}	Batch	1.67 x 10^{-5}	3.00 x 10^{-5}
Electrical energy input, W	400	960	126	40
Efficiency*, μmol/s/m^3/ W	9.50 x 10^{-3}	2.10 x 10^{-2}	7.55 x 10^{-2}	5.09 x 10^{-2}
% increase in efficiency	1	121	695	436
Scale-up possibilities	no	no	yes	yes

* Efficiency is expressed as 90 % pollutant (SBB dye) converted (μmol/s) from a starting concentration of 0.024 mol/m^3 per unit reactor volume (m^3) per unit electrical energy (W) used.

\# The value will be much lower than 6139 m^{-1} as all the suspended catalyst particles are not effectively illuminated and the assumption of average particle diameter of 0.3 μm may be too low.

Both the MTR and TLR design concept creates great opportunities for building much more efficient photocatalytic reactors for water purification as the reactors will be more economical. From Tables 1-2 it can be seen that higher values for the parameter κ can be achieved for both MTR and TLR than other reactor configurations. It is expected that the performance of TLR will surpass that of MTR because of superior catalyst activation, but the overall reactor efficiency may be much lower due to the application of a large excess of light energy than is required for catalyst activation. It is apparent that MTR design idea creates great opportunities for building much more efficient photocatalytic reactor for water purification, as the reactor most likely will be economical. We believe that MTR reactor will be cost effective compared to other photocatalytic reactors since it consists of inexpensive hollow glass tubes, cheap catalyst and requires low wattage lamps. It needs a reflector, which usually comes with the lamp and of course, a lens to direct the light entry at proper angle. Moreover, the hollow test tubes could easily be replaced. It is well known that water

purification by photocatalysis will not be cheaper than for example, by bio-treatment. However, if one is interested in purifying water containing toxic chemicals the best method may be to break open the benzene ring first by photocatalysis to eliminate the toxic chemicals and then send the water for bio-treatment. It would then not be necessary to completely mineralise the pollutants present in water by a photocatalytic reactor. A combination of the two methods could be best suited for water purification and may be more economical.

A problem for TLR is still the burning stability and lifetime of the lamps, particularly when the lamps are used immersed in water containing toxic chemicals. The main obstacle in the development of MTR design concept is that it is impossible to obtain uniform light distribution along the length of the tubes and thereby severely restricting the maximum length of tubes that can be used. One way of avoiding both the problems is to place one extremely narrow diameter novel tubelight lamp inside each of the hollow tubes. In this way, all the advantages of the MTR concept can be utilised while eliminating the basic drawback of uniform light distribution dilemma. Moreover, this will also eliminate the main problem experienced in the TLR with the prolonged use of novel lamps immersed in polluted water. A comprehensive experimental program investigating the influence of operating parameters on the conversion rates is presently being carried out for both reactors.

4. COMPUTER SIMULATION

The increase in reactor efficiency over conventional photocatalytic reactor was inspite that the design of the test reactor was far from optimum with respect to mass transfer, flow distribution and efficiency of packing of the tubes inside the reactor. Computer simulation was used to fine tune the reactor design to achieve better fluid-catalyst contacting to minimize mass transfer limitation.

Numerical simulation of the reactor was performed using a commercial CFD package FLUENT to determine effects of flow rates, diffusion coefficients, reaction rate constants, and inter tube spacing on the conversion of pollutants. The reactor considered in the simulation consisted of a cylindrical vessel (diameter 0.05m, length 0.25m) within which 7 hollow tubes (diamter 0.006m) coated on its peripherial surface with catalyst were placed in staggered manner with 0.006m pitch. The liquid was introduced and collected through an inlet and a outlet port placed tangentially to achieve greater mixing. In computer simulation, less number of tubes with less packing density was considered in order to achieve convergence in the simulation runs.

In order to get accurate results, the 3-D model of the reactor required control volume ranging from 500,000 to 1,000,000 cells distributed unevenly in the computational domain. Computation of the velocity components, pressure and six species components had to be carried out for at least 2000 iterations for convergence, which was very time consuming, and required couple of days on a single SGI workstation. In the wake of this, a state-of-the-art computational technique, viz., distributed computing, to expedite the calculation and overcoming the memory bottleneck present in single workstations was applied [13].

Simulation of the complex and computationally intensive physico-chemical phenomena using the distributed computing technique expedited the progress of the present research manifold. The time taken to produce the desired result plummeted from days to hours. Besides the speed-up, visualisation of the data by the powerful SGI machines facilitated in the final analysis. The results showed that the distributed computing technique was one of the most economical and efficient method for overcoming difficulties, such as the memory bottle-neck present in single workstations and long computation time associated with computer simulations of reacting flows [13].

Initially a reasonably converged solution was obtained for the velocity and pressure equations. The conservation equations were solved in Fluent using RNG (Re-normalized group) k-ε model. The reaction part of the solver was then activated, and using the almost converged solution as the initial condition, a complete solution of the reacting flow model was obtained. The converged velocity profiles at various regions of the reactor were observed to determine the degree of mixing (Figure 5). Fluid mixing was used as one of the important criteria in efficient design of photocatalytic reactor as transport of reactants from the bulk of the liquid to the catalyst surface determines the extent of fluid-catalyst contacting and overall conversion.

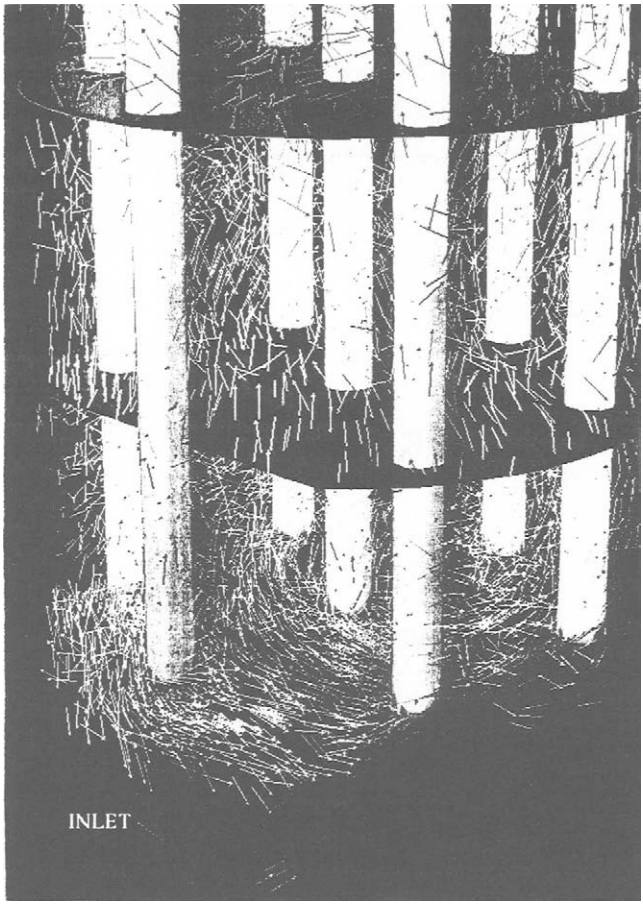

Figure 5. Mixing inside the reactor

Figure 6 shows the effect of various parameters on the conversion of dye pollutant. As the flow rate was increased, conversion decreased since the residence time of pollutant decreased. However, the capacity of the reactor will be low when slow flow rate is used. When reaction rate constant was increased beyond 0.1 $\mu mol/m^2/s$, conversion did not improve much implying that overall rate is not controlled by reaction kinetics. When the reaction rate constant was reduced to 0.001 $\mu mol/m^2/s$,. a factor of 100, conversion decreased only by 1.4% confirming that overall reaction is mass transfer controlled. This is further justified when diffusion coefficient was varied keeping other parameters fixed at the reference value.

Diffusion coefficient of pollutant in aqueous phase is normally of the order of 1.0×10^{-9} m^2/s, and figure 6 reveals that conversion is controlled by diffusion of pollutant from bulk to the catalyst surface. This was further confirmed by varying the inter tube spacing. By reducing the pitch, one would reduce the distance a species has to travel to come in contact with the catalyst surface. Hence, conversion will increase with the decrease of tube clearance, particularly when the flow is laminar as there is no mixing of fluid particles. The effect was more pronounced at smaller pitch (34.3% decrease in conversion when pitch was increased from 0.003 to 0.004m), while drop in conversion is less noticeable when lamp spacing is large (only 15% drop when pitch was increased from 0.006 to 0.007m).

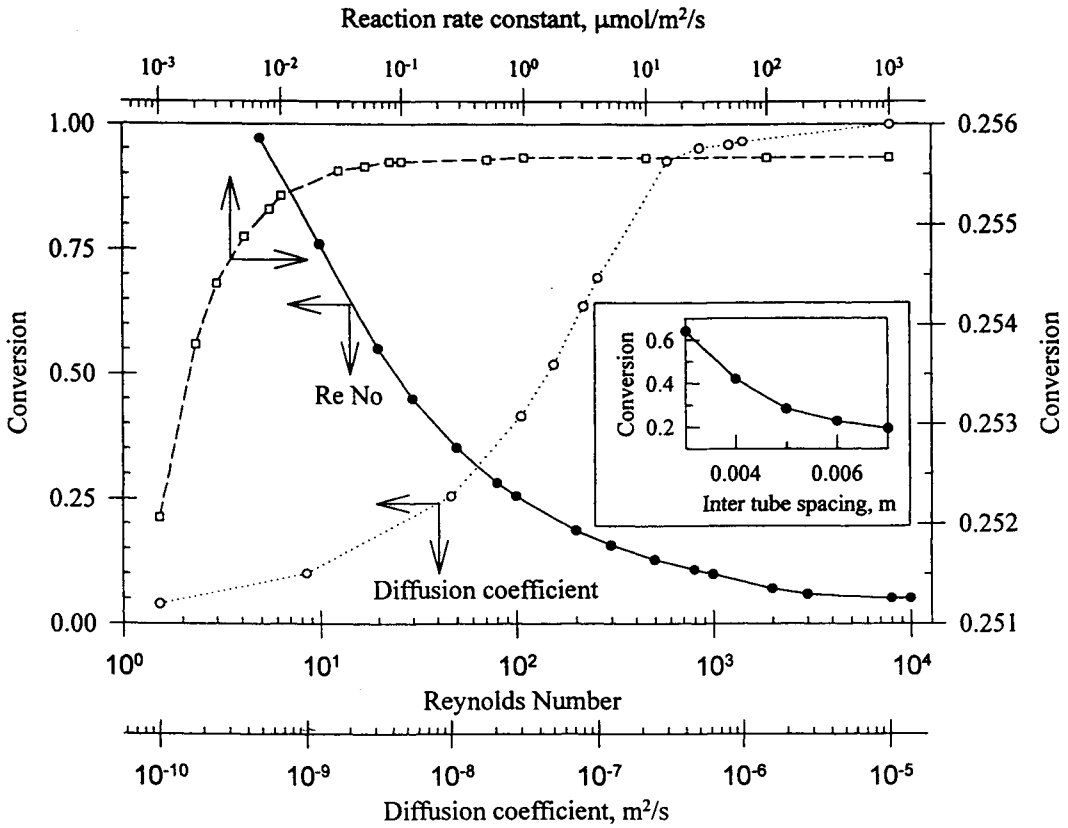

Figure 6. Effect of Re, D, k and P on conversion of pollutants.

Figure 6 reveals the importance of diffusion in the design of photocatalytic reactor. Conversion is primarily controlled by flow and diffusion of pollutant and is practically independent of reaction rate. When diffusion coefficient is very low, low flow together with smaller inter tube spacing must be used to ensure high conversion. However, low flow rate results in low throughput. Conversion can be improved if mixing of fluids in the reactor is enhanced by creating turbulance. But, if turbulance is generated only by increasing flow rate, residence time of pollutant in the reactor will decrease and conversion will subsequently decrease. Therefore, one must find optimal flowrate first, and then maximize both mixing of

fluid and residence time of pollutant in the reactor, by introducing baffles and selecting proper reactor configurations.

A comprehensive computer simulation on the design of the reactor is currently being carried out using distributive computing to expedite the calculation of coupled non-linear PDEs and in overcoming memory bottle-neck present in single workstation. The advantage of using computer simulations is that the length of the reactor required for complete degradation of a particular pollutant can be determined easily compared to time consuming expensive experimental studies. The result will then be verified experimentally.

5. CONCLUSIONS

The central problems in the development of a photocatalytic reactor, namely light distribution inside the reactor and providing high surface areas for catalyst per unit reactor volume, are addressed in this paper. Two reactor concepts, one of which is a distributive-type fixed-bed reactor system that employs hollow glass tubes as a means of light delivery to the catalyst particles, while the other is an immersion-type reactor where new extremely narrow diameter artificial fluorescent lamps, are discussed. Both reactors result in a 100 to 150 fold increase in surface area per unit volume of reaction liquid inside the reactor relative to a classical annular reactor design and a 10 to 20 fold increases relative to an immersion-type reactor using classical lamps. The design of both reactors increases the surface-to-volume ratio while eliminating the prospect of light loss by absorption and scattering in the reaction medium. Experiments performed to study the degradation of a textile dye showed promising results for the two test reactors. Both reactor configurations are flexible to be scaled-up for commercial applications.

Acknowledgements: The author wishes to thank Professor A. A. C. M. Beenackers, University of Groningen, Mr. P. A. W. Tielemans, Philips Lighting, Eindhoven, and Mr. T. P. M. Koster and Mr. J. W. Assink, TNO, The Netherlands, for their advice and many helpful discussions.

Notation

		Subscripts and superscripts	
C	concentration, mol/m^3		
d	diameter, m		
ε	fractional volume of reactor covered with lamps	0	outer
k	reaction rate constant, mol/s/kg-cat	c	catalyst
κ	illuminated catalyst density, m^2/m^3	i	inner
λ	wavelength, nm	in	inlet
ρ	density, kg/m^3	max	maximum
R	reactor	o	outside
X	fractional conversion	p	particle

REFERENCES

1. Fox, M.A. and Dulay, M.T., *Heterogeneous photocatalysis*, Chem. Rev., (1993) **93**, 341.
2. Ollis, D. F., Pelizzetti, E. and Serpone, N., 1989, *Photocatalysis: Fundamentals and Applications*, Wiley, New York.
3. Mills, A., Davies, R. H. and Worsley, D., *Water purification by semiconductor photocatalysis*, Chemical Society Reviews, December, (1993) pp.417.
4. Ray, A. K., New photocatalytic reactors for destruction of toxic water pollutants, Dev. Chem. Eng. Mineral Process., (1997) 5(1/2), pp.115.

5. Ray, A.K. and Beenackers, A.A.C.M., Novel swirl-flow reactor for kinetic studies of semiconductor photocatalysis, AIChE J., (1997) 43(10), pp.2571.
6. Legrini, O., Oliveros, E. and Braun, A. M., *Photochemical processes for water treatment,* Chem. Rev., (1993) **93**, pp.671.
7. Hagfeldt, A. and Grätzel, M., *Light-induced redox reactions in nano-crystalline systems*, Chem. Rev., (1995) 95, pp.49.
8. Ollis, D. F., Pelizzetti, E. and Serpone, N., *Destruction of water contaminants*, Env. Sci.Technol., (1991) 25 (9), pp.1523.
9. Braun, A. M., Maurette, M.T. and Oliveiros, E., 1993, *Photochemical Technology*, John Wiley & Sons, Chichester, England.
10. Matthews, R.W., *Photocatalytic oxidation of organic contaminants in water: An aid to environmental preservation,* Pure and Applied Chemistry, (1992) **64** (9),1285
11. Hoffmann, M.R., Martin, S.C., Choi, W. and Bahnemann, D.W., *Environmental applications of semiconductor photocatalysis*, Chem. Rev., (1995) **95**, 69.
12. Ray, A. K. and Beenackers, A.A.C.M., (1996), A photocatalytic reactor suitable for water purification as well as a process for the purification of waste water by means of such a photocatalytic reactor, Eurpean patent 96200942.9-2104.
13. Periyathamby, U. and Ray, A. K., Reactive flow modelling on a distributive computing environment, Chem. Eng. Technol., (1999), in press.
14. Ray, A.K. and Beenackers, A.A.C.M., *Novel photocatalytic reactor for water purification*, AIChE J., (1998) **44**(2), pp.477.
15. Chen, D. and Ray, A. K., Photodegradation kinetics of 4-nitrophenol in TiO_2 suspensions, Water Research, (1998) 32(11), pp.3223.
16. Chen, D. and Ray, A. K., Photocatalytic kinetics of phenol and its derivatives over UV irradiated TiO2, Applied Catalysis B: Environmental, (1999), in press.
17. Mukherjee, P. S. and Ray, A. K., Major challenges in the design of a large-scale photocatalytic reactor for water treatment, Chem. Eng. Technol., (1999), 22, pp253.
18. Ray, A. K., A new photocatalytic reactor for destruction of toxic water pollutants by advanced oxidation process, Catalysis Today, (1998), 44, pp357.
19. Assink, J. W., Koster, T.P.M. and Slaager J.M., (1993), Fotokatalytische oxydatie voor afvalwater behandeling, Internal report reference no. 93-137, TNO - Milieu en Energie, Apeldoorn, The Netherlands.
20. Ray, A. K. and Beenackers, A.A.C.M., Development of a new photocatalytic reactor for water purification, Catalysis Today, (1998) 40(1), pp.73.
21. Ray, A. K., Design, Modelling and Experimentation of a New Large-scale Photocatalytic Reactor for Water Treatment, *Chemical Engineering Science*, 54 (15-16), 3133-3125, 1999.
22. Peill, N. J. and Hoffmann, M. R., Development and optimization of a TiO2 coated fiber optic cable reactor, Env. Sci. Technol., (1995) 29, pp.2974.
23. Sato, K., 1992, *Drinking water container capable of decomposing organic halogen compounds by light irradiation*, patent JP 04114791 A2 920415.
24. Taoda, H., 1993, *Water treatment*, patent JP 05076877 A2 930330.
25. Matthews, R.W., 1990, *Coating photoactive metal oxides onto substrates and their use in water purification*, patent AU 600289 B2 900809.
26. Anderson, M.A., Tunesi, S. and Xu, Q., 1991, *Degradation of organic chemicals with titanium ceramic membranes*, US 5035784 A 910730.
27. Cooper,G.A., 1989, *Photocatalyst in a glass wool matrix between plates*, US 4888101.
28. Miano, F. and Borgarello, E., 1991, *Method for the heterogeneous catalytic photodegradation of pollutants*, patent EP 417847 A1 910320.

29. Oonada, J., 1994, *Water purifying method*, patent JP 06071256 A2 940315.
30. Hosokawa, M. and Yukimitsu, K., 1988, *Treatment of waste fluids with titania particles*, patent JP 63042793 A2 880223.
31. Henderson, R.B. and Robertson, M.K., 1989, Fluid purification by photodegradation of organic pollutants and microorganisms, patent EP 3063301 A1 890308.
32. Heller, A. and Brock, J.R., 1993, M*aterials and methods for enhanced photocatalysis of organic compounds in oil spill treatment*, patent WO 9317971 A1 930916.
33. Hofstadler, K., Bauer, R., Novalic, S. and Helsler, G., 1994, *New reactor design for photo-catalytic treatment with TiO2 immobilized on fused-silica glass fibers: photomineralization of 4-chlorophenol*, Environmental Science and Technology, **28**, 670.
34. Haneda, K., 1992, *Photocatalytic element pipe and photocatalytic chemical reactor*, patent JP 04061933 A2 920227.
35. Masuda, R., Kawashima, K., Takahashi, W., Murabayashi, M. and Ito, K., 1994, *Photocatalysts for treatment of harmful substances and its apparatus*, patent JP 06320010 A2 941122.
36. Ritchie, D.G., 1991, *Photocatalytic fluid purification apparatus having helical nontransparent substrate*, patent US 5069885 A 911203.
37. Matthews, R.W., 1988, *Semiconductor photocatalytic method and system for determining organic matter in an aqueous solution including an oxidizing agents*, patent WO 8806730 A1 880907.
38. Cooper, G.A. and Ratcliff, M.A., 1991, *System for and method for decontaminating a contaminated fluid by using photocatalytic particles*, WO 9108813 A1 910627.
39. Wake, H. and Matsunaga, T., 1994, *Redox reaction using photocatalysis of semiconductor*, patent JP 06134476 A2 940517.
40. Ray, A. K., Simulation of a photocatalytic reactor using CFD, J. Inst. Eng. Singapore, (1998) 38(3), pp.22.

Reaction Engineering for Pollution Prevention
M.A. Abraham and R.P. Hesketh (Editors)

Asymmetric Catalytic Hydrogenation in CO_2 Expanded Methanol – an Application of Gas Anti-Solvent Reactions (GASR)

G. B. Combes, F. Dehghani, F. P. Lucien, A. K. Dillow[a] and N. R. Foster
School of Chemical Engineering and Industrial Chemistry,
The University of New South Wales, Sydney, 2052, Australia

[a]Department of Chemical Engineering and Materials Science,
University of Minnesota, 421 Washington Ave. SE, Minneapolis, MN 55455, USA

The technical feasibility of performing reactions in a novel solvent medium was investigated. The reaction considered was the asymmetric hydrogenation of 2-(6'-methoxy-2'-naphthyl) acrylic acid to (S)-Naproxen using a [(S)-Ru(BINAP)Cl]Cl *p*-cymene catalyst. The reaction was performed in methanol at 298 K, and in methanol expanded with carbon dioxide at both 288 K and 298 K. Preliminary results showed that the reaction rate was significantly faster in expanded methanol than in pure methanol at the same temperature. The increase in rate is probably due in part to the higher hydrogen solubility attainable in the expanded liquid phase compared with pure methanol.

1. INTRODUCTION

Economic and environmental regulatory pressures are two of the major driving forces behind efforts in the chemical process industries to maximise efficiency and to minimise waste. The traditional methods for producing optically pure compounds involve preferential crystallisation or diastereomeric crystallisation, kinetic resolution and catalytic asymmetric synthesis. Catalytic asymmetric synthesis has significant advantages over conventional technology, including waste minimisation and a reduction or elimination of separation requirements with associated savings in energy consumption.

There is significant scope for increasing the productivity of catalytic asymmetric hydrogenation reactions by reducing reaction times and enhancing enantioselectivities. The two major factors that determine enantioselectivity are the catalyst and solvent, the nature of the latter being of greater significance [1]. However once an optimum solvent and catalyst is chosen, there is limited scope in the manipulation of process variables to further enhance selectivities.

The major focus of research relating to asymmetric hydrogenations has been on the development of enantioselective catalysts. The incentives for such research are the

economic and environmental advantages to be gained by reducing the complexity of procedures involved in purifying the final product. Catalysts have been developed that can yield over 99% enantioselectivity [2]. As acceptable catalyst selectivities can now be achieved, attention should focus on improving the actual rates, which typically require tens of hours for complete conversion. Hydrogenation reaction rates are often limited by the actual hydrogen (H_2) concentrations in solution, since hydrogen has relatively poor solubility in conventional organic solvents [3]. Unlike other gases, the solubility of gaseous hydrogen increases with increasing temperature. If a reaction produces higher enantioselectivity for the desired product at lower temperatures, then this is obviously a concern for hydrogenation reactions. Thus we arrive at a conundrum - do we increase the reaction rates at the expense of enantioselectivity or do we seek to minimise the purification steps downstream and settle for a slower reaction rate?

The solubility of gases is considerably higher in supercritical fluids (SCF) than in conventional solvents. This property has been taken advantage of in much of the supercritical water oxidation research that has been undertaken. Hydrogenation reactions have also been carried out in SCF such as carbon dioxide and propane. The addition of SC-CO_2 has produced faster rates compared to those obtained in conventional solvent mediums [4,5]. A significant factor in this regard is the improved solubility of the hydrogen [6]. There are other solvent effects such as viscosity, polarity and local solvent density effects which may also impact favourably on kinetics, but they are as yet unquantified. As the solubility of large substrate molecules is significantly less in SCF than in conventional solvents, it would seem that the choice of solvent mediums must be a compromise between solubility of catalyst and reactants, and the reaction rates.

Supercritical fluids provide a very promising medium for homogeneous catalysis. Solvolytic homogeneous catalysis in SC-CO_2 has been reported and it was shown that, under supercritical conditions, formic acid can be produced from the hydrogenation of CO_2 in the presence of certain ruthenium (II)-phosphine complex catalysts [6]. Notably, higher initial reaction rates were achieved in the supercritical CO_2 than in conventional liquid organic solvents. Jessop and coworkers (1995) also investigated the synthesis of methyl formate by hydrogenation of SC-CO_2 in the presence of methanol [7]. The turn over numbers and yields were an order of magnitude higher than any previously reported. The hydrogenation of CO_2 actually reached a stage where it was thought that hydrogen was the limiting reactant. Tacke and coworkers (1996) have successfully conducted a homogeneous hydrogenation reaction in SC-CO_2 [8]. Hydrogenation rates as high as 52.3 (mole H_2 per hour per gram active metal) at 60°C were reported.

Xiao et al. (1996) have published the first reported study of asymmetric hydrogenations in supercritical systems using tiglic acid and a variety of Ru(BINAP) catalysts [9]. The study demonstrated that reaction in SC-CO_2 produced selectivities and yields that were comparable to those obtained for conventional solvent systems such as methanol and hexane. The addition of a small amount of fluorinated alcohols to the SC-CO_2 was also observed to improve both the conversion and selectivity compared to that achieved in conventional solvents. Tumas and co-workers (1995) have also reported the successful use of enantioselective catalysis in a number of hydrogenation applications in SC-CO_2 [10]. The above examples demonstrate that the use of high pressure carbon

dioxide as a reaction medium can result in higher yields and selectivity and hence is a concept with significant potential for the production of high value-added pharmaceuticals.

In recent years, work has been carried out using Gas Anti-Solvent (GAS) media for the purpose of precipitating particles of uniform morphology and size [11]. The addition of a dense gas (a near critical or supercritical fluid) to a conventional solvent produces expansion of the solvent, provided that the dense gas is miscible with the solvent. The dense gas is termed the anti-solvent because it lowers the solvation power of the solution. The anti-solvent alters the properties of the solution but as yet, only the impact on solvent density (and hence solvation power of the solution) has been investigated. Work by Dixon and Johnston (1991) showed the effect of adding anti-solvent to a solution of toluene and naphthalene [12]. The naphthalene solubility was maintained at levels similar to that of the conventional solvent but at CO_2 mole fractions in excess of 60%. From the aforementioned work, it is clear that the concentration of substrate in solution can be held at levels attainable in conventional solvent in the presence of a considerable amount of anti-solvent.

As the characteristics of the solvents are fixed in conventional systems (P and T have limited affect on solvent characteristics), improvements in selectivity will most likely arise only from developments in catalyst technology. Undertaking reactions in dense gas expanded media is an alternative approach in which a far greater range of solvent properties is achievable. As rates are dependent on concentrations and rate constants, it may be possible to increase reaction rates, whilst maintaining the selectivity, by manipulating solvent parameters in a solution expanded with a dense inert gas. The physical (viscosity, diffusivity, density) and chemical properties (dielectric constant, polarizability) of the expanded reaction medium can be manipulated to suit the reaction by adjusting the concentration of CO_2 in the reaction medium.

The objective of the project was to investigate the feasibility of conducting an enantioselective catalytic hydrogenation reaction in a solvent (methanol) expanded with a dense gas (CO_2). It is stressed that whilst the results presented here are preliminary, the technical feasibility of the GASR is clearly demonstrated.

1.1 The Reaction

The catalytic asymmetric hydrogenation of 2-(6'-methoxy-2'-naphthyl) acrylic acid (or PreNap) using Ru(BINAP) type catalysts to S-Naproxen has been studied previously by others [13-16]. The reaction is typically conducted at temperatures less than 273 K, in a methanol solvent environment, under hydrogen pressures in the range 50 to 100 bar. Ashby and Halpern (1991) determined the need for a basic environment for the reaction to proceed [16]. To achieve this, triethylamine (TEA) was added to the reaction medium. In general it has been found that the catalyst is an important factor in determining enantiomeric selectivity. Two other factors affecting the selectivity are temperature and hydrogen pressure (H_2 concentration in solution). It has been reported that high selectivity is favoured by lower temperatures and high H_2 pressure [13, 15]. There are no comprehensive published studies of reaction rates for this reaction. The influence of temperature has as yet only been determined qualitatively. Although in

general terms one would expect the reaction rate to increase with an increase in temperature, this particular reaction exhibits a loss in selectivity as temperature increases which is only partially offset by the increase in hydrogen solubility and hence reaction rate. Due to this selectivity/temperature dependence, and on the basis of prior work, pure SC-CO_2 as a reaction medium must be ruled out since the optimum reaction temperature lies below that of the critical temperature of carbon dioxide [17].

It has been shown that the presence of an anti-solvent (such as CO_2) in a solvent does increase the amount of H_2 dissolved in the liquid phase [18]. Thus it is expected that adding CO_2 to methanol would improve the solubility of H_2 in the liquid phase containing the dissolved substrate and catalyst. Naproxen has relatively high solubility in methanol ($X_{Nap} = 10^{-2}$ - 10^{-3} mole fraction) but is only sparingly soluble in SC-CO_2 (10^{-5} to 10^{-6} mole fraction) [19]. Its solubility in CO_2 containing 5% methanol as cosolvent is approximately 10^{-4} mole fraction. Data reported by Francis [20] show that the density of the CO_2-MeOH solution system does not change significantly with increasing CO_2 content until the mole fraction of carbon dioxide exceeds 0.85 ($X_{CO2} \simeq 85$ mol%), thus providing a wide range of CO_2 concentrations for which high Naproxen concentrations might be maintained [20]. It was expected that the reactant would exhibit a similar solubility to Naproxen due to the very similar nature of the major functional groups on both compounds. To illustrate the above concept, qualitative solubility curves for the solid solute and gases appear in Fig. 1. The solid solubility curve is based on the phenomena seen in GAS precipitation studies. However only the limits of the H_2 solubility curve are known and the solubility curve displayed is simply an indication of a trend.

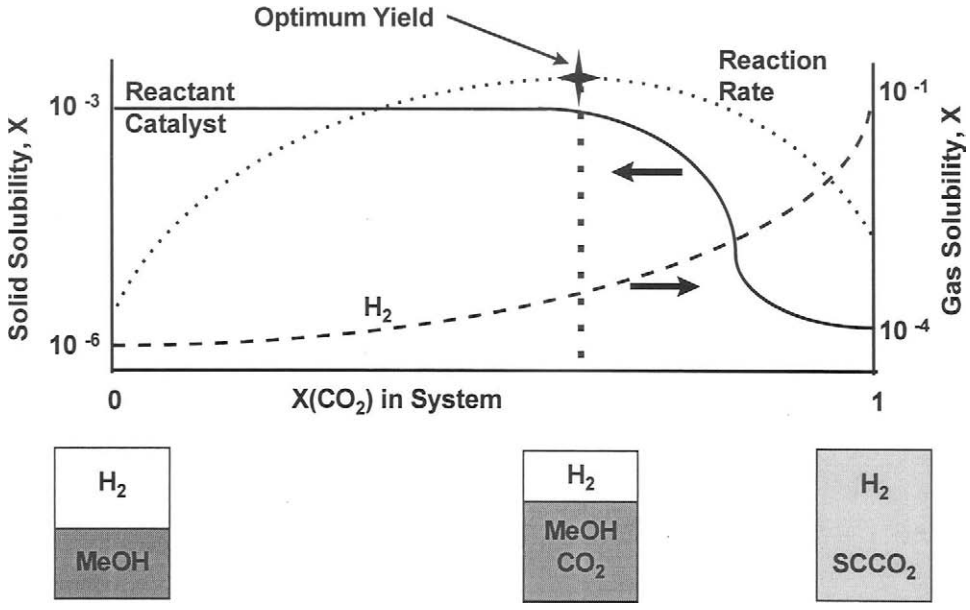

Fig. 1 - Schematic Diagram of Solubility Curves for Solid and Gaseous Components

2. EXPERIMENTAL

The system investigated was the asymmetric hydrogenation of 2-(6'-methoxy-2'-naphthyl) acrylic acid (or PreNap) to (R,S) Naproxen, an anti-inflammatory pharmaceutical used widely throughout the world. The (S)-Naproxen (98% purity), the catalyst ([(S)-Ru(BINAP)Cl]Cl *p*-cymene) and the TEA (+99% purity) were all supplied by Sigma-Aldrich. The reactant was synthesised and analysed by NMR for purity. The reaction was performed in both pure methanol (HPLC grade min 99.8%, BDH) and dense CO_2 expanded methanol at temperatures of 298 K and 288 K. The CO_2 was SCF grade (99.999% purity) and the H_2 of 99.999% purity (BOC Gases).

Expansion studies of the methanol with CO_2 were carried out using a travelling telescope and a high pressure Jerguson sight gauge to visually determine the degree of expansion at given temperatures. Sufficient information was obtained to enable the required conditions to perform the reaction to be determined. Expansion data was obtained over the temperature range of 278 K- 308 K.

The reaction was carried out in a magnetically stirred, stainless steel optical cell (path length 68 mm, volume 18 mL) complete with jacket. The pressure and temperature were measured with a Druck 911 pressure transducer and a Pt100 RTD respectively and logged to a computer. The reaction was monitored using a single beam, UV-visible spectrometer (Hewlett Packard model HP8453) together with kinetic software. The conversion was verified and selectivity determined using HPLC on a Chromtech AGP (150 × 4 mm) column eluting a 10 mM phosphate buffered solution.

Methanol solutions were placed into the cell using a Hamilton airtight glass syringe with a repeatability of 0.1%. The solutions were prepared with a [TEA]:[PreNap] of one and a [PreNap]:[Catalyst] of 10 and 190. In the initial studies conducted at a substrate:catalyst ratio of ten (S:C =10), the TEA-catalyst-methanol solution was placed into the cell and a background spectrum was taken after the spectra showed insignificant change (less than 0.002 AU over a period of 30 mins). Hydrogen does not absorb in the UV-vis spectrum and hence it was not necessary to include in the background spectrum. The cell was then cleaned, dried and purged with nitrogen (N_2). The combined reactant and TEA-catalyst solution in methanol was then placed into the cell, sealed and purged with 0.5 bar. Hydrogen at 50 bar was added to the reaction cell when the system was stable and no further change in spectra was observed. The hydrogen flow was controlled by a regulator from the gas cylinder and a continuous positive feed of hydrogen gas was provided to the cell. Excess hydrogen was used and thus should not be rate limiting in either case. The stirrer speed was set at 380 rpm.

The monitoring of the reaction began upon the introduction of the hydrogen to the vessel. The magnetic stirrer was used throughout the spectral studies to eliminate mass transfer effects and decrease the time required for equilibrium to be reached. The action of the stirrer had a negligible effect on the variance of the spectral data. Dilute solutions were used to eliminate any problems associated with solubility limitations thus minimising the risk of mass transfer limitations. However, running at low concentrations of catalyst has the disadvantage of raising the susceptibility of the catalyst to becoming deactivated through reacting with the dissolved oxygen. The reactions in

expanded solutions were performed similarly, except that the purging of the cell was carried out with CO_2 instead of N_2. The anti-solvent, CO_2, was added once the solution had been injected into the cell. The cell was slowly pressurised over a period of one hour to the pressure required to achieve a 200% expansion. The CO_2 was then stopped and H_2 was supplied to the vessel.

3. RESULTS AND DISCUSSION

Results for the expansion of methanol with CO_2 appear in Fig. 2. The data indicated that the pressure at which methanol expanded dramatically decreased as the temperature was decreased. This was due to the fact that the solubility of carbon dioxide in methanol increased as the temperature was decreased.

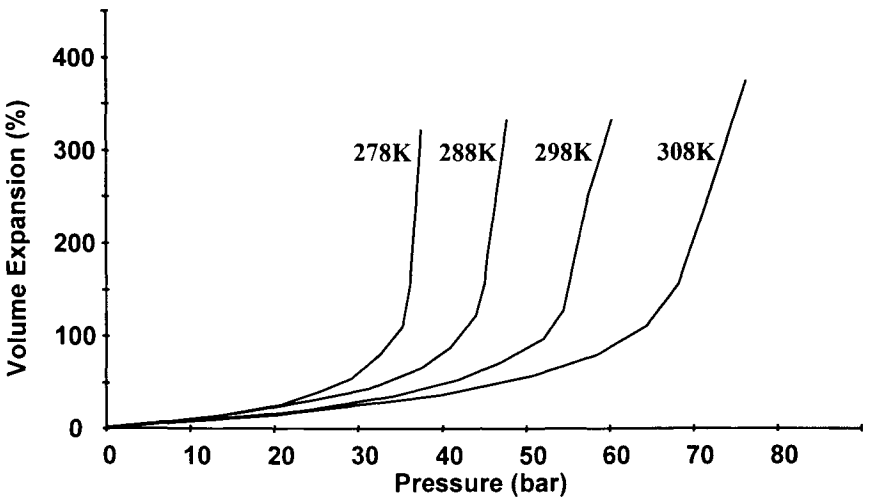

Fig. 2 : Expansion of methanol with dense CO_2

Reproducible spectra for the reaction were obtained in preliminary trial runs using the non-selective Wilkinson's catalyst in both methanol and expanded methanol solutions. The results obtained from repeated runs under the same physical conditions with the Ru(BINAP) catalyst appear in Table 1. Selectivity is reported as enantiomeric excess.

The first four results were obtained using a S:C = 10. It is clear that, for a given temperature, the average time required to attain a specific conversion in the expanded medium was significantly less than for neat methanol. It can be seen that the increased rate of reaction is obtained with only a minor loss in selectivity. Repeatability of the reaction was difficult to obtain when using the [(S)-Ru(BINAP)Cl]Cl *p*-cymene catalyst. It was thus inferred that catalyst deactivation through oxygen poisoning may be the major reason behind this problem. Catalyst deactivation may also have influenced the selectivity results in a negative manner.

Table 1 - Conversion and Enantioselectivity Using (S)-Ru(BINAP) catalyst

Medium	Temp. (K)	P(total) (bar)	S:C	Time (hrs)	X (%)	ee. * (%)
Methanol	298	50	10	7.5	96	86
Methanol	288	50	10	14	12	57
Methanol/CO_2	298	106	10	3.8	96	80
Methanol/CO_2	288	95	10	10.6	93	84
Methanol	298	50	190	6	48	60
Methanol/N_2	298	88	190	6	27	42

* ee. = enantiomeric excess or (S-R)/(S+R)

The high substrate to catalyst ratio (kept constant at 10) can also present problems in such an environment. The Ru(BINAP) catalyst has been known to form H_8-Ru(BINAP) catalyst species [21]. A disadvantage of using a single beam UV-vis spectrometer is that no correction can be made for drift in the light emitted, hence the reaction time period was limited to 14 hours. The reason for operating at the high ratio was to obtain a fast enough reaction in the given time period of 14 hours. In light of the information gained with respect to catalyst handling, it is now apparent why such a high ratio was required to obtain a suitably fast reaction.

In more recent work, changes have been made to the handling procedures for the solutions involved, which has seen all work conducted under atmospheres of either Argon or Nitrogen and rigorous degassing procedures followed. Significant improvements in catalytic activity and repeatability have been realised, allowing methanol studies to be conducted at a S:C = 190. Also of significance is that a higher speed of 750 rpm has been used in the studies at the higher S:C ratios, thus further decreasing potential mass transfer limitations to the system. At a S:C = 190, the addition of Nitrogen (N_2) to the system retards the reaction rate. The last two entries in Table 1 show that, over the same time period, the degree of conversion of the reactant under 50 bar H_2 and 38 bar N_2 was only 56% when compared to the reaction under 50 bar H_2 alone. This may be due to the N_2 bonding with the catalyst-reactant complex, thus decreasing the amount of active sites available for the hydrogen to bond to the reactive complex. In future studies argon will be used instead of nitrogen to avoid this possibility. Through the improvements in experimental technique, the reaction rates as depicted by the UV-vis spectra (and correlated with the conversion) have also suggested that there is an optimum equilibrium time for the substrate and catalyst.

CONCLUSION

The technical feasibility of conducting an asymmetric catalytic hydrogenation reaction in a GAS medium has been demonstrated. It has been shown that improved rates can be obtained using dense CO_2 expanded methanol compared with those attainable in the conventional neat methanol system. The improvement is achieved with only a minimal

loss of enantioselectivity. Handling of the Ru(BINAP) catalyst was found to be crucial in obtaining repeatable results. The exact reasons for the improved reaction rates are still under investigation, however it is suspected that improved mass transfer of the hydrogen gas into the liquid phase and improved solubility are significant factors. Further improvements are being made to reduce the oxygen in the reaction system to minimal levels. The reaction kinetics, as well as the impact of both the hydrogen concentration in the liquid and mass transfer resistances on the reaction, are the subjects of on going investigations.

ACKNOWLEDGMENTS

Thanks must be extended to Dr Sergei Kazarian, of Imperial College ,London, UK, for the useful discussions on high pressure spectroscopic cell design and to Jessica Wu for assistance with the methanol expansion studies. The financial support of the Australian Government for the provision of an APRA is appreciated greatly.

REFERENCES

[1] C. Reichardt, Solvents and Solvent Effects in Organic Chemistry 2nd Edition, VCH, Germany, pp 203-205 1990
[2] T. Naota, H. Takaya and S. Murshashi, Chem. Rev., 98 (1998) 2599-2660
[3] Y. Sun, R.N. Landau, J. Wang, C. LeBlond, D.G. Blackmond, J. Am. Chem. Soc, 118 6 (1996) 1348-1353
[4] P.G. Jessop, T. Ikariya, R. Noyori, Nature, 368 17th Mar (1994) 231-233
[5] L. Devetta, A. Giovanzana, P. Canu, A. Bertucco, B.J. Minder, Catalysis Today, 48 (1999) 337-345
[6] C.Y. Tsang and W.B. Streett, Chem. Eng. Sci., 36 (1981) 993-1000
[7] P.G. Jessop, Y. Hsiao, T. Ikariya, R. Nortori, J. Chem. Soc. Chem. Comm., Mar 21 (1995) 707-708
[8] T. Tacke, S. Wieland, P. Panster, High Pressure Chem. Eng, R. von Rohr and C.H. Trepp (Eds) Elsevier, 1996
[9] J. Xiao, S.C.A. Nefkens, P.G. Jessop, T. Ikariya, R. Noyori, Tet. Letters, 37, 16, (1996) 2813-2816
[10] M.J. Burk, S. Feng, M.F. Gross, W. Tumas, J. Am. Chem. Soc, 117 (1995) 8277-8278
[11] R. Thiering, F. Dehghani, B. Warwick, L. Sze Tu, N.R. Foster, "A Critical Review Of Dense Gas Anti-Solvent Precipitation", (1999), [in press]
[12] D.J. Dixon and K.P. Johnston, AIChE Journal, 37, 10, (1991) 1441-1449
[13] A.S.C. Chan, S.A. Laneman, R.E. Miller, ACS Symposium Series No. 517, American Chemical Society, Washington, D.C., (1993) pp27-39
[14] M. Davis, K.T. Wan, J. Catal., 148 (1994) 1-8
[15] H. Takaya, K. Ohta, K. Mashima, Homogeneous Transition Metal Catalyzed Reactions, N.R. Moser and D.W. Slocum (Eds.), Am. Chem. Soc., USA, 1992
[16] M.T. Ashby, J. Halpern , J. Am. Chem. Soc, 113 (1991) 589-594

[17] E. Birnbaum, g. Brown, S. Buelow, P. Dell'Orco, S. Feng, L. Luan, D. Morita, D. Morgenstern, D. Pesiri, T. Walker, W. Tumas, *4th Int'l Symp. on SCF*, Japan, 11-14th May 1997.
[18] H.S. Phiong, D.M. Pryor, F.P. Lucien "The Effect of SC-CO_2 on the Solubility of H_2 in α-Methyl Styrene", paper accepted for CISF99, Garda, 13th-16th June 1999
[19] S.S.T. Ting, S.J. Macnaughton, D.L. Tomasko, N.R. Foster, Ind. Eng. Chem. Res., 32 (1993) 1471-1481
[20] A.W. Francis, Ternary Systems of Liquid Carbon Dioxide, 10 (1965) 1
[21] X. Zhang, T. Uemura, K. Matsumura, N. Sayo, K. Hidenori, H. Takaya, Synlett, July (1994) 501-503

Reaction Engineering for Pollution Prevention
M.A. Abraham and R.P. Hesketh (Editors)

Rhodium Catalyzed Homogeneous Hydroformylation of Unsaturated Compounds in Supercritical Carbon Dioxide

D. R. Palo and C. Erkey

Department of Chemical Engineering and Environmental Engineering Program, University of Connecticut, 191 Auditorium Road, Storrs, CT 06269

A novel catalyst, $HRh(CO)[P(p\text{-}CF_3C_6H_4)_3]_3$, was synthesized for homogeneous catalytic hydroformylation of unsaturated compounds in supercritical carbon dioxide. The incorporation of *para*-trifluoromethyl groups to the conventional hydroformylation catalyst, $HRh(CO)[P(C_6H_5)_3]_3$, provided enhanced solubility in supercritical carbon dioxide while maintaining catalyst activity. The substrates 1-octene, 1-decene, 1,7-octadiene, styrene, allylbenzene, *trans*-2-octene, 2-methyl-1-heptene, and cyclohexene were hydroformylated at 50°C and 273 atm. Selectivities were found to be similar to those for the conventional catalyst in organic solvents.

1. INTRODUCTION

Over 6 million tons of aldehydes are produced annually by the homogeneous catalytic hydroformylation of olefins[1]. The shares of the various aldehydes are: C_3 (2%), C_4 (73%), C_5-C_{12} (19%), and C_{13}-C_{18} (6%). The catalysts generally employed are of the form $H_xM_y(CO)_zL_n$; the two transition metals utilized are rhodium and cobalt and the most commonly utilized ligands are phosphines (PR_3 where R = C_6H_5 or n-C_4H_9). Production of C_4 aldehydes from hydroformylation of propene is dominated by rhodium based catalysts whereas higher aldehydes are produced mainly by cobalt catalysts. Since rhodium is about 1000 times more active than cobalt, processes based on Rh catalysts operate at significantly lower temperatures and pressures than processes based on Co catalysts. For example, the UCC liquid recycle process for hydroformylation of propene which uses $HRh(CO)[P(C_6H_5)_3]_3$ operates in the temperature range 85-90°C and at a pressure of 18 bar. In contrast, the BASF process for hydroformylation of 1-octene which uses $HCo(CO)_4$ operates in the temperature range 160-190°C and in the pressure range 250-300 bar. Therefore, substantial savings in operating and capital costs can be achieved if hydroformylation of higher olefins is conducted using Rh based catalysts.

One of the major issues in switching to Rh is the difficulty of the separation of products and catalyst by distillation of the aldehydes. The high boiling points of aldehydes beyond C_7 makes such an operation impractical even under reduced pressure due to thermal stability considerations for the catalyst. A relatively recent development in this field has been the commercialization of a biphasic hydroformylation process by RCH/RP. In this process, the hydroformylation reaction is conducted in the aqueous phase using water-soluble rhodium complexes as catalysts, thus eliminating the problem of separating the catalyst from the product mixture. The process is utilized for production of C_4 and C_5 aldehydes, however

application of this concept to higher olefin production is highly unlikely due to the extremely low solubilities of higher olefins in water. An alternative may be to utilize supercritical fluids as hydroformylation solvents.

A supercritical fluid (SCF) is a fluid that has been heated and compressed above its critical temperature and pressure. At these conditions, SCFs have densities that are greater than those of gases but comparable to those of liquids, thus enabling them to function as solvents. Using SCFs as solvents may have great advantages in catalyst recovery. The solubility of a compound in SCFs is a strong function of temperature and pressure in the vicinity of the critical point. Therefore, the catalyst, products, and reactants may be separated in an efficient manner through temperature and/or pressure programming. Among the SCFs, supercritical carbon dioxide ($scCO_2$) is particularly attractive as a solvent since it is non-toxic, environmentally acceptable, inexpensive, readily available in large quantities, and has a low critical temperature and a moderate critical pressure. It is non-flammable unlike some other SCFs such as ethane and propane, thus its use does not constitute a safety hazard. Today, there are many $scCO_2$ extraction plants operating around the world, indicating the technical and economic feasibility of CO_2-based processes.

Even though $scCO_2$ has many favorable properties as a solvent for homogeneous hydroformylation, there have been surprisingly few pertinent studies in this area. Rathke et al. investigated the cobalt catalyzed hydroformylation of olefins in $scCO_2$,[2] and also performed a number of thermodynamic studies on oxo catalysts in $scCO_2$ using high pressure NMR techniques.[3] The rate of propylene hydroformylation in these studies was found to be comparable to values for other linear-terminal olefins in non-polar liquid media. A more detailed study of cobalt catalyzed propylene hydroformylation was conducted by Guo and Akgerman in the temperature range 66-108°C and the pressure range 93-186 atm.[4] The activation energy of the reaction in $scCO_2$ was found to be comparable to values obtained in conventional organic solvents.

Recently, Kainz et al. described the first rhodium catalyzed hydroformylation in $scCO_2$ using perfluoroalkyl substituted arylphosphanes as ligands.[5] The CO_2-philic fluoroalkyl chains provided the solubility enhancement necessary to dissolve the catalytically active species at high concentrations in the fluid phase. A more detailed study on utilization of such ligands of the form PR_3 (where R = *p*-$C_8H_4F_{13}C_6H_4$, *m*-$C_8H_4F_{13}C_6H_4$, or *p*-$C_8H_4F_{13}C_6H_4O$) for hydroformylation of olefinic substrates in $scCO_2$ was recently reported by Koch and Leitner.[6] Higher regioselectivities were obtained with the modified ligands in $scCO_2$ than those obtained in conventional organic solvents. Another group recently reported hydroformylation in $scCO_2$ using a non-fluorinated trialkylphosphine/rhodium system, finding similar rates and slightly higher n:iso ratios.[7]

In contrast, our group previously described a trifluoromethylated hydroformylation catalyst, *trans*-$RhCl(CO)[P(p\text{-}CF_3C_6H_4)_3]_2$ which exhibited moderate solubility in $scCO_2$. This species efficiently catalyzed the hydroformylation of 1-octene at 343 K and 273 atm after an initial induction period.[8] More recently, we reported on an even more effective catalyst, $HRh(CO)[P(p\text{-}CF_3C_6H_4)_3]_3$, **1**, which exhibits much higher activity for the conversion of 1-octene to C_9-aldehydes in $scCO_2$ with no induction period.[9] Preliminary experiments employing these two catalysts indicate that small amounts of fluorination lead to large increases in solubility in $scCO_2$. In addition, the method employed is much less synthetically demanding than the "long chain" approach described above. In the current

paper, we report the hydroformylation of several different unsaturated compounds in $scCO_2$ using **1**.

2. EXPERIMENTAL

Tris(*para*-trifluoromethylphenyl)phosphine (**2**) was synthesized from 4-bromobenzotrifluoride (**3**) and phosphorus trichloride through a standard Grignard reaction. Under nitrogen, a three-necked flask containing magnesium turnings (2.16 g) in diethyl ether (40 mL) was vigorously stirred while **3** (20 grams) dissolved in diethyl ether (12 mL) was added dropwise at room temperature. The reaction initiated after a small amount of the starting material was added, evidenced by a darkening of the solution and the refluxing of the ether. Once all the starting material was added, the reaction was allowed to proceed to completion, indicated by the dark, brownish-red solution and the disappearance of the magnesium turnings. After cooling the solution to 0°C, phosphorus trichloride (2.3 mL) dissolved in diethyl ether (10 mL) was added dropwise over a period of 30 minutes. The solution was then heated and refluxed for one hour, allowed to cool, and acidified with hydrochloric acid (22 mL, 6 molar). The two-phase solution was then separated, and the ether phase was washed with 3×20 mL of water. The ether solution was reduced, forming a reddish-brown colored solid. The phosphine **2** was recrystallized from isopropyl alcohol, yielding 10 grams of yellowish-white crystals (yield = 24%). ^{1}H NMR [(400 MHz, $CDCl_3$, 30°C, $CHCl_3$) δ = 7.62 (d, J = 7.9), δ =7.40 (t, J = 7.6)]; ^{31}P NMR [(400 MHz, $P(O)Ph_3$, 30°C, $CHCl_3$) δ = -6.3 (s)].

The catalyst **1** was prepared by a modification of the procedure employed by Ahmad, et al. for producing $HRh(CO)[P(C_6H_5)_3]_3$.[10] Under nitrogen, rhodium chloride trihydrate (0.45 g) dissolved in ethanol (20 mL) was added to a refluxing solution of **2** (7.95 grams) in ethanol (60 mL). After 10 minutes, aqueous formaldehyde (19 mL, 37% solution) and ethanolic potassium hydroxide (1.39 g in 35 mL hot ethanol) solutions were added rapidly and successively to the refluxing rhodium/phosphine solution. The solution turned from deep red to yellow over a period of about one minute, after which a large amount of a bright yellow crystals began to precipitate. The solution was refluxed for an additional 10 minutes, then cooled for 15 minutes before filtering off the precipitate. The crystals were then washed with 1:1 ethanol/water, ethanol, and cyclohexane, then dried under vacuum, yielding 2.09 grams (80.3% yield based on rhodium chloride) of bright yellow crystals. The catalyst was weighed into glass ampuoles, which were then sealed under vacuum for use in hydroformylation experiments. FTIR [ν(CO) = 1950 cm^{-1}, ν(RhH) = 2038 cm^{-1}]; ^{1}H NMR [(400 MHz, $CDCl_3$, 30°C, $CHCl_3$) δ = -9.9 (q, J(H,P)=14]; ^{31}P-NMR [(400 MHz, $CDCl_3$, 30°C, $P(O)Ph_3$) δ = 40.2 (d, J(P,Rh)=156).

A schematic diagram of the experimental apparatus for hydroformylation reactions is given in Figure 1. For a typical hydroformylation experiment, a custom manufactured, 54 mL stainless steel reactor (3) fitted with two sapphire windows (Sapphire Engineering, Inc.) and poly-ether-ether-ketone o-rings (Valco Instruments, Inc.), was charged with catalyst (0.065 mmol), a stir bar, and olefin (0.054 mole) under nitrogen. The reactor was sealed and then heated to reaction temperature by a circulating heater (12-Haake FJ) via a machined internal heating coil. The reactor rested on a magnetic stir plate (4), being fitted with a T-type thermocouple assembly (5-Omega Engineering, DP41-TC-MDSS), pressure transducer (6-Omega Engineering, PX01K1-5KGV), vent line (7), and rupture disk assembly (9-Autoclave

Engineers). At reaction temperature, the system was pressurized to 69 atm with equimolar amounts of H_2 and CO from gas cylinders (1), and then further pressurized with CO_2 from a syringe pump (2-ISCO, 260D) to the desired reaction pressure (273 atm). The ampoule shattered upon pressurization of the reactor with CO, marking the beginning of the reaction. The sapphire windows allowed confirmation of a single fluid phase and that the catalyst was completely dissolved in the reaction mixture. For kinetic information, periodic samples were taken through a high pressure sample loop (10) by filling with the supercritical fluid mixture, depressurizing into a sample vial (11), and flushing with solvent from a reservoir (8). The solvent/sample was then analyzed by NMR spectroscopy (Bruker, DX-400 NMR) to determine reactant and product concentrations, and to check for side reactions.

CO_2, H_2, and CO gases (99.999% purity) were obtained from Northeast Airgas, and were further deoxygenated before use. Substrates were obtained either from Acros Chemicals or Aldrich Chemicals, and were freshly distilled from sodium metal under nitrogen or vacuum before each experiment. Hydrated rhodium(III) chloride (99.9%, Alfa Aesar), formaldehyde solution (Fisher Scientific), potassium hydroxide (Fisher Scientific) and magnesium metal (99.8%, Acros Chemicals) were used as received.

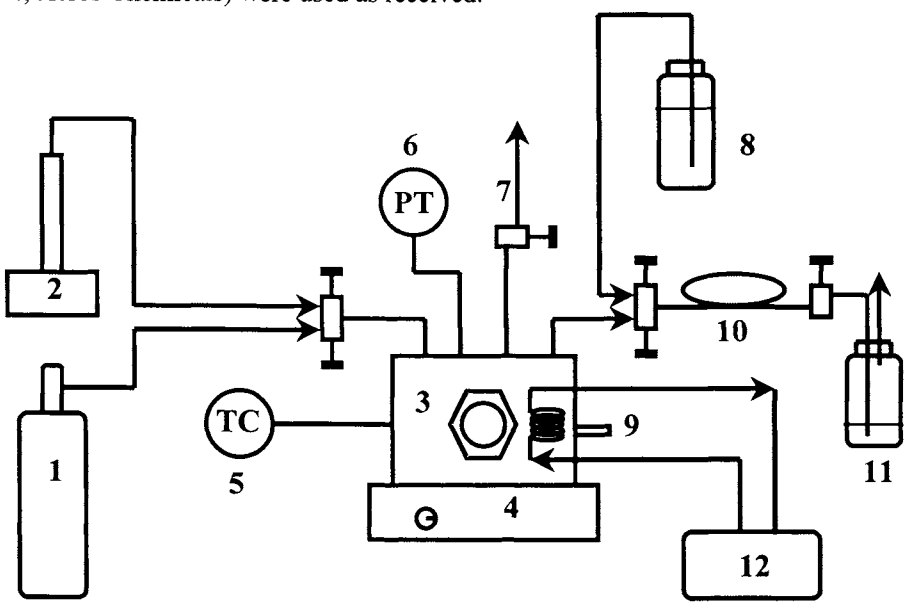

Figure 1. High pressure windowed reactor setup for hydroformylation experiments in $scCO_2$.

3. RESULTS AND DISCUSSION

The concentration versus time data for a typical hydroformylation experiment are shown in Figure 2. The hydroformylation of 1-decene in $scCO_2$ using **1** proceeds with no observable hydrogenation or isomerization. Selectivity was found to be relatively constant during the course of the reaction. However, significant isomerization occurs in the absence of CO/H_2, producing internal double bonds from terminal ones. For this reason, the catalyst was sealed in glass ampuoles to keep it separate from the substrate until CO and H_2 were admitted to the reactor.

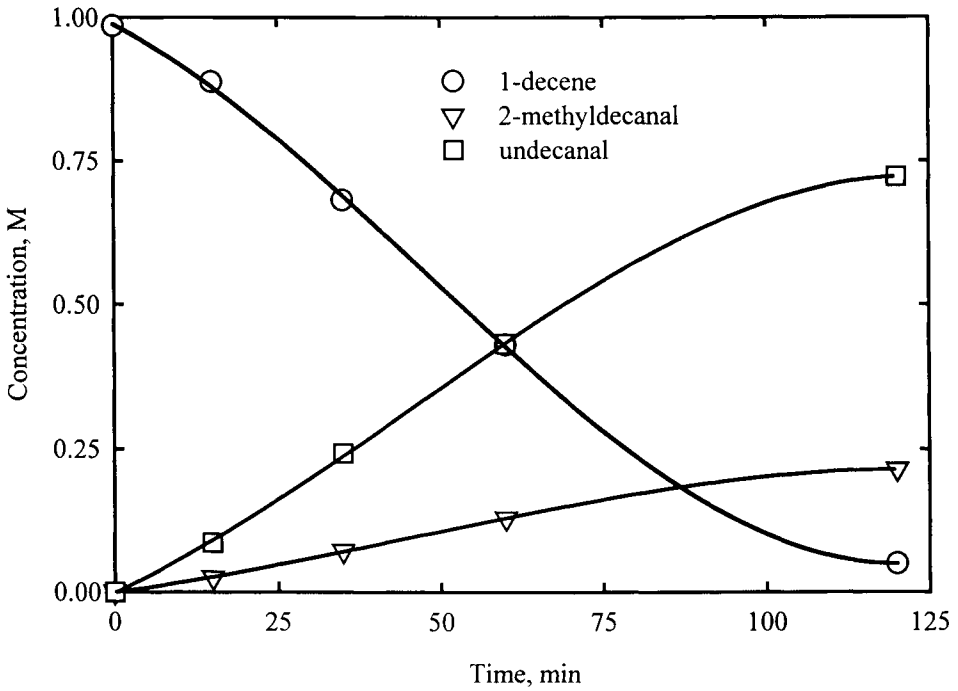

Figure 2. Hydroformylation of 1-decene in $scCO_2$ (T = 50°C, P = 273 atm, V = 54 mL, $[CO]_0 = [H_2]_0 = 1.1$ M, [catalyst] = 1.2 mM, $[substrate]_0 = 0.96$ M).

Reactions involving the five substrates containing unsubstituted terminal double bonds had roughly the same initial rate, as can be seen from Table 1 and showed similar behavior throughout the reaction, as illustrated in Figure 3. For each reaction, 80-90% conversion was achieved in around two hours.

Table 1 lists the initial rates and selectivities observed for various substrates under standard reaction conditions. Initial rates were calculated from the linear portion of each rate curve by estimating the slope in mol dm^{-3} min^{-1}. Not surprisingly, the reaction rates for compounds with unsubstituted terminal double bonds were more than an order of magnitude higher than for compounds with substituted or internal double bonds. Furthermore, the reaction rate for cyclohexene was an additional order-of-magnitude lower than for 2-octene, while 1-octyne was not converted at all.

The trends in reaction rate and selectivity are quite similar to those obtained by Wilkinson using the standard triphenylphosphine catalyst in benzene.[11] It is difficult, however, to compare the two systems directly, owing to the drastically different reaction conditions necessary for $scCO_2$ experiments. The selectivity behavior of the unsubstituted terminal double bonds was similar to that observed previously for 1-octene[9] with n:iso ratios between 2.7 and 3.5. Hydroformylation of styrene, however, produced an 11:1 ratio in favor of the branched product. In the case of 2-methyl-1-heptene, 3-methyloctanal was formed exclusively, and hydroformylation of *trans*-2-octene produced almost equal amounts of the two isomers, 2-methyloctanal and 2-ethylheptanal.

Table 1
Initial rate and selectivity data for hydroformylation of various substrates in $scCO_2$

Substrate	10^4 × Initial Rate[a] mol dm^{-3} min^{-1}	Selectivity (n:iso ratio)
1-Octene	123	3.3
Styrene	111	0.090
1,7-Octadiene	109	3.5
1-Decene	90.1	3.4
Allylbenzene	81.3	2.7
2-Methyl-1-heptene	6.87	∞
Trans-2-octene	3.53	1.3[b]
Cyclohexene	0.246	--
1-Octyne	0.0	--

[a] Conditions: T = 50°C, P = 273 atm, V = 54 mL, $[H2]_0 = [CO]_0$ = 1.1 M, [catalyst] = 1.2 mM, $[substrate]_0$ = 0.96 M
[b] Ratio of 2-methyloctanal to 2-ethylheptanal

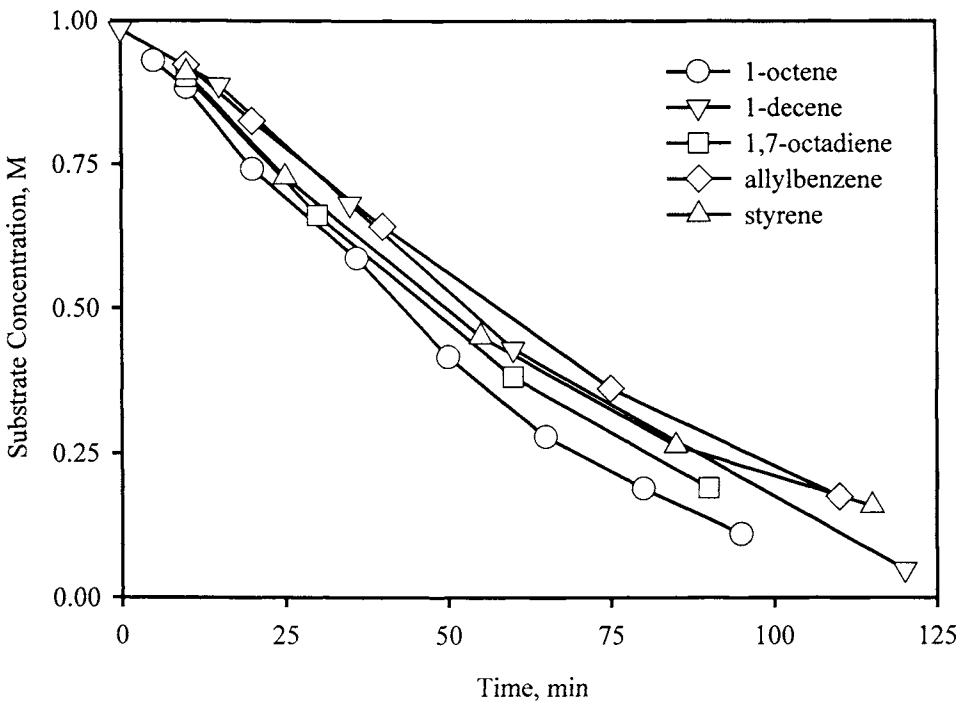

Figure 3. Hydroformylation of various unsaturated compounds in $scCO_2$ (T = 50°C, P = 273 atm, V = 54 mL, $[H_2]_0 = [CO]_0$ = 1.1 M, [catalyst] = 1.2 mM, $[substrate]_0$ = 0.96 M).

ACKNOWLEDGMENTS

Acknowledgement is made to the donors of the Petroleum Research Fund, administered by the ACS, for partial support of this research (ACS-PRF 32299-AC1).

REFERENCES

1. B. Cornils and W. A. Hermann (eds.), Applied Homogeneous Catalysis with Organometallic Compounds, VCH Publishers, New York, NY, 1996.
2. J. W. Rathke, R. J. Klingler and T. R. Krause, Organometallics, 10 (1991) 1350; J. W. Rathke and R. J. Klingler, Cobalt Carbonyl Catalyzed Olefin Hydroformylation in Supercritical Carbon Dioxide, US Patent No. 5 198 589 (1993).
3. R. J. Klingler, and J. W. Rathke, Inorg. Chem., 31 (1992) 804; J. W. Rathke, R. J. Klingler, and T. R. Krause, Organometallics, 11 (1992) 585; R. J. Klingler, and J. W. Rathke, J. Am. Chem. Soc., 116 (1994) 4772.
4. Y. Guo and A. Akgerman, Ind. Eng. Chem. Res., 36 (1997) 4581.
5. S. Kainz, D. Koch, W. Baumann, and W. Leitner, Angew. Chem. Int. Ed. Engl., 36 (1997) 1628; Angew. Chem. 109 (1997) 1699.
6. D. Koch and W. Leitner, J. Am. Chem. Soc., 120 (1998) 13398.
7. I. Bach and D. J. Cole-Hamilton, Chem. Commun., (1998) 1463.
8. D. R. Palo and C. Erkey, Ind. Eng. Chem. Res., 37 (1998) 4203.
9. D. R. Palo and C. Erkey, Ind. Eng. Chem. Res., 38 (1999) 2163.
10. N. Ahmad, J. J. Levison, S. D. Robinson, M. F. Uttley, Inorg. Synth., 28 (1990) 81.
11. C. K. Brown and G. Wilkinson, Tett. Lett., (1969) 1725.

Reaction Engineering for Pollution Prevention
M.A. Abraham and R.P. Hesketh (Editors)

Production of Hydrogen Peroxide in CO_2

D. Hâncu and E. J. Beckman

Chemical Engineering Department, University of Pittsburgh
1249 Benedum Hall, Pittsburgh, PA 15261

H_2O_2 production via sequential hydrogenation-oxidation of anthraquinones represents a potentially efficient process application of liquid or supercritical CO_2. Both mono- and di-functionalized anthraquinones (FAQs) were synthesized by attaching CO_2-philic polymers chains (-$CF(CF_3)CF_2O$-) either to mono- or diaminoanthraquinones or to (hydroxymethyl)-anthraquinone. All FAQs synthesized were highly soluble in CO_2 and presented liquid-liquid phase behavior with minimum miscibility pressure between 170 and 210 bar. Cloud-point pressures were shifted to lower values by using non-hydrogen bonding linkers between AQ block and CO_2-philic tails or by increasing the CO_2-philic content of FAQs. Pd-catalyzed hydrogenations of fluoroether functionalized anthraquinones (FAQs) were conducted in liquid CO_2 (P=235 bar) at room temperature in a high-pressure batch reactor under a ten fold excess of hydrogen, while varying the catalyst loading and catalyst particle size. True kinetic constants, diffusion coefficients and effective diffusivities were determined by simultaneous regression of the kinetic data. The ^1H NMR analysis of the FAQs after a hydrogenation-oxidation cycle showed no indication for "deep" hydrogenation or degradation of the linker. Using FAQs with relatively short fluoroether tails, we could readily achieve conditions where hydrogenation in CO_2 was kinetically controlled.

1. INTRODUCTION

Carbon dioxide is generally considered to be an environmentally benign solvent because it is naturally abundant, relatively non-toxic and non-flammable. Although CO_2 itself is inexpensive, the capital and operating costs for a CO_2-based process can be prohibitively high if the technology is misapplied or if process is not optimized. The current use of liquid or supercritical CO_2 in chemical applications reveals that the replacement of an organic solvent with CO_2 becomes advantageous if the process contains some special characteristics. Process attributes, which invites discussion of the use of CO_2 as solvent include: (1) food or pharmaceutical processing; (2) gas-liquid reactions; (3) liquid-liquid extraction involving hydrophobic and hydrophilic phases; (4) plasticization of polymers; (5) generation of "unavoidable" emissions; (6) CO_2 as raw material.

The use of CO_2 in the above listed processes can produce better products in a more sustainable fashion if one considers certain process constraints while using CO_2 as a working solvent.

(1) The operating pressure should be minimized by using CO_2-philic compounds. Due its low dielectric constant, high-pressures are often required to dissolve large amounts of organics in CO_2.

(2) The products should be recovered with the lowest pressure drop possible. The use of high-pressure drop will increase the operating costs, due the need to recompress the gas after each reaction cycle.
(3) Even though the use of CO_2-philic materials lowers the operating pressure, they are more expansive than their CO_2-phobic counterparts, therefore they should be recycled in the process as much as possible.
(4) The CO_2 flow rate should be minimized in order to reduce the equipment size. However, if the use of more CO_2 will lower the viscosity of the working solutions and in this way, the operating costs and the diffusional effects, the use of more CO_2 could become economically advantageous.

In the light of the previous process constraints imposed by using CO_2 as a working solvent, the anthraquinone / anthrahydroquinone process to produce hydrogen peroxide appears to be a good application target for CO_2 technology (Figure 1). In the conventional process, an alkylanthraquinone (AQ) dissolved in a mixture of solvents (usually a combination of aromatic hydrocarbons with an aliphatic alcohol) is hydrogenated over a Pd-supported catalyst in a three-phase reactor to produce anthrahydroquinone (AQH_2). The latter is then transferred to the second reactor where is oxidized back to the initial AQ while forming one mole of hydrogen peroxide; the latter is stripped into water via liquid-liquid extraction. The hydrogenation-oxidation cycle is completed by transferring the AQ back to the hydrogenation reactor [1].

Although the anthraquinone / anthrahydroquinone process has been used to produce hydrogen peroxide for over 40 years, it exhibits a number of innate disadvantages from the use of an organic solvent and from the phase behavior in each of the reactors [2].
(1) Energy and raw material consumptions are greater than optimal. Both the hydrogenation and oxidation processes are limited by the transport of the gases (hydrogen and oxygen) through the gas-liquid (g-l) and / or liquid-solid (l-s) interfaces and consequently higher reactor volumes and temperatures than optimum are required to compensate for these limitations.

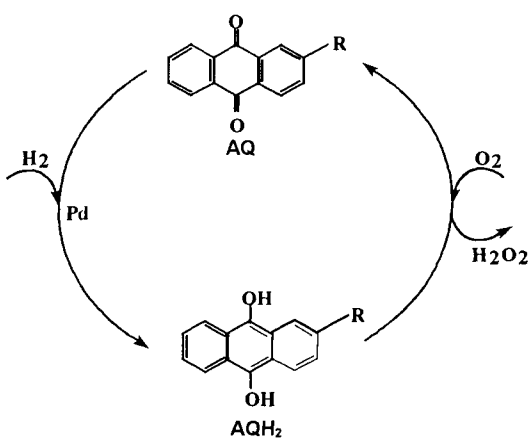

Figure 1. Anthraquinone-anthrahydroquinone process of generation of hydrogen peroxide

(2) The conventional process uses a mixture of solvents because no single solvent was found to meet all the criteria required by the cyclic process. An ideal solvent would exhibit as many as possible of the following properties: (a) good solvent power for both AQ and AQH_2; (b) good solvent for both hydrogen and oxygen; (c) low solubility in water and (d) high distribution coefficient for hydrogen peroxide in a mixture with water.
(3) The aqueous solution of hydrogen peroxide is contaminated with traces of organics during the extraction stage and further purification is required. During the purification and concentration (normally by distillation), hydrogen peroxide can be thermally decomposed or can form explosive mixtures with the organic impurities.
(4) Anthraquinone is degraded during the hydrogenation-oxidation cycles due to the hydrogenation of the aromatic rings or due to hydrogenolysis of the C=O bonds [3]. The side products have to be continuously removed, increasing the consumption of the raw materials. To minimize the formation of the side products, the conversion of the hydrogenation reaction is kept between 40-50%.

The CO_2-based process for production of hydrogen peroxide can benefit from the environmental advantages of using CO_2 and the process is also economically feasible. The environmental and economic advantages are summarized below.

Environmental Advantages

1. Elimination of the organic solvent via replacement by CO_2 eliminates the contamination of the aqueous product. This solves both the economic and environmental problems associated with the extraction and purification stages of the process.
2. Waste generated in the process is reduced due to the minimization of the side reactions. Due to the high miscibility of hydrogen and oxygen in CO_2 at elevated pressures, the mass transfer limitations during hydrogenation/oxidation are eliminated and the reactions can be conducted under kinetically controlled regimes. Hence, one could move to a plug-flow operation in the hydrogenation reactor, minimizing the backmixing and the side reactions.
3. The use of CO_2 as the working fluid eliminates the gas phase in the hydrogenation reactor and the safety hazard of having a hydrogen headspace at high-pressure.
4. Emissions are significantly reduced.

Economic Advantages

The high capital and operating costs often times associated with the use of elevated pressure can be lowered owing to the special features of the AQ/AQH_2 process:

1. In a CO_2-based $AQ\text{-}AQH_2$ process, the CO_2 travels in a loop (where pressure is relatively constant), and the product can be recovered without a large pressure drop. The operating costs are lowered because there is no need to recompress the gas after each reaction cycle.
2. The use of kinetically controlled regimes will increase the amount of hydrogen peroxide produced per cycle while reducing the equipment size and lowering the reaction temperature. Also, anthraquinone degradation is diminished, lowering raw material consumption.
3. Continuous processing is feasible, minimizing the equipment size.
4. The operating pressure can be minimized, or the concentration of AQ in the system maximized at constant pressure, via use of a CO_2-philic AQs.
5. AQ is continuously recycled during the process, and thus the financial impact of anthraquinone redesign for use in CO_2 is minimized.

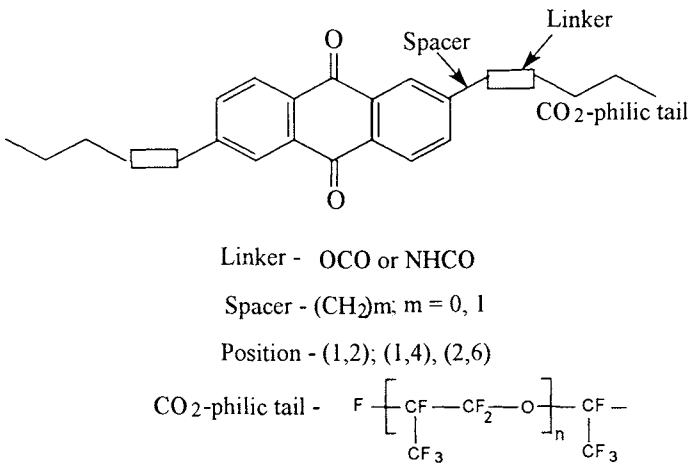

Figure 2. General chemical formula of functionalized anthraquinone

The primary obstacle to the use of CO_2 as the working fluid in hydrogen peroxide production from the AQ-AQH_2 system is that conventional 2-alkylAQs exhibit poor to negligible solubility in carbon dioxide at pressures up to 200 bar [4]. Thus, the initial focus of our research has been to design and generate CO_2-philic analogs of 2-ethylAQ that would support the production of hydrogen peroxide via sequential hydrogenation and oxidation. A family of functionalized anthraquinones (FAQs) has been designed and synthesized by attaching perfluoroether tails to either amino or hydroxyanthraquinones. In a typical FAQ, a CO_2-philic tail (perfluoroether polymer), is attached through an amidic or ester linker and a spacer to different positions of the anthraquinone rings (Figure 2). Both the phase behavior of FAQs in CO_2 and the reactivity of these materials in the hydrogenation process were studied as a function of the following structural parameters: (1) length of the CO_2-phlic tail; (2) nature of linker / spacer; (3) topology of the tails on the anthraquinone rings.

2. EXPERIMENTAL

2.1. Synthesis of perfluoroether acid chloride (Kr-COCl)

Poly(perfluoropropylene oxide) monofunctionalized with a terminal acid chloride group (Kr-COCl) (FW= 2500, 5000, and 7500) was prepared from the reaction between the corresponding carboxilic acid (Krytox functional fluids, FSL (FW=2500), FSM (FW=5000), FSH (FW=7500), Dupont) and thionyl chloride (Aldrich) as described elsewhere [5].

2.2. Synthesis of Functionalized Antraquinones (FAQs)

Typically, 2 mmol of poly(perfluoropropylene oxide) acid chloride (FW = 2500, 5000, and 7500) and 0.892 g (4 mmol) of monoaminoanthraquinone (1 or 2-aminoanthraquinone, Aldrich) were heated at 100 °C under a nitrogen atmosphere for five hours. After completion, the product was dissolved in perfluoro-1,3-dimethylcyclohexane, and the excess amino-anthraquinone was removed by filtration and the solvent evaporated under vacuum.

The same method was used to synthesize di-amido FAQs. 4.5 mmol (0.356 g, 0.36 ml) of pyridine (as HCl scavenger) was added to a mixture of 4 mmol of perfluoroether acid chloride

and 2 mmol (0.472 g) of diaminoanthraquinone (1,2; 1,4 and 2,6-diaminoanthraquinone, Aldrich). After heating at 100 °C for 5 h, the final product was dissolved in perfluoro-1,3-dimethylcyclohexane, washed with 10% HCl solution, and the solvent was then evaporated under vacuum. Finally, the product was washed with acetone. [IR: disappearance of 1806 cm^{-1} peak (COCl) and appearance of a new peak at 1720-1740 cm^{-1} (CONH)].

In a typical experiment for synthesis of ester FAQs, 3.5 mmol of fluoroether acid chloride (FW = 700 (Lancaster), FW = 2500, 5000, 7500 (prepared as above)), was added dropwise to a mixture of 0.953 g (4 mmol) of 2-(hydroxymethyl)anthraquinone (Aldrich) and 0.32 ml (0.31 g, 4 mmol) of pyridine. After 10-15 min, 30 cm^3 of 1,1,2-trifluorotrichloroethane was added and the mixture was refluxed for 3 h. After completion, pyridinium chloride (white salt) formed in the reaction was removed by vacuum filtration. Excess pyridine was removed by washing with a 5 % HCl solution (3 x 10 ml), and the solvent (along with water emulsified during the washing) was removed by evaporation under vacuum in the presence of 5 ml of benzene. [IR: appearance of the ester peak at 1780-1785 cm^{-1} and the disappearance of the peak at 4.7 ppm (OH) in the ^1H NMR spectrum].

2.3. Phase behavior measurements

The phase diagrams of FAQs were determined in a high-pressure, variable-volume view cell (D. B. Robinson and Associates) as described previously [6].

2.4. Hydrogenation of FAQ and oxidation of $FAQH_2$ in liquid CO_2

Both hydrogenation of FAQ and oxidation of $FAQH_2$ were conducted in high-pressure batch reactors at room temperature and P=235 bar. The experimental setup shown in Figure 3 consists of: (1) two 35 cm^3 high-pressure batch reactors constructed at the University of Pittsburgh; (2) two syringe pumps (High-pressure Equipment, 30 cm^3) where the H_2–CO_2 and O_2–CO_2 mixtures were prepared; (3) a high-pressure recirculating pump (Micropump); (4) high-pressure UV spectrometer (Linear Systems).

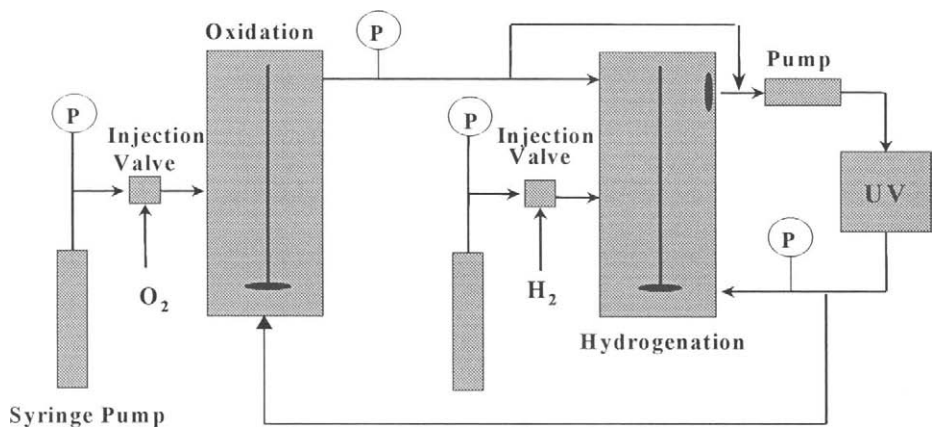

Figure 3. Experimental setup for generation of hydrogen peroxide in CO_2

In a typical experiment, known amounts of Pd/Al_2O_3 catalyst (Aldrich) and FAQ were charged to the hydrogenation reactor and the system was then evacuated to eliminate traces of oxygen which might interfere with the hydrogenation reaction. The solution of FAQ in CO_2 was prepared in the hydrogenation reactor and the CO_2-H_2 and CO_2-O_2 mixtures in the syringe pumps. After injection of H_2 to the hydrogenation reactor, the reaction mixture was recirculated through the UV spectrometer, and the kinetics of hydrogenation reaction was followed by measuring the disappearance of the FAQ peak in the UV spectrum. After completion, the solution of $FAQH_2$ was transferred to the oxidation reactor, oxygen was injected, and the oxidation was followed by measuring the rate of appearance of the FAQ peak (310-330 nm^{-1} region) in the UV spectrum.

3. RESULTS AND DISCUSSION

3.1. Phase behavior of binary system CO_2-FAQ

All functionalized anthraquinones are liquids at room temperature or amorphous materials which liquify almost immediately in the contact with CO_2. The phase diagrams determined experimentally represent only a portion of the generalized liquid-liquid phase envelope shown in Figure 4. Above the minimum miscibility pressure (P_{min}), CO_2 and FAQ are miscible in any proportion and the process can be conducted either in a dilute regime to accommodate concentration constraints of the UV detector or in a concentrated regime where CO_2 acts more as a viscosity reducing-agent. Phase behavior studies revealed that all FAQs investigated exhibit liquid-liquid phase behavior which is influenced by (1) length of the CO_2-philic tail; (2) nature of the linker and spacer; (3) topology of the tails on the anthraquinone rings.

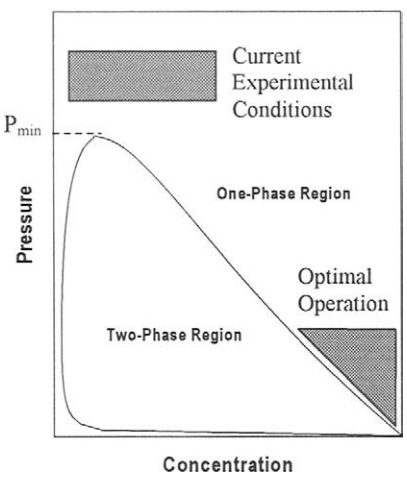

Figure 4. Generalized liquid-liquid phase diagram.

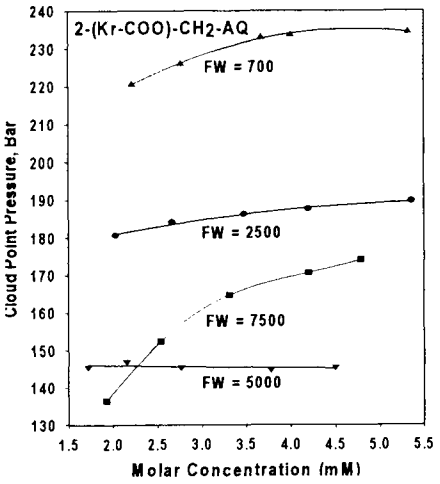

Figure 5. Effect of tail length on phase behavior of 2-(Kr-COO)-CH_2-AQ (T =25 °C) (Kr – perfluoroether polymer)

The dependence of the cloud-point pressure curves on the molecular weight of the CO_2-philic tail shows that there is an optimum chain length for which the cloud-point pressures are minimized. As shown in Figure 5, as one increases the length of the CO_2-philic tail in the series of ester FAQs, the cloud-point curves shift to lower pressures for the lower molecular tails. For FW = 5000, the cloud-point curve reaches a minimum, while a further increase in CO_2-philic tail length brings about a shift of the cloud-point pressures to higher values.

We studied the influence of the linker on the phase of behavior of FAQ in CO_2 for a family of FAQs having the same length of the CO_2-philic tail (Figure 6). We designed four types of linkers: (1) a secondary amidic linker bonded to the 2 position on the AQ rings which can form only intermolecular H bonds; (2) a secondary amidic linker bonded to the 1 position of the AQ rings that can form either inter or intramolecular H bonds and (3-4) a tertiary amidic and an ester linker, which cannot form H bonds with the AQ carbonyl groups. As expected, the capability of the linker to form intermolecular H bonds produces cloud-point curves at higher pressures as seen for 1 and 2-amido FAQs. Between the tertiary amide and the ester, the ester FAQ has the lower cloud-point curve, revealing a thermodynamic preference by CO_2 for the less polar linker.

Diamido functionalized AQs were synthesized by attaching two 2500 FW CO_2-philic tails in three different configurations on the anthraquinone rings: (1,2), (1,4) and (2,6). Their cloud-point curves are shown in Figure 7. The high cloud-point pressures exhibited by the 2,6-Twin(2500) isomer can be the result of both high molecular symmetry and intermolecular H bonding of the secondary amidic linker. These results suggest that a strategy to lower the minimum miscibility pressure of FAQ in CO_2 would be to attach a number of small to medium CO_2-philic tails in an asymmetric configuration through non-H bond donating linking groups such as esters or ethers.

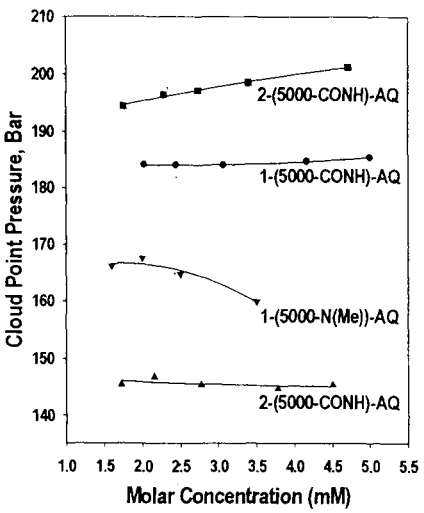

Figure 6. Effect of head group on phase behavior of FAQs in CO_2: (T = 25 °C, Number in chemical formula shows the molecular weight of the CO_2-philic tail)

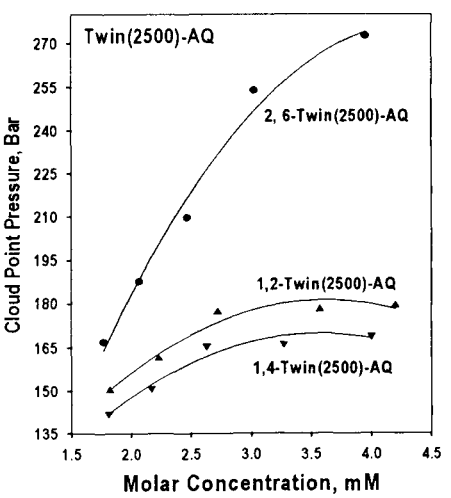

Figure 7. Effect of the topology of tails on phase behavior of di-amido FAQs in CO_2 (Number in chemical formula shows the molecular weight of the CO_2-philic tail)

3.2. Hydrogenation of Functionalized Anthraquinone in CO_2

3.2.1. General procedure for evaluation mass transfer and kinetic parameters

For a given FAQ, we ran a series of hydrogenations while varying the particle size (d_p) of the catalyst and the catalyst loading (w) to identify the controlling regimes in the process and to determine the true kinetic constant (k_c), diffusion coefficient (D_e) of FAQ in bulk CO_2 and the effective diffusivity (D_{eff}) of FAQ inside the catalyst pores. The model includes the following assumptions:

(1) The reaction is first order with respect to FAQ.
(2) The only transport limitations considered are because of the liquid-solid mass transfer of FAQ and intraparticle diffusion of FAQ inside the catalyst pores, due to the total miscibility of hydrogen and CO_2 at elevated pressures [7].
(3) FAQ is considered the limiting reactant inside the pores of the catalyst, because of the large excess of hydrogen in the system.

Under these assumptions, the reaction rate (R) is given by

$$R = k_g \cdot c_{FAQ} \tag{1}$$

The global rate constant (k_g) can be written in terms of the l-s mass transfer coefficient (k_s), the true kinetic constant (k_c), the catalytic effectiveness factor (η), the catalyst loading (w) and the external surface area of the catalyst particle (a_p) as in reference [8]:

$$\frac{1}{k_g} = \frac{1}{k_s \cdot a_p} + \frac{1}{w \cdot \eta \cdot k_c} \tag{2}$$

We then expand equation (2) using expressions previously derived for k_s for the case of mass transport to particles in agitated tanks, the expression for the catalytic effectiveness factor (η) written for a first order reaction, and the area of a spherical particle. The global rate constant k_g can then be written as [5]:

$$\frac{1}{k_g} = \frac{1}{w} \cdot \frac{1}{k_{eff}} \tag{3}$$

where k_{eff} is given by

$$\frac{1}{k_{eff}} = \frac{\rho_p}{6 \cdot F_c \cdot \omega(D_e, d_p)} + \frac{\phi(D_{eff}, d_p)}{k_c} \cdot \frac{1}{\left(\coth(3\phi) - \frac{1}{3\phi}\right)} \tag{4}$$

In Eq. 4, ϕ is Thiele modulus written for a first order reaction, F_c is the shape factor as defined in ref. [9], while ω (D_e, d_p) is given by [5]:

$$\omega(D_e, d_p) = \frac{2 \cdot D_e + 0.4 \cdot Q \cdot d_p \cdot D_e^{\frac{2}{3}}}{d_p^{\,2}} \quad (5)$$

and Q is a constant:

$$Q = \frac{e^{\frac{1}{4}} \cdot \rho_L^{\frac{5}{12}}}{\mu_L^{\frac{5}{12}}} \quad (6)$$

where ρ_L and μ_L are the density and viscosity of liquid CO_2 calculated at the experimental conditions and e is the energy supplied per unit mass by the stirring unit, calculated as in [8].

The following steps were followed to determine k_c and D_e's and D_{eff}'s for a certain group of functionalized anthraquinones having the same AQ block, spacer, and linker, but different CO_2-philic tail lengths:

(1) Determine global rate constant (k_g) by fitting the experimental data ($c_{FAQ} = f(t)$) with an exponential 1st order function while varying the particle size catalyst and catalyst loading.
(2) Determine k_{eff} by plotting k_g as a function of the catalyst loading (w) for different particle size catalysts (Eq. 3).
(3) Determine k_c, D_e's, and D_{eff}'s by fitting experimental data $1 / k_{eff} = f(d_p)$ with the function given in Eq. 4. The simultaneous regression was run considering that for all FAQs in the group the intrinsic rate constant (k_c) is the same, while D_e and D_{eff} depend on the length of the CO_2-philic tail.

3.2.2. Mass transfer effects

Figure 8 shows the experimental and regressed effective rate constant for the group of amide-FAQs with different lengths of the CO_2-philic tails. For all three FAQs, k_{eff} is dependent on d_p indicating that the reaction is under a mixed "diffusional-kinetic" regime.
To quantify the diffusional effects, the regressed value of k_c was used to calculate the overall effectiveness factor β ($\beta = k_{eff} / k_c$). Table 1 lists the overall effectiveness factors for both amide and ester FAQs at varying particle sizes and varying CO_2-philic tail lengths. For small CO_2-philic tails and small particle size catalysts, β is close to 1 and the reaction is kinetically controlled. By increasing either the particle size of the catalyst or the size of the CO_2-philic tail, beta drops to values of 0.1-0.3 indicating that in this case the diffusion of FAQ within the catalyst pores is the controlling step in the process. The individual contribution of the liquid-solid diffusion to the mass transfer limitations was studied by varying the mixing rate in the hydrogenation of 2-(5000-CONH)AQ catalyzed by two different catalyst sizes. As shown in Figure 9, for the powdered catalyst (d_p = 0.0032 cm) the reaction rate is not influenced by the stirring rate, indicating that the l-s mass transfer resistances are negligible in this case. For the 0.04 cm catalyst, the reaction rate constant depends on the stirring rate and therefore the mass transfer limitations are due to both liquid-solid and intraparticle diffusion.

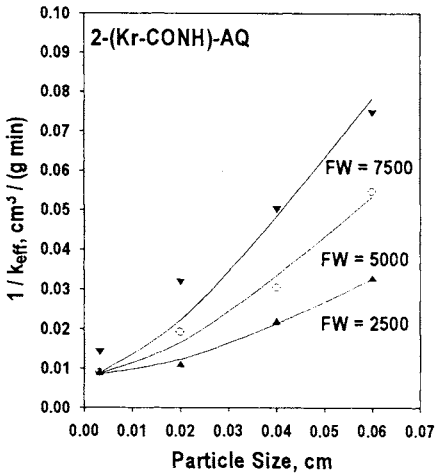

Figure 8. Effect of d_p on $1/k_{eff}$ for 2-(Kr-CONH)-AQ.(Kr-perfluoroeter polymer).

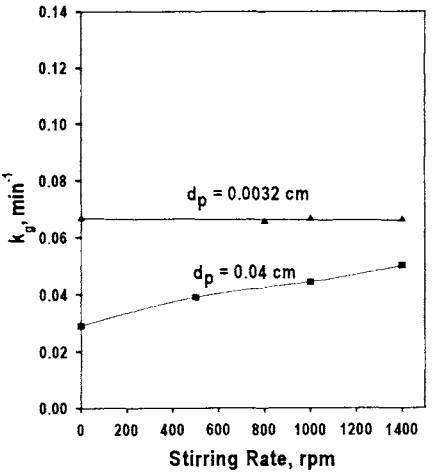

Figure 9. Effect of the stirring rate on reaction rate for 2-(5000-CONH)-AQ: (▲) 0.0032 cm (w = 1.4 g/l); (■) 0.04 cm (w = 2.5 g/l)

3.2.3. Diffusion Coefficients of FAQs in CO_2

The resulting diffusion coefficients are in the range of 10^{-3} -10^{-4} cm^2/s, in good agreement with other values reported in the literature for diffusion coefficients of organic substances in supercritical CO_2 away from the critical point (Table 2) [10]. The fact that the diffusion coefficients vary inversely with the molecular weight of FAQs can explain the dependence of the controlling regimes on the length of the CO_2-philic tail. For small CO_2-philic tails, diffusion is fast, and the reaction is kinetically controlled. When increasing the length of the CO_2-philic tail, the diffusion coefficients decrease and diffusion becomes the rate determining step of the process.

Table 1
Overall effectiveness factors (β) for hydrogenation of FAQs in CO_2 (P = 235 Bar; T =25 °C)

d_p[(a)] cm	$\beta = k_{eff} / k_c$[(b)] 2-(Kr-COO-CH_2)-AQ[(c)]			$\beta = k_{eff} / k_c$ 2-(Kr-CONH)-AQ		
	700[(d)]	2500	5000	2500	5000	7500
0.0032	~1	0.92	0.55	0.9	0.9	0.65
0.02	0.71	0.84	0.37	0.75	0.4	0.3
0.04	0.55	0.42	0.26	0.35	0.25	0.15
0.06	0.32	0.21	0.11	0.25	0.15	0.1

(a) d_p - Average catalyst particle diameter. (b) k_{eff} – effective rate constant calculated from Eq. 3; k_c – "true" kinetic constant regressed from Eq. 4. (c) Kr – perfluoroether polymer. (d) Molecular weight of the perfluoroether polymer attached to AQ block.

Table 2
Kinetic and mass transfer parameters determined by regression (P = 235 bar, T = 25 °C)

2-(Kr-NHCO)AQ[a]				2-(Kr-COO-CH_2)AQ			
FW	k_c[b]	D_e[c]	D_e / D_{eff}	FW	k_c[c]	D_e[c]	D_e / D_{eff}
700	-	-		700	3.8	13.5	4.3
2500	2.0	4.8	5.1	2500	3.8	7.0	3.5
5000	2.0	2.1	4.7	5000	3.8	2.5	3.8
7500	2.0	1.13	4.4	7500	-	-	
2-etAQ	0.47 [4]						

(a) Chemical formula defined as in Table 1. (b) [cm^3 / (g s)]. (c) [cm^2/s 10^4]. (d) reference 11.

3.2.4. Intrinsic reactivity of functionalized anthraquinones

In Table 2, the true kinetic constants (k_c) for the amide and ester FAQs are compared to the corresponding value calculated for 2-etAQ in organic solvents. Ester FAQs are twice as reactive as the amide variants while the amide FAQs in CO_2 are 4 times more reactive than 2-etAQ in organic solvents. We suspect that the electronic effect of the group attached to the AQs block plays an important role. The acyl-amino group (NHCO) is a mildly electron donating group, stabilizing the quinone in the redox equilibrium quinone-hydroquinone. The ester group separated by the methylene spacer from the aromatic rings has an opposite effect, stabilizing the hydroquinone by its electron withdrawing effect.

3.2.5. Side reactions

Hydrogenation of anthraquinone can form a wide range of products, depending on the catalyst loading, temperature, and amount of hydrogen allowed to react. Under an excess of hydrogen and long reaction time, two type of side products can be formed: (1) products of aromatic ring hydrogenation; (2) products of hydrogenolysis (anthrone and derivatives) [3]. The behavior of 2-(5000-COO-CH_2)AQ in a hydrogenation-oxidation cycle was followed by NMR spectroscopy, as shown in Figure 10. The ratio of the integrated peaks in the aromatic region remained unchanged after the reaction cycle, indicating that no deep hydrogenation or degradation of the ester linker took place under the experimental conditions.

3.3. Oxidation of functionalized anthrahydroquinone ($FAQH_2$) in CO_2

Oxidation of functionalized anthrahydroquinone ($FAQH_2$) was followed by measuring the rate of appearance of the FAQ peak in the UV spectrum. Preliminary oxidation experiments performed using 2-(7500-CONH)AQ show that (1) the initial FAQ is fully recovered after one hydrogenation–oxidation cycle, based on the initial and final values of the UV absorbance of FAQ (Figure 11); (2) the oxidation reaction is fast, probably because of the homogeneity of the reaction mixture. We are currently investigating the reactivity of $FAQH_2$ as a function of the length of the CO_2-philic tail and the nature of the linker – spacer.

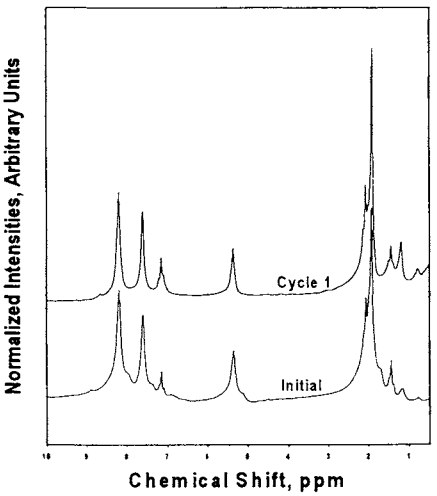

Figure 10. Performance of 2-(5000-COO-CH_2)AQ during a hydrogenation-oxidation cycle

4. CONCLUSIONS

All functionalized anthraquinones (FAQs) synthesized exhibit a liquid-liquid phase envelope in CO_2 with a minimum miscibility pressure between 170 and 210 bar. A strategy to lower the minimum miscibility pressure is to use non-H bonding linkers and multiple CO_2-philic tails attached in a non-symmetrical configuration on the AQ rings. Reactivity of FAQs in Pd-catalyzed hydrogenation is enhanced by including a spacer between the AQ block and the CO_2-philic tails. For small particle size catalyst and low molecular weight tails, hydrogenation of FAQ is kinetically controlled.

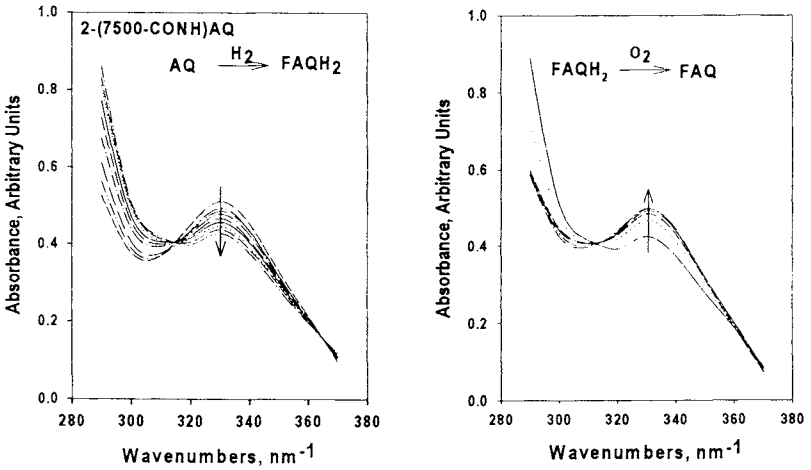

Figure 11. Hydrogenation and oxidation of 2-(7500-CONH)-AQ in liquid CO_2 followed by UV spectroscopy

REFERNCES

1. R. Powell, Hydrogen Peroxide Production, Noyes Develop. Corp., Park Ridge, 1968.
2. (a) H. T. Hess, Hydrogen Peroxide. in Kirk-Othmer Encyclopedia of Chemical Engineering, 4th edition, Vol. 13, John Wiley & Sons, Inc., New York, 1995, 961. (b) T. E. Guenter,. Hydrogen Peroxide. in Encyclopedia of Chemical Processing and Design. Vol. 27, Marcel Dekker, New York, 1988, 27.
3. (a) A. Drelinkiewicz, J. Mol. Catal., *75* (1992), 321. (b) A. Drelinkiewicz, J. Mol. Catal A: Chem., 101, (1995), 61. (c) E. Santacesaria, M. Di Serio, R. Velloti, U. Leone, J. Mol. Catal. 94, (1994), 37.
4. (a) P. Swidersky,. D. Tuma, G. M. Schneider, J. Supercrit. Fluids, 9, (1996), 12. (b) S. N. Joung, K. P. Yoo, J. Chem. Eng. Data, 43, (1998), 9.
5. D. Hâncu, E.J. Beckman, Ind. Eng. Chem. Res., (1999), in press.
6. A. V. Yazdi, E. J, Beckman,. Ind. Eng. Chem. Res., 35, (1996), 3644.
7. C. Y. Tsang, W. B. Streett, Chem. Eng. Sci. 36, (1981), 993.
8. P. A. Ramachandran,, R.V. Chaudhari, Three-Phase Catalytic Reactors, Gordon and Breach, Science Publishers, Inc., New York, 1983.
9. Y. Sano, N. Yamaguchi, T. Adachi, J. Chem. Eng. Jpn., 7, (1974), 255.
10. (a) A. Akgerman, C. Erkey, M. Orejuela, Ind. Eng. Chem. Res., 35, (1996), 911.(b) C. M. Silva, E. A. Macedo, Ind. Eng. Chem. Res., 37, (1998), 1490.
11. E. Santacesaria, M. Di Serio, R. Velloti, U. Leone, Ind. Eng. Chem. Res., 33, (1994), 277.

Reaction Engineering for Pollution Prevention
M.A. Abraham and R.P. Hesketh (Editors)

Cellulose hydrolysis in supercritical water to recover chemicals

T. Adschiri, M. Sasaki, Z. Fang, Y. Fukushima and K. Arai*

Department of Chemical Engineering, Faculty of Engineering, Tohoku University,
07 Aza-Aoba, Aramaki, Aoba-Ku, Sendai 980-8579, Japan

Cellulose decomposition experiments were conducted in subcritical and supercritical water (25 MPa, 320 – 400 °C and 0.05 – 10.0 s). At 400 °C hydrolysis, products were mainly obtained, while in 320 - 350 °C water, pyrolysis products were main products. To understand this change of product distributions around the critical temperature, kinetic studies were conducted for reactions of cellulose, cellobiose and glucose in subcritical and supercritical water. Below 350 °C, the cellulose hydrolysis rate was slower than glucose or cellobiose decomposition rate. However, above 350 °C, the cellulose hydrolysis rate drastically increased and became higher than glucose or cellobiose decomposition rate. For understanding the change of cellulose hydrolysis rate around 350 °C, direct observation of the reaction field by using a diamond anvil cell (DAC) was conducted. Below 280 °C, cellulose particles became gradually smaller with time. However, the shrinking rate of the particles increased greatly around 300 °C. In the range of temperature from 300 to 320 °C, cellulose disappeared without changing its particle shape. After 2 hours cooling of the produced solutions at room temperature, white precipitates came out from the solutions, which was found to be cellulose-like materials which had been solubilized in high temperature water. These results suggest that cellulose can be dissolve in high temperature water, which is probably because of the cleavage of intramolecular and intermolecular hydrogen linkages in cellulose crystal. Thus, a homogeneous hydrolysis atmosphere is formed in high temperature water and this probably results in the drastic increase of the cellulose hydrolysis rate above 350 °C.

1. INTRODUCTION

Development of global economies that can be sustained in view of the environment is of great importance. The concept of sustainability includes the issue of carbon dioxide emission, which leads to the green house effect on the planetary climate, as well as the waste environmental problem. Efficient energy use and material recycle are the key for solving these problems. For the reduction of carbon dioxide emissions, the use of fossil fuels can be substantially reduced by introducing high efficiency energy conversion systems or methodologies. In other words, material recycle has the potential to solve many environmental waste problems and also to reduce petroleum consumption, which is important for creating and maintaining economies.

A major component of the wastes is the municipal and agricultural wastes, namely, biomass waste. Biomass works for fixing carbon dioxide during their growing stage, but the wastes becomes an emission source with the bacteria oxidation. Thus the conversion of biomass wastes into chemicals or materials would lead to the reduction of the petroleum use, the reduction of carbon dioxide emission from the bacteria oxidation, and the solution of waste environmental problems.

So far, various studies have been reported that relate waste biomass conversion to chemicals including reactions with acid-catalysis [1-3] or enzymes [4]. One method is non-catalytic hydrolysis in high temperature water. Some researchers have reported that hydrolysis takes place for the ether or ester bonds without any catalyst in near-critical or supercritical water (T_C = 374.2 °C; P_C = 22.1 MPa; ρ_C = 323.2 kg/m^3) [5-10] and recently the detailed mechanism has been elucidated [11]. This noncatalytic hydrolysis in high temperature water can be applied to the chemical recycle of wastes, since costly catalysts and the process of the waste treatment and catalyst recovery are not necessary. Also, the process will be an environmentally benign one. Some researchers have studied biomass or cellulose conversion in high temperature water [12-15] and reported the high yield of oils or hydrogen gas from biomass. However, the selective production of chemicals is never expected by a simple method, since biomass is a complicated mixture of variety of components and various reactions should take place.

Recently, Antal and his colleagues demonstrated that cellulose could be separated as a

solid residue from other components, lignin or hemi-cellulose, by the high temperature extraction of biomass. We thought that selective recovery of sugars or oligosackarides is expected by the combination of his proposed method to recover cellulose from biomass with the noncatalytic hydrolysis of the cellulose in high temperature water and have studied on cellulose hydrolysis in high temperature water[11,16,17,20-22] for several years. This paper describes the specific features of hydrolysis of cellulose in SCW, which has been elucidated in our research.

2. EXPERIMENTAL AND ANALYTICAL PROCEDURES

2.1. Materials

Cellulose used was de-ashed microcrystalline cellulose (Avicel No. 2331; particles diameter 20 - 100 μm) purchased from Merck. The reagents used for the high performance liquid chromatography (HPLC) analysis are as follows. Cellobiose (99+%), cellotriose (95+%), cellotetraose (95+%), cellopentaose (95+%) and cellohexaose (95+%) (Seikagaku Industrieal Co. Ltd., Tokyo); glucose (99+%), fructose (99+%), erythrose (60+%), dihydroxyacetone (99+%), 1,6-anhydroglucose (99+%), glyceraldehyde (97+%), pyruvaldehyde (40 %), 5-hydroxymethyl-2-furaldehyde (60+%) and furfural (80 %) (Wako Pure Chemicals Industries Ltd., Osaka).

2.2. Cellulose decomposition experiments and analyses

Experiments were conducted at temperatures ranging from 320 °C to 400 °C and at the pressures of 25 MPa. Residence times were between 0.05 and 10.0 s.

A flow type reactor was used in cellulose hydrolysis experiments. A schematic diagram of the apparatus is shown in Figure 1. The slurry feed pump has dual pistons of 300 ml capacity each of which is stirred by a magnetically coupled static mixer externally propelled by an external permanent magnet. Cellulose-water slurry of 10 wt% was fed to the reactor at a flow rate of 5.0 ml/min and mixed at a T-junction with preheated water fed from another line at a flow rate of 20.0 ml/min by three high-pressure pumps. At the mixing point, the slurry was rapidly heated up to the reaction temperature (320 - 400 °C), which was monitored by a chromel-alumel thermocouple set at a distance of about 20 mm from the mixing T-junction. To terminate the reaction rapidly, the reactor outlet was rapidly cooled by introducing cool water directly into the system at a rate of 10.0 ml/min as well as by externally with a cooling water jacket. The residence time of the solution in the

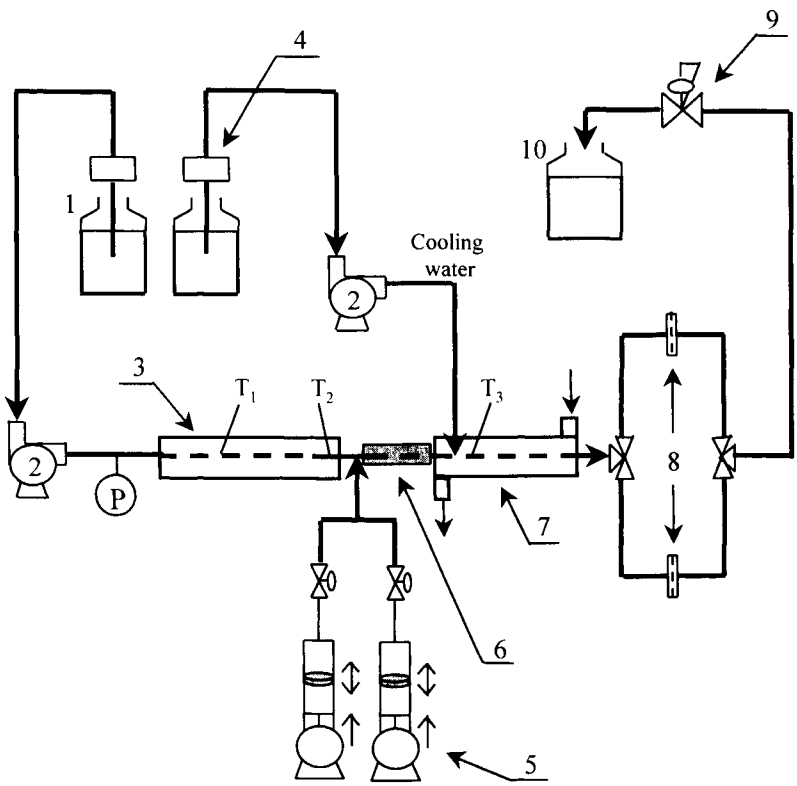

Figure 1. Schematic diagram of experimental setup [16].
1: Distilled water storage; 2: High-pressure pump; 3: Electric furnace; 4: Degassing unit; 5: Slurry feed pump; 6: Reactor; 7: Cooling water jacket; 8: Inline filter; 9: Back-pressure regulator; 10: Sampling bottle.

reactor (t [s]) could be accurately determined by this rapid heating and quick quenching method.

The reaction pressure was controlled by a back-pressure regulator (TESCOM, Model 26-1721-24). Liquid products were filtered with inline filters of 0.5 μm pore size and continuously recovered through the back-pressure regulator in a sampling bottle.

The liquid products obtained in the experiments were submerged in the cool water bath kept at 20 °C for 2 hours and then incubated in an air bath at a constant temperature of 20 °C for 2 days. In case that the white precipitates appeared in the solution, the liquid sample was filtered and dried at 60 °C for 24 hours. After that, they were analyzed by the Fourier-transfer infrared spectroscopy (FTIR) (Bio-rad, Digilab FTS-60A). On the other hand, the water-soluble products were analyzed by ^{1}H nuclear magnetic resonance (^{1}H-NMR) and the fast atom bombardment mass spectrometry (FAB-MS). They were also analyzed for the total organic carbon (TOC) by TOC analyzer (Shimadzu, Model TOC-5000A), and their compositions were quantified by high performance liquid chromatography (HPLC). The HPLC equipment consisted of an isocratic pump, an autosampler, and and integrator (Thermoseparation Products, Model P1000, Model AS3000, and Model SP4400, respectively). The column used for analysis was a SUGAR KS-801 (Shodex). The HPLC was operated at an oven temperature of 80 °C with 1.0 ml/min flow of water solvent. The detectors used were an ultraviolet detector (UV) (Thermoseparation Products, Model Spectra 100) set at 290 nm and a refractive index detector (RI) (ERC, Model 7515A). The RI detector provided quantitative analysis, while the UV detector was used to confirm the presence or absence of compounds with double bonds such as C=O and C=C in the products. Peak identification was established by the comparison of sample peak retention times with the standard solution of the pure compound. The calibration of the peaks was performed using standard solutions of varying concentrations to develop a linear relationship between the peak area and corresponding concentration [19].

Solid residues trapped in the inline filters for 30 minutes were dried at 60 °C for 24 hours after the experiment and weighed. This residue was also analyzed by Infrared spectroscopy (FITR) and scanning electron microscopy (SEM).

Cellulose conversion was evaluated by Eq 1, as follows:

$$X = \frac{W_O - W}{W_O} \tag{1}$$

where W_O is the total amount of cellulose introduced in 30 min, which is nearly 18 g and W is the amount of cellulose recovered after the experiment.

Product yield (Y) and product selectivity (S) were defined as follows:

$$Y_i = \frac{W}{W_O} \tag{2}$$

$$S_i = \frac{Y_i}{X} \tag{3}$$

where Y_i and S_i are the yield and the selectivity of product component *i*, respectively.

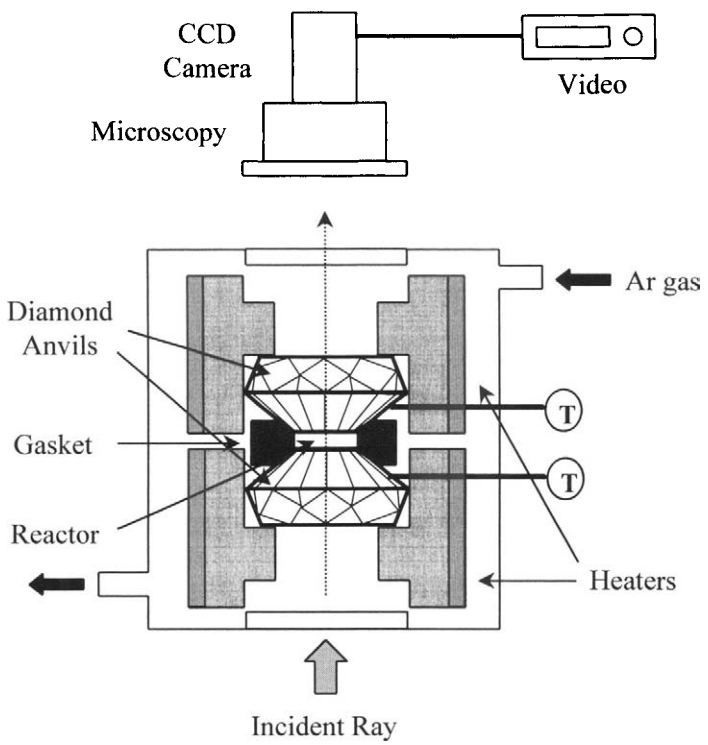

Figure 2. Experimental apparatus of DAC.

2.3. Direct observation of cellulose-water reaction field

For the direct observation of cellulose-water reaction field, the diamond anvil cell (DAC) which was developed by Bassett [18] was used. Figure 2 shows the schematic diagram of this apparatus. A rhenium (Re) gasket was sandwiched with two diamond windows and the enclosed space with the gasket (0.5 mm i.d. hole size and 0.25 mm thickness) and the diamonds was used as a reaction field. Cell temperature was controlled by two heaters and thermocouples attached on the diamond windows and recorded with a scanner (Hewlett Packard; Model 37970A). To prevent oxidation of diamonds, argon gas with 1.0 % hydrogen was introduced into the cell.

First, both a ruby chip and cellulose particles were introduced into the gasket hall on the lower diamond. Then, a small water droplet was loaded into the gasket hole with a micro-syringe. The sample was enclosed in the cell by installing the upper diamond anvil. Finally, the heaters and thermocouples were connected in preparation for heating, while the sample was observed at 100× magnification and the images were recorded with a CCD camera (Olympus KY-F55MD, Tokyo) system. The pressure in the cell was evaluated from the shifts of the raman spectrum of the ruby [19].

3. RESULTS AND DISCUSSION

3.1. Cellulose decomposition product distribution

The cellulose decomposition products identified and qualified in the experiments are shown in Table 1. Cellohexaose, cellopentaose, cellotetraose, cellotriose, cellobiose, glucose and fructose are "hydrolysis products", and glucose decomposition products, namely 1,6-anhydroglucose, erythrose, glycolaldehyde, glyceraldehyde, dihydroxyacetone, pyruvaldehyde, 5-HMF, furaldehyde and acids are defined as "pyrolysis products". In this study, though furaldehyde was identified, it was not quantified.

The HPLC chromatograms of the solvated products obtained at almost 100 % conversion level at the temperatures of 320, 350 and 400 °C at 25 MPa are shown in Figures 3(a)-(c), respectively. The product distributions are also shown in Table 2. At 320 °C, it took 9.9 s for 100 % cellulose conversion. Under these conditions, the main products were

Table 1.
Chemical species of cellulose decomposition.

Products detected	Analytical method
Hydrolysis products of cellulose	
Cellohexaose	HPLC, FAB-MS
Cellopentaose	HPLC, FAB-MS
Cellotetraose	HPLC, FAB-MS
Cellotriose	HPLC, FAB-MS
Cellobiose	HPLC, FAB-MS
Glucose	HPLC, ^{1}H-NMR
Fructose	HPLC, ^{1}H-NMR
Pyrolysis products of glucose	
1,6-Anhydroglucose	HPLC, 1H-NMR, traces
Erythrose	HPLC, ^{1}H-NMR
Glycolaldehyde	^{1}H-NMR
Glyceraldehyde	HPLC, ^{1}H-NMR
Dihydroxyacetone	HPLC, ^{1}H-NMR
Pyruvaldehyde	HPLC, ^{1}H-NMR
5-Hydroxymethyl-furaldehyde (5-HMF)	HPLC
Furaldehyde	HPLC

erythrose, pyruvaldehyde, 1,6-anhydroglucose, 5-HMF and furaldehyde, acids. In other series of studies on decomposition of cellobiose, glucose, fructose, glyceraldehyde, dihydroxyacetone, the main reaction pathways of cellobiose decomposition in SCW were elucidated as shown in Figure 4 [20-22]. The main products obtained in the 320 °C experiment were found to be pyrolysis products of glucose (31.2 %). The yield of hydrolysis product yield was 14.7 %, mainly monomers (glucose and fructose). At 350 °C as shown in Figure 3(b), cellulose conversion reached approximately 100 % at 8.8 s. Also in this case, pyrolysis products were mainly obtained (34.4 %). However, at 400 °C, cellulose was completely converted even at very short residence times (0.05 s). As shown in Figure 3(c), most of the products obtained were hydrolysis products, including cellohexaose, cellopentaose, cellotriose, cellobiose, glucose and fructose. The total yield of these hydrolysis products reached 75.8 %.

Table 2.
Product distributions of cellulose hydrolysis in sub- and supercritical water at 25 MPa [a].

T [°C]	t [s]	Conv. [C%]	Product yield [C%]											
			Hydrolysis products					Pyrolysis products						Others
			4-6 mers	CT	CB	Glc	Fru	GA	DA	AG	Ery	PA	HMF	
320	9.9	99.3	0.7	0.1	0.4	7.6	5.9	11.0	0.3	6.2	4.2	0.2	9.3	53.5
350	8.8	99.3	0.3	0.1	0.4	1.6	1.9	14.2	0.3	3.0	5.1	0.9	10.9	61.0
400	0.05	98.6	16.7	1.4	13.8	28.4	15.5	8.8	0.4	5.8	7.6	0.3	0.5	0.2

[a] Symbols: 6 mer, Cellohexaose; 5 mer, Cellopentaose; 4 mer, Cellotetraose; CT, Cellotriose; CB, Cellobiose; Glc, Glucose; Fru, Fructose; GA, Glyceraldehyde; DA, Dihydroxyacetone; AG, 1,6-Anhydroglucose; Ery, Erythrose;PA, Pyruvaldehyde; HMF, 5-Hydroxymethyl-2-furaldehyde; Others, mainly acids.

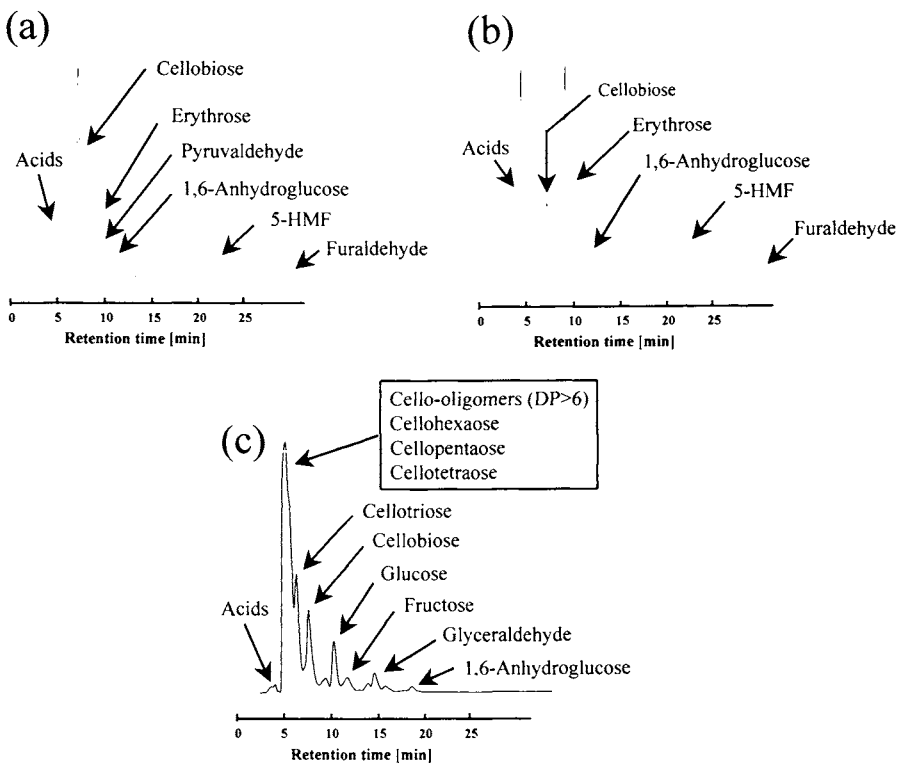

Figure 3. HPLC chromatograms of recovered liquid samples at 100 % cellulose conversion level.
(a) 320 °C, 9.9 s; (b) 350 °C, 8.8 s; (c) 400 °C, 0.05 s. [16]

For some cases especially for the experiments in the short residence time around the critical temperature (370 - 400 °C), we found that the white precipitates appeared in the product solutions after cooling for several hours at room temperature. Thus we conducted a controlled incubation for the precipitation. As described, after the sample was submerged

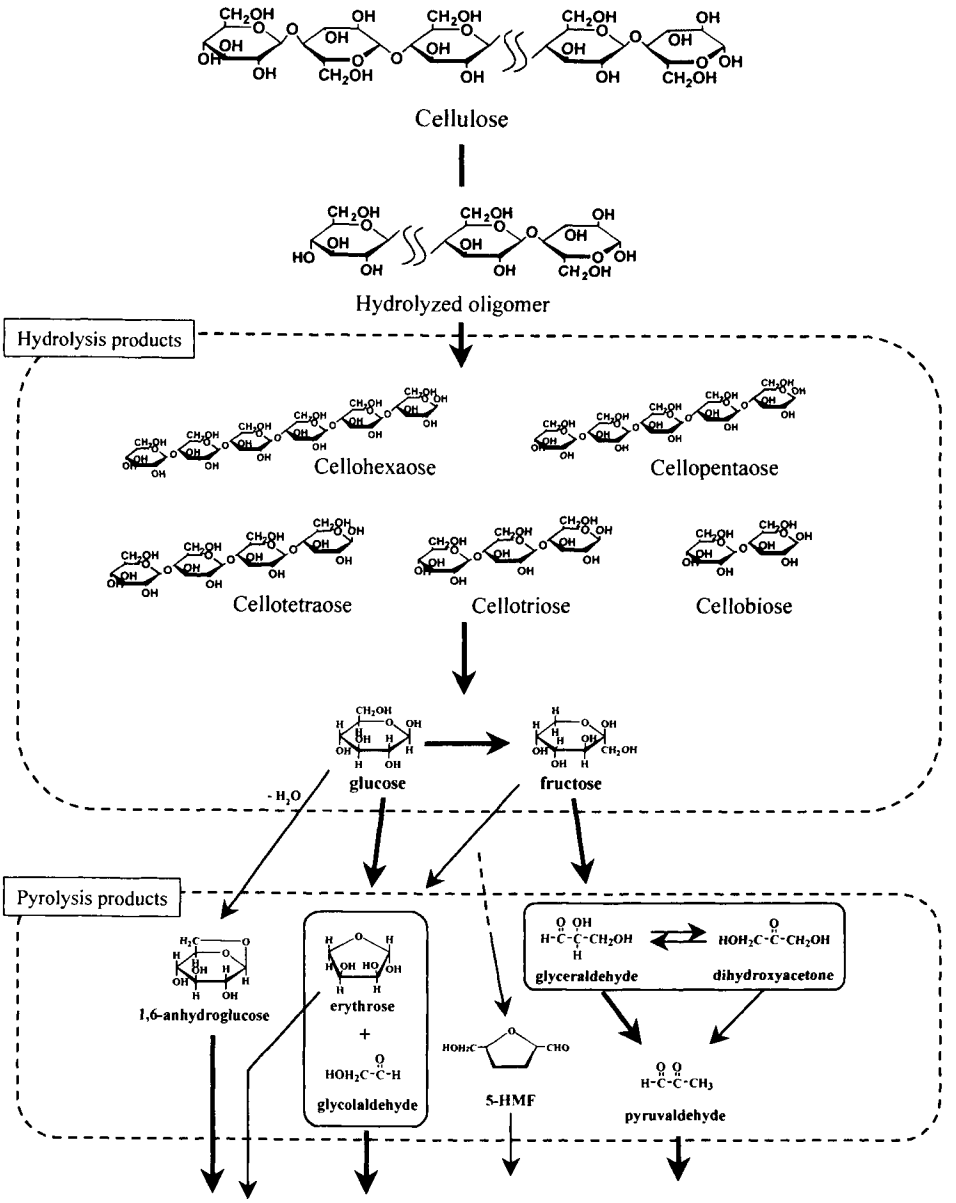

Figure 4. Main reaction pathways of cellulose hydrolysis and glucose decomposition in supercritical water [16,19-21].

in a water bath of 20 °C for 2 hours, it was incubated in an air bath at the temperature of 20 °C for 2 days. The precipitates were analyzed by FTIR after drying at 60 °C for 24 hours. The IR spectra of the precipitates are more or less the same as that of the original cellulose. When the precipitates were hydrolyzed in sulfuric acid aqueous solution [23], only glucose was obtained as product. These results indicate that the precipitates have a cellulose-like molecular structure.

3.2. Cellulose decomposition rate in subcritical and supercritical water

The first order rate constant of cellulose hydrolysis around the critical temperature was evaluated by the following equation:

$$k = -\frac{\ln(1-X)}{t} \tag{4}$$

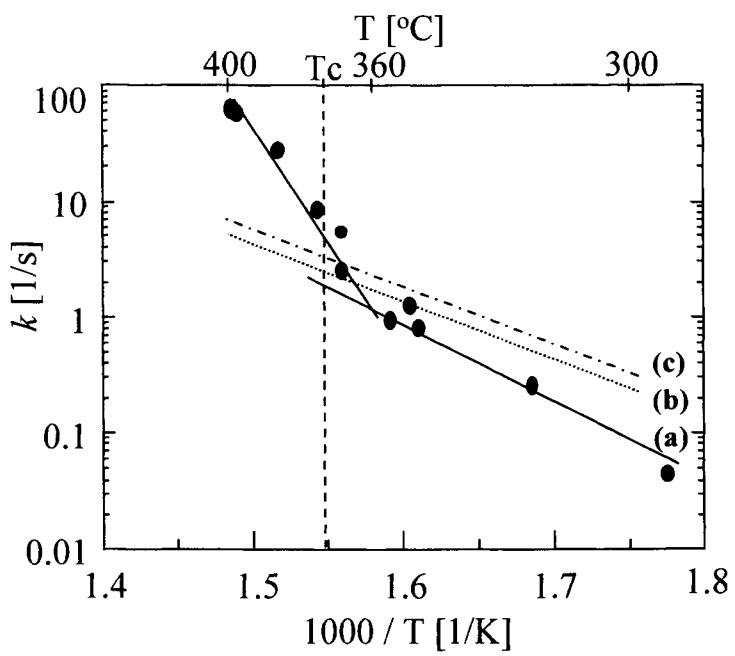

Figure 5. Arrhenius plot of cellulose and related cellulosic compounds in subcritical and supercritical water at 25 MPa. (a) Cellulose [16]; (b) Cellobiose [19]; (c) Glucose [20].

The evaluated first order rate constants (k [1/s]) were plotted against reciprocal temperature in Figure 5. The decomposition rates of glucose and cellobiose, both of which are the hydrolysis products of cellulose, evaluated in our previous works [20,21] are also shown in this figure. In the lower temperature region, both glucose and cellobiose conversion rates were much faster than the hydrolysis rate of cellulose. However, above 350 °C, the reaction rate drastically increased and at 400 °C it became much faster than the conversion rates of glucose and cellobiose. This is the reason why we obtained high yield of hydrolysis products at 400 °C.

3.3. DAC experiments

The direct observation of cellulose in high temperature water was performed by using the DAC. The typical examples of the observation result are shown in Figure 6. After heating the temperature at 250 °C for 30 min, the reaction temperature has been elevated at 10 °C/s. Below 280 °C, the change of the cellulose particle size was barely observed. However, at 280 °C, the phase boundary between cellulose and water began to become unclear and particle size of cellulose became smaller gradually. At around 300 - 320 °C, cellulose particles seemed to disappear without changing their particle shape (Figures 6 (b)-(f)). It appears that the cellulose particles dissolved into the high temperature water.

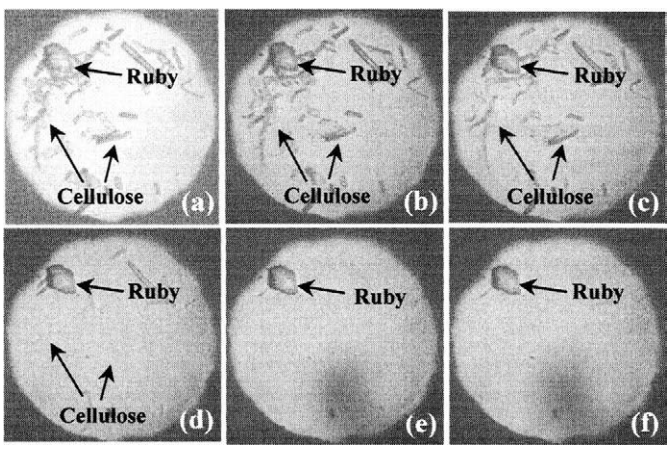

Figure 6. Diamond anvil cell study of cellulose in water at 60 MPa. Conditions: (a) 22 °C; (b) 280 °C; (c)-(f) photos at approximately 1 second intervals with heating from 280 °C at a rate of 10 °C/s. Diameter of Re gasket hole is 500 μm with a thickness of 250 μm Ruby is for pressure measurement.

3.4. Mechanism of cellulose hydrolysis in high temperature water

Combination of the finding of the recrystallization of cellulose-like materials at around the critical temperature and the result of the DAC observation leads us to the hypothesis that cellulose dissolution took place in high temperature water and thus the homogeneous hydrolysis atmosphere is formed. We think this is the reason why the drastic change in the cellulose reaction rate around 350 °C.

Cellulose is a homopolymer, in which 100 to 3,000 glucose molecules are straightly combined with each other at β(1,4) position. Each glucose unit has three hydroxyl groups having high affinity to water. Thus, basically cellulose molecule can be dissolved in water. However, because of intermolecular and intramolecular hydrogen linkages through the

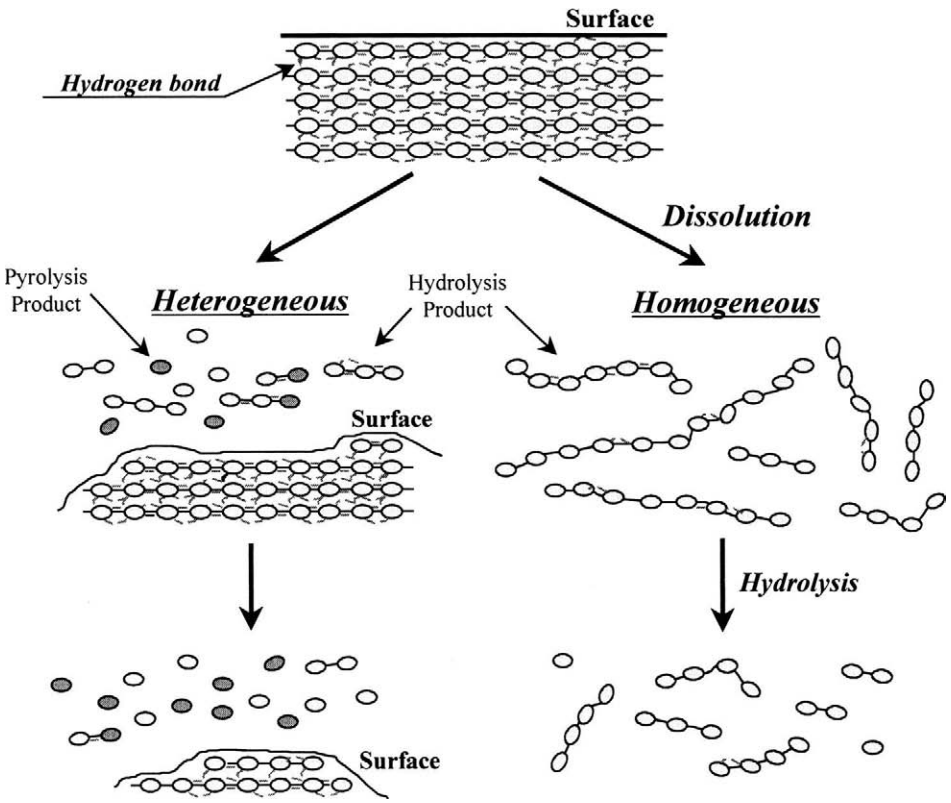

Figure 7. Cellulose hydrolysis pathways of both a heterogeneous reaction and a homogeneous reaction [24].

hydroxyl groups, cellulose can have high crystallinity at room temperature. However, at high temperatures, the cleavage of hydrogen bonds probably occurs. Once the hydrogen bonds are broken, the cellulose molecule with many hydroxyl groups can be solubilized in high temperature water to form a homogeneous phase.

Based on these experimental results, cellulose reaction pathways in subcritical and supercritical water were elucidated and schematically shown in Figure 7 [24]. Below 350 °C, cellulose decomposed only on the surface of the cellulose particles. The decomposition rate of cellobiose and glucose were faster than the heterogeneous cellulose hydrolysis rate. Therefore, hydrolysis products formed from cellulose hydrolysis further decomposed. On the other hand, above 350 °C, a homogeneous hydrolysis atmosphere exists.

4. CONCLUSIONS

The specific features of hydrolysis of cellulose in SCW are elucidated. At 400 °C, the yield of hydrolysis products (water soluble oligomers and monomers) was 75.8 % at 100 % cellulose conversion level and was much higher than that at 320 °C and 350 °C. Below 350 °C, cellulose hydrolysis rate was slower than glucose or cellobiose decomposition rate. Kinetic studies of cellulose and cellulose related compounds also showed that above 350 °C, cellulose hydrolysis rate drastically increased and became higher than glucose or cellobiose decomposition rate. This is the reason why hydrolysis products were the main products at 400 °C. Judging from the newly found recrystallization of cellulose-like species from the product solutions and the observation results of DAC experiments, it was concluded that dissolution of cellulose takes place in high temperature water. The drastic changes of the cellulose hydrolysis rate are probably because of the formation of homogeneous hydrolysis reaction atmosphere in high temperature water.

ACKNOWLEDGMENTS

The authors thank to the Grants in Aid for Scientific Research on Priority Areas (0621402, 0423803) and for General Scientific Research (07455433) of the Ministry of Education, Science and Culture, NEDO and RITE.

REFERENCES

1. I. A. Malester, M. Green, G. Shelef, Ind. Eng. Chem. Res., 31 (1992) 1998.
2. J. F. Saeman, Ind. Eng. Chem., 37(1) (1945) 43.
3. K. Belkacemi, N. Abatzoglou, R. P. Overend, E. Chornet, Ind. Eng. Chem. Res., 30 (1991) 2416.
4. M. Mandels, L. Hontz, J. Nystrom, Biotech. Bioeng., 16(2) (1974) 1471.
5. S. H. Townsend, M. A. Abraham, G. L. Huppert, M. T. Klein, S. C. Paspec, Ind. Eng. Chem. Res., 27 (1988) 27.
6. M. L. Penninger, J. M. M. Kolmschate , In Proceedings of American Chemical Society Symposium Series, Vol. 406 (1989) 242.
7. M. T. Klein, L. A. Torry, B. C. Wu, S. H. Townsend, J. Supercrit. Fluids, 3 (1990) 222.
8. M. J. Antal Jr., W. S. L. Mok, Carbohydr. Res., 199 (1990) 91.
9. M. J. Antal Jr., W. S. L. Mok, Carbohydr. Res., 199 (1990) 111.
10. T. Adschiri, S. Hirose, R. M. Malaluan, K. Arai, J. Chem. Eng. Jpn., 26(6) (1993) 676.
11. C. L. Harrell, M. T. Klein, T. Adschiri, Adv. Environ. Res., 1(3) (1997) 373.
12. W. S.-L. Mok, M. J. Antal, Jr., Ind. Eng. Chem. Res., 31 (1992) 1157.
13. O. Bobleter, Progr. Polym. Sci., 19 (1994) 797.
14. S. G. Allen, L. C. Kam, A. J. Zemann, M. J. Antal, Jr., Ind. Eng. Chem. Res., 35 (1996) 2709.
15. J. M. Martinez, J. Reguant, M. A. Montero, D. Montane, J. Sovado, X. Rarriol, Ind. Eng. Chem. Res., 36 (1997) 688.
16. R. M. Malaluan, Ph.D. Dissertation, Tohoku University, Sendai, Japan (1995).
17. M. Sasaki, B. M. Kabyemela, R. M. Malaluan, S. Hirose, N. Takeda, T. Adschiri, K. Arai, J. Supercrit. Fluids, 13 (1998) 261.
18. W. A. Bassett, A. H. Shen, M. Bucknum, Rev. Sci. Instrum., 64(8) (1993) 2340.
19. R. A. Forman, G. J. Piermarini, J. D. Barnett, S. Block, Science, 176 (1972) 284.
20. B. M. Kabyemela, M. Takigawa, T. Adschiri, R. M. Malaluan, K. Arai, Ind. Eng. Chem. Res., 37(2) (1998) 357.
21. B. M. Kabyemela, T. Adschiri, R. M. Malaluan, K. Arai, Ind. Eng. Chem. Res., 36(5)

(1997) 1552.

22. B. M. Kabyemela, T. Adschiri, R. M. Malaluan, K. Arai, Ind. Eng. Chem. Res., 36(6) (1997) 2025.

23. J. F. Saeman, J. L. Bubl, E. E. Harris, Ind. Eng. Chem., 17(1) (1945) 35.

24. M. Sasaki, Z. Fang, Y. Fukushima, T. Adschiri, K. Arai, Submitted for publication to J. Am. Chem. Soc. (1999).

Reaction Engineering for Pollution Prevention
M.A. Abraham and R.P. Hesketh (Editors)

Operation of Reactor-Adsorber Systems for Minimization of Exhaust Gases Emissions

Jiří Jirát[1], František Štěpánek[1], Milan Kubíček[2], Miloš Marek*,[1]

[1]Department of Chemical Engineering, [2]Department of Mathematics
Prague Institute of Chemical Technology, Technická 5, 166 28 Praha 6, Czech Republic
Phone: +4202 2435 3104; Fax: +4202 311 7335
*E-mail: marek@vscht.cz

The cold-start problem of an automobile catalytic converter is considered. A solution based on the interconnection of an adsorber (hydrocarbon trap) with a monolithic reactor is investigated by means of numerical simulations, using the European and FTP driving cycles as standards for a time-variable input. It is shown that the cumulative emissions of hydrocarbons are minimized in the case of a configuration where the direction of exhaust gas flow is adaptively switched from the reactor-adsorber arrangement before the lightoff to the adsorber-reactor arrangement (with partial bypass) after the ignition. For proper parameter setting, up to 99% integral conversion of HC can be achieved by solely systems-engineering approaches (i.e. by an appropriate dynamic interconnection of reactor-adsorber unit operations), with no need to preheat the reactor.

1. INTRODUCTION

The use of automobile catalytic converters in the last ten years contributed to a remarkable reduction of the emissions of carbon monoxide (CO), nitrogen oxides (NO_x), and unburned hydrocarbons (HC). Two qualitatively different periods can be distinguished during a typical operation cycle of a car engine – a start-up ("cold start") period and a "steady driving" period. The dynamics of catalyst operation has a different character during the two operation periods mentioned above. During the start-up, the so called cold start problem is most eminent, i.e. a situation where despite the engine producing exhaust gas with high content of HC's, the catalytic afterburner has not yet reached its ignition temperature, therefore most pollutants pass through. Driving in a town is characterized by frequent accelerations and stops, causing fluctuations in inlet conditions at several different time-scales, the result being that neither in this period does the converter reach a steady state even in this period. A further problem stems from the fact that the lean burn conditions (stoichiometric excess of oxygen in the fuel-air mixture) can lead to a higher content of nitrogen oxides in exhaust gases. Lean-burn engines operate generally at higher fuel efficiencies but the problem of NO_x reduction is difficult to solve, cf. [1, Chapter 12]. Currently available catalysts use hydrocarbons for the reduction but they operate in a rather narrow temperature window.

One approach to the problem of keeping the catalyst temperature in a "window" favorable to selective NO_x reduction has been described earlier [2], [3]. It is based on periodic cooling of a system of thermally coupled monoliths. Another approach, common to both the cold start (HC) and the NO_x problem, is based on the idea that during unfavourable conditions, certain reaction components can be stored (selectively adsorbed), and then released when conditions in the catalytic converter become favorable to their specific reactions. Application of this concept to the cold start problem has the form of the so called hydrocarbon traps, i.e. "in-line" adsorbers whose goal is to accumulate HC's while the converter is inactive (below its ignition temperature) and release them once the converter reaches its operating state.

A complementary solution is to shorten the start-up time of the catalyst, e.g. by electrical pre-heating, as it was considered for example in [4] or [5]. The hydrocarbon traps are likewise the subject of intensive research, both experimental and computational, cf. [1], [6]–[9]. From the systems engineering point of view can the HC-trap be seen as an additional unit operation which modifies (and shifts in time) the physico-chemical properties of a stream (exhaust gases) in such a way that the overall performance of the system – reactor + adsorber – measured by the mean conversion of HC's, be maximized. Research efforts in the field of development of proper catalysts is very intense, and may lead to robust low-temperature light-off catalysts relatively soon [10]. However, given the number of catalytic converters currently installed a solution based on existing catalysts is still of high interest.

2. PROBLEM FORMULATION

In this contribution we consider several arrangements and nonstationary modes of operation of system of an adsorber and a catalytic monolith. Contrary to the static "in-line" HC traps, we concentrate primarily on a configuration with adaptive switching of streams, which has not been comprehensively treated to date. As a standard for the simulation of inlet conditions (reflecting the typical variations of composition, flowrate and temperature during the first few minutes of a driving cycle) we took the data used by Koltsakis et al. [11], based on the European driving cycle, and the first part of the FTP cycle (Federal Test Procedure), which is used as a standard for emissions testing in the US. Figure 1 shows the temporal evolution of the inlet gas temperature for the European cycle, inlet conditions according to the FTP cycle are shown in Fig. 2. The goal is to minimize the integral amount of hydrocarbons exiting the reactor-adsorber system over one driving cycle, including adsorbent regeneration as part of the cycle.

We assume that the cycle starts with both the reactor and the adsorber cold, the temperature of exhaust gases is also relatively low and the mole fraction of HC's relatively high. Before the monolith is warmed up to the ignition temperature, the hydrocarbons are selectively adsorbed in the adsorber. Since low temperature favors adsorption equilibrium towards the solid phase, we wish to bring the gas to the adsorber as cold as possible. Therefore is the exhaust first lead through the reactor, which in this phase acts only as a heat exchanger, and then to the adsorber. In this initial phase, there is a temperature front propagating through the reactor monolith and a concentration front through the adsorber. When the temperature in the monolith exceeds the HC light-off temperature,

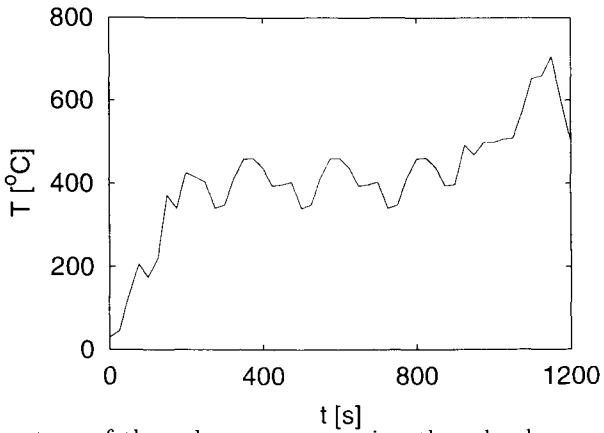

Figure 1: Temperature of the exhaust gas entering the adsorber-reactor system – European driving cycle [11].

the catalytic converter starts to perform its function and it is no longer necessary to direct the gas from the reactor into the adsorber, as it is essentially free of hydrocarbons. On the contrary, now the HC's previously entrapped in the adsorber can be released by letting a fraction of the hot inlet gas pass through the adsorber – regeneration by a temperature swing. The desorption can be done either co- or counter-currently, but it is essential to choose the flowrate of the desorption gas neither too small (risk of an insufficient adsorbent regeneration), nor too high ("hydrocarbon shock" in the reactor possibly leading to overheating and irreversible changes in the catalyst activity). In practical operation, the time of switching can either be set *a priori*, based on mean expected parameters of the driving cycle, or the switching can be adaptive, according to the values of temperatures. The switching time settings will be also determined by the type of engine and activity and capacity of the actual catalyst and the adsorbent. Neural network algorithm may be also used to adapt the control to local conditions and the behaviour of a particular driver [3]. Quantitative results of our simulations of several arrangements and a parametric study of the effect of switching time and desorption ratio on mean HC conversion are discussed in the section Results.

3. MODELS AND THEIR SOFTWARE IMPLEMENTATION

3.1. Reaction scheme

A simplified mixture containing only CO and two representative hydrocarbons (C_3H_6 with a lower ignition temperature and C_3H_8 with a higher one) was considered, hence the following oxidation reactions take place:

1. $CO + O_2 \longrightarrow CO_2$
2. $C_3H_6 + O_2 \longrightarrow CO_2 + H_2O$
3. $C_3H_8 + O_2 \longrightarrow CO_2 + H_2O$

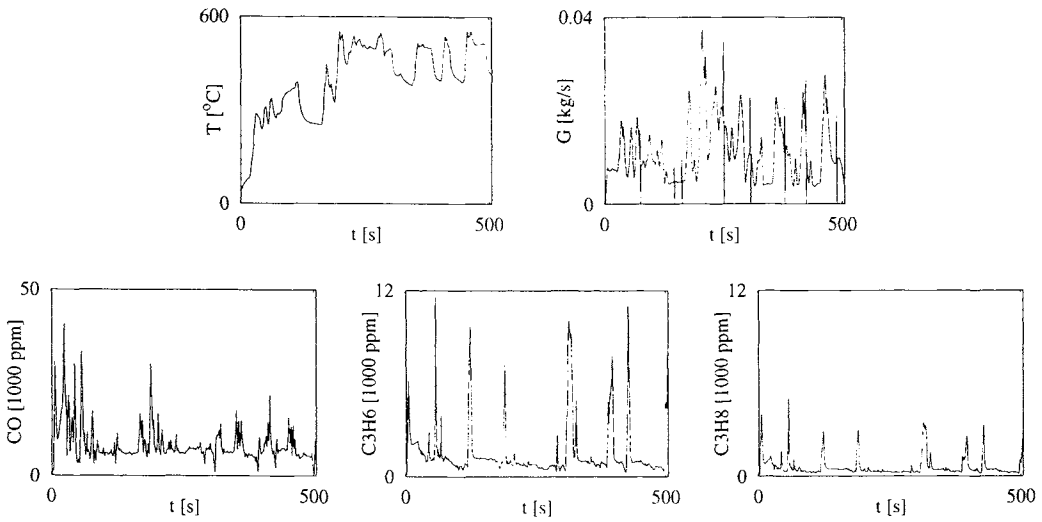

Figure 2: Part of the FTP-cycle, all concentrations at the inlet are considered time-dependent, only O_2 concentration was considered constant (2%).

3.2. Model of a monolithic converter

The reactor was described by a 1-D, two-phase model, incorporating the axial conduction of heat. The mass and enthalpy balances were used in the form

$$\frac{\partial c_k}{\partial t} = -\frac{\partial (v c_k)}{\partial z} - k_c(z)\frac{a}{\varepsilon}(c_k - c_k^*) \tag{1}$$

$$\varrho c_p \frac{\partial T}{\partial t} = -v\varrho c_p \frac{\partial T}{\partial z} - k_h(z)\frac{a}{\varepsilon}(T - T^*) \tag{2}$$

$$\varepsilon^* \frac{\partial c_k^*}{\partial t} = k_c(z)\frac{a}{1-\varepsilon}(c_k - c_k^*) + \sum_{j=1}^{J} \nu_{k,j}\Re_j \tag{3}$$

$$\varrho^* c_p^* \frac{\partial T^*}{\partial t} = \lambda_z \frac{\partial^2 T^*}{\partial z^2} - \sum_{j=1}^{J} \Delta H_{r,j}\Re_j + k_h(z)\frac{a}{1-\varepsilon}(T - T^*) - k_{w,r}(T^* - T_w) \tag{4}$$

The meaning of symbols is as follows: c_k concentration of k-th component in the gas phase, c_k^* in the solid, T temperature in the gas phase, T^* temperature of solid, v gas flow linear velocity, t time, z axial coordinate (reactor length $L = 11$ cm), k_c mass-transfer coefficient and k_h heat transfer coefficient between gas and solid, k_w heat transfer coefficient to wall, ε void fraction, ϱ density, c_p heat capacity, $\Delta H_{r,j}$ reaction enthalpies, $\Re_j$ reaction rates, a specific surface area, λ_z axial heat conductivity, ϱ^* solid phase density, c_p^* solid phase heat capacity, ε^* washcoat porosity, T_w wall temperature and ν stoichiometric coefficients ($\nu < 0$ for reactants). The dependence of k_c and k_h on axial coordinate z reflects the effects of an undeveloped laminar flow at the inlet to monolith channels. The used correlations [12], [5] in principle describe the increase of k_c and k_h values in the entrance region of the channel (approx. 10% of the channel length). The above mentioned model is in the form, which includes all significant terms commonly used in the modelling of monolithic converters cf. [13], [11].

3.3. Reaction kinetics

The Langmuir-Hinshelwood kinetics was used, with parameters chosen according to [11].

$$\Re_1 = \frac{k_1 y_{CO} y_{O_2}}{Q} \qquad \Re_2 = \frac{k_2 y_{C_3H_6} y_{O_2}}{Q} \qquad \Re_3 = \frac{k_3 y_{C_3H_8} y_{O_2}}{Q} \tag{5}$$

$$Q = T^*(1 + K_1 y_{CO} + K_2 y_{C_3H_6})^2 (1 + K_3 y_{CO}^2 y_{C_3H_6}^2) \tag{6}$$

The constants K_i assume the values $K_1 = 65.5\exp(961/T^*)$, $K_2 = 2.08 \cdot 10^3 \exp(361/T^*)$, and $K_3 = 3.98\exp(11611/T^*)$. The rate constants depend on temperature according to the Arrhenius relationship $k_i = A_i \exp(-E_i/RT^*)$, values of the activation energies and the pre-exponential factors are listed in the following table:

reaction no.	A_i [mol K m^{-3} s^{-1}]	E_i [kJ mol^{-1}]
1	$5 \cdot 10^{16}$	95
2	$1 \cdot 10^{18}$	105
3	$1.2 \cdot 10^{18}$	125

3.4. Model of an adsorber

The adsorber is described by a 1-D model (pseudohomogeneous for the enthalpy balance). The balance equations lead to

$$\frac{\partial c_k}{\partial t} = -\frac{\partial (v c_k)}{\partial z} - \frac{1-\epsilon}{\epsilon} \frac{\partial \bar{q}_k}{\partial t} \tag{7}$$

$$\frac{\partial \bar{q}_k}{\partial t} = k_{LDF}(q_k^* - \bar{q}_k) \tag{8}$$

$$\left[\varrho_g C_{p,g} + \frac{1-\epsilon}{\epsilon} \varrho_s C_{p,s}\right] \frac{\partial T}{\partial t} = -\varrho_g C_{p,g} \frac{\partial (v c_k)}{\partial z} - \frac{1-\epsilon}{\epsilon} \sum_{k=1}^{K} \Delta H_{a,k} \frac{\partial \bar{q}_k}{\partial t} - k_{w,a}(T - T_w) \tag{9}$$

Here $\bar{q}_k$ is loading of the k-th component in the solid phase, k_{LDF} is linear driving force mass transfer coefficient, $\Delta H_{a,k}$ is adsorption heat, ρ_g and ρ_s are fluid and solid phase density, respectively, $C_{p,g}$ and $C_{p,s}$ are fluid and solid phase heat capacity, respectively, and $k_{w,a}$ is wall heat transfer coefficient. The adsorption equilibrium was described by the extended Langmuir isotherm

$$q_k^* = q_{m,k} \frac{b_k c_k}{1 + \sum_k b_k c_k} \tag{10}$$

where the equilibrium constants b_k depend on temperature according to

$$b_k = b_{k,0} \exp\left[-\frac{\Delta H_{a,k}}{R}\left(\frac{1}{T} - \frac{1}{T_0}\right)\right] \tag{11}$$

The reference temperature was $T_0 = 298$ K, and the values of other parameters were taken from [14], i.e. $q_m = 367$ mol/m^3, $b_0 = 28.5$ m^3/mol, $\Delta H_a = -33500$ J/mol. For simplicity we have assumed that CO is not adsorbed and the two model hydrocarbons have identical adsorption characteristics.

3.5. Inlet conditions

For the European driving cycle, inlet temperature was varied according to Fig. 1, the composition of the inlet gases was set so as to correspond to the average composition of exhaust gases leaving a typical gasoline engine given in the table below:

component	inlet concentration
CO	1 %
C_3H_6	320 ppm
C_3H_8	160 ppm
O_2	1 %

The space velocity was assumed equal to 50000 h^{-1}. The second example was part of the FTP cycle, where all inlet values are time-dependent (with the exception of O_2), cf. Fig. 2. The purpose of modelling studies was to demonstrate that the proposed way of operation of the monolith reactor-adsorber system is able to achieve very high conversions of HC's for average exhaust gas temperatures, compositions and flowrates. In applications to concrete type and size of engine the operational parameters have to be optimized with a view to actual catalyst and adsorbent properties.

3.6. Numerical methods and Software

The Crank-Nicolson method with the quasi-linearization of nonlinear terms was used for the solution of the reactor model. Fixed spatial grid of 50 nodes was used, the time step was adaptively varied. The adsorber model was solved by the method of lines on a spatial grid of 60 nodes, using the LSODE integrator. For the dynamical simulation of the system of the monolithic reactor and the adsorber was used a software whose detailed description is given in [15]. This software enables the simulation of defined sequences of coupled monolithic reactors and other flow-through unit operations (adsorber in this particular case). The biggest advantage of the software is its modularity which allows for rapid and flexible changes of physical models, kinetics, numerical methods or the calculation of transfer coefficients. The mutual connection of individual modules is defined in a MASTER program. The modularity also enables to vary the structure of interconnections of individual units and operational conditions in time. The integrations in individual modules take place sequentially, each time a single time step is computed. In the case solved here, where no recycle is considered, the use of the LSODE integrator enables to increase the overall speed of the integration as longer time intervals can be used for each unit separately. The structure and mutual relationship of individual modules of the SW are shown in Fig. 3.

4. RESULTS OF SIMULATIONS

After an initial evaluation, two configurations were studied in detail and their HC-removal efficiency compared with that of a stand-alone monolith reactor. All simulations assumed the same inlet (as specified above) and initial conditions: *(i)* empty adsorber, and *(ii)* initial temperature of all modules equal to 298 K. A schematic flowsheet diagram of the configurations (a)-(c) studied is shown in Fig. 4.

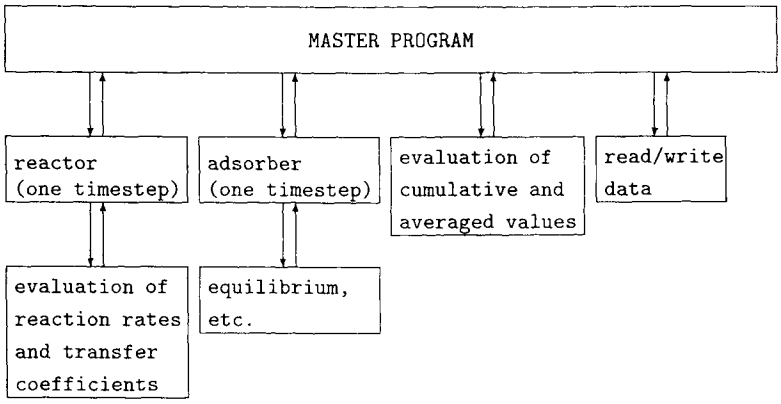

Figure 3: Schematic block diagram of the software used for simulations.

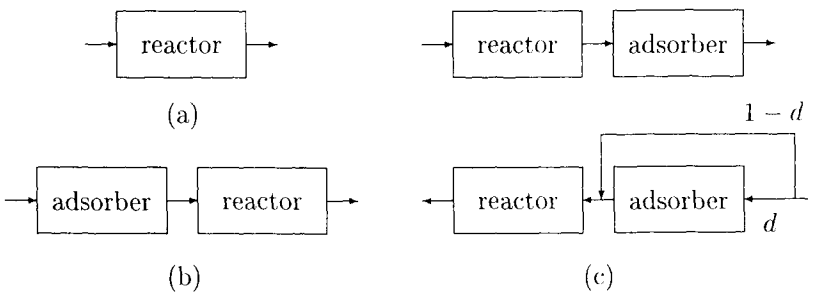

Figure 4: The arrangements considered: (a) reactor only, (b) adsorber before reactor, (c) reactor before adsorber with subsequent switching of the flow (d – desorption ratio, cf. text).

Let us study the single monolithic reactor (case (a), Fig. 4) first. For comparison with the results obtained for different configurations containing the adsorber, the mean (i.e. averaged over the European driving cycle) integral conversions of CO, C_3H_6, and C_3H_8 for a single-pass monolithic reactor were 83 %, 84 %, and 82 %, respectively. The temporal evolution of mole fractions of the components in the outlet stream is given in Fig. 5; it can be seen that after the ignition (approx. at $t = 200$ s), almost complete conversion is achieved in the reactor. For the FTP-cycle, the temporal evolution of the outlet temperature and cumulative emissions from a single monolith are shown in Fig. 6. The temporary increase in the emissions of CO and HC's just after the lightoff is caused by an excess of reducing components in the inlet mixture (inlet O_2 concentration is held at a fixed value, which can sometimes be too low).

The case where the adsorber preceded the reactor (situation (b) in Fig. 4) was studied next. This static configuration with an "in-line" adsorber brought no improvement to the overall performance of the system, it even lead to a slight increase in the cumulative

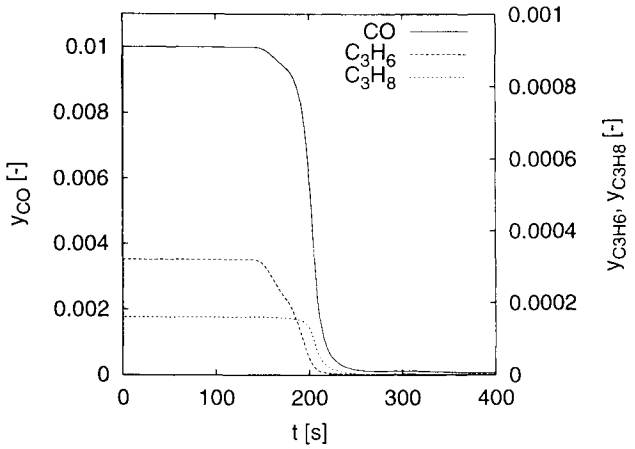

Figure 5: Outlet mole fractions (y) of CO, C_3H_6, and C_3H_8 during the first 400 s of European driving cycle (configuration (a) from Fig. 4).

emissions. The reason is that the reactor ignition time was delayed due to the considered heat capacity of the adsorber. Although some hydrocarbons were initially retained in the adsorber, this had no net effect on the total mean conversion because thermal desorption occurs at significantly lower temperatures than the ignition temperature. As a result, the initially adsorbed hydrocarbons leave the system even before the catalytic combustion begins in the converter. As a matter of interest we tried to change the adsorption capacity of the adsorber, q_s. Neither this lead to an improvement, though, as is demonstrated in the following table, showing total conversions of individual pollutants.

component	q_s [mol/m^3]		
	200	367	600
CO	82 %	82 %	82 %
C_3H_6	83 %	83 %	83 %
C_3H_8	80 %	80 %	80 %

It can thus be concluded that the limiting factor here is not the adsorption capacity, but the temperature-dependence of the adsorption isotherms. Let us estimate the contribution of the heat of adsorption to the overall heat flow in the adsorber. We have approximately

$$\frac{\dot{H}_{ads}}{\dot{H}_{flow}} = \frac{F \cdot \sum_k y_k \cdot (-\Delta H_{a,k})}{\dot{m} \cdot c_p \cdot (T - T_{ref})}$$

where F is molar flow, $\dot{m}$ is mass flow, c_p is fluid specific heat capacity, T_{ref} is reference temperature ($= T_{initial}$), then we obtain for Fig. 1 with the European driving cycle, that in the first 25 seconds is this ratio $< 4\%$ and it decreases with the fastly increasing inlet temperature. Thus the evolved adsorption heat has minor effects in comparison with the variations of inlet temperature. The intensity of cooling required in order to avoid an early breakthrough from the adsorber depends on the temperature-dependence of the adsorption equilibrium constants b given by Eq. (11), i.e. on $|-\Delta H_a|$.

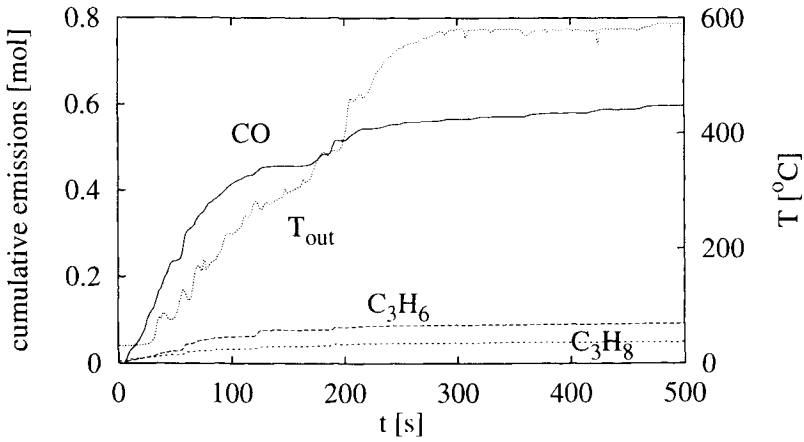

Figure 6: Cumulative emissions and outlet temperature – reactor only (inlet conditions defined in Fig. 2). Total conversions: CO - 0.64, C_3H_6 - 0.65, C_3H_8 - 0.47.

Finally, the arrangement (c) (Fig.4) was considered, where the reactor initially preceeds the adsorber, but when the ignition temperature is reached, the inlet gas stream is switched so that a part of it flows through the adsorber (in order to thermally desorb the accumulated hydrocarbons), then re-joins the rest of the stream (which was lead through a by-pass), and eventually enters the reactor where the hydrocarbons are incinerated. A parametric study was performed with respect to the switching time t_s and the desorption ratio d (defined as the fraction of the original inlet stream that enters the adsorber). The results of parametric study are summarized in Fig. 7. As can be deduced from the results obtained for a single reactor, the optimum switching time should lie somewhere around 200 s, which is the ignition time. However, simulations with an adiabatic adsorber showed that the elevated temperature of the gas leaving the reactor leads to early, thermally induced break-through of HC's from the adsorber even before the ignition in the reactor. The break-through occured around $t = 100$ s, thus the maximum integral conversions attainable in the adiabatic adsorber correspond to this switching time (compare Fig. 7 (a), (c), and (e)). To avoid the undesirable early thermal desorption, either the adsorber or the gas entering it must be cooled so that the temperature in the adsorber remains at levels which favour adsorption equilibrium towards the solid phase. We therefore considered an adsorber intensively cooled during $t < t_s$. It was considered that the adsorber is operated simultaneously as a heat exchanger. Alternatively the use of a cold shot air cooling (mixing of the gas exiting the monolith with a cold air) could be considered. The integral conversions of both hydrocarbons increased significantly (up to 99 % for C_3H_6), which means that the HC trap fulfilled its main function, i.e. it accumulated hydrocarbons until the ignition occured in the converter. Temporal development of concentration profiles in the reactor and both the adiabatic and the cooled adsorber for switching time of 200 s is shown on Fig. 8. As can be seen, the propagation patterns of the mass transfer zone in the cooled and adiabatic adsorbers are qualitatively different; the early break-through on Fig. 8 (b) is evident.

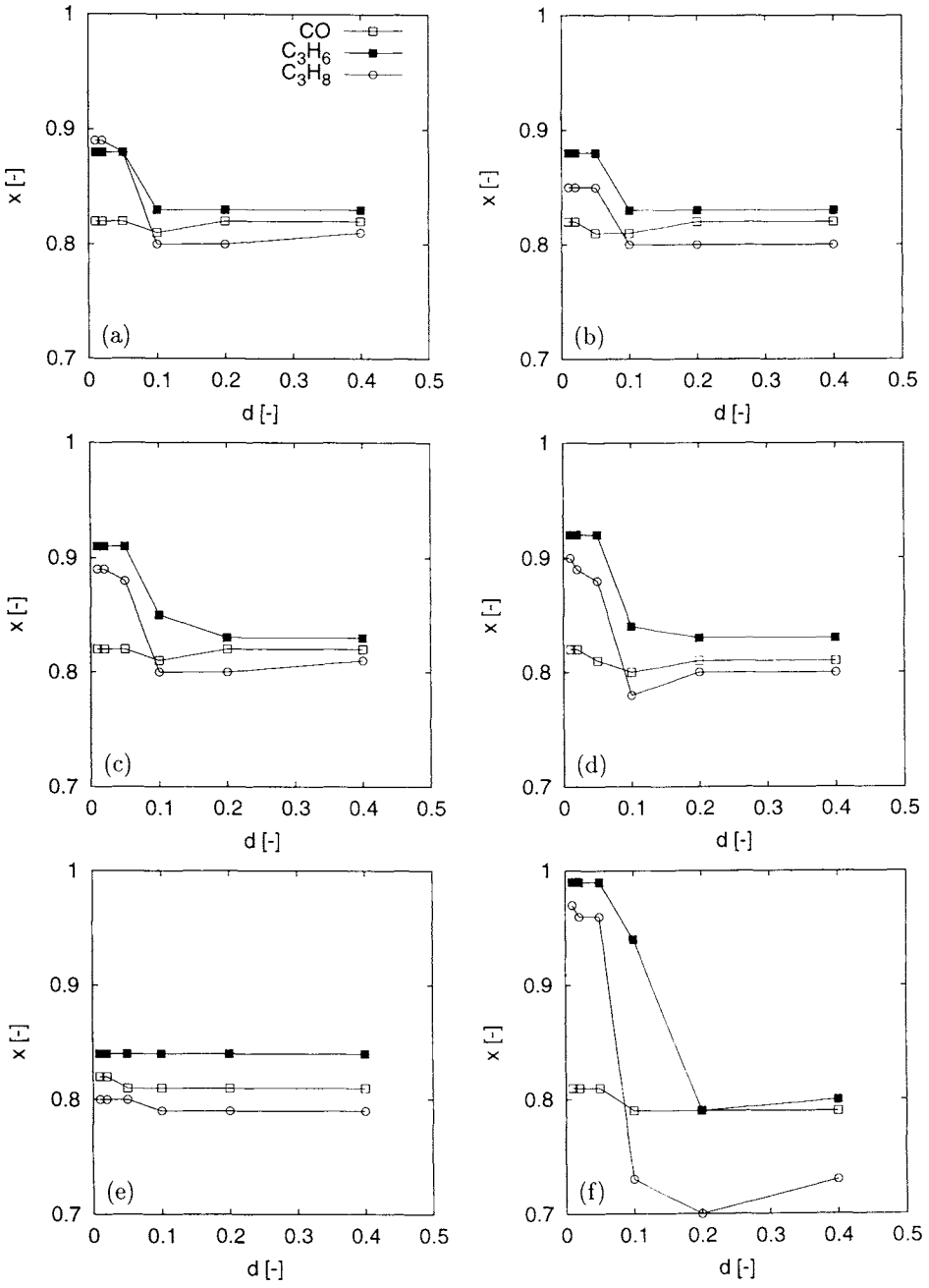

Figure 7: Dependence of total conversion of CO, C_3H_6, and C_3H_8 on the desorption ratio d for different switching times: (a) and (b) $t_s = 50$ s, (c) and (d) $t_s = 100$ s, (e) and (f) $t_s = 200$ s. Graphs (a), (c), and (e) – adiabatic adsorber, graphs (b), (d), and (f) – intensively cooled adsorber ($k_{w,a} = 3 \cdot 10^5$ J m^{-3} s^{-1} K^{-1}, $T_w = 298$ K), SV = 50000/h. Total conversion is defined as a ratio of converted to entering mass of pollutant over the 1200 s cycle.

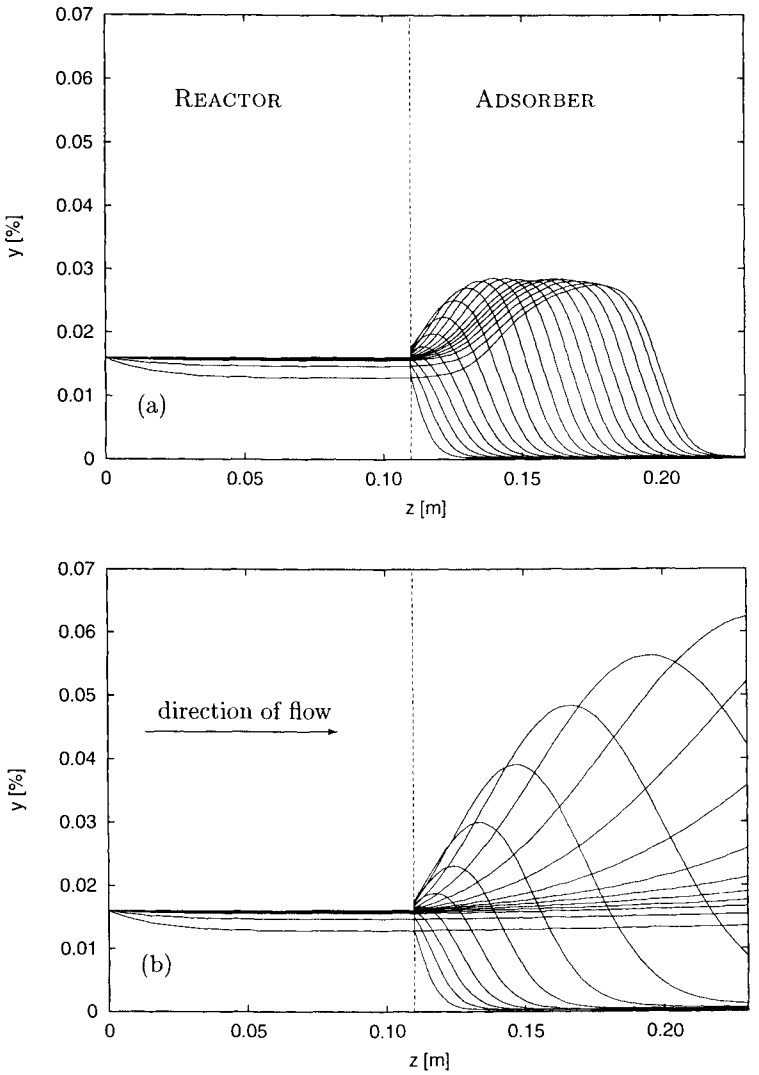

Figure 8: Propagation of concentration fronts in a downstream connected adsorber. During the first 200 s (a) intensively cooled adsorber, (b) adiabatic adsorber.

Interesting to observe is the effect of the desorption ratio d on the mean conversion. In both cases (adiabatic and cooled adsorber) can an improperly chosen value of d cause either a delay in the ignition or an extinction of an already propagating reaction in the reactor, both of which result in lower mean conversions. The reason for the extinction is that if too much gas is passed through the cool adsorber, the resulting temperature after mixing with the by-pass is below the extinction temperature. At the other extreme, the hot spot formation has been observed as a result of a "hydrocarbon shock", i.e. a sharp increase of HC concentration at the inlet to the ractor corresponding to the desorption peak. The maxima with respect to d can be found in the range of 0.01–0.05. A qualitatively different behavior can be observed for C_3H_8 in the case $t_s = 200$ s (Fig. 7 (f)). The conversion goes through a minimum for $d = 0.2$. A possible explanation is that this higher-igniting hydrocarbon is more sensitive to a delay in the ignition of the reaction. For comparison, the same parametric study was conducted with lower flowrate, SV = 25000/h. The results are qualitatively similar in this case, the only difference being that the lower flowrate allows to use higher values of d without decreasing conversions significantly.

Results from simulations with the FTP-cycle (cf. Fig. 9) reveal that an adaptive switching of streams is applicable also to cases where all inlet values are time-dependent. The dominant factor is in fact the temperature of the inlet stream, time variations of composition do not cause a significant change in the trends observed during the parametric study performed with the Euro-cycle. Fig. 9(f) ($t_s = 200$ s) shows that if the reactor is hot enough, then the effect of d is very low. On the contrary, for $t_s = 50$ and 100 s, the dependencies of conversion on d are very significant. An interesting example is the behavior for $d = 0.2$ (Fig. 10), where cumulative emissions are decreasing nonmonotously. This can be explained by comparing the dependence of inlet temperature (Fig. 2) with the results from Fig. 10. The relatively large temperature drop (occuring around 100 s) causes for $t_s = 50$ or 100 s a significant delay in the reactor start-up, because the inlet gas is brought into a still cool reactor end (countercurrently), which blows out the developing reaction zone. For $t_s = 200$ s, the inlet temperature is already high enough and the early switch does not matter.

5. CONCLUSIONS

It has been shown that an adsorber connected in series with a catalytic converter with a switching of the order of units in the desorption part of the dynamic operation cycle, can improve the efficiency of HC removal from automobile exhaust gases during the cold start period. The possible range of applications of the system studied here is not limited just to the treatment of gases from mobile sources. The computational design methodology proposed here (i.e. accumulation of some species in an adsorber with a subsequent thermal regeneration when conditions in the complementary reactor become favorable), can also be used in other VOC combustion situations where it is desirable to modify (delay) the properties of a stream in time.

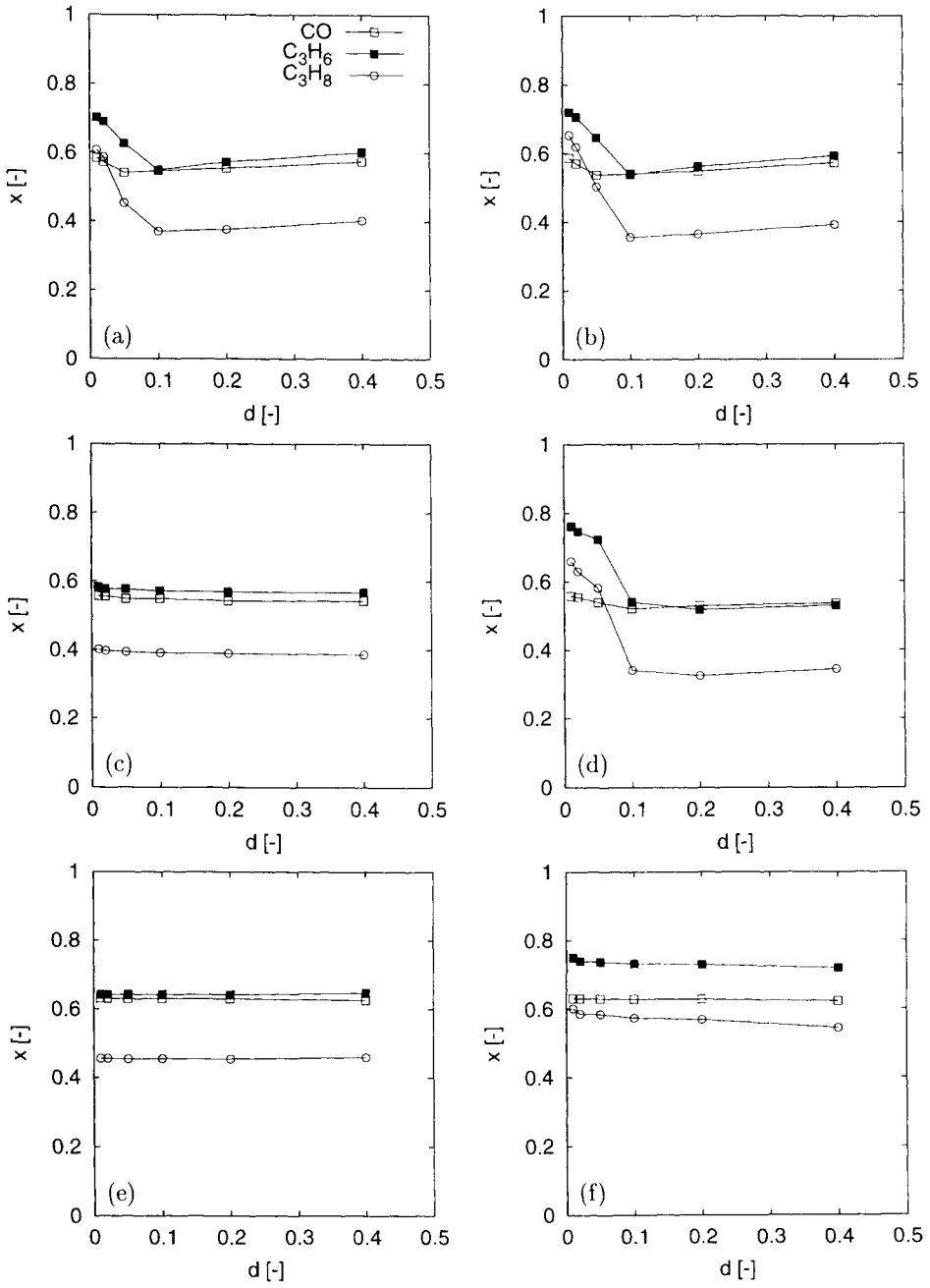

Figure 9: Dependence of total conversion of CO, C_3H_6, and C_3H_8 on the desorption ratio d for different switching times: (a) and (b) $t_s = 50$ s, (c) and (d) $t_s = 100$ s, (e) and (f) $t_s = 200$ s. Graphs (a), (c), and (e) – adiabatic adsorber, graphs (b), (d), and (f) – intensively cooled adsorber ($k_{w,a} = 3 \cdot 10^5$ J m^{-3} s^{-1} K^{-1}, $T_w = 298$ K). Total conversion is defined as a ratio of converted to entering mass of pollutant over the part of FTP-cycle.

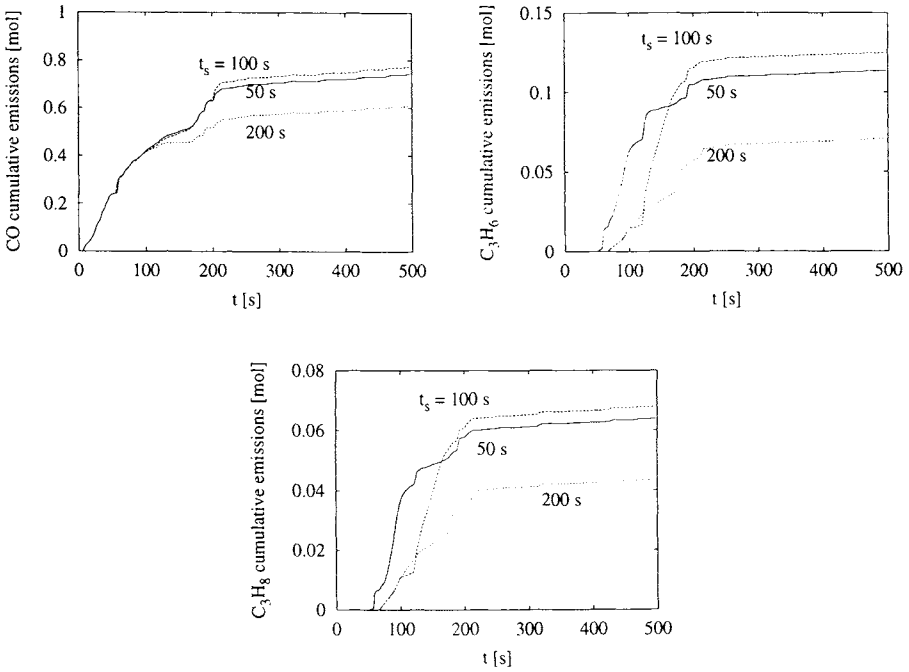

Figure 10: Cumulative emissions – reactor - adsorber arrangement, cf. Fig. 4c; t_s = 50, 100, 200 s, d = 0.2 (inlet conditions defined in Fig. 2).

REFERENCES

1. R.M. Heck and R.J. Farrauto, Catalytic Air Pollution Control – Commercial Technology. Van Nostrand Reinhold, New York, 1995.
2. J. Jirát, F. Štěpánek, M. Kubíček, and M. Marek, Chem. Eng. Sci., in press, (1999).
3. F. Štěpánek, J. Jirát, M. Kubíček, and M. Marek, Comp. Chem. Eng., accepted, (1999).
4. P. Pinkas, D. Šnita, M. Kubíček and M. Marek, Chem. Eng. Sci., 49 (1994), 5347–5358.
5. T. Kirchner and G. Eigenberger, Chem. Eng. Sci. , 51 (1996), 2409–2418.
6. P.L. Burk, J.K. Hochmuth, D.R. Anderson, S. Sung, A. Punke, E. Dahle, S.J. Tauster, C.O. Tolentino, J. Rogalo, G. Miles, M. Mignano and M. Niejako, Stud. Surf. Sci. Catal., 96 (1995), 919–930.
7. T. Cnop and G. Baron, Proc. 1st ECCE, Florence, Italy, (1997).
8. J.K. Lampert, M. Deeba and R.J. Farrauto, 2nd World Congress on Environmental Catalysis, Miami Beach, FL, USA, November 15-20, (1998).
9. L. Xinsheng, D.A. Arendarskii and J.K. Lampert, Hydrocarbon trapping in promoted zeolites for gasoline cold start conditions. 2nd World Congress on Environmental Catalysis, Miami Beach, FL, USA, November 15-20, (1998).

10. D.S. Lafyatis, G.P. Ansell, S.C. Bennett, J.C. Frost, P.J. Millington, R.R. Rajaram, A.P. Walker and T.H. Ballinger, Appl. Cat. B, 18 (1998), 123–135.
11. G.C. Koltsakis, P.A. Konstantinidis and A.M. Stamatelos, *Appl. Catal. B* **12** (1997), 161–191.
12. W.M. Kays and M.E. Crawford, Convective heat and mass transfer, McGraw-Hill, New York, 1993.
13. S. H. Oh, Chap. 8, E. R. Becker and C. J. Pereira (editors), M. Dekker, New York, 1993
14. S. Farooq, M.M. Hassan and D.M. Ruthven, Chem. Eng. Sci., 43 (1998), 1017–1031.
15. M. Kubíček, P. Pinkas, J. Jirát, D. Šnita and M. Marek, Comp. Chem. Eng., 21 (1997), S757–S762.

Reaction Engineering for Pollution Prevention
M.A. Abraham and R.P. Hesketh (Editors)

Reactive distillation for synthesizing ethyl *tert*-butyl ether from bioethanol

A. T. Quitain, H. Itoh and S. Goto*

Department of Chemical Engineering, Nagoya University, Chikusa, Nagoya 464-8603, Japan

Reactive distillation, a configuration in which the reaction section is located inside the column is employed to continuously synthesize ethyl *tert*-butyl ether (abbreviated as ETBE) from bioethanol (2.5 mol% ethanol in aqueous solution) and *tert*-butyl alcohol (TBA) using Amberlyst 15 in the pellet form as a catalyst. Results under standard operating conditions indicate that ETBE at about 60 mol% could be obtained in the distillate, and almost pure water in the residue. The conversion of TBA and the selectivity of ETBE were 99.9 and 35.9 %, respectively. The effects of operating conditions on conversion and selectivity are also investigated. Further purification of the distillate using the residue resulted into 95 mol% ETBE.

The experimental results are compared with the results calculated by using ASPEN PLUS simulator.

1. INTRODUCTION

Environmental regulations on emissions of carbon monoxide and unburned hydrocarbon especially from automobile exhaust are becoming more strict worldwide. These regulations would further increase the demand for ethers such as methyl *tert*-butyl ether (MTBE) and ethyl *tert*-butyl ether (ETBE) as gasoline oxygenates. Although MTBE produced directly from the reaction of isobutene (IB) and methanol (MeOH) is currently predominant in industry, ETBE may become a better option since this is derived mainly from ethanol (EtOH), which can be obtained from renewable resources like biomass. Also, ETBE having a blending Reid vapor pressure (BRvp) of 4 psi outranks MTBE as an octane enhancer and is more attractive than MTBE since low BRvp blends less than 8 psi is required in some places during summer. Furthermore, the supply of IB, which is mostly derived from non-renewable crude oil, may become limited, and for this reason alternative routes for the synthesis of ETBE are currently being explored [1]. *tert*-Butyl alcohol (TBA), which is a major byproduct of propylene oxide production from isobutane and propylene, can be employed instead of IB as a reactant [2].

*Author to whom correspondence should be addressed.
E-mail address: goto@park.nuce.nagoya-u.ac.jp

The primary concern of the present study is to continuously synthesize ETBE from TBA and EtOH at a concentration as low as that obtained from fermentation of biomass. EtOH concentration obtained from the fermentation of carob pod, for example, was reported by Roukas [3] to be maximum at 1.40 x 10^3 mol/m^3 (about 2.67 mol% in aqueous solution). In the present study, the aqueous solution of EtOH at 2.5 mol% is used to represent bioethanol.

Reactive distillation, a configuration in which the reaction section is located within the distillation column is employed. The use of this type of configuration to the direct synthesis of ETBE from TBA and bioethanol may reduce the energy requirement in separating EtOH from bioethanol. Sneesby *et al.* [4] investigated this column configuration in the synthesis of ETBE from IB and EtOH at operating pressure of 950 kPa. In this present study, however, the system is operated at mild temperature and pressure.

Moreover, in the separation of alcohol or hydrocarbons from compounds like ethers, purification with water is an effective separation technique. For example, industrial processes for obtaining high-grade MTBE utilize water to separate methanol (MeOH) from ethers or hydrocarbons by extraction [5]. This purification method is applied to concentrate ETBE in the distillate in this study.

The experimental results are compared with the results calculated by using ASPEN PLUS, a sequential modular simulation software package.

2. EXPERIMENTAL

2.1 Apparatus

Figure 1a shows the schematic diagram of the set-up. A vacuum-insulated column (inside diameter = 3.5 cm, height = 85 cm) was connected to the central opening of the flask. Catalysts (Amberlyst 15 in pellet form) of 100 g were placed inside the column to allow simultaneous reaction and separation of products. Stainless steel mesh saddles (48 mesh, 3 mm diameter, 6 mm height) were used as packing materials for the rectifying and stripping sections of the column (height = 30 and 35 cm, respectively). Thermocouples were connected to measure the temperature profiles inside the column. A circulating water at a temperature of about 278 K served as a coolant for the condenser located at the top. A gas meter was connected to measure the amount of IB gas escaping from the condenser. The reflux ratio was controlled by the solenoid valve with a multitimer.

2.2 Procedure

A mixture of TBA, EtOH and H_2O was placed inside the bottom flask and heated up to its boiling point. When the distillate appeared at the top, the feed mixture of TBA, EtOH and H_2O at room temperature was introduced to the lower part of the reaction section by using a peristaltic pump. At the same time, liquid from the reboiler was withdrawn by another peristaltic pump. Then, continuous operation was started. The liquid level in the reboiler was maintained by adjusting the tip of the withdrawing pipe connected to the pump. The experiment was conducted for about 7 hours. After every hour, the distillate and the residue were collected, weighed and analyzed.

Samples of the distillate and the residue were analyzed using Shimadzu Gas Chromatograph with 3.0 m column filled with Gaskuropack 54 serving as packing materials. The column temperature was set at 443 K while injection port temperature at 453 K.

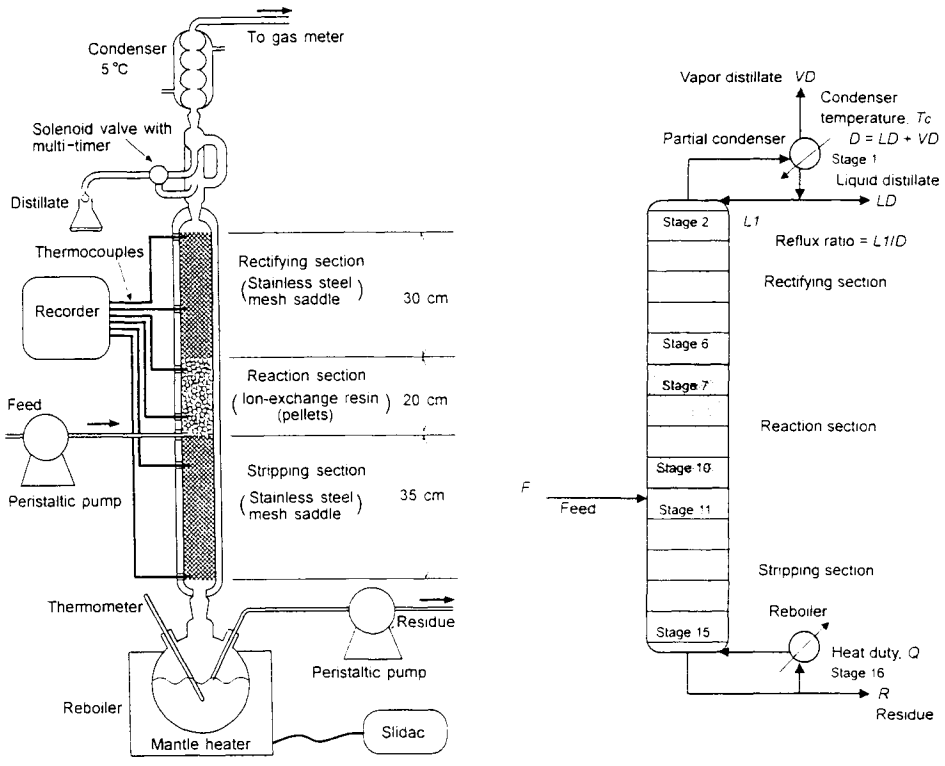

a) Experimental set-up b) Simulation's column configuration

Figure 1. Diagram of experimental set-up and column configuration for simulation of reactive distillation

3. SIMULATION

3.1 ASPEN PLUS

Venkataraman *et al.* [6] applied ASPEN PLUS to simulation of reactive distillation. The RADFRAC module of ASPEN PLUS can also be used to simulate the reactive distillation column shown in Fig. 1b. In the simulation, a property option set PSRK based on the predictive Soave-Redlich-Kwong equation of state was used. The Soave-Redlich-Kwong method has been widely used for the prediction of enthalpy and other properties (Sneesby *et al.*, 1997). Using UNIFAC, the PSRK method is predictive for any interaction that can be predicted by UNIFAC at low pressure.

The column consisted of 16 stages, including a partial reboiler and a partial condenser. The reaction section in the middle of the column was represented by four reactive stages. The reaction was assumed to take place in the liquid phase.

In the simulation, reaction kinetics obtained from the experiments using a CSTR was used [7]. The reaction kinetics considered the production of ETBE from TBA and EtOH, dehydration of TBA and the inhibition effect of H_2O and EtOH. The results were verified by experiments using a batch reactor.

3.2 Preliminary study on ASPEN PLUS simulation of distillation system without reaction

The RADFRAC module in ASPEN PLUS is a rigorous model for all types of multistage vapor-liquid fractionation operations. However, our experiments used packing materials in the column. In simulating a packed column, an infinite number of stages should be assigned due to very high vapor-liquid interaction within the column. However, certain problems such as convergence and long computation time may be encountered in employing an infinite number of stages. In this study, based on the geometric configuration of the column used in the experiment, rectifying, reaction and stripping section were first allocated for 5, 4 and 5 stages, respectively for a total of 16 stages (including a condenser and a reboiler). The results of the simulation did not change when the number of stages in each section was doubled. Thus, a total of 16 stages is considered sufficient to simulate our system.

The simulation was then verified by the distillation experiments without reaction. The same experimental apparatus in Fig. 1 was used. To remove the catalytic activity, the ion exchange resins in the H^+ form were treated overnight with NaCl solution to change to Na^+ form and then washed with distilled water. Experimental data at the steady state were obtained after 4 hours of continuous operations.

Figure 2 shows the temperature profiles of the column for three different cases, that is, ternary and quaternary systems without reactions and the standard condition with reactions (described in section 3.1).

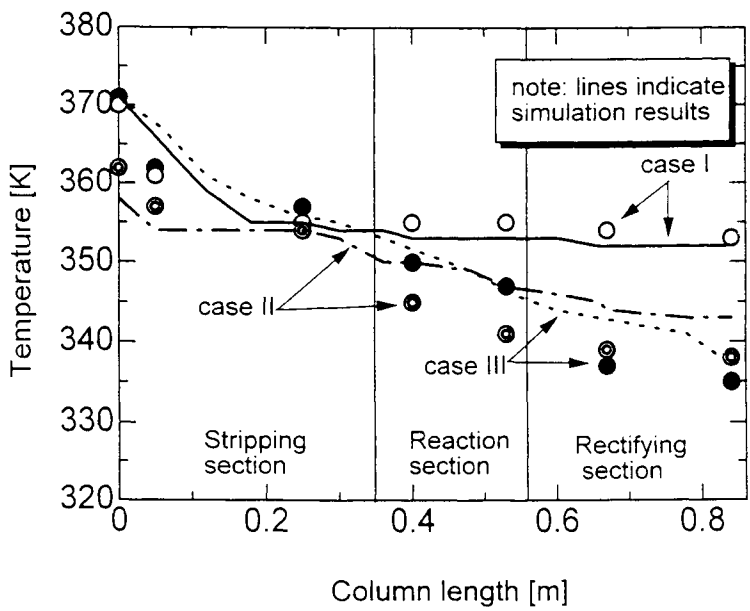

Figure 2. Experimental column temperature profiles and simulation results at three different cases (Case I -Ternary distillation without reaction, Case II - Quaternary distillation without reaction, Case III - Reactive distillation at the standard condition)

For the ternary system (TBA-ETOH-H_2O), the simulation results of compositions in both the liquid distillate and the residue and the column temperature agree well with the experimental data. This may imply that ASPEN PLUS can be used for the simulation of the packed bed column in this work.

On the other hand, for quaternary system (ETBE-TBA-ETOH-H_2O), the simulation results of the compositions in the liquid distillate and the column temperature are a little different from the experimental data. This may be due to inaccurate UNIFAC-prediction of the interaction parameters between the components for the quaternary system [8].

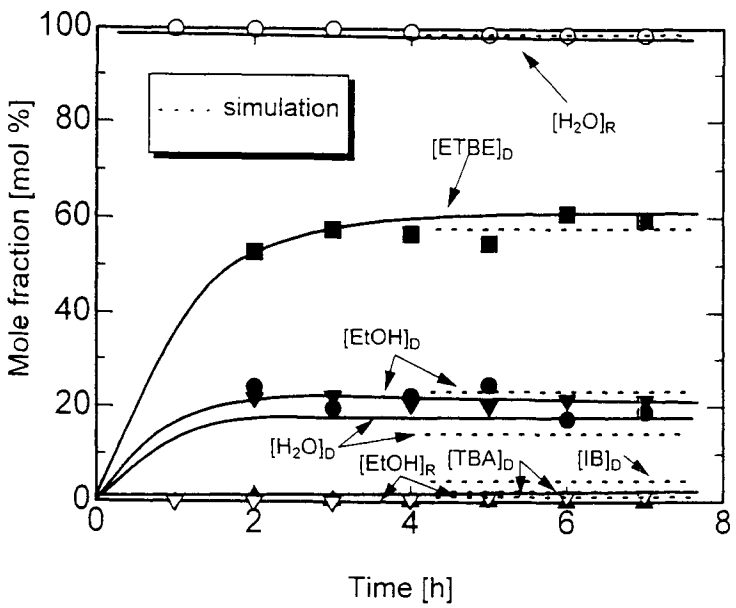

Figure 3. Concentration profiles of distillate and residue under standard conditions (Total feed molar flowrate = 4.13 x 10^{-3} mol/s, Reflux ratio = 7.0, Catalyst = 0.1 kg, Feed molar ratio = 1:1:38(TBA:EtOH:H_2O))

4. RESULTS AND DISCUSSIONS

4.1 Standard condition

The experimental column temperature profile under standard conditions with reactions agrees well with the simulation as shown in Fig.2 (Case III), although slight differences can be observed at the temperatures above the reaction section.

Figure 3 shows the mole fraction profiles for both the distillate and the residue under standard conditions. At about 55 mol% ETBE, two layers appeared in the distillate as observed in the previous work [9]. The lower layer consisting of mostly water (about 91 mol%) was negligible compared to the ETBE-rich upper layer. For this reason, only the mole fractions of the upper layer are shown in Fig. 3.

The steady state can be attained after about 4 hours. The mole fraction of ETBE in the distillate at the steady state ($[ETBE]_D$) is about 60 mol%. Both the mole fractions of EtOH and H_2O in the distillate ($[EtOH]_D$ and $[H_2O]_D$) are about 20 mol%, while TBA is negligible. The residue consists of mostly H_2O and slight amount of EtOH. The dotted lines in Fig. 3 indicate the simulation results by using ASPEN PLUS. The agreements between experimental and simulation results are comparable to the quaternary system without reactions.

The flow rate of gaseous product consisting of mostly IB (about 99.2 mol%), *VD*, was determined as 1.34×10^{-5} mol/s by a soap film meter. The flow rate of liquid distillate, *LD*, was obtained as 6.98×10^{-6} mol/s from the increase of weight in the reservoir during a specified period.

It is important to convert TBA into more useful products (IB and ETBE) and to obtain ETBE in the distillate as high as possible. Then, the conversion of TBA and the selectivity of ETBE are defined as follows:

$$\text{Conversion} = \frac{\text{molar flowrate of ETBE and IB in the distillate}}{\text{feed molar flowrate of TBA}} \tag{1}$$

$$\text{Selectivity} = \frac{\text{molar flowrate of ETBE in the distillate}}{\text{molar flowrate of ETBE and IB in the distillate}} \tag{2}$$

The conversion of TBA and the selectivity of ETBE under standard conditions are 99.9 and 35.9 %, respectively. The operating conditions were varied to study the effect on conversion of TBA and selectivity of ETBE.

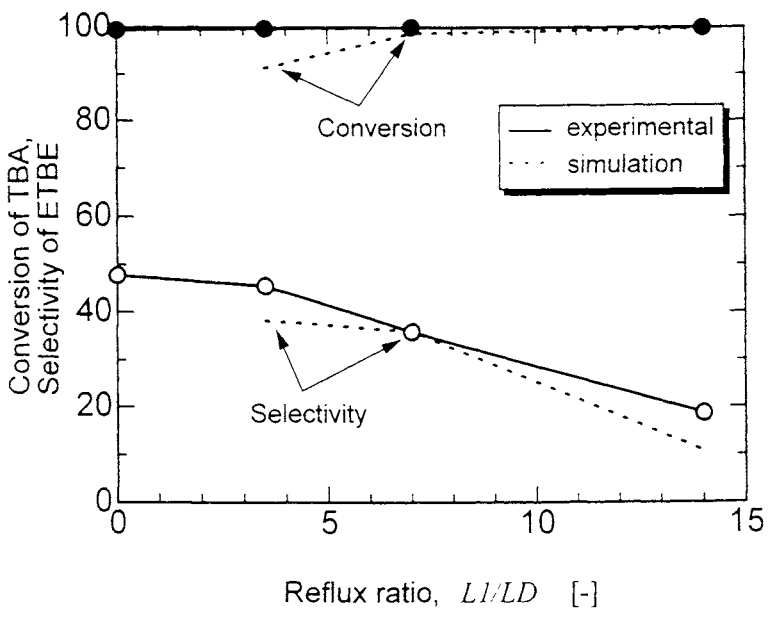

Figure 4. Effect of reflux ratio on conversion of TBA and selectivity of ETBE

4.2 Effect of reflux ratio

Figure 4 shows that the increase in reflux ratio only decreases the selectivity of ETBE resulting to increase of unconverted EtOH in the residue. Although the selectivity of ETBE decreases with increasing reflux ratio, the conversion of TBA is still high at 99.9 %. This implies that TBA dehydrates fast at any values of reflux ratio. The simulation results represented by dotted lines are in good agreement with the experimental results.

4.3 Effect of total feed flowrate

An increase in the feed molar flowrate from 2.06 x 10^{-3} to 4.13 x 10^{-3} mol/s doesn't have a significant effect on the selectivity of ETBE. However, further increasing the flowrate to 5.16 x 10^{-3} mol/s decreases the selectivity. The lowering of column temperature resulting from an increase in the feed flowrate may account for this decrease in ETBE production. The conversion is not affected by the change in flowrate which means that an increase in flowrate favors the dehydration of TBA to IB gas.

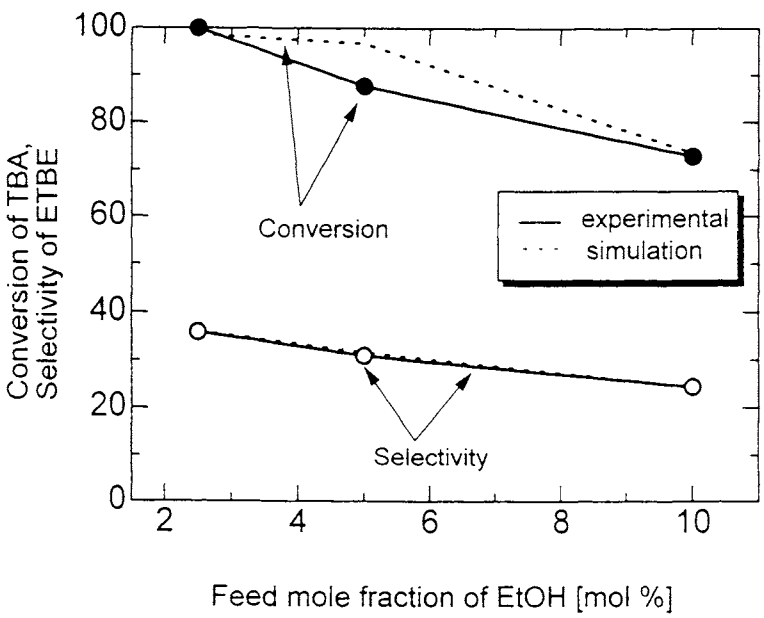

Figure 5. Effect of feed mole fraction of EtOH on conversion of TBA and selectivity of ETBE (Feed molar ratio of TBA to EtOH = 1)

4.4 Effect of feed mole fraction of EtOH

The feed concentrations were changed with equimolar ratio of TBA to EtOH. When the feed mole fraction of EtOH is 10 %, the conversion of TBA and the selectivity of ETBE are low at 73 and 24 %, respectively as shown in Fig. 5. Decreasing the feed mole fraction of EtOH to 2.5 % increases the conversion and the selectivity. This suggests that bioethanol, that is, 2.5 mol% EtOH in the feed is suitable to produce ETBE.

4.5 Effect of feed molar ratio of TBA to EtOH

In order to reduce the production of IB gas, the molar ratio of TBA to EtOH was decreased from the standard operating condition of 1 to 0.5 while maintaining the values of other parameters. The selectivity of ETBE increases with decreasing molar ratio of TBA. However, the decrease in the amount of TBA in the feed increases the amount of unconverted EtOH in both the residue and the distillate. Increasing the molar ratio to 2 did not increase the production of ETBE but only accelerates the dehydration of TBA.

4.6 Effect of catalyst on the selectivity of ETBE

The selectivity of ETBE can be improved by using catalysts other than Amberlyst 15 which favors dehydration of TBA to IB. It was reported in the previous works of Matouq *et al.* [10] and Yin *et al.* [11] that the selectivity of ethers over IB is high for $KHSO_4$ and HPA catalysts. However, pellets cannot be formed from these catalysts and cannot be utilized in the reactive distillation column being used in this study.

The gaseous IB products in this work can be utilized for the direct synthesis of ETBE and is currently being studied in our laboratory by ASPEN PLUS simulation.

5. ETBE PURIFICATION

To purify ETBE, the liquid distillate obtained under standard operating conditions (reflux ratio = 7.0) was mixed with the residue (almost pure water). Purification was done by adding different volumes of residue to 2.0 x 10^{-5} m^3 of liquid distillate initially at 60 mol % ETBE. It was mixed thoroughly and then was allowed to stabilize. The upper layer consisting of mostly ETBE was analyzed using the gas chromatograph.

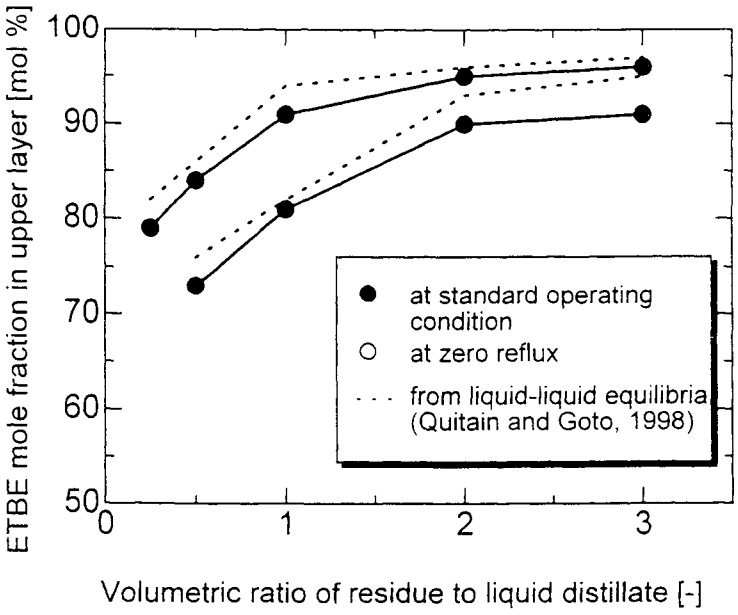

Figure 6. ETBE mole fraction in upper layer

Figure 6 shows that ETBE mole fraction in the upper layer increases to as high as 95 mol%. Other components in the upper layer are 3 mol% EtOH and 2 mol% H_2O. The aqueous phase contains only about 1 mol% EtOH.

The same procedure is carried out for the liquid distillate of 53 mol% ETBE obtained at zero reflux. Results in Fig. 6 show that ETBE mole fraction increases to as high as 91 mol%.

The mole fractions of ETBE in the upper layer is determined from ETBE-ETOH-H_2O liquid-liquid equilibrium diagrams (Fig. 1 in Quitain and Goto [8]). Figure 6 shows that the liquid-liquid equilibrium compositions are always a little higher than the experimental results.

6. CONCLUSIONS

Reactive distillation was employed to synthesize continuously ETBE from bioethanol (2.5 mol% ethanol in aqueous solution) and TBA catalyzed by Amberlyst 15 in the pellet form. At the standard condition, ETBE at about 60 mol% could be obtained in the distillate and almost pure water in the residue. The conversion of TBA and the selectivity of ETBE were found to be 99.9 and 35.9 %, respectively. At zero reflux, the selectivity was high at 48 %, but the ETBE concentration was low at 53 mol%. Further extraction of the distillate obtained at the standard condition by using the residue as an extractant resulted into ETBE concentration as high as 95 mol%. The ASPEN PLUS simulation results are in good agreements with the experimental data.

NOMENCLATURE

D	=	total distillate flowrate (=LD+VD)	[mol/s]
F	=	feed flowrate	[mol/s]
LD	=	liquid distillate flowrate	[mol/s]
$L1$	=	liquid flowrate to return from stage 1 to stage 2	[mol/s]
Q	=	heat duty at the reboiler	[J/s]
T_C	=	temperature at the condenser	[K]
VD	=	vapor distillate flowrate	[mol/s]

<Subscripts>

D	=	distillate
L	=	liquid
R	=	residue
F	=	feed

<Abbreviations>

ETBE	=	ethyl *tert*-butyl ether, 2-ethoxy 2-methyl propane (IUPAC)
EtOH	=	ethanol
H_2O	=	water
IB	=	isobutene
TBA	=	*tert*-butyl alcohol, 2-methyl 2-propanol (IUPAC)

REFERENCES

1. K. L. Rihko, A. Outi and L. Krause, Ind. Eng. Chem. Res., 35 (1996) 2500.
2. B. Yang and S. Goto, Sep. Sci. Tech., 32 (1997) 971.
3. T. Roukas, Food Biotechnology (N.Y.), 9 (1995) 175.
4. M. G. Sneesby, M. O. Tade, R. Datta and T. N. Smith, Ind. Eng. Chem. Res., 36 (1997) 1855.
5. "Refining 1996", Hydrocarbon Processing, 75 (1996) 113.
6. S. Venkataraman, W. K. Chan and J. F. Boston, Chem. Eng. Proc., 86 (1990) 45.
7. A. T. Quitain, H. Itoh and S. Goto, J. of Chem. Eng. Japan, 32 (1999) 280.
8. A. T. Quitain and S. Goto, Can. J. Chem. Eng., 76 (1998) 828.
9. M. Matouq, A.T Quitain, K. Takahashi and S.Goto, Ind. Eng. Chem. Res., 35 (1996) 982.
10. M. Matouq, T. Tagawa and S. Goto, J. of Chem. Eng. Japan, 27 (1994) 302.
11. X. Yin, B. Yang and S. Goto; Int. J. Chem. Kinetics, 27 (1995) 1065.

Reaction Engineering for Pollution Prevention
M.A. Abraham and R.P. Hesketh (Editors)

Environmentally benign hydrocarbon processing applications of single and integrated permreactors

Savvas Vasileiadis* and Zoe Ziaka

ZiVaTech, 15549 Dearborn Street, North Hills, CA 91343, USA and
University of Southern California, University Park, Los Angeles CA 90089, USA

ABSTRACT

Experimental, modeling and design results are presented here for methane-steam reforming and the propane dehydrogenation reaction in various catalytic inorganic permreactors. The proposed permreactors can be beneficially used as reactant and/or product recycling and distributing devices, also as two side (tube and shell) feed acceptors and distributors to contact reforming and dehydrogenation reactions. Enhanced conversions and yields (beyond the equilibrium and conventional PFR reactor levels) can be achieved for various types of permreactor operation (i.e., CFBP, FBP, CP) for the methane steam reforming and propane dehydrogenation as demonstrated by comprehensive experimental studies at various reaction, separation conditions and permreactor configurations (i.e., temperature, two sides pressure, feed flowrate and composition, sweep gas flowrate and composition). Modeling results of these two reaction schemes simulate the operation of the various permreactors and fit satisfactory the experimental data over a wide range of parameters. The models can be used also for designing and optimizing the permreactor systems. The recovered H_2, and H_2 rich mixtures from the membrane reactor operations can be used as fuel in power generation systems, and in chemical synthesis reactions.

New process designs are also presented for steam hydrocarbon reforming, the water gas shift, and paraffin (e.g., propane, ethane, n/i-butane) dehydrogenation in inorganic, metal, and organic-polymer permreactors and permeators. These constitute the basis for designing improved, environmentally benign, integrated hydrocarbon upgrading and in-situ CO_2 abatement systems for hydrogen, H_2-CO_2, synthesis gas, and hydrogen rich hydrocarbon generation. The permeated or combined product gases can be utilized in-line for synthesis (e.g., methanol, ammonia, hydrogenations) or as feed in molten carbonate and other types of hydrogen based fuel cells, and in power generation systems (e.g., gas turbines and engines). The rejected from downstream permeator streams can be recycled into reformer, water gas shift reactor or used in consecutive reforming, water gas shift steps. In dehydrogenator case, rejected olefin streams such as propylene, ethylene, n/i-butene can be used for polymer production (e.g., polypropylene,

*corresponding author

polyethylene) or in other chemical synthesis.

Use also of catalytic permreactors and possible membrane materials is presented for the still non-commercialized, methane-CO_2 reforming route with and without steam. The process can be applied effectively for converting landfill and coal gases, acidic natural gas, flue gases rich in CH_4 and CO_2, and CO_2 and CH_4 mixtures to synthesis gas (a CO and H_2 rich mixture).

Environmentally benign utilization of product gases from the CO_2 reforming process, especially dry synthesis gas product, is proposed for use in integrated power generation systems, fuel cells and in chemical feedstock synthesis. Overall thermal efficiency of the proposed processes can be increased by utilizing heats of reactions, thermal content of exiting from reactor streams and external waste heat sources to cover respective thermal requirements of reactors, permreactors and permeators in an autothermic type of operation.

Keywords: H_2 generation, in-situ CO_2 abatement, steam-CO_2 hydrocarbon reforming, paraffin dehydrogenation, membranes, permreactors, permeators.

1. INTRODUCTION

Permreactors or most commonly called membrane reactors in relevant chemical engineering literature, integrate reaction and separation processes into a single engineering operation. If the membrane unit is used only for separating processing fluids (e.g., gases, liquids or mixtures of the two) then it is called membrane separator or permeator. The membrane reaction and separation technology has been implemented extensively during the last years in both the commercial and experimental bench scale level as well as theoretically and computationally. It covers a wide variety of reactions and separations. Those vary from liquid phase filtrations and separations of both aqueous and non-aqueous mixtures to gas phase homogeneous and heterogeneous (catalytic) reactions to multiphase processes [1-56,93,94].

Membrane reactor and/or permeator materials can be inorganic ceramics or glasses such as alumina, silica, titania, zirconia or metals such as palladium, nickel, palladium-silver alloys or organic polymers, carbon based materials, and organic polymer-inorganic composites.

Permreactors have been applied in the past to both thermodynamically and kinetically limited reactions for increasing conversion, yield and/or selectivity towards conventional reactors. Concomitant effects of such an operation is elimination of by-product formation (i.e., selectivity increases), low temperature permreactor operation, reduced catalyst deactivation and process energy savings; they can also offer innovative designs for unreacted materials recovery, recycling and reuse including processing of toxic and hazardous chemicals [93].

Utilization of the above merits of membrane reactors in hydrocarbon processing and upgrading reactions such as reforming and dehydrogenations is certainly an appealing engineering task. We have worked during the last years on experimental and modeling studies of ceramic alumina-based membrane reactors for the methane steam reforming and propane dehydrogenation reactions. Partial data of the related work have

been reported in earlier communications [19,20,22-23,36-38], while a comprehensive presentation is given in [21,35].

The purpose of the current communication is to review our research work on membrane reactors and permeators for hydrocarbon processing and upgrading and specifically experiments and modeling results with methane steam reforming and propane dehydrogenation reactions; also to present new process designs for steam and CO_2 reforming, water gas shift and paraffin dehydrogenation. In methane steam reforming and propane dehydrogenation we present additional work in ceramic alumina permreactors in the areas of experiments, design, operation, parameter selection and optimization of such systems. The data presented can be used as useful reference by other researchers for selecting catalysis, permreactor design and configurations, operating parameters, and optimized range of conditions for permreactor operation. The presented experiments and simulation by models are of current significance in the area of membrane reactor design and operation. This is because of the unique experimental characteristics of the examined permreactor systems and respective modeling analysis in terms of catalytic permreactor modification (CP, CFBP), permreactor configurations examined (e.g., shell and tube distributed feed permreactor) and utilized operating permreactor parameters (reaction and separation conditions). The results are also important for comparison purposes with similar permreactor systems applied to same reactions [24,39]. They confirm the equilibrium shift in reactant (i.e., methane, propane) conversion and product yield (i.e., hydrogen, CO, CO_2, propylene) by use of specific permreactor configurations, in such thermodynamically limited reactions and in comparison with the results obtained in conventional (non-permeable) reactors.

In methane steam reforming permreactor experiments the data which report on CO_2 yield is presented for first time in related literature. It is indicative of the extent of the simultaneously occurring water gas shift reaction in the methane steam reforming reaction scheme. Modeling results presented for reforming and dehydrogenation reactions describe the effect of variation of key design parameters in final performance measures such as reactant conversion, product yield, species partial pressures.

The blank (non-modified) ceramic membranes used, were commercially provided sol-gel type alumina tubes, of asymmetric multilayer structure, with top permselective layer of 40-50Å pore diameter and have been used as well in related membrane reactor studies [19-24,35-38,43-47].

Moreover, the goal in this communication is to present single and integrated permreactor and permeator systems related to environmentally benign and energy efficient steam ($H_2O(g)$) and/or CO_2 reforming of feedstocks such as natural, coal, landfill and flue gases and to paraffin dehydrogenation reactions. Further, it presents processing applications of the produced synthesis gas (H_2, CO), H_2-CO_2, H_2-hydrocarbon mixtures, and pure H_2 gas. Several chemical commodities today such as pure hydrogen fuel, synthesis gas (a H_2, CO mixture), and olefins of polymer/synthesis grade (e.g., propylene, ethylene, n-butene, isobutene) are produced from petroleum, light naphtha, coal or natural gas steam reforming and paraffin (e.g., ethane, propane, n/i-butane) catalytic dehydrogenation reactions.

The objective of these studies is the development of permreactor and permeator technology for increased conversion, separation, and additional utilization (e.g., through membrane unit recycling processes) of primary and secondary hydrocarbon feedstocks and their products. Membrane processes can be used as example, in both early purification stage of sulfur, nitrogen, halogenes containing compounds (NH_3, H_2S, HCl) of natural, coal, landfill gas and other gaseous hydrocarbon feedstocks (e.g., paraffins) as well as in main conversion and upgrading sections (e.g., reforming, dehydrogenation, oxidation) of these feedstocks through permreactors and permeators [51,54].

It is also discussed the use of systems of permeable reactors and permeators or conventional reactors and permeators in methane steam reforming and water gas shift processing cycles for separation of H_2 and H_2, CO_2 products from the exit reformed gases for use in chemical synthesis or power generation (e.g., fuel cells, gas turbines). Various materials, including high Tg polymers, ceramics and metals can be used in these operations for recovery of H_2 and CO_2 from the reacted streams [51,53,54]. The rejected CH_4 and/or CO streams from the permeator can be recycled into the inlet of the reformer/water gas shift reactor for increasing the process efficiency through unreacted materials utilization. Utilized process feedstocks include natural gas, types of coal gas (mainly mixtures rich in CH_4 and CO) , light hydrocarbons (naphtha) and CO. Products H_2 and CO_2 can be used directly, or after the CO_2 condensation, pure H_2 can be recovered and used in synthesis or as fuel.

Furthermore, we report the use of systems of permeable reactors and permeators and conventional reactors and permeators in ethane, propane, n/i-butane dehydrogenation reactions for production of respective olefins; these can be considered sample reactions for hydrogen production from low carbon paraffin hydrocarbons. According to the newly proposed processes, product H_2 can be recovered/separated from synthesis grade olefin products (ethylene, propylene, butylene) through permselective membranes and can be used in subsequent chemical synthesis (e.g., CH_3OH, NH_3, hydrogenations) or as a fuel in gas turbine and engine cycles (as H_2/O_2, or H_2/hydrocarbon/O_2 mixture) and in anode of various types of fuel cells.

Moreover, we seek to design membrane reactors and processes which eliminate greenhouse gas emissions from reaction and separation sources. CO_2 is a main component of coal, landfill and acidic natural gas, and byproduct of all fossil and upgraded hydrocarbon combustion processing; also is usually a product in methane steam reforming and water gas shift reaction schemes. CO_2 from the above sources, if not utilized, contributes together with unreacted CH_4, as greenhouse gases, to global warming. Recent environmental legislation calls for global reduction of CO_2 and CH_4 emissions from fossil fuel processing/combustion and other relevant sources. The proposed reforming processes seek for in-situ CO_2 conversion and abatement of its greenhouse effects. It is highly desirable from an environmentally benign and cost effective standpoint to seek for ways of reducing CO_2 emissions in the source, that is by utilizing alternative reaction routes and special catalysts in the reformer, such as this of reforming CH_4 with CO_2 instead of steam in an all dry gas reforming process. The product in specific catalyst formulations, is mostly an equimolar synthesis gas mixture of H_2 and CO. Alternatively, both CO_2 and steam can react with CH_4 over specific catalysts

to yield synthesis gas. The developing technology controls (concentrates and/or converts) the CO_2 containing streams by using integration of membrane reactors and permeators or conventional reactors and permeators. The synthesis gas product can be used directly for production of methanol, gasoline type hydrocarbons through Fischer Tropsch synthesis, or in power generation systems.

As follows, we include our detailed experimental and modeling studies with different catalytic membrane reactor configurations for methane steam reforming (including the water gas shift) [35] and propane dehydrogenation reactions [21]. Key process parameters such as reaction temperature, two side pressures, space time, feed composition, sweep gas flow and composition (e.g., inert and reactive sweep gases) and catalytic permreactor configurations (i.e., CP, FBP, CFBP) were varied experimentally to yield applicable permreactor designs with gas flow configurations for improved operation in the above described and related processes.

2. DESIGN EQUATIONS FOR PERMREACTOR MODELING (METHANE STEAM REFORMING, PROPANE DEHYDROGENATION)

Related modeling of such permreactors (membrane reactors) have been described in earlier communications [19,20,21,35-37,45,46]. Here we provide an overview of the models used, with specific details for the reactions studied, the applied reactor configurations and the numerical methods of solution.

We developed and implemented numerically membrane reactor models adapted to the specific studied configurations of methane steam reforming and propane dehydrogenation experiments [21,35]. The models simulate the acquired data and predict conditions for best membrane reactor module operation. Thus far, we have worked and present experimental and computational results with three types of membrane reactors as defined below: 1) FBP, fixed bed permreactor. The catalyst is a fixed bed of particles packed within the tubeside of the ceramic tube which remains inert (noncatalytic membrane) 2) CP, catalytic permreactor. The tubeside is empty but the membrane tube becomes catalytic by wet impregnation 3) CFBP, catalytic fixed bed permreactor. It combines the previous two permreactors; the tubeside contains a fixed bed of catalytic particles and the ceramic membrane is catalytically impregnated. The conventional tubular reactor is defined as PFR (plug flow reactor). It is the nonpermeable mode of the above described permreactors. The shellside is closed and flow directed only axially through the tubeside. The tubeside contains a fixed bed of catalyst (nonpermeable FBP) or is empty (nonpermeable CP). Similar membrane reactor configurations and definitions are described elsewhere [19,46].

The models describe numerically reaction and separation operations in these reactors which are cylindrical multilayer asymmetric alumina tubes with about 40-50Å pore diameter permselective layers. Thermal and mass balances describe transport and reaction operations through inert and catalytic membranes in cylindrical coordinates. Tubeside and shellside of permreactors are described by plug flow type mass and heat balances and axial pressure drop equations along the catalytically packed sides. The kinetic and transport parameters used in modeling were obtained experimentally by

independent kinetic and permeability experiments described in detail elsewhere [21,35]. For the kinetic experiments the nonpermeable plug flow fixed or catalytic reactor (PFR) was used with the shellside closed and flow allowed only through the tubeside. The final derived design equations are based on the following assumptions [19,21,35]:

- The permreactors and conventional reactors operate at steady state, isothermal conditions (catalytic packed phase, membrane tube, fluid phase in both sides of the membrane are at same temperature). Plug flow conditions exist in tubeside and shellside with no radial concentration gradients in either of the sides. Sweep gas in shellside is flown concurrently with the tubeside gas. No mass transfer limitations exist between fluid phase and catalyst particles and between the tubeside/shellside and the membrane interface. For FBP, CFBP and the fixed type PFR, catalyst particles are fixed in the tubeside while the shellside is empty and with negligible pressure drop. No internal diffusion limitations exist in the catalyst particles. Ideal gas mixtures are assumed. A two layer structure is assumed for modeling the membrane operation. A permselective layer in the inner surface of the cylindrical alumina tube with Knudsen type diffusion, and a support with negligible mass transfer resistance. Gas permeabilities or diffusivities are independent of each other and independent of concentration or pressure.

The CP and FBP membrane reactors are subsystems of the CFBP configuration and their equations are derived accordingly from those of CFBP by rearrangement of the respective terms. The same also happens with the PFR equations. The initial dimensional equations are rendered dimensionless for use in modeling.

Below we present the dimensionless forms of the CFBP design equations and their incorporated dimensionless parameters.

In the Catalytic Membrane:

$$\frac{d^2 Y_j^m}{d\omega^2} = -\sum_{i=1}^{M} \frac{\nu_{ij}}{\delta_j} exp\,(2\alpha\omega)\,\Phi_i^2 r'^m_i \qquad (A)$$

With boundary conditions:

at $\omega = 0$ $\qquad Y_j^m = X_j^F \psi^F$

at $\omega = 1$ $\qquad Y_j^m = X_j^P \psi^P$

where r'^m_i is the dimensionless form of r_i^m.

In the Tubeside of the Membrane:

$$\frac{dy_j^F}{d\varsigma} = \frac{Q\delta_j}{\alpha}\left(\frac{dY_j^m}{d\omega}\right)_{\omega=0} + \sum_{i=1}^{M} \nu_{ij} Da_i^F R'^F_i \qquad \text{(B)}$$

with the initial condition:

at $\zeta = 0$ $\qquad y_j^F = X_{jo}{}^F$

where $R'_i{}^F$ is the dimensionless form of R_i^F.

In the Shellside of the Membrane:

$$\frac{dy_j^P}{d\varsigma} = -\frac{Q\delta_j}{\alpha}\left(\frac{dY_j^m}{d\omega}\right)_{\omega=1} \qquad \text{(C)}$$

with the initial condition:

at $\zeta = 0$ $\qquad y_j^P = Fr\,\psi^{PF} X_{jo}{}^P$

The pressure drop equation in the tubeside becomes:

$$-\psi^F \frac{d\psi^F}{d\varsigma} = \frac{f\left(\frac{F_o^F}{\pi R_1^2}\right)^2 M_A L\left(\sum_j y_j^F \nu_j\right)^2}{g_c d_p RT\left(\sum_j X_j^F \nu_j\right)} \qquad \text{(D)}$$

with the following initial condition:

at $\zeta = 0$ $\qquad \psi^F = 1$

Where the friction factor f is given by:

$$f = \left(\frac{1-\varepsilon_\upsilon}{\varepsilon_\upsilon^3}\right)\left(1.75 + \frac{150\,(1-\varepsilon_\upsilon)}{N_{Re}}\right)$$

this equation is valid for $N_{Re}<500(1-\varepsilon_u)$, with $N_{Re} = d_p G^F/\mu$

The following dimensionless quantities have been defined in the above equations:

$$Y_j^m = \frac{P_j^m}{P_o^F},\ X_j^{F(P)} = \frac{P_j^{F(P)}}{P^{F(P)}},\ \psi^{PF} = \frac{P_o^P}{P_o^F},\ y_j^F = \frac{n_j^F}{n_o^F},\ y_j^P = \frac{n_j^P}{n_o^F}$$

$$v_j = \frac{M_j}{M_A},\ \xi = \frac{r}{R_1},\ \delta_j = \frac{D_{je}}{D_{Ae}},\ \zeta = \frac{z}{L},\ K'^F_{ei} = K^F_{ei}\left(P_o^F\right)^{\beta_i^f - \beta_i^r}$$

$$Q = \frac{2\pi D_{Ae} L}{F_o^F},\ Fr = \frac{F_o^P}{F_o^F},\ \varepsilon = \frac{R_2 - R_1}{R_1},\ \omega = \frac{ln\xi}{\alpha},\ \alpha = ln\,(1+\varepsilon)$$

$$\Phi_i = \alpha R_1 \sqrt{\frac{k_i' RT}{D_{A\,e}}}$$

$$Da_i^F = \frac{\pi R_1^2 L k_i^F \left(P_o^F\right)^{\beta_i^f}}{n_o^F},\ \psi^{F(P)} = \frac{P^{F(P)}}{P_o^F},\ Fm_j = \frac{n_{jo}^P}{n_{CH_4 o}^F (C_3H_8{}^o)}$$

The definition of each parameter and its respective units is given in notation at the end of the paper. ***j,*** in the equations can be any of the species in methane steam reforming or propane dehydrogenation reactions; ***i,*** is a reaction index corresponding to a specific reaction equation.

$r_i'^m$, $R_i'^F$ in equations (A), (B) are respectively the reaction rates within the catalytic membrane and in the fixed catalyst in tubeside. These are usually of heterogeneous form and are functions of reaction and adsorption constants and of reactant and product partial pressures and the reaction equilibrium constants. Thereby, their dimensional forms can be represented as follows:

$$r_i^m, R_i^F = f(k_i^F, k'_i, K_j, P_j^F, Pj^m, K_{ei}) \qquad (E)$$

The rate constants and final reaction rate expressions (for methane steam reforming and propane dehydrogenation) were obtained from independent kinetic experiments with the PFR configuration and incorporated within equations (A) and (B). Fixed bed PFRs were used for determining the rate constants in the catalyst particles. The same catalyst particles were used in the permreactor experiments (FBP and CFBP modules). Empty PFRs were used for determining the rate constants in the catalytic membranes. The membrane tubes were impregnated with suitable catalytic solutions and were consequently used as permreactors (CP modules).

The reaction rate expressions, reaction, adsorption and equilibrium constants and their experimental and computational estimation for methane steam reforming and propane dehydrogenation have been presented in detail elsewhere [21,35]. For methane steam reforming, the rate expressions used in PFR and membrane reactors are based on the heterogeneous kinetic model developed originally by Xu and Froment based on reactions (1-3) below [60].

For the reaction in fixed bed catalyst in PFR tubeside, the first two reactions (1-2) were used to interpret the experimental data from the PFR and obtain values for the kinetic constants k_1^F and k_2^F. The rate expressions for the two reactions with the derived constants were used subsequently in modeling the membrane reactors and the PFR and in simulating the experimental results:

$$CH_4 + H_2O = CO + 3H_2, \quad -\Delta H^o_{298} = -206.1 \text{ kJ/mol, (reverse of methanation)} \quad (1)$$

$$CO + H_2O = CO_2 + H_2, \quad -\Delta H^o_{298} = 41.15 \text{ kJ/mol, (water gas shift)} \quad (2)$$

For the reaction in empty catalytic PFR and CP modules, no CO was detected, thus the following combined reforming reaction was used to interpret experimental results and obtain values for the kinetic constant within the membrane (k'_3), and subsequently in modeling:

$$CH_4 + 2H_2O = CO_2 + 4H_2, \qquad -\Delta H^o_{298} = -165.0 \text{ kJ/mol,} \qquad (3)$$

For the experiments with the propane system, the main dehydrogenation reaction was occurring, and no byproducts were detectable for reaction temperatures up to 500°C, in the fixed bed catalyst and catalytic membrane. The respective reaction rates and derived rate constants for the fixed bed (k_4^F) and empty PFR (k'_4) modes were calculated from such experiments, based on the stoichiometry of the main dehydrogenation reaction given below:

$$C_3H_8 = C_3H_6 + H_2 \qquad -\Delta H^o_{298} = -124.3 \text{kJ/mol} \qquad (4)$$

Equilibrium constants for the above reactions, used within the rate expressions (E), were calculated computationally by using tabulated data of heat capacities, standard heats of reactions and standard Gibbs free energy changes.

The FBP design model is derived from above set of equations (A through E) by eliminating only the reaction term in catalytic membrane given in equation (A). Similarly, the CP design model is represented by same set of equations (A-E) by eliminating only the reaction term in fixed bed catalyst given in equation (B). The PFR model is derived by eliminating equations (A) and (C), and using equation (B) without the permeation term and equation (D) for the pressure drop in tubeside.

The above design equations for the permreactors were solved numerically [21,35,53]. The differential equations (A) in the membrane were solved as a two point boundary value problem by using a variable order, variable step size finite difference method with deferred conditions. The DBVPFD routine of IMSL was used to perform this numerical task. The axial differential equations (B,C,D) in tubeside and shellside of membrane reactors were solved as an initial value problem by using the Adams Moulton integration method (routine DIVPAG of IMSL). The same routine was also used to solve the respective differential equations in the plug flow reactor (PFR) to obtain the rate constants [21,35]. To achieve this, an optimization procedure had to be used. This was done by minimizing the sum of squares of residuals of the experimental molar flowrates at the reactor exit with those calculated using the PFR model equations (the material balance and pressure drop equations in tubeside). The DUNLSF optimization routine which involves a modified Levenberg-Marquardt algorithm was combined with the DIVPAG to perform these computations. For the permreactors and PFRs, the species mole fractions or partial pressures were obtained axially in the reactor and radially across the membrane and translated into reactant conversion and product yield.

3. METHANE STEAM REFORMING PERMREACTORS; EXPERIMENTAL AND MODELING RESULTS

The reaction of methane reforming by steam is the traditional complete methane oxidation route which uses steam as an alternative route oxidant instead of oxygen or air. Its kinetics and catalysis have been studied extensively in the literature due to its industrial significance in converting fossil hydrocarbon feedstocks to synthesis gas or hydrogen [57-60,85-88]. In most cases, it is the parallel reaction scheme of the endothermic reverse of methanation (1) combined with the slightly exothermic water gas shift (2). The composition of the product stream in H_2, CO, CO_2 depends on the activity and specificity of the catalyst to carry out these two independent reactions. Usually, for H_2 production, most of the CO produced is furthermore converted in the same catalyst to CO_2 via the water gas shift. This increases the H_2 throughput from the reformer and eliminates the need for a subsequent water gas shift reactor. Even if the water gas shift is part of the methane steam reforming process (reactions (1) and (2)), in the text below for clearness purposes, we are referring on this reaction separately.

The experimental and modeling studies of the methane steam reforming and water gas shift reactions in various catalytic membrane reactor configurations are presented. One of the tasks of these studies is to compare the performance of membrane reactors with this of an nonpermeable plug flow-packed bed catalytic reactor to project advances and drawbacks of the permreactor technology in these applications. For each

permreactor experiment, we have also calculated and include within the same plot, the thermodynamic equilibrium values of conversion, yield and/or selectivity at the specific experimental conditions (i.e., reaction temperature, pressure and feed composition). In FBP and CFBP modules, reactions (1) and (2) were assumed to occur simultaneously and equilibrium conversions, yields were calculated accordingly. In CP module no CO was detected and reaction (3) was assumed to take place. Equilibrium values were also calculated based on reaction (3); its equilibrium constant is the product of equilibrium constants of reactions (1) and (2). It is necessary to report equilibrium values in the experiments below in order to verify equilibrium shift and improvement in conversion, yield obtained with the membrane reactors.

3.1 Experimental Section

Sol-Gel type hollow cylindrical alumina tubes (Membralox) supplied by Alcoa were used as membrane reactors. They were of ID=7mm, OD=10mm and length=254mm. The membranes were asymmetric consisting of three thin microporous layers on the top of a macroporous thick support (15μm average pore diameter and 1.5mm thick). Reported average pore diameters of the three consecutive layers starting with the top inner layer were 40Å, 2000Å and 8000Å, having 5, 30 and 50μm thickness respectively. Top layer was a sol-gel made γ-Al_2O_3 with the remaining two layers and the support consisting of α-Al_2O_3.

The steam reforming catalyst was supplied by Katalco, it was 15% NiO supported on a calcium aluminate support enriched with earth metals. Particles of 0.92mm average diameter were used as fixed bed catalyst in the tubeside of the membrane tubes to make FBP, CFBP and conventional PFR configurations. For the CP and CFBP membrane configurations nickel salts in aqueous solutions (i.e., $NiNO_3$) were used to impregnate the alumina tubes to make catalytic membranes [35].

The experiments for methane steam reforming were done with the apparatus/experimental set-up described already in earlier communications [20,35-38]. Gas flowrates were measured before the inlet of the reactor. The feed gases were premixed with prepurified steam in a steam generator operated under saturation conditions and after preheating in a stainless steel coil the final mixture was introduced into the membrane reactor assembly.

The membrane reactor works in a tube and shell configuration. The ceramic tube is placed symmetrically inside the cylindrical openings of an HK40-stainless steel shell (reactor) to make the feedside (tubeside) and shellside (permeate side) of the membrane reactor. The external stainless steel reactor shell has additional inlet and outlet ports for the influx and discharge of the sweep gas in permeate side (shellside). The two ends of the ceramic tube are sealed inside the shell openings with a compressible, high temperature resistant graphitized string and compression fittings. The entire cylindrical SS shell with the membrane tube inside was thermally controlled by means of three Omega CN2000 temperature controllers, six semi-cylindrical ceramic heaters and three Ni-Cr thermocouples attached to the external membrane surface at equidistant points. Additional temperature control was applied into the catalyst bed in tubeside by means of two additional thermocouples placed in the inlet and outlet. For the experiments reported

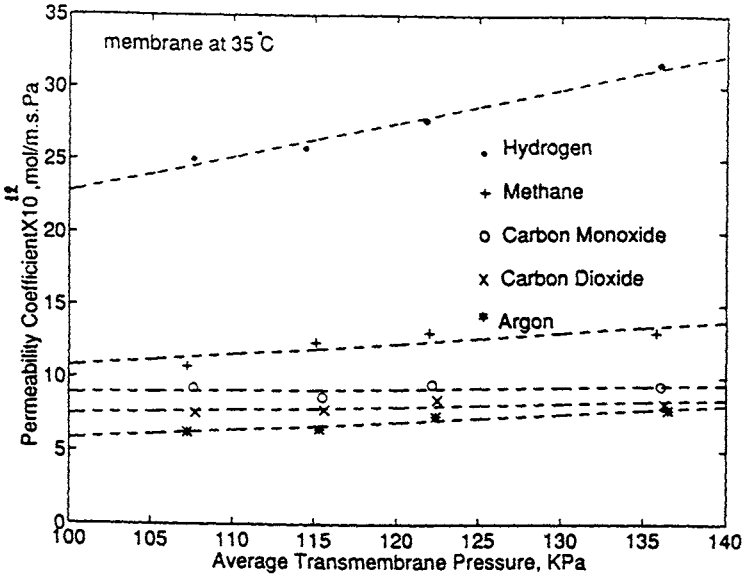

Fig.1 Permeability coefficients versus average transmembrane pressure at 308K (35°C) for unmodified alumina membranes

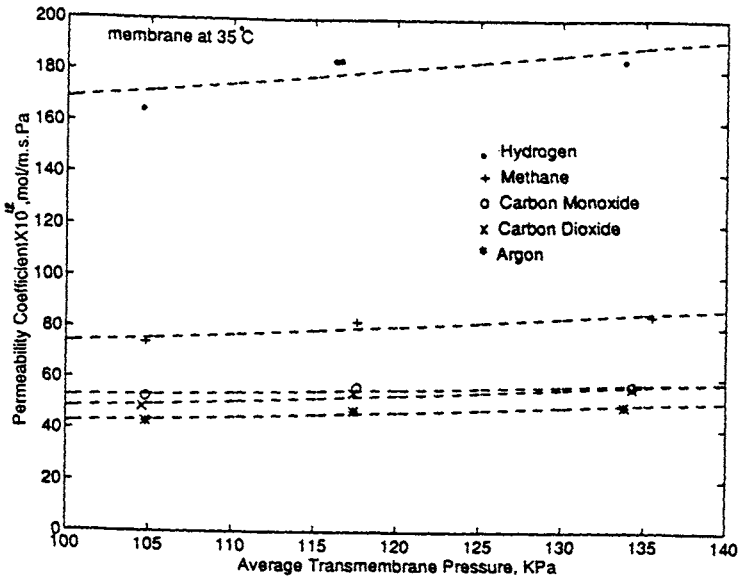

Fig.2 Permeability coefficients versus average transmembrane pressure at 308K (35°C) for catalytically modified alumina membranes

here isothermicity of the reactor axially and radially, within ±2°C was maintained. The membrane reactor pressure was adjusted by means of two needle valves placed in the tubeside and shellside exits. Pressure transducers were used to detect the pressure in tubeside and shellside (two transducers in each side). The effluent streams from the tubeside and shellside were condensed to remove the unreacted steam, then each of them was dried separately through a packed bed of calcium sulphate. Steam from the two sides was collected in separate vessels and measured volumetrically to satisfy the reacting water mass balance. After drying, the two side effluents were separately analyzed in composition by using an online gas chromatograph with a thermal conductivity detector. Volumetric flow rates of the two side effluents were separately measured by a wet flowmeter at room conditions.

The described experimental set-up was used for both the permreactor and conventional reactor (PFR) experiments. In the latter case the shellside ports were closed and the reactor assimilated a fixed bed catalytic reactor (the non permeate FBP case) or an empty tubular one (the non permeate CP case). The experiments listed here performed under constant catalytic activity. The activity of the catalytic reactors was checked daily in the conventional reactor mode at a standard reference temperature (550°C), pressure (10psig) and feed composition (CH_4:H_2O:H_2=1:4:0.2) conditions. To perform an experiment, first the catalyst bed was heated slowly to the reaction temperature under hydrogen flow. After temperature stabilization the steam flow was initiated and the tubeside pressure was adjusted to the desired value, then methane and hydrogen flow was turned on. A conventional reactor experiment was first performed at the set reaction conditions followed by a membrane reactor experiment with the shellside open. Next, new conditions were applied and another membrane reactor experiment was performed and recorded. The catalyst was reduced initially at 600-650°C under hydrogen flow for 24hrs. Also, the catalyst was reduced (activated) overnight in flowing hydrogen to reverse any oxidation from steam or deactivation from coke formation. For the methane space times used in these experiments coke deactivation was typically not a problem, and activity was almost unchanged by the end of the daily experiments as indicated by overall carbon balances. A carbon balance at every point of the reactor is given by, CH_4+CO_2+CO=CH_4(feed).

The following definitions apply:

(methane conversion)=CH_4(feed)-CH_4(exit)/CH_4(feed)
(carbon dioxide yield)=CO_2(exit)/CH_4(feed)
(carbon monoxide yield)=CO(exit)/CH_4(feed)

Experimental errors of the data obtained were estimated with the method of propagation of errors and were about 5% of the conversion, yield values for the methane steam reforming and propane dehydrogenation experiments.

3.2 Results and Discussion

We report in Fig.1 the permeability of the methane steam reforming gas species H_2, CH_4, CO, CO_2 and Ar (inert), through a blank (unmodified) alumina membrane tube

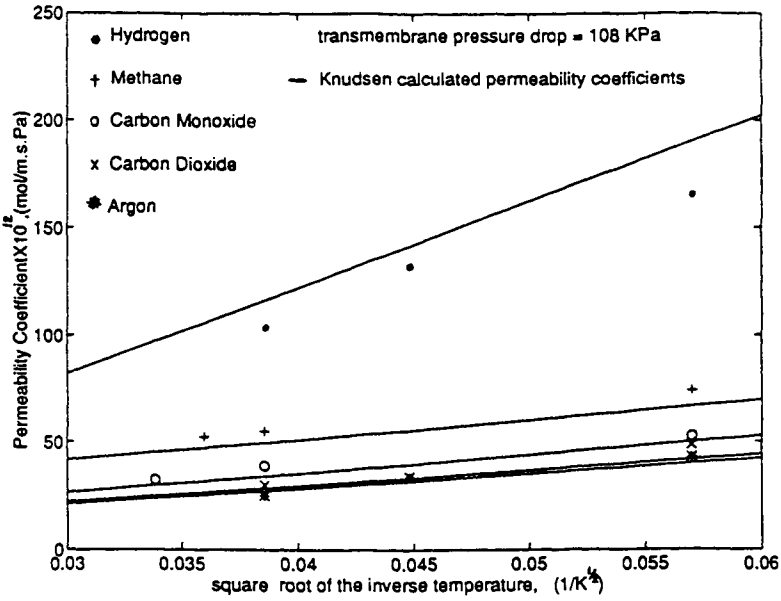

Fig.3 Permeability coefficients versus the square root of the inverse temperature for unmodified alumina membranes

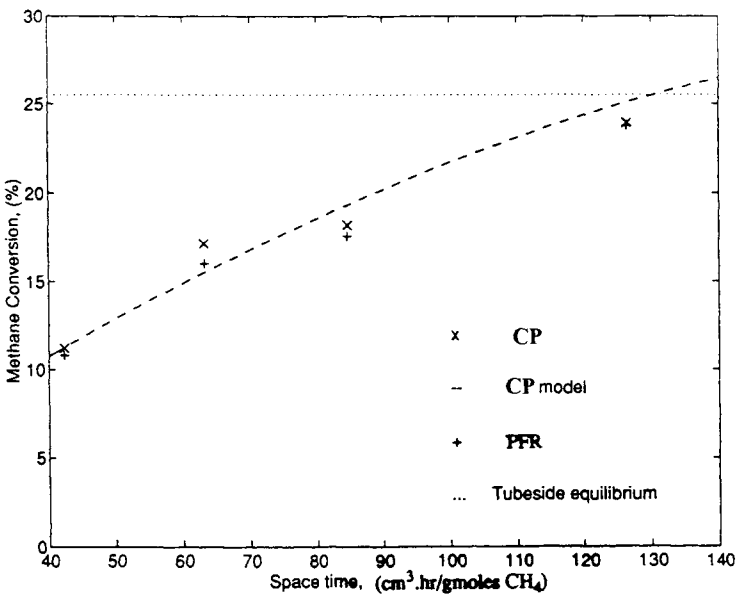

Fig.4 Effect of space time on CH_4 conversion in the CP and conventional empty catalytic reactor (PFR) at 475°C (tubeside feed: CH_4:H_2O:H_2 =1:2.5:0.2)

[35]. The permeabilities follow the Knudsen diffusional regime (horizontal lines) with a positive deviation as pressure increases due to a laminar flow contribution in the membrane [25,26]. Fig.2 reports on reduced permeability of the same gases in nickel oxide catalytically modified alumina membranes (incipient wetness impregnation with nickel nitrate solution was used) [35]. The wet tubes were dried at room temperature, subsequently in air flow at 100°C, and finally the catalyst was activated in H_2 flow at 600°C.

Catalytic modification tailors the product/reactant permeability (e.g., H_2/CH_4, CO/CH_4, CO_2/CH_4, H_2/C_3H_8, C_3H_6/C_3H_8) of ceramic membrane reactors by changing the species diffusivity (D_i) ($\bar{P}_i=D_i/RT$). There was an increase in selectivity of impregnated membranes with respect to the values of blank ones towards the Knudsen calculated values, as indicated by comparing respective values from the related plots (Figs.1&2 for methane steam reforming species, and Fig.25 below for propane dehydrogenation species).

The dependence of gas permeability ($\bar{P}_i$) on temperature is shown in Fig.3. The linear dependence on $1/\sqrt{T}$ is indicative of a Knudsen diffusion mechanism within the pores of the 40-50Å top permselective membrane layer. The deviation for H_2 from the Knudsen calculated lines, is again due to a laminar flow contribution.

In the described experiments below for methane steam reforming and propane dehydrogenation, transmembrane pressure drops were between 2.0-3.5 psig in various membrane reactor configurations. Pressure drops across the membrane for the CFBP and CP configurations were higher than those in FBP. Inert sweep gases were not used in the reported experiments except if otherwise indicated in the experimental description. However, experiments are reported with use of reactive sweep gases in shellside. Process simulations by use of models with use of inert and reactive sweep gases are also reported for both reaction schemes.

Fig.4, shows the exit methane conversion obtained with an impregnated tubular catalytic permreactor (CP) and also with its nonpermeable mode (i.e., with the shellside closed) at different residence times and constant temperature of 475°C and tubeside pressure of about 4.0 psig [35]. It is shown that the activity and/or amount of the impregnated $NiNO_3$ catalyst within the porous membrane was not enough for the membrane reactor conversion to exceed the PFR and equilibrium conversions at the temperature and space times used. However, methane conversion increases by increasing the space time and for high space times it approaches the equilibrium one. The CP model using kinetics based on reaction (3) simulates well the permreactor data.

Fig.5 shows the dependence of the exit CH_4 conversion on reaction temperature in the FBP, CFBP and PFR modules [35]. These are isothermal experiments with no pressure drop along the reactor tube and shell sides. In CFBP, in addition to the packed catalyst, the ceramic alumina tube became catalytic by incipient impregnation of $NiNO_3$ solution. The methane residence time for all reactors was about 50 $gr_{cat}.hr/gmole_{CH4}$, at tubeside pressures of about 10psig. The feed composition in tubeside was $CH_4:H_2O:H_2=1:4:0.20$. The conventional plug flow catalytic reactor (PFR) experiments were conducted at same conditions as those of membrane reactors with the shellside closed. The respective equilibrium points are also shown for comparison in the plots. The

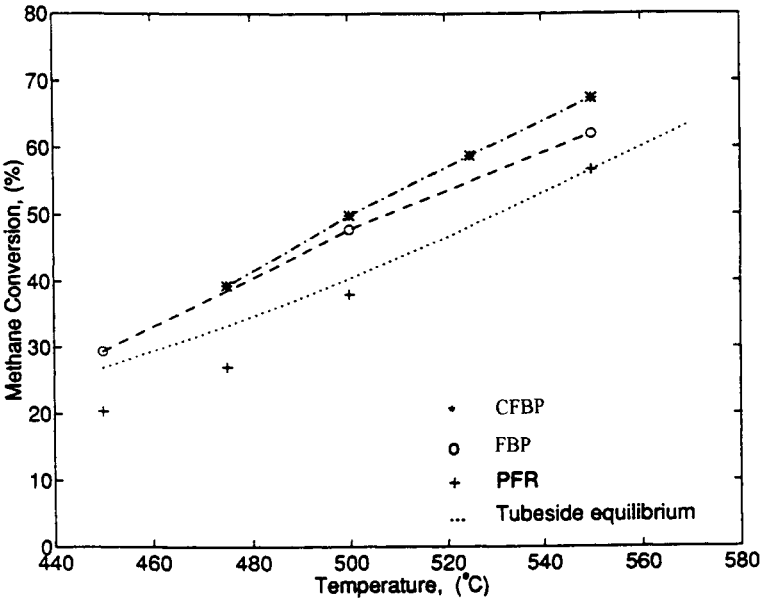

Fig.5 Effect of temperature on CH_4 conversion in the CFBP, FBP, and PFR (tubeside feed: CH_4:H_2O:H_2=1:4:0.2)

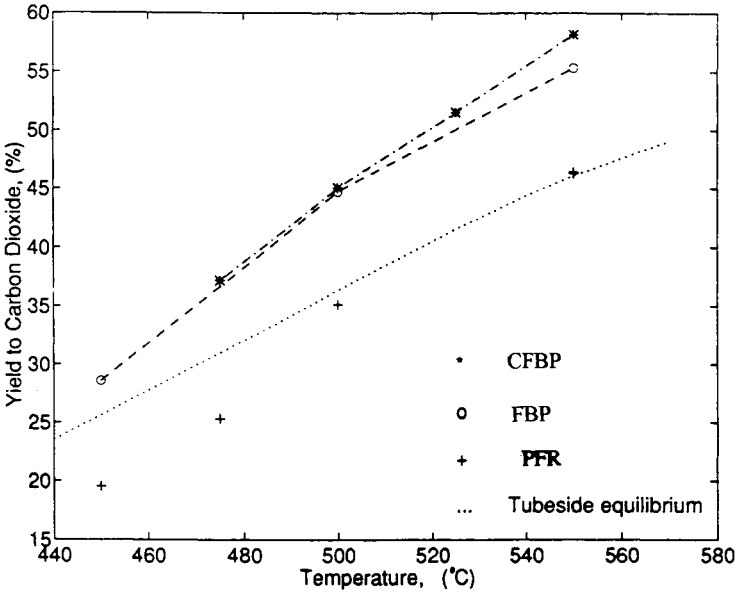

Fig.6 Effect of temperature on CO_2 yield in the CFBP, FBP, and PFR (tubeside feed: CH_4:H_2O:H_2=1:4:0.2)

conversion and yield improvements by using the permreactors can be practically implemented to increase hydrogen or synthesis gas production from related natural gas, coal gas (rich in CH_4) and methane feedstocks; also in applications where mixed streams of hydrogen and unreacted methane are desirable for cleaner and higher calorific value fuel, as in power or heat generation cycles. Similar results on CH_4 conversion have been obtained by Chai et al. [39], for similar methane steam reforming permreactors by using metal (Ru, Rh, Pt, Pd) dispersed alumina (Al_2O_3) membrane tubes either empty (CP type modules), or filled with Ru/Al_2O_3 catalyst pellets (CFBP, FBP, PFR type modules). Better than Knudsen permeabilities were reported for these membranes. They also observed larger improvements between CFBP and FBP modules by using the Ru and Rh impregnated membrane tubes.

We are also uniquely reporting on the corresponding experimental CO_2 yields in Fig.6 for the various reactor configurations, at the same with Fig.5 conditions. CO_2 product yield is a measure of the extent of the water gas shift (reaction (2)). Corresponding improvements by using membrane reactors correspond to increases in CO_2 yield with respect to the equilibrium and the PFR yields, as shown in Fig.6. A CO consumption (conversion) can be defined as: CO(formed)-CO(exit)/CH_4(feed). The CO consumption will be equal with the CO_2 yield because we assume that all CO_2 formed comes as product of the water gas shift.

The effect of permreactor tubeside pressure on methane conversion and carbon dioxide yield (indicative of the extent of the water gas shift reaction) is shown in Fig. 7 in CFBP module with respect to the equilibrium values [35]. The methane residence time in tubeside was fixed at 25 $gr_{cat}.hr/gmole_{CH4}$ at reaction temperature of 500°C. The conversion and yield of the overall reforming process [reactions (1) and (2) combined] are favored by high temperatures (endothermic) and low pressures (volume expansion). Therefore, it is necessary to operate the permreactor at reduced pressures to maximize methane conversion and hydrogen yield. For high pressure applications, such as in gas turbines (Figs.42-45), the exit reformed stream needs to be pressurized subsequently in the combustor inlet at the operating pressure of the turbine. The variable pressure experiments in Fig.7 are simulated well by the CFBP model, shown with dashed lines.

Figs. 8&9 report on the total increased H_2 production in FBP with respect to equilibrium and conventional packed bed reactor values for two different steam to methane feed ratios and feed compositions [35]. In Fig.8, the residence time was fixed at 48 $gr_{cat}.hr/gmole_{CH4}$ at about 10psig tubeside pressure; in Fig.9 the respective value was 54 $gr_{cat}.hr/gmole_{CH4}$ at about 3psig. Operation of a membrane reactor at various steam to methane to hydrogen to carbon oxide exit compositions can be applied to provide fuel for combustion with an adjustable calorific value content [52].

It is important to note in Figs.5-9 that the permreactors offer conversions and yields above equilibrium levels, even at the lower temperature of 400-450°C. These results can be effectively implemented in utilizing various low temperature, reject heat sources (e.g., flue gases from gas and steam turbines, combustion chambers, boilers, superheaters, or heat exchangers) to provide for the necessary endothermic heat of reaction for low temperature methane reforming, water gas shift, and dehydrogenation permreactor operations, with increased hydrogen or synthesis gas production and thermal

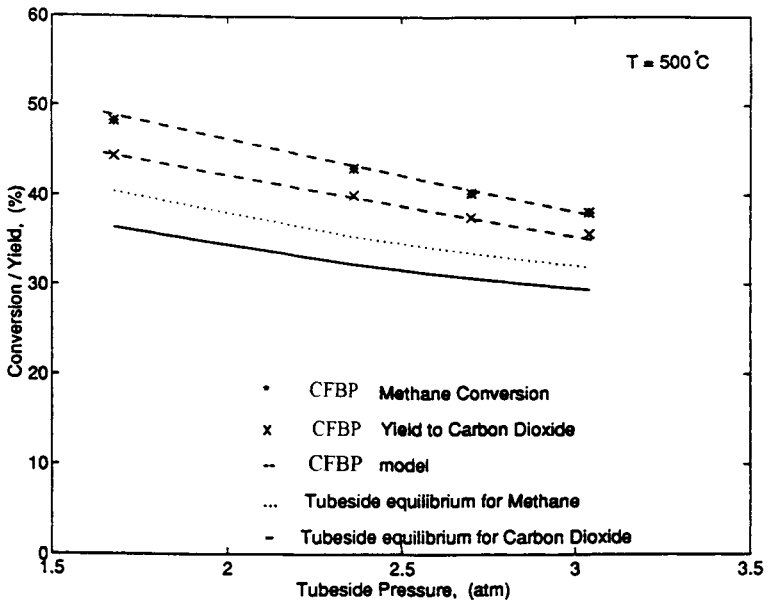

Fig.7 Effect of reaction pressure on CH_4 conversion and CO_2 yield in the CFBP (tubeside feed: CH_4:H_2O:H_2=1:4:0.2)

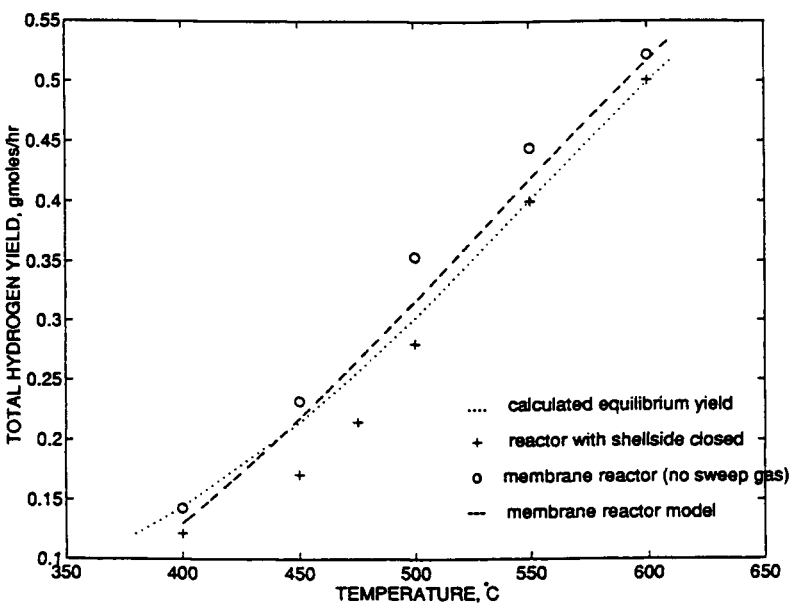

Fig.8 Effect of temperature on H_2 yield in the FBP and PFR (tubeside feed: CH_4:H_2O:H_2=1:4:0.2)

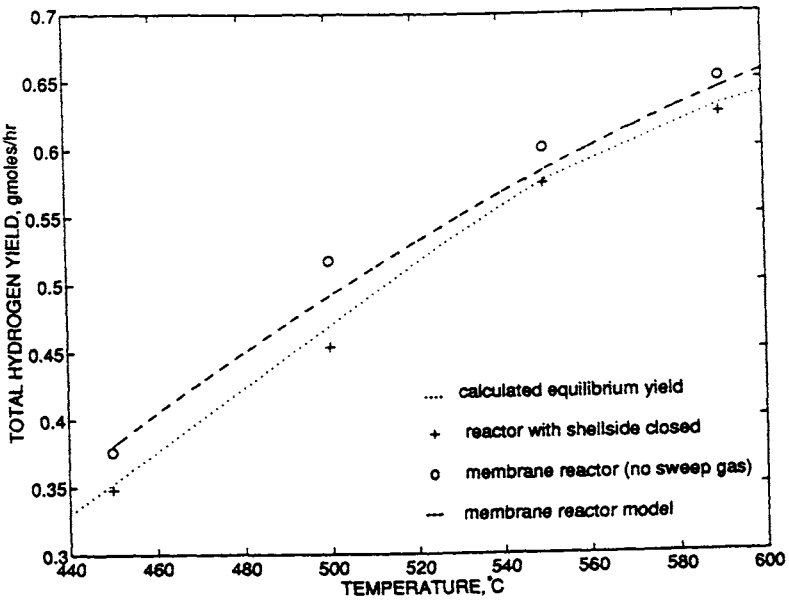

Fig.9 Effect of temperature on H_2 yield in the FBP and PFR (tubeside feed: CH_4:H_2O:H_2:Ar=1:7:1:0.75)

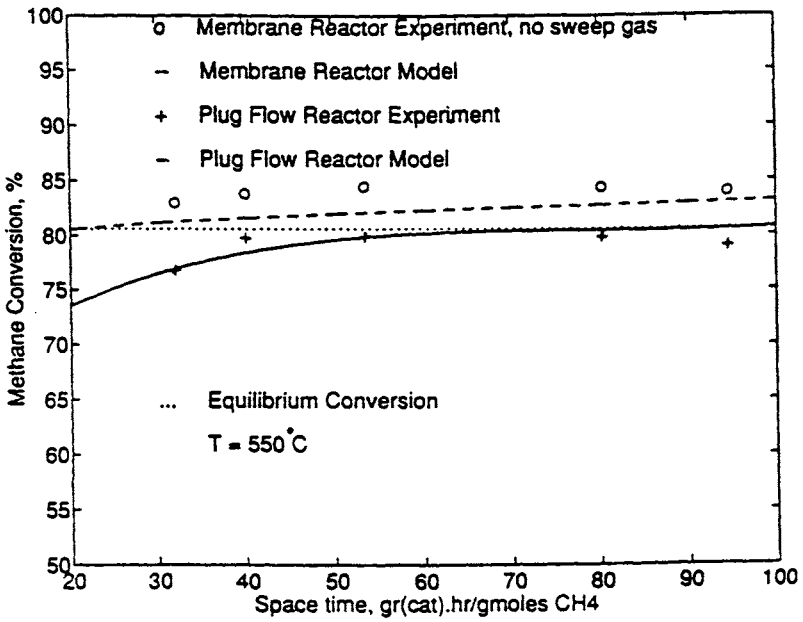

Fig.10 Effect of space time on CH_4 conversion in the FBP and PFR at 550°C, (tubeside feed: CH_4:H_2O:H_2:Ar=1:7:1:0.75)

efficiency as shown in Figs.42-45. This improved low temperature mode of permreactor operation, is combined with a concomitant beneficial extension of the life of reactor materials and catalysts (decreased sintering and coking). Increased thermal efficiency of membrane reactors and related processes is achieved through utilization of the heat of reaction of exothermic type reactions such as the water gas shift, and the waste heat from exit gas streams as shown in these Figures.

At lower inlet flowrates of reactants (methane and steam) in the tubeside, the reactant space time is increased and both conversions and yields are enhanced. An example of this effect is shown in Figs.10&11 for the CH_4 conversion and CO_2 yield in FBP and PFR modules at 550°C and about 3psig tubeside pressure [35]. A high steam to carbon ratio (i.e., H_2O:CH_4=7) has been used in these experiments to demonstrate membrane reactor operation at dilute hydrocarbon conditions. Similar improvements in conversion and yield have been obtained by using a lower steam to methane ratio in feed (i.e. H_2O:CH_4=4) with both the FBP and CFBP modules [35]. For the membrane reactor operation however, to be practically effective and economically feasible, the methane flowrate in inlet must be comparable with this of conventional industrial steam reformers currently in use. The experimental results shown in Figs.7-11 have been simulated by means of the FBP and CFBP computational models [35], which account for the reforming reaction in the tubeside bed of particles and within the pores of the catalytic ceramic membrane with simultaneous species separation via the inert or catalytic alumina membrane walls.

A practical point in membrane reactor operation is use of sweep gas along the shellside annulus in contact with the external membrane surface to suppress the build up of concentration (mole fraction) of the permeating products (H_2, CO, CO_2) and thereby increase conversions and yields. Both inert and reactive gases have be flown through the shellside [35,38]. For designing an effective membrane reactor operation under such flow mode one should take into account the counter-diffusion of sweep gas from the shell annulus into the reaction tubeside via the permeable membrane; also the available volume of the shell annulus and the sweep (shellside) and feedside (tubeside) gas flowrate and composition. Counter-diffusion of sweep gas dilutes the species concentrations in tubeside and changes the permeation driving force from one side to the other and vice versa, thus possibly affecting the overall CH_4 and other hydrocarbon conversion and the product yield.

Use of an inert sweep gas in shellside (e.g., nitrogen, argon) may increase the operating cost of the permreactor process and also makes more difficult the downstream separation of hydrogen or synthesis gas for use in subsequent processes. Therefore, reported increases in conversion, yield which can be achieved with appropriate permreactor design by the use of inert sweep gases are offset by increased operating and product separation costs [33-35,38,39,49] . Use of steam or methane in shellside seems to be a better process and economic alternative because both are reacting species, must be consumed during reaction and eventually separated from the products in downstream; thus these process modifications can be regarded as environmentally benign in terms of efficient materials utilization.

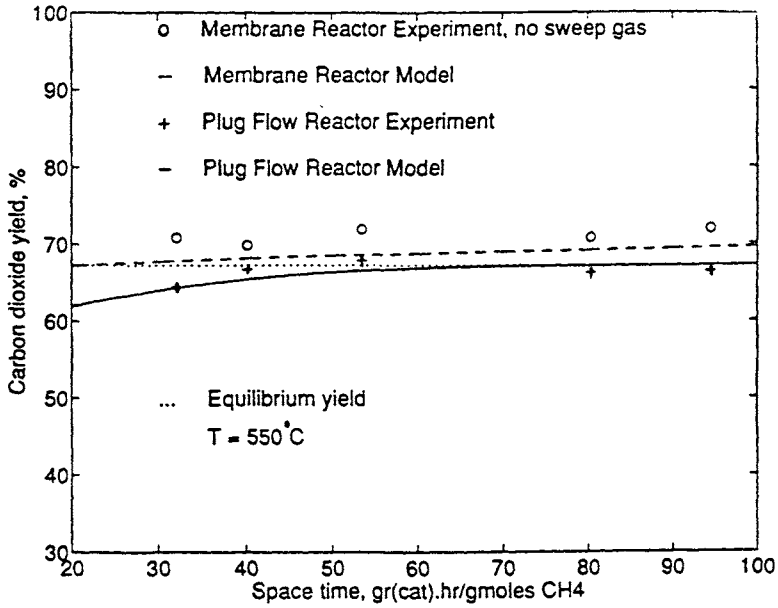

Fig.11 Effect of space time on CO_2 yield in the FBP and PFR at 550°C, (tubeside feed: CH_4:H_2O:H_2:Ar=1:7:1:0.75)

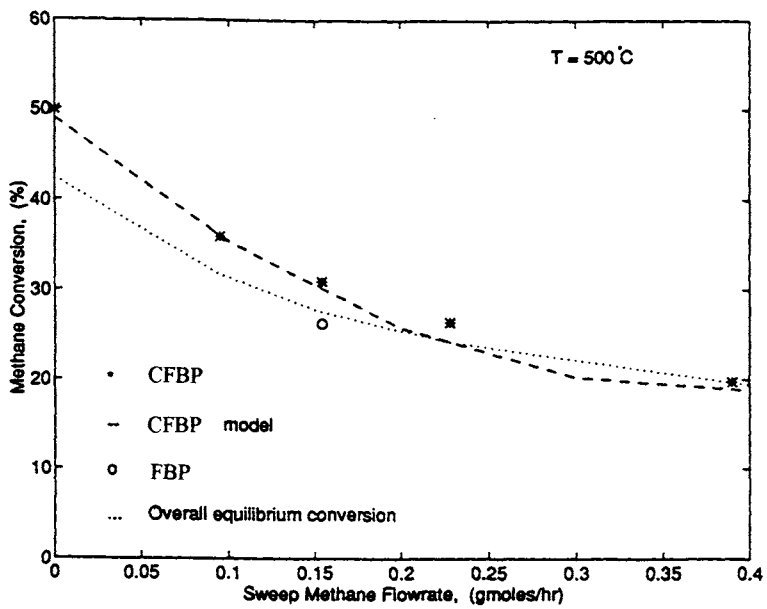

Fig.12 Effect of sweep methane flowrate on CH_4 conversion in the CFBP at 500°C (tubeside feed: CH_4:H_2O:H_2=1:4:0.2)

Application of this alternative proposition is implemented in Figs. 12, 13 for the CH_4 conversion and CO_2 yield respectively, in CFBP and FBP modules [35]. Methane residence time in tubeside, and pressure and feed composition in tubeside were the same with these in Fig.5. As the CH_4 flowrate increases in shellside, the overall CH_4 conversion and yield to CO_2 decreases due to increase of unreacted CH_4 in the exit streams. It is important to note for these runs that the overall methane to steam ratio increases significantly from its initial value in the tubeside inlet. However, even under the increased CH_4 feed composition the overall CH_4 conversion and CO_2 yield in permreactor are still close or above the overall equilibrium calculated values. The equilibrium values for these experiments are calculated at shellside pressure and by taking into account the combined tube and shell feed composition. This operation mode is a significant advantage of the permreactor process. Such dense methane feed compositions (low steam to methane ratios through single reactor inlet) cannot be used in conventional plug flow catalytic reformers due to significant carbon deposition on the catalyst located close to inlet. It is expected that plug flow reformers under similar integrated single feed conditions will yield lower than equilibrium conversions and yields.

The carbon deposition on nickel based catalyst comes primarily from the following reactions: $CH_4=C+2H_2$, $2CO=C+CO_2$, and from various other recombination reactions between CH_4, CO, CO_2 and H_2 [60]. To prevent carbon from being deposited in the reactor inlet, H_2 has to be added in the feed and higher steam to methane ratios (e.g., above 2.5) to be used. H_2 in feed lowers the equilibrium yield and conversion of the reaction, and a high steam feed oxidizes the reduced metallic Ni back to inert NiO. Improvement from these drawbacks can be accomplished with the proposed split CH_4 feed through both the tubeside and shellside. Each of the experiments in Figs. 12,13 lasted for about half an hour and the experiments were run consecutively by changing the CH_4 flow rate in shellside. For those experiments at the higher CH_4 flowrates in shellside, deactivation of catalyst by carbon deposition was observed and thus catalyst regeneration under flowing H_2 took place overnight. After overnight regeneration, the catalyst was used in subsequent experiments the next day, after its activity was checked and found to be at the same reference state as before deactivation. Similar procedure was followed with the experiments with C_3H_8 flowing in shellside, shown in Fig.29 below.

It is important to note in Figs.12&13 that the highest CH_4 flowrate in shellside corresponds to an overall mixed composition of H_2O:CH_4:H_2=1.21:1.0:0.06. This overall steam to methane feed ratio is far lower from the one used during the described single feed experiments with either the membrane reformer (single reactant feed in membrane tubeside inlet) or the plug flow catalytic reformer (single reactant feed in stainless steel tube inlet). Preliminary experiments were performed with the single dense methane feed in the membrane and plug flow reactors at various feed compositions and low steam to methane ratios. Deactivation was much more severe than the respective experiments with the split feed membrane reactor at same time intervals. Most of the deposition was occurring in the reactor inlet with subsequent build up of pressure drop along the tubeside. The split feed membrane reactor outperforms in terms of operational capacity

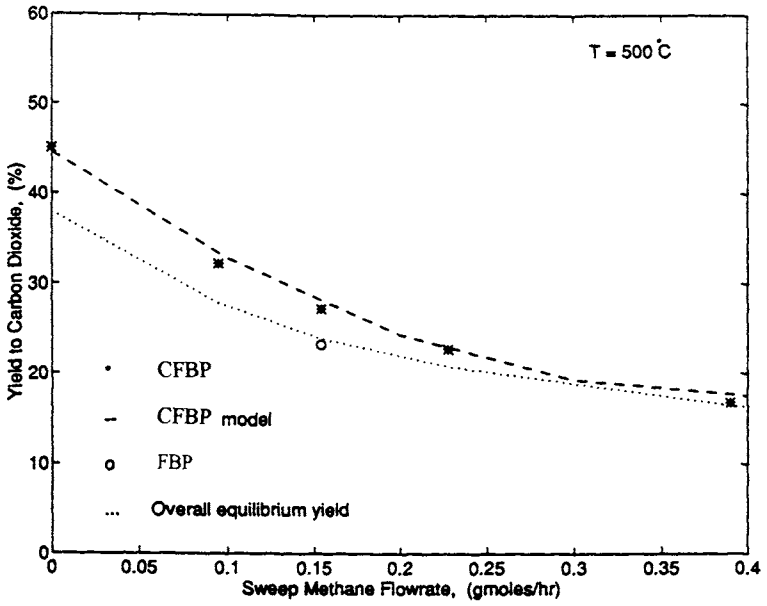

Fig.13 Effect of sweep methane flowrate on CO_2 yield in the CFBP at 500°C (tubeside feed: CH_4:H_2O:H_2=1:4:0.2)

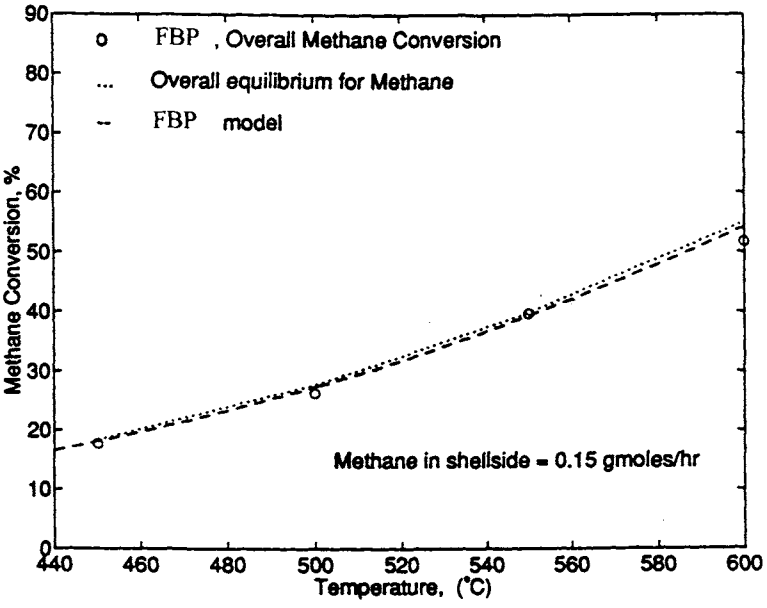

Fig.14 Effect of temperature on CH_4 conversion in the FBP with sweep methane gas (tubeside feed: CH_4:H_2O:H_2=1:4:0.2)

and time and obtained conversions, yields the single feed membrane and conventional plug flow reactors with dense methane composition.

The split feed membrane reactor operation seems to offer also additional benefits in overall process improvement. Methane from the shellside diffuses and reacts through the catalytic membrane and part of it is transported along the catalyst zone in the tubeside. This provides an effective way of feeding metered amounts of methane for reaction within the catalytic membrane pores and the tubeside catalysts pellets. Also, the thermal efficiency of the entire permreactor becomes superior by utilizing the external heat provided through the outer surface of the shellside annulus not only for heating the reaction fluid in tubeside but also for heating the flowing CH_4 in shellside to endothermically react both in catalytic membrane and in tubeside. The metered mass of reactant and heat flow along the shellside annulus can also possibly extend the life of the catalyst within the membrane and in tubeside as demonstrated with the high CH_4 concentrations used in the above experiments.

Additional results with use of reactive methane in shellside of the permreactor are shown in Fig.14 for the FBP module as function of the reaction temperature in the 450-600 °C range, at similar operating conditions as those shown previously in CFBP. The overall mixed (tube plus shell) feed composition was fixed at H_2O:CH_4:H_2=2.12:1.0:0.11. The experimental conversions are well close to those corresponding at overall equilibrium conditions, which are calculated for a mixed tube-shell composition and at shellside pressure, indicating the utilization of the split feed process over a wide temperature range. Similar results were obtained for the yield to CO_2 indicative of the extent of the water gas shift reaction and are shown in Fig.15, [35]. A comparison of the obtained results in the two types of permreactors (Figs.12-15) indicates the effective use of the catalytic membrane in CFBP for increasing conversion and yield beyond the values obtained by using only the packed catalyst zone in FBP. Furthermore, the described experiments were confirmed by the use of the numerical permreactor models applied at the conditions of the experiments; the model results are shown within the Figures as dashed lines.

Moreover, the above experiments with methane used in shellside both as reactant and sweep gas, can simulate closely the performance of impermeable plug flow reactors with multiple side feed ports or with recycled side streams of unreacted methane. The results indicate possibilities for improved performance of these concepts/operations for dense methane feeds in terms of obtained conversion and yield in comparison with the PFR operation.

Beyond the experimental results obtained above computational simulations using the developed process models gave information for additional useful process operating conditions. These simulations were done to verify the experimental results and obtain new effective operating conditions and process configurations for the permreactors in an attempt to design better permreactor-methane reforming processes.

Figs.16-19 simulate an FBP reactor with CH_4 used as sweep gas in shellside of the reactor. This is a process simulation case of one of the experimental points shown in Figs.14 and 15, at 450°C. The axial molar flowrate profiles from the inlet to the reactor outlet, for methane, steam, hydrogen, carbon dioxide and carbon monoxide are plotted in

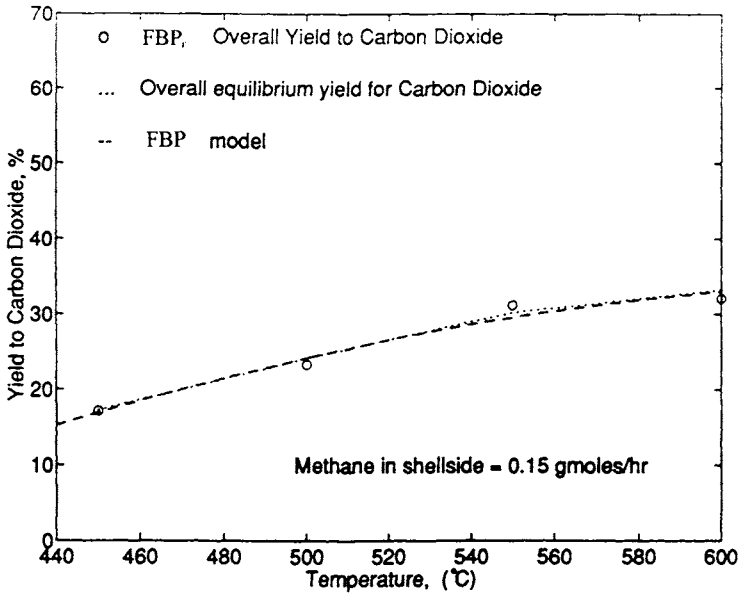

Fig.15 Effect of temperature on CO_2 yield in the FBP with sweep methane gas (tubeside feed: CH_4:H_2O:H_2=1:4:0.2)

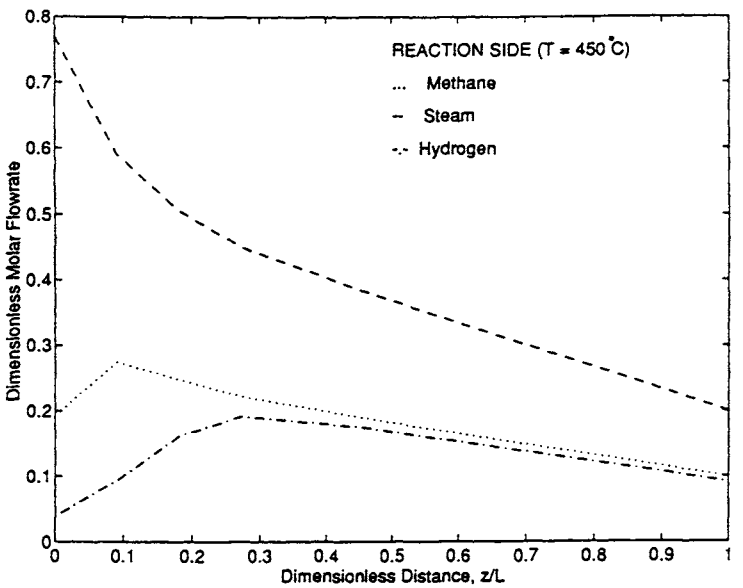

Fig.16 Dimensionless molar flowrate at reaction side (tubeside) versus axial distance for CH_4, H_2O and H_2 in the FBP. T=450°C,P_o^F=1.68atm, P_o^P=1.47atm, sweep methane (Fm_{CH4}=1), (tubeside feed: CH_4:H_2O:H_2=1:4:0.2)

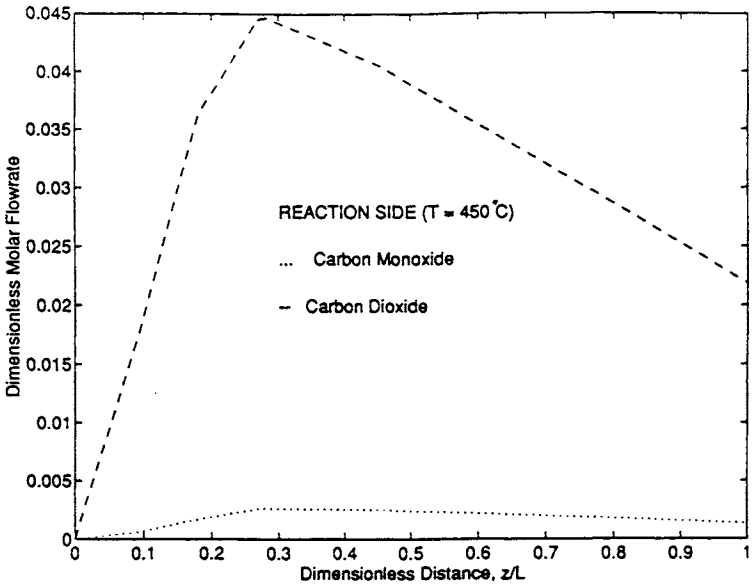

Fig.17 Dimensionless molar flowrate at reaction side (tubeside) versus axial distance for CO, CO_2, in the FBP. T=450°C, P_o^F=1.68atm, P_o^P=1.47atm, sweep methane (Fm_{CH4}=1), (tubeside feed: CH_4:H_2O:H_2=1:4:0.2)

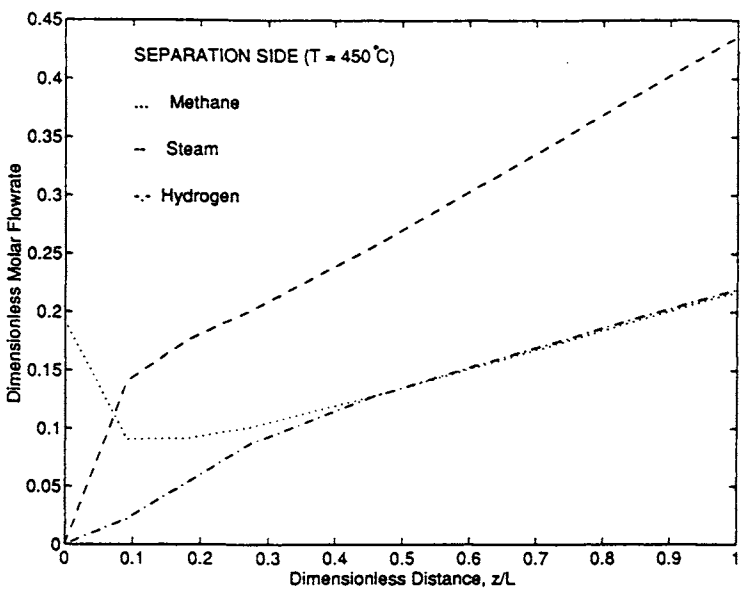

Fig.18 Dimensionless molar flowrate at separation side (shellside) versus axial distance for CH_4, H_2O and H_2 in the FBP. T=450°C, P_o^F=1.68atm, P_o^P=1.47atm, sweep methane (Fm_{CH4}=1), (tubeside feed: CH_4:H_2O:H_2=1:4:0.2)

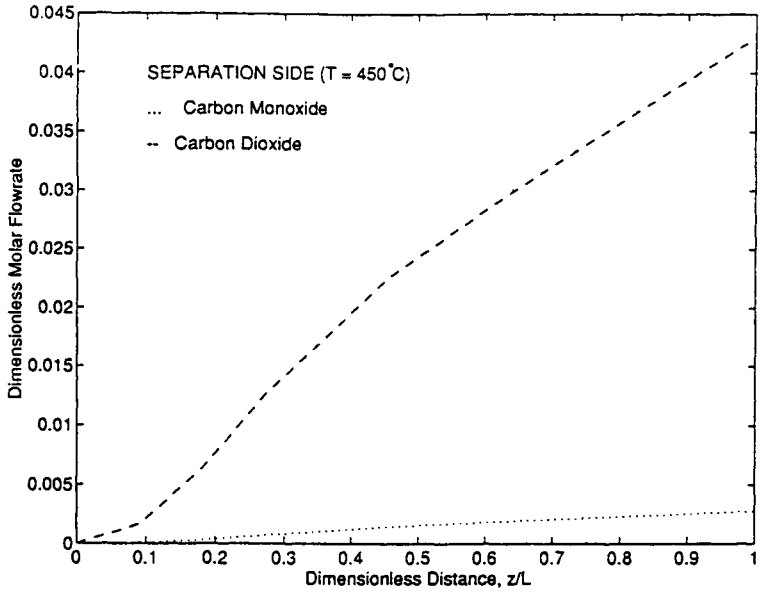

Fig.19 Dimensionless molar flowrate at separation side (shellside) versus axial distance for CO, CO_2, in the FBP. T=450°C, P_o^F=1.68atm, P_o^P=1.47atm, sweep methane (Fm_{CH4}=1), (tubeside feed: CH_4:H_2O:H_2=1:4:0.2)

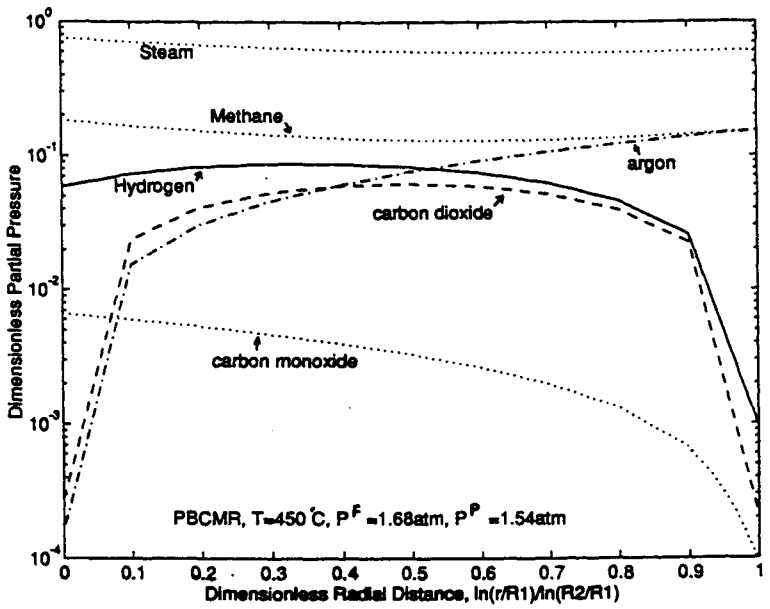

Fig.20 Dimensionless partial pressures across the membrane for CH_4, H_2O, H_2 CO, CO_2 and Ar in the CFBP. In shellside: sweep argon (Fm_{Ar}=1), sweep methane (Fm_{CH4}=1), sweep steam (Fm_{H2O}=4), (tubeside feed: CH_4:H_2O:H_2=1:4:0.2)

tubeside (reaction side) and shellside (separation side) of the FBP module. It is characteristic the maxima in the molar flowrate profiles of methane in tubeside (due to its diffusion from the shellside) and of hydrogen and both carbon oxides (CO, CO_2). The profile of methane in shellside passes through a minimum, again due to its diffusion and loss in the tubeside.

An additional demonstration of the numerical model vigorous simulation capacity is shown in Figs.20 for the CFBP module. The plot shows the variation of partial pressures across the catalytic membrane radius in CFBP mode at z=1/20cm axial distance from the membrane reactor inlet. A mixture of methane diluted in steam and argon was simulated to flow in the shellside. The other conditions are shown within the plot [35].

Figs.21&22 refer to the FBP module [35]. They show how the variation of the dimensionless number $Q=2\pi D_{Ae}L\,F_o^F$, (a unified measure of the species diffusivity through the membrane), affects the CH_4 and CO_2 conversions for a fixed tubeside pressure and different pressures in shellside. Note the precipitous drop in conversion, yield for the lower shellside pressure for $Q>5\text{x}10^{-3}$. Figs.23&24 show the effect of varying the dimensionless Damkohler number for the reverse of methanation reaction (reaction (1)) in conversion and yield by varying the shellside pressure. $Da^F_1=\pi R_1^2 L k^F_1/n_o^F.(P_o^F)^{0.5}$, is a product of the reaction rate constant for reaction (1) and the reactor residence time in tubeside. In the above equations, D_{Ae} ,(cm^2/hr) is the diffusivity, through the membrane, of the reference compound A (i.e., CH_4); k^F_1 is the rate constant for reaction (1) in tubeside catalyst bed of the FBP, and it is in gmole.$atm^{1/2}$/hr.cm^3 [35]. Increase in Da^F_1 values affects strongly the relative conversion, yield at various values of shellside pressure.

The described results for blank and nickel modified ceramic aluminas used as FBP, CP and CFBP modules, and those from PFR modules, agree well with the ones presented by Chai et al. [39] for similar inorganic reactors. Most of the studies on membrane reactors for methane steam reforming have reported solely on CH_4 conversions indicative only of the extent of the reverse of methanation reaction (reaction 1) [e.g.,32,33,39]. The studies presented here, report however comprehensively as well on the extent of the parallel water gas shift reaction (reaction (2)) which is proportional to the magnitude of the CO_2 yield.

For the ceramic alumina membrane tubes utilized in the described reforming and dehydrogenation experiments hydrothermal stability has been tested in several occasions. Constant hydrothermal stability of the tubes has been reported after several hundred hours in steam flow [44]. Some increase in gas permeabilities (up to about 25%) with a similar magnitude decrease in permselectivity was observed for the various gases with regard to initial values, after final permeation tests for some of the discharged ceramic tubes which were used in the described methane steam reforming experiments. These tubes were tested for several months under reaction conditions and steam flow and underwent several heating-cooling thermal cycles, reaction pressure cycles, and catalyst regenerations under hydrogen flow. Thus, their reported stability can be considered satisfactory to the specific application. Metal dispersed membranes used in methane steam reforming experiments [39] prepared by dip-coating method were shown high

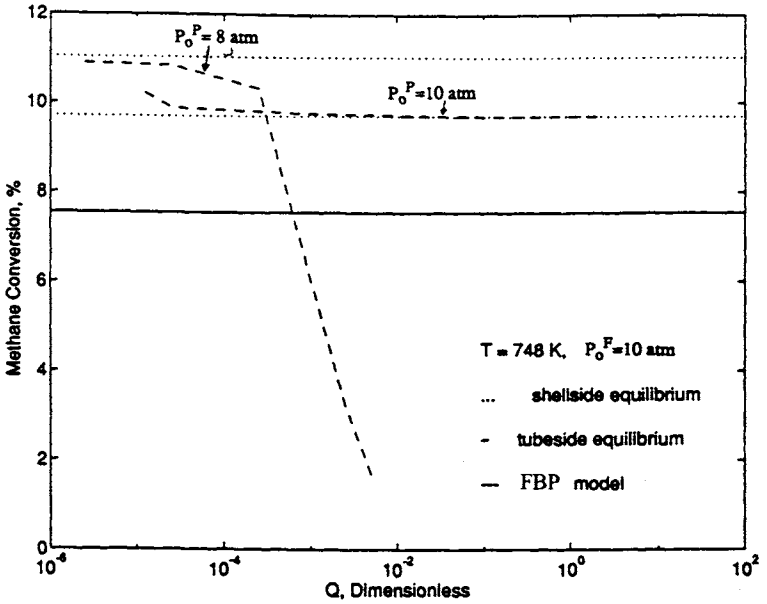

Fig.21 Effect of Q on CH_4 conversion at different shellside pressures in the FBP.
(tubeside feed: CH_4:H_2O:H_2:CO_2=1:3:0.2:0.5)
(shellside feed same with tubeside without hydrogen)

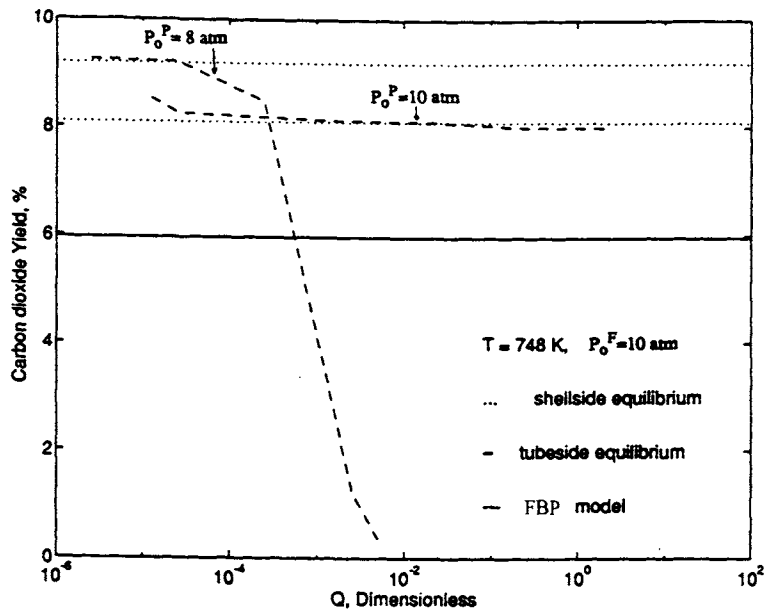

Fig.22 Effect of Q on CO_2 yield at different shellside pressures in the FBP.
(tubeside feed: CH_4:H_2O:H_2:CO_2=1:3:0.2:0.5)
(shellside feed same with tubeside without hydrogen)

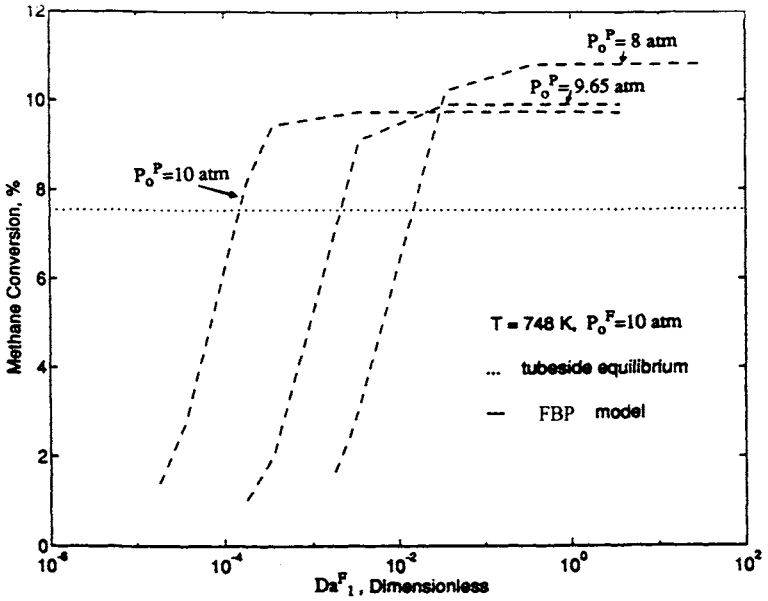

Fig.23 Effect of Da_1^F on CH_4 conversion at different shellside pressures in the FBP.
(tubeside feed: CH_4:H_2O:H_2:CO_2=1:3:0.2:0.5)
(shellside feed same with tubeside without hydrogen)

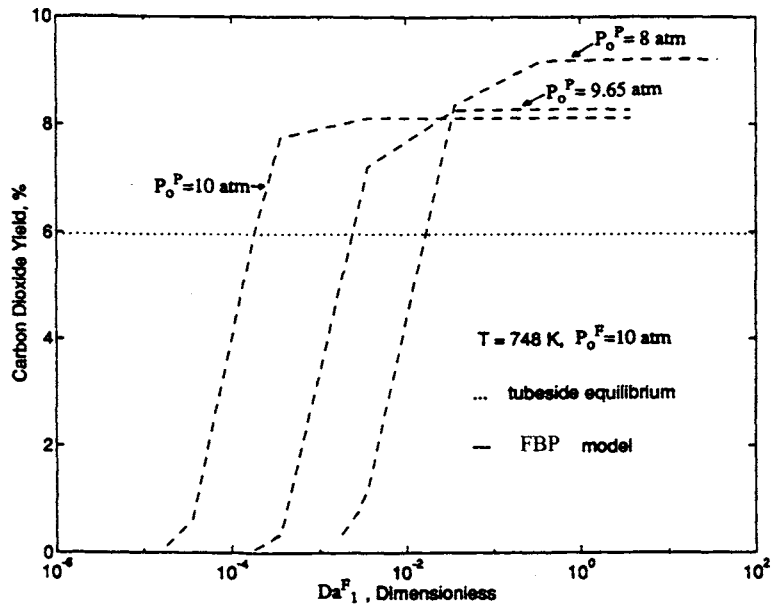

Fig.24 Effect of Da_1^F on CO_2 yield at different shellside pressures in the FBP.
(tubeside feed: CH_4:H_2O:H_2:CO_2=1:3:0.2:0.5)
(shellside feed same with tubeside without hydrogen)

hydrothermal susceptibility and their permselectivity changed after a couple of hours on reaction stream.

The above studies have provided means for designing and improving membrane reactor operations for methane steam reforming processes. If successfully implemented these reactors can be considered environmentally benign due to their ability of yielding higher conversions and product yields at lower temperatures; also because they can increase thermal efficiency of the application cycle, and provide integrated materials recovery and recycling under improved and cost effective process conditions. The H_2 and H_2 rich hydrocarbon, carbon oxides mixtures exiting from the membrane reactors can be used either as mixture or as pure H_2 in chemical synthesis, hydrogenation and hydrotreating of oil, petroleum and coal feedstocks. Also, as fuel in power generation systems (gas turbines and engines) and in anode of fuel cells (i.e., solid oxide, molten carbonate, phosphoric acid, alkaline, proton exchange). Integration of similar reformers, for reforming various hydrocarbon feedstocks mentioned above, within transportation and stationary sources is of significant importance in related energy generation systems. The presented studies can provide guidelines in design of such systems.

The studies are involved as well with design aspects and parametric analysis of permeable reformers with objective the process improvement. Parameters that are involved in process operation and need to be selected for permreactor optimization are the reaction temperature, reactant space time (or space velocity) and feed composition, sweep gas flowrate and composition, the operating pressures in the tubeside and shellside, the flow pattern between sweep gas and feed gas (e.g., concurrent, countercurrent, perfect mixing, cross flow [82]) and the type of the applicable catalytic permreactor (e.g., CP, FBP, CFBP). Standard modeling techniques applied to heterogeneous catalysis and reactor design are also applicable in the catalytic permreactor design. Models applied in fixed bed catalytic reactor design such as the one- and two- dimensional pseudo-homogeneous and heterogeneous ones can be applied as well in the various permreactor cases [90].

Membrane reactors of the catalytic design configurations discussed above with the appropriate sweep gas and feed gas composition and flow mode, can be used also for steam and/or CO_2 reforming of various hydrocarbon feedstocks. Catalysts for the CO_2 reforming route is currently under development. The successful implementation of this reaction route can provide several environmentally benign conversions of CO_2 to synthesis gas; this endothermic reforming route can be used as a dry energy storage and transformation reaction [67]. The provided endothermic thermal energy to drive the reaction is stored as chemical bond energy in the CO and H_2 conversion products which can be subsequently utilized, as example, for various power generation applications [91].

4. PROPANE DEHYDROGENATION

Next, we describe and analyze the use of similar catalytic permreactors in conducting effectively paraffin catalytic dehydrogenation reactions such as this of propane to propylene.

4.1 Experimental Section

The experimental set-up for the propane dehydrogenation experiments was similar with this described for methane steam reforming. Lack of steam in these reaction experiments made the apparatus simpler, which is described in detail elsewhere [21-23]. The same type of membrane tubes and permreactor configurations (FBP, CP, CFBP) were used in these experiments and results were compared with respective PFR experiments and equilibrium calculated values for propane dehydrogenation (reaction(4)). The fixed bed catalyst particles were from commercial 5% $Pt/\gamma\text{-}Al_2O_3$. Mg was added to the catalyst particles in the form of $Mg(NO_3)_2.6H_2O$ in NH_4OH solution (pH=10) by impregnation. This was done to improve coking and sintering resistance. In CP, CFBP modes the catalytic membrane was impregnated with hexachloroplatinic acid (H_2PtCl_6) of 24.5% Pt and $Mg(NO_3)_26H_2O$ in NH_4OH solution (pH=10). The tubes were dried overnignt in situ at 130°C. Then, they were calcined at 400°C in air flow for 12hrs to oxidize the catalyst and consequently brought at 550°C in hydrogen flow for 24hrs to activate the catalyst. The catalyst was also kept overnight in flowing hydrogen at 550°C after each experiment in order to be active for the next experiment. Occasional regeneration of the catalyst was carried out when activity was lower than the reference activity, by treating the catalyst with air at 450°C overnight, and then with hydrogen at 550°C for 24hrs.

Experimental conversion, yield values obtained with membrane reactors were compared with the respective thermodynamic equilibrium values from propane dehydrogenation reaction (4), which were calculated at same experimental conditions (at same reaction temperature, pressure and feed composition). Overall carbon balances in the reactor: $C_3H_8(exit)+C_3H_6(exit)=C_3H_8(feed)$ were closed with an up to 6% estimated error. Moreover, the following definitions apply:

(Yield to propylene): $C_3H_6(exit)/C_3H_8(feed)$;

(Propane conversion): $C_3H_8(feed)-C_3H_8(exit)/C_3H_8(feed)$.

4.2 Results and Discussion

Previous results from propane dehydrogenation permreactors have been reported by Ziaka et al. [21-23]. Here we present a more detailed description aiming in analysis of various propane dehydrogenation permreactors (FBP, CP, CFBP) and in related design and application issues.

The permeabilities of the blank and Pt/Mg impregnated alumina membranes were measured as in the methane steam reforming work. Fig.25 reports on permeabilities of propane dehydrogenation species, H_2, C_3H_8, C_3H_6, Ar (inert gas) for blank and incipient impregnated alumina membrane tubes (0.8g of catalyst were applied in the membrane) [21]. The dependence of species permeability (P_i/d) on temperature is shown in Fig.26. Previous reports have described experiments with the FBP configuration at various reaction and feed composition conditions, including tubeside feed compositions with propane and propylene [22,23].

Reaction runs at different temperatures by using the catalytic fixed bed permreactor (CFBP) with tubeside catalyst particles and a catalytic membrane, are shown in Fig.27, [21]. There is a propylene yield improvement by the use of the membrane

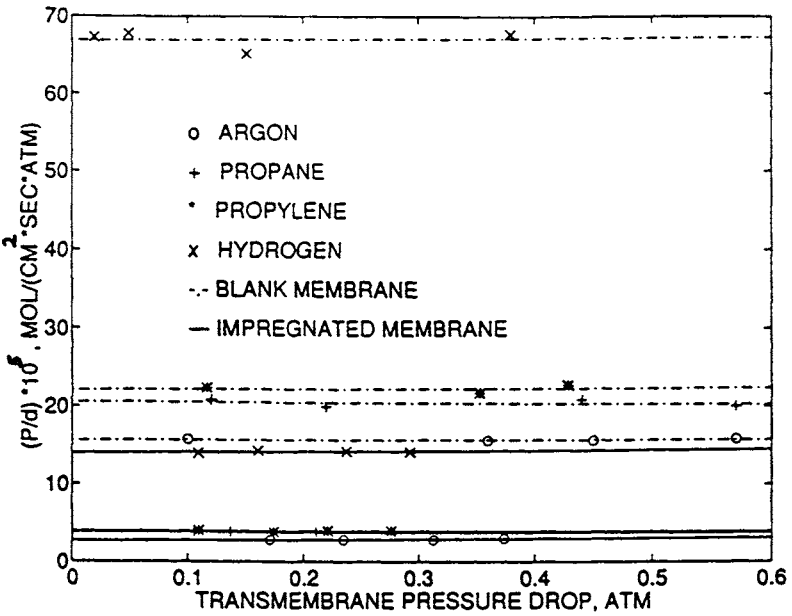

Fig.25 Permeability coefficient over membrane thickness versus average transmembrane pressure drop at 473K (200°C) for blank and modified alumina membranes with 0.8g of catalyst

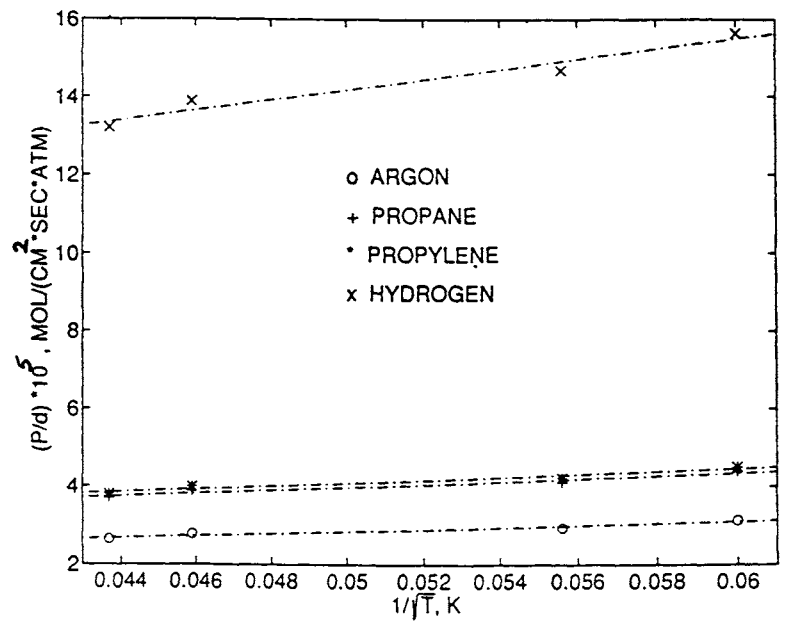

Fig.26 Permeability coefficient over membrane thickness versus square root of inverse temperature for blank and modified alumina membranes with 0.8g of catalyst

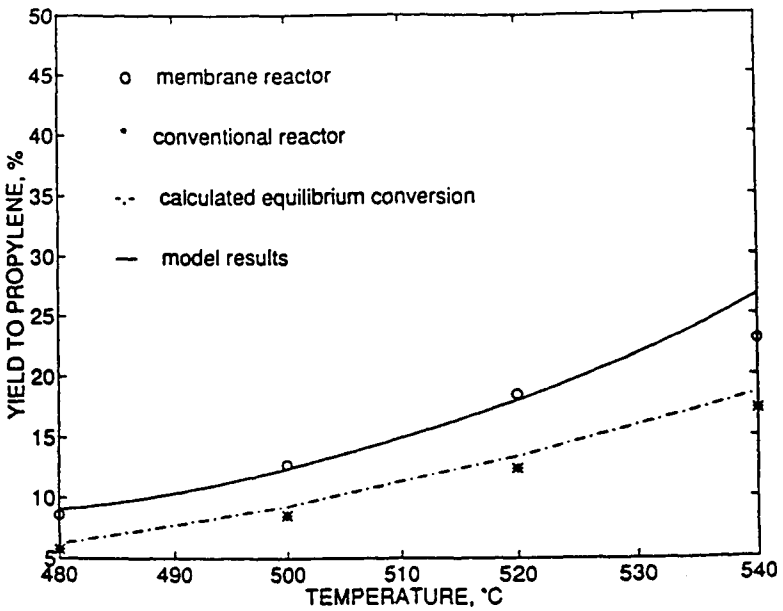

Fig.27 Yield to propylene versus reaction temperature for the CFBP. Reactor residence time=2sec, P_o^F=6psig, P_o^P=3psig, sweep ratio Fr=0, (tubeside feed: C_3H_8:H_2:Ar=1:0.2:0)

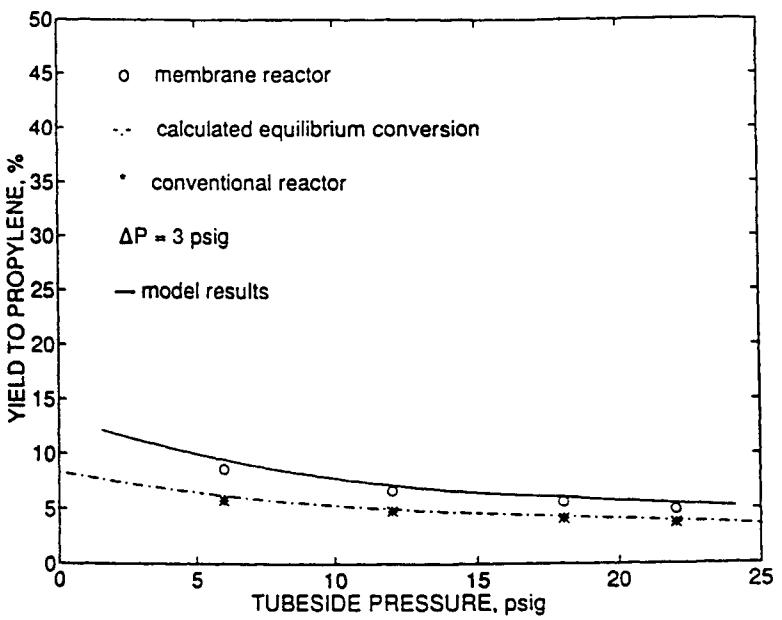

Fig.28 Yield to propylene versus tubeside pressure for the CFBP. Reactor residence time=2sec, transmembrane pressure drop=3psig, sweep ratio Fr=0, (tubeside feed: C_3H_8:H_2:Ar=1:0.2:0)

reactor (shown also by the model solid line) with respect to the mode in which no permeation occurs (conventional tubular reactor with shellside closed) and the equilibrium one; this equilibrium shift effect is attributed to the increased dual catalyst activity and the permselective separative membrane action. As with the methane steam reforming permreactors, catalytically impregnated alumina tubes for propane dehydrogenation show significant permeability drop in comparison with blank membrane tubes (Fig.25). This effect can be used to control (adjust) the composition of the permeate or reject streams from the membrane dehydrogenator directly into the combustor inlet of gas turbine power generation cycles or in synthesis reactors, similar to those shown in Fig.43. Catalytic combustion of H_2 with O_2 over metallic catalysts or noncatalytic homogeneous combustion can be used as effective alternatives for reduction of NOx emissions in flue gases and extended flammability ratios for various H_2/O_2 mixtures diluted with inert gases [52,73-75].

The effect of tubeside pressure on propylene yield in CFBP is shown in Fig.28. Paraffin dehydrogenation is an endothermic volume expansion process and its conversion and yield are favored by increasing the temperature and by lowering the reactor pressure [21]. Increases in overall propane conversion and propylene yield were also observed by increasing the reactant space time in tubeside, the inert sweep gas (argon) flowrate in shellside, and by diluting the tubeside feed with argon [21]. The application of CFBP as a two side propane feed membrane reactor is shown in Fig.29. The reaction temperature was kept at 480°C, at tubeside pressure of about 3psig. Propane was fed in both the tubeside and shellside inlets at respective ratios shown in the abscissa. The overall equilibrium yield increases by increasing the relative propane shell to propane tube ratio, due to the decrease of the relative H_2:C_3H_8 ratio in reactor inlet. Improved membrane reactor yields to propylene can be achieved, especially at low propane shell to tube ratios as shown. The split feed propane system offers similar benefits with those described earlier in the respective methane steam reforming experiments and can be used in related applications.

For reaction temperatures up to 540°C, the main reaction product was propylene in yields usually better than 90% for the CFBP and conventional reactors. Reaction by-products were methane and ethylene. In most cases, the CFBP configuration improved also the selectivity to propylene and the overall propane conversion with respect to the conventional reactor. Similar to our studies results, have been reported recently using mesoporous ceramic and metal membrane reactors. Hughes et al. [24] utilized porous ceramic alumina reactors modified with silica and impregnated catalytically, and dense metal Pd/Ag composite permreactors. Both types of membrane reactors were filled with catalyst pellets (Pd, Pt on Al_2O_3) and reported significant conversion improvements which increased even further with use of inert (N_2) and reactive sweep gases (mixture of CO and air).

Presented below are computational results with the membrane reactor configurations obtained by using the numerical models [21]. They provide insights into design, operation and optimization of the propane membrane dehydrogenators.

Fig.30, is referred to the FBP mode. It plots the increase in propylene yield by increasing the Damkholer number for propane dehydrogenation reaction (4), given as:

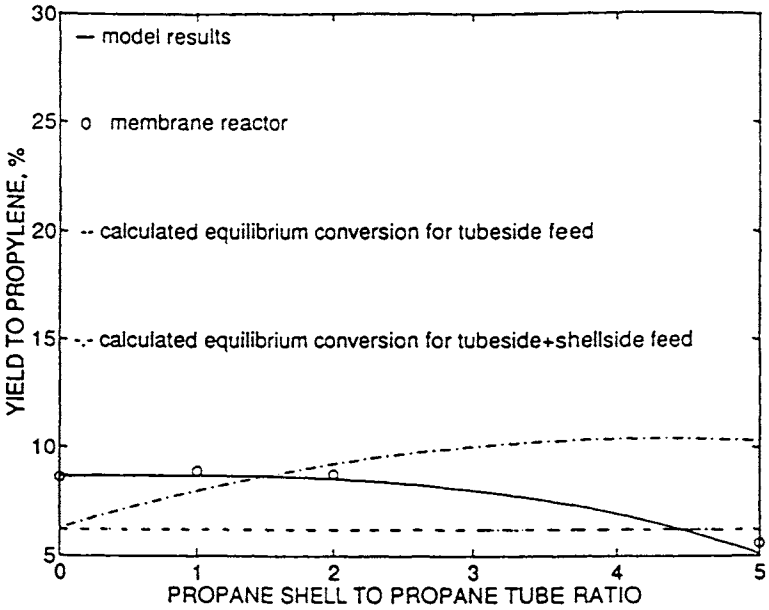

Fig.29 Yield to propylene (with respect to total propane feed) versus propane shell to propane tube ratio in the CFBP. Reactor residence time=2sec, P_o^F=6psig, P_o^P=3psig, sweep ratio Fr=0, (tubeside feed: C_3H_8:H_2:Ar=1:0.2:0)

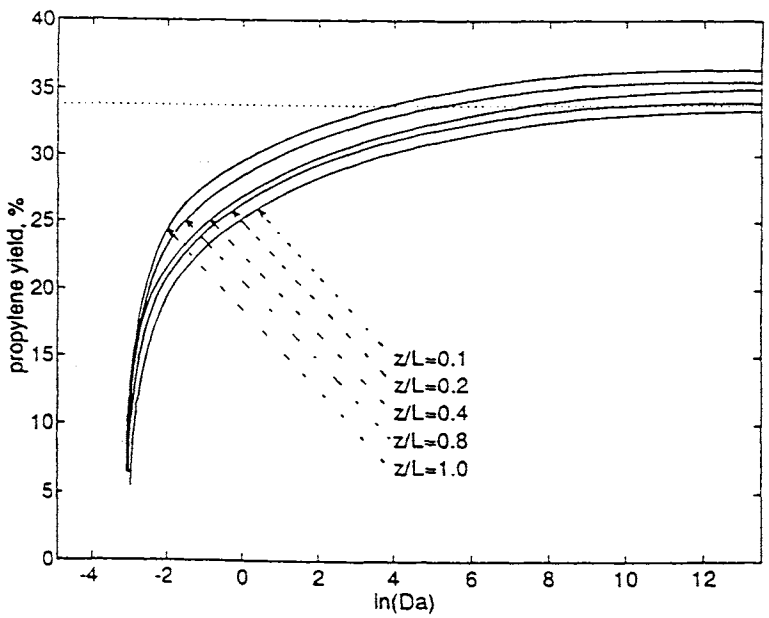

Fig30. Yield to propylene versus ln(Da^F) at various axial distances z/L for the FBP module. ψ^{PF}=1, sweep ratio Fr=0, (tubeside feed: C_3H_8:H_2:Ar=1:0.2:0)

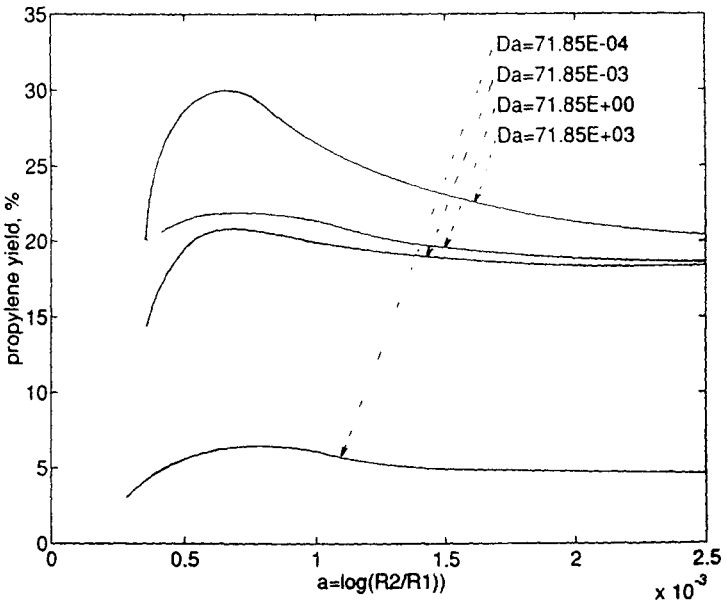

Fig31. Yield to propylene versus $\alpha=\ln(R_2/R_1)$ at various Da^F values for the FBP module. $\psi^{PF}=1$, sweep ratio Fr=0, (tubeside feed: C_3H_8:H_2:Ar=1:0.2:0)

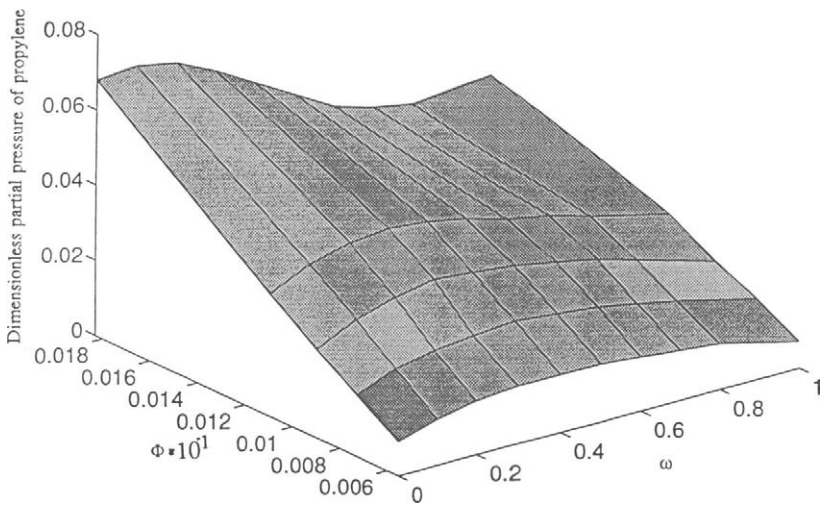

Fig.32 Dimensionless partial pressure of propylene versus dimensionless radial distance ω and Thiele modulus Φ in CP. Pressure ratio $\psi^{PF}=0.88$, sweep argon with Fr=0.28, (tubeside feed: C_3H_8:H_2:Ar=1:0.2:0)

$Da^F=\pi R_1^2 L k^F{}_4 P_o^F/n_o^F$, at various dimensionless axial lengths (z/L) from the inlet. The catalytic reaction occurs in the fixed bed of pellets located in tubeside. For a fixed Da^F value the propylene yield increases monotonically along the reactor length. Fig.31, refers also in FBP and shows the effect of radial variation across the membrane (α) and Da^F on the propylene yield. It is characteristic that the maxima in yield, for various Da^F values, occur at values of α between about 0.6-0.75. For the same value of α, an increase in Da^F results to higher yields.

Figs.32&33 describe the CP model operation. Only the dehydrogenation reaction (4) takes place and is used within the model. The two figures plot the propylene and hydrogen partial pressures respectively, as function of the Thiele modulus Φ in catalytic membrane, across the dimensionless catalytic membrane radius ω. z/L=1 (permreactor exit) for these simulations; with $\Phi=\alpha R_1\sqrt{k'_4 RT/D_{Ae}}$, to be the Thiele modulus for the reactive catalytic membrane, and k'_4 is the rate constant for the reaction in catalytic membrane in gmol/cm^3.sec.atm, [21]. For every point across the membrane (various values of $\omega=ln(r/R_1)/ln(R_2/R_1)$ an increase in Thiele modulus and thereby in reactant propane consumption, increases the partial pressure of both products.

The application of the fixed bed catalytic membrane reactor (CFBP) with dual reactor function (along the fixed bed catalytic tubeside and within the catalytic porous membrane) is seen in Figs.34-38, [21]. Figs.34,35 show the effect of Damkholer number (defined above) across the membrane dimensionless radius ω on the partial pressures of propylene and hydrogen products. The simulation is at the permreactor exit (z/L=1). There is a monotonic increase in partial pressure of both products by increasing the Damkohler number at every ω value; this is similar with the increase in Thiele modulus in CP for the same species (Figs.32,33). The partial pressure of hydrogen is also increased across the membrane (across ω) for various Damkohler numbers, while this is not the case for propylene due to the difference in molecular weight between the two products which is translated in differences in permeabilities across the catalytic membrane. Similar plots corresponding to the reactant propane and inert sweep argon partial pressure variations are shown in Figs.36,37 respectively, revealing the intrinsic behavior of the CFBP in propane consumption and inert sweep argon distribution. To provide further analysis of the CFBP dehydrogenator, the next Fig.38 shows the propylene partial pressure variation along the permreactor axial length (z/L) and across the membrane radius (ω) for fixed Da and Φ values. There is an agreement in variation of propylene partial pressure profiles from a comparison of the described related plots, which shows that the model can be an effective tool in permreactor analysis and design.

Finally, Figs. 39&40 show the increase in propylene yield from the inlet to exit along the reactor length for various Φ and Da values respectively. Da and ω are fixed in Fig.39; Φ and ω are fixed in Fig.40. By increasing the Φ and Da values in the model, higher propylene yields are obtained at every axial point of the permreactor.

The described numerical simulations can be especially useful in the design and operational optimization of catalytic membrane dehydrogenators where new operating conditions need to be applied and new or scaled up reactor modules have to be tried. In general, the above plots show a strong dependence of partial pressure distribution of

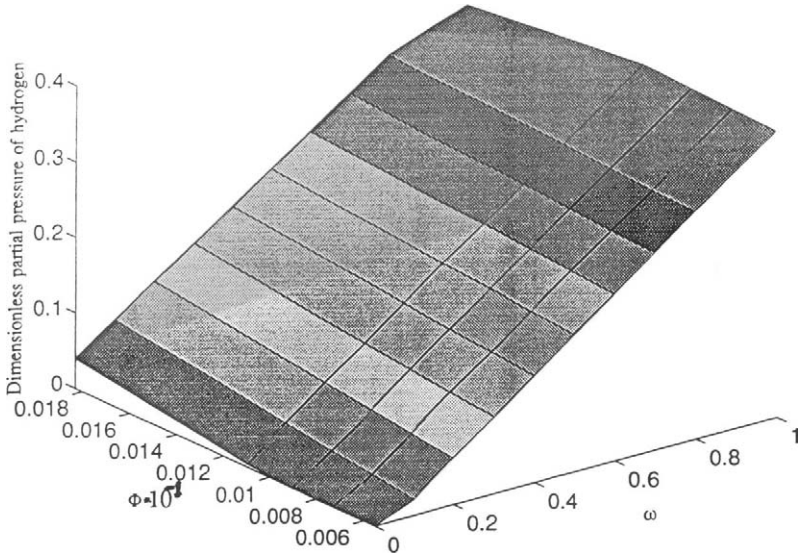

Fig.33 Dimensionless partial pressure of hydrogen versus dimensionless radial distance ω and Thiele modulus Φ in CP. Pressure ratio ψ^{PF}=0.88, sweep argon with Fr=0.28, (tubeside feed: C_3H_8:H_2:Ar=1:0.2:0)

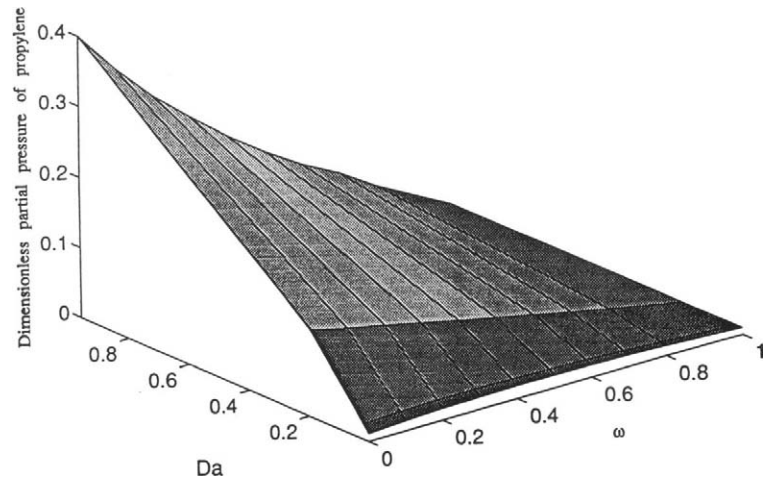

Fig.34 Dimensionless partial pressure of propylene versus dimensionless radial distance ω and Damkohler number Da^F in CFBP. Pressure ratio ψ^{PF}=0.85, sweep argon with Fr=0.20, (tubeside feed: C_3H_8:H_2:Ar=1:0.2:0)

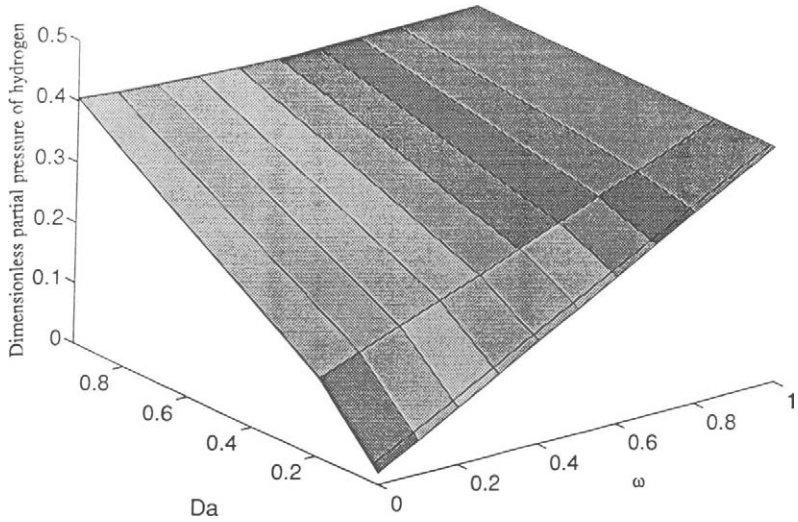

Fig.35 Dimensionless partial pressure of hydrogen versus dimensionless radial distance ω and Damkohler number Da^F in CFBP. Pressure ratio ψ^{PF}=0.85, sweep argon with Fr=0.20, (tubeside feed: C_3H_8:H_2:Ar=1:0.2:0)

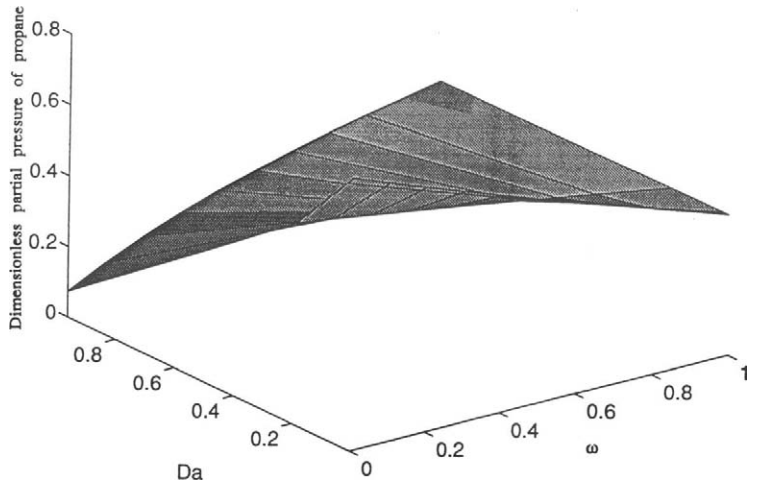

Fig.36 Dimensionless partial pressure of propane versus dimensionless radial distance ω and Damkohler number Da^F in CFBP. Pressure ratio ψ^{PF}=0.85, sweep argon with Fr=0.20, (tubeside feed: C_3H_8:H_2:Ar=1:0.2:0)

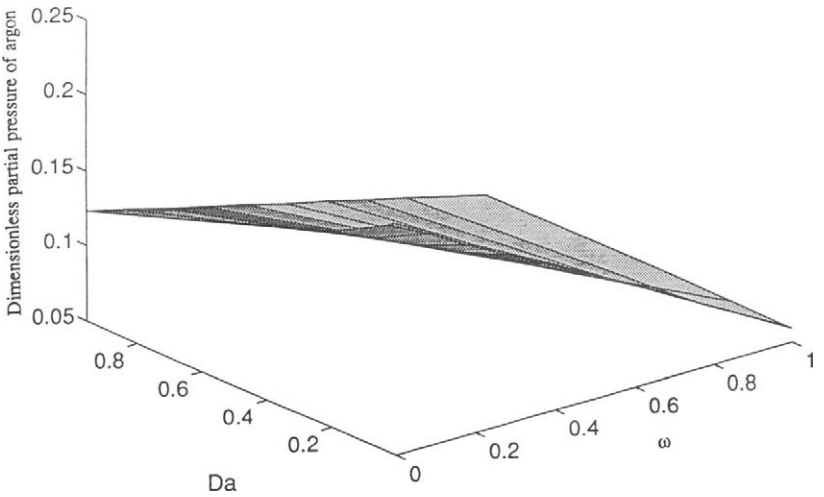

Fig.37 Dimensionless partial pressure of argon versus dimensionless radial distance ω and Damkohler number Da^F in CFBP. Pressure ratio ψ^{PF}=0.85, sweep argon with Fr=0.20, (tubeside feed: C_3H_8:H_2:Ar=1:0.2:0)

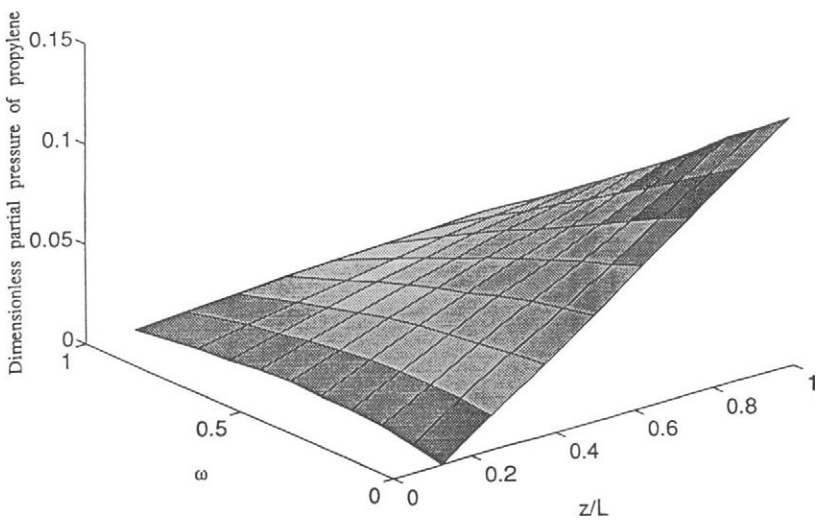

Fig.38 Dimensionless partial pressure of propylene versus dimensionless radial distance ω and axial distance z/L in CFBP. Pressure ratio ψ^{PF}=0.85, sweep argon with Fr=0.20, (tubeside feed: C_3H_8:H_2:Ar=1:0.2:0)

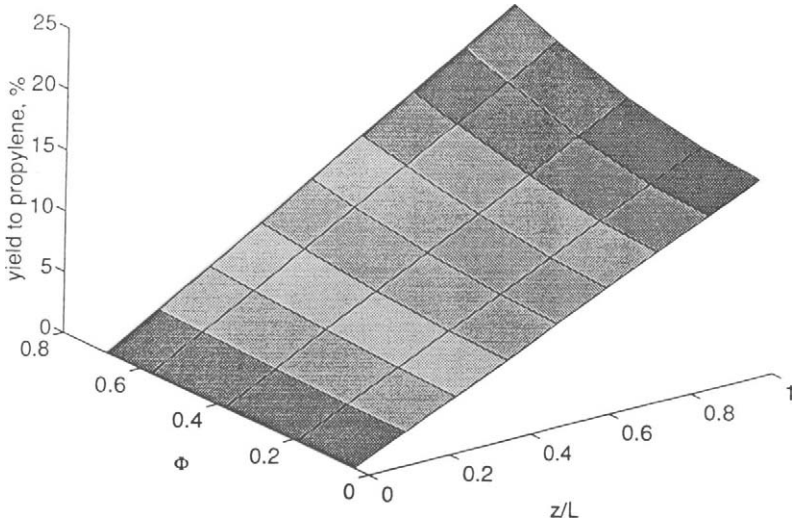

Fig.39 Yield to propylene versus Thiele modulus Φ and axial distance z/L in CFBP. Pressure ratio ψ^{PF}=0.85, sweep argon with Fr=0.20, (tubeside feed: C_3H_8:H_2:Ar=1:0.2:0)

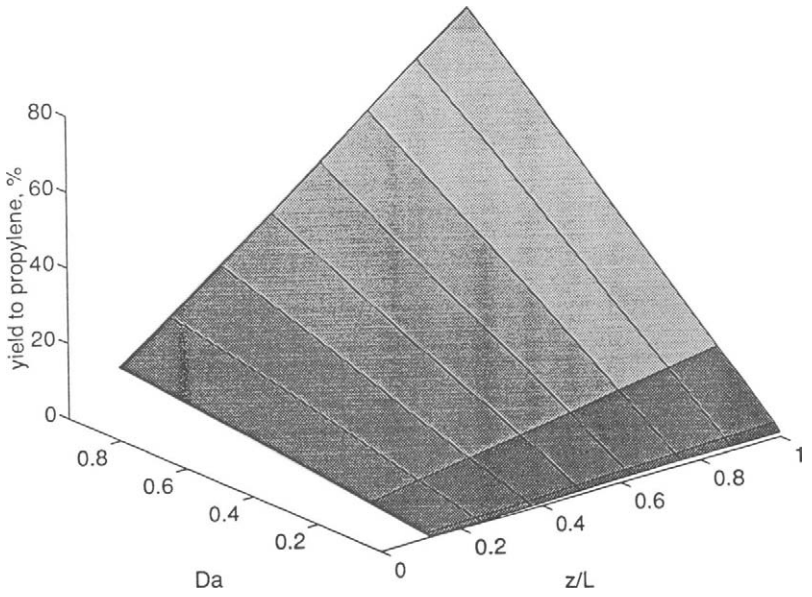

Fig.40 Yield to propylene versus Damkohler number Da^F and axial distance z/L in CFBP. Pressure ratio ψ^{PF}=0.85, sweep argon with Fr=0.20, (tubeside feed: C_3H_8:H_2:Ar=1:0.2:0)

dehydrogenation species on the axial and radial dimensions of the membrane reactor, the rates of reaction in membrane and tubeside catalyst, the feed composition in the reactor and the total pressure in the two membrane sides. Difference in partial pressures of various species between the two sides are driving the membrane separation. Translation of the partial pressure profiles in above plots to profiles of species conversions, yields is especially useful for selecting the final parameter values for related process applications.

H_2 and H_2 rich hydrocarbon mixtures produced from propane dehydrogenators like the ones described here can be used in the aforementioned applications of integrated chemical synthesis and power generation systems.

Below we give additional emphasis in new applications for methane (hydrocarbon) steam, and CO_2 reforming and paraffin dehydrogenation processes.

5. REACTOR PERMEATOR PROCESS INTEGRATION AND RELATED APPLICATIONS

Systems (cascades) of membrane permeators (separators) and conventional plug flow catalytic reformers, as well as membrane permeators and catalytic membrane reformers can be also applied for environmentally benign and cost effective conversion and upgrading of CH_4, higher hydrocarbons (e.g., C_2H_6, C_3H_8, n/i-C_4H_{10}) and CO to synthesis gas, hydrogen gas, or H_2 and CO_2 mixture, through reforming, water gas shift and dehydrogenation routes. The permeators discussed here can be of hollow fiber type, made from asymmetric polymer membranes of high glass transition temperature [77-83]. These membrane process systems were modeled appropriately by using permeators made by polyimide membranes such as 6FDA-pPDA, 6FDA-3,3',5,5'-TMB or other high Tg polymers [79-81]. These polymers have high glass transition temperatures of about 350-380°C and therefore an expanded operating temperature span in comparison with ordinary organic polymers. Such type of polyimides and related polymers (e.g., polybenzimidazoles, polycarbonates, polysulfones, polyphosphazenes) can separate selectively H_2 and CO_2 from CH_4 and CO [53]. Thus, they can be used not only as gas separation devices but also as single unit catalytic permreactors (of FBP type) for conducting low temperature methane steam reforming. Alternatively, such unit polymer permreactors can be used for conducting solely the lower temperature water gas shift reaction, which again has as products the permselective H_2 and CO_2 gases [51,53]. For the above permreactor applications, polymers can be also fabricated in combination with ceramics, metals or composites to constitute for more durable reactor wall materials.

Alternatively, microporous ceramic permreactors and permeators selective to H_2 and carbon oxides or metal ones selective to H_2 can be used in single unit and cascade configurations for these and related applications (Figs.42-45). In these cases, the high temperature permeators following the reactors will be used for highly selective separation and purification of the related gases from the feed mixtures in a thermally efficient manner. Polymer permeators can be also used for processing higher temperature gas mixtures (products of CH_4, natural gas, CO or paraffin conversion) which are exiting from conventional plug flow reformers or catalytic membrane reformers (made by metal alloys or ceramic materials) as shown in Figs.42,43. In these cases, the temperature of the exit stream needs to be reduced (e.g., by generating steam in an exit heat exchanger to be

used as feed in the reactors) to ensure long term operation of the polymer membranes in permeator as shown in the figures.

Similar types of high Tg polymers, ceramics, metals, and composites which are permselective only to H_2 can be used in applications shown in Fig.43. This is in propane (or other paraffin, e.g., ethane, n/i-butane) dehydrogenation reactions. After the cooling of the stream exited from the reactors/permreactors, H_2 is separated in the subsequent permeator. The rejected C_3H_6 , C_2H_4, n/i-C_4H_8 can be used for polymerization (i.e., polyolefin production) or other chemical synthesis.

The performance of the above described permeators (using polyimide polymers) in series with conventional plug flow reformers has been modeled through appropriate model equations which take into account the catalytic methane steam reforming and water gas shift reactions in the reformer and the species permeation through the polymer membranes [53].

Fig.41, shows the improvement in total CH_4 conversion and CO_2 yield at different first reactor inlet pressures by using a two reformer-one intermediate polymer permeator in a series process for methane steam reforming. Improvements in CH_4 conversion and CO_2 yield result to subsequent increases in H_2 yield by using the membrane process with respect to conventional PSA process (pressure swing adsorption). The latter one assumes a 90% separation capacity of the produced H_2 out of the first reformer exit stream [53]. Similar improvements in H_2 yield from increases in CH_4 conversion and CO_2 yield by use of the membrane process are reported at different reforming reaction temperatures (400-600 °C). The membrane permselectivity and thickness values are important parameters for the permeator, together with its module dimensions, total pressure and molar flowrate and composition in permeator inlet. These parameters define the margin of improved conversions and yields by using the series of two reformers with an intermediate permeator [53]. When the first reformer operates at higher temperatures it can deplete CH_4 or CO almost completely. In this case there is no need of using a second reformer or water gas shift reactor after the permeator (e.g., Fig.42). The produced H_2 and CO_2 are recovered almost completely in permeate stream of the permeator (almost 100% H_2 and CO_2 membrane recovery is reported based on specific simulation cases) [53].

6. NEW ENVIRONMENTALLY BENIGN PROCESS APPLICATIONS-A REVIEW

Based on the above process experiments and parametric analysis, one can design systems of conventional reactors and permeators, and those of permreactors and permeators which can be successfully utilized to process hydrocarbon feedstocks by converting them to hydrogen or synthesis gas or H_2 and CO_2 if needed, with subsequent selective product separation-recovery through permselective membranes. These membrane systems can be also used for adjusting process gas compositions in consecutive processes such as gas turbines, fuel cells or synthesis reactors. As an example the H_2 and CO_2 mixture, which is coming from methane steam reforming and water gas shift reactions, in membrane or conventional reactors, can be separated effectively (about 100% permeate recoveries of both components, [53]) from the unreacted components and other products with the membrane permeator, shown in

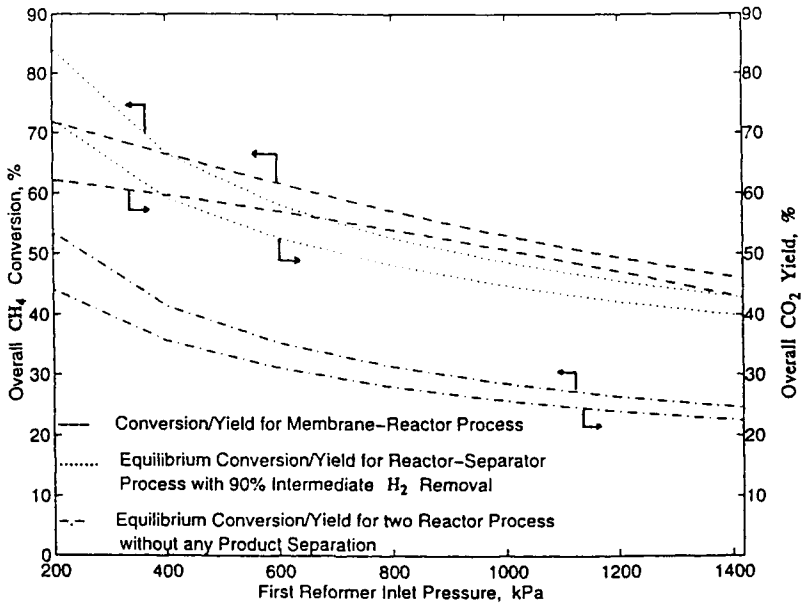

Fig.41 Overall CH_4 conversion and CO_2 yield versus first Reformer inlet pressure for three methane steam reforming systems. A polyimide was used in the reactor-membrane permeator system; T(of both reformers)=823K (550°C) (feed in first reformer: CH_4:H_2O:H_2=1:4:0.2)

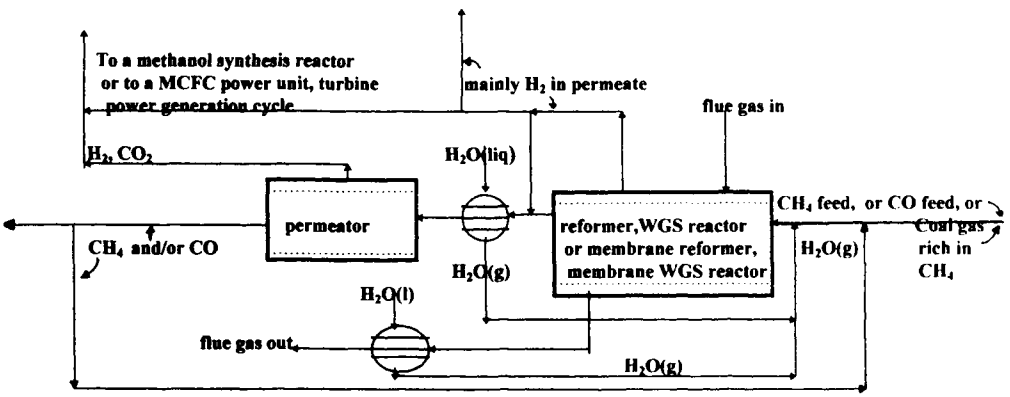

Fig.42 Permreactor-Permeator or Reactor-Permeator process for methane steam reforming or the water gas shift reactions. Membranes in permreactor: microporous ceramics or metals/alloys; same materials in permeator or high Tg polymers

Fig.42. The gas mixture entered in permeator is free of water by passage through a steam condenser/heat exchanger for removal of unreacted steam. The separated stream contains excess H_2 and can be used directly for methanol synthesis on specific catalyst formulations (e.g., iron, zinc, chrome, copper oxides) via the exothermic reaction:

$$3H_2+CO_2=CH_3OH+H_2O \qquad -\Delta H°_{298}=49.5kJ/mol$$

In the case of conducting the water gas shift alone in the process shown in Fig.42, CO constitutes only for the feed into the water gas shift reactor, which can be a conventional PFR or a permreactor. CO is converted to H_2 and CO_2 in the reactor. In both cases the reactors are followed by a permeator which separates the H_2 and CO_2 mixture as shown in the Figure.

An important application of the recovered H_2 and CO_2 mixture by using the reactor-permeator cascade process is as direct feed in molten carbonate fuel cells (MCFC), as shown in Fig.42. The gas mixture of H_2 and CO_2 is coming as product of the steam methane reforming or the water gas shift reactions in the preceded reforming or water gas shift vessels. In both cases, the recovered permeate mixture of H_2 and CO_2 is fed into the MCFC anode together with O_2 fed in cathode. Electricity is generated in the cell via the following overall reaction:

$$H_2+CO_2+1/2O_2 \dashrightarrow H_2O+CO_2$$

The oxidation reaction occurring in anode for current generation is:

$$H_2+CO_3^{2-} \dashrightarrow H_2O+CO_2+2e^-$$

while the reaction occurring in cathode is:

$$1/2O_2+CO_2+2e- \dashrightarrow CO_3^{2-}$$

Alternatively, after the CO_2 condensation from the binary mixture in permeate, pure H_2 can be recovered from the process and used in chemical synthesis or as fuel in anode of various types of H_2 based fuel cells and power generation cycles. H_2 can be used in H_2/O_2 advanced type combustors or in traditional H_2/hydrocarbon/O_2 type ones.

Similarly, propane, ethane or n/i-butane dehydrogenation to the corresponding olefins in conventional or membrane reactors can be used for direct H_2 production. Hydrogen can be separated from the produced olefins (e.g., propylene) and the unreacted paraffins (e.g., propane) in the following permeators and directed for chemical synthesis (e.g., ammonia, methanol synthesis, hydrogenations) or used in gas turbine and engine cycles or in fuel cell units as shown in Fig.43. Hydrogen can be consumed directly as fuel in anode of most fuel cell systems such as molten carbonate, solid oxide, alkaline, phosphoric acid, proton exchange. Propylene or ethylene will be rejected by the polymer membrane and can be fed to a polypropylene or polyethylene polymerization reactor while n/i-butene can be used in various chemical synthesis applications. Usually various configurations of stirred or fluidized bed reactors can be used as consecutive polymerization vessels [89].

An important related separation application is the use of CO_2 permselective polymer permeators for removal of CO_2 from CH_4 which are both the main components of landfill gas. Improved polymer membranes such as the desrcibed polyimides, polybenzimidazoles and others, become effective permselective barriers through materials-fabrication process optimization, and can be compared successfully with currently applied cellulose acetate membranes. Process superiority by using the new

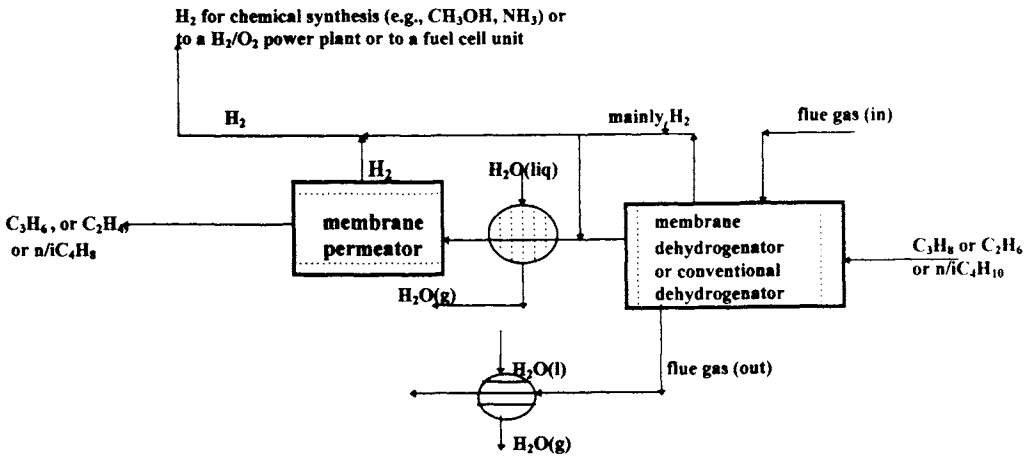

Fig.43 Permreactor-Permeator or Reactor-Permeator process for paraffin dehydrogenation and production of olefins. Membranes in permreactor: microporous ceramics or metals/alloys; same materials in permeator or high Tg polymers

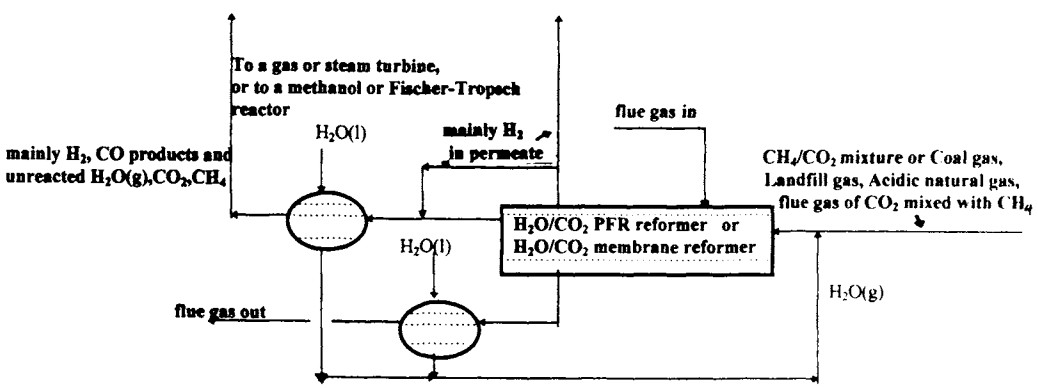

Fig.44 Combined H_2O-CO_2-CH_4 reforming process for chemical synthesis or power generation cycles. The membrane reformer can be from microporous ceramics or metals/alloys

proposed glassy polymers can be achieved by increasing simultaneously species permeability and CO_2:CH_4 selectivity, also due to their fabrication capacity in multiple hollow fiber permeator or permreactor configurations. Even if these new polymers bring improved thermal, chemical and mechanical resistance (e.g., lack of plasticization) in comparison with earlier generation used polymers, they are still sensitive to feed contaminants which must be removed before the stream enters into the membrane modules.

A related potential application, mentioned above, is use of the first reactor or permreactor alone to conduct CO_2-methane reforming. CO_2-CH_4 reforming without or with steam will mostly yield CO and H_2. In the first case, the main reaction occurring is as follows: $CH_4+CO_2=2CO+2H_2$, $-\Delta H^o_{298}=-247.3$ kJ/mol. Also, the reverse water gas shift reaction may occur. This is an applicable route for producing high grade synthesis gas without any moisture content, by directly eliminating the associated downstream gas drying processing. Dry synthesis gas is especially useful as fuel and in chemical synthesis (Fig.45).

In the CO_2-H_2O-CH_4 system the same CO_2 reforming reaction takes place together with reaction (1) and possibly the reverse of water gas shift, to yield synthesis gas (CO and H_2) with traces of CO_2, CH_4 and H_2O. In both of mentioned systems the need for the subsequent permeator can be eliminated and all mixture out of the reformer (e.g., H_2, CO, unreacted CO_2, CH_4, $H_2O(g)$) can be fed directly to a power generation cycle (e.g., steam or gas turbine, gas engine) or to a direct methanol synthesis ($CO+2H_2=CH_3OH$, $-\Delta H^o_{298}=128.2$kJ/mol) or to a Fischer Tropsch reactor, as shown in Figs.44&45. This is because most of the exit gas from the reactor consists of H_2 and CO which is synthesis gas with high calorific value and there is no need for species separation. The H_2 rich fuel can contribute to the adjustment of combustion conditions in the combustor with environmentally benign reduction of NOx and SOx emissions in flue gases, an effect that can possibly eliminate the downstream NOx, SOx removal steps [35-38,52,72]. Alternatively, produced H_2 gas exiting the permeate side of the permreactor can be used in synthesis applications and in aforementioned power generation and fuel cell systems.

The process can be also applied to convert prepurified landfill gas (CH_4, CO_2 mixtures) to synthesis gas. Landfill gas, which is mentioned above, needs to be prepurified form sulfur, hydrogen sulfide, ammonia, halogens and other contaminants before entering into the reformer to prevent catalyst deactivation and poisoning. Types of coal gas (mixtures of CH_4 and CO_2) coming from coal gasifiers can be also used as feed in CO_2 reforming processes shown in Figs. 44&45. Moreover, flue streams which come from hydrocarbon combustion systems and contain CO_2 are also applicable, after the removal of unwanted components and mixing with CH_4, for in-situ abatement and reduction of their greenhouse effects through the proposed processes. Another important new proposed application is in direct reforming of acidic natural gas, which after the H_2S removal contains hydrocarbons such as methane or higher, and CO_2 and is directly suitable for the catalytic CO_2 reforming process for upgraded synthesis gas production.

The dry CH_4-CO_2 reforming reaction or the CO_2-H_2O-CH_4 reaction can be applied in a microporous or mesoporous ceramic reactor or metal/metal composite (e.g.,

Pd, Pd/Ag) membrane reactor for integrated H_2 separation and concomitant increase of the CH_4, CO_2 conversion and H_2, CO yields per reactor pass. Today's drawback for dry reforming is the lack of selective catalysts to make this conversion without severe carbon deposition and eventual complete catalyst deactivation with time on stream. Research towards improved catalyst process developments for CO_2/CH_4 reforming such as Rh/Al_2O_3, Pd/TiO_2, Ni/TiO_2, $CaO\text{-}TiO_2\text{-}Al_2O_3$ has been reported [67-71].

Efforts are currently underway to fabricate membranes from inorganic materials and polymers (e.g., silica, titania, zirconia, glass composites, various zeolite types) and composites of organic and inorganic materials and polymers (carbons, organics) [29,30,51,76,93,94] with even higher permeabilities and permselectivities to H_2 in comparison with CH_4, CO, CO_2 and higher hydrocarbons or to H_2 and CO_2 in comparison with same species. These membranes can be used at higher temperature applications than the currently used organic polymer membranes. In these cases they can constitute permreactors which integrate reaction and separation in a single unit process and vessel, as mentioned in Section 5 above. Current developmental efforts are hampered by hydrothermal stability problems of these materials, increased susceptibility to poisoning compounds (e.g., sulfur, ammonia, hydrogen halides), and deactivation of the permselective layer by carbon deposition (with subsequent permeability and selectivity loss). Operational life times of these permeable materials may be currently short, due to their susceptibility as well to mechanical and thermal stresses. Thus, an ultimate goal in these applicable process designs from a materials point of view is development of specifically permselective, process resistant, high flux materials or composites (e.g., organics and inorganics) able to withstand as high as possible operating process temperatures and pressures. This accomplishment will increase the overall process

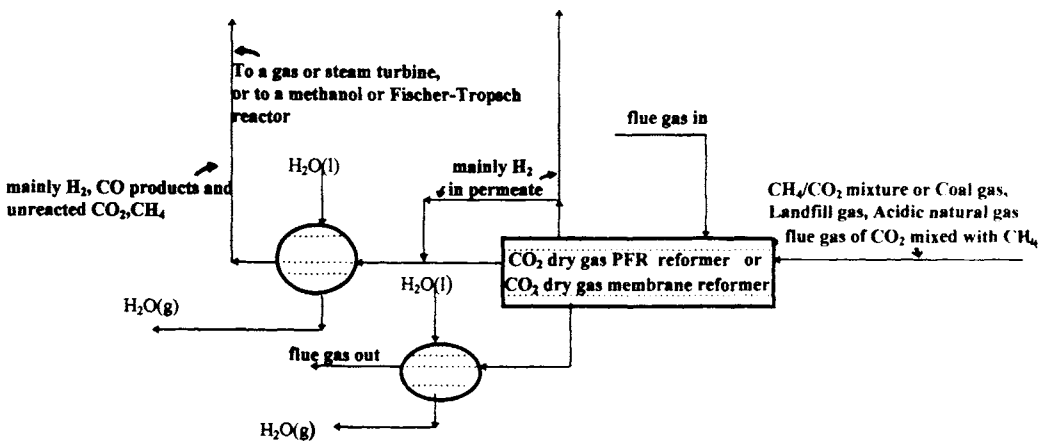

Fig.45 CO_2-CH_4 dry gas reforming process for chemical synthesis or power generation cycles. The membrane reformer can be from microporous ceramics or metals/alloys

efficacy due to the reduction of thermal losses between reactor and permeator.

Ultimately, the ideal process design is integration of reactor and permeator in a single permreactor vessel, suited to the specific reaction/process and operated in the process temperature and pressure, which reacts with efficient yields and separates selectively the desired product and/or unreacted reactant compounds out of the reaction zone. Moreover, utilization of the thermal energy of flue or waste gases from turbines, boilers, superheaters, heat exchangers and other low temperature heat resources, to provide the endothermic heat load to the permeable reformers or dehydrogenators can increase the overall process efficiency in such systems [35-38,52]. Also, an autothermic type of operation can be designed in which the exit streams are used to supply heat to the reactant streams fed into the reactor (e.g., steam) as shown in Figs.42 and 44.

The use of the above described permreactor/reactor-permeator systems for separation of the H_2, CO_2 mixtures or of the H_2, CO_2 separate compounds, must be comparable (in terms of system yield and conversion measures) to the operational use and performance of currently applied single ceramic or metal membrane reactors. Further, these membrane processes-systems must compare successfully to currently used reaction and separation integrated processes (e.g., plug flow reactors combined with pressure swing adsorption, solvent absorption units).

7. CONCLUSIONS-REMARKS

The above studies have demonstrated the importance of using permreactors and system configurations of permreactors or conventional reactors with permeators for processing and upgrading methane, natural gas, landfill, coal and flue gases, and light hydrocarbon feedstocks (such as propane, ethane, n/i-butane) to hydrogen or synthesis gas via the catalytic steam and/or CO_2 reforming, water gas shift, and dehydrogenation routes. The use of ceramic catalytic membrane reactors provides versatile design tools for contacting hydrocarbon to hydrogen and carbon oxide chemical transformations. These processes may offer increased hydrocarbon conversion and yield to H_2 gas, synthesis gas, H_2 and CO_2 mixture, H_2 and unreacted hydrocarbon mixture, product olefins (e.g., propylene, ethylene, n/i-butene), product H_2 and olefin mixture, olefin and unreacted paraffin mixture, which are all valuable synthesis and fuel species.

The results presented here with mesoporous ceramic permreactors are promising. Better conversions and yields can be further obtained by using improved membranes made by microporous ceramics, dense metals, organic materials and composites of the previous, by using recent advances in materials processing and fabrication. Long term thermo-mechanical durability, with hydrothermal, and deactivation-poisoning resistance, are the ideal candidate-permreactor and permeator properties for steam reforming, CO_2 reforming, water gas shift and dehydrogenation processes.

The studies presented here lay out the design principles, process criteria, parameter value range, and selection of membrane reactor operations and catalytic configurations which must be followed, for environmentally benign and cost effective implementation of the ceramic permreactor technology for H_2 and H_2 rich mixtures generation from methane steam reforming and propane dehydrogenation.

Guidelines for related ceramic catalytic permreactor design based on our studies can be derived. Increases in Damkholer number and Thiele modulus in FBP, CP and CFBP lead to increases in product yield and reactant conversion. There is a range of values for the parameter Q, and thus for the values of species permeability, which improve the product yields above the respective at equilibrium, for fixed values of species selectivity through the membrane and pressure difference across it. The higher the selectivity of the membrane to the permeating product, the higher the product yield improvement. Variation in pressure values in permeate and in tubeside are strongly affecting the reaction and permeation process and thereby the product yield and reactant conversion. Steam reforming and dehydrogenation of paraffins are volume expansion reactions, thereby product yields are favored by low pressures. These reactions are also endothermic and are favored by increased temperatures in contrary to exothermic ones. Thereby, selection of operating pressure and temperature of a permreactor (FBP, CP, CFBP) depends on the level of its desired conversion and yield and exit gas composition. A basis for optimum temperature and pressure selection in these type of reactions is to exceed the thermodynamic equilibrium and PFR reactor yield, conversion values.

There is also a strong dependence of the species partial pressures and consequently of product yield and reactant conversion on permreactor length, its radius and the membrane thickness. The last two variables are introduced within the dimensionless radius ω, and its variation affects product yield. Reactive sweep gases such as methane and steam for the reforming reaction and propane for the dehydrogenation one are more effective species than inerts for sweep gas-membrane reactor synergy. Reactive sweep gas double effect as sweep gas and reactant, increases permreactor process efficacy. Inert gases need to be separated in downstream from permeated and non-permeated products and reactants which require increased capital and operational costs. Though, there are cases in which specific inert gases can fit better to a permreactor process application. Thermal efficiency in endothermic membrane reformers and dehydrogenators can be increased by utilizing the thermal content of the exiting permreactor streams to heat reactant streams (such as steam, methane, propane) before they introduced in reactor inlet, providing for an autothermic mode of operation. Use also of waste, flue gases to provide endothermic heat in the permreactors contributes to the same purpose. Optimization and modeling studies of various reaction systems by use of permreactors have been reported which provide additional insights to such systems performance [16-18,92].

For the specific reactions, catalysts, membranes, and permreactor configurations studied, the CFBP mode is more effective than the FBP and CP to achieve conversion and yield improvements towards the equilibrium and PFR modes.

Beyond the concluded remarks, the described reforming and dehydrogenation studies show possible proposed configurations of high temperature permreactos (CFBP and FBP) to be used as catalytic reaction carriers with multiple or alternative reactant feed ports and multiple or alternative relative reactant/reactor flow configurations. Also membrane reactors can be used as reactant recycling providers or acceptors from the tubeside and/or shellside for increasing the reactant conversion and utilization per reactor pass. Moreover, permreactors can be used in series or parallel configurations in

combination with membrane permeators and conventional catalytic reactors for various chemical synthesis applications such as methanol and synthetic gasoline, polyolefin production, and for providing fuel in fuel cells and power generation systems.

Catalytic alumina membrane reactors studied, demonstrated specifically, effectiveness in increasing both CH_4 conversion and CO_2 yield, and C_3H_6 yield, C_3H_8 conversion, above the values obtained in respective experiments with nonpermeable catalytic reactors. Moreover, for several conditions, the obtained membrane reactor conversion/yield values exceeded those calculated at thermodynamic equilibrium.

The porous ceramic reactors were also tested as double side (both shellside and tubeside) feed (split feed) reactors for CH_4 steam reforming and C_3H_8 dehydrogenation with success. Conversions and yields same or higher than the equilibrium were obtained which otherwise can not be achieved with use of conventional reactors.

Both methane steam reforming and propane dehydrogenation permreactors were modeled appropriately with computational models that account for simultaneous reaction and species separation. The models can simulate any of FBP, CFBP and CP configurations. Several model parameters were varied and their effect on species partial pressure and respectively on product yield and reactant conversion was studied. Based on selection of parameter values such as temperature, pressure, reactant space time, feed composition, sweep gas flow rate and composition, optimization of the permreactor can take place in terms of increased conversion and yield above the equilibrium and PFR values.

Hydrocarbon and CO -environmentally benign conversion technology- to CO_2 and H_2 mixture, or to H_2 gas after the CO_2 condensation, with subsequent conversion of these products to useful chemical feedstocks or utilization in power generation cycles and fuel cells is presented. CO_2 in-situ mitigation and elimination technology from landfill, coal, flue gases, acidic natural gas rich in CO_2, and other CO_2, CH_4 mixtures via the CO_2 reforming route with or without H_2O is also presented. Also described are new process designs for paraffin dehydrogenation. These integrate permreactors or conventional reactors with permeators for downstream separation of the produced H_2 through the membrane from the produced olefins and unreacted paraffins.

Subsequently, membrane reaction and separation processes can be applied in CH_4-steam, CH_4-CO_2 or combination of the two reforming routes for elimination of these and relevant greenhouse process gases through chemical conversion. The related in-situ CO_2 reforming technology, produces directly synthesis gas which can be used to make methanol, synthetic gasoline via Fischer Tropsch synthesis, or as alternative fuel for power generation under reduced NOx emissions due to increased H_2 concentration in the fuel.

Usage of specifically tailored permselective membranes from high Tg polymers, also from alternative ceramics and metals, can be effective in separating H_2 and CO_2 from CH_4, CO and higher hydrocarbons, H_2 from hydrocarbons and carbon oxides, or H_2 from olefins and paraffins. This technology shows potential application for integrated methanol synthesis and polyolefin production (e.g., polypropylene, polyethylene). Also, as hydrogen supply in various types of H_2 based fuel cells (H_2 and CO_2 combined, are

especially suited for molten carbonate fuel cells) and in gas turbine, engine cycles for power generation.

The proposed membrane reactor configurations and their described applications seek to perform multiple unit operations within a single or integrated module/s which makes them advanced in comparison with up to now proposed and utilized membrane reactors.

Based on the above experimental, modeling and design studies such type of permreactors and related permreactor/reactor-permeator systems can be a promising replacement technology for conventional reaction, reaction-separation systems for hydrocarbon-steam, CO_2 reforming, water gas shift, paraffin dehydrogenations and other related reactions. The laboratory scale experiments shown here need to be complemented by scale up and optimization studies to verify their applicability with industrial scale permreactors. Actual process conditions need to be optimized as well by the use of models and process tests, to ensure efficacy in production capacity and operation costs. Long term operation of these membrane reactors/systems under steady state improved conversion, yield and selectivity to specific species, and without catalyst deactivation is the applicable objective.

REFERENCES

1. M.P. Harold and P. Cini, AIChE Symp. Ser., 286, 85 (1989) 26.
2. J.N. Armor, Appl. Catal., 49 (1989) 1.
3. V.M. Sun and S.J. Khang, Ind. Eng. Chem. Res., 27 (1988) 1136.
4. T. Kameyama, M. Dokiya, M. Fujishige, H. Yokokama and K. Fukuda, Ind. Eng. Chem. Fund., 20 (1981) 97.
5. D. Edlund and W.A. Pledger, J. Memb. Sci., 77 (1993) 255.
6. V.M. Gryaznov, V.S. Smirnov, and G. Slinko, "Heterogeneous Catalysis with Reagent Transfer through the Selectively Permeable Catalysis, Catalysis, J.W. Hightower, (ed.), American Elsevier, New York, (1973).
7. V.M. Gryaznov, Platinum Met. Rev., 30 (1986) 68.
8. V.M. Gryaznov, V.P. Polyakova, E.M. Savitsky, and E.V. Khrapova, US Patent No. 4 026 958 (1977).
9. W.E. Pfefferle, US Patent No. 3 290 406 (1966).
10. T.J. Stanley and J.A. Quinn, J. Memb. Sci., 30 (1987) 243.
11. H.N. Chang and S. Furusaki, Adv. Biochem. Eng. Biotechnol., 44 (1991) 27.
12. M. Cheryan and M.A. Mehaia, Chemtech, 16 (1986) 676.
13. N. Itoh, Y. Shindo, K. Haraya, K. Obata, T. Hakuta, and H. Yoshitome, AIChE J., 25,1 (1985) 138.
14. N. Itoh, AIChE J., 33,9 (1987) 1576.
15. N. Itoh, Y. Shindo, and K. Haraya, J. Chem. Eng. Japan, 23,4 (1990) 420.
16. K. Mohan and R. Govind, AIChE J., 32,12 (1986) 2083.
17. K. Mohan and R. Govind, AIChE J., 34,9 (1988) 1493.
18. K. Mohan and R. Govind, Ind. Eng. Chem. Res., 27 (1988) 2064.

19. T.T. Tsotsis, A.M. Champagnie, S.P. Vasileiadis, Z.D. Ziaka and R.G. Minet, Chem. Eng. Sci., 47(9-11) (1992) 2903.
20. T.T. Tsotsis, A.M. Champagnie, S.P. Vasileiadis, Z.D. Ziaka and R.G. Minet, Sep. Sci. Technol., 28(1-3) (1993) 397.
21. Z. Ziaka, "Experimental and modeling studies of the catalytic propane dehydrogenation reaction in ceramic membrane reactors", Ph.D. dissertation, University of Southern California (ed.), (1994).
22. Z. Ziaka, T. Tsotsis, and R.G. Minet, AIChE J., 39 (1993) 3.
23. Z. Ziaka, T.Tsotsis, and R.G. Minet, J. Memb. Sci., 77 (1993) 221.
24. R. Hughes, K. Hou, and Y. Yildirim, Paper#314d, AIChE Annual Meeting, Miami Beach, Nov. (1998).
25. V.T. Zaspalis, W. van Praag, K. Keizer, J.G. van Ommen, J.R.H. Ross, and A.J. Burggraaf, Appl. Catal., 74 (1991) 223.
26. V.T. Zaspalis, W. van Praag, K. Keizer, J.G. van Ommen, J.R.H. Ross, and A.J. Burggraaf, Appl. Catal., 74 (1991) 249.
27. J.W. Veldsink, R.M.J. Van Damme, G.F. Versteeg and W.P.M. Van Swaaij, Chem. Eng. Sci., 47, 9-11 (1992) 2939.
28. H.J. Sloot, C.A. Smolders, W.P.M. Van Swaaij and G.F. Versteeg, AIChE J., 38,6 (1992) 887.
29. G.R. Gavalas, M. Tsapatsis and S. Kim, #13B, 4thNAMS meeting, San Diego, CA (1991).
30. J. Lewis, G. Gavalas, and M. Davis, AIChE J., 43,1 (1997) 83.
31. T. Okubo, K. Haruta, K. Kusakabe, S. Morooka, H. Anzai, and S. Akiyama, Ind. Eng. Chem. Res., 30(4) (1991) 614.
32. M. Ortel, J. Schmitz, W. Welrich, D.J. Neumann and R. Schulten, Chem. Eng. Technol., 10 (1987) 248.
33. S. Uemiya, N. Sato, H. Ando, T. Matsuda, and E. Kikuchi, Appl. Catal., 67 (1991) 223.
34. S. Uemiya, N. Sato, H. Ando, and E. Kikuchi, Ind. Eng. Chem. Res., 30(3) (1991) 585.
35. S.P. Vasileiadis, "Catalytic Ceramic Membrane Reactors for the Methane Steam Reforming Reaction; Experiments and Simulation", Ph.D. Dissertation, University of Southern California (ed.), (1994).
36. S. P. Vasileiadis, R.G. Minet, and T.T. Tsotsis, AIChE Annual Meeting, Saint Louis, MO, Nov. (1993).
37. S. P. Vasileiadis, R.G. Minet, and T.T. Tsotsis, 7th NAMS Meeting, Breckenridge, CO (1994).
38. R.G. Minet, S.P. Vasileiadis, and T.T. Tsotsis, Proceedings of Amer. Chem. Soc., Div. of Petrol. Chem., San Francisco, CA (1992).
39. M. Chai, M. Machida, K. Eguchi, and H. Arai, Appl. Catal., 110 (1994) 239
40. T. Nozaki, O. Yamazaki, K. Omata, and K. Fujimoto, Chem. Eng. Sci., 47(9-11) (1992) 2945.
41. A. Tonkovich, R. Carr, and R. Aris, Science, 262 (1993) 221.

42. M.P. Harold, V.T. Zaspalis, K. Keizer, and A.J. Burggraaf, 5th NAMS Meeting, Lexington, KY (1992).
43. J. Wu, T. Gerdes, J.L. Pszczolkowski, R. Bhave, and P. Liu, Sep. Sci. Technol., 25, (1990) 1489.
44. C.L. Liu, D.F. Flowers, G.R. Gallagher, and P.K.T. Liu, paper 13D, 4th NAMS Meeting, San Diego, CA (1991).
45. A.M. Champagnie, T.T. Tsotsis, R.G. Minet and E. Wagner, J. Catal., 134 (1992) 713.
46. T.T. Tsotsis, A.M. Champagnie, R.G. Minet and P.K.T. Liu, "Catalytic Membrane Reactors", Vol. 51, E.R. Becker, and C.J. Pereira (eds.), Marcel Dekker, NY (1993).
47. Y.L. Becker, A.G. Dixon, W.R. Moser, and Y.H. Ma, J. Memb. Sci., 77 (1993).
48. A.M. Adris, S.S.E.H. Elnashaie, and R. Hughes, Can. J. Chem. Eng., 69 (1991) 1061.
49. A.M. Adris, C.J. Lim and J.R. Grace, Chem. Eng. Sci., 152, 10 (1997) 1609.
50. J.L. Troutman, "Linear Boundary Value Problems", Syracuse University(ed.), (1988).
51. S. Vasileiadis and Z. Ziaka, Paper No. 275c, AIChE Annual Meeting, Los Angeles, CA (1997).
52. Z. Ziaka and S. Vasileiadis, No. 2p, AIChE Annual Meeting, Nov. (1998).
53. Z. Ziaka and S. Vasileiadis, Chem. Eng. Comm., 156 (1996) 161-200.
54. Z. Ziaka and S. Vasileiadis, Paper#318bp, AIChE Annual Meeting, Miami Beach, Nov. (1998).
55. Z. Ziaka and S. Vasileiadis, 5th World Congress of Chemical Engineering, Vol.3 pp.114-119, San Diego, CA (1996).
56. N. Itoh, M.A. Sanchez, W. Xu, K. Haraya and M. Hongo, J. Membr. Sci., 77 (1993) 245.
57. I.M. Bodrov, L.O. Apelbaum, and M.I. Temkin, Kinet. Katal., 5,4 (1964) 614.
58. M.E. Agnelli, E.N. Ponzi, and A.A. Yeramian, Ind. Eng. Chem. Res., 26,8 (1987) 1707.
59. J.R.H. Ross and M.C.F. Steel, J. Chem. Soc. Faraday Trans., 1,69 (1972) 10.
60. J. Xu and G.F. Froment, AIChE J., 35,1 (1989) 88.
61. R.D. Farr and C.G. Vayenas, J. Electrochem. Soc., 127(7) (1980) 1478.
62. M. Stoukides and C.G. Vayenas, J. Catal., 70 (1981) 137.
63. T.M. Gur and R.A. Huggins, Science, 219 (1983) 967.
64. E.A. Hazburn, US Patent No. 4 791 079 (1988).
65. M.P. Harold and K.M. Ng, AIChE J., 33 (1987) 9.
66. K.M. Ng and K.D. Samant, Paper No. 143b, AIChE Annual Meeting, Miami Beach, FL (1998).
67. J.H. McCrary, G.E. McCrary, T.A. Chubb, J.J. Nemecek, and D.E. Simmons, Solar Energy, 29,2 (1982) 141.
68. A.M. Gadalla and B. Bower, Chem. Eng. Sci., 43,11 (1988) 3049.
69. J.T. Richardson and S.A. Paripatyadar, Appl. Catal., 61 (1990) 293.
70. J.T. Richardson, M. Lei, B. Turk, K. Forster, and M.V. Twigg, Appl. Catal., 110 (1994) 217.
71. A. Erdohelyi, J. Cserenyi, E. Papp, and F. Solymosi, Appl. Catal., 108 (1994) 205.

72. F.L. Robson, W.A. Blecher, and C.B. Colton, Rep. No. EPA-600/2-76-153, USEPA, Washington, D.C. June (1976).
73. W.C. Pfefferle and L.D. Pfefferle, Prog. Energy Combust. Sci., 25 (1986) 2.
74. W.R. Williams, C.M. Marks, and L.D. Schmidt, J. Phys. Chem., (1992) 5922.
75. Y.K. Park, N.E. Fernandes, and D.G. Vlachos, Paper No. 62cb, AIChE Annual Meeting, Nov. (1998).
76. C.J. Brinker, T.L. Ward, R. Sehgal, N.K. Raman, S.L. Hietala, D.M. Smith, D.-W. Hua, and T.J. Headley, J. Memb. Sci., 77 (1993) 165.
77. K. Toi, Y. Maeda and T. Tokuda, J. Appl. Polym. Sci., 28 (1983) 3589.
78. J. Shu, B.P.A. Grandjean, A. van Neste, and S. Kaliaguine, Can. J. Chem. Eng., 69 (1991) 1036.
79. S.A. Stern, Y. Mi, H. Yamamoto and A.K.S. Clair, J. Polym. Sci., Part B, Polym. Phys. Ed., 27 (1989) 1887.
80. H. Yamamoto, Y. Mi, S.A. Stern and A.K.S. Clair, J. Polym. Sci., Part B, Polym. Phys. Ed., 28 (1990) 2291.
81. S. Vasileiadis, "Gas Transport through Aromatic Polyimides", MS independent research study, Syracuse University, NY (1990).
82. W.J. Koros and R.T. Chern, "Separation of Gaseous Mixtures Using Polymer Membranes", in Handbook of Separation Process Technology, R.W. Rousseau Ed., pp. 862-953, Wiley Interscience, (1987).
83. K.C.O. Brien, W.J. Koros, and G.R. Husk, J. Memb. Sci., 35 (1988) 217.
84. S.Y. Lim, B.G. Park and T.T. Tsotsis, Paper#143h, AIChE Annual Meeting, Miami Beach, Nov. (1998).
85. M.A. Soliman, S.S.E.H. Elnaahaie, A.S. Al-Ubaid and A.M. Adris, Chem. Eng. Sci., 43,8 (1988) 1801.
86. M.A. Soliman, A.M. Adris, S.S.E.H. Elnaahaie, and A.S. Al-Ubaid, J. Chem. Technol. Biotechnol. 55 (1992) 131.
87. J.R. Rostrup-Nielsen, J. Catal., 33 (1974) 184.
88. J.R. Rostrup-Nielsen, J. Catal., 85 (1984) 31.
89. F. Rodriguez, "Principles of Polymer Systems", Hemisphere Publishing Corp., 3rd Ed. (1989).
90. G.F. Froment and K.B. Bischoff, "Chemical Reactor Analysis and Design", J.Wiley & Sons, (1979).
91. J.M. Smith and H.C. Van Ness, "Introduction to Chemical Engineering Thermodynamics", McGraw Hill, (1983).
92. Z. Ziaka and V. Manousiouthakis, Ind. Eng. Chem. Res., 37, (1998) 3551.
93. W. Ho and K. Sirkar, Eds., "Membrane Reactors", in Membrane Handbook, Van Nostrand Reinhold, (1992).
94. R.R. Bhave, Ed., "Inorganic Membrane Reactors", in Inorganic Membranes Synthesis, Characteristics and Applications, Van Nostrand Reinhold, (1991).

NOTATION

$Q=2\pi LD_{Ae}/F_o^F$, dimensionless
R=gas constant, J/gmol.K
R_1=inner radius of membrane tube, cm
R_2=radius of membrane tube including the permselective layer, cm
r=radial distance, cm
r_i=rate of reaction i, gmol/hr.g_{cat}
R_{CH4}=rate of CH_4 consumption in methane steam reforming process, gmol CH_4/hr.g_{cat}
R_{CO2}=rate of CO_2 formation in methane steam reforming process, gmol CO_2/hr.g_{cat}
R_1^F, R_3^F =modified reaction rate expression for reactions (1) and (3) in tubeside catalyst, $1/atm^{1/2}$
R_2^F= modified reaction rate expression for reaction (2) in tubeside catalyst, atm
R'^F_i= modified reaction rate expression for reaction i in tubeside catalyst, dimensionless
r_i^m=reaction rate expression for reaction i in the catalytic membrane, gmol/hr.cm^3
r'^m_i=reaction rate expression for reaction i in the catalytic membrane, dimensionless
T= temperature, K or °C
W=catalyst weight in tubeside, g
$X_j^{F(P)}$=mole fraction of species j in feedside (tubeside) or permeate side (shellside), dimensionless
X^{CH4}=total methane conversion, gmol CH_4/gmol CH_4 in feed
Y_j^m=partial pressure of species j across the membrane with respect to the total tubeside pressure at the inlet, dimensionless
Y^{CO2}=CO_2 yield, gmol CO_2/gmol CH_4 in feed
$y_j^{F(P)}$=molar flowrate of species j in feedside (tubeside) or permeate side (shellside) with respect to the total molar flowrate in tubeside inlet, dimensionless
z= reactor axial distance, cm
Da_i^F=Damkohler number for reaction i in feedside (tubeside), dimensionless
D_{je}=effective diffusion coefficient (diffusivity) for species j, cm^2/hr or cm^2/s
d_p=equivalent particle diameter, cm
f=friction factor, dimensionless
$F^{F(P)}$=volumetric flowrate in tubeside or shellside, cm^3/hr
Fr=volumetric flowrate ratio, dimensionless
F_{mj}= molar flowrate of sweep gas (j) in shellside inlet with respect to the molar flowrate of methane or propane in tubeside inlet, dimensionless
g_c=conversion factor, g/cm.atm.hr^2
G^F=superficial flow velocity in tubeside, g/cm^2.s
K_{e1}, K_{e3} =equilibrium constants for reactions (1) and (3), atm^2
K_{e2}=equilibrium constant for reaction (2), dimensionless
K'_{ei}=dimensionless equilibrium constant for reaction i
K_j=adsorption constant of species j
k_1^F, k_3^F=kinetic constants for reaction (1) and (3) in tubeside catalyst, gmol.$atm^{1/2}$/hr.cm^3
k_2^F=kinetic constant for reaction (2) in tubeside catalyst, gmol/hr.atm.cm^3
k_4^F=kinetic constant for reaction (4) in tubeside catalyst, gmol/s.atm.cm^3
k'_i=kinetic constant for the reaction in catalytic membrane, gmol/hr.atm.cm^3

L=axial length in membrane tube or conventional reactor, cm
Mj =molecular weight of species j, g/gmol
$N_{Re}=d_p G^F/\mu$, Reynolds number, dimensionless
$n_j^{F(P)}$=molar flowrate of species j in tubeside or shellside, gmol/hr
n_o^F=total molar flowrate in tubeside inlet, gmol/hr
$P^{F(P)}$=total pressure in tubeside or shellside, atm
$P_j^{F(P)}$=partial pressure of species j in tubeside or shellside, atm
P_j^m=partial pressure of species j through the porous membrane, atm
$\bar{P}j$=permeability coefficient (permeability) of species j, gmol/m.s.Pa or gmol/cm.s.Pa

Greek Symbols

$\alpha=\ln(1+\varepsilon)$, dimensionless
$\beta_i^{f(r)}$=order of the forward or reverse reaction i, dimensionless
$\delta_j=D_{je}/D_{Ae}$, diffusion coefficient of species j with respect to diffusion coefficient of reference species A, dimensionless
$\varepsilon=R_2-R_1/R_1$, dimensionless
ε_u=void fraction of catalyst bed, dimensionless
ζ=z/L, axial distance, dimensionless
μ=viscosity of gas mixture, g/cm.hr
$\xi=r/R_1$, radial distance, dimensionless
v_{ij}=stoichiometric coefficient of species j in reaction i, dimensionless
$v_j=M_j/M_A$, molecular weight of species j with respect to molecular weight of reference component A, dimensionless
Φ_i=Thiele modulus for reaction i, dimensionless
$\psi^{F(P)}$=total tubeside or shellside pressure with respect to total tubeside pressure in reactor inlet, dimensionless
ψ^{FP}=ratio of shellside (permeate side) to tubeside (feedside) total pressure in reactor inlet, dimensionless
$\omega=\ln\xi/\alpha$, dimensionless

Superscripts

F=tubeside (feedside)
P=shellside (permeate side)
m=membrane
f=forward
r=reverse

Subscripts

A=reference species (CH_4), (C_3H_8)
I=inert species (Ar)
i=reaction index
j=species index
o= reactor inlet conditions
p=particle
e=at equilibrium
je=effective parameter for species j

Reaction Engineering for Pollution Prevention
M.A. Abraham and R.P. Hesketh (Editors)

Pollution Prevention Education in Chemical Reaction Engineering

Robert P. Hesketh[a], and Martin A. Abraham[b]

[a]Dept of Chemical Engineering, Rowan University, Glassboro, NJ, 08081-1701, (hesketh@rowan.edu)

[b]Dept of Chemical and Environmental Engineering, The University of Toledo, Toledo, OH 43606 (mabraham@eng.utoledo.edu)

During the last 10 - 20 years, the need to introduce pollution prevention concepts to undergraduate students has become recognized.[1] This need has now been codified in the chemical engineering accreditation criteria, through the ABET engineering criteria 2000. This specifies, in part, that chemical engineering departments must incorporate "ethics, safety and the environment" into the curricula. Originally, many chemical engineering programs responded by introducing a senior/graduate level elective course on environmental engineering, with emphasis on end of the process treatment. Recently, courses have been developed that focus on methods to minimize or prevent waste streams from exiting chemical plants. These trends mirror those in industry, in which initial efforts were applied to waste treatment whereas current efforts are aimed at reducing the total volume of effluent treated as well as the nature of the chemicals treated. Efforts are now underway to incorporate aspects of pollution prevention throughout the curriculum. This paper reviews the current status of pollution prevention courses in the chemical engineering curriculum and presents ideas on implementing pollution prevention case studies in the reaction engineering course.

Pollution Prevention Courses

A quick survey of chemical engineering course catalogs will reveal that most departments throughout the United States list at least one course devoted to environmental training. Further analysis reveals that many of these are survey courses on Environmental Engineering. Some more extensive programs provide additional courses at higher levels, including courses on air or water pollution and waste treatment. While these courses certainly provide good educational experiences, this paper is intended to focus attention on education opportunities in pollution prevention. We differentiate between waste treatment and pollution prevention as follows:

- Waste treatment and minimization refers to methods and processes for treating or removing wastes from effluent streams.
- Pollution prevention refers to the design of new processes or modification of existing processes with a specific goal of producing minimal wastes.

While the distinction between these concepts is subtle, it clearly falls along the lines of the pollution prevention hierarchy recommended by the Pollution Prevention Act of 1990, which lists source reduction and recycling as the highest forms of pollution prevention, followed by waste treatment and then secure disposal.

Specific course opportunities on pollution prevention have existed for at least the past decade. The National Pollution Prevention Center web site lists 19 courses in the general area of pollution prevention on their web site.[2] This list summarizes the courses that were added between 1988 and 1995; the majority of courses that have a significant pollution prevention component were added around 1993. Nearly all of the courses listed were designed as electives for graduate students or upper division undergraduates. Of the 19 courses listed, approximately one-half might be better classified as courses on waste treatment and minimization rather than pollution prevention.

In order to get a more recent assessment of the state of pollution prevention education, we have completed a survey of chemical engineering departments throughout the USA. A survey form was sent to each department asking for information on how they taught pollution prevention within their curriculum. The responses can be loosely classified into three categories:

1. Programs in which pollution prevention is taught as a separate elective class (30%).
2. Programs that offer a course in air pollution or waste treatment and include pollution prevention as a component within these elective courses (40%).
3. Programs that do not provide any specialized training in pollution prevention but may include some material within the regular course sequence, usually, the senior design course (30%).

In nearly all cases, the courses are targeted at upper division undergraduate or graduate students and are elective courses. To the best of our knowledge, only our program at The University of Toledo requires a course in pollution prevention for all its chemical engineering seniors. Although the number of survey responses represents a minority of chemical engineering departments, these results would appear to be consistent with anecdotal information that many chemical engineering programs are now looking into ways in which pollution prevention can be incorporated into the graduate and undergraduate curriculum.

The required course at The University of Toledo follows the same general outline as the electives taught at other locations, and follows the textbook of Allen and Rosselot[3]. Within the chemical and environmental engineering department at the University of Toledo, we have recently implemented a required course entitled "Pollution Prevention" and focused on the chemical process industry. The course contains three components, an introduction to chemical pollutants, a discussion of life cycle analysis, and an environmental analysis of a chemical process. As a component of the course, we included a case study provided by a local chemical manufacturer. Personnel from the US EPA in Cincinnati provided training on the WAR (Waste Reduction) algorithm, which the students used in conjunction with the process simulator to propose modifications to the process in an effort to minimize its environmental impacts.

Pollution Prevention Texts and References

Based on the chemical engineering pollution prevention survey, the most popular textbook for an advanced elective course is the text by Allen and Rosselot[3] titled, "Pollution Prevention for Chemical Processes." Allen and Rosselot start their text by defining pollution prevention as the more efficient use of raw materials and energy and avoiding the use or generation of hazardous materials. They give a short introduction on the legislative history of pollution prevention with emphasis on the Pollution Prevention Act of 1990 (42 13101-13109). In this act the national policy of the US that pollution should be prevented or reduced at the source whenever feasible was placed into law.

The text is divided into three sections that describe macro, meso and micro-scale pollution prevention. In the first section an overview of waste generation is given and the term industrial ecology, coined by Frosch and Gallopoulos[4], and life cycle assessment is introduced. The mesoscale section concentrates on conducting waste audits and emission inventories of plants and examining individual unit operations. Techniques for preventing fugitive and secondary emissions are given and a flowsheet analysis tool is presented which includes an economic analysis. In this section 2 large case studies are presented. The final chapter on microscale pollution prevention is a very brief introduction on reaction pathway analysis which is used to elucidate alternate chemical pathways for producing chemical products.

A large number of the examples described within the text center on decreasing the amount of water used within a process. For example, methods can be employed to minimize water brought into the plant by reusing process water streams from internal unit operations. Allen and Rosselot[3] give an excellent example originally reported by Griffin[5] of the impact of using water in a refinery. As process water is used in the refinery, losses occur in the production of steam, evaporation in the cooling tower, and miscellaneous valves and fittings. In evaporation and boiling the impurities in the process water are concentrated leading to problems with process equipment.

The new text by Mulholland and Dyer[6] gives examples in which pollution prevention not only allows the company to comply with regulations, but it is also financially responsible.[7] Both of these authors are from DuPont's waste reduction team and provide a practical guide for practicing pollution prevention in the chemical process industries. The authors use the classic unit operations approach and show how chemical engineering principles can be used to implement pollution prevention strategies. These authors utilize a problem solving strategy similar to that given by Fogler and LeBlanc[8]. The authors start by defining the process variables and constraints, brainstorm to develop numerous options, search the literature and examine case studies from other industries, and finally decide on a economically viable solution, implement it into the facility, and evaluate the effectiveness.

Pollution prevention educators also mention other books that can be used in a course. For example, Freeman[9] has produced a handbook referenced by many pollution prevention educators. Other general texts include those by Rossiter[10] and Theodore[11], and a new text that is being completed by Paul Bishop at University of Cincinnati. For those courses with an emphasis on mass integration, the text by El-Halwagi[12] is available.

For case studies and pollution prevention problems, one can consider the compilation of problems by Allen[13] titled, "Pollution Prevention: Homework and Design Problems for Engineering Curricula." This 155 page problem set can be ordered from the AIChE for $35 and contains examples involving fugitive and process emissions during cleaning operations, and examples of life cycle assessment are contained within a smaller volume. Other resource texts can be found on National Pollution Prevention Center for Higher Education web site.

There are several recent articles on pollution prevention courses given in the senior and graduate years. For example, Grant et al.[14] describes a senior/graduate elective taught at North Carolina State University that focuses on environmental management, while Simpson and Budd[15] describe a similar course developed at Washington State University. These courses are designed to provide a select set of students that are interested in the environment, an excellent set of tools to tackle problems in pollution prevention. When pollution prevention is taught as an elective course, the majority of students will pass through the curriculum without the knowledge regarding the impact of chemical technology on the environment. To reach all students in the engineering curriculum and satisfy EC2000, aspects of pollution prevention should be introduced in courses throughout the curriculum. Recent advances toward this approach of spreading pollution prevention ideas in the curriculum were most recently presented at an EPA workshop titled, "Green Engineering Educators Workshop," that was held at the 1999 ASEE conference in Charlotte, North Carolina.

Pollution Prevention throughout the Curriculum

As a result of the environmental movement, most universities have instituted environmental courses that can be taken by all university students to fulfill their humanities requirements. These courses typically have titles such as Man and the Environment or Environmental Ethics and have a goal of making students more aware of their actions in a global environment. A recent paper from the Colorado School of Mines by Wiedenhoeft[16], shows how they introduce basic concepts of pollution prevention to freshman students. These courses are valuable and are useful to show students the environmental impact of our lifestyle and give students a technological background for their future courses.

Also in the freshman year many universities have placed topics on environmental issues in freshman engineering courses. A typical method employed is to invite environmental engineers to give a lecture on their profession. These lecture style courses are ineffective, since the students are not actively engaged in the learning process. Active learning processes are vital in the freshman year to engage the students in engineering problem solving. At Rowan University, freshman students investigate commercial household products through reverse engineering. The students are very familiar with products such as coffee machines, computers, and hair dryers, and common household toys, because they have been exposed to these items since birth.

An example given here is with the coffee machine from Hesketh *et al.* [17]. Students conduct experiments at Rowan to competitively assess the operation of a coffee machine. They dissect coffee machines to find out how they work. They discover a large number of individual components that are inside coffee machines including electrical circuit boards,

thermal switches, one-way valves, tubular heaters, silicone tubing. The housing of most coffee machines, and other appliances, is molded polypropylene. Students are then asked to conduct a life cycle assessment of these materials. Extensive use is made of the Kirk-Othmer and McKetta references volumes.

Other freshman engineering programs, such as the one at New Jersey Institute of Technology presented by Golub *et al.*[18], use a case study approach in which students have to site and design a manufacturing facility that either uses or generates hazardous materials. In this example, students are asked to consider pollution prevention strategies in their process plant design. The philosophy is to make a typical senior level design problem accessible to freshman students. In this simple design problem the students are guided into the concepts of pollution prevention in chemical process design. NJIT also uses an aspirin plant siting in the freshman engineering course.

Pollution prevention examples can also be incorporated within the more traditional chemical engineering courses. For example, Rochefort[19] introduces pollution prevention in his material balances course using the Ford Wixom material balances module developed by the Multimedia Engineering Laboratory at the University of Michigan[20] and adds a pollution prevention component in which the "bad actors" are identified.

The chemical engineering departments at the University of Notre Dame, West Virginia University and the University of Nevada at Reno, are implementing through courseware, research and design projects a program on pollution prevention.[21] The overall program includes the development of three new courses: 1) Environmentally Conscious Chemical Process Design, 2) Ecology and the Environment and 3) Environmental, Flows. In addition, they are incorporating research results into instructional modules that are integrated throughout the chemical engineering curriculum, with a special emphasis on the design sequence. Information on the entire project can be found at http://www.nd.edu/~enviro.

In the Green Engineering Educators Workshop, six case studies were presented, as summarized in Table 1. These case studies are designed to be applied in a range of courses from second year chemical engineering principles to senior year plant design. Copies of these materials can be obtained from the U.S. EPA.[22]

Pollution Prevention in Chemical Reaction Engineering Courses

The synthesis of a process design represents a hierarchical decision process, in which the choice of a particular component impacts all other process decisions. The central feature of most chemical processes is the conversion of raw materials into useful products. As a result, the reactor design is one of the central tasks in the synthesis of a chemical process. The selection of design characteristics, *i.e.*, conversion, reaction temperature, use of solvent, etc. dictate many of the remaining process considerations associated with separations and recycle, heat exchange, and use of utilities. Thus, it is appropriate to consider the environmental impacts of a reactor design problem in the context of pollution prevention.[23]

Numerous traditional topics of reaction engineering can be applied to pollution prevention. For example, in a parallel reaction scheme wherein one reaction leads to the desired product, the reaction temperature, the concentration of the reactant, or the reactor type can often be used to control the selectivity. Similarly, the incorporation of a heterogeneous catalyst can

Table 1
Green Engineering Modules in Chemical Engineering Courses

Module	Appropriate Courses
Evaluating Environmental Partitioning and Fate: Approaches based on chemical structure	Plant Design Materials/thermodynamics Mass and energy balances
Estimating emissions and exposures: Case studies from the EPA PreManufacture Notice (PMN) process	Plant Design Industrial chemistry Polymers Electronic materials
Evaluation the Environmental Performance of a Flowsheet	Plant Design Transport Phenomena
Improving the Environmental Performance of Unit Operations and Flowsheets	Plant Design Reactor Design Unit Operations
Environmental Cost Accounting	Plant Design
Life Cycle Assessment	Mass and Energy Balances Freshman level design course

accelerate the rate of reaction or effect the reaction selectivity. Multiphase reactions, and in particular gas-liquid reactions, and the impact of mass transfer on the rate and selectivity also have a significant role in controlling the reactor design. In an elective course on Environmental Reaction Engineering taught several years ago at The University of Toledo, we covered several of these topics. These topics may also be covered in a conventional chemical reactor design course, but it is generally not emphasized to students that waste minimization and pollution prevention are direct results of optimizing reactor performance by minimizing production costs.

Bourne and Gablinger[24] have shown how process chemistry developed in the laboratory can go awry when scaled to industrial reactors. An excellent example of the classic series-parallel reaction using an azo dye chemistry is presented by Bourne and Gholap.[25] The chemist will optimize the reaction to obtain very high reaction rates for the desired reaction. However, in the industrial reactor, micromixing occurs, negatively impacting the process chemistry.[26] However, as explained by Etchells[27] (1998), a typical undergraduate reactor design course focuses on ideal reactors and would overlook the impacts of mixing on the reaction chemistry and the formation of trace byproducts.

The Green Engineering Educators workshop developed a case based on the production of acrylonitrile. In this example, Shonnard[28] illustrates a risk-based approach for reactor optimization based on reactor type, temperature, residence time, mixing, and selectivity. He shows that the mass-based approach gives avenues that minimize HCN generation whereas the risk based approach indicates that the formation of acetonitrile should be minimized. Acetonitrile is about three times more toxic than HCN and the downstream removal rate of acetonitrile is very low. This is an excellent example of optimizing reactor operating

conditions to reduce the production rate of a toxic chemical instead of the classic maximum yield of a desired product.

An additional element of pollution prevention in reaction engineering is the development of new reactor separator configurations. Combined reactor separators may be used in driving a reaction beyond the chemical equilibrium, such that higher conversion can be obtained in a single vessel. An excellent industrial example of this technique has been employed by Eastman Chemical[29], in which they utilize a single reactive distillation unit for the production of methyl acetate. An essentially pure product stream is obtained from acetic acid and methanol feeds, with only water produced as the by-product.

Allen and Rosselot[3] give an example based on the production of MTBE using two routes. The first is the traditional reaction scheme followed by a separation process. The second uses a catalytic distillation tower that drives the equilibrium-limited reaction by separating MTBE from the reactants. Additionally several units are eliminated reducing fugitive emissions and using fewer heat exchangers and process water. A second reactor-separator technology is the membrane reactor, which can be used to selectively remove one of the products from the reactive environment, minimizing the possibility of sequential conversion to undesirable products, or driving the reaction beyond the single-phase equilibrium point. Oyama[30] shows for the reforming of methane using CO_2, that higher yields of CO and H_2 can be achieved in a membrane reactor than possible in a fixed bed, because the H_2 product passes through the membrane. Thus, the reverse reaction cannot occur. The use of the membrane catalyst also provides a feasible route to the production of a pure hydrogen stream, an important element in the future development of fuel cell technology.

A final area in which pollution prevention can be emphasized in the chemical engineering curriculum is the area of green chemistry. Here, one investigates whether a new reaction route can be identified that minimizes the possibility of worker or surrounding environmental exposure? Alternatively, can one of the products be used as a raw material for another feed stream?

As an example, consider the production of phthalic anhydride, used as an additive to PVC to impart flexibility.[31] Phthalic anhydride can be produced from the partial oxidation of either o-xylene or naphthalene. Considering only sources of raw materials, we note that naphthalene is recovered from coal tar, which is a by-product of coking operations used in the steel industry. Napththalene has a lower price than o-xylene but the raw material (obtained from steel-making operations) contains sulfur compounds.[32] Wiedemann and Gierer[33] describe an alternative low energy process for phthalic anhydride production from naphthalene run by Veba Chemie AG. In this process one of the byproducts, maleic acid, is recovered through a scrubbing operation and used to produce maleic anhydride. For each metric ton of phthalic anhydride produced 40 to 50 kg of maleic anhydride can be reclaimed. This example shows how a byproduct can be recovered and sold as high value chemical.

The production of maleic anhydride is a second example in pollution prevention. The predominate feedstock for commercial production is benzene, which is a recognized toxic compound. Unfortunately benzene is still the predominant feedstock outside the US.[34] In addition to the reduced health risks the n-butane route has several economic advantages including, cheaper feedstock and a higher theoretical yield than benzene.[35]

Table 2
Reaction Engineering Case Studies from the Combined Research and Curriculum Development Program[21]

Project	Comments	Contact
New route for production of p-nitroaniline	Eliminates need for chlorine and chlorinated organics	Brennecke
Production of dimethyl carbonate	DMC is a potential oxygenated fuel additive, it can also replace phosgene as raw material. Phosgene is not used as a raw material in this process.	Shaeiwitz
Production of polyurethanes from dimethyl carbonate	Phosgene replaced as raw material	Shaeiwitz

The Combined Research and Curriculum Development program supported by the National Science Foundation provides three examples of alternate process chemistry, summarized in Table 2. In each case, a potentially hazardous starting material or intermediate is eliminated from the reaction process. For example, in the production of p-nitroaniline, the formation of a chlorobenzene intermediate is replaced by a reaction step involving nucleophilic aromatic substitution for hydrogen (NASH). This novel chemistry is now being incorporated into the development plans of Monsanto's Rubber Chemicals Division (now Flexsys America, Inc), and has been cited by the Environmental Protection Agency as a Presidential Green Chemistry Challenge Award recipient in 1998. Several additional examples of green chemistry that have been cited as Award recipients, including

- The development of surfactants to be used in conjunction with supercritical CO_2 as an alternative reaction solvent
- Conversion of glucose into chemical feedstocks using microbial pathways
- Production of lactate esters from carbohydrate feedstocks using selective membrane reactors
- The use of novel non-biological catalysts in the manufacture of pharmaceuticals.

Information about each of these processes can also be found on the EPA web-site (http://www.epa.gov/greenchemistry/presgcc.htm).

Summary

The chemical engineer, as the designer of chemical processes, also has a central role in designing chemical processes that have a minimal impact on the environment. As a result, pollution prevention should be a central component of the chemical engineering curriculum. Within this paper, we have provided several examples of pollution prevention case studies that may be used in courses from the freshman through graduate level. Because of its central

role in the development of the chemical process, reaction engineering and reactor design has an especially strong impact on the environmental acceptability of a chemical process. Thus, specific examples have been given for pollution prevention in chemical reaction engineering. Additional pollution prevention examples are being developed on a regular basis and can be located through one of the web-sites listed in Table 3.

Table 3
Useful Web-sites for pollution prevention information

Site information	Web address
Toxic Release Inventory area, facility or industry searches	http://www.rtk.net/www.data/tri_gen.html
Biennial Reporting System area, facility or industry searches	http://www.rtk.net/www.data/brs_gen.html
National ambient air quality standards	http://ttnwww.rtpnc.epa.gov/naaqspro
University of Michigan's National Pollution Prevention Center Homepage	http://www.snre.umich.edu/nppc
Curriculum materials from the Combined Research Curriculum Development Program of Notre Dame, University of Nevada and West Virginia University (Contains pdf files of their case studies.)	http://www.nd.edu/~enviro
Pollution Prevention web site from Michigan Tech and Univ. of Arizona	http://www.p2workshop.org
EPA's green chemistry web site	http://www.epa.gov/greenchemistry

References

1 Bakshani, Nandkumar, and David T. Allen. "In the States: Pollution Prevention Education at Universities in the United States." Pollution Prevention Review 3, no. 1 (December 1992): 97-105.

2 www.umich.edu/~nppcpub, National Pollution Prevention Center, viewed 9/21/99.

3 Allen, David T., and Kirsten Sinclair Rosselot, *Pollution Prevention for Chemical Processes*. John Wiley & Sons, Inc., New York (1997) ISBN 0-471-11587-8.

4 Frosch, R. A. and N. E. Gallopoulos, "Strategies for manufacturing," *Sci. Am.*, Sept. (1989), 144-152

5 Griffin, D. G., "Feed Water pretreatment to Reduce Process Wastewater," ENV-94-160, National Petroleum Refining Association, Washington, DC., (1994).

6 Mulholland, K. L., and J. A. Dyer, *Pollution Prevention: Methodologies, Technologies, and Practices*, AIChE Press: ISBN 0-8169-0782-X

7 Cooper, C. "Voluntary 'Green' Efforts Pay Off," *Chemical Engineering*, **105**(3) 60 (1998).

8 Fogler, H. S., S. E. LeBlanc, *Strategies for Creative Problem Solving*, Prentice Hall, Englewood Cliffs, NJ, 1995.

9 Freeman, H. M., *Industrial Pollution Prevention Handbook*, McGraw Hill, Inc., New York, NY (1995).

10 Rossiter, Alan P., *Waste Minimization through Process Design*, McGraw Hill, New York (1995).

11 Theodore, Louis, and Young C. McGuinn. *Pollution Prevention.* New York: Van Nostrand Reinhold, 1992.

12 El-Halwagi, M.M. *Pollution Prevention through Process Integration*, Academic Press, New York, (1997).

13 Allen, David T., Nandkumar Bakshani, and Kirsten Sinclair Rosselot. *Pollution Prevention: Homework and Design Problems for Engineering Curricula.* New York: American Institute of Chemical Engineers, American Institute for Pollution Prevention, and Center for Waste Reduction Technologies, 1992.

14 Grant, C.S., M.R. Overcash, and S.P.Beaudoin. "A Graduate Course on Pollution Prevention in Chemical Engineering." *Chemical Engineering Education* **30**(4) 246 (1996).

15 Simpson, J. D., Budd, W.W. "Toward a Preventive Environmental Education Curriculum: The Washington State University Experience", *J. Environ. Educ.*, **27**(2), 18-24 (1996).

16 Wiedenhoeft, Ronald V, "Historic Background for Colorado School of Mine's Nature and Human Values Course" *Proc. Conf. Amer. Soc. Eng. Educ.*, Charlotte, NC (1999).

17 Hesketh, R. P., K. Jahan, A.J. Marchese, C. S. Slater, J. L. Schmalzel, T. R. Chandrupatla, R. A. Dusseau, "Multidisciplinary Experimental Experiences in the Freshman Engineering Clinic at Rowan University," *Proc. Conf. Amer. Soc. Eng. Educ.*, Session 2326 (1997).

18 Golub, E., D. Hanesian, H. Hsieh and A. J. Perna The Siting and Design of a Manufacturing Facility Using Hazardous Materials, *Proc. Conf. Amer. Soc. Eng. Educ.*, Charlotte, NC (1999).

19 Rochefort, W. E., "A Traditional Material Balances Course Sprinkled with "Non-Traditional" Experiences," ASEE 1999 Annual Conference Proceedings, Charlotte, NC. Jun (1999).

20 Montgomery, Susan, Multimedia Education Laboratory, University of Michigan, http://www.engin.umich.edu/labs/mel/meBalances.html, 9/21/99.

21 Brennecke, J. F, Joseph A. Shaeiwitz, Mark A. Stadtherr, Richard Turton, Mark J. McCready, Roger A. Schmitz, and Wallace B. Whiting, "Minimizing Environmental Impact of Chemical Manufacturing Processes," *Proc. Conf. Amer. Soc. Eng. Educ.*, Charlotte, NC. June (1999).

22 Sharon Weil, Green Engineering Program coordinator, USEPA, Chemical Engineering Branch, Washington, D. C. 20460.

23 Smith, R., and E. Petela, "Waste minimization in the Process Industries: Part 2. Reactors," *Chemical Engineer* (London) n 509-510 Dec 12 (1991).

24 Bourne, J.R.; Gablinger, H., "Local pH gradients and the selectivity of fast reactions. II. Comparisons between model and experiments." *Chemical Engineering Science* **44** (6) p 1347-1352 (1989).

25 Bourne, J.R.; Gholap, R.V, "Approximate method for predicting the product distribution of fast reactions in stirred-tank reactors," *Chemical Engineering Journal and Biochemical Engineering Journal* **59**(3) 293-296 (1995)

26 Baldyga, J.; Bourne, J.R.; Hearn, S.J., "Interaction between chemical reactions and mixing on various scales," *Chemical Engineering Science* **52** (4) p 457-466 (1997).

27 Etchells, A., Notes on Mixing in the Process Industries, lecture and short course material, DuPont USA, Wilmington, DE., 1998.

28 Shonnard, D.R. *Unit Operations and Pollution Prevention*, Chapter 9, forthcoming from U.S. EPA, presented at Green Engineering Educators Workshop, Charlotte, NC June (1999).

29 Siirola, J. "Industrial Examples of Process Synthesis and Integration", presented at NSF Workshop on Hybrid Technologies for Waste Minimization, Breckenridge, CO, July 16, 1999.

30 Prabhu, A.K., Radhakrishnan, R., Oyama, S. Ted " Supported nickel catalysts for carbon dioxide reforming of methane in plug flow and membrane reactors" *Appl. Catal. A: General* **183** (1999) 241-252.

31 Hesketh, R. P., "Incorporating Reactor Design Projects into the course," Group 4a, 1999 AIChE Annual Meeting, Dallas, TX, Nov, 1999.

32 Dengler, H. P. "Phthalic Anhydride," in Encyclopedia of Chemical Processing and Design, executive editor, John J. McKetta, associate editor, William A. Cunningham. New York, M. Dekker, c1976.

33 Wiedemann, and W. Gierer, "Phthalic anhydride made with less energy," *Chemical Engineering*, 29 Jan 1979 p. 62.

34 Cooley, S. D. and J. D. Powers, "Maleic Acid and Anhydride," in Encyclopedia of Chemical Processing and Design, executive editor, John J. McKetta, associate editor, William A. Cunningham. New York, M. Dekker, c1976.

35 Robinson, W. D., and R. A. Mount, "Maleic Anhydride, Maleic and Fumaric Acid," Kirk-Othmer Encyclopedia of Chemical Technology. editorial board, Herman F. Mark .et al. ; executive editor, Martin Grayson, associate editor, David Eckroth. 4th ed. New York, Wiley, c1991.